Nanorobotics

Constantinos Mavroidis • Antoine Ferreira
Editors

Nanorobotics

Current Approaches and Techniques

Springer

Editors
Constantinos Mavroidis
Department of Mechanical
and Industrial Engineering
Northeastern University
Boston, MA, USA

Antoine Ferreira
Laboratoire PRISME
Ecole Nationale Supérieure
d'Ingénieurs de Bourges
Bourges, France

ISBN 978-1-4614-2118-4 ISBN 978-1-4614-2119-1 (eBook)
DOI 10.1007/978-1-4614-2119-1
Springer New York Heidelberg Dordrecht London

Library of Congress Control Number: 2012952154

© Springer Science+Business Media New York 2013
This work is subject to copyright. All rights are reserved by the Publisher, whether the whole or part of the material is concerned, specifically the rights of translation, reprinting, reuse of illustrations, recitation, broadcasting, reproduction on microfilms or in any other physical way, and transmission or information storage and retrieval, electronic adaptation, computer software, or by similar or dissimilar methodology now known or hereafter developed. Exempted from this legal reservation are brief excerpts in connection with reviews or scholarly analysis or material supplied specifically for the purpose of being entered and executed on a computer system, for exclusive use by the purchaser of the work. Duplication of this publication or parts thereof is permitted only under the provisions of the Copyright Law of the Publisher's location, in its current version, and permission for use must always be obtained from Springer. Permissions for use may be obtained through RightsLink at the Copyright Clearance Center. Violations are liable to prosecution under the respective Copyright Law.
The use of general descriptive names, registered names, trademarks, service marks, etc. in this publication does not imply, even in the absence of a specific statement, that such names are exempt from the relevant protective laws and regulations and therefore free for general use.
While the advice and information in this book are believed to be true and accurate at the date of publication, neither the authors nor the editors nor the publisher can accept any legal responsibility for any errors or omissions that may be made. The publisher makes no warranty, express or implied, with respect to the material contained herein.

Printed on acid-free paper

Springer is part of Springer Science+Business Media (www.springer.com)

Preface

Nanorobotics is an emerging interdisciplinary technology area raising new scientific challenges and promising revolutionary advancements in applications such as medicine, biology, and industrial manufacturing. Nanorobots could be defined as intelligent systems with overall dimensions at or below the micrometer range that are made of assemblies of nanoscale components with individual dimensions ranging between 1 and 100nm. Nanorobots would be able to perform at least one of the following actions: actuation, sensing, signaling, information processing, intelligence, swarm behavior at the nanoscale. In an effort to disseminate the current advances in nanorobotics, and to stimulate a discussion on future research directions in this field, this book addresses the current state of the art and the growing interest of the robotics community. The editors believe that this book can invigorate new research interests in the development of nanorobotic systems and their use in different applications. The various chapters demonstrate that the area of nanorobotics can attract multidisciplinary teams of researchers, assembling skills and expertise from different disciplines, such as biology, robotics, engineering, medicine, nanotechnology, chemistry, and computer science.

The present book "*Nanorobotics: Current Approaches and Techniques*" is a collection of 21 excellent chapters that represent the large variety and high quality of nanorobotics research in terms of robot design and fabrication, actuation and sensing, manipulation, and control at the nanoscale. The editors have classified the authors' contributions into five main application domains. The volume begins with a part of six chapters introducing the vision and applications of nanorobotics. These chapters provide an overview of the state-of-the-art methodology and the foreseen applications of nanorobotics, such as space, environmental, biological, or medical applications. The next four parts are focusing on the various types of nanorobotic systems and their applications.

Section 2, "Nanomanipulation and Industrial Nanorobotics," collects three chapters addressing the problem of robotic manipulation at the nanoscale for industrial processes. These chapters are relevant to industrial nanorobotics (or otherwise called nanomanipulators) that can be used in the fabrication, manipulation, control, and assembly at the nanoscale. Techniques of nanomanipulation of 1D and 2D

nanomaterials through an imaging atomic force microscope (AFM) device or a scanning electron microscope (SEM) device are presented. Finally, mass transport at attogram (10^{-18}g) level using carbon nanotubes is introduced for the manipulation and assembly tasks in nanofluidics.

Section 3, "Nanomanipulation in Biomedical Applications," addresses the increasing interest in handling, understanding, and integrating biological systems, important to the fields of biomedicine, process industry, pharmacy, and biomaterial research. Three chapters demonstrate the nanomanipulation and nanohandling capabilities of nanorobots in a wide variety of biological materials such as cells, viruses, proteins, DNA, and RNA. Techniques related to noncontact manipulation (including fluidic force, magnetic force, electrical force, and optical tweezers) and contact manipulation (atomic force microscope probes, nano-grippers) are presented.

Section 4, "Inside the Body Nanorobotic Applications," describes different technologies for developing nanorobotic drug carriers including nanotubes, nanowires, nanoparticles, or biological bacteria. A major issue is the powering and steering control of these untethered devices in order to allow in vivo interaction with the human body. Three chapters describe wireless magnetic control of nano-drug delivery systems and, in particular, the generation of the required magnetic fields in dedicated magnetic setups or magnetic resonance imagery (MRI) systems. The advantages and limitations of both synthetic relying on magnetism and bacterial carriers relying on a self-propelling flagellated system are described and the advantages of combining both approaches for navigation in the vascular network are demonstrated. Finally, two other chapters describe the sensing strategies for early diagnosis of cancer by using different visual modalities.

Section 5, "Bio-Nano Actuators for Nanorobotics," presents bio-inspired mechanisms, actuators, sensors, and systems using biological elements. Four chapters expose the recent advances in protein, bacterial flagellar, and DNA-based nanorobotic systems.

It is difficult to cast a vision for the future of this newly sprung field. We hope that such ventures will be facilitated by this volume. We would like to express our gratitude to the authors for providing excellent contributions and descriptive illustrations. We would also like to acknowledge the tremendous efforts of the reviewers to complete this task on time. Finally, we would like to thank Alison Waldron, Senior Editor, and Merry Stuber, Editorial Assistant of Springer, for their enthusiastic support for this book, their continuous patience, and their skillful handling of technical issues related to publication of this book.

Boston, MA, USA — Constantinos Mavroidis
Bourges, France — Antoine Ferreira

Contents

Part I Nanorobotics: The Vision and Applications

1 Nanorobotics: Past, Present, and Future 3
Constantinos Mavroidis and Antoine Ferreira

2 Nanomechanical Cantilever-Based Manipulation for Sensing and Imaging 29
Nader Jalili

3 Swarms of Self-Organized Nanorobots 41
Ari Requicha

4 Reservoir Nanoagents for In-Situ Sensing and Intervention 51
Mazen Y. Kanj

5 Miniaturization and Micro/Nanotechnology in Space Robotics 69
Evangelos Papadopoulos, Iosif Paraskevas, and Thaleia Flessa

6 Diamondoid Nanorobotics 93
Robert A. Freitas Jr.

Part II Nano-Manipulation and Industrial Nanorobotics

7 Virtual Tooling for Nanoassembly and Nanomanipulations 115
Zhidong Wang, Lianqing Liu, Jing Huo, Zhiyu Wang, Ning Xi, and Zaili Dong

8 Nanorobotic Mass Transport 137
Lixin Dong, Xinyong Tao, Zheng Fan, Li Zhang, Xiaobin Zhang, Bradley J. Nelson, Mustapha Hamdi, and Antoine Ferreira

9 Nanorobotic Manipulation of 1D Nanomaterials in Scanning Electron Microscopes 155
Yan Liang Zhang, Yong Zhang, Changhai Ru, Jason Li, and Yu Sun

Part III Nano-Manipulation in Biomedical Applications

10 Nanorobotic Manipulation and Sensing for Biomedical Applications 169
Fumihito Arai and Hisataka Maruyama

11 Nanohandling of Biomaterials 191
Michael Weigel-Jech and Sergej Fatikow

12 Apply Robot-Tweezers Manipulation to Cell Stretching for Biomechanical Characterization 223
Youhua Tan and Dong Sun

Part IV Inside the Body Nanorobotic Applications

13 Propulsion and Navigation Control of MRI-Guided Drug Delivery Nanorobots 243
Laurent Arcese, Matthieu Fruchard, and Antoine Ferreira

14 Generating Magnetic Fields for Controlling Nanorobots in Medical Applications 275
Simone Schürle, Bradley E. Kratochvil, Salvador Pané, Mohammad Arif Zeeshan, and Bradley J. Nelson

15 Techniques for MRI-Based Nanorobotics 301
Christian Dahmen, Tim Wortmann, and Sergej Fatikow

16 Therapeutic Bacterial Nanorobots for Targeted Drug Delivery Deep Inside Tumors 323
Sylvain Martel

17 Sensing Strategies for Early Diagnosis of Cancer by Swarm of Nanorobots: An Evidential Paradigm 331
G. F. Cerofolini and P. Amato

Part V Bio-Nano Actuators for Nanorobotics

18 DNA Nanorobotics 355
Harish Chandran, Nikhil Gopalkrishnan, and John Reif

19 DNA for Self-Assembly 383
Ahlem Abbaci and Stéphane Régnier

20 Local Environmental Control Technique for Bacterial Flagellar Motor 411
Toshio Fukuda, Kousuke Nogawa, Masaru Kojima, Masahiro Nakajima, and Michio Homma

21 Protein-Based Nanoscale Actuation 425
Gaurav Sharma, Atul Dubey, and Constantinos Mavroidis

Index 457

Contributors

Ahlem Abbaci Université Pierre et Marie Curie, Paris cedex 05, France

Paolo Amato Department of Informatics, Systems and Communication (DISCo), University of Milano-Bicocca, Milano, Italy

Fumihito Arai Department of Micro-Nano Systems Engineering, Nagoya University, Furo-cho, Chikusa-ku, Nagoya, Japan

Department of Mechanical Science and Engineering, Nagoya University, Furo-cho, Chikusa-ku, Nagoya, Japan

Laurent Arcese Laboratoire PRISME, University of Orleans, Bourges, France

Gianfranco Cerofolini Department of Materials Science, University of Milano-Bicocca, Milano, Italy

Harish Chandran Department of Computer Science, Duke University, Durham, NC, USA

Christian Dahmen Division Microrobotics and Control Engineering (AMiR), University of Oldenburg, Oldenburg, Germany

Lixin Dong Department of Electrical and Computer Engineering, Michigan State University, East Lansing, MI, USA

Zaili Dong State Key Laboratory of Robotics, Shenyang Institute of Automation, Chinese Academy of Sciences, Shenyang, China

Atul Dubey Department of Chemical and Biochemical Engineering, Rutgers University, Piscataway, NJ, USA

Zheng Fan Department of Electrical and Computer Engineering, Michigan State University, East Lansing, MI, USA

Sergej Fatikow Division Microrobotics and Control Engineering (AMiR), University of Oldenburg, Oldenburg, Germany

Antoine Ferreira Laboratoire PRISME, Ecole Nationale Supérieure d'Ingénieurs de Bourges, Bourges, France

Thaleia Flessa Department of Mechanical Engineering, National Technical University of Athens, Athens, Greece

Robert A. Freitas Institute for Molecular Manufacturing, Palo Alto, CA, USA

Pilot Hill, CA, USA

Matthieu Fruchard Laboratoire PRISME, University of Orleans, Bourges, France

Toshio Fukuda Department of Micro-Nano Systems Engineering, Nagoya University, Furo-cho, Chikusa-ku, Nagoya, Japan

Nikhil Gopalkrishnan Department of Computer Science, Duke University, Durham, NC, USA

Mustapha Hamdi Ecole Nationale Supérieure d'Ingénieurs, Laboratoire PRISME, de Bourges, Bourges, France

Michio Homma Division of Biological Science, Nagoya University, Furo-cho, Chikusa-ku, Nagoya, Japan

Jing Hou College of Information Science and Engineering, Northeastern University, Shenyang, China

Nader Jalili Department of Mechanical and Industrial Engineering, Northeastern University, Boston, MA, USA

Mazen Y. Kanj Saudi Aramco, Dhahran, KSA

Masaru Kojima Department of Systems Innovation, Osaka University, Machikaneyama-cho, Osaka, Japan

Bradley K. Kratochvil Institute of Robotics and Intelligent Systems, ETH Zurich, Zürich, Switzerland

Jason Li Department of Mechanical and Industrial Engineering, University of Toronto, Toronto, ON, Canada

Lianqing Liu State Key Laboratory of Robotics, Shenyang Institute of Automation, Chinese Academy of Sciences, Shenyang, China

Sylvain Martel Department of Computer and Software Engineering, Institute of Biomedical Engineering, École Polytechnique de Montréal (EPM), Montréal, QC, Canada

Hisataka Maruyama Department of Micro-Nano Systems Engineering, Nagoya University, Furo-cho, Chikusa-ku, Nagoya, Japan

Constantinos Mavroidis Department of Mechanical and Industrial Engineering, Northeastern University, Boston, MA, USA

Masahiro Nakajima Center For Micro-nano Mechatronics, Nagoya University, Furo-cho, Chikusa-ku, Nagoya, Japan

Bradley J. Nelson Institute of Robotics and Intelligent Systems, ETH Zurich, Zürich, Switzerland

Kousuke Nogawa Department of Micro-Nano Systems Engineering, Nagoya University, Furo-cho, Chikusa-ku, Nagoya, Japan

Salvador Pané Institute of Robotics and Intelligent Systems, ETH Zurich, Zürich, Switzerland

Evangelos Papadopoulos Department of Mechanical Engineering, National Technical University of Athens, Athens, Greece

Iosif Paraskevas Department of Mechanical Engineering, National Technical University of Athens, Athens, Greece

Stéphane Régnier Institut des Systémes Intelligents et Robotique, Université Pierre et Marie Curie, Paris Cedex 05, France

John Reif Department of Computer Science, Duke University, Durham, NC, USA

Ari Requicha Department of Computer Science, University of Southern California, Los Angeles, CA, USA

Changhai Ru Robotics and Microsystems Center, Soochow University, Suzhou, China

Simone Schürle Institute of Robotics and Intelligent Systems, ETH Zurich, Zürich, Switzerland

Gaurav Sharma Battelle Memorial Institute, Columbus, OH, USA

Dong Sun Department of Mechanical and Biomedical Engineering, City University of Hong Kong, Kowloon, Hong Kong, China

Yu Sun Department of Mechanical and Industrial Engineering, University of Toronto, Toronto, ON, Canada

Xinyong Tao College of Chemical Engineering and Materials Science, Zhejiang University of Technology, Hangzhou, China

Youhua Tan Department of Mechanical and Biomedical Engineering, City University of Hong Kong, Kowloon, Hong Kong, China

Zhidong Wang Department of Advanced Robotics, Chiba Institute of Technology, Narashino, Chiba, Japan

Zhiyu Wang State Key Laboratory of Robotics, Shenyang Institute of Automation, Chinese Academy of Sciences, Shenyang, China

Michael Weigel-Jech Division Microrobotics and Control Engineering (AMiR), University of Oldenburg, Oldenburg, Germany

Tim Wortmann Division Microrobotics and Control Engineering (AMiR), University of Oldenburg, Oldenburg, Germany

Ning Xi Department of Electrical and Computer Engineering, Michigan State University, East Lansing, MI, USA

Arif M. Zeeshan Institute of Robotics and Intelligent Systems, ETH Zurich, Zürich, Switzerland

Li Zhang Department of Mechanical and Automation Engineering, The Chinese University of Hong Kong, Hong Kong SAR, China

Yan Liang Zhang Department of Mechanical and Industrial Engineering, University of Toronto, Toronto, ON, Canada

Yong Zhang Department of Mechanical and Industrial Engineering, University of Toronto, Toronto, ON, Canada

Xiaobin Zhang Department of Materials Science and Engineering, Zhejiang University, Hangzhou, China

Part I
Nanorobotics: The Vision and Applications

Chapter 1
Nanorobotics: Past, Present, and Future

Constantinos Mavroidis and Antoine Ferreira

Abstract This chapter focuses on the state of the art in the field of nanorobotics by presenting a brief historical overview, the various types of nanorobotic systems, their applications, and future directions in this field. Nanorobots are basically any type of active structure capable of any one of the following (or any of their combination): actuation, sensing, manipulation, propulsion, signaling, information processing, intelligence, and swarm behavior at the nanoscale (10^{-9} m). The following four types of nanorobotic systems have been developed and studied so far (a) large size nanomanipulators with nanoscale manipulation capability; (b) protein- and DNA-based bionanorobotic systems; (c) magnetically guided nanorobotic systems; and (d) bacterial-based nanorobotics. Nanorobotic systems are expected to be used in many different areas that range from medical to environmental sensing to space and military applications. From precise drug delivery to repairing cells and fighting tumor cells, nanorobots are expected to revolutionize the medical industry in the future.

1.1 Overview and Brief History of Nanorobotics

Robotic devices able to perform tasks at the nanoscale (i.e., scale of a nanometer) are called "***NanoRobots***." A nanometer is a billionth of a meter, that is, about 1/80,000 of the diameter of a human hair, or ten times the diameter of a hydrogen atom.

C. Mavroidis (✉)
Department of Mechanical and Industrial Engineering, 334 Snell Engineering Center, Northeastern University, 360 Huntington Avenue, Boston, MA 02115, USA
e-mail: mavro@coe.neu.edu

A. Ferreira
Laboratoire PRISME, Ecole Nationale Supérieure d'Ingénieurs de Bourges, 88 Boulevard Lahitolle, 18000 Bourges, France
e-mail: antoine.ferreira@ensi-bourges.fr

C. Mavroidis and A. Ferreira (eds.), *Nanorobotics*, DOI 10.1007/978-1-4614-2119-1_1,
© Springer Science+Business Media New York 2013

The size-related challenge is the ability to measure, manipulate, and assemble matter with features on the scale of 1–100 nm. The field of nanorobotics studies the design, manufacturing, programming, and control of nanorobotic systems. Nanorobots are also referred to as ***nanobots*** or ***nanites*** by some enthusiasts of the field, although these terms do not accurately represent the engineering aspects of the system.

Nanorobotics is a relatively new field that grew out of the merging of robotics and nanotechnology during the late 1990s and early 2000s. This came as a natural evolution of the microrobotics field that grew rapidly in the 1990s and of the nanotechnology field that exploded in the 2000s. The term *NanoRobot* started being used by the robotics community in the late 1990s. Some of the earliest appearances of the term occur (a) in 1998 in the paper by Requicha et al. that focused on *NanoRobotic Assembly* [1]; (b) in Sitti and Hashimoto's paper on *Tele-Nanorobotics* [2]; and (c) in 1999 in Freitas' book on *NanoMedicine* where one can find a nice historical presentation of the nanorobotic concept for medical applications [3]. Prior to 1998 we rarely meet the term nanorobot although the concept of a nanorobot has been clearly described by several researchers and was referred to as "molecular machine" or "nanomachine" or "cell repair machine" [4, 5].

Two of the pioneers in the nanorobotics field are Eric K. Drexler and Robert A. Freitas. Drexler described the concept of molecular machinery and molecular manufacturing [6–8] while Freitas developed in great detail the concept of medical nanorobotics [3, 9, 10]. Prior to late 1990s the limited amount of scientific work on nanorobotics was mostly focused on concept generation, design, and modeling. Thorough computational and experimental studies on nanorobotics started being published only after the late 1990s. Nowadays, the nanorobotics field keeps expanding and many laboratories around the world are focusing their activities on this topic.

As with the robotics field, nanorobotics became known to the large audience through science fiction movies, TV series, and books. For example, Isaac Asimov in his 1966 book "Fantastic Voyage" (following the completion of the science fiction movie with the same name at the same year) described a miniscule submarine able to travel through the human bloodstream [11] while Michael Crighton in 2002 in his popular book "Prey" introduced a swarm of intelligent nanorobots that threaten humankind [12]. Although the nanorobotic concept being described in these fiction stories is far from being close to what a nanorobot is or will be for the scientific community, it helped generate public interest in this topic which is very important for the future growth of the field.

The term *NanoRobot* is being used by the scientific community in the broadest possible way. This term basically includes any type of active structure capable of anyone of the following (or any of their combination): actuation, sensing, manipulation, propulsion, signaling, information processing, intelligence, and swarm behavior at the nanoscale. For example, the term nanorobot includes large-scale manipulators with nanoscale precision accuracy and manipulation capabilities and microscale robotic devices with at least one nanoscale component [13]. It also includes molecular machines that are based on biological entities such as

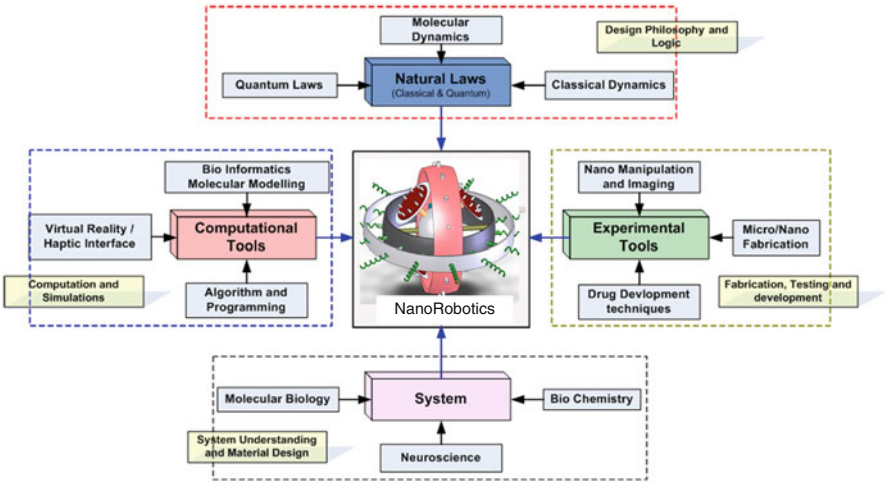

Fig. 1.1 Nanorobotics—a multidisciplinary field

proteins and DNA [14] and magnetic nanoparticles that can be guided by an external magnetic field [15].

In addition to the capabilities described above, in the future it is desirable that nanorobots have the following unique characteristic abilities associated with their nanoscale size and their presence in large numbers in a remote environment:

1. *Swarm intelligence* ([16, 17], Chaps. 3 and 17 of this book).
2. *Self-assembly and replication*—assemblage at the nanoscale and "*nanomaintenance*" [18, 19].
3. Nano- to macro-world *interface architecture*—an architecture enabling instant access to the nanorobots and its control and maintenance including haptics and virtual reality [20].

Nanorobotics is a field which calls for collaborative efforts between physicists, chemists, biologists, computer scientists, engineers, and other specialists to work towards this common objective as shown in Fig. 1.1 (this is just a representative figure and not exhaustive in nature).

Fully functional, autonomous nanorobots with completely artificial nanocomponents have not been realized yet. This is an open problem for the nanorobotics community that could easily be characterized as the "***Mount Everest of Nanorobotics***" paraphrasing Ferdinand Freudenstein who characterized in a similar way some important open kinematic problems of his time [21]. So far the nanorobotics community was able to develop large-scale manipulators with nanoscale precision and manipulation capability called nanomanipulators. The community was also able to demonstrate experimentally the development of several nanocomponents such as various types of nanostructures, nanosensors, nanomotors, nanocomputers, etc. that eventually could be used in the assembly of nanorobots. Finally, simple

nanorobots based on molecular machines and nanoparticles have also been developed and successfully tested. We believe that the time is right to try to assemble the first ever fully functional and autonomous nanorobot.

1.2 Types of NanoRobotic Systems

In this section, we present the various types of nanorobotic devices that have been developed so far by scientists and engineers. These nanorobotic types are very different than the science fiction concept of nanorobots that are usually presented as nano-bugs as shown in Fig. 1.2 or such as the nanobots described in [22].

1.2.1 NanoManipulators

The first nanorobotic systems were not "nano" at all. Instead, they were large manipulator-like structures that had the capability of nanopositioning. The robotics community was not the first to get involved in the nanomanipulation field but was preceded and got inspired by the work of their colleagues from the physics and chemistry fields that used ***scanning probe microscopes*** (SPM) such as ***scanning tunneling microscopes*** (STM) and ***atomic force microscopes*** (AFM) to nanomanipulate atoms and molecules [23]. The first example of atom nanomanipulation using

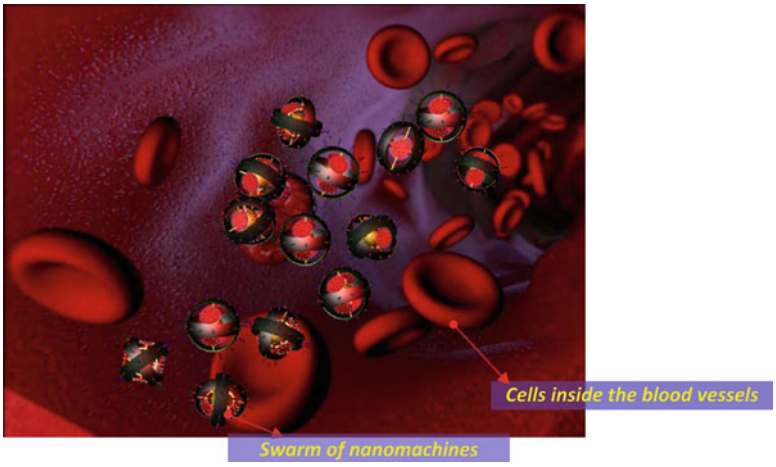

Fig. 1.2 Fictional concept of swarms of nanorobots inside the blood vessels. These nanomachines would detect and treat the effected cells. They would also deliver the targeted drug to the specific cells

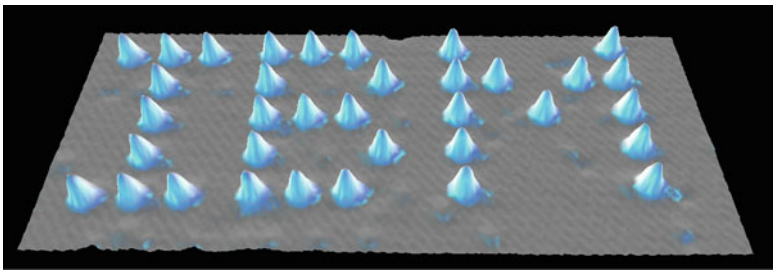

Fig. 1.3 STM manipulated zenon atoms form the word IBM [24] (image originally created by IBM Corporation, STM Image Gallery, http://www.almaden.ibm.com/vis/stm/library.html)

an STM was performed by Eigler and Schweizer in [24] where they nanopositioned 35 Zenon atoms to write the name of IBM, their employer (see Fig. 1.3).

As Requicha points out in one of the first reviews published on nanomanipulation from the robotics community in 1999 [25] initially a SPM is like a three degree-of-freedom (DOF) robotic manipulator, having x–y–z positioning capability at its tip but with no orientation capability. The manipulation capability of a SPM is based on the inter-atomic forces developed between the SPM's tip and the atoms to be manipulated. The SPM's tip serves as the manipulator end-effector and is the main nanocomponent of the nanomanipulator. At that time, there was no possibility for direct feedback for the SPM's tip positioning while the task is performed so the SPM played a dual role of manipulator and sensor at the nanoscale. Requicha in his prophetic review of 1999 describes a number of research topics that should be studied by the robotics community to improve the state of the art of nanomanipulation. For example, Requicha describes the needs for (a) developing 6 DOF nanomanipulators; (b) providing real-time feedback from the task space while the nanomanipulator is performing the task; (c) developing nanogrippers; (d) performing nanomanipulation tasks in liquid environments; (e) enhancing SPM's performance by the development of clever nanomanipulation strategies; (f) coupling of SPM manipulation with self-assembly properties for building nanostructures, etc. Since then, all these topics have been studied thoroughly by the robotics community in the context of nanomanipulation.

As the robotics community was getting more and more involved in the nanomanipulation field, we have observed the development of new nanorobotic manipulation systems that presented more capabilities, similar to those that are met in industrial manipulators. These new systems that are called nanorobotic manipulators (NRM) present higher number of DOFs at their end-effectors, higher end-effector dexterity, higher positioning accuracy, and higher end-effector tool possibilities. To increase positioning accuracy of the NRM and to improve the efficiency of its control and planning algorithms, NRMs were placed inside electron microscopes, such as scanning electron microscopes (SEMs) and transmission electron microscopes (TEMs). One of the first multi-degree-of-freedom NRMs was developed by

Fig. 1.4 DCG Systems' nProber Solution (http://www.dcgsystems.com). Eight probe nanomanipulator encoded positioners may be placed with 2nm resolution probe steps. The XYZ encoded center stage provides step and repeat capability, while allowing the probes to remain in registration while the sample is moved to the next bit (published with permission from DCG Systems, Inc., http://www.dcgsystems.com)

Dong, Arai, and Fukuda in 2001 where they demonstrated successful operation of a 10-DOF NRM system [26]. They then developed a 16-DOF NRM system [27] equipped with a SEM for real-time imaging of the manipulation task and a nanofabrication system based on electron-beam-induced deposition [28].

Nowadays, multi-DOF NRM systems are commercially available. Examples are the DCG Systems NanoManipulators (formerly the Zyvex NanoManipulators; http://www.dcgsystems.com/product.line.NI.html) shown in Fig. 1.4 and the Klocke Nanotechnik nanorobotic systems (http://www.nanomotor.de/m_nanorobotics.htm).

During the last 10 years, there have been several review papers that covered in great detail the subjects of *NanoManipulation* and *NanoRobotic Manipulators* [13, 29–31] including Chaps. 2, 7–12 of this book. The reader is referred to these papers and chapters for further information on this topic.

1.2.2 *BioNanorobotics (DNA- and Protein-Based NanoRobotic Systems)*

During the same period that nanorobotic manipulators were developed and studied, a second type of nanorobotic system, that of ***BioNanorobotics***, appeared and grew independently of the first. The term bionanorobotics, that was first introduced in 2003 [32, 33], denotes all nanorobotic systems that include nanocomponents that are based on biological elements such as proteins and DNA. Bionanorobotic systems are different than medical nanorobots in that even though bionanorobotic systems include components based on biological elements they may not be used in medical applications. Bionanorobotics is a subset of a more general field that of molecular machines and machine components that grew rapidly during the last decades [34].

The main goal in the field of bionanorobotics is to use various biological elements—whose function at the cellular level creates motion, force, or a signal—as nanorobotic components. These components perform their preprogrammed biological function in response to the specific physiochemical stimuli but in an artificial setting. In this way, proteins and DNA could act as motors, mechanical joints, transmission elements, or sensors. If all these different components were assembled together in the proper proportion and orientation they would form nanorobotic devices with multiple degrees of freedom, able to apply forces and manipulate objects in the nanoscale world. The advantage of using nature's machine components is that they are highly efficient and reliable. Just as conventional macrorobotic systems are used to generate forces and motions to accomplish specific tasks, bionanorobots could be used to manipulate nano-objects; to assemble and fabricate other machines or products; to perform maintenance, repair, and inspection operations. Figure 1.5 shows one such concept of a bionanorobot, with its "feet" made of helical peptides and its body using carbon nanotubes while the power unit is a biomolecular motor.

A plethora of molecular machines and machine components that could be used in nanorobotics has already been developed by scientists coming from the fields of physics, chemistry, biology, chemical and biomedical engineering [14, 19, 34]. Some very well-known examples are (a) the work of Ned Seeman's group in DNA-based nanomachine components including the development of a DNA bipedal walking device [35]; (b) the work of Carlo Montemagno's group that developed several protein-based nanomotors that rely on an energy-rich molecule known as adenosine triphosphate (ATP) [36, 37]; (c) Yurke et al. DNA-based nanotweezers [38]; and (d) the recent DNA-based nanorobot, shown in Fig. 1.6, for payload transport and delivery to cells by George Church's group [39]. Although these bionanorobots and components are important scientific achievements, all of them are lacking one major factor: the robotics science and engineering in their design, fabrication, control, and planning.

In an effort to bridge the gap between physicists, chemists, and biologists developing bionanorobotic systems and components on one side and the robotics community on the other, Dinos Mavroidis' group in US and Antoine Ferreira's group

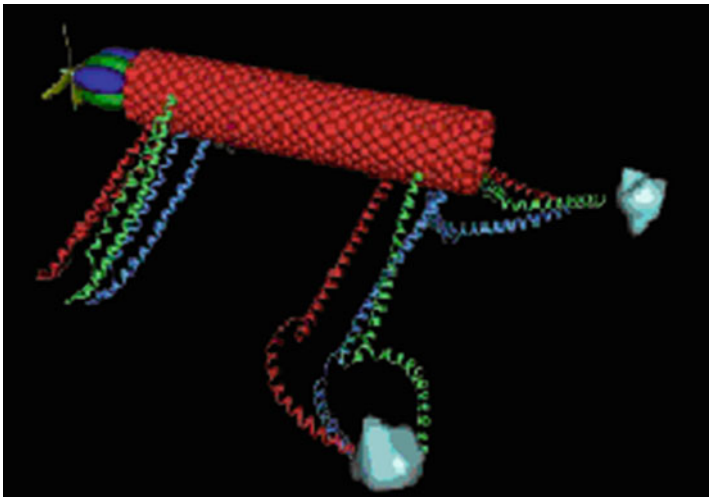

Fig. 1.5 Biological elements will be used to fabricate robotic systems. A vision of a bio-nanorobotic organism: carbon nanotubes form the main body; peptide limbs can be used for locomotion and object manipulation; a biomolecular motor located at the head can propel the device in various environments

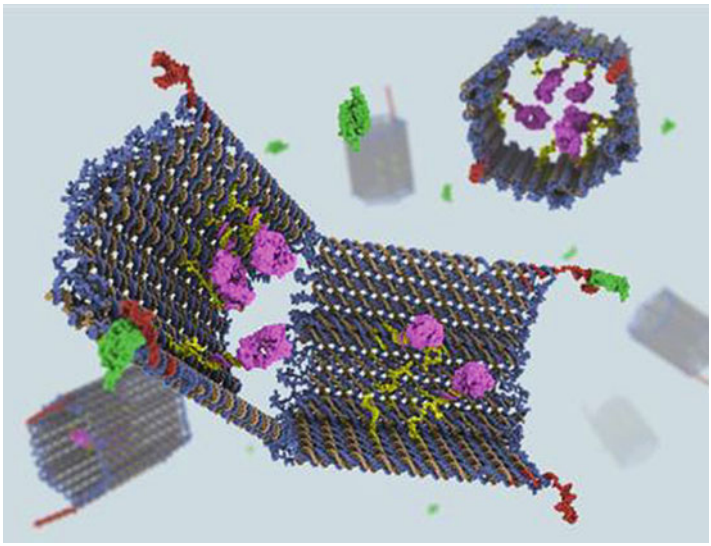

Fig. 1.6 CAD drawing of DNA nanorobots carrying protein-based payloads for targeted drug delivery [39] (published with permission from George Church)

in France proposed several new bionanorobots based on a bottom-up approach inspired by equivalent approaches in the macro-robotics field [40]. The Mavroidis' group focused on two different protein-based nanomotors: (a) a viral-based linear

nanomotor called VPL [41] and (b) a protein-based nanogripper [42–44]. For the latter experimental validation was presented in [45]. More details about these two protein-based nanomotors could be found in Chap. 21 of this book. Ferreira's group focused more on the design, modeling, and virtual reality problems of bionanorobotic systems [46–49].

To complete successfully the activities described above, virtual prototyping tools based on molecular dynamics (MD) simulators had to be developed in order to understand the protein molecular mechanics and to develop dynamic and kinematic models to study the bionano-system performance and control aspects. The ability to visualize the atom-to-atom interaction in real time and observe the results in a fully immersive 3D environment was an additional feature of such simulations [46–49]. Virtual reality (VR) technology was applied in these MD simulators, which not only provided immersive visualization but also gave an added functionality of CAD-based design, simulation, navigation, and interactive manipulation of molecular biological components. The simulation system shown in Fig. 1.7 allows manipulation, connection, and assembly of bio-nanorobotic components in molecular dynamic simulations using real-time VR devices such as stereo glasses, 3D trackers, force-feedback devices, and 3D graphical display.

Research in the field of bionanorobotic system continues. However, it is clear that there is still a lot more that needs to be done in order to bring together the two scientific communities involved with the development of bionanorobotics. Additional information about this topic could be found in Chaps. 18, 19, and 21 of this book and in [50].

1.2.3 Magnetically Guided NanoRobotic Systems

The third type of nanorobotic system developed so far is much simpler than the previous two types but closer to the concept of a full nanoscale robotic system as the one shown in Fig. 1.2 in the sense that its dimensions are at the nanoscale and it is composed of artificial nanocomponents. This nanorobot is basically a simple nanoparticle comprising a ferromagnetic material. The obvious question of course is, "how can a nanoparticle be considered as a nanorobot?" The answer to this is that all components and functions that constitute a robotic system have been moved outside of the robot structure. Actuation and propulsion could be achieved using an external magnetic field and its gradients that could apply a six degree-of-freedom magnetic force on the nanoparticle(s) (see Fig. 1.8). Sensing and tracking of the nanoparticle motion could be done using external imaging modalities such as microscopes or magnetic resonance imaging (MRI) scanners (see Fig. 1.8). Once the actuation and sensing has been achieved using the external magnetic field and imaging modalities then it is possible to implement a closed loop control algorithm as shown in Fig. 1.8 that will guide the nanoparticle/nanorobot at the desired location. A nice literature review on this topic can be found in [51].

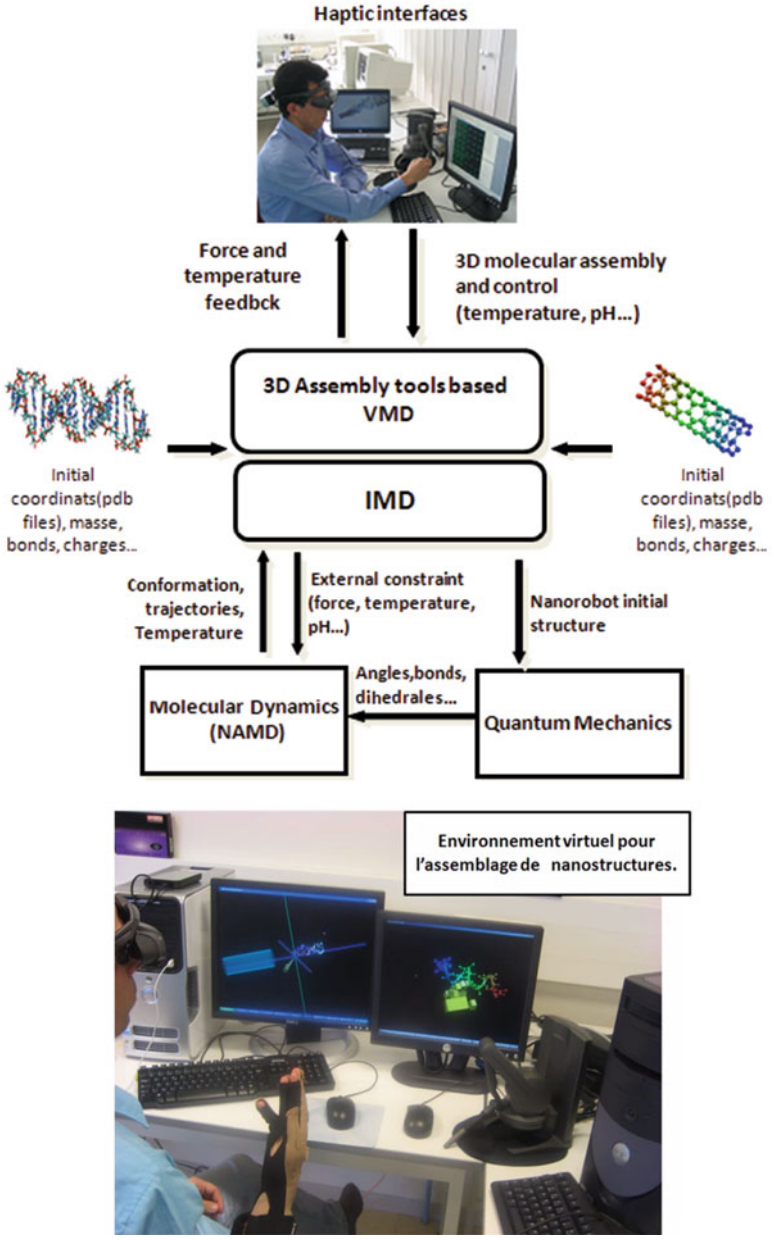

Fig. 1.7 *Top*: Basic concept of virtual environment and haptics technology coupled to multi-physics computational methods for drug delivery nanovector simulation. *Bottom*: Experimental interactive simulation platform using virtual reality interfaces. In the virtual molecular dynamics (VMD) environment, the user applies forces to simulated bio-nanorobotic structures via a force-feedback haptic interface while manipulation is performed through a virtual hand. The headtracker is mounted on a pair of shutter glasses for operator immersion

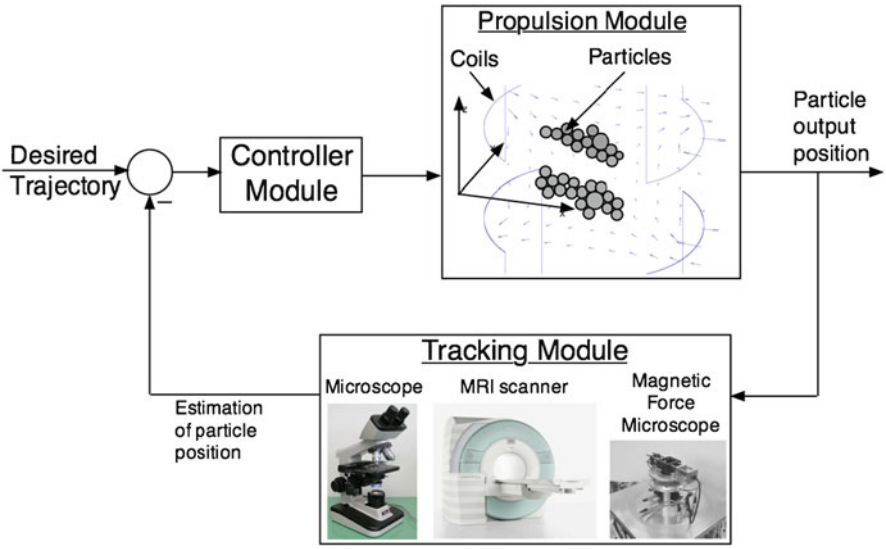

Fig. 1.8 General concept of closed-loop system for propulsion and guidance of magnetically driven nanoparticles using external magnetic fields and imaging modalities (published with permission from Panagiotis Vartholomeos)

Research in this field has been pioneered since 2003 by Sylvain Martel at the Ecole Polytechnique de Montréal [52–55]. He has used clinical MRI to navigate an inflow of 10.9-μm magnetic microparticles into a branch of a Y-shaped microchannel [54] and was the first to perform in vivo experiments on a living animal where he demonstrated propulsion and navigation of an untethered device in the blood vessel [55]. His analytical and experimental research results have been limited to millimeter- and micrometer-sized nonfunctionalized magnetic particles.

A systematic approach towards MRI-based guidance of nanoscale functionalized robotic capsules began for the first time, in the summer of 2008 in the context of the European Project NANOMA. Researchers of the NANOMA team have successfully developed a process for producing agglomerates of ferromagnetic filled multi-walled carbon nanotubes (FMWCNT) that were able to be steered in a MRI system. Their process is capable of producing vertically aligned multi-walled carbon nanotubes filled with high aspect ratio *nickel* (Ni), *iron* (Fe), and *cobalt* (Co) with a sufficient magnetic susceptibility artifact [56, 57] to be detected by the MRI modality. The direction and magnitude of the forces that are applied on the magnetic microparticles are generated according to a control law, where the feedback (i.e., the endovascular position of the microparticles) is calculated by the processing of the MRI data [58, 59]. Navigation techniques in combination with appropriate chemical modification of the nanoparticles' surfaces yield a more localized and controlled treatment as well as controlled drug-release mechanisms [60].

One of the limitations of MRI scanners for being used in the guidance of magnetic nanoparticles is the generation of weak magnetic gradients that are much smaller than those required to produce adequate propulsion forces that can move and guide the nanorobots at the nanoscale [51]. One way to resolve this challenge is to develop specially designed electromagnetic systems that can generate strong external magnetic fields with high magnetic gradients that can be used in the manipulation of magnetic nanoparticles at the nanoscale. Towards this goal, a five degree-of-freedom electromagnetic manipulator has been developed in Brad Nelson's laboratory [61] that in its newer version can steer and control magnetic drug delivery nanoagents [62].

Research in this field is currently showing a rapid expansion. The reader may find additional information regarding magnetically guided nanorobots in Chaps. 13–15 of this book.

1.2.4 Bacterial-Based Nanorobotics

The fourth type of nanorobotic system that exists today is based on the way that bacteria move in a fluidic environment [63]. This is a "biomimetic" type of nanorobot as it uses systems or concepts developed by nature but it is also a very "unusual" type of nanorobot from an engineering point of view. The bacterial-based nanorobotic systems and some of their versions could also be considered (depending on their fabrication technique and actuation) as either a bionanorobotic system or a magnetically guided nanorobotic system as presented earlier. However, because of the uniqueness in their design, control, and guidance we consider them to be an independent type of nanorobotic system.

Unicellular organisms such as *E. coli* and other bacteria have an interesting mode of motility [64, 65]. They have a number of molecular motors, about 45nm in diameter, that drive their "feet" or the flagella that help the cell to swim. Motility is critical for cells, as they often have to travel from a less favorable to a more favorable environment. The flagella are helical filaments that extend out of the cell into the medium and perform a function analogous to what the oars perform to a boat. The flagella and the motor assembly are called a flagellum. The flagella motors impart a rotary motion into the flagella [66]. The flagella motors allow the bacteria to move at speeds that can reach 25 μm/s while their torque output could range from 2,700 to 4,600 pN-nm making them one of the most powerful nanomotors found in nature.

There are two different approaches in developing bacterial-based nanorobotic systems. The first approach is using living bacteria to serve as the nanorobotic system that will move in the fluidic environment and manipulate objects in it. The other approach is developing fully artificial bacteria-like nanorobots that are powered using an external magnetic field.

The first approach is trying to take advantage of the biological engineering already in place in living bacteria and most importantly their propulsion capability through their flagella motors. From the robotics point of view, the goal is to use

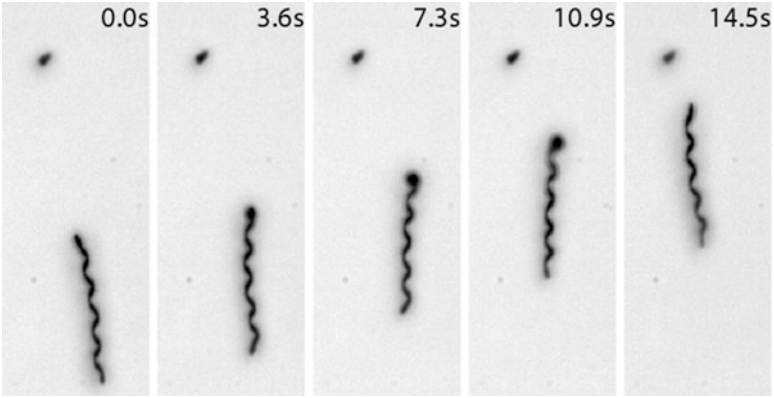

Fig. 1.9 Artificial bacterial microswimmers developed at ETH Zurich. By adjusting the rotating speed and direction of the external magnetic field, velocity and direction of the motion of the helical swimmers can be tuned in a controlled fashion (published with permission from B.J. Nelson, ETH Zurich, http://www.iris.ethz.ch/)

a team of bacteria to move forward a small object (e.g., a tiny bead) in a fluidic environment and be able to control this process, i.e., control the speed, direction, amount of displacement, and on demand stop and resume of this process. So far it was shown that bacteria can move a micro-object in a random, i.e., uncontrolled direction [67] while the stop and resume phases of this process could be controlled either by light [68] or chemically [69, 70].

A special type of bacteria called magnetotactic bacteria (MTB) offer more possibilities for manipulation of objects at the micro and nanoscale. MTB are bacteria that possess magnetic nanoparticles on their membrane. A direct result of this is that their main functional characteristic is magnetotaxis, i.e., they can orient along the Earth's geomagnetic field lines [71]. Using the naturally embedded magnetic nanoparticles of MTBs, it was shown that well-controlled manipulation of micro-objects could be performed by MTBs once an external magnetic field is used to generate a torque for MTB steering control [72, 73].

The second approach in developing bacterial-based nanorobotic systems is a biomimetic one, i.e., the goal is to create completely artificial nanoswimmers by copying nature's design from bacteria. Inspired by the motion of spermatozoa, Dreyfus et al. [74] developed a microswimmer consisting of a thin paramagnetic filament that attached itself to a blood cell. By applying an oscillating magnetic field the swimmer propelled the cell through continuous deformation of the filament in a manner somewhat similar to a eukaryotic flagellum. Recent examples of artificial flagellum in the form of a nanocoil that has been propelled using a rotating magnetic field have been proposed by Brad Nelson's group [75] (see Fig. 1.9). The self-scrolling fabrication technique to fabricate helical swimmers of a size comparable to *E. coli* which are capable of swimming in both water and paraffin oil [76] has recently been performed as well by the same group.

It is clear that a lot needs to be done in this area of nanorobotics. Most of the work that has been done so far is still in a preliminary phase and the systems that have been developed are far from being ready to be used in a real application. The reader may refer to Chaps. 14, 16, and 20 for more detailed presentation on bacterial nanorobots.

1.3 Applications of NanoRobotic Systems

One of the more frequent questions that a nanorobotic engineer or researcher has to answer is the following: "Where nanorobotic systems could be used commercially and how soon could a nanorobotic product be on the market?" This is a very important question and a very difficult to respond if we have to be realistic.

In general, nanorobotic systems are expected to be used in many different areas. Their possible uses range from medical to environmental sensing to space and military applications. Molecular construction of complex devices could be possible by nanorobots of the future. From precise drug delivery to repairing cells and fighting tumor cells, nanorobots are expected to revolutionize the medical industry in the future [3, 9].

All these potential, future applications of nanorobotic systems stay mostly in the area of "science fiction" for the time being as a lot of basic research still needs to be performed. An exception is the large size nanomanipulator type of nanorobotic systems where, as we described earlier in this chapter, several commercially available models exist. However, strictly speaking, true nanoscale size robotic systems developed so far are at a very preliminary phase of their development, and their commercial use is many years away.

One indication for the present lack of commercialization of nanorobotic systems is the limited number of currently issued patents in this area. A simple search within US patents issued up to the moment when this chapter was being written revealed that only three patents exist that use the word "nanorobot" [77–79]. One of them issued in 2005 presents a nanomanipulator system [77] while the most recent ones (issued in 2011 and 2012) focus on nanoscale systems such as nanoelectronics for nanorobotics [78] and swarms of magnetically driven nanosensors for in situ spinal cord imaging [79]. We would also like to mention a recent patent by Sylvain Martel's group on MRI guided microrobots in a blood vessel, even if the systems covered by this patent are at the microscale [80]. In addition, there are many patent applications under consideration and it is expected that the number of patents issued in the area of nanorobotics will increase in the near future.

In general, nanorobotic systems should be used to perform tasks at the nanoscale that cannot be performed with other means, that are of high importance for humankind, and that present a significant business opportunity for future investors. In addition, the nanoscale environment could be considered as a remote, difficult to reach, and sometimes hazardous location for the humans and these site limitations add additional technical challenges for their successful deployment. Given these

constraints, we foresee the following generic tasks at the nanoscale that nanorobotic systems should perform (a) in situ sensing; (b) manipulation of nano-objects; and (c) accurate nanopayload (e.g., drug) transportation and delivery.

In the rest of this section, we will try to present potential applications of nanorobotic systems that we believe are very promising for developing new commercial products in the years to come and for which there was substantial research activity recently. We would like to emphasize that we will not be exhaustive in our listing of applications but rather we will present the ones that we believe are the more promising at the moment for commercial use.

1.3.1 Medical Applications

Medicine has been a major application field for nanotechnology. In a similar way, medicine will be one of the most important applications areas for nanorobotics. Performing tasks inside the human body requires in many cases the use of nanosystems. For example, any task performed inside a cell will require nanoscale components. Furthermore, studies have shown that only objects 30–300nm in size can be circulated through the thinnest sections of the vasculature system. Therefore, nanorobotic systems will be needed to perform important tasks in these tiny locations inside the body.

One of the most representative medical tasks that nanorobots could perform is schematically shown in Fig. 1.10. This is the task of targeted drug delivery for localized therapy with improved efficiency and minimization of side effects. As shown in the figure, numerous nanorobotic agents carrying a drug for cancer therapy could be injected inside the body. The nanorobotic agents using their propulsion and guidance capabilities travel to the cancer location and deliver at that location only the drug that they are carrying. In a similar scenario, the nanorobotic agents could be equipped with nanosensors for in situ sensing and monitoring. A large number of technical papers have been written to describe how such a scenario (or similar scenarios for many other diseases that require targeted drug delivery) could become a reality [3, 9, 81–84].

There are several studies that tried to demonstrate experimentally the validity of the scenario described in Fig. 1.10. Most of the nanorobotic types presented earlier such as bionanorobotics, magnetically guided nanorobots, and bacterial-based nanorobotics have been developed for a medical application along the lines described above even if they are still at a preliminary development phase. We would like to highlight the application of nanorobotics in delivering a drug in the brain by bypassing the blood–brain barrier [85]. This is a very challenging task that cannot be performed with conventional ways and is an excellent example in medicine of where nanorobots are actually needed. Recently, intraocular microrobots have been employed for targeted drug delivery and for procedures such as retinal-vein cannulation that require a high degree of dexterity as shown in Fig. 1.11 [86, 87].

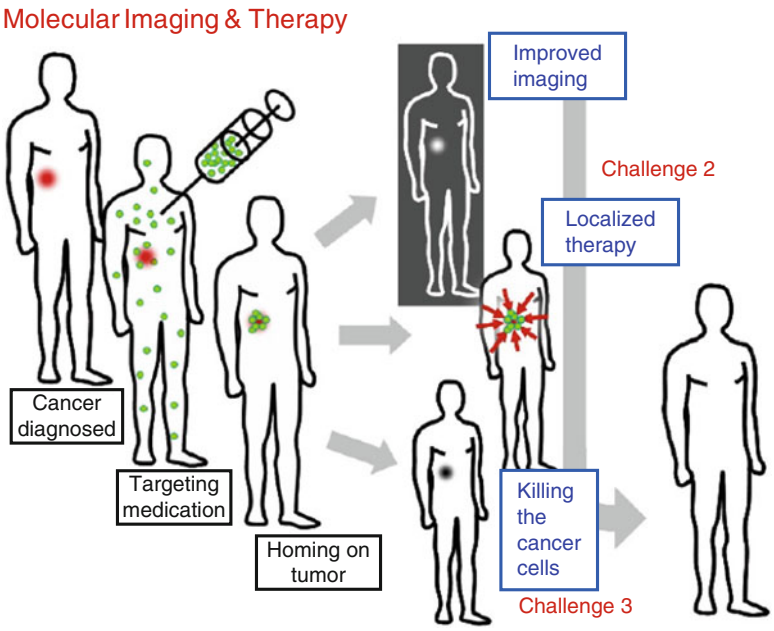

Fig. 1.10 Nanorobotics for targeted drug delivery (*Opensource Handbook of Nanoscience and Nanotechnology*)

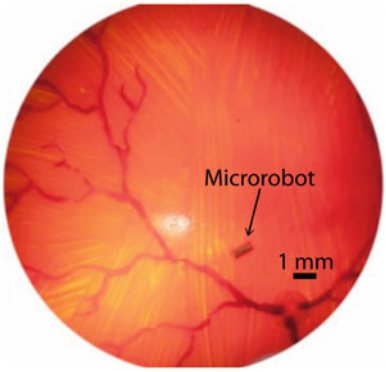

Fig. 1.11 Intraocular microdevices for retinal-vein canulation, drug delivery, or oxygen sensing (published with permission from B.J. Nelson, ETH Zurich, http://www.iris.ethz.ch/)

It is clear that nanomedicine is a perfect application area for nanorobotics. We definitely expect commercial products in this area in the near future (even if this near future is at least a decade), most probably relevant to nanosensing and targeted drug delivery. Most of the chapters in this book discuss one way or other medical applications of nanorobots. Specifically Chaps. 10–21 are focused on medical applications.

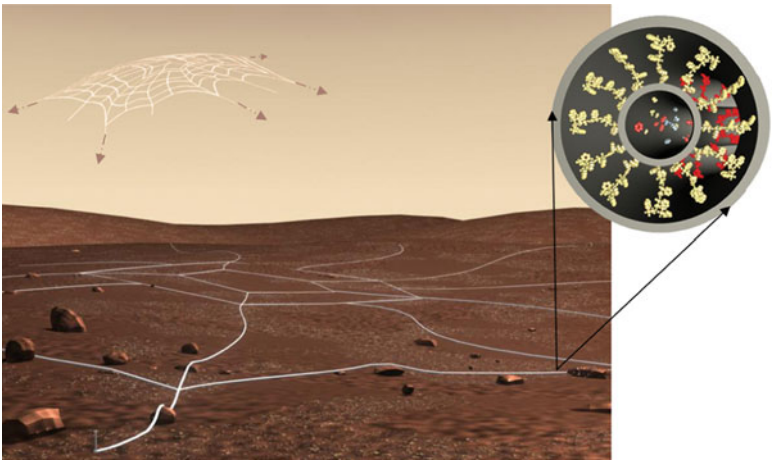

Fig. 1.12 A realistic scenario where the Networked TerraXplorers (NTXp) are employed. These meshes will be launched through the parachute and these will be spread open on the target surface. These NTXps could be launched in large quantities (hundreds) and hence the target terrain could be thoroughly mapped and sensed. A single NTXp could run into miles and when integrated with other NTXps could cover a vast terrain

1.3.2 Space Applications

Another application area where nanorobotics could be of great use is space. It is well known that the smaller a system launched in space is the smaller the mission cost is as well. In addition, for planetary exploration, due to the hazardous environment there is a need to deploy redundant systems for fault tolerance. The smaller and hence cheaper systems are much better for planetary deployment in large numbers. Nanotechnology and nanorobotics could provide solutions in the problem of miniaturization of space systems [88–90]. As an example of a possible future space application of nanorobotics we will present a concept developed by Dinos Mavroidis' group at Northeastern University during a NASA-funded project that targeted the development of revolutionary space systems [91].

Mapping and surveying a vast planetary terrain is a very difficult task. Some of the difficulties faced are limited area of landing for sophisticated planetary probes and rovers. It has been estimated that only a very small percentage of a planet's area is suited for landing. The planetary terrains and the atmospheric conditions pose a lot of difficulties for surface as well as air probes. Hence, only limited mobility could be achieved. Also, the investment required will be enormous for designing such rovers with capabilities of exploring the vast and difficult terrains.

Networked TerraXplorers is a concept shown in Fig. 1.12 in which various advantages of nanorobotic systems are being exploited such as their extremely light weight, low cost of manufacturing, mass scale production and bulk usage (billions), and their ability to self-assemble and self-organize. NTXp is a network of channels

containing the nanorobots having enhanced sensing and signaling capabilities. This essentially is a static device, which could be easily projected onto a planetary surface, which is intended for exploration. The length of this device could be in miles, and yet it will be very light in weight. These could be easily packaged into small volumes appropriate for space missions. Also the power consumption for this device will be considerably less. The main consumption of power will be to maintain gradients for transporting the nanorobotic components inside these channels and for signaling and communicating with the main receiver.

The nanorobots will move inside the channels of the network and will have "limited" window of interaction through special valves with the outside environment. They will interact with the outside terrain and chemically sense the presence of water or other targeted resources/minerals. They will also act like a position sensor on the surface of the terrain enabling it with the capability to map the terrain geometrically. They will communicate with their main nodes and will pass the information about the terrain through them to the main receiver (which could be an altitude orbiter). These networks could be spread throughout the terrain irrespective of the topological constraints. Their mass production will be cheap as compared to any technology available now, which could be used to map a terrain. Furthermore, these networks could be used by future rovers or human explorers for tracing out the vast terrain and thereby guiding them to the direction they should follow. Discovery of caves and low-lying surfaces could be possible with the help of these networks. This information will be very crucial for future human explorations to any planetary terrains.

Chapter 5 discusses in more detail the use of nanorobotics in space applications.

1.3.3 Subterranean Exploration of Oil Reservoirs

The next application is an "unusual" one for nanorobotics: exploration of subterranean oil reservoirs and maximization of hydrocarbon recovery [92].

Although found in the subsurface, hydrocarbon is essentially located in a complex mix of water and in the pores of the "reservoir rock." A large amount of the removed oil is embedded in reservoir rock (most commonly limestone or sandstone) much like water in a sponge. The challenge is determining the reservoir rock's 3D geometry. Because of the reservoir rock's unpredictable shape and size, large amounts of oil are unaccounted because "pockets" are created rich with oil. Current technologies are restricted to analyzing the rock's properties within a 2 m radius around the drilled hole or from hundreds of meters above (at the surface) which tends to give vague results. Removing oil from the reservoir rocks is usually compared to "squeezing water out of a sponge." Due to the limitations in the current methods and technologies, large amounts of oil remain stranded in the already drilled wells. The August 2006 issues of the World Oil Magazine reported that an estimated 374 billion barrels (approximately 66 %) of the discovered oil remain stranded in the wells. Oil recovery can be substantially improved and facilitated

if an accurate mapping of the oil reservoir "tubing" is known, i.e., getting 3D representation of the oil pathways (i.e., cracks in the rocks) in the reservoir. The network of cracks in the reservoir rocks and its properties is usually referred to as the "reservoir permeability field." Therefore, detection, mapping, and predictive modeling of high permeability pathways in oil reservoir are of primary importance for efficient oil recovery.

Recently, nanotechnology has been proposed as a new technology field for assisting the oil industry in oil discovery, recovery, and processing. The Advanced Energy Consortium (AEC) was recently created by the Bureau of Economic Geology at the University of Texas in the Austin Jackson's school of Geosciences (http://www.beg.utexas.edu/aec/index.htm) with the goal to improve energy production using micro and nanoscale technologies. The consortium includes members such as BP, Baker Hugnes, Conoco Phillips, Halliburton, Marathon, Occidental, and Schlumberger. Nanorobotics could be an important tool in this endeavor as it is shown by Saudi Aramco's initiative on the development of nanoscale ***Resbots***, i.e., reservoir robots [92, 93]. More information on this subject can be found in Chap. 4.

1.4 NanoRobots: The Future

In this chapter we presented an overview of the nanorobotics field. This is a relatively new field where the robotics community started to be involved in a systematic way less than 15 years ago. Starting from large-scale manipulators that have nanoscale manipulation capability the robotics community quickly expanded into magnetically guided nanoparticles and protein, DNA, and bacterial-based nanorobotics. Definitely, we are still in a preliminary phase of the field and commercial applications have not been realized yet. However, it is clear that the future of nanorobotics is bright. We are at the dawn of a new era in which many disciplines are merging including robotics, mechanical, chemical and biomedical engineering, chemistry, biology, physics, and mathematics so that fully functional nanorobotic systems will be developed and used in important applications for humankind.

We foresee two major future research directions in this field. The first will focus on developing fully functional nanorobotic systems where all technological challenges due to the nanoscale environment will be resolved. The second research direction will focus more on applications where new nanorobotic products will be commercially available and new applications fields will be added.

There is no doubt that future technology development in nanorobotics will target to the development of fully functional and autonomous systems. Figure 1.13 shows a generic, futuristic, concept of a nanorobot in the form of a fish-like nanocapsule so that it can move in a fluidic environment. All the components needed for autonomous functionality of such a nanorobot are on-board. Most notably, propulsion, power generation, various types of sensing, wireless communication, and some computing power for limited intelligence have to be integrated into a small

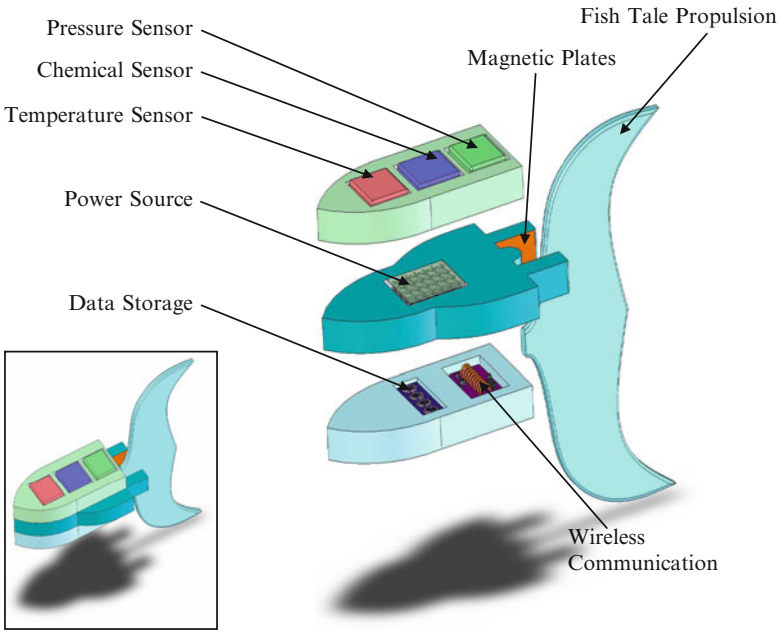

Fig. 1.13 Detailed view of a fully functional, autonomous nanorobot for in situ monitoring and its individual components

and strong structure so that the nanorobot could move in the fluidic environment using its own resources and be able to perform its task that in this case will be in situ monitoring.

Some of the components needed to materialize this concept exist today while others still need to be developed or improved before being used in a nanorobot. Manufacturing nanostructures, nanosensors of different types, and nanomotors are in an advanced development phase so we may consider that these components are one way or another available for integration in a nanorobot. However, onboard power generation, wireless communication, and computing capability have not been developed yet at a state where they could be used in a nanorobot even if some preliminary proof-of-concept prototypes for each one of these components have already been developed. Therefore, the robotics community in collaboration with the nanotechnology community should focus their near future efforts on improving the state of the art on onboard power, computing, and communication capabilities.

Furthermore, it is expected that the nanorobotics community will be actively working on new applications. Not only nanorobotic systems for the applications named earlier in this chapter (medical, space, oil industry) will be expanded and improved but new nanorobots for new applications will also emerge. Food industry, environmental monitoring and cleaning, military and counterterrorism systems, and industrial manufacturing are some of the applications areas where new nanorobotic systems are expected to be developed.

"There is plenty of room at the bottom" said Richard Feynman in his famous speech in 1959 at the California Institute of Technology raising for the first time the problem of manipulating and controlling objects at the nanoscale and setting this as one of the goals to achieve for future generations of scientists and engineers [94]. As a true prophet of the nanorobotics field he described in his talk for the first time ever his "small machines" being able to move in the blood vessel and perform surgeries. He raised numerous questions that relate to the manufacturing and operation of these "small machines" at the nanoscale. How can these "small machines" be manufactured? How can they be tele-operated in a "master–slave" configuration? How can power be generated for these small machines? "What would be the utility of such machines?" How do we perform assembly in a high viscosity nanoscale environment? All these very important questions raised over 50 years ago by an impressive pioneer of science are now ready to be answered by the current generation of nanoroboticists. But above all, as Richard Feynman suggested, let's "... have some fun" while we develop the next generation of nanorobotic systems!!

References

1. Requicha AAG, Baur C, Bugacov A, Gazen BC, Koel B, Madhukar A, Ramachandran TR, Resch R, Will P (1998) Nanorobotic assembly of two-dimensional structures. In: Proceedings of the IEEE international conference on robotics and automation, Leuven, Belgium, 16–21 May 1998, pp 3368–3374
2. Sitti M, Hashimoto H (1998) Tele-nanorobotics using atomic force microscope. In: Proceedings of the IEEE/RSJ international conference on intelligent robots and systems, IROS'98, Victoria, Canada, October, pp 1739–1746
3. Freitas RA Jr (1999) Nanomedicine, volume I: basic capabilities. Landes Bioscience, Georgetown, TX, http://www.nanomedicine.com/NMI.htm
4. Wowk B (1988) Cell repair technology. Cryonics Magazine, Alcor Foundation Reprint, pp 7–10
5. Dewdney AK (1988) Nanotechnology – wherein molecular computers control tiny circulatory submarines. Sci Am 258(101):100–103
6. Drexler KE (1986) Engines of creation: the coming era of nanotechnology. Anchor, New York
7. Drexler KE, Peterson C, Pergamit G (1991) Unbounding the future: the nanotechnology revolution. William Morrow, New York
8. Drexler KE (1992) Nanosystems: molecular machinery, manufacturing, and computation. Wiley, New York
9. Freitas RA Jr (2003) Nanomedicine, volume IIA: biocompatibility. Landes Bioscience, Georgetown, TX, http://www.nanomedicine.com/NMIIA.htm
10. Freitas RA Jr (2005) Current status of nanomedicine and medical nanorobotics. J Comput Theor Nanosci 2:1–25
11. Asimov I (1966) Fantastic voyage. Houghton Mifflin, Boston, MA
12. Crichton M (2002) Prey. Avon, New York
13. Weir NA, Sierra DP, Jones JF (2005) A review of research in the field of nanorobotics. Sandia National Laboratories Report SAND2005-6808. http://prod.sandia.gov/techlib/access-control.cgi/2005/056808.pdf
14. Ummat A, Dubey A, Sharma G, Mavroidis C (2006) Bio-nano-robotics: state of the art and future challenges (chapter 19, invited chapter). In: Bronzino JD (ed) Tissue engineering and artificial organs, The biomedical engineering handbook. CRC, Boca Raton, FL. ISBN 0849321239

15. Vartholomeos P, Fruchard M, Ferreira A, Mavroidis C (2010) MRI-guided nanorobotic systems for drug delivery (chapter 45). In: Klaus S (ed) Handbook of nano-physics, vol 7. Taylor & Francis, Boca Raton, FL. ISBN 978-1-4200753-8-0
16. Bonabeau E, Dorigo M, Theraulaz G (1999) Swarm intelligence: from natural to artificial systems. Oxford University Press, New York
17. Arbuckle DJ, Requicha AAG (2010) Self-assembly and self-repair of arbitrary shapes by a swarm of reactive robots: algorithms and simulations. Auton Robot 28(2):197–211
18. Freitas RA Jr, Merkle RC (2004) Kinematic self-replicating machines. Landes Bioscience, Georgetown, TX, http://www.MolecularAssembler.com/KSRM.htm
19. Ummat A, Dubey A, Mavroidis C, Mavroidis C (2010) Bionanorobotics: a field inspired by nature (chapter 7, invited chapter). In: Bar-Cohen Y (ed) Biomimetics – biologically inspired technologies. CRC, Boca Raton, FL, pp 201–227. ISBN 0849331633
20. Ferreira A, Mavroidis C (2006) Virtual reality and haptics in nano robotics: a review study. IEEE Robot Autom Mag 13(2):78–92
21. Freudenstein F (1973) Kinematics: past, present and future. Mech Mach Theory 8:151–160
22. Cray D (2000) Incredible shrinking doctors. Pop Sci July:63–65
23. Stroscio JA, Eigler DM (1991) Atomic and molecular manipulation with the scanning tunneling microscope. Science 254(5036):1319–1326
24. Eigler DM, Schweizer EK (1990) Positioning single atoms with a scanning tunneling microscope. Nature 344:524–526
25. Requicha AA (1999) Nanorobotics. In: Shimon YN (ed) Handbook of industrial robotics. Wiley, New York
26. Dong LX, Arai F, Fukuda T (2001) 3-D nanorobotic manipulation of nanometer-scale objects. J Robot Mechatron 13(2):146–153
27. Fukuda T, Arai F, Dong L (2003) Assembly of nanodevices with carbon nanotubes through nanorobotic manipulation. Proc IEEE 91(11):1803–1818
28. Fukuda T, Arai F, Dong LX (2005) Nanorobotic systems. Int J Adv Robot Syst 2(3):264–275
29. Du E, Cui H, Zhu Z (2006) Review of nanomanipulators for nanomanufacturing. Int J Nanomanufacturing 1(1):83–104
30. Dong LX, Nelson BJ (2007) Robotics in the small, part II: nanorobotics. IEEE Robot Autom Mag 14(3):111–121
31. Dong LX, Subramanian A, Nelson BJ (2007) Carbon nanotubes for nanorobotics. Nano Today 2(6):12–21
32. Dubey A, Mavroidis C, Thornton A, Nikitczuk KP, Yarmush ML (2003) Viral protein linear (VPL) nano-actuators. In: Proceedings of the 2003 IEEE – NANO conference, San Francisco, CA, 12–14 August 2003, vol 2, pp 140–143
33. Dubey A, Sharma G, Mavroidis C, Tomassone SM, Nikitczuk KP, Yarmush ML (2004) Dynamics and kinematics of viral protein linear nano-actuators for bio-nano robotic systems. In: Proceedings of the 2004 IEEE international conference of robotics and automation, New Orleans, LA, 26 April–1 May 2004, pp 1628–1633
34. Mavroidis C, Dubey A, Yarmush M (2004) Molecular machines. Annu Rev Biomed Eng 6:363–395
35. Sherman WB, Seeman NC (2004) A precisely controlled DNA bipedal walking device. Nano Lett 4:1203–1207
36. Montemagno CD, Bachand GD (1999) Constructing nanomechanical devices powered by biomolecular motors. Nanotechnology 10:225–331
37. Bachand GD, Montemagno CD (2000) Constructing organic/inorganic NEMS devices powered by biomolecular motors. Biomed Microdevices 2:179–184
38. Yurke B, Turberfield AJ, Mills AP Jr, Simmel FC, Neumann JL (2000) A DNA-fuelled molecular machine made of DNA. Nature 406:605–608
39. Douglas SM, Bachelet I, Church GM (2012) A logic-gated nanorobot for targeted transport of molecular payloads. Science 335(6070):831–834
40. Hamdi M, Ferreira A, Sharma G, Mavroidis C (2008) Prototyping bio-nanorobots using molecular dynamics simulation and virtual reality. Microelectron J 30(2):190–201

41. Dubey A, Mavroidis C, Tomassone SM (2006) Molecular dynamic studies of viral-protein based nano-actuators. J Comput Theor Nanosci 3(6):885–897
42. Sharma G, Rege K, Budil D, Yarmush M, Mavroidis C (2008) Reversible pH-controlled DNA binding peptide nano-tweezers – an in-silico study. Int J Nanomed 3(4):505–521
43. Sharma G, Rege K, Budil D, Yarmush M, Mavroidis C (2009) Computational studies of a protein based nanoactuator for nanogripping applications. Int J Robot Res 28(4):421–435
44. Sharma G, Rege K, Budil D, Yarmush M, Mavroidis C (2009) Biological force measurement in a protein based nano-actuator. IEEE Trans Nanotechnol 8(6):684–691
45. Gullà S, Sharma G, Borbat P, Freed J, Ghimire H, Lorigan G, Rege K, Mavroidis C, Budil D (2009) Molecular-scale force measurement in a coiled-coil peptide by electron spin resonance. J Am Chem Soc 131(15):5374–5375
46. Hamdi M, Ferreira A (2009) Multiscale design and modeling of protein-based nanomechanisms for nanorobotics. Int J Robot Res 28:436–449
47. Ferreira A, Sharma G, Mavroidis C (2005) New trends in bio-nanorobotics using virtual reality technologies. In: Proceedings of the IEEE international conference on robotics and biomimetics (IEEE ROBIO 2005), Hong Kong SAR and Macau SAR, China, 29 June–03 July 2005, pp 89–94
48. Hamdi M, Sharma G, Ferreira A, Mavroidis C (2005) Molecular mechanics simulation of bionanorobotic components using force feedback. In: Proceedings of the IEEE international conference on robotics and biomimetics (IEEE ROBIO 2005), Hong Kong SAR and Macau SAR, China, 29 June–03 July 2005, pp 105–110
49. Hamdi M, Sharma G, Ferreira A, Mavroidis C (2006) Characterization of protein based spring-like elastic joints for biorobotic applications. In: Proceedings of the 2006 IEEE international conference on robotics and automation, Orlando, FL, 15–19 May 2006
50. Hamdi M, Ferreira A (2008) DNA nanorobotics. Microelectron J 39:1051–1059
51. Vartholomeos P, Fruchard M, Ferreira A, Mavroidis C (2011) MRI-guided nanorobotic systems for therapeutic and diagnostic applications. Annu Rev Biomed Eng 13:157–184
52. Martel S, Mathieu JB, Felfoul O, Chanu A, Aboussouan E, Tamaz S, Pouponneau P, Yahia L, Beaudoin G, Soulez G, Mankiewicz M (2008) A computer-assisted protocol for endovascular target interventions using a clinical MRI system for controlling untethered microdevices and future nanorobots. Comput Aided Surg 13(06):340–352
53. Mathieu J-B, Beaudoin G, Martel S (2006) Method of propulsion of a ferromagnetic core in the cardiovascular system through magnetic gradients generated by an MRI system. IEEE Trans Biomed Eng 53:292–299
54. Mathieu J-B, Martel S (2007) Magnetic microparticle steering within the constraints of an MRI system: proof of concept of a novel targeting approach. Biomed Microdevices 9:801–808
55. Martel S, Mathieu J-B, Felfoul O, Chanu A, Aboussouan E, Tamaz S, Pouponneau P, Beaudoin G, Soulez G, L'H Y, Mankiewicz M (2007) Automatic navigation of an untethered device in the artery of a living animal using a conventional clinical magnetic resonance imaging system. Appl Phys Lett 90:114105–114108
56. Zeeshan M, Shou K, Pané S, Pellicer E, Sort J, Sivaraman K, Baró MD, Nelson BJ (2011) Structural and magnetic characterization of batch-fabricated nickel encapsulated multi-walled carbon nanotubes. Nanotechnology 22:275713
57. Folio D, Dahmen C, Wortmann T, Zeeshan M, Shou K, Pane S, Nelson BJ, Ferreira A, Fatikow S (2011) MRI magnetic signature imaging, tracking and navigation for targeted micro/nano capsule therapeutics. In: IEEE international conference on intelligent robots and systems, San Francisco, 23–29 September 2011
58. Arcese L, Fruchard M, Ferreira A (2012) Endovascular magnetically-guided robots: navigation, modeling and optimization. IEEE Trans Biomed Eng 59(4):977–987
59. Belharet K, Folio D, Ferreira A (2011) Three dimensional controlled motion of a microrobot using magnetic gradients. Adv Robot 25:1069–1083
60. Wortmann T, Dahmen C, Fatikow S (2010) Study of MRI susceptibility artifacts for nanomedical applications. ASME J Nanotechnol Eng Med 1(4):041002

61. Kummer MP, Abbott JJ, Kratochvil BE, Borer R, Sengul A, Nelson BJ (2010) OctoMag: an electromagnetic system for 5-DOF wireless micromanipulation. IEEE Trans Robot 26(6):1006–1017
62. Schürle S, Peyer KE, Kratochvil BE, Nelson BJ (2012) Holonomic 5-DOF magnetic control of 1D nanostructures. In: Proceedings of the 2012 IEEE international conference on robotics and automation, Minnesota, pp 1081–1086
63. Sitti M (2009) Miniature devices: voyage of the microrobots. Nature 458:1121–1122
64. Berry RM, Armitage JP (1999) The bacterial flagella motor. Adv Microb Physiol 41:291–337
65. Berg HC (2003) The rotary motor of bacterial flagella. Annu Rev Biochem 72:19–54
66. Berg HC, Anderson RA (1973) Bacteria swim by rotating their flagellar filaments. Nature 245:380–382
67. Darnton N, Turner L, Breuer K, Berg HC (2004) Moving fluid with bacterial carpet. Biophys J 86:1863–1870
68. Steager E, Kim C-B, Patel J, Bith S, Naik C, Reber L, Kim MJ (2007) Control of microfabricated structures powered by flagellated bacteria using phototaxis. Appl Phys Lett 90:263901–263903
69. Behkam B, Sitti M (2007) Bacterial flagella-based propulsion and on/off motion control of microscale objects. Appl Phys Lett 90:023902–023904
70. Behkam B, Sitti M (2008) Effect of quantity and configuration of attached bacteria on bacterial propulsion of microbeads. Appl Phys Lett 92:223901
71. Ardelean I, Ignat M, Moisescu C (2007) Magnetotactic bacteria and their significance for P systems and nanoactuators. In: Gutierrez-Naranjo MA, Paun G, Romero-Jimenez A, Riscos-Nunez A (eds) Proceedings of the 5th brainstorming week on membrane computing, Seville, pp 21–32
72. Martel S, Tremblay C, Ngakeng S, Langlois G (2006) Controlled manipulation and actuation of microobjects with magnetotactic bacteria. Appl Phys Lett 89:233804–233806
73. Martel S, Mohammadi M, Felfoul O, Lu Z, Pouponneau P (2009) Flagellated magnetotactic bacteria as controlled MRI-trackable propulsion and steering systems for medical nanorobots operating in the human microvasculature. Int J Robot Res 28:571–582
74. Dreyfus R, Baudry J, Roper ML, Fermigier M, Stone HA, Bibette J (2005) Microscopic artificial swimmers. Nature 437:862–865
75. Zhang L, Abbott JJ, Dong LX, Peyer KE, Kratochvil BE, Zhang HX, Bergeles C, Nelson BJ (2009) Characterizing the swimming properties of artificial bacterial flagella. Nano Lett 9(10):3663–3667
76. Zhang L, Peyer KE, Nelson BJ (2010) Artificial bacterial flagella for micromanipulation. Lab Chip 10:2203–2215
77. Xi N, Fung WK, Yu M, Li G (2005) Augmenting reality system for real-time nanomanipulation using atomic force microscopy. US Patent 6,862,924, 8 Mar 2005
78. Solomon N (2011) System, methods and apparatuses for integrated circuits for nanorobotics. US Patent 7,921,384, 5 Apr 2011
79. Jonckheere E, Lou M (2012) Spinal injury imaging by magnetically levitated sensors. US Patent 8,200,310, 12 June 2012
80. Martel S, Mathieu JB, Yahia L'H, Soulez G, Beaudoin G (2011) Method and system for propelling and controlling displacement of a microrobot in a blood vessel. US Patent 7,962,194, 14 June 2011
81. Cavalcanti A, Shirinzadeh B, Fukuda T, Ikeda S (2009) Nanorobot for brain aneurysm. Int J Robot Res 28(4):558–570
82. Cavalcanti A, Shirinzadeh B, Kretly LC (2008) Medical nanorobotics for diabetes control. Nanomedicine 4(2):127–138
83. Cavalcanti A, Shirinzadeh B, Zhang M, Kretly LC (2008) Nanorobot hardware architecture for medical defense. Sensors 8(5):2932–2958
84. Cavalcanti A, Shirinzadeh B, Freitas RA Jr, Hogg T (2008) Nanorobot architecture for medical target identification. Nanotechnology 19(1):015103 (15pp)

85. Tabatabaei SN, Duchemin S, Girouard H, Martel S (2012) Towards MR-navigable nanorobotic carriers for drug delivery into the brain. In: Proceedings of the 2012 IEEE international conference on robotics and automation, Minnesota, pp 727–732
86. Bergeles C, Shamaei KG, Abbott JJ, Nelson BJ (2010) Single-camera focus-based localization of intraocular devices. IEEE Trans Biomed Eng 57(8):2064–2074
87. Bergeles C, Kratochvil BE, Nelson BJ (2012) Visually servoing magnetic intraocular microdevices. IEEE Trans Robot. doi:10.1109/TRO.2012.2188165
88. Clark S (2012) Nanotechnology can launch a new age of space exploration. The Guardian (UK), 17 Apr 2012
89. Chui B, Kissner L (2000) Nanorobots for Mars EVA Repair. In: Proceedings of the international conference on environmental systems, Toulouse. doi: 10.4271/2000-01-2478
90. Mavroidis C, Ummat A (2005) Space bionanorobotic systems: design and applications. In: Proceedings of the 7th NASA/DoD conference on evolvable hardware (EH-2005), Washington, DC, 29 June–1 July 2005
91. Mavroidis C (2006) Bionano machines for space applications. Final Phase II Report to the NASA Institute of Advanced Concepts, July 2006. http://www.coe.neu.edu/Research/robots/papers/NIAC06.pdf
92. Sanni M, Kamal R, Kanj MY (2008) Reservoir nanorobots. Saudi Aramco J Technol Spring:44–52
93. Saudi Aramco (2012) Resbots reservoir robots. http://www.saudiaramco.com/content/mobile/en/home/innovation2/innovation-at-saudi-aramco/resbots-reservoir-robots.html?switchToMobile=1
94. Feynman RP (1959) Plenty of room at the bottom. California Institute of Technology. http://www.its.caltech.edu/~feynman/plenty.html

Chapter 2
Nanomechanical Cantilever-Based Manipulation for Sensing and Imaging

Nader Jalili

Abstract This brief chapter provides an overview of nanomechanical cantilever (NMC) systems with their applications in cantilever-based imaging and manipulation platforms such as atomic force microscopy (AFM) and its varieties. Some new concepts in modeling these systems are also introduced along with practical applications in laser-free imaging and nanoscale manipulation and positioning. In an effort to keep this chapter focused, only a brief overview of these topics is presented in this chapter. Finally, the outlook in NMC-based imaging and manipulation is given.

2.1 Classification of Control and Manipulation at the Nanoscale

Advancement of emerging nanotechnological applications such as nanoelectromechanical systems (NEMS) require precise modeling, control and manipulation of objects, components and subsystems ranging in sizes from few nanometers to micrometers. The added complexity of uncertainties and nonlinearities at nanoscale combined with the sub-nanometer precision requirement calls for the development of fundamentally new techniques and controllers for these applications. This area of research has recently received widespread attention in different technologies such as fabricating electronic chipsets, testing and assembly of MEMS and NEMS, micro-injection and manipulation of chromosomes and genes [1]. For example, in nanofiber manipulation, the ultimate goal is to grasp, manipulate and place nanofibers in certain predefined arrangement (see Fig. 2.1). Other applications could include defining materials properties, fabricating electronic chipsets, testing

N. Jalili (✉)
Department of Mechanical and Industrial Engineering, 334 Snell Engineering Center, Northeastern University, 360 Huntington Avenue, Boston, MA 02115, USA
e-mail: n.jalili@neu.edu

C. Mavroidis and A. Ferreira (eds.), *Nanorobotics*, DOI 10.1007/978-1-4614-2119-1_2,

© Springer Science+Business Media New York 2013

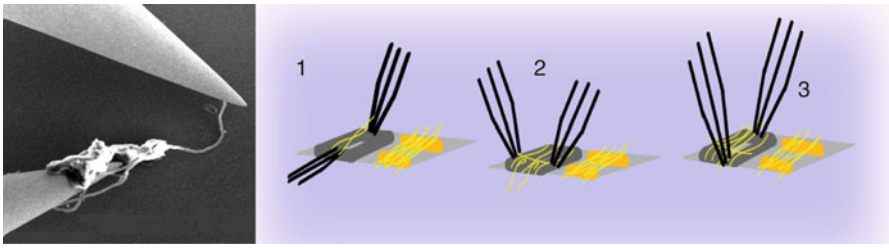

Fig. 2.1 (*Left*) Manipulation of nanofiber using MM3A® Nanorobot from Kleindiek®, (*right*) schematic representation of automated weaving process; (1) placement of the fibers and folding in the warp direction, (2) fiber placement in the weft, and (3) unfolding of the warp. Reprinted with permission

microelectronics circuits, assembly of MEMS and NEMS, teleoperated surgeries, microinjection, as well as manipulation of chromosomes and genes.

In general, nanoobject manipulation is defined as grasping, manipulating and placing nanoobjects in certain predefined arrangement. The strategies for control and manipulation at the nanoscale can be divided into the following two general categories:

1. Scanning probe microscopy (SPM)-based techniques
2. Nanorobotic manipulation (NRM)-based techniques

Under the first category, the following platforms can be utilized: scanning tunneling microscope (STM) and nanomechanical cantilever (NMC)-based systems (e.g., atomic force microscopy, AFM). On the other hand, NRM-based systems are more flexible and versatile in nanoscale manipulations. However, due to complexity and difficulty in sensing requirements (e.g., low-speed imaging acquisition and capturing in scanning electron microscopy (SEM) systems), control and manipulation using these systems might be limited, and hence, not discussed here.

2.1.1 Scanning Probe Microscopy-Based Control and Manipulation

In SPM systems, a probe is scanned over the surface at a small distance, where an "*interaction*" between the probe and the surface is present. This interaction can be of various nature (e.g., electrical, magnetically, mechanical) and provides the measured signal (tunnel current, force, etc.), see Fig. 2.2. SPM systems have numerous applications in a variety of disciplines and fields such as materials science, biology, chemistry, and many more areas.

As mentioned earlier and depicted in Fig. 2.2, under SPM-based control and manipulation techniques, STM and AFM platforms are referred to as the two most widely accepted techniques. As a matter of fact, early efforts on nanomanipulation

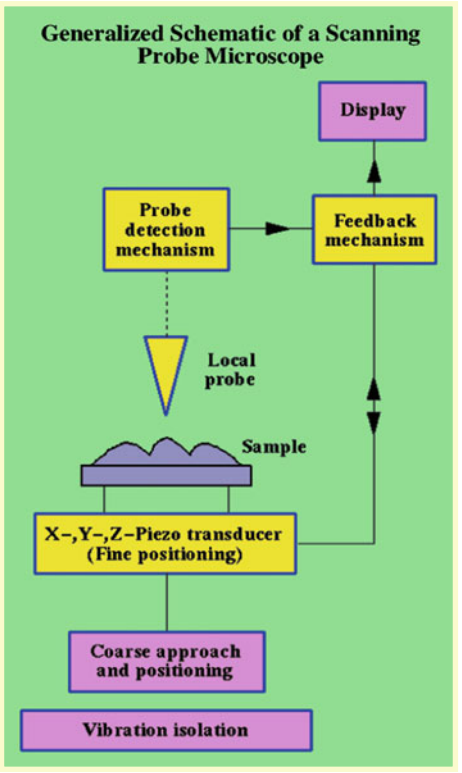

Fig. 2.2 Generalized schematic of scanning probe microscopy (SPM) system. Reprinted with permission

were initiated by both STM [2] and AFM [3]. Other techniques such as optical tweezers [4] and magnetic tweezers [5] have been also used for this purpose. Although this chapter focuses on NMC-based imaging/manipulation platform, other techniques are briefly reviewed to provide a comparative basis.

2.1.1.1 Scanning Tunneling Microscope, an Electrical SPM-Based Control and Manipulation

The STM, invented in 1982 by Binnig and Rohrer [2], was originally designed to perform real space atomic resolution imaging of a material's surface. The ability to obtain atomic resolution images with the STM arises from its unique operating principles. The microscope uses a sharp, metallic tip that is placed only a few Angstroms (10^{-10} m) from a conducting surface. At this distance, the tip conducts tunneling electrons or "tunnel current" from the surface and probes the surface electron density at that point. The electron density is exponentially dependent on the tip-surface separation, which makes the tunnel current a highly sensitive measure of this relative distance.

The strong interactions that can exist between a scanning tip and atoms/molecules at the surface can lead to alterations in surface chemical structure and, if controlled properly, can be used to move atoms or molecules and build nanoscale structures. It is this feature of the STM that forms the basic concept in nanomanipulation, i.e., due to its ultrahigh imaging resolution, nanoparticles as small as atoms can be manipulated.

2.1.1.2 Atomic Force Microscope, an Electromechanical SPM-Based Control and Manipulation

As mentioned earlier, AFM systems belong to the category of NMC-based systems, a subcategory of SPM systems. A typical AFM system consists of a micromachined cantilever probe with a sharp tip that is mounted to a piezoelectric actuator with a position-sensitive photo detector that receives a laser beam reflected off the back of the AFM tip. Roughly speaking, AFM is operated by moving the sample under the AFM tip and then recording the vertical displacement of the tip as the samples moves. As the AFM tip hovers across the surface of the sample, the tip moves up and down with the contour of the surface. A laser beam, deflected off the back of the AFM tip, is captured by a detector. This laser/detector configuration could provide displacement measurements that are utilized to generate topographical images and to control the piezoelectric actuators.

The AFM system has evolved into a useful tool for direct measurements of microstructural parameters and the intermolecular forces at the nanoscale level. Similar to STM, AFM system can also be used for manipulation at the nanoscale. In manipulation via AFM in non-contact mode, the image of nanoparticle is taken, the tip oscillation is removed and the tip is approached to particle while maintaining contact with the surface. In manipulation via AFM, larger forces can be applied to the nanoparticle and any object with arbitrary shape can be manipulated in 2D space. However, the manipulation of individual atoms or nanofibers with an AFM is still a major challenge and practically difficult task [6].

2.1.2 Nanorobotic Manipulation-Based Control and Manipulation

In manipulation via NRMs, much more degrees of freedom (DOFs) including rotation for orientation control of nanoparticle are feasible. For this reason, NRMs can be used for manipulations in 3D space. However, the relatively low resolution of electron microscope in manipulation with NRMs is a limiting factor in this nanomanipulation. A NRM system generally utilizes nanorobot as the manipulation device, microscopes or CCD camera as visual feedback, end-effectors including cantilevers and tweezers or other type of SPM and some sensors (e.g., force, displacement, tactile and strain) to manipulate nanoparticles [6].

Fig. 2.3 MM3A nanomanipulator [7], reprinted with permission

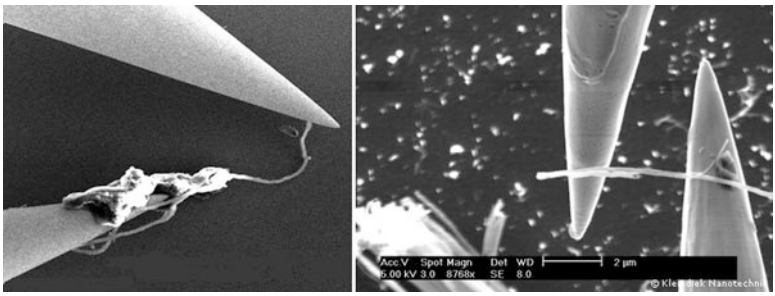

Fig. 2.4 MM3A manipulating nanofibers under scanning electron microscope (SEM). *Source*: [7], reprinted with permission

Among the variety of available NRM-based configurations, an attractive platform is a 3DOF nanomanipulator. This nanomanipulator, named as MM3A® and depicted in Fig. 2.3, consists of two rotational motors and one linear Nanomotor® [7]. The MM3A travels a distance of 1 cm within a second, with up to 1nm step precision. Using a single drive system, it integrates both coarse and fine manipulations [5]. It also offers a high degree of flexibility, that is, the nanomanipulator is capable of approaching a sample at any angle along the *X*, *Y* and *Z*-axes [7, 8].

As mentioned earlier, one attractive application of NRMs is to manipulate nanofibers, weave and utilize them in a variety of textile-related applications (see Fig. 2.4). The MM3A nanomanipulator combined with a novel fused vision force feedback controller can be utilized to address such a critical need in nano-fabric production automation [8–11].

2.2 Nanomechanical Cantilever-Based Imaging

As mentioned in the preceding subsection, AFM serves as one of the most effective tools in imaging at the nanoscale. In an effort to reduce the cost and improve the speed of AFM in molecular scale imaging of materials, a laser-free AFM proposition augmented with an accurate control strategy for its scanning axes is presented here. To replace the bulky and expensive laser interferometer, a piezoresistive sensing device with an acceptable level of accuracy is employed. Change in the resistance of piezoelectric layer due to the deflection of microcantilever, caused by the variation

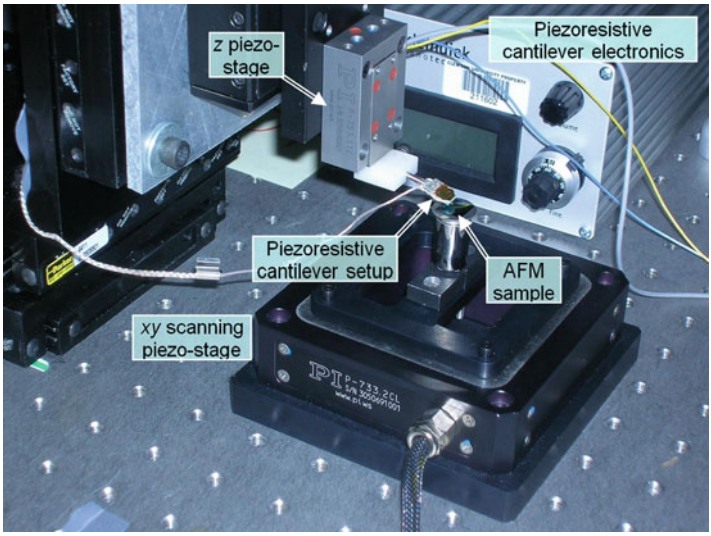

Fig. 2.5 Piezoresistive cantilever-based laser-free AFM setup. *Source*: [13], reprinted with permission

of surface topography, is monitored through a Wheatstone bridge. Hence, the surface topography is captured without the use of laser and with nanometer scale accuracy.

2.2.1 A NMC-Based Laser-Free AFM System for Fast Imaging

Figure 2.5 depicts the proposed laser-free AFM setup. The sample to be imaged is mounted on the double-axes parallel piezo-flexural stage, while a piezoresistive microcantilever is mounted on another piezoelectric z-stage for acquiring sample topography. The z-stage is used only for the initial adjustment and to bring the cantilever into a desired contact with the sample. During scanning, z-stage does not move; hence, the cantilever deflection corresponds to the surface topography (see Fig. 2.6 for the schematic view of laser-free AFM setup).

A self-sensing microcantilever, PRC-400, is utilized here for imaging purpose. Figure 2.7 depicts the piezoresistive cantilever image under a 100× magnification light microscopy consisting of a silicon microcantilever with a piezoresistive layer on its base, a sharpened tip, and a piezoresistive reference lever. The piezoresistive layers on cantilever and reference lever are utilized as resistances in a Wheatstone bridge. Due to the external force on the piezoresistive cantilever's tip, it bends and results in a change of resistance in the piezoresistive layer. This change of resistance can be monitored utilizing the output voltage of the Wheatstone bridge. Figure 2.7 depicts a schematic of the PRC-400 self-sensing cantilever, with external

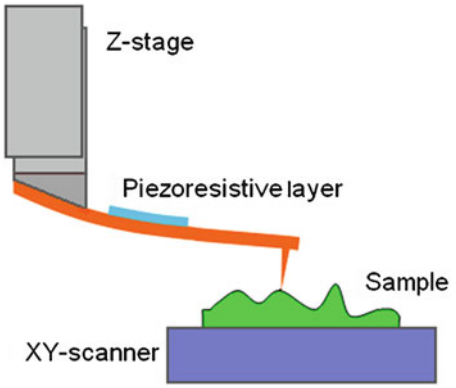

Fig. 2.6 Schematic representation of laser-free AFM setup. *Source*: [13], reprinted with permission

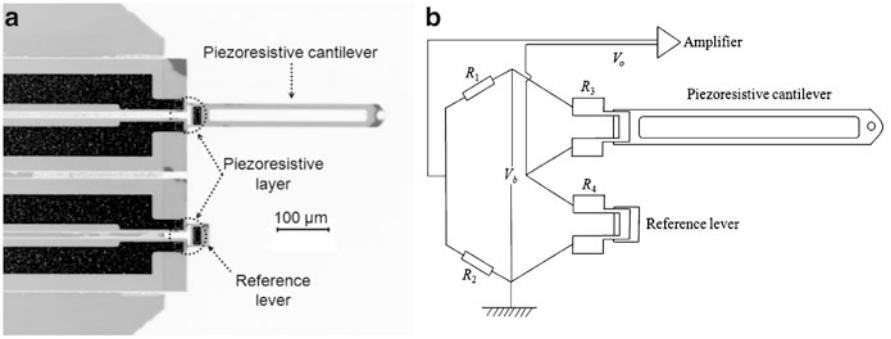

Fig. 2.7 Piezoresistive microcantilever with Weston bridge circuit. *Source*: [12], reprinted with permission

Wheatstone bridge and amplifier. The relation between the cantilever deflection and output voltage of the Wheatstone bridge is typically linear [12]. Thus, the cantilever deflection can be estimated through the deflection-to-voltage gain of the piezoresistive cantilever.

At the tip/sample contact point, the magnitude of the force applied to the cantilever tip is equally the same as the magnitude of the force applied to the sample surface. Cantilever's dimensions are, however, extremely small, and it only undergoes bending. Hence, the high flexibility of the cantilever is realized compared to the sample that distributes the force around the contact point and resists against it. As a result, the vertical deformation of sample at the contact point becomes negligible compared to that of the cantilever. This assumption is valid unless ultrasoft samples (e.g., liquids, soft biological species or ultrathin polymeric layers) are under study. Within the scope of this chapter, only stiff enough samples are addressed. Imaging ultrasoft samples requires further experiments to identify the local stiffness of the material, and is better done using non-contact or tapping AFM modes. On the other hand, the variation of surface topography in contact mode AFM

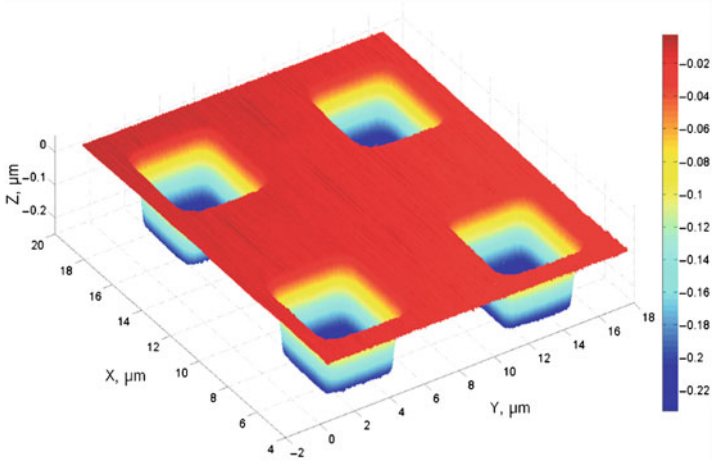

Fig. 2.8 3D image of an AFM calibration sample with 200nm steps captured by the developed laser-free AFM setup at 10 Hz raster scanning. *Source*: [13], reprinted with permission

should not exceed a certain value beyond which the cantilever would experience plastic deformation or yield. Since the length of a typical AFM cantilever is in the order of several hundred micrometers, it can safely bend for few tens of microns. This flexibility is sufficient for most of the current AFM applications with micro- and nano-scale topographical variations.

2.2.2 *Development of a Robust Adaptive Controller for Laser-Free Imaging*

Utilizing a robust adaptive controller for *x*–*y* nano-positioner, an AFM calibration sample with 5×5 μm^2 cubic pools with 200nm depth, uniformly distributed on its surface, is considered for the experimental implementation of the proposed laser-free AFM setup. Figure 2.8 demonstrates the 3D image of the sample within a 16×16 μm^2 scanning area at 10 Hz scanning frequency. It is particularly desired to observe the quality of images acquired in different scanning speeds (or in the other words, scanning frequencies). Figure 2.9 demonstrates the top view of images at frequencies varying from 10 to 60 Hz with 10 Hz increments. It is seen that as the frequency increases, the quality drops and images become more blurry. This effect could have been originated from the increased transversal vibrations of microcantilever due to facing with the steeper steps in the surface at higher speeds, and/or the sensitivity reduction of piezoresistive layer due to the frequency increase. Further information such as cross-sectional view (line scan) of the surface could yield better judgment in this regard.

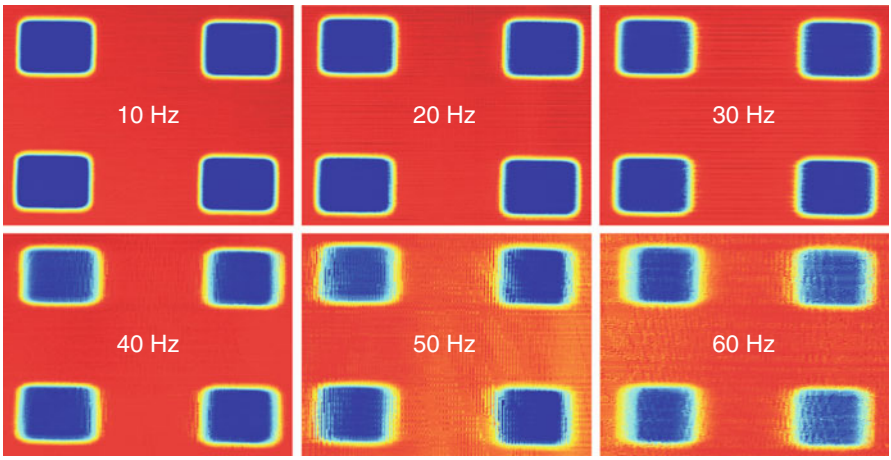

Fig. 2.9 Effects of raster scanning frequency on the image quality of laser-free AFM. *Source*: [13], reprinted with permission

As seen from Fig. 2.9, it reveals that at frequency of 30 Hz or less, the steep topographical steps are captured clearly by the cantilever and its piezoresistive sensor. However, when the frequency increases to 40 Hz and more, the stepped edges seem smoother and the image loses accuracy around the step areas. Moreover, at high frequencies, particularly at 60 Hz, the measured topography finds a negative slope which leads to further accuracy loss. Both of these effects cannot originate from the cantilever's vibrations, neither can they come from cantilever's irresponsiveness. This is due to the ultrahigh natural frequency of microcantilevers (in the order of several kHz) which significantly reduces their rise time and makes them extremely responsive. Hence, we may conclude that the degradation of image at high frequencies is due to the deficiency of the piezoresistive measurement at high frequencies which sets the limit to the proposed laser-free AFM device. Hence, one of the important future directions of piezoresistive-based AFMs would be improving the accuracy of piezoresistive sensors through their manufacturing process and electronics integration.

Nevertheless, acquiring high-quality images at frequencies up to 30 Hz could imply the effectiveness of the proposed control framework in increasing the speeds of current AFMs which typically suffer from the low speed of commonly used PID controllers.

2.3 Nanomechanical Cantilever-Based Manipulation

A relatively common manipulation configuration using AFM is to maintain a desired force, mostly constant, at the cantilever tip. Hence, the control objective is to move the cantilever base in order to acquire this desired force at the tip. This

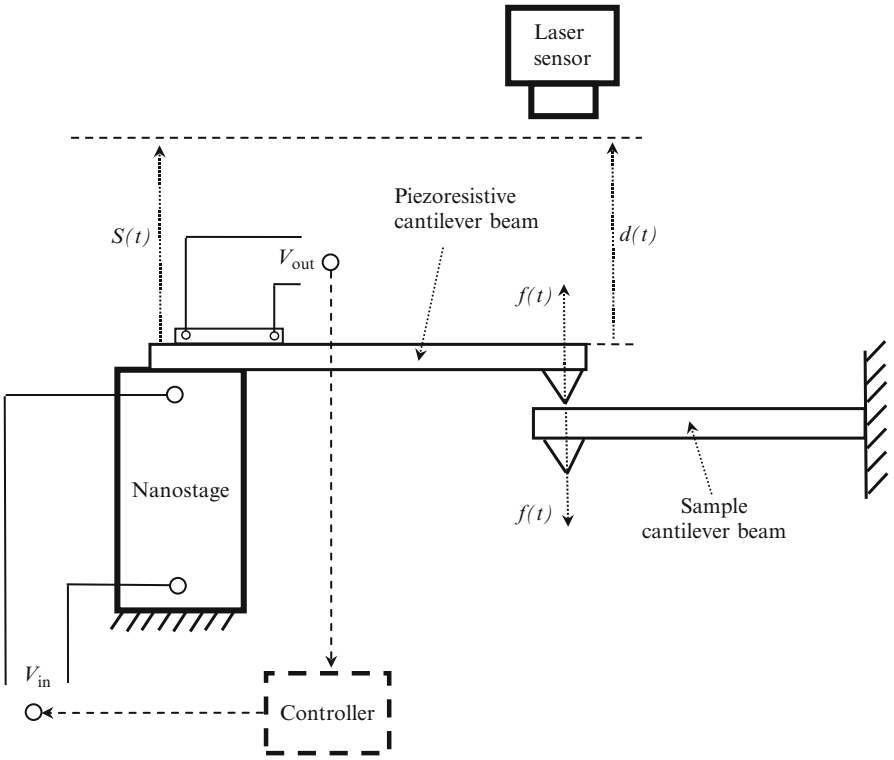

Fig. 2.10 Schematic of the NMC-based force sensing experimental setup. *Source*: [12], reprinted with permission

is a highly demanding mission in nanomanipulation and imaging; for instance, in contact imaging in AFM, there is a need to keep the force at the cantilever's tip in a constant value [12, 14]. Moreover, in almost all of the non-destructive materials characterization and nanomanipulation tasks, there is a need to control the interaction force between the cantilever's tip and the surface or nanoparticle.

2.3.1 *Nanoscale Force Tracking Using NMC-Based Manipulation*

Figure 2.10 depicts the schematic of such nanoscale force tracking using a piezoresistive cantilever with a PZT-actuated base. The objective here is to sense the force acting on the piezoresistive cantilever's tip utilizing the output voltage of the piezoresistive beam and smoothly move its base to acquire the desired force on the piezoresistive cantilever's tip. The control objective is to obtain the desired force at the cantilever's tip, which is measured utilizing the output voltage of the

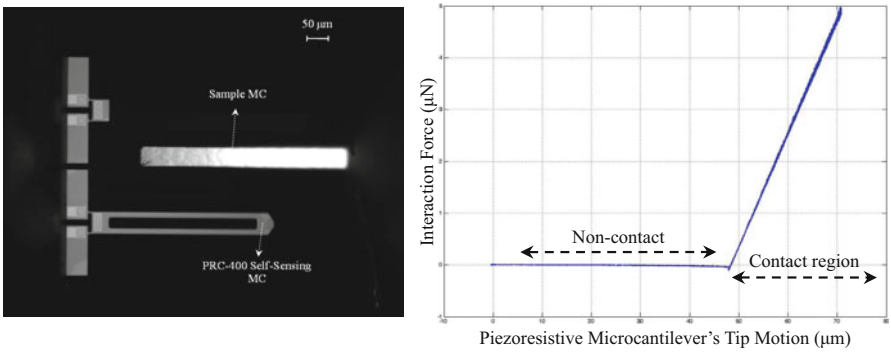

Fig. 2.11 (*Left*) Experimental setup of pushing sample NMC with piezoresistive NMC, and (*right*) the interaction force between sample and piezoresistive NMCs. *Source* (for the left figure only): [12], reprinted with permission

piezoresistive layer, V_{out}. Acquiring the force acting on the tip, this force and the desired value for the force are fed back to the controller that generates the suitable control command and sends it to the nanostage as the input voltage V_{in}.

2.3.2 Controlled Tip Force-Based Manipulation

A set of experimental results are presented for tracking a desired nanoscale force at the tip of NMC. For this, the piezoresistive NMC is brought close to a sample NMC (see Fig. 2.11, left) and the output voltage from piezoresistive layer is utilized to predict the force acting on the NMC's tip. By comparing the predicted force with the desired trajectory, the error which should be regulated can be easily determined. However, in order to identify the actual force acting on the NMC and compare it with the estimated force through the modeling, another measurement mechanism is employed using a laser-based measurement technique, for instance. Figure 2.11, right depicts the experimental results to identify the sample NMC's stiffness. The slope of the line depicted in Fig. 2.11, right in the contact region represents the force acting on the sample NMC's tip over the sample NMC's deflection which is also the sample NMC's stiffness. Utilizing the sample NMC's stiffness and its deflection, the actual force acting on the NMC's tip can be determined.

2.4 Summary

This chapter briefly provided a relatively general overview of NMC-based imaging and manipulation systems with their applications in many cantilever-based systems such as AFM and its varieties. It specifically presented some new concepts in

imaging at the nanoscale using laser-free setup and highlighted the issues related to nonlinear effects at such small scale, piezoelectric materials nonlinearity and remedies for control at these scales. The concepts of NMC-based manipulation and tip force-based control were presented with their applications in numerous biological species manipulation, cell mechanics and ultrasmall mass sensing and detection.

References

1. Kallio P, Koivo HN (1995) Microtelemanipulation: a survey of the application areas. In: Proceedings of the international conference on recent advances in mechatronics. ICRAM'95, Istanbul, August 1995, pp 365–372
2. Binnig G, Rohrer H, Gerber C, Weibel E (1982) Surface studies by scanning tunneling microscopy. Phys Rev Lett 49:57–61
3. Binnig G, Quate CF, Gerber C (1986) Atomic force microscope. Phys Rev Lett 56:93–96
4. Ashkin A, Dziedzic JM, Bjorkholm JE, Chu S (1986) Observation of a single-beam gradient force optical trap for dielectric particles. Opt Lett 11:288–290
5. Crick FHC, Hughes AFW (1950) The physical properties of cytoplasm: a study by means of the magnetic particle method. Exp Cell Res 1:37–80
6. Fukuda T, Dong L (2003) Assembly of nanodevices with carbon nanotubes through nanorobotic manipulations. Proc IEEE 91:1803–1818
7. Kleindiek S. Nanorobots for material science, biology and micro mounting. Kleindiek Nanotechnik Technical Report. http://www.nanotechnik.com/mm3a.html
8. Saeidpourazar R, Jalili N (2008) Towards fused vision and force robust feedback control of nanorobotic-based manipulation and grasping. Mechatron Int J 18:566–577
9. Baumgarten PK (1971) Electrostatic spinning of acrylic microfibers. J Colloid Interface Sci 36:71
10. Laxminarayana K, Jalili N (2005) Functional nanotube-based textiles: pathway to next generation fabrics with enhanced sensing capabilities. Textil Res J 75(9):670–680
11. Hiremath S, Jalili N (2006) Optimal control of electrospinning for fabrication of nonwoven textile-based sensors and actuators. In: Proceedings of 3rd international conference of textile research, Cairo, Egypt, April 2006
12. Saeidpourazar R, Jalili N (2009) Towards microcantilever-based force sensing and manipulation: modeling, control development and implementation. Int J Robot Res 28(4):464–483
13. Bashash S, Saeidpourazar R, Jalili N (2010) Development of a high-speed laser-free atomic force microscopy. Rev Sci Instrum 81-023707:1–9
14. Abramovitch DY, Anderson AB, Pao LY, Schitter G (2007) A tutorial on the mechanics dynamics and control of atomic force microscopes. In: Proceedings of the 2007 American control conference, New York, 11–13 July

Chapter 3
Swarms of Self-Organized Nanorobots

Ari Requicha

Abstract This chapter begins with a brief assessment of the state of the art in nanorobot hardware. Then, it focuses on programming and coordination issues that arise when large numbers of nanorobots are used for tasks such as building prescribed shapes. The active self-assembly system developed at the University of Southern California is discussed as an example of a proposed system that is capable of constructing arbitrary shapes. The system compiles the desired shape into a set of reactive, stateless rules to drive a large swarm of identical and identically programmed robots. Extensive simulations show that the system self-organizes and is capable of self-repair when numerous faults are present. The chapter concludes with a brief discussion of the current limitations of nanorobotic swarms, and an outlook on future developments.

3.1 Autonomous Nanorobots

A robot, at any spatial scale, is a system that can sense its environment, "think" (i.e., process information), and act. One of the most important actions normally associated with a robot is propulsion, but additional actions are required if the robot is to perform a useful function. Ideally, one would like a robot to be initially programmed and then go about its task autonomously, adapting itself to any unexpected situation. In practice, the degree of autonomy of today's robots is relatively low, and varies widely among robots.

A nanorobot is usually defined as a robot with overall dimensions not exceeding a few micrometers and built from nanoscale components. The nanoscale ranges from 1 to 100nm. A nanorobot, therefore, has a size comparable to that of a small

A. Requicha (✉)
Department of Computer Science, University of Southern California,
941 Bloom Walk, Los Angeles, CA 90089-0781, USA
e-mail: requicha@usc.edu

C. Mavroidis and A. Ferreira (eds.), *Nanorobotics*, DOI 10.1007/978-1-4614-2119-1_3,
© Springer Science+Business Media New York 2013

biological cell. This simple fact is expected to have major consequences, because nanorobots should be able to intimately interact with cells, and this may bring about a revolution in our understanding of biology and in medical applications. One can even envision malfunctioning biological cells being replaced by robotic "artificial cells."

Human-made, artificial nanorobots do not yet exist. The nanoparticles currently being developed at many laboratories for drug delivery are perhaps the closest relatives of nanorobots that we have today. They can sense by molecular recognition of surface markers on (for example) some cancer cells, and act by releasing drugs in the neighborhoods of the cells. But these nanoparticles are not self-propelled, and one would be hard pressed to attribute any thinking abilities to them. Clearly, they are very primitive devices. Swarms of such nanoparticles require essentially no coordination among particles' behaviors, in contrast with some of the systems discussed below.

Natural, biological nanorobots do exist. For example, certain cells in the human immune system are capable of sensing bacterial intruders, following them, and engulfing and destroying them. They sense and act, and have enough intelligence to pursue the pathogens and kill them.

3.2 Nanorobot Hardware

Robots of any size need sensors, actuators (including means of propulsion), control logic, power sources, and communication capabilities. Attempts to scale down macro or even microscopic designs for robots or their components are often doomed to failure, because the physics at the nanoscale is different from its counterparts at larger scales. Inertia is largely irrelevant in the nanoscopic world, and one must contend with Brownian motion and low Reynolds number flows, which often lead to counter-intuitive situations.

Nanosensors are relatively well developed. For example, nanowire chemical sensors (reviewed in [1]) are approaching acceptable performance for robotic applications. How to ensure that the analytes reach the sensor's active area is still an issue. In addition, certain materials, e.g., mammalian proteins, are "sticky" and may attach nonspecifically to the sensing wires. If the concentration of such materials is high compared to that of the targeted analytes, reliable detection may be impossible.

The literature on nanoactuators is burgeoning. There are now many examples of molecular machines, DNA-based machines, and larger actuators based on catalytic reactions or carbon nanotubes—see for example [2–5]. However, to my knowledge, none of these nanomachines has been used to build anything resembling an autonomous nanorobot. Perhaps more promising, at least in the short term, are approaches that use magnetic fields to rotate helicoidal propellers [6] or that involve live magnetotactic bacteria propelled by flagella [7].

Closely related to actuation is the issue of power. How are these nanomachines and robots to be powered? Ideally, they should scavenge energy from their

environment, and that is precisely what the bacteria mentioned above do. The helicoidal propellers are driven by an external magnetic field; this approach may be acceptable for operation in a relatively small environment, for example, within a human body. The other nanomachines briefly discussed above typically use a chemical "fuel" or are driven by light. The chemical approach is ubiquitous in nature, but is difficult to control; for example, to stop a nanomachine, one may have to wait for it to run out of fuel; light-driven approaches seem to be more promising.

Control of the actuators and of the whole robot presumably could be accomplished using the nanoelectronic circuitry being developed at many laboratories, worldwide. However, how the electronics interfaces with the other components and how well it works in environments such as the human body, are unresolved issues. It is worth noting here that sometimes very simple control schemes elicit relatively complex behaviors, as demonstrated by the elegant Braitenberg's vehicles [8] or by chemotaxis in bacteria [9]. Steering of magnetic bacteria and propellers may be accomplished by external magnetic fields.

Communication is essential for robot coordination and for exchanging information with the outside world, for example, for robots operating within the human body. Outside communication might be relayed by larger embedded devices ("mother ships") that can muster significant power, and with which the nanorobots exchange messages. Biological cells communicate primarily through chemical signals, and recent research is addressing the topic of chemical communication for artificial devices [10]. Communication by releasing chemicals relies on diffusion and is very slow for distances beyond a micrometer or so. Stigmergy, i.e., indirect signaling by writing and reading messages to and from the environment may be useful. Recent work on plasmonic antennas shows that it may be possible for nanorobots to communicate electromagnetically by carrying antennas with sizes below the micrometer [11, 12]. The near infrared seems especially suitable for communication within the human body, because it is not strongly attenuated and there is little noise in the body at such frequencies. Nevertheless, the range achieved by such an approach is likely to be very short, which implies that many hops will be required for reaching macroscopic distances.

Attempts to integrate several of the components discussed above are virtually non-existent. One of the very few examples of integration is the work in Lieber's laboratory at Harvard that demonstrates a photovoltaic receptor powering a nanowire sensor [13]. A biofuel cell that uses glucose as a fuel to power a nanowire sensor has been demonstrated in [14].

3.3 Tasks for Nanorobot Swarms

A single nanorobot is likely to have severely limited capabilities because of its minute size. Swarms of thousands or millions of nanorobots will be needed to accomplish significant tasks. Programming and coordination of such swarms raises a host of difficult problems. A decentralized approach to control is required to

ensure that the swarm continues to operate in the presence of faults, which are to be expected. There can be no "boss," or the swarm will not accomplish its mission if the boss fails. The environment in which the robots operate is likely to evolve, and the ability to adapt to such dynamic environments is crucial. Robustness to noise and failures of many sorts, plus the ability to self-heal (or self-repair) or perhaps even self-reproduce are essential characteristics of nanorobot swarms. The swarm must exhibit the desired, emergent behavior (a bit of an oxymoron . . .) and accomplish a global goal using only local rules. This is known as the "global-to-local compilation" problem, and has only been achieved in a very small number of proposed systems.

If we succeed in building a nanorobot swarm, what will we do with it? There are only two tasks that have been investigated in some depth. The first involves responding to a cell-size source releasing chemicals in a blood vessel [15]. A related task would be to identify areas of a blood vessel that have large cholesterol deposits and remove them.

The second generic task that has been investigated in detail is the construction of specified shapes by robot swarms. The main research groups addressing this problem are my own group at the Laboratory for Molecular Robotics (LMR) of the University of Southern California (USC), Wei-Min Shen's also at USC [16], Radhika Nagpal's at Harvard [17], Eric Klavins' at the University of Washington [18], and Marco Dorigo's at the Free University of Brussels, Belgium [19]. Of this research, only LMR's addresses specifically the case of nanoscopic robots. The various approaches that have been proposed make different assumptions and are hard to compare.

The primary application of shape construction by robot swarms is in building scaffolds of prescribed shapes for nanoelectronic or biomedical purposes. For example, a scaffold could be built with nanorobots that together define a specific shape, and that possesses attachment points for, say, metallic nanoparticles. Similarly, scaffolds for biological cells could be constructed. Once a scaffold is available, the desired structure itself would be built in parallel by traditional, passive self-assembly. For example, gold nanoparticles in a liquid suspension could be flown over a nanorobotic scaffold with suitable attachment sites.

Traditional tasks discussed in the distributed robotics literature, such as area coverage or surveillance, may also be relevant at the nanoscale. A thorough investigation of the tasks that might be tackled by nanorobot swarms has not yet been done, as far as I know.

3.4 Simulation

Roboticists are understandably skeptical of robotic systems that have not been validated experimentally. Given that physical nanorobot swarms do not yet exist, what should we do? There are two main options. The first is to work with small groups of macroscopic robots. With current technology and funding constraints,

it is unfeasible to build swarms of more than a few dozen robots. This is too small for convincing demonstrations. More pointedly, it is unclear what are the nanoscopic implications, if any, of macroscopic demonstrations, because the physics at the two scales are quite different, and this changes trade-offs, robot capabilities, strategies, and algorithms.

The second option is to simulate the swarms in software. This is non-trivial because of the large number of robots (ideally, a swarm should have tens of thousands of robots, or even more), and because of the nanoscale physics involved. Simulations over significant time periods (not nano or microseconds) are required. For a faithful treatment of the relevant physics, one would need to consider a variety of issues: collisions between robots; collisions between robots and obstacles, including, for example, cells or molecules in the environment; temperature effects, including random motion; robot energy levels; and so forth. In addition, one must take into account failures of many types, from catastrophic robot failures to failures of communication links. This is a tall order, and I do not know of any simulator that correctly addresses all these issues.

Here I will discuss briefly the simulator built at the LMR, as an example of an existing system. Our simulator is stochastic and driven by a priority queue. Entries in the queue correspond to events, and each event is associated with the time at which it will occur in the future. A lower time implies a higher priority. Events include robot motion in either the current direction or a different one; receiving messages; and decreasing the strength of the attachment between two robots. Initially, the positions of the robots are determined by sampling a Gaussian random variable. We also associate with each robot a "displacement" variable, which is a proxy for the robot velocity, or its kinetic energy, and is also obtained by sampling another Gaussian. Each robot has a time at which the next event involving that robot will occur. These time values are also sampled values of yet another Gaussian variable. When the time increments are small, the temporal density of the events increase, as it would in a physical system at high temperature.

The simulation proceeds by removing from the queue the entry with highest priority, i.e., containing the event with lowest associated time. The action specified in the event is executed, and usually creates new events that are entered in the queue. When the action is a motion, the displacement vector associated with the target robot is added to the current position of that robot. The trajectory thus defined is compared with the positions of all the other robots to determine if there are collisions. If so, the motion is stopped at the collision point and the robots become attached to each other with a given strength. The motion of the robot is assumed to be instantaneous and all the other robots are kept stationary. This is physically wrong, but is very convenient computationally. Robot attachment triggers a "decay" event that will decrease the strength of the binding between the two involved robots as time goes by.

If the action is a message from an adjacent robot, the program of the receiving robot (a set of reactive rules—see next section) is executed, and the strength of the attachment between the two communicating robots is increased. A decay event is scheduled as well. When the binding strength between two robots reaches zero, the robots detach from each other.

The discussion above is oversimplified but serves to point out a few interesting characteristics of the simulator (for a detailed description, see [20]). Time does not increase by a constant time step, but rather at distinct points when something interesting is happening. Instead of implementing the correct physics, we make simplifications (such as the instantaneous motion assumption above), and we replace a complex behavior by a few stochastic actions. The random variable distributions and the other various parameters involved in the simulation must be chosen carefully, and, at the moment, this has to be done empirically, by trial and error.

3.5 The Active Self-Assembly Approach

I will now summarize the approach we have been pursuing at LMR, and which we call active self-assembly. Our system is described in detail in [20], and earlier versions are discussed in [21–25].

The global goal of the system is to construct a specified shape (a polygon) in the plane. A global-to-local compiler, working off line, processes the input shape and produces, fully automatically, a program to drive the robots.

The robots are assumed to be identical, and identically programmed by a set of rules generated by the compiler. These rules are reactive, i.e., the robots have no computational state. When a robot receives a message, it consults a table of rules and executes the action that corresponds to that message. There are two main messages: one corresponds to a rule to keep growing an edge of the polygon and another to start a new edge at a vertex.

Initially, the robots are in random, Brownian motion. They could be moving under their own power, or be driven by thermal agitation of the medium. When two robots come into contact, they may exchange messages and physically connect themselves. If there is no contact, no messages propagate; conversely, if no messages are being exchanged between two adjacent robots, they will eventually detach from each other.

The boundary of the given polygon is constructed by executing the growing rules mentioned above. The interior of the polygon is built by a simple process that emulates the behavior of a porous, unidirectional membrane. When a robot hits the boundary under construction, it replaces the robot lying on the boundary, while this latter moves to the interior side of the polygon.

Our earlier work with robots driven by finite state machines ran into severe problems when we attempted to ensure that the system would repair itself in the presence of various faults. In essence, we were unable to find a strategy that would maintain consistency between the actual physical state of the robot and its computational state. For example, a sensor's faulty reading could indicate that a robot was attached to the desired structure when in fact it was not. Such inconsistencies almost invariably resulted in overall system failures.

We decided to take a different approach and completely externalized the state. In the current version of the active self-assembly system, robots have no internal state. All the necessary information circulate in the messages exchanged between adjacent robots. The new system is remarkably impervious to malfunctions—see [20] for examples—and is self-repairing. It can even self-reproduce to a limited extent. Robustness, however, came at a price: two sets of messages, grow and acknowledge messages, must now circulate. The grow messages are propagated forward, in the direction of the growth of the polygon's boundary, whereas the acknowledge messages move in the opposite direction.

The swarm algorithms and the simulation depend on a dozen or more parameters, which range from the assumed time to process a message to the standard deviations of the random variables used in the simulation. Some of these parameters can have subtle effects. Currently, most of the parameter values are determined empirically, by trial and error. This is clearly undesirable, but a better approach is yet to be found.

How well does our system perform? This is an important and simple question that does not have a simple answer. Traditionally, computer science approaches such questions by expressing the execution time of an algorithm as a function of the input size. The execution time in our case can be measured as the number of simulation time steps until the boundary of a polygon is completed or, perhaps, until some given percentage of the entire polygon interior has been filled. But how is input size to be measured? There are several possibilities, such as, for example, the number of vertices of the polygon, the number of robots needed to complete the boundary, or the total number of robots to fill the polygon. Our investigations indicate that different measures lead to substantially different results. Even more pernicious is the fact that the actual shape of the polygon has a strong impact on the performance measures. For example, two polygons with the same number of vertices may have very different execution times. In our initial work aimed at assessing the system's performance, we finessed input size issues by assuming that all the input polygons were squares of varying sizes, with the size measured as the length of a square's edge [26]. We were still left with the thorny issue of what parameter values to use. Given the large number of parameters and their nonlinear effects on performance, we chose a set of parameter values that our experience suggested as reasonable. We found that the time for completion of the polygon's boundary was roughly linear on the size of the input, but this result is subject to the numerous caveats discussed above.

Even less understood is the assessment of self-repairing and self-reproducing performance. Thus far, all we (and others) have been able to do is to present evidence that for certain faults, the system repairs itself. A more systematic approach, with quantitative measures of reliability, is needed. At a minimum, one might agree on a set of benchmarks, although it may be difficult to conceive benchmarks that apply to several systems, because the existing systems make different assumptions and are largely incompatible.

3.6 Outlook

We are currently limited by nanorobot hardware. Components such as sensors and actuators are emerging from various labs, but integration of these into systems is almost completely lacking. Power and communication are especially pressing issues. Nevertheless, I believe that swarms of autonomous nanorobots will be built in the not-so-distant future. The implications are staggering, and likely to go well beyond what we can think about today.

If we manage to solve the communication and power problems we could begin by building nanosensor networks. Deploying such networks in cell cultures, i.e., building instrumented cell systems would open new vistas in biological research by providing unprecedented capabilities for acquiring data in many modalities with high spatial and temporal resolutions. This might contribute to a dramatic increase of our understanding of biology. Eventually, nanosensor nets would be deployed in explants and the human body itself, yielding an Instrumented Body. Next, actuation would be added to the sensors. A sensor/actuator network would be very close to a robot swarm. It would be capable not only of supporting basic biological research and early detection of disease but also its treatment.

Interesting nanoswarm algorithms and systems are being investigated. How to simulate their execution with the correct physics, and how to assess their performance are areas that need more research. Finally, potential connections with developmental biology are extremely intriguing and, for the most part, not studied thus far.

References

1. Currelli M, Zhang R, Ishikawa FN, Chang H-K, Cote RJ, Zhou C, Thompson ME (2008) Real-time, label-free detection of biological entities using nanowire-based FETs. IEEE Trans Nanotechnol 7:651–667
2. Browne WR, Feringa BL (2006) Making molecular machines work. Nat Nanotechnol 1:25–35
3. Bath J, Turberfield AJ (2007) DNA nanomachines. Nat Nanotechnol 2:275–284
4. Wang J, Manesh K (2010) Motion control at the nanoscale. Small 6:338–345
5. Dong L, Nelson BJ, Fukuda T, Arai F (2006) Towards nanotube linear servomotors. IEEE Trans Autom Sci Eng 3:228–235
6. Zhang L, Abbott JJ, Dong L, Kratochvil BE, Bell D, Nelson BJ (2009) Artificial bacterial flagella: fabrication and magnetic control. Appl Phys Lett 94:064107
7. Martel S, Mohammadi M, Felfoul O, Lu Z, Pouponneau P (2009) Flagellated magnetotactic bacteria as controlled MRI-trackable propulsion and steering systems for medical nanorobots operating in the human microvasculature. Int J Robot Res 28:571–582
8. Braitenberg V (1984) Vehicles: experiments in synthetic psychology. MIT Press, Cambridge, MA
9. Dhariwal A, Sukhatme GS, Requicha AAG (2004) Bacterium-inspired robots for environmental monitoring. In: Proceedings of the IEEE international conference on robotics & automation (ICRA '04), New Orleans, LA, 25–30 April, pp 1436–1443
10. Akyildiz IF, Brunetti F, Blazquez C (2008) Nanonetworks: a new communication paradigm. Comput Netw 52:2260–2279

11. Cubukcu E, Cort EA, Crozier KB, Capasso F (2006) Plasmonic laser antenna. Appl Phys Lett 89:093120
12. Kosako T, Kadoya Y, Hofmann HF (2010) Directional control of light by a nano-optical Yagi-Uda antenna. Nat Photon 4:312–315
13. Tian B, Zheng X, Kempa TJ, Fang Y, Yu N, Yu G, Huang J, Lieber CM (2007) Coaxial silicon nanowires as solar cells and nanoelectronic power sources. Nature 449:885–889
14. Pan C, Fang Y, Wu H, Ahmad M, Luo Z, Li Q, Xie J, Yan X, Wu L, Wang ZL, Zhu J (2010) Generating electricity from biofluid with a nanowire-based biofuel cell for self-powered nanodevices. Adv Mater 22:5388–5392
15. Hogg T (2008) Distributed control of microscopic robots in biomedical applications. In: Prokopenko M (ed) Advances in applied self-organizing systems. Springer, London
16. Shen W-M, Will P, Galstyan A, Chuong C-M (2004) Hormone-inspired self-organization and distributed control of robotic swarms. Autonom Robot 17:93–105
17. Werfel J, Ingber D, Nagpal R (2007) Collective construction of environmentally-adaptive structures. In: Proceedings of the IEEE/RSJ international conference on intelligent robots and systems (IROS ‘07), San Diego, CA, 29 October–2 November, pp 2345–2352
18. Klavins E (2004) Directed self-assembly using graph grammars. Foundations of Nanoscience: Self Assembled Architectures and Devices, Snowbird, UT
19. Christensen AL, O’Grady R, Dorigo M (2008) SWARMORPH-script: a language for arbitrary morphology generation in self-assembling robots. Swarm Intell 2:143–165
20. Arbuckle DJ, Requicha AAG (2009) Self-assembly and self-repair of arbitrary shapes by a swarm of reactive robots: algorithms and simulations. Autonom Robot 28:197–211, Published online on 7 November 2009 (Published also as Tech. Rept. AR-07, Laboratory for Molecular Robotics, University of Southern California, 2007)
21. Arbuckle DJ, Requicha AAG (2004) Active self-assembly. In: Proceedings of the IEEE international conference on robotics & automation (ICRA ‘04), New Orleans, LA, 25–30 April, pp 896–901
22. Arbuckle DJ, Requicha AAG (2005) Shape restoration by active self-assembly. Appl Bionics Biomech 2:125–130 (An earlier version appeared in Proc Int’l Symp on Robotics & Automation (ISRA ‘04), Querétaro, Mexico, 25–27 Aug 2004, pp 173–177)
23. Arbuckle DJ, Requicha AAG (2006) Self-repairing self-assembled structures. In: Proceedings of the IEEE international conference on robotics & automation (ICRA ‘06), Orlando, FL, 15–19 May, pp 4288–4290
24. Arbuckle DJ, Requicha AAG (2007) Global-to-local rule generation for self-assembly and self-repair by robot swarms. In: Proceedings 4th conference on foundations of nanoscience (FNANO ‘07), Snowbird, UT, 18–21 April, pp 251–255
25. Requicha AAG, Arbuckle DJ (2006) CAD/CAM for nanoscale self-assembly. IEEE Comput Graph Appl 26:88–91
26. Tangchoopong T, Requicha AAG (2009) An empirical study of the performance of active self-assembly. In: Proceedings of the IEEE/RSJ international conference on intelligent robots and systems (IROS ‘09), St. Louis, MO, 11–15 October, pp 1838–1842

Chapter 4
Reservoir Nanoagents for In-Situ Sensing and Intervention

Mazen Y. Kanj

Abstract Nanotechnology is often associated with the alternate clean energy technologies of tomorrow, from the super efficient solar and fuel cells to hydrogen economy and the extreme lasting batteries. As only recently, the Oil and Gas industry started uncovering the great potentials of this field for its use, upstream E&P professionals need to be able to clarify facts from misconceptions and have a basic understanding of the physical phenomena that govern the behavior of things at the nanoscale. This chapter introduces the potentials of nanotechnology in E&P. It highlights current and anticipated benefits in the upstream sector and explores the feasibility of having molecular agents (Resbots) in the subsurface. The future reality of reservoir nanoagents is demonstrated in a suite of nanofluid coreflood experiments targeting stability and survivability of the nanoagents at reservoir conditions.

4.1 Introduction

The promise of nanotechnology provides fertile grounds for much of the highly thought after breakthroughs in many of the upstream E&P[1] challenges of today. The industry[2] desires strong, stable, friction-resistant, and corrosion-combatant materials in virtually all of its operations and processes (e.g., pipes, casings, drill strings,

[1] Upstream E&P is one of the major sectors of the petroleum (or oil and gas, O&G) industry. E&P refers to Exploration and Production. The sector is concerned with the discovery of, the drilling for, and the production and recovery of oil and gas from the subsurface.

[2] In this chapter, unless otherwise specified, the term industry refers to the O&G industry.

M.Y. Kanj (✉)
Saudi Aramco, Dhahran, KSA 31311, Saudi Arabia
e-mail: mazen.kanj@aramco.com

C. Mavroidis and A. Ferreira (eds.), *Nanorobotics*, DOI 10.1007/978-1-4614-2119-1_4,
© Springer Science+Business Media New York 2013

production tubings, and drill bits). These requirements lend itself more favorably to a bottom-up approach for material design and fabrication. Also, it is hoped that by employing nanofabricated particles in drilling, completion, stimulation, and injection fluids, one can drill faster, prevent or remove near wellbore damage, mineback hydraulic fractures, plug water-thief zones, reduce waterflood fingering, encourage oil production, and prevent water breakthroughs. The industry looks also to capitalize on a new set of high-pressure/high-temperature small-scale sensors that are disposable and more reliable and economical than their predecessors. It is hoped that this may soon lead to the development and deployment of sensing and intervention devices that can help delineate the waterflood front, identify bypassed oil, and map super-permeability zones in-situ in the underground. The capabilities become limitless with the possibility of having functionalized molecular agents that "illuminate" the reservoir and intervene to alter adverse transport conditions. As such, it has been stated on numerous occasions the prospect of nanotechnology in different areas of upstream E&P from the reality of corrosion resistant alloys and loss control materials to the vision of self-healing materials and look-ahead drilling agents [1–3]. Potential dream applications for reservoir nanoagents (Resbots[3]) include mapping tortuosities in the rock, identifying bypassed oil location and optimizing well placement, formulating realistic geological models of the underground, optimizing well design, delineating the extent of the asset, and target delivering chemicals to support enhanced oil recovery (EOR) objectives.

It is envisioned that waterflooding will be used to inject and displace functionalized hydrophilic nanoagents that can be interrogated for their 3D location and the in-situ reservoir environment and condition (Fig. 4.1). Remote interrogation templates could include magnetic/electromagnetic contrast agents or acoustic/seismic noise agents. Similarly, the process could postulate a nanoscale chemical delivery system to alter wettability, reduce interfacial tension, and enhance oil recovery deep into the reservoir. Means of activations in the latter case could include chemical, pH, electrical, or thermal. As such, a number of Resbot types can be postulated based on functionality and the breakups of the nanotechnology definition. The broad categories are:

Passive agents These can be thought of as a form of advanced DNA tracers. Passive agents are bar coded with the intent to cross-correlate injectors with producers in the field. These are examples of the incremental nanotechnology in upstream E&P.

Active agents These in-situ sensing agents are basically reservoir environment markers. Active agents work to capture (sense and record) the reservoir environment and perform fluid-typing activities during their journey between wells. This category is part of the evolutionary nanotechnology in upstream E&P.

Reactive agents These are in-situ intervention agents that work to rectify unfavorable hydrocarbon recovery conditions as they are encountered in the

[3]The term Resbots was coined at Saudi Aramco in 2006 to reflect on the futuristic reservoir nanorobots concept.

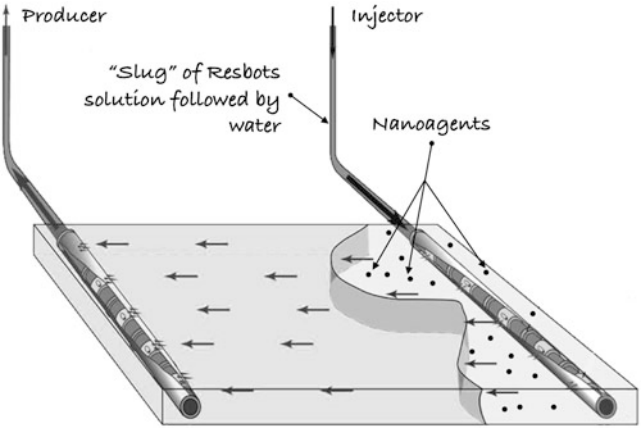

Fig. 4.1 Procedure for deploying nanoagents (Resbots) into the reservoir. It is hoped that these will be interrogated (remotely) for their location and (directly or remotely) for the reservoir environment and properties. The waterflood schematic is reworked from [4] (Adopted and reworked with permission)

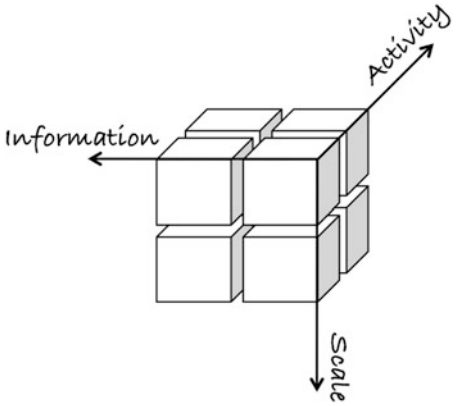

Fig. 4.2 A generalized approach to MNT in upstream E&P in the petroleum industry

underground. For example, these may act as shear-thickening agents to optimize hydrocarbon sweep efficiency or as nanocarriers to target deliver chemicals (e.g., surfactant) deeper into the reservoir. These could be classified under radical or revolutionary nanotechnology in upstream E&P.

This classification is only one dimensional in the space domain envisioned for micro-nanotechnology (MNT) applications in upstream E&P. It reflects the activity dimension in the cube of Fig. 4.2. Figure 4.2 adds two additional dimensions: the agents' scale (e.g., micro vs. nano) and its information or reporting capability (remote vs. direct interrogation). As such, sophisticated Resbots are active/reactive agents that can be interrogated remotely about its status and the underground environment. This complexity is yet magnified several folds with the capability of

these agents to propel itself beyond the constraints of the hydrodynamics of the fluid in which it resides; either by simple diffusion or via capitalizing on some form of phoretic gradients in the environment.

This chapter addresses a critical step on the road to having in-situ reservoir agents. It targets the limiting size of these devices and endeavors to reflect on their transport mechanisms in the rock matrix. It also details an experimental study on nanofluid coreflood experiments in the prolific carbonate reservoir rocks of Saudi Arabia. The study aims to test the feasibility and future reality for displacing molecular agents in the reservoir. It starts by a notion on the scaling laws and progresses to demonstrate some physics-based effects that are commonly overlooked in the macroworld but are greatly pronounced at the scale of these entities.

4.2 Nanotechnology Efficiency Index

Unlike biotechnology or information technology, nanotechnology is a scale not a domain technology. Naturally in this context, one ought to think about miniaturization and scaling. A fundamental question in this regard is: "How a nanoscale design is needed or justified?" or alternatively "What is the generated impact by miniaturization on some engineering design parameters?" This calls for a nanotechnology efficiency index, α, to be introduced. The index basically characterizes how the length scale influences the physical and mechanical properties at hand. Ultimately, this involves looking into the impact of using one, two, or several orders of magnitude change in the length scale, ℓ, on the parameters in a given objective function. (ℓ is the characteristic length scale dimension and not a length value.) For a given parameter Q, the change is introduced via a multiplier, λ, according to:

$$Q(\lambda\ell) = \lambda^{-\alpha} Q(\ell). \tag{4.1}$$

Scaling laws with negative efficiency indices (positive exponents, $-\alpha$) become more important as things get larger with $\lambda > 1$ (e.g., $\lambda = 10^3$). On the other hand, scaling laws with positive efficiency indices become more important as things get smaller with $\lambda < 1$ (e.g., $\lambda = 10^{-3}$). In this context, we are assuming that the same material properties are maintained over different length scales. For example, the material density and the fluid viscosity do not change as the engineering design is made smaller. The objective is to find "back-of-the envelop" means to effectively estimate how the characteristics of something improve or inhibit performance as its dimensions change. Scaling laws are intended simply as rules-of-thumb to help us understand the behavior and the different modifications of physical effects in the transition from the macro- to the micro- and ultimately to the nano-worlds [5, 6]. In general, miniaturization brings on multifunctionality in the same volume, $V \propto \ell^3$, or weight, $W \propto \ell^3$, of the material.

$$V(\lambda\ell) = \lambda^3 V(\ell). \tag{4.2}$$

For example, molecular electronics (or moletronics) may yield a 100-fold improvement in the linear scale of the transistor (i.e., $\lambda = 0.01$). Volumetrically, this translates into a million-fold improvement in the number of circuitry. Macroscale sensing and intervention assemblies can barely fit in the slim-sized oil and gas wells of today. Similarly, the intricate micro and sub-micro scale pathways of the reservoir are practically off-limits to anything exceeding few hundred nanometers in size. This issue will be revisited in later sections in the chapter with more detail and specificity.

At small scales, both the inertia effects and the object mass are small. Accordingly, products can perform tasks faster at minimal power consumption. In addition, the surface effects dominate at this level. This is true as the surface to volume ratio, S/V, is inversely proportional to ℓ. The surface to volume ratio is a mean to predict power and energy consumptions of things. Scalewise, it is equivalent to the total strength[4] to weight ratio and reflects the power density, P_{D}, of the object. Accordingly,

$$P_{\mathrm{D}}(\lambda\ell) = \lambda^{-1} P_{\mathrm{D}}(\ell). \tag{4.3}$$

Using this logic, one may conclude that a group of one thousand cubical nanomachines each having a side of 100 nm provides 10 times the power output of a single $1\,\mu\mathrm{m}^3$ cubical micromachine though both groups occupy the same bulk volume in space. Nanoscale electric motors may have an astonishing power density on the order of $1\,\mathrm{MW/cm}^3$ [7].

Some of the implications of scaling laws in porous media for the transport of fluids maybe illustrated by examining Darcy's equation (or alternatively the Hagen-Poiseuille equation in fluid mechanics that addresses the flow of fluids in pipes). This is a simple proportional relationship between the instantaneous discharge rate through the porous medium and the pressure drop over a given distance.

$$q = -\frac{k}{\mu}\frac{\Delta P}{L}. \tag{4.4}$$

The total pore fluid discharge per cross-sectional flow area, q, is equal to the product of the hydraulic permeability of the rock medium, k, and the pressure drop, ΔP, all divided by the fluid dynamic viscosity, μ, and the length, L, the pressure drop is taking place over. This value of flux can be related to the pore fluid velocity through the intrinsic porosity of the formation. Thus, $\Delta P/L \propto \ell^{-2}$ and reducing the average pore throat radius by a factor of 10 (i.e., $\lambda = 0.1$) leads to 100-fold increase in pressure drop per unit length (as $\alpha = 2$). This is an important design problem and the reason that engineers have devised alternative methods of pumping at the micron and submicron scales (e.g., electrohydrodynamic pumping including electro-osmotic and electrophoretic pumping such as the one demonstrated in Fig. 4.3).

[4]Given constancy of stress and material strength, the strength of a structure and the force it applies scale with the object's cross-sectional area (i.e., Strength $\propto \ell^2$).

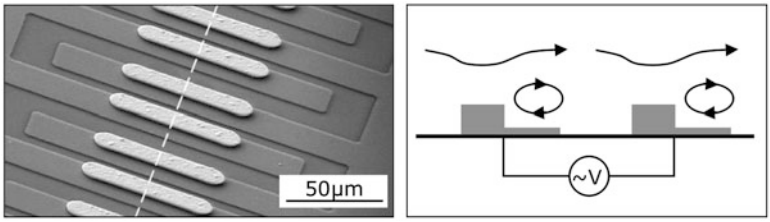

Fig. 4.3 A 3D electroosmosis micropump. The design allows high-speed flows through microchannels with an input of only a few AC volts of electricity [8] (Adopted with permission)

4.3 Some Physics-Based Effects

At the nanoscale, different forces become dominant over those experienced in everyday life at the macroscale. The effects that become dominant at the small scale include laminar flow, diffusion, stickiness, surface area to volume ratio (ρ_{sv}), and surface tension [9]. Also, electromagnetic rather than either inertia or gravity effect dominates, and overall quantum rather than classical mechanics applies.

4.3.1 Low Reynolds Number

At the nanoscale, the Reynolds number, Re, is extremely small. The Reynolds number is the dimensionless ratio of inertial forces to viscous forces, and consequently, it quantifies the relative importance of these two forces for given flow conditions. At small scales, viscous forces dominate.[5] Smaller objects generate smaller inertia forces and are less capable to drive adjacent layers of fluid past each other. In fact, it can be easily shown that $\text{Re} \propto \ell^2$. Relying on the previously defined scaling equation (Eq. 4.1), one concludes that, for example, while the Reynolds number for a human being might be 10^4, this number goes down for a small goldfish to about 100 and for a bacterium to a mere 10^{-4}. A bacterium is roughly a million times smaller than a human being. A bacterium feels water a million times more viscous than what a human being would feel it like. And water to a bacterium feels like molasses or treacle to a human being. This is why at this scale, bacteria and viruses do not have arms and legs to swim. They have flagella with a corkscrew-like propulsion system which is more efficient in this medium for their size.

[5]Typically, Re is much less than 1 at the nanoscale [10] and much less than 100 at the microscale [11].

4.3.2 Brownian Universe

Although a nanoscale entity (nanoagent) cannot swim freely and steer itself in the reservoir medium, this does not mean that it stays stationary in the fluid. It will be constantly undergoing random jolts called the Brownian motion effect. This effect is discovered by a botanist named Robert Brown in 1827. He noted that tiny objects (pollen particles floating in water) appear to be undergoing continuous random motion jiggling. This is due to the constant bombardment of a microscopic object by atoms and molecules in the fluid medium. Brownian motion is inescapable at the nanoscale. Most importantly, one cannot engineer around this effect, as it is a property of the medium not the object.

4.3.3 Stickiness

At the nanoscale, electromagnetic (EM) forces of adhesion are dominating in importance. Various manifestations of these forces are known as van der Waals forces, London dispersion forces, and Casimir effect. These are negligible at the macroscale but dominating at the nanoscale. van der Waals forces arise between molecules that are nanometer apart. London dispersion forces (part of the van der Waals forces) are temporary electrostatic attractions between two atoms or molecules. Casimir forces is the attraction between plates that are nanometer apart (even grounded plates with no charges) due to the wave nature of quantum particles outside and inside the plates. For example, geckos and spiders capitalize on nanoscale setules to generate adhesive forces strong enough to counterbalance up to 170 times their weight on the smoothest of surfaces. The key challenge in Resbots is not making the active or reactive agents. It is rather in creating agents with the proper functionalities and surface chemistry that can secure their long-term colloidal stability and survivability in the harsh reservoir conditions. These conditions include 100 °C or more temperature and 120, 000 ppm or more salinity with both monovalent and divalent ions and varying rock charges.

4.3.4 Surface Tension

Finally, there is the high surface or interfacial tension arising at the interface between two phases (e.g., liquid–liquid or liquid–gas). Surface tension is the result of cohesion between liquid molecules at the interface. The smaller the object, the more difficult it becomes for it to break this interface. A water strider standing on the surface of the water creates dents on the surface without breaking this interface. This situation is definitely more pronounced with a nanoagent that is 5 orders of magnitude smaller than a water strider. While a nanoagent cannot swim like a fish

in water, it definitely cannot jump out of the water (or cross the oil-water interface) like a dolphin. Though physical jumping across the interface by these nanoagents is not plausible, chemical partitioning of the agents between the different phases is very much possible.

4.4 Proposed Nanoagent Model

The previous section highlighted the difficulties associated with living at the nanoscale. However, this is not to be misinterpreted as a call to abandon the Resbots dream. If and whenever possible, nanoagents will have to be properly designed and functionalized around or with consideration of these constraints for them to overcome and maybe "adapt" to these challenges. Our Resbots lead a life dominated by viscous forces. Though possible, it is unlikely that in the coming few years, the industry will demonstrate a form of nanoagents with motorized mobility. For the time being, the nanoagents' mobility remains passive or possibly driven by a phoretic gradient. Our Resbots live in a Brownian universe. Brownian motion is a characteristic of the medium and not of the system. (Thus, one cannot engineer around it [12].) Though it is neither expected nor desired, Resbots cannot perform intervention tasks with "atomic" precision in the underground. Our Resbots reside in a sticky environment. Surface chemistry will have to play a major role in the agents' stability and dispersion in the fluid medium and the agents' compatibility as they come in contact with the reservoir rocks in-situ. This has been mastered in other disciplines but has yet to be proven in a reservoir environment for the upstream E&P. The experimental research initiative described in the following sections is a first but critical step in this regard.

Many of these concerns have already been examined and partially addressed in domains like pharmacology for drug delivery in biological systems. The nanoagent model featured in Fig. 4.4 is a general nanocarrier design. Nanocarriers work by bringing drugs directly to diseased parts of the body. It has an inorganic core and an organic corona or shell. The thickness of the corona is usually in the order of 2–10 nm. The core can be as small as 5 nm or as large as few 100 nm. The core emits or is tagged to emit a strong fluorescent signal following the excitation by a specific wavelength of light. The corona can be functionalized to allow attaching peptides to make the agent stealthy to the body immune system or antibody to help it find its way to diseased cells in the body. Bioactive/sensing molecules can be attached to the shell to help monitor pH changes and detect specific enzymes for use as a trigger mechanism for drug delivery. Basically, this model exhibits many of the sensing and intervention capabilities that we desire in our reservoir nanoagents. These agents are designed to go into the cell's body. It is also possible to manipulate the hydrophilicity of the ligands on the corona to allow varying degrees of partitioning of these agents between the oil and the water phases or for them to reside at the interface. The analogy and relevance to the oil industry becomes

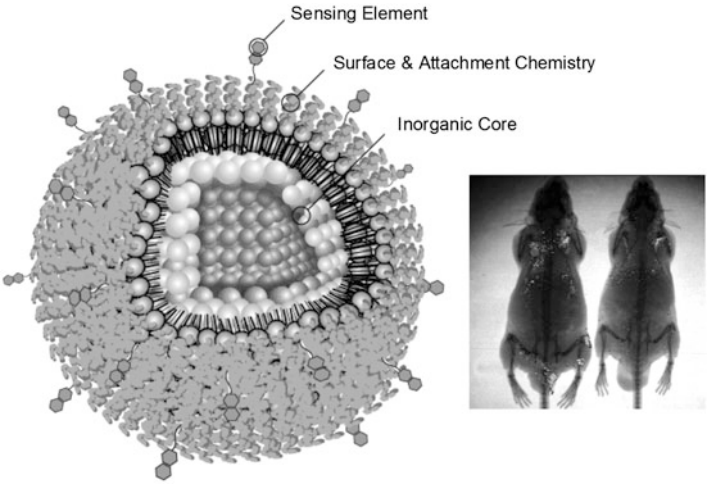

Fig. 4.4 A nanoagent model in the life sciences. Injected into a mouse, these stick to the tumor in the mouse's body glowing red under IR light (Image Courtesy of Evident Technologies. Adopted and reworked with permission)

even more evident when one compares the blood in a biological system to the brine (sea)water that we inject into the reservoir and the human fatty cells in the body to the oil present in the reservoir. However, though that these nanoagent models of the pharmacology and life sciences have many of the functionalities that the O&G industry strives for, these neither have the proper material structure nor have a ready-made design for immediate use in the oil reservoir. Merely, these constitute research subjects of adaptation but not off-the-shelf/ready-made solutions.

4.5 Experimental Program

Logically, having nanodevices that can function in-situ in the oil and gas reservoir underground will require first and foremost determining the maximum usable size of these devices before attempting to develop interrogatable (passive) nanosensors or steerable (active) nanomachines. And this critical step requires (1) making an assessment of the rock's pore throat size distribution to establish a rough estimate on a usable size or size range for these agents, (2) formulating stable, uniform, and inert nanoparticles suspensions with narrow distributions of different particle sizes, and (3) conducting coreflood experiments to validate the particles' stability and their transport continuity under realistic conditions. Conceptually, a coreflood experimental procedure involving nanofluid is rather simple. It involves injecting a slug (about one-tenth of a pore volume or 1 cc) of a well characterized nanofluid

solution at one end of a core sample[6] and follows this with continuous injection of particle-free water or brine. The effluent fluid at the other end of the core is then monitored and characterized for its content in nanoparticles. As such, it is hoped to formulate an idea on the transport potential of these particles within the rock matrix. In the particle concentration vs. injected volume plot, the influent response is a Heaviside step function and the effluent response is generally a skewed bell-shaped function. Though the concept is simple, the process is rather involving. The rest of the chapter elaborates further on the elements that are ultimately geared toward testing the concept in the field [13].

4.6 Pore Size Characterization

The Jurassic Arab-D is the most prolific oil-bearing formation of the Ghawar field in the Kingdom of Saudi Arabia. Ghawar is the largest oil field discovered in the world today. From its northern extremity, the field extends southward some 150 miles (240 km) as essentially one long continuous anticline, about 25 miles (40 km) across at its widest point. As such, the Arab-D formation was picked as the subject of this study. The Arab-D is predominately a bimodal pore system that spans the skeletal-oolitic, Cladocoropsis, stromatoporoid red algae coral, and bivalve-coated grain-interlast lithofacies. A cross-sectional sampling of high-pressure mercury injection tests that were performed on nearly 850 Arab-D core plugs from different parts of Ghawar is shown in Fig. 4.5 (see also [14]). The histogram illustrates the partitioning of pore throat sizes in this dominant distribution. The two general peaks of the response are located around 40 μm (a macro-sized pore network system) and 0.8 μm (a microsized pore network system). This fact is further supported by the pore cast inset (adopted from [15]) in Fig. 4.5. As a preliminary rule-of-thumb, one may set a 500 nm upper usable limit for nanoagents because the limit covers all samples in the macro-system as well as the majority (more than 90 %) of the samples in the micro-system. The 500 nm size is a starting upper limit of the nanoparticles for direct plugging. Obviously, any particle larger than 500 nm will have a very slim chance of staying mobile in the microsized pore network systems of the rock. Smaller particles in large enough quantities or concentrations may also come together to form a bridge across the pore-throat entry and impact the rock permeability. ("Bridging" is a well-known phenomenon in sanding mitigation and the design of sand control measures in producing wells.) This sets the usable size of the nanoagents well below the 500 nm limit. A second rule-of-thumb is needed. This one limits the size of the nanoparticles in solution to $\frac{1}{7}$th to $\frac{1}{5}$th the critical pore throat size (i.e., 70–100 nm range).

[6] A rock core plug measures about 1.5 in. in diameter and 3 in. in height.

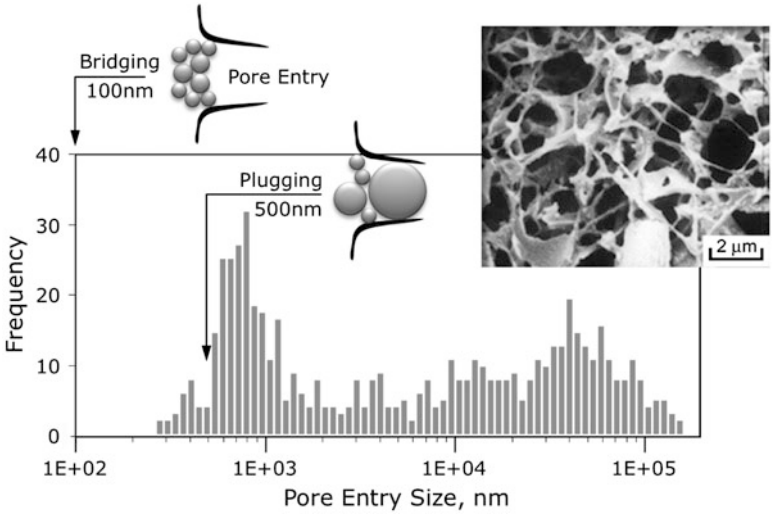

Fig. 4.5 A bimodal response of the pore size distribution in the Arab-D. The nanoparticles' upper size limit for direct plugging is inferred at about 500 nm and for bridging at about 100 nm. The inset SEM image of an Arab-D pore cast is adopted and reworked with permission from [15]

4.7 Nanoparticle Suspensions

Nanoagents should be safe to handle and dispose of. They should be environmentally friendly so that they can be injected into reservoir formations with little or no concern. The particles should be stable in suspension, should remain dispersed in solution, and should have little or no affinity (tendency to get adsorbed) to the carbonate rocks of the Arab-D under reservoir conditions. The stability should be measured in years instead of days or weeks. A host of potential nanoparticle solutions were examined. The requirement on surface chemistry sophistication to properly suspend particles is also a key controlling factor in the selection of any one particle type. Copolymer suspensions satisfied the majority of the set conditions for preliminary testing under room temperature conditions. These are polystyrene beads cross-linked with di-vinyl benzene (DVB) solubilized in ultra pure water. One polymeric nanoparticle type was provided in solution as water turbidity standards. Samples with 50, 500 and 800 NTU turbidity values are demonstrated in Fig. 4.6b. A scanning electron micrograph (SEM) of an evaporated solution with a reported turbidity of 500 NTU is shown in Fig. 4.6d, e. Though we confirmed the particles mean size and size distribution in solution, particle concentration in relation to turbidity was not possible. Accordingly, the test results obtained with this fluid using an in-house turbidity meter were more qualitative than they were quantitative. Next, we opted for research grade solutions. These included white latex spheres (Fig. 4.6c) and colored fluorescent latex spheres (Fig. 4.6a) [16]. The polymer microspheres were acquired commercially from Duke Scientific Corporation (Thermo Fisher

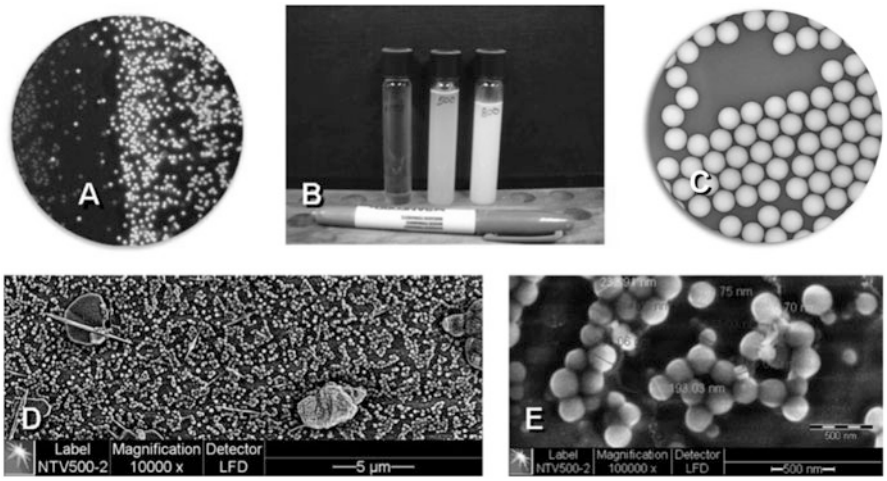

Fig. 4.6 General purpose commercial latex particles (polymer microspheres) were used in the coreflood experiments. These included Fluorescent polymer beads (**a**), turbidity standards as cross-linked copolymer microspheres in ultrapure water (**b**), and calibration latex particles (**c**). Insets (**d**) and (**e**) demonstrate scanning electron microscopy images of the turbidity standard nanofluid solution with an average particle size in the order of 120 nm

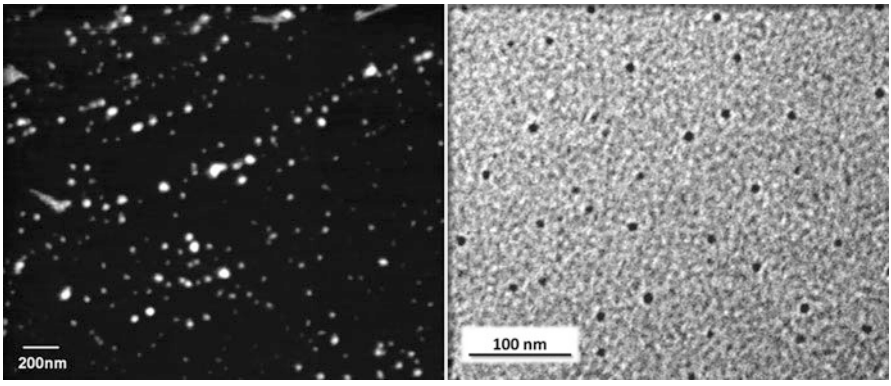

Fig. 4.7 AFM (*left*) and TEM (*right*) images of the A-Dots. These demonstrate a particle size in the order of 5–10 nm

Scientific). Ultimately, specialized carbogenic nanoparticles proved to be most reliable for in-situ reservoir conditions. These are made inherently fluorescent and named Arab-D Dots, or A-Dots (Fig. 4.7) [13]. They are developed with a functional stability to survive a lengthy transit in the harsh environment in an oil reservoir, and which can be read and interrogated reliably when the nanoparticles are recovered. This translates into required stability at temperatures exceeding 100 °C and salinities exceeding 120, 000 ppm in total dissolved solids (TDS) in the presence of divalent (as well as monovalent) ions such Ca^{++}, Mg^{++} and SO_4^{--}.

4.8 Coreflood Experiments

The experimental process starts with a well-characterized (cylindrical) rock plug sample. The sample is mounted in the coreflood apparatus and a 3, 000 psi confining pressure is applied. Up to 40 pore volumes (PV) of ultrapure water is then injected at flow rates up to 6 cc/min through the sample to fully saturate the sample, mobilize the fines, and establish a base permeability. A slug (of varying amount) of the nanofluid is injected on one end of the core followed by continuous injection of particle-free water. Then, the effluent is sampled and characterized using dynamic light scattering and asymmetric flow field-flow fractionation (qualitative measurements) and a photospectrometer or a fluorometer (quantitative measurements). This allowed making an assessment on how much of the particles are getting trapped in the core. During testing, the change in pressure is monitored constantly in order to get an idea on the change in permeability of the core. Following each test, the core plug is dismounted from the coreflood apparatus, the sample is sliced, and pieces of the rock is taken at different distances from the inlet end of the sample for environmental SEM analysis. This allowed characterizing the nanoparticles' morphology inside the sample as well.

The experimental procedure is supported by an optimized testing program (Fig. 4.8). Coreflooding starts with a continuous injection of particle-free water or brine after injecting a slug of the nanoparticle fluid (WAN test) (The slug volume varied from 5 % to 100 % of the total pore volume of the core sample at hand.).

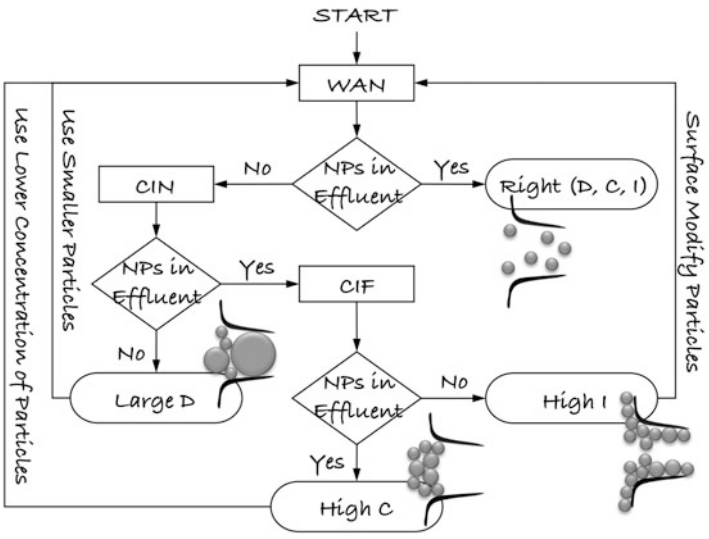

Fig. 4.8 Nanofluid coreflood testing program. The program involves three types of tests: a WAN test that follows nanofluid injection with water; a CIN test that continuously inject nanofluid into the core sample; and a CIF test that continuously inject particle-free water into the core

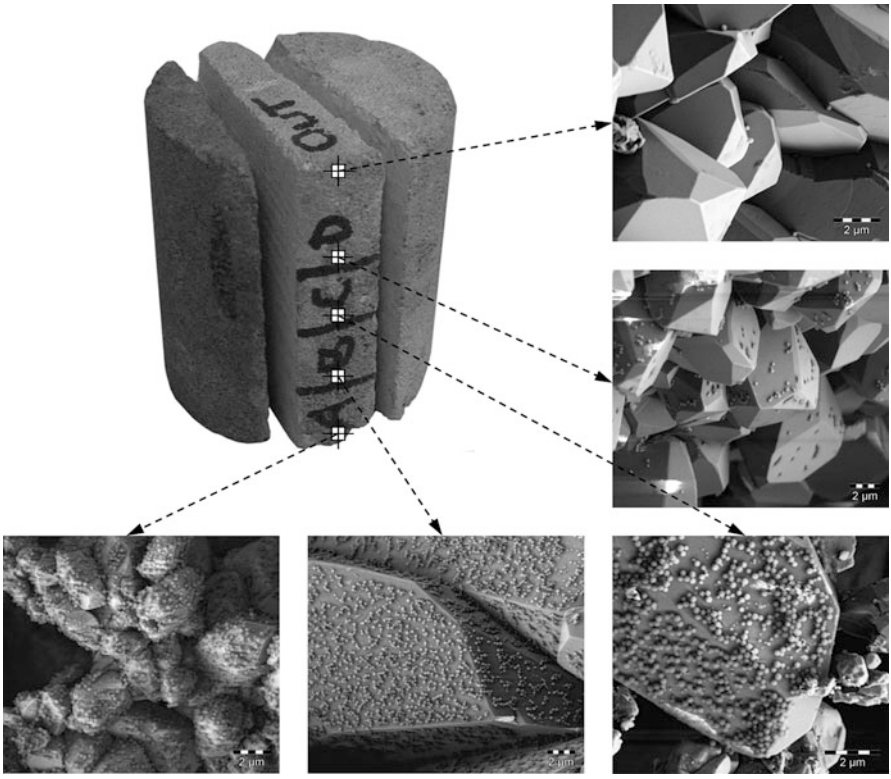

Fig. 4.9 Environmental SEM results from a coreflood test using a commercially acquired polymeric nanofluid with a mean particles size in the order of 100 nm

If nanoparticles are not detectable in the effluent during a WAN test, a continuous injection of nanofluid is attempted (CIN test). Now, if nanoparticles were detected in the effluent during the CIN phase, continuous ultrapure water injection is applied (CIF test). This multistage heuristic process is needed to establish the suitability of a particle size and concentration selection and identify any interaction affinity to the rock carbonate matrix.

At any given water injection rate, one of four outcomes maybe reached. These are demonstrated in Fig. 4.8. The first outcome is indicative of a successful test with the right combination of particle size (D), particle concentration (C), and minimal particle-rock interaction level (I). The remaining outcomes are indicative of plugging, bridging, or interaction problems. Interaction between the nanoparticles and the rock matrix is probably the most critical as the nanoagents would need to be properly refunctionalized.

The rock sample demonstrated in Fig. 4.9 was tested using a commercially acquired 100 nm copolymer beads solution. WAN testing at varying injection rates demonstrated no nanoparticle flow on the effluent side. Similar tests on plugs from

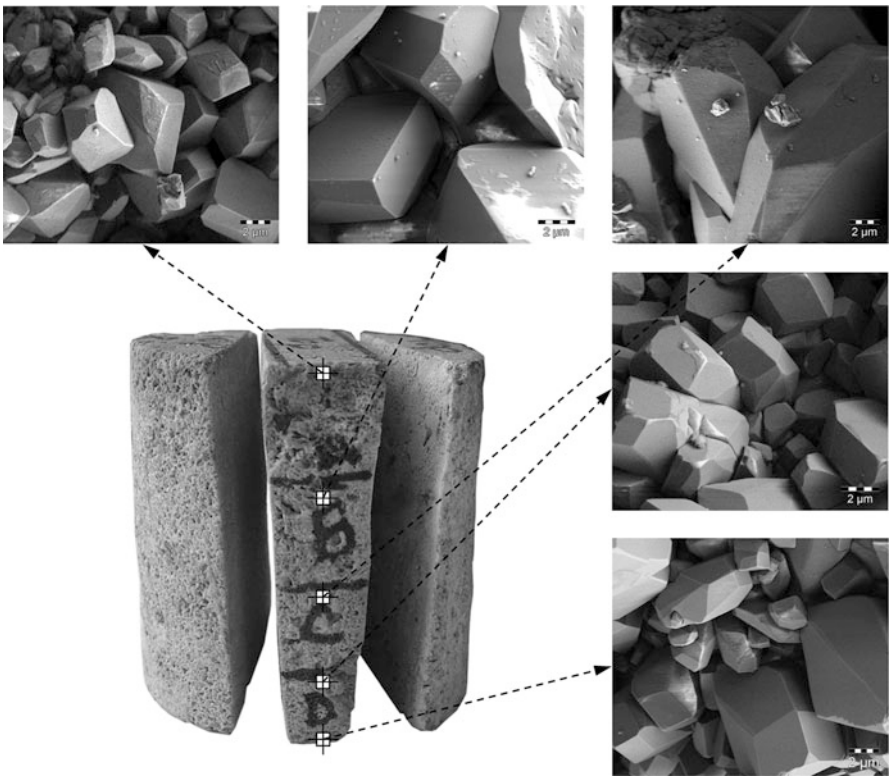

Fig. 4.10 Typical images from a successful nanofluid coreflood test. The SEM micrographs demonstrate that the sample is practically particle-free

the same core added that particles are detectable in CIN but not in CIF testing. This fact led us to conclude that there is high interaction between the particles and the carbonate matrix. The resulting particle retention was viewed using the environmental SEM images taken from the inside of the rock at different distances from the inlet. These images and their location in the sample are shown in the figure. In Fig. 4.9, "A" marking indicates the inlet end (injection side) of the core. The photomicrographs show reduced particle deposition with increased distance from inlet. In slides closer to the inlet end of the core, the particles coated the carbonate crystals in a fashion similar to chicken pox. Stability tests conducted in our labs demonstrated the flocculations and agglomerations that took place in the original solution in the presence of salt and carbonate fines (limestone). Instabilities were also confirmed by examining the absorbance spectra generated following mixing the nanofluid in the synthetic injection seawater or synthetic Arab-D connate water. By placing PEG/polymer chains (ligands) on the surface of the nanoparticles, the modified solution is rendered favorably stable in the medium (Fig. 4.10) at the targeted experimental conditions.

4.9 Summary and Outlook

Reservoir nanoagents are the ultimate dream tools for the upstream industry. They may help delineate the extent of the assets, map tortuosities in the rock, layout super-permeability pathways, map fractures and faults, identify bypassed oil locations in the field, optimize well placement and design, generate realistic geological models of the asset, and may be used for chemical delivery deep into the reservoir to support EOR objectives.

To test the future reality of having active/reactive nanoagents in the reservoir, a series of nanofluid coreflood experiments were run on carbonate samples from the Arab-D formation. The aim of these tests is to correlate transport potentials with size and concentration of the nanoparticles in suspension. These experiments supported the possibility of having the right functionalization, size, and concentration of the particles to maintain the mobility of the nanoparticles in the reservoir. A critical step on the road to having in-situ reservoir nanoagents (sensors or devices) to illuminate the reservoir has been established.

Proper functionalization or surface chemistry is a crucial first step on road to realizing the reservoir nanoagents' concept. It enhances the nanoparticles' stability, reduces flocculation/aggregation, enhances colloidal homogeneity, and most importantly reduces the nanoagents' interaction with the rock matrix. In the near-term plan, the nanoagent concept could simply be materializing as smart tracers and in-situ reservoir chemical markers. In the medium term, however, this could enable traceable nanofluids and chemical delivery agents. And on the long run, the concept will mature to realize remotely interrogatable nanosensors and maybe even steerable nanomachines to undertake real intervention tasks in the reservoir.

References

1. Kanj MY (ed) (2008) Nanotechnology in Upstream E&P: Nano-Scale Revolutions to Mega-Scale Challenges? Workshop Report, SPE Applied Technology Workshop. Dubai, U.A.E.
2. Saggaf MM (2008) A vision for future upstream technologies. J Petroleum Tech, March, 54–98
3. Sanni M, Kamal R, Kanj MY (2008) Reservoir nanorobots. Saudi Aramco J Technol, Spring, 44–52
4. Brouwer DR, Jansen JD (2004) Dynamic optimization of water flooding with smart wells using optimal control theory. SPE J 9(4):391–402
5. Wautelet M (2001) Scaling laws in the macro-, micro- and nanoworlds. Eur J Phys 22:601–611
6. Rogers B, Pennathur S, Adams J (2008) Nanotechnology: understanding small systems. CRC Press. 398pp
7. Phoenix C (2004) Responsible nanotechnology: scaling laws–back to basics. Science and Technology Essays from CRN. Series 7
8. Urbanski JP, Levitan JA, Burch DN, Thorsen T, Bazant MZ (2007) The effect of step height on the performance of three-dimensional AC electro-osmotic microfluidic pumps. J Colloid Interface Sci 309:332–341
9. Beebe DJ, Mensing GA, Walker GM (2002) Physics and applications of microfluidics in biology. Annu Rev Biomed Eng 4:261–286

10. Cavalcanti A, Hogg T, Shirinzadeh B (2006) Nanorobotics system simulation in 3D workspaces with low Reynolds number. In: Proceedings of the IEEE international symposium on micro-nanoMechatronics and human science. Nagoya, Japan, 05–08 Nov
11. deMello AJ (2006) Control and detection of chemical reactions in microfluidic systems. Nature 442(7101):394–402
12. Jones RAL (2004) Soft machines. Oxford University Press, NY
13. Kanj MY, Rashid MH, Giannelis EP (2011) Industry first field trial of reservoir nanoagents. SPE-142592. In: 17th middle east oil & gas show and conference. Manama, Bahrain, 25–28 Sep
14. Clerke EA (2007) Permeability and microscopic displacement efficiency of M1 bimodal pore systems in Arab-D limestone. SPE-105259. In: 15th SPE middle east oil & gas show and conference. Manama, Bahrain, 11–14 Mar
15. Cantrell DL, Hagerty RM (1999) Microporosity in arab formation carbonates, Saudi Arabia. GeoArabia 4(2):129–154
16. Kanj MY, Funk JJ, Yousif Z (2009) Nanofluid coreflood experiments in the Arab-D. SPE-126161. In: SPE Saudi Arabia section technical symposium and exhibition. Alkhobar, Saudi Arabia, 09–11 May

Chapter 5
Miniaturization and Micro/Nanotechnology in Space Robotics

Evangelos Papadopoulos, Iosif Paraskevas, and Thaleia Flessa

Abstract Space is an exciting but fundamentally unfriendly environment for humans. Space robotic systems (robots in orbit, planetary rovers, or even satellites) are of great importance to space exploration and perform tasks hazardous or impossible for humans. Using micro and nanotechnologies in space robotic systems results either in miniaturized systems in terms of volume and mass, while retaining or increasing their capabilities, or in space robots with increased capabilities while retaining their size due to the nature of their tasks. Examples of miniaturization possibilities for space robots and satellites are given, focusing on the challenges and the enabling technologies. The miniaturization process and the use of advanced micro and nanotechnologies in space will have a large beneficial impact in the years to come.

5.1 Introduction

Space is an exciting area of activities for mankind. These activities allow us answering fundamental questions about the origins of the universe, assist our life on earth (e.g., meteorological and GPS satellites), and improve our scientific and technological capabilities resulting in a wide range of inventions and new processes. However, space is a highly unfriendly environment for humans. Harmful radiations, extreme temperatures, lack of suitable or lack of any atmosphere, huge distances to be covered, and long communication lags and interruptions are only a few of the

E. Papadopoulos (✉) • I. Paraskevas • T. Flessa
Department of Mechanical Engineering, National Technical University of Athens,
9 Heroon Polytechniou Street, 15780 Athens, Greece
e-mail: egpapado@central.ntua.gr; isparas@mail.ntua.gr; tflessa@mail.ntua.gr

C. Mavroidis and A. Ferreira (eds.), *Nanorobotics*, DOI 10.1007/978-1-4614-2119-1_5,

© Springer Science+Business Media New York 2013

factors that render space a hostile environment for humans. It is well known that the need for astronaut extravehicular activities (EVA) increases the cost of a mission dramatically, due to the life support systems and precautions that must be taken to ensure astronaut safety during EVA.

A solution to these problems is the use of robotic devices, capable of operating for long times with minimum supervision or even autonomously. Such devices have been developed during the last 50 years and include robotic spacecraft, on-orbit robotic arms, rovers for planetary exploration, robots for space structures, and satellites. Additional plans for robotic space hardware of all types are in the development phase. Clearly, the future of space exploration and commercialization will include robots as a vital enabling technology.

Space robotic devices tend to be very big in size. For example, in orbital systems, the Canadarm of the Space Shuttle is 15 m long, weighs 431 kg, and handles payloads up to 14 tons [1]. The reason is that it must be able to handle satellites and other equipment, which are of large dimensions due to the instruments they carry, or due to the need for being compatible with the human scale. For exploration systems, the small Sojourner Mars rover was also at the human scale, weighing about 10.6 kg with its dimensions being 0.65 m high, 0.30 m wide, and 0.48 m long [2]. Subsequent rovers were bigger and heavier by at least one order of magnitude due to the need for carrying instruments and for traveling larger distances.

On the other hand, on earth an important current trend is miniaturization of devices and processes and the capability of acting at very small scales, including and in some cases less than the nanoscale. Such miniaturization offers significant gains in volume, mass, and power for devices; leads to materials with unparalleled properties; and capabilities of intervening at the cell level. Miniature mobile robots at the scale of a few cm and with resolution of a few microns have been developed to provide mobile microinstrumentation, to assist in cell manipulation in biological experiments, and in micromechanism or microelectromechanical system (MEMS) assembly. Besides mobility, these robots include capabilities such as object manipulation with force feedback, two way communications, onboard controllers, visual feedback, and significant power autonomy. In addition to the above developments, smaller robots operating at the nanometer scale are being envisaged. The size of such nanorobots may be in the range of 0.1–10 μm and could be implemented through the use of controlled biological microorganisms [3] or the use of magnetic nanocapsules steered by improved gradient coils provided by magnetic resonance imaging (MRI) systems [4].

A natural question appears then regarding the degree to which space robotic activities are affected by the miniaturization trend observed on terrestrial applications in general, and more specifically in robotics. One can identify similarities and differences. For example, in robotics the terms micro or nano refer either to the size of the robot itself in terms of micrometers or nanometers, or to the resolution in micrometers or nanometers that this robot has in dealing with its environment. This is because human scale robots that operate in human scale tasks are taken as the basis for comparison. However, in space the scale of tasks is very different and to be more exact, much bigger. Both space exploration and orbital systems scales in

terms of orbits, distances, power requirements, etc. are very large compared to the terrestrial human scale. Therefore, despite the evolving miniaturization process, the same terms refer in most cases to different scales of magnitude. This can be seen clearly in the case of nano or even picosatellites, both of which will not qualify as such according to terrestrial robotic terminology.

Miniaturization affects space robotic systems in two fundamental ways (a) by reducing the size and weight of components, thus allowing a space robotic system to increase its overall capabilities by maintaining more or less its size and (b) by reducing its overall size, maintaining the same capabilities. In the first case, the robotic system cannot be reduced in size, because the objects it operates on remain of large size, for example the case of the International Space Station (ISS) robotic manipulators. In the second case, the size can be reduced by maintaining more or less, the initial capabilities; this is the case of nanosatellites. As mentioned earlier, the base scale is large enough so that any size reductions at the device or component scale will not qualify as nanodevices on earth.

In the subsequent sections, we examine the existing space robotics applications and classify the robots that are being used. The ways in which these robots can be miniaturized, using our terrestrial experience are addressed. The interesting subject of satellite miniaturization and subsequent proliferation is presented next. Finally, we outline the future trends for miniaturization of space robotics systems and components and address briefly the challenges ahead.

5.2 Space Robotics Applications

Usually the term space robotics is used to characterize semi or fully autonomous, teleoperated exploration and servicing systems, and a few specialized experimental systems. However on a broader sense, almost everything that has been sent into space, integrates a form of automation in some degree, and therefore can be characterized as “automated” or “robotic.” The emphasis here is given to systems that are flight proven, they still operate, or are in the final construction phases and the state of the art in their class.

5.2.1 Exploration

From the very beginning of the space exploration age, rovers were considered as the main exploration platform and appeared early in the space programs of both the USA (with the Surveyor Lunar Rover Vehicle, 1963) and the USSR (with Lunokhod, 1970). The former program was canceled and substituted by the Lunar Roving Vehicles of the Apollo program, while the latter (Lunokhod 1 in 1970) was the first remote controlled rover to land on the moon [5]. NASA has also sent to the Moon stationary explorers (Rangers and Surveyors [6]).

Table 5.1 Characteristics of different rover generations from JPL

Rover	Mass (kg)	Instrument mass (kg)	Average speed (m/h)	Distance traveled (km)	Largest object over (m)	Approx. volume (m^3)
Sojourner (1996)	10.6	<4.5	3.5	≈0.1	N/A	$0.7 \times 0.5 \times 0.3$
MER (2003)	176.5	6.8	34.0	Spirit ≈ 8, Opportunity >28	0.26	$1.5 \times 1.6 \times 2.3$
MSL (2011)	900.0	80.0	30.0	N/A	0.75	$2.7 \times 3.0 \times 2.2$

Since the late 1970s, the exploration focus turned to Mars and other distant bodies. At first, it was necessary to achieve the goal of reaching the target, e.g., the Viking Landers in 1975 [7]; however, it appeared soon that the scientific objectives should not be limited to the landing area. Time delays due to the distance to Mars rendered teleoperation impossible; this paved the way for semi and fully autonomous systems. Due to technological limitations, early designs such as Marsokhod and Robby were massive and frequently impossible to fit in the available launchers [8]. Smaller systems could not be autonomous and/or integrate adequate scientific instrumentation.

The radical changes in microtechnology enabled prototype miniaturization, which led in 1996 to the first flight proven planetary explorer with advanced capabilities, the Sojourner Rover [2]. After some unsuccessful efforts, the Mars Exploration Rovers Spirit and Opportunity were sent to Mars in 2003 [9]. The two identical rovers were larger than the Sojourner; however, they included more scientific instrumentation and were capable to travel for kilometers. Today, rovers are a main programmatic goal of all space agencies. Primary missions include the Mars Science Laboratory (MSL, 2011) [10], and the ESA and Roscosmos ExoMars Rovers Mission (est. launch 2018), still in the design phase [11]. Stationary explorers, such as ESA's Beagle 2 [12] and the successful Phoenix Mars Lander [13] were and still are in agency programmatics.

A number of alternative concepts are tested for planetary exploration, which include surface explorers based on legged locomotion [14, 15], the exploitation of swarm capabilities [16, 17], or flying systems [18]. However, no such working prototype that has operated in space exists currently. Planetary orbital explorers, such as the Mars Odyssey, are examples of relatively small autonomous systems [19]. Other interesting concepts in this category include those that release a landing probe (to a planet, asteroid, or comet) like Cassini-Huygens [20], Deep Impact-EPOXI [21] and Rosetta [22], or that land themselves, such as NEAR Shoemaker [23] and Hayabusa [24].

From the above examples, a trend is observed, from the large and massive systems to the small and lightweight ones and again towards larger exploration rovers, the difference in mass is obvious; Table 5.1 and Fig. 5.1 show clearly this trend as exhibited by NASA's rovers. The first rovers were large because of the then available technology. The development of microtechnology enabled miniaturization

Fig. 5.1 Full-scale models of three generations of exploration rovers. Sojourner (*centre*), MER (*left*), and MSL (*right*) (*courtesy of NASA/JPL-Caltech*)

and development of designs that could be accommodated in a launcher. At the same time, the requirements of the scientific community were the main design consideration for the development of larger systems. The size of the MSL is comparable to that of the Rocky I; however, earlier designs had almost no space for scientific payloads.

5.2.2 Servicing

To sustain a constant presence in space and to enable longer exploration missions, it is necessary to develop servicing systems. Such systems are used in servicing or removal of malfunctioning satellites, removal of space debris, inspection and construction of space structures, or, in the future, in astronaut assistance at planetary outposts. These robotic systems must be able to manipulate objects with various characteristics, making them more complex.

Currently, the most successful space robots, such as the Shuttle Remote Manipulator System (SMRM) or "Canadarm," the Space Station Remote Manipulator System (SSMRM) or "Canadarm 2," and the Special Purpose Dexterous Manipula-

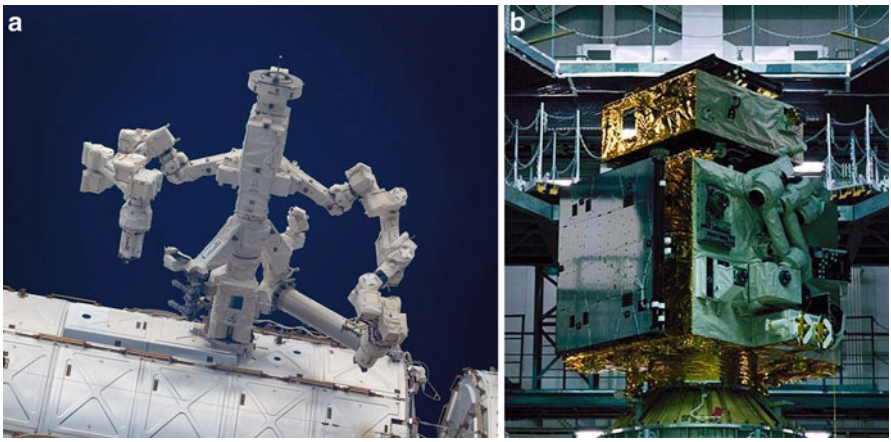

Fig. 5.2 (**a**) Dextre on ISS (*courtesy of NASA*) and (**b**) ETS-VII prior to launch (*courtesy of JAXA*)

tor (SPDM) or "Dextre" on ISS ([1], Fig. 5.2a) are mainly teleoperated via dedicated remote interfaces. The European Robotic Arm (ERA) [25] (est. launch in 2013) and the Japanese Experiment Module Remote Manipulator System (JEMRMS) [26], currently at the ISS, have a greater level of autonomy but still require a human operator.

To overcome the increasingly important problem of space debris and malfunctioning satellites, a greater level of autonomy is required. The first mission that demonstrated autonomous in space servicing was JAXA's ETS-VII (Fig. 5.2b, [27]). NASA and DARPA extended the concept, initially with the unsuccessful DART mission and later with the successful Orbital Express mission [28]. ESA and others pursue similar designs for on-orbit servicing, like the TECSAS and the DEOS [29]. Additionally, ESA and JAXA have developed fully autonomous human-class systems for logistic purposes for the ISS. Both the Automated Transfer Vehicle (ATV) [30] and the H-II Transfer vehicle operated smoothly [31].

5.2.3 Experimental Systems

Space agencies, R&D institutes, universities, and companies have developed a number of designs to test future space robotic systems and enabling technologies. The systems that have been tested in space are presented here.

During the STS-55 mission (1993), various control modes in space were tested using DLR's ROTEX [32], a small, six-axis robot equipped with a gripper and mounted inside a space-lab rack. On behalf of DLR, the Robotic Components Verification on the ISS (ROKVISS) was installed in 2005 and removed in 2010. Its main purpose was to update and validate space robot dynamic models, to verify

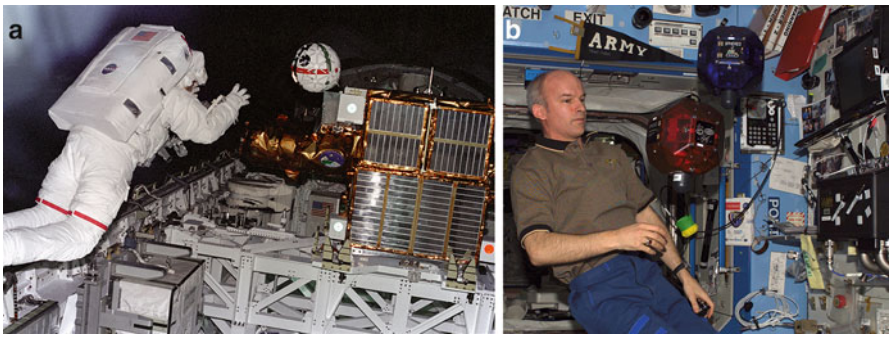

Fig. 5.3 (**a**) AERCam Sprint, (**b**) SPHERES in on-orbit experiments (*courtesy of NASA*)

DLR's proprietary modular joints, and to verify telepresence methods [33]. The most recent experimental system in space is the Robonaut 2 by NASA and GM [34], which will test the performance of an anthropomorphic robot, resembling future robots that can replace astronauts, while retaining at the same time the dexterity of the human body.

The need for miniature robotic systems to assist the astronauts and capable of performing a number of tasks led to the development of the AERCam Sprint [35] and the MIT SPHERES [36], Fig. 5.3. Their performance proved that small autonomous robots could indeed assist humans. Various small robots have been proposed since then, but few designs have been tested. An interesting example is Robyspace [37], which was developed to examine the capabilities of small robotic systems operating in specialized nets. The integration of a large number of electronics for sensing and actuation in a small volume enabled the development of all these experimental systems. However, a greater degree of integration is necessary in order to increase redundancy and functionality.

5.3 Robotics Miniaturization in Space

5.3.1 Motivation

The wealth of available micro and nanotechnologies (MNT), such as MEMS and microelectronics, the exciting and innovative prospects they present combined with the importance of space robotics for space exploration, lead us to the conclusion that the introduction of micro and nanotechnologies in space robotics will significantly augment the capabilities of space robotics and will pave the way for further space robotic exploration missions. Space robotics is an area of particular importance to future missions; the introduction of MNT, either sourced from terrestrial applications (spinning-in) or specifically designed for space robotics, results in their

overall miniaturization. However, as noted earlier, the term miniaturization when applied to space robotics has a somewhat different meaning than the traditional one. Therefore, for such systems the miniaturization process refers to (a) reduction of component size and mass, with increased functionality and unchanged total size and (b) reduction in overall size, while maintaining capabilities.

The terms MNT and microsystems are used in the present chapter with a broader meaning; they encompass MEMS technologies, nanotechnologies, and miniature or microrobotic technologies, collectively referred as MNT or microsystems. Electronic devices (e.g., processors) are not generally recognized as examples of microsystems; however, in order to benefit from the reductions achieved with microsystems and from the integration of devices and electronics, they are considered here as microsystems. Additionally, any enabling technologies that allow for the miniaturization of space robotics are also of interest. Further clarification on the terms MEMS and microsystems can be found at [38].

There are several reasons why the miniaturization of space robotics is desirable. An important motivation for the systematic miniaturization of robotic systems is that launch vehicles have tight constraints with respect to the payload's mass and volume characteristics and therefore successful miniaturization directly results in an improved, more compact and less expensive system. The cost to place 1 kg in Low Earth Orbit is approximately $10k and can rise up to $20k; this cost is significantly increased for long space exploration missions (e.g., Moon, Mars, asteroids, etc.), therefore any weight and volume reduction would significantly decrease the launch cost. Another benefit of the miniaturization process is that the total resources required for space systems (e.g., mass, volume, power) are substantially reduced. Furthermore, systems such as proprioceptive and exteroceptive sensors, wireless communications, control units power generation and transmission units can be integrated into small packages at a system level, thus allowing for a substantial increase in payload, reduction in power losses, and more efficient thermal management. Integrating several microsystems into a silicon wafer and introducing redundancy by design, results in increased reliability and flexibility, lower risk and greater functionality compared to conventional robotic space systems. Silicon wafer microsystems are subject to economies of scale and therefore reduce the overall cost. Additional benefits of terrestrial microtechnologies in particular often include better performance compared to those in space; significantly smaller development costs since investments on non-space technology exceed by orders of magnitude those of space; and sustainability of capabilities, reliability, and strict quality procedures due to the presence of strong markets.

A successful miniaturization (1) results in a compact system, (2) reduces the required power budget, (3) reduces the development cost, (4) requires fewer resources and smaller testing facilities, (5) lessens complexity and improves overall performance. These benefits are particularly important for space applications, therefore the adaptation and implementation of microtechnologies in space robotics is of great interest and expected to yield substantial benefits.

The field of MEMS is the most important in terms of commercialization, range of applications, and technological maturity. The worldwide market for MEMS, boosted

Table 5.2 MEMS market forecast 2011–2015 in millions of units [39]

MEMS device	2011	2012	2013	2014	2015
Accelerometers	1,362	1,630	1,838	2,002	2,194
RF MEMS	805	987	1,190	1,551	2,023
Inkjet heads	673	683	691	706	719
Microphones	579	816	995	1,186	1,381
Pressure sensors	389	488	571	633	689
Digital compass	340	441	542	652	770
Gyroscopes	325	402	510	587	722
Microfluidics for IVD (in vitro diagnostics)	312	394	493	621	785
Oscillators	72	138	248	421	674
Microdispensers	55	68	118	141	168
Projection systems	9	21	44	79	136
Optical MEMS	2.2	3.7	6.6	12.8	18.3
Micro displays	2	5	10	15	20
Microbolometers	0.3	0.4	0.4	0.6	0.7
Other (microstructures, microtips, flow meters, micro speakers, microfluidics for research)	6	15	43	112	209

by automotive applications and by mobile handsets, gaming controllers, digital cameras, and other consumer electronics devices, exhibits nowadays an increasing growth and has expanded to cover nearly all critical technological domains. The MEMS market reached $6.9 billion in 2009, approximately $8 billion in 2010, and is expected to be $9 billion in 2011, with an expected compound annual growth rate (CAGR) in revenue for the next 5 years equal to 13% [39]. The MEMS accelerometer, gyroscope, and inertial measurement unit (IMU) market and in general the motion sensing industry is especially robust. For 2011, the MEMS gyroscope market is estimated at $1 billion and the MEMS accelerometer market at $1.3 billion [40]. This growth will be mostly driven by the deployment of more motion control user interfaces on consumer electronics and drop detection and protection features in portable systems. Table 5.2 presents the MEMS market volume in millions of units.

The major terrestrial technological areas that employ MEMS are automotive, aerospace, defense, industrial processes, consumer products, biotechnology, and telecommunications. Solutions provided by MEMS are finding their way into an increasing number of automation and robotics applications, such as motion sensing, impact detection, and rollover prevention. Commercial microsystem industries provide reliability procedures and yield management systems for microsystems and microsensor systems that offer excellent data return performance, redundancy, and reduced power budget integrated in a very small package. A good example are inertial navigation systems, where inertial measurement sensors from the automotive industry and complete inertial measurement units from oil drilling, offer increased performance, and reduced power and space requirements. MEMS and microsystems have a large and diverse market that enables cost reduction and sustainability of available resources. It is also worth noting that the fraction of the

MEMS market solely dedicated to space applications is very small, often the MEMS that have been used in space have been developed exclusively for the targeted application; the situation is directly opposite to the case of solar cells, where solar technology was first used in space and then on terrestrial applications.

5.3.2 State of the Art

Microtechnologies for space systems in general and robotics in particular have attracted the interest of the scientific community during the past decade. The Jet Propulsion Laboratory (JPL) discussed the role of MEMS in the development of smaller robotic systems in 1999 [41] and the MEMS technology developments at JPL, such as LIGA-based devices, micro-propulsion, microvalves, optics, microactuators, system on a chip, microinstruments, biomedical devices, and packaging were analyzed in [42]. A 1998 work also discusses the use of MEMS and microtechnologies in propulsion, inertial navigation, and wireless sensors in space systems [43]. More recently, the use of microrobotics in space, and the use of MEMS, nanoelectromechanical systems (NEMS), and microtechnologies towards a miniaturized robot in terms of mass and volume has attracted a lot of interest [44]. While not strictly related to the use of microtechnologies [45] discusses the use of length scaling in space dynamics; a method for simulating the orbit and attitude of small objects and therefore provide insights for the dynamics of very small spacecrafts ESA has organized several roundtables on MNT for space applications [46]. Finally, the results of a recent ESA initiative for the introduction of terrestrial MNT to space robotics can be found at [47]. In addition to the small exploration systems, several studies exist on the design of miniaturized space systems, such as the mobile micro-robot Alice [48] developed at École Polytechnique Fédérale de Lausanne (EPFL), ESA's Nanokhod exploration rover [49], and the spider inspired climbing robot (Abigaille-I) for space at [50].

Despite these reports and studies and the benefits highlighted in the above section, microtechnology is still sporadically used in space robotics. An overview of the more developed areas of microtechnology in space is at [51] and [52] provides a thorough review of the current and future use of MEMS and microsystems in space systems. The most developed areas of use in space are inertial navigation, where accelerometers and gyroscopes (e.g., in the current Mars rovers) are sourced from commercial and military applications, atomic force microscopes, and propulsion. MEMS-based propulsion that produces small thrusts in the order of μN–1 N (micropropulsion), especially cold gas thrusters and ion thrusters (colloid and FEEP thrusters), is particularly suitable for fine control, positioning formation flying applications and for primary acceleration of small spacecrafts [53–58]. NASA has used miniature science instruments for the Phoenix Mars Mission (2008) and for the Mars Science Laboratory (MSL) mission, which was launched in November 2011 and the Curiosity rover which became operational in August 2012 [59]. Finally, the James Webb Space Telescope (est. launch 2018) will use a MEMS based

Table 5.3 MEMS in space applications and estimated TRL [51]

MEMS device	Flown in space?	Estimated TRL
Inertial navigation	Yes	High
Pressure sensors	Yes (launch vehicles, propulsion)	High
Magnetometer	Yes (CubeSats)	High
Atomic force microscope	Yes (Phoenix mission)	Medium–high
Sun sensor	Yes (Delfi C3)	Medium–high
Microfluidics	Yes (space shuttle, satellites)	Medium
Bolometer	Yes (Planck 2009)	Medium–high
Optical switching	No	Medium–high
Propulsion: ion, cold gas, colloid, solid	Yes (ST5, small satellites)	Medium
Thermal control	Yes	Medium
RF switch and variable capacitor	Yes (2000, OPAL picosatellites)	Low–medium
Adaptive optics and MOEMS instruments	James Webb Telescope (est. 2014)	Low–medium
MEMS oscillator	No	Low–medium

microshutter array for the Near InfraRed Spectrometer (NIRSpec) of the telescope [60, 61]. Table 5.3 provides a summary of the MEMS technologies flown in space and their technology readiness levels (TRL) [51]. Devices that were used in satellites (CubeSats, ST5, Delfi C3) are discussed in Sect. 5.4.

5.3.3 Miniaturization Challenges

In order to assess the areas where the introduction of miniaturization in space robots is essential, it is necessary to identify the main challenges during design and operation. The candidate areas for miniaturization in space robotics should be searched within their subsystems' components. The difference between the target applications for microrobotics on Earth and space robotics must be stressed again; a robot cannot be miniaturized if this negatively affects its objectives, e.g., a rover should be able to travel for kilometers and gather samples, this is not possible with a microrover. The miniaturization challenges interest greatly the space agencies, such as the work presented in [47].

Space systems in general and space robotics in particular have the following subsystems: Power, Propulsion, Structure, Attitude and Orbital Control (AOCS); On Board Data Handling (OBDH); Locomotion, Guidance, Navigation and Control (GNC); Communication, Thermal, Manipulators and End-Effectors [62]. Depending on the application of each space robot, a subsystem might not be applicable, for example a rover requires no propulsion; however, this categorization is standard for all space systems. The subsystems that have the greatest demands (1) in terms of mass and volume are Power, Propulsion, and Structure; (2) in terms of required computational power are OBDH, AOCS, GNC, and the motion of manipulators; and (3) in terms of power demands from the Power subsystem are Thermal, Locomotion, and Propulsion. Therefore, the focus of R&D in Micro and Nanotechnology (MNT)

should be given in these areas to efficiently address the current challenges. Table 5.4 presents the main challenges per space robot class and where the introduction of MNT is expected to have the highest impact.

Table 5.4 Challenges for MNT R&D per space robot class

Class	Subsystem	Challenges for micro- and nano-technology
1. Rovers/other means of locomotion	Power	• Solution for solar cell efficiency decrease by dust
		• Large and heavy batteries: higher density required
	OBDH	• Low computational power: more efficient electronics, decentralized architectures
	Thermal	• Improved materials, spot cooling/heating
	Actuation	• Low eff. DC motors: better materials required
		• Low integration of electronics
	Navigation	• Slow in rough terrains due to computational restrictions
2. Stationary planetary explorers	Power	• See Class 1 above
	Propulsion	• Landing with retros has mass and volume penalty: better properties for fuels
	Mechanisms	• See Class 6 below
	Thermal	• See Class 1 above
3. Orbital planetary explorers	Power and OBDH	• See Class 1 above
	AOCS	• High electrical power consumption: better electronics required
		• More efficient and smaller sensors required
	Comms	• High power consumption: better electronics req.
	Propulsion	• ≈50% of mass and volume of the system: better fuel properties
		• Electrical propulsion requires high power reqs.
	Structure	• ≈20% of total mass: lightweight materials
		• Enhanced properties required: active materials
4. Aerobots/balloons	Power	• No efficient flexible solar cells
		• Large Batteries: see Class 1
	Structure	• Restrictive space for all the necessary subsystems
		• Corrosive environments: protection required
	AOCS, OBDH, comms, thermal	• High integration needed: better electronics required
		• High efficiency required: better sensors required
	Propulsion	• Use mainly of propellers: see Actuation of Class 1
	Power	• Highly efficient flexible cells required

(continued)

Table 5.4 (continued)

Class	Subsystem	Challenges for micro- and nano-technology
5. Orbital servicers	AOCS	• See Class 3 above
		• Reqs. during rendezvous, docking and manipulation
	Comms	• See Class 3 above
	OBDH	• See Class 1
		• Reqs. during rendezvous, docking and manipulation
	Propulsion	• See Class 3 above
	Structure	• See Class 3 above
	GNC	• Massive sensors
		• High power consumption
	Manipulators	• See Class 6 below
		• Computational intensive: complex dynamics
6. Manipulators	Sensors	• Integration of more sensors for high autonomy
	Structure	• Large mass
		• Massive and confusing cabling
		• Increased stiffness of cabling affects movement
	Actuation	• See Class 1 above
	End-effector	• End-effectors designed for specific tasks
		• Higher dexterity and sensory information required

5.3.4 General Selection Criteria

Not all MNT components can be used in miniaturizing space robotic devices, as their reliability in space condition varies. This is especially pertinent to those systems that are sourced from terrestrial applications. A set of criteria for the selection of microsystems (MEMS, micro and nanotechnologies, etc.) is presented here.

To access the compatibility of the selected MNT components with the space environment and functionality requirements of space robotics the following criteria are proposed (1) applicability to space robotics, (2) launch conditions, (3) external space environment requirements (LEO, GEO, Mars, Moon, Near Earth Asteroid), (4) required technical lifetime. Additionally, microsystems that are part of the scientific payload must also comply with the scientific objectives of the experiment. Each component should be able to withstand mechanical shocks of 6,000–10,000 $\times g$ and be able to at least operate in a temperature range of -50 to $+80$ °C. A study on the reliability of MEMS under vibration and shock can be found at [63]. Vacuum conditions are detrimental to MEMS performance and out-gassing in a vacuum environment has also adverse effects on a device's performance; however, it has been observed that a nitrogen atmosphere inside the MEMS packaging has a

positive effect on the device's performance and reduces drift. An additional criterion is the maximum operating voltage, which is limited at approximately 2 kV for space applications due to electrical insulation specifications. Space radiation is an important problem that is experienced by all structures operating in space. The high energy particles present in space radiation can trigger single-event effects (SEE) in all digital electronics. MEMS based on capacitive sensors (accelerometers, gyroscopes, proximity sensors) exhibit certain problems when exposed to radiation, due to their operating principle; radiation effects result in creating output drifts and generate noise; packaging is not always a sufficient solution, especially when volume and mass limitations are imposed. The effect of radiation on devices in space is a subject of great interest [52, 64]. Reference [64] provides also a list of radiation tested MEMS and microsystem devices.

For each microsystem, it is important to consider the development risk, time, and cost required to reach the maturity necessary for use in space. Currently, there is no general qualification process for space MNT, it is done on a case-by-case basis and usually there is no volume production of those devices that are space compliant. The general standards for European space activities can be found at [65], while a study on the reliability of MEMS in space can be found at [66]. Problems are usually addressed by correct design while the applicability of packaging techniques of MEMS devices for space is limited; for example, the packaging of heterogeneous MEMS is problematic because the metallic parts cannot withstand the high temperatures of the packaging process. The reliability of MEMS is discussed in [67]. As a final guideline, a terrestrial component that has been tested and verified by being used in the industrial or commercial sector would require an additional 10% cost to be made space compliant. If the terrestrial component or technology has not been extensively tested, the cost of technology transfer to space increases above this 10% figure, and in proportion to the number of tests required.

The proposed set of criteria will aid in the selection of MNT components for space robotics; however, ideally a streamlined selection process would enable the miniaturization of space robotics to a significantly greater degree.

5.3.5 Enabling Technologies

MNT can greatly benefit space robotics; the miniaturization of critical components of the subsystems provide to the designers more solutions and flexibility during development. The efficient, systematic introduction of MNT to space robotics requires the fusion of the challenges and requirements of the future robotic systems. The most important technologies and how they will affect space robots and their subsystems are outlined here.

Sensor Islands. Sensor Islands are known as Power and Computational Autonomous Remote Sensors, a research area highly pursued and MNT dependent.

This concept is very important because it can increase the autonomy and flexibility of space systems. A sensor island should be able to (a) receive or harvest power with minimal cabling; (b) have high electronics integration; (c) be computational autonomous and perform data fusion and signal processing, without need to send or receive any data, except for the final data packages; (d) wirelessly communicate with a central computer for the overall control; and (e) integrate sensors of different functionalities. In this way, the computational architecture becomes completely decentralized and the overall system more compact and robust.

Power. The upgrade of current power subsystems is strongly related to the advances in power density for batteries (Ah/kg) and higher efficiency for solar cells. Nanomaterials and microelectronics can harvest and exploit more energy than current technological solutions, reducing the mass and weight of current power production and storage systems. Efficient electronics reduce the power requirements and have positive impact in power management.

Structure. The target technology is the development of structural elements with advanced capabilities. Robust but lightweight materials like carbon fiber reinforced plastics (CFRP) are already available and in production; however, their capabilities should be augmented by ejecting specialized nanoparticles and general use of nanotechnology and nanomaterials. These new structural elements can be combined with techniques for embedding sensors, cables, and piping inside the structure, thus lowering mass penalties and thermal losses and increasing flexibility and environmental protection. The technology of electroactive polymers (EAP) and piezoelectric elements can also be used as sensors and/or actuators (e.g., as vibration suppressors).

OBDH & GNC. Developments here should be aimed towards a decentralized architecture; therefore, the enabling technologies are based on those for Sensor Islands. Dedicated image processors would lower the computational burden, and miniaturized cameras and optics would render the navigation capabilities more efficient. There are MNT systems with small footprints and low consumption offering superior functionalities for commonly used sensors, such as GPS, gyroscopes, and IMUs. Additionally, for electronics and microcontrollers 64 bit solutions would increase the overall computational power.

Actuators. Reduction of motor volume and mass require advanced materials enhanced with nanoparticles. The new materials could lower the power losses and increase the magnetic flux and therefore the produced torque and/or speed. Additionally, higher integration would minimize the essential electronics volume.

All subsystems could benefit by the introduction of MNT and terrestrial MNTs exhibit a significant potential for use in space systems. In general, MNTs can lead to smaller, lighter, less power consuming, and with higher functionality parts, which in turn means (a) lighter and more compact systems (without affecting capabilities); (b) more space for payload (e.g., scientific instrumentation, cargo, etc.); (c) higher autonomy capabilities; (d) higher security, operational flexibility, greater redundancy; (e) lower development costs and time; and (f) lower launch costs.

5.4 Micro/Nanosatellites

5.4.1 State of the Art

MNTs and miniaturization in terms of weight and volume also have been introduced in satellites. Although satellites are not strictly considered as robotics systems, they are automated space systems, and therefore pertinent to this chapter. The satellite market is the most mature and well-known segment of space systems. Since the launch of Sputnik 1 in 1957, more than 4,900 launches have placed approximately 6,000 satellites into orbit, of which, as of April 2011, about 957 are operational per the latest available satellite database available at [68]. Of those operational, 463 (49%) are in Low Earth Orbit (LEO, 160–2,000 km), 397 (41%) are in Geostationary Orbit (GEO, 36,000 km), 63 (6%) are in Medium Earth Orbit (MEO, 2,000–36,000 km), and 34 (4%) are in Elliptical Orbits. These satellites are of government, military, commercial, or civil nature. Their uses in orbit are given in Table 5.5, using data from [68]. The majority (93%) of commercial satellites are communication satellites, 4% are Earth Observation/Remote Sensing satellites, 2% are Technology Development, and 1% are for Navigation Demonstration (prototype satellites for the Galileo system).

For the next decade, there will be an average of 122 satellites launches per year, a 60% increase compared to the average annual rate of 77 per year in the 2000s, with a total of 1,220 satellites build in the decade 2010–2020. The total revenue from the manufacturing and launch of these 1,220 satellites will reach $194 billion worldwide for the decade 2010–2020, while currently 60% of the total 5 billion € annual revenue of the European space industry comes from the manufacture and launch of communications satellites. The average satellite mass is estimated to be 1,890 kg in the coming decade [69, 70]. For the satellites currently in orbit, the average wet mass at launch (mass including fuel at launch) is 2,139 kg and the average dry mass (mass in orbit) is 1,190 kg. Table 5.6 presents the mass (wet mass) distribution of the satellites in orbit using data from [68].

Table 5.5 Function of satellites on orbit

Function	Percentage
Communication	59
Earth observation/remote sensing	9
Navigation	8
Military surveillance	7
Astrophysics/space science	5
Earth Science/meteorology	4
Other	7

Table 5.6 Mass distribution of satellites on orbit

Weight (kg) (wet mass)	Percentage
<500	26.40
500–1,000	13.69
1,000–1,500	8.98
1,500–2,000	5.37
2,000–2,500	9.75
2,500–4,000	18.07
4,000–5,000	11.39
>5,000	6.35

5.4.2 Miniaturization Efforts in Satellites

It is clear from the above statistics that the satellite market is growing fast and the average mass is quite high. Similarly to space robotic systems, the cost/launch is proportional to the wet mass of each satellite and higher mass means higher systems and development complexity. It is clear that any mass and volume reduction would significantly decrease the launch cost. Within this context, the term miniaturization of satellites in terms of mass and volume has a different meaning compared to the traditional one used in terrestrial applications.

The miniaturization in satellites is achieved in three ways: (a) by scaling down the satellite's mass and volume while retaining functionality (small satellites), (b) by implementing micro/nanotechnologies for the subsystems, mostly in the form of microelectronics and MEMS, and (c) by combining (a) and (b). A small satellite is defined as a satellite of wet mass of less than 500 kg. Within this range, a microsatellite has a wet mass between 10 and 100 kg, a nanosatellite between 1 and 10 kg, and a picosatellite between 0.1 and 1 kg. Compared to the average wet mass of 2,139 kg or with an average telecommunication satellite with a mass of 1,000–5,000 kg, a 100 kg satellite is at 10–50 times smaller, a significant weight decrease. The development of nano, micro, and picosatellites requires decreased infrastructures and cost, making them ideal candidates for academic institutions and research centers that have a limited budget for space activities, and for novel technology demonstrations which would be otherwise difficult and costly to put in orbit. The importance of small satellites, especially in the weight range of 1–30 kg, is also recognized by the United Nations, which led to the establishment in 2009 of the Basic Space Technology Initiative, a new area of activity of the United Nations Programme on Space Applications [71].

The majority of the miniaturization efforts have been concentrated in case (a), where MEMS and microelectronics are mostly used. In general, the implementation of MNT is still sporadic and mostly occurs at small satellites. A review of MEMS used in pico to microsatellites can be found at [51]. A successful example of the miniaturization of satellites is the CubeSat standard [72, 73]. A CubeSat is a miniaturized satellite that weighs no more than 1.33 kg, therefore it is classified as a

nanosatellite; its dimensions are $10 \times 10 \times 10$ cm and usually uses commercial off-the-shelf (COTS) electronics components. CubeSats are scalable in 1U increments; a 2U CubeSat is $20 \times 10 \times 10$ cm and a 3U CubeSat is $30 \times 10 \times 10$ cm. The CubeSat standard was developed in 1999 by the California Polytechnic State University (Cal Poly) and Stanford University, with the aim of providing a standard design for picosatellites, while reducing cost and development time, increasing accessibility to space, and sustaining frequent launches. CubeSats are used for educational purposes and technology demonstrations, such as testing microtechnologies in space, earth remote sensing, tethers, and biological experiments.

CubeSats are launched and deployed using a common deployment system, the Poly-PicoSatellite Orbital Deployer (P-POD). The P-PODs are mounted on the launch vehicle and carry a maximum of three CubeSats into orbit. Additionally, CubeSats are usually "piggy-back" launches; the launch vehicle is used for another purpose (e.g., for a commercial, full-size satellite) and the CubeSats are put into orbit once the main spacecraft has been deployed. The minimized mass and volume, in conjunction to the use of COTS components and the "piggy-back" launch, results in a significantly less expensive system that is developed much faster compared to bigger satellites. As a guideline, a CubeSat costs approximately $40k, including launch costs and has an average development time of 1–2 years, whereas a 500 kg satellite requires 3 years and bigger ones require 5 and more years. However, CubeSats have a smaller lifetime compared to that of bigger satellites (weight >500 kg), since they use COTS that have not been fully tested and qualified for the harsh space environment (vacuum, radiations, extreme thermal conditions); for example, the typical lifetime of a telecommunications satellite is 15 years, whereas CubeSats have a lifetime of months to 3 years. It should be noted that the benefits of CubeSats are also applicable to micro and nanosatellites.

From 2003 to 2009, more than 45 CubeSat missions have been successfully launched, such as ESA's SSETI Express [74] and the SwissCube. The EPFL developed and successfully launched in 2009 the SwissCube, with the aim of taking pictures of the atmospheric airglow using a small low cost earth sensor [75]. The earth sensor weighted less than 50 g, the optics volume was $30 \times 30 \times 65$ mm^3, and the payload board was $80 \times 35 \times 15$ mm^3. To acquire quality airglow images, the required attitude determination accuracy was better than 1°.

There are several small satellite missions that employ microtechnologies. MEMS are mostly used in the CubeSat attitude determination subsystem, such as inertial sensors (gyroscopes), magnetometers, and optical sensors (sun sensors, star trackers). Magnetometers and gyroscopes are typically COTS devices, while sun sensors and star trackers are space specific. The SwissCube-1 mission used the MEMS gyroscope ADXRS614 manufactured by Analog Device and the 3 axis Honeywell magnetometer HMC1053. Another example is the AAUSAT-II Cubesat developed at Aalborg University, Denmark (2008), which used six Analog Devices single chip yaw rate gyroscopes (model ADXRS401) and one 3 axis magnetometer (model HMC1053) from Honeywell as part of the attitude determination system [51]. In both cases, the sensors operated satisfactorily in orbit. MEMS-based propulsion that produces small thrusts in the order of μN–1 N (micropropulsion) has also been used in pico to nanosatellites.

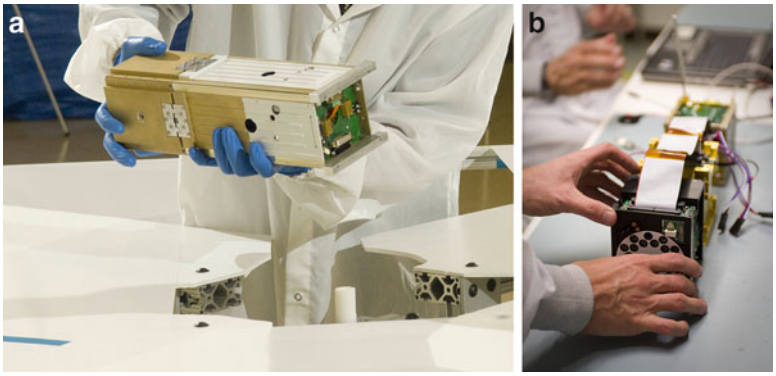

Fig. 5.4 (**a**) NanoSail-D stowed and ready for deployment test and (**b**) test of an early prototype of O/OREOS bus (*courtesy of NASA*)

The PRISMA mission (2010) used a MEMS micropropulsion system. The mission consisted of two satellites, Mango (140 kg) and Tango (40 kg), with the aim of demonstrating autonomous satellite formation flying. Mango was equipped with a hydrazine propulsion system, a high performance green propellant (HPGP) system and a MEMS cold gas micropropulsion system manufactured by Nanospace. The system consisted of a four thruster array, orthogonally distributed in the equator plane of the golf ball sized thruster module, with a thrust range of 10 μN–1 mN and used nitrogen as propellant. The micropropulsion system was used successfully during the mission and is candidate for future missions where extremely low and accurate thrust is required [76]. The Delft University of Technology in the Netherlands launched Delfi-C3, a 3U CubeSat in 2008 and its follow-up will be Delfi-n3Xt, which test several innovative technologies, including a micropropulsion system and micro sun sensors [77]. The University of Toronto's Institute of Aerospace Studies Space Flight Laboratory has successfully launched a number of nanosatellites, such as MOST (2003) [78]. MOST incorporated a small optical telescope (15 cm aperture) equipped with a CCD photometer designed to return high photometric precision and frequency on stars other than the Sun and successfully demonstrated the capabilities of a significantly smaller telescope. NASA's Space Technology 5 mission (2006) demonstrated the operation of three 25 kg, fully functional spacecrafts that functioned as a single constellation and implemented multiple new technologies and miniaturized components [79]. The miniaturized technologies that were successfully validated include the following: cold gas microthrusters (CGMT), designed by Marotta Scientific Controls, Inc., variable emittance coatings for thermal control, which consisted of an electrically tunable coating that could change properties (absorbing heat when cool to reflecting or emitting heat when in the Sun) [80] and CULPRiT, a microelectronic device that allows circuits to operate at 0.5 V, a technology that is expected to reduce power consumption while achieving a high radiation and latch-up immunity. Recent examples of successful nanosatellite missions are NASA's NanoSail-D (2010), Fig. 5.4a, and the O/OREOS (2010), Fig. 5.4b [81, 82]. NanoSail-D's objective

was the experimental validation of solar sail capabilities, with the sail packed inside the $9.9 \times 9.9 \times 37.9$ cm^3 satellite. NanoSail-D successfully deployed the 100 sq. ft. polymer sail in January 2011. O/OREOS is the first nanosatellite to operate in the exosphere, conducting autonomous biological and chemical measurements, weighs 5.5 kg, and will use a propellant-less mechanism for de-orbiting.

5.5 Future Trends

As discussed above, the design of robotic devices for space applications is in general affected by the ongoing miniaturization efforts in two ways. Those systems that must be of certain size become more capable, while the rest shrink in size. However, the size of all space systems remains much larger from that of the terrestrial systems, due to the different scale of the actual space tasks, the conservatism of the space industry [76] (it may lag 10 years with respect to the same technologies on earth), the need for extreme reliability and the inability for in situ repairs, and the requirement for survivability in extreme space conditions (radiation, atomic oxygen, extreme atmospheres).

It is expected though that a number of drastically smaller devices will be considered and employed in space applications. For these to be adopted, the operating scenarios will have to exploit the capabilities of micro and nanotechnologies in innovative ways. For example, an alternative to some functions provided by lander-deployed rovers can be the deployment of a large number of microrobotic planet monitoring modules with low flying balloons. These can cover great areas; establish a redundant communications network; transmit temperature, seismic, or other data; and even change their position periodically using spring loaded mechanisms, with all their functions powered by harvesting solar energy. A similar scenario includes a parachute-deployed network of interconnected channels, covering vast planetary areas and containing sensing bionanorobots [83]. Micro or bionanorobots can also be envisioned to act as rover or mother station linked disposable "scouts," exploring hazardous zones in "one-shot" missions [44]. Another possibility is using swarm nanorobots for inspection and repair of space structures on orbit or on planets, or for checking the status of spacecraft thermal shielding before reentry. Researchers also envision applications such as spacesuit repairs by suit embedded nanorobots [84].

The driving forces that will further strengthen the trend towards miniaturization of robotic devices for space applications are many. The demand for small volume and mass of space systems will continue to be important, due to launch volume and mass technology constraints. As mentioned earlier, the cost of launching a kilogram exceeds $10k, reaching even twice as more. Clearly, adding mass increases the cost. Miniaturization will continue occurring also due to component size reduction and to higher level of integration between platforms providing mobility (such as spacecrafts or rovers) and instruments or sensors [85]. Downscaling of systems and components has some interesting properties. For example, the inertia forces on a component are proportional to the cube of its characteristic length (size), while

its stiffness is inversely proportional to it. Therefore, a decrease in size reduces the inertial forces and increases its rigidity, with an obvious benefit to its overall robustness to shocks [44]. Also, since the ratio of area to volume is inversely proportional to length, smaller systems can have higher power densities and can dissipate power more effectively [86]. It is also important to note that a large number of inexpensive robotic devices are obviously more effective against failures versus a single large and expensive one, as the failure of a few of the miniature devices will not jeopardize the entire mission.

Miniaturization will have to overcome formidable technological obstacles. For example, it is very difficult to have high voltages required in electron spectrometry in a very confined space [85], to produce radiation hardened chips with the same capabilities as those for terrestrial applications, or to cover great distances at reasonable times with millimeter size rovers. Despite factors that hinder the proliferation of miniaturized robotic devices in space, the trend is clear and will continue for many years to come.

Acknowledgments Part of the work presented in this chapter was conducted under the ESA Project "Identification and Assessment of Existing Terrestrial Micro-systems and Micro-technologies for Space Robotics," 22110/08/NL/RA. Mr. Paraskevas has been co-financed by the European Union (European Social Fund—ESF) and Greek national funds through the Operational Program "Education and Lifelong Learning" of the National Strategic Reference Framework (NSRF)—Research Funding Program: Heracleitus II. Investing in knowledge society through the European Social Fund.

References

1. http://is.mdacorporation.com/mdais_canada/Programs/Programs_SRMS.aspx. Accessed May 2011
2. http://www.jpl.nasa.gov/missions/missiondetails.cfm?mission=Pathfinder. Accessed May 2011
3. Martel S, Felfoul O, Mathieu J-B, Chanu A, Tamaz S, Mohammadi M, Mankiewicz M, Tabatabaei N (2009) MRI-based nanorobotic platform for the control of magnetic nanoparticles and flagellated bacteria for target interventions in human capillaries. Int J Robot Res 28(9):1169–1182, Special Issue on Medical Robotics
4. Vartholomeos P, Fruchard M, Ferreira A, Mavroidis C (2011) MRI-guided nanorobotic systems for therapeutic and diagnostic applications. Annu Rev Biomed Eng 13:157–184
5. Seeni A, Schäfer B, Hirzinger G (2010) Robot mobility systems for planetary surface exploration – state-of-the-art and future outlook: a literature survey. In: Thawar TA (ed) Aerospace technologies advancements. InTech, Croatia
6. http://www.jpl.nasa.gov/jplhistory/mission/apollo-t.php. Accessed May 2011
7. http://nssdc.gsfc.nasa.gov/planetary/viking.html. Accessed May 2011
8. Muirhead BK (2004) Mars rovers, past and future. In: Proceedings of the IEEE aerospace conference, Big Sky, MT. doi: 10.1109/AERO.2004.1367598
9. http://marsrovers.jpl.nasa.gov/home/index.html. Accessed May 2011
10. http://marsprogram.jpl.nasa.gov/msl/. Accessed May 2011
11. Baglioni P, Fisackerly R, Gardini B, Gianfiglio G, Pradier AL, Santovincenzo A, Vago JL, van Winnendael M (2006) The mars exploration plans of ESA. IEEE Robot Autom Mag 13:83–89

12. http://www.beagle2.com/index.htm. Accessed May 2011
13. http://www.jpl.nasa.gov/news/phoenix/main.php. Accessed May 2011
14. Ji LY, Bartsch S, Kirchner F (2011) Distributed compliance controller for legged-robot with geared brushless DC joints. In: 11th Symposium on advanced space technologies in robotics and automation (ASTRA), ESTEC, Noordwijk, The Netherlands
15. Silva MF, Machado JAT (2010) A survey of technologies and applications for climbing robots locomotion and adhesion. In: Miripour D (ed) Climbing and walking robots. InTech, Croatia
16. Curtis SA, Brandt M, Bowers G et al (2006) Mobile science platforms for impassable terrain. In: Proceedings of the IEEE aerospace conference, Big Sky, MT. doi: 10.1109/AERO.2006.1655722
17. Truszkowski W, Hallock H, Rouff C, Karlin J, Rash J, Hinchey M, Sterritt R (2009) Swarms in space missions. In: Autonomous and autonomic systems: with applications to NASA intelligent spacecraft operations and exploration systems, 1st edn. Springer, London
18. Kerzhanovich VV, Hall JL, Faibrother D, Said M (2007) Progress in planetary aerobot technologies. In: Proceedings of the IEEE aerospace conference, Big Sky, MT. doi: 10.1109/AERO.2007.352742
19. http://mars.jpl.nasa.gov/odyssey/. Accessed May 2011
20. http://saturn.jpl.nasa.gov/. Accessed May 2011
21. http://www.nasa.gov/mission_pages/epoxi/index.html. Accessed May 2011
22. Ulamec S, Biele J (2010) From the Rosetta Lander Philae to an asteroid hopper: lander concepts for small bodies missions. In: 7th International planetary probe workshop (IPPW), Barcelona
23. http://near.jhuapl.edu/. Accessed May 2011
24. Kawaguchi J, Uesugi K, Fujiwara A (2008) Hayabusa – its technology and science accomplishment summary and Hayabusa-2. Acta Astronaut 62(10–11):639–647
25. http://www.esa.int/esaHS/ESAQEI0VMOC_iss_0.html. Accessed May 2011
26. Sato N, Wakabayashi Y (2001) JEMRMS design features and topics from testing. In: 6th International symposium on artificial intelligence, robotics and automation in space (iSAIRAS), Quebec
27. Oda M (2001) ETS-VII: achievements, troubles and future. In: 6th International symposium on artificial intelligence, robotics and automation in space (iSAIRAS), Quebec
28. Ogilvie A, Allport J, Hannah M, Lymer J (2008) Autonomous satellite servicing using the orbital express demonstration manipulator system. In: 9th International symposium on artificial intelligence, robotics and automation in space (i-SAIRAS), Los Angeles
29. http://www.dlr.de/rm/en/desktopdefault.aspx/tabid-3825/5963_read-8759/. Accessed May 2011
30. http://www.esa.int/SPECIALS/ATV/index.html. Accessed May 2011
31. http://www.jaxa.jp/projects/rockets/htv/index_e.html. Accessed May 2011
32. Hirzinger G, Brunner B, Dietrich J, Heindl J (1993) Sensor-based space robotics-ROTEX and its telerobotic features. IEEE Trans Robot Autom 9(5):649–663. doi:10.1109/70.258056
33. Rebele B, Schaefer B, Albu-Schaeffer A, Bertleff W, Landzettel K (2006) Robotic joints and contact dynamics experiments: lessons learned from ROKVISS. In: 9th ESA workshop on advanced space technologies for robotics and automation (ASTRA), ESTEC, Noordwijk, The Netherlands
34. http://robonaut.jsc.nasa.gov/default.asp. Accessed May 2011
35. Choset H, Knepper R, Flasher J, Walker S, Alford A, Jackson D, Kortenkamp D, Burridge R, Fernandez J (1999) Path planning and control for AERCam, a free-flying inspection robot in space. In: Proceedings of the IEEE robotics and automation international conference, Detroit, MI. doi: 10.1109/ROBOT.1999.772556
36. Nolet S, Saenz-Otero A, Miller DW, Fejzic A (2007) SPHERES operations aboard the ISS: maturation of GN&C algorithms in microgravity. AAS Guidance, Navigation & Control, Breckenridge, CO
37. Summerer L, Putz B, Kopacek P, Kaya N (2006) Robots moving on a loose net in microgravity – results from the Japanese Furoshiki sounding rocket experiment. In: 9th ESA workshop on advanced space technologies for robotics and automation (ASTRA), ESTEC, Noordwijk, The Netherlands

38. http://www.wtec.org/loyola/mcc/mems_eu/Pages/Chapter-3.html. Accessed May 2011
39. Yole Développement (2010) Status of the MEMS industry. http://www.yole.fr. Accessed May 2011
40. Yole Développement (2009) MEMS accelerometer, gyroscope and IMY market, 2008–2013. http://www.yole.fr. Accessed May 2011
41. Miller LM (1999) MEMS for space applications. Proc SPIE 3680:2. doi:10.1117/12.341193
42. George T, Bae Y, Chakraborty I, Cherry H et al (2000) MEMS technology at NASA's Jet Propulsion Laboratory. Proc SPIE 4134:16. doi:10.1117/12.405340
43. Janson S, Helvajian H, Amimoto S, Smit G, Mayer D, Feuerstein S (1998) Micro-technology for space systems. IEEE Proc 1:409–418. doi:10.1109/AERO.1998.686938
44. Corradi P, Menciassi A, Dario P (2005) Space applications of micro-robotics: a preliminary investigation of technological challenges and scenarios. In: Proceedings of the 5th round table on micro/nano technologies for space, Noordwijk, The Netherlands
45. Atchison J (2011) Length scaling in spacecraft dynamics. J Guid Control Dyn 34(1):231–246. doi:10.2514/1.49383
46. http://www.congrex.nl/10C03/. Accessed May 2011
47. Paraskevas I, Flessa T, Papadopoulos E (2011) Spinning-in of terrestrial micro systems and technologies to space robotics: results and technology roadmaps. In: 11th Symposium on advanced space technologies in robotics and automation, ESTEC, Noordwijk, The Netherlands
48. Caprari G, Siegwart R (2005) Mobile micro-robots ready to use: Alice. In: Proceedings of the IEEE/RSJ international conference on intelligent robots and systems, pp 3295–3300. doi: 10.1109/IROS.2005.1545568
49. Schiele A, Romstedt J, Lee C, Henkel H, Klinkner S et al (2008) NanoKhod exploration Rover – a Rugged Rover suited for small, low-cost, planetary lander mission. IEEE Robot Autom Mag 15(2):96–107. doi:10.1109/MRA.2008.917888
50. Menon C, Li Y, Sameoto D, Martens C (2008) Abigaille-I: towards the development of a spider-inspired climbing robot for space use. In: 2nd IEEE RAS & EMBS international conference on biomedical robotics & biomechatronics, pp 384–389. doi: 10.1109/BIOROB.2008.4762903
51. Shea HR (2009) MEMS for pico- to micro-satellites. Proc SPIE 7208. doi:10.1117/12.810997
52. Osiander R, Darrin MAG, Champion JL (2006) MEMS and microstructures in aerospace applications. CRC, Boca Raton, FL
53. Köhler J, Bejhed J, Kratz H et al (2002) A hybrid cold gas microthruster system for spacecraft. Sens Actuators A Phys 97–98:587–598. doi:10.1016/S0924-4247(01)00805-6
54. Mitterauer J (2002) Micropropulsion for small spacecraft: a new challenge for field effect electric propulsion and microstructured liquid metal ion sources. Surf Interface Anal 36:380–386. doi:10.1002/sia.1693
55. van der List MCAM, van Put PAG, Yüce V, Kuiper J (2006) Next generation electrical propulsion feed systems and spin-off micro-propulsion components. In: ISU 2006 conference, Strasbourg
56. Rossi C, Briandb D, Dumonteuila M, Campsa T, Phamb PQ, de Rooijb NF (2006) Matrix of 10×10 addressed solid propellant microthrusters: review of the technologies. Sens Actuators A Phys 126(1):241–252. doi:10.1016/j.sna.2005.08.024
57. Krpoun R, Rdber M, Shea HR (2008) Microfabrication and test of an integrated colloid thruster. In: Proceedings of 21st IEEE international conference on micro electro mechanical systems, Tucson, AZ, pp 964–967. doi: 10.1109/MEMSYS.2008.4443818
58. Snyder JS, Randolph TM, Hofer RR, Goebel DM (2009) Simplified ion thruster xenon feed system for NASA science missions. In: 31st International electric propulsion conference, Ann Arbor, MI
59. Kim SS, Hayati S, Lavery D, McBride KS (2006) Mars miniature science instruments. In: Proceedings of the IEEE aerospace conference, Big Sky, MT. doi: 10.1109/AERO.2006.1655786
60. Kutyrev AS, Arendt R, Moseley SH, Boucarut RA et al (2004) Programmable microshutter arrays for the JWST NIRSpec: optical performance. IEEE J Sel Top Quant Electron 10(3):652–661. doi:10.1109/JSTQE.2004.830614

61. Buchner S, Rapchun DA, Moseley H, Meyer SE et al (2007) Response of a MEMS microshutter operating at 60 K to ionizing radiation. IEEE Trans Nucl Sci 54(6):2463–2467. doi:10.1109/TNS.2007.910040
62. Sellers JJ (2005) Understanding space – an introduction to astronautics, 3rd edn. McGraw-Hill, New York
63. Sundaram S, Tormen M, Timotijevic B, Lockhart R et al (2011) Vibration and shock reliability of MEMS: modeling and experimental validation. J Micromech Microeng 21(4):doi: 10.1088/0960-1317/21/4/045022
64. Shea H (2011) Effects of radiation on MEMS. Proc SPIE 7928. doi: 10.1117/12.876968
65. http://www.ecss.nl. Accessed May 2011
66. Shea H (2006) Reliability of MEMS for space applications. Proc SPIE 6111. doi:10.1117/12.651008
67. Hartzell AL, da Silva MG, Shea HR (2011) MEMS reliability, 1st edn. Springer, New York
68. UCS Satellite Database (2011). http://www.ucsusa.org/nuclear_weapons_and_global_security/space_weapons/technical_issues/ucs-satellite-database.html. Accessed May 2011
69. Euroconsult (2010) Satellites to be built & launched by 2019, World Market Survey, 13th edn. http://www.euroconsult-ec.com/research-reports/space-industry-reports/satellites-to-be-built-launched-by-2019-38-29.html. Accessed May 2011
70. ADS – Eurospace (2010) European space industry activity – facts and figures, 14 edn. http://www.eurospace.org/. Accessed May 2011
71. UN General Assembly Committee on the Peaceful Uses of Outer Space (2010) Report on the second United Nations/Austria/European Space Agency symposium on small satellite programmes for sustainable development: payloads for small satellite programmes
72. http://cubesat.org/. Accessed May 2011
73. Toorian A, Diaz K, Lee S (2008) The CubeSat approach to space access. In: IEEE aerospace conference, Big Sky, MT. doi: 10.1109/AERO.2008.4526293
74. http://www.esa.int/SPECIALS/sseti_express/index.html. Accessed May 2011
75. http://swisscube.epfl.ch/. Accessed May 2011
76. Gronland T, Rangsten P, Nese M, Lang M (2007) Miniaturization of components and systems for space using MEMS-technology. Acta Astronaut 61(1–6):228–233. doi:10.1016/j.actaastro.2007.01.029
77. Bouwmeester J, Brouwer GF, Gill EKA, Monna GLE, Rotteveel J (2010) Design status of the Delfi-Next nanosatellite project. In: Proceedings of the 61th international astronautical congress, Prague
78. http://www.utias-sfl.net/microsatellites/MOST/MOSTIndex.html. Accessed May 2011
79. http://www.nasa.gov/mission_pages/st-5/main/index.html. Accessed May 2011
80. Beasley MA, Firebaugh SL, Edwards RL, Keeney AC, Osiander R (2004) MEMS thermal switch for spacecraft thermal control. Proc SPIE 5344:98. doi:10.1117/12.530906
81. http://www.nasa.gov/mission_pages/smallsats/nanosaild.html. Accessed May 2011
82. http://www.nasa.gov/mission_pages/smallsats/ooreos/main/. Accessed May 2011
83. Mavroidis C, Ummat A (2005) Space bionanorobotic systems: design and applications. In: Proceedings of the 7th NASA/DoD conference on evolvable hardware (EH-2005), Washington, DC
84. Chui B, Kissner L (2000) Nanorobots for Mars EVA repair. In: International conference on environmental systems, Toulouse. doi: 10.4271/2000-01-2478
85. Dorsky LI (2001) Trends in instrument systems for deep space exploration. IEEE Aerosp Electron Syst Mag 16(12):3–12. doi:10.1109/62.974833
86. Menon C, Ayre M, Ellery A (2006) Biomimetics – a new approach for space system design. ESA Bull 125:20–26

Chapter 6
Diamondoid Nanorobotics

Robert A. Freitas Jr.

Abstract Activity in the field of nanorobotics, as measured by published literature, has been growing at +30 % per year for the last decade. A wide variety of simple nanorobotic mechanisms have already been fabricated, but much of the interest in nanorobotics is focused on the future of medicine. Diamondoid nanorobots potentially offer the most powerful medical applications. Technologies required for the atomically precise fabrication of diamondoid nanorobots in macroscale quantities at low cost require the development of a new nanoscale manufacturing technology called positional diamondoid molecular manufacturing, enabling diamondoid nanofactories that can build nanorobots. Achieving this new technology will require the significant further development of four closely related technical capabilities: (1) diamond mechanosynthesis, (2) programmable positional assembly, (3) massively parallel positional assembly, and (4) nanomechanical design.

6.1 Introduction

Nanorobotics most broadly involves the study of robotic mechanisms and devices that either possess functional features or components with nanoscale size (i.e., below 100 nm, all the way down to single atom) in one or more dimensions or can produce effects or influence processes that are taking place at nanoscale dimensions. A narrower definition that hints at the tremendous future importance of this discipline regards the primary object of the field of nanorobotics to be the "nanorobot," which has been defined as "a computer-controlled robotic device constructed of nanometer-scale components to molecular precision, usually microscopic in size" [1]. The nanorobotics field has been quickly attracting interest and activity, as

R.A. Freitas Jr. (✉)
Institute for Molecular Manufacturing, 555 Bryant Street, Suite 354, Palo Alto, CA 94301, USA
e-mail: rfreitas@rfreitas.com

C. Mavroidis and A. Ferreira (eds.), *Nanorobotics*, DOI 10.1007/978-1-4614-2119-1_6,

© Springer Science+Business Media New York 2013

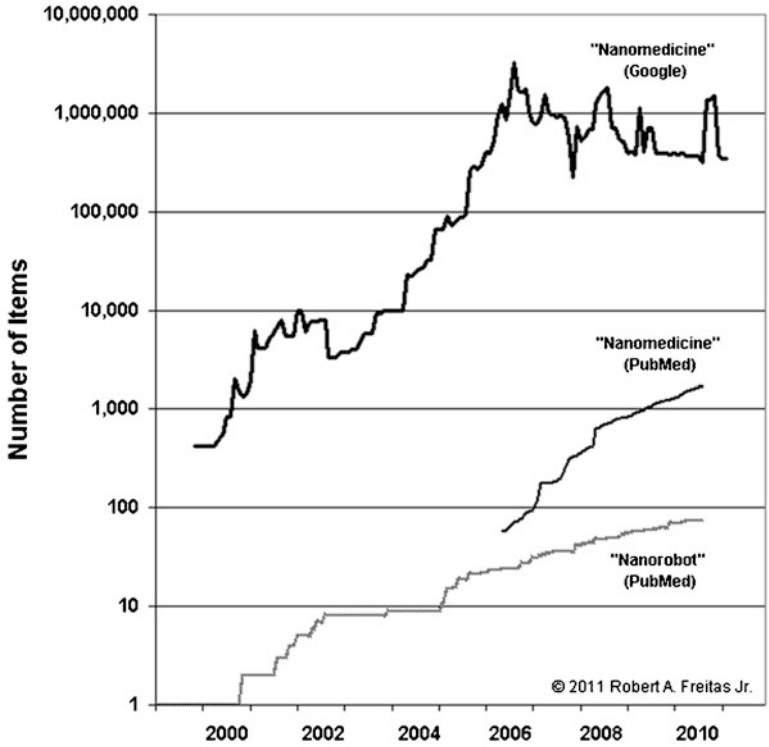

Fig. 6.1 Number of papers mentioning "nanorobot*" in the PubMed database, 2000–2010. © 2011 Robert A. Freitas Jr. (http://www.rfreitas.com). All rights reserved

measured by the growing number of unique literature references to nanorobots or nanorobotics in the PubMed database (Fig. 6.1) which during the past decade have been climbing at a +30 % per year rate (∼2.4-year doubling time).

Seeman and others have published numerous nanorobotics papers describing a variety of robotic nanomechanisms fabricated via DNA nanotechnology [2–5], while others are investigating DNA-based nanotransport devices [6], DNA-based actuation of carbon nanotube-based servomotors for drug delivery [7], protein-based nanoactuators [8], biological molecular motors [9], and bionanorobot prototyping methodologies [10] as alternative approaches to the field of bionanorobotics. Chemically actuated cantilever arrays that transform biochemical reactions into nanomechanical motion may be useful for biosensing and other nanorobotic applications [11]. Mobile wireless nanorobots, for example, with motion control and onboard power supplies, are being more widely discussed than even just a few years ago [12–16].

Much of the interest in nanorobotics—and its brightest future—is focused on the medical and surgical applications areas [17]. There have already been early attempts to build less sophisticated stand-alone microrobots for near-term in vivo

surgical use. For example, Ishiyama's group [18] at Tohoku University developed tiny magnetically driven spinning screws intended to swim along veins and carry drugs to infected tissues or even to burrow into tumors and kill them with heat. Martel's group at the Nanorobotics Laboratory of Ecole Polytechnique in Montreal has used variable magnetic resonance imaging (MRI) magnetic fields to generate forces on an untethered microrobot containing ferromagnetic particles, developing sufficient propulsive power to direct the small device through the human body [19]. In 2007, they reported injecting, guiding via computer control, and propelling at 10 cm/s a prototype untethered microdevice (a ferromagnetic 1.5-mm-diameter sphere) within the carotid artery of a living animal placed inside a clinical MRI system [20]—the first time such in vivo mobility has been demonstrated. Martel's group continues to make progress using this approach [21, 22].

Nelson's team at the Swiss Federal Institute of Technology in Zurich has pursued a similar approach, in 2005 reporting [23] the fabrication of a microscopic robot small enough ($\sim$200 μm) to be injected into the body through a syringe and which they hope might someday be used to perform minimally invasive eye surgery. Nelson's simple microrobot has successfully maneuvered through a watery maze using external energy from magnetic fields, with different frequencies able to vibrate different mechanical parts on the device to maintain selective control of different functions. More recently, the team has fabricated oxygen-sensing microrobots [24] and investigated artificial bacterial flagella for lab-on-a-chip applications [25], and Nelson has reviewed progress in the medical microrobotics field [26]. The Mavroidis group is also investigating MRI-based guidance of nanoparticulate and nanorobotic systems for targeted drug delivery [27].

Sitti's group at Carnegie Mellon's Nanorobotics Laboratory investigated [28] a <100-μm swimming microrobot using biomimetic flagellar motors borrowed from *S. marcescens* bacteria "having the capability to swim to inaccessible areas in the human body and perform complicated user directed tasks." Sitti believes that tiny, tetherless microrobots might be able to access small spaces inside the human body that can currently be reached only using invasive surgical methods [29]. Friend's group in the Micro/Nanophysics Research Laboratory at Monash University in Australia began designing a 250-μm microrobot [30, 31] to perform minimally invasive microsurgeries in parts of the body outside the reach of existing catheter technology—such as delivering a payload of expandable glue to the site of a damaged cranial artery, a procedure typically fraught with risk because posterior human brain arteries lay behind a complicated set of bends at the base of the skull beyond the reach of all but the most flexible catheters. The completed device was to have been inserted and extracted using a syringe and driven by an artificial flagellar piezoelectric micromotor; however, there have been no updates on this project since 2008 [32].

Nanosurgery has been reported on subcellular and even nanoscale structures deep inside individual living cells without killing them. For instance, femtolaser surgery has performed the following: (1) microtubule dissection inside live cells [33–35], (2) severing a single microtubule without disrupting the neighboring microtubules <1 μm away [36], (3) altering depolymerization rate of cut microtubules by varying

laser pulse duration [37], (4) dissection of individual dendritic spines of a specific neuron in a live brain without damaging adjacent structures [38], (5) selective removal of submicron regions of the cytoskeleton and individual mitochondria without altering neighboring structures [39], (6) noninvasive intratissue nanodissection of plant cell walls and selective destruction of intracellular single plastids or selected parts of them [40], and even (7) the nanosurgery of individual chromosomes (selectively knocking out genomic nanometer-sized regions within the nucleus of living Chinese hamster ovary cells) without perturbing the outer cell membrane [41]. Zettl's group has demonstrated a nanoinjector consisting of an AFM-tip-attached carbon nanotube that can release injected quantum dots into cell cytosol, with which they plan to carry out organelle-specific nanoinjections [42].

Nanomedicine [1, 43] is the application of nanotechnology to medicine: the preservation and improvement of human health, using molecular tools and molecular knowledge of the human body. Nanomedicine encompasses at least three types of molecularly precise structures [44]: nonbiological nanomaterials, biotechnology materials and engineered organisms, and nonbiological devices including diamondoid nanorobotics. In the near term, the molecular tools of nanomedicine will include biologically active nanomaterials and nanoparticles having well-defined nanoscale features. In the midterm (5–10 years), knowledge gained from genomics and proteomics will make possible new treatments tailored to specific individuals, new drugs targeting pathogens whose genomes have been decoded, and stem cell treatments. Genetic therapies, tissue engineering, and many other offshoots of biotechnology will become more common in therapeutic medical practice. We also may see biological nanorobots derived from bacteria or other motile cells that have had their genomes reengineered and reprogrammed [45], along with artificial organic devices that incorporate biological motors or self-assembled DNA-based structures [46] for a variety of useful medical purposes.

The greatest power of nanomedicine [1, 43] will emerge, perhaps starting in the late 2020s, when we can design and construct complete artificial nanorobots using rigid diamondoid nanometer-scale parts like molecular gears and bearings [47]. These medical nanorobots will possess a full panoply of autonomous subsystems including onboard sensors, motors, manipulators, power supplies, and molecular computers. But getting all these nanoscale components to spontaneously self-assemble in the right sequence will prove increasingly difficult as machine structures become more intricate. Making complex nanorobotic mechanical systems requires new manufacturing techniques that can build a molecular structure by what is called positional assembly. This will involve picking and placing molecular parts one by one and moving them along controlled trajectories much like the robot arms that manufacture cars on automobile assembly lines. The procedure will then be repeated until the final product, such as a medical nanorobot, is fully assembled, inside a desktop nanofactory [47–49].

6.2 Nanorobotic Treatments for Most Human Diseases

The ability to build complex diamondoid medical nanorobots [44, 50–53] to molecular precision, and then to build them cheaply enough in sufficiently large numbers to be useful therapeutically, will revolutionize the practice of medicine [17] and surgery [54].

The first theoretical design study of a complete medical nanorobot ever published in a peer-reviewed journal described a hypothetical artificial mechanical red blood cell or "respirocyte" made of 18 billion precisely arranged structural atoms [50]. The respirocyte would be a blood-borne spherical 1-μm diamondoid 1,000-atm pressure vessel with reversible molecule-selective surface pumps powered by endogenous serum glucose. This nanorobot would deliver 236 times more oxygen to body tissues per unit volume than natural red cells and would manage carbonic acidity, controlled by gas concentration sensors and an onboard nanocomputer. A 5-cm^3 therapeutic dose of 50 % respirocyte saline suspension containing five trillion nanorobots could exactly replace the gas-carrying capacity of the patient's entire 5.4 l of blood. Of course, nanorobots, no matter how capable, always have very well-defined physical limitations. In general, they are limited by mobility constraints, by the availability of energy, by mechanical and geometric constraints, by diffusion limits and biocompatibility requirements, and by numerous other constraints [1, 43]. Nanorobots cannot act instantly—they take time to effect their cure. Biocompatibility issues related to diamondoid medical nanorobots have been examined elsewhere at length [43].

Nanorobotic artificial phagocytes called "microbivores" could patrol the bloodstream, seeking out and digesting unwanted pathogens including bacteria, viruses, or fungi [44]. Microbivores would achieve complete clearance of even the most severe septicemic infections in hours or less. This is far better than the weeks or months needed for antibiotic-assisted natural phagocytic defenses. The nanorobots do not increase the risk of sepsis or septic shock because the pathogens are completely digested into harmless sugars, amino acids, and the like, which are the only effluents from the nanorobot. Similar nanorobots can digest cancer cells and vascular blockages that produce heart disease and stroke.

Even more powerful applications—most importantly, involving cellular replacement or in situ repair of individual cells—are possible with medical nanorobotics. For example, most diseases involve a molecular malfunction at the cellular level, and cell function is significantly controlled by gene expression of proteins. As a result, many disease processes are driven either by defective chromosomes or by defective gene expression. So in many cases, it may be most efficient to extract the existing chromosomes from a diseased cell and insert fresh new ones in their place. This cell repair procedure is called "chromosome replacement therapy" [53]. During this future procedure, your replacement chromosomes first would be manufactured to order, outside of your body, in a clinical benchtop production device that includes a molecular assembly line. The patient's individual genome is used as the blueprint. If the patient wants, acquired or inherited defective genes could be replaced with non-defective base-pair sequences during the chromosome manufacturing process, thus

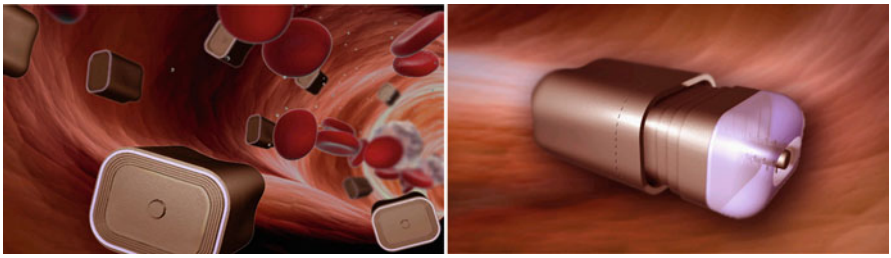

Fig. 6.2 Chromallocytes. *Left*: Artist's conceptions of the basic chromallocyte [53] design. Devices walk along luminal wall of blood vessel using an array of cilia-like mechanical manipulator arms (not shown in the illustration) that emerge from silos embedded in the nanorobot hull. *Right*: Artist's conceptions of the basic chromallocyte [53] design. Schematic of nanorobot operation in which a large central manipulator (the proboscis) extends from the nanorobot core and spools existing nuclear DNA into a bolus which is then surrounded and enclosed by a telescoping funnel assembly. Images © 2006 Stimulacra LLC (http://www.stimulacra.net) and Robert A. Freitas Jr. (http://www.rfreitas.com). All rights reserved

permanently eliminating any genetic disease. Nanorobots called chromallocytes [53], each carrying a single copy of the revised chromosomes, would be injected into the body and travel to the target tissue cells (Fig. 6.2). Following powered cytopenetration and intracellular transit to the nucleus [1], the chromallocytes would remove the existing chromosomes and then install the properly methylated replacement chromosomes in every tissue cell of your body (requiring a total dose of several trillion nanorobots), then exit the cell and its embedding tissue, reenter the bloodstream, and finally eliminate themselves from the body either through the kidneys or via intravenous collection ports (coincident, most likely, with the original injection mechanism).

The development pathway for diamondoid medical nanorobots will be long and arduous. First, theoretical scaling studies [44, 50–53, 55, 56] are used to assess basic concept feasibility. These initial studies must then be followed by more detailed computational simulations of specific nanorobot components and assemblies and ultimately full-system simulations, all thoroughly integrated with additional simulations of massively parallel manufacturing processes from start to finish consistent with a design-for-assembly engineering philosophy. Once nanofactories implementing molecular-manufacturing capabilities become available, experimental efforts may progress from fabrication of components (using small-molecule or atomic precursors) and testing to the assembly of components into nanomechanical devices and nanomachine systems and finally to prototypes and mass manufacture of medical nanorobots, ultimately leading to clinical trials. By 2011, there was some limited experimental work with microscale-component microscopic microrobots (see Sect. 6.1), but progress on nanoscale-component microscopic diamondoid nanorobots today is largely at the concept feasibility and preliminary design stages and will remain so until experimentalists develop the capabilities required for diamondoid molecular manufacturing, as reviewed below.

Of all possible materials that might be used to build medical nanorobots—including borrowed biological components, dendrimers, polymers, and various linked or tethered nanoparticles—diamondoid (Sect. 6.4.1) is the best possible material for constructing rigid molecular machine systems exhibiting reliable repeatable mechanical operations because of its special properties including extraordinary strength, stiffness, and chemical stability.

6.3 Positional Diamondoid Molecular Manufacturing

Complex molecular machine systems, including microscale robotic mechanisms comprised of thousands or millions of nanoscale mechanical components such as gears, motors, and computer elements, probably cannot be manufactured using the conventional techniques of self-assembly. As noted in the final report [57] of the 2006 congressionally mandated review of the US National Nanotechnology Initiative (NNI) by the National Research Council (NRC) of the National Academies and the National Materials Advisory Board (NMAB): "For the manufacture of more sophisticated materials and devices, including complex objects produced in large quantities, it is unlikely that simple self-assembly processes will yield the desired results. The reason is that the probability of an error occurring at some point in the process will increase with the complexity of the system and the number of parts that must interoperate." Error detection and correction requires a minimum level of complexity that cannot easily be achieved via thermodynamically driven self-assembly processes.

The opposite of self-assembly processes is positionally controlled processes, in which the positions and trajectories of all components of intermediate and final product objects are controlled at every moment during fabrication and assembly. Positional processes should allow more complex products to be built with high quality and should enable rapid prototyping during product development. Positional assembly is the norm in conventional macroscale manufacturing (e.g., cars, appliances, houses) but is only recently [49, 58] starting to be seriously investigated experimentally for nanoscale manufacturing. Of course, we already know that positional fabrication will work in the nanoscale realm. This is demonstrated in the biological world by ribosomes, which positionally assemble proteins in living cells by following a sequence of digitally encoded instructions (even though ribosomes themselves are self-assembled). Lacking this positional fabrication of proteins controlled by DNA-based software, large, complex, digitally specified organisms would probably not be possible, and biology as we know it would not exist. Guided self-assembly—a hybrid approach combining self-assembly and positional assembly—is also being investigated experimentally [59, 60].

The most important materials for positional assembly may be the rigid covalent or "diamondoid" solids, since these could potentially be used to build the most reliable and complex nanoscale machinery. Preliminary theoretical studies have suggested great promise for these materials in molecular manufacturing. The

NMAB/NRC Review Committee recommended [57] that experimental work aimed at establishing the technical feasibility of positional molecular manufacturing should be pursued and supported: "Experimentation leading to demonstrations supplying ground truth for abstract models is appropriate to better characterize the potential for use of bottom-up or molecular manufacturing systems that utilize processes more complex than self-assembly." Making complex nanorobotic systems requires manufacturing techniques that can build a molecular structure by positional assembly [61]. This will involve picking and placing molecular parts one by one, moving them along controlled trajectories much like the robot arms that manufacture cars on automobile assembly lines. The procedure is then repeated over and over with all the different parts until the final product, such as a medical nanorobot, is fully assembled inside a desktop nanofactory.

Technologies required for the atomically precise fabrication of diamondoid nanorobots in macroscale quantities at low cost require the development of a new nanoscale manufacturing technology called positional diamondoid molecular manufacturing, enabling diamondoid nanofactories. Achieving this new technology over the next one to three decades will require the significant further development of four closely related technical capabilities: diamondoid mechanosynthesis (DMS) (Sect. 6.4), programmable positional assembly (Sect. 6.5), massively parallel positional assembly (Sect. 6.6), and nanomechanical design (Sect. 6.7).

6.4 Diamondoid Mechanosynthesis

Mechanosynthesis, or molecular positional fabrication, is the formation of covalent chemical bonds using precisely applied mechanical forces to build atomically precise structures. Mechanosynthesis will be most efficient when automated via computer control, enabling programmable molecular positional fabrication of nanostructures of significant size. Atomically precise fabrication involves holding feedstock atoms or molecules, and separately a growing nanoscale workpiece, in the proper relative positions and orientations so that when they touch they will chemically bond in the desired manner. In this process, a mechanosynthetic tool is brought up to the surface of a workpiece. One or more transfer atoms are added to, or removed from, the workpiece by the tool. Then the tool is withdrawn and recharged (Fig. 6.3). This process is repeated until the workpiece (e.g., a growing nanopart) is completely fabricated to molecular precision with each atom in exactly the right place. The transfer atoms are under positional control at all times to prevent unwanted side reactions from occurring. Side reactions are also avoided using proper reaction design so that the reaction energetics avoids undesired pathological intermediate structures and atomic rearrangements.

The positional assembly of diamondoid structures, some almost atom by atom, using molecular feedstock has been examined theoretically [47, 62–71] via computational models of DMS. DMS is the controlled addition of individual carbon atoms, carbon dimers (C_2), single methyl (CH_3), or like groups to the growth surface

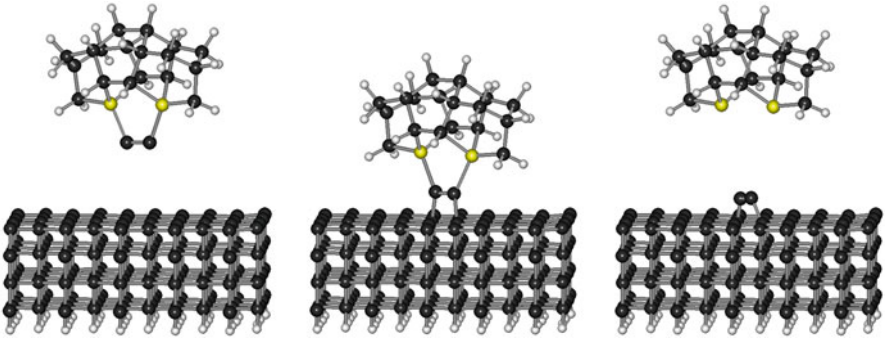

Fig. 6.3 Diamondoid mechanosynthesis: DCB6Ge dimer placement tool shown depositing two carbon atoms on a diamond surface (C = *black*, H = *white*, Ge = *yellow*/*gray*) [49]. © 2011 Robert A. Freitas Jr. All rights reserved

of a diamond crystal lattice workpiece in a vacuum manufacturing environment. Covalent chemical bonds are formed one by one as the result of positionally constrained mechanical forces applied at the tip of a scanning probe microscope (SPM) apparatus, usually resulting in the addition of one or more atoms having one or more bonds into the workpiece structure. Programmed sequences of carbon dimer placement on growing diamond surfaces in vacuo appear feasible in theory [67, 71].

6.4.1 Diamondoid Materials

Diamondoid materials include pure diamond, the crystalline allotrope of carbon. Among other exceptional properties, diamond has extreme hardness, high thermal conductivity, low frictional coefficient, chemical inertness, a wide electronic bandgap, and is the strongest and stiffest material presently known at ordinary pressures. Diamondoid materials also may include any stiff covalent solid that is similar to diamond in strength, chemical inertness, or other important material properties and possess a dense three-dimensional network of bonds. Examples of such materials are carbon nanotubes and fullerenes, atomically precise "doped" diamond, several strong covalent ceramics such as silicon carbide, silicon nitride, and boron nitride, and a few very stiff ionic ceramics such as sapphire (monocrystalline aluminum oxide) that can be covalently bonded to pure covalent structures such as diamond. Of course, pure crystals of diamond are brittle and easily fractured. The intricate molecular structure of a diamondoid atomically precise product will more closely resemble a complex composite material, not a brittle solid crystal. Such products, and the nanofactory systems that build them, should be extremely durable in normal use.

6.4.2 Minimal Toolset for DMS

It is already possible to synthesize bulk diamond today. In a process somewhat reminiscent of spray painting, layer after layer of diamond is built up by holding a cloud of reactive hydrogen atoms and hydrocarbon molecules over a deposition surface. When these molecules bump into the surface, they change it by adding, removing, or rearranging atoms. By carefully controlling the pressure, temperature, and the exact composition of the gas in this process—called chemical vapor deposition or CVD—conditions can be created that favor the growth of diamond on the surface. But randomly bombarding a surface with reactive molecules does not offer fine control over the growth process. To achieve atomically precise fabrication, the first challenge is to make sure that all chemical reactions will occur at precisely specified places on the surface. A second problem is how to make the diamond surface reactive at the particular spots where we want to add another atom or molecule. A diamond surface is normally covered with a layer of hydrogen atoms. Without this layer, the raw diamond surface would be highly reactive because it would be studded with unused (or "dangling") bonds from the topmost plane of carbon atoms. While hydrogenation prevents unwanted reactions, it also renders the entire surface inert, making it difficult to add carbon (or anything else) to it.

To overcome these problems, a set of molecular-scale tools must be developed that would, in a series of well-defined steps, prepare the surface and create hydrocarbon structures on a layer of diamond, atom by atom and molecule by molecule. A mechanosynthetic tool typically will have two principal components—a chemically active tooltip and a chemically inert handle to which the tooltip is covalently bonded. The tooltip is the part of the tool where site-specific single-molecule chemical reactions are forced to occur by the application of mechanical energy. The much larger handle structure is big enough to be grasped and positionally manipulated using an SPM or similar macroscale instrumentality. At least three types of basic mechanosynthetic tools (Fig. 6.4) have already received considerable theoretical (and some related experimental) study and are likely among those required to build molecularly precise diamond via positional control:

1. *Hydrogen abstraction tools*. The first step in the process of mechanosynthetic fabrication of diamond might be to remove a hydrogen atom from each of two specific adjacent spots on the diamond surface, leaving behind two reactive dangling bonds. This could be done using a hydrogen abstraction tool [68] that has a high chemical affinity for hydrogen at one end but is elsewhere inert. The tool's unreactive region serves as a handle or handle attachment point. The tool would be held by a high-precision nanoscale positioning device, initially perhaps a SPM tip but ultimately a molecular robotic arm, and moved directly over particular hydrogen atoms on the surface. One suitable molecule for a hydrogen abstraction tooltip is the acetylene or "ethynyl" radical, comprised of two carbon atoms triple bonded together. One carbon of the two serves as the handle connection and would bond to a nanoscale positioning device through a larger handle structure. The other carbon of the two has a dangling bond where

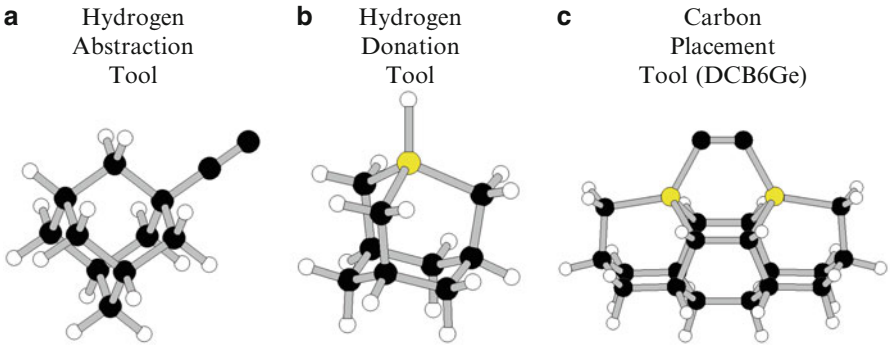

Fig. 6.4 Examples of three basic mechanosynthetic tool types that are required to build molecularly precise diamond via positional control (C = *black*, H = *white*, Ge = *yellow*/*gray*) [71] © 2011 Robert A. Freitas Jr. All rights reserved. (**a**) Hydrogen abstraction tool, (**b**) hydrogen donation tool, and (**c**) carbon placement tool (DCB6Ge)

a hydrogen atom would normally be present in a molecule of ordinary acetylene (C_2H_2), which can bond and thereby abstract a hydrogen atom from a workpiece structure. The environment around the tool would be inert (e.g., vacuum or a noble gas such as neon). The recharge sequence for this tool has been studied rather extensively [72].

2. *Carbon placement tools*. After the abstraction tool has created adjacent reactive spots by selectively removing hydrogen atoms from the diamond surface but before the surface is re-passivated with hydrogen, carbon placement tools may be used to deposit carbon atoms at the desired reactive surface sites. In this way, a diamond structure can be built up on the surface, molecule by molecule, according to plan. The first complete tool ever proposed for this carbon deposition function is the "DCB6Ge" dimer placement tool [63]—in this example, a carbon (C_2) dimer having two carbon atoms connected by a triple bond with each carbon in the dimer connected to a larger unreactive handle structure via two germanium atoms. This dimer placement tool, also held by a nanoscale positioning device, is brought close to the reactive spots along a particular trajectory, causing the two dangling surface bonds to react with the ends of the carbon dimer. The dimer placement tool would then withdraw, breaking the relatively weaker bonds between it and the C_2 dimer and transferring the carbon dimer from the tool to the surface. A positionally controlled dimer could be bonded at many different sites on a growing diamondoid workpiece, in principle allowing the construction of a wide variety of useful nanopart shapes. As of 2007, the DCB6Ge dimer placement tool remains the most studied of any mechanosynthetic tooltip to date [63, 64, 66, 67, 69, 71], having had more than 150,000 CPU hours of computation invested thus far in its analysis, and it remains the only tooltip motif that has been successfully simulated and theoretically validated for its intended function on a full 200-atom diamond surface [67]. Other proposed dimer (and related carbon

transfer) tooltip motifs [47, 62, 63, 65, 69, 71] have received less intensive study but are also expected to perform well.

3. *Hydrogen donation tools*. After an atomically precise structure has been fabricated by a succession of hydrogen abstractions and carbon depositions, the fabricated structure must be passivated to prevent additional unplanned reactions. While the hydrogen abstraction tool is intended to make an inert structure reactive by creating a dangling bond, the hydrogen donation tool [70] does the opposite. It makes a reactive structure inert by terminating a dangling bond by adding an H atom. Such a tool would be used to stabilize reactive surfaces and help prevent the surface atoms from rearranging in unexpected and undesired ways. The key requirement for a hydrogen donation tool is that it includes a weakly attached hydrogen atom. Many molecules fit that description, but the bond between hydrogen and germanium is sufficiently weak so that a Ge-based hydrogen donation tool should be effective.

A recently completed 3-year study [71] representing 102,188 CPU hours of computing time has computationally analyzed a comprehensive set of DMS reactions and an associated minimal set of nine specific DMS tooltips that could be used to build basic diamond, graphene (e.g., carbon nanotubes), and all of the tools themselves including all necessary tool recharging reactions. The research defined 65 DMS reaction sequences incorporating 328 reaction steps, with 354 pathological side reactions analyzed and with 1,321 unique individual DFT-based (density functional theory) quantum chemistry reaction energies reported. These mechanosynthetic reaction sequences range in length from 1 to 13 reaction steps (typically 4) with 0–10 possible pathological side reactions or rearrangements (typically 3) reported per reaction.

The first practical proposal for building a DMS tool experimentally was published in 2005 and is the subject of the first mechanosynthesis patent ever issued, in March 2010 [66]. According to this proposal, the manufacture of a complete "DCB6Ge" positional dimer placement tool would require four distinct steps: synthesizing a capped tooltip molecule, attaching it to a deposition surface, attaching a handle to it via CVD, and then separating the tool from the deposition surface. An even simpler practical proposal for building DMS tools experimentally, also using only experimental methods available today, was published as part of the aforementioned minimal toolset work [71]. Processes are identified for the experimental fabrication of a hydrogen abstraction tool, a hydrogen donation tool, and two alternative carbon placement tools (other than DCB6Ge). These processes and tools are part of the second mechanosynthesis patent ever filed and provide clear developmental targets for a comprehensive near-term DMS implementation program to begin working toward a more mature set of efficient, positionally controlled mechanosynthetic tools that can reliably build atomically precise diamondoid structures—including more DMS tools.

6.4.3 *Experimental Successes to Date*

The first experimental proof that individual atoms could be manipulated was obtained by IBM scientists in 1989 when they used a scanning tunneling microscope to precisely position 35 xenon atoms on a nickel surface to spell out the corporate logo "IBM." However, this feat did not involve the formation of covalent chemical bonds. One important step toward the practical realization of DMS was achieved in 1999 [73] with the first site-repeatable site-specific covalent bonding operation of a two diatomic carbon-containing molecules (CO), one after the other, to the same atom of iron on a crystal surface, using an SPM. The first experimental demonstration of true mechanosynthesis, establishing covalent bonds using purely mechanical forces—albeit on silicon atoms, not carbon atoms—was reported [74] in 2003. In this landmark experiment, the researchers vertically manipulated single silicon atoms from the Si(111)–(7×7) surface, using a low-temperature near-contact atomic force microscope to demonstrate (1) removal of a selected silicon atom from its equilibrium position without perturbing the (7×7) unit cell and (2) the deposition of a single Si atom on a created vacancy, both via purely mechanical processes. The same group later repeated this feat with Ge atoms [75].

By 2008, the Custance group in Japan [76] had progressed to more complex 2D structures fabricated entirely via mechanosynthesis using more than a dozen Si/Sn or Pb/In atoms, with a 12-atom 2D pattern created in 1.5 h (∼450 s/atom). In late 2008, Moriarty's group at the University of Nottingham (UK) began a $3-million 5-year effort [77] employing a similar apparatus to produce 2D patterns using carbon atoms, to validate previous theoretical DMS proposals [71]. If successful, Moriarty's work could lead to subsequent studies extending DMS from 2D to small 3D carbon nanostructures.

6.5 Programmable Positional Assembly

Atomically precise nanoparts [78], once fabricated, must be transferred from the fabrication site and assembled into atomically precise complex components containing many nanoparts. Such components may include gear trains in housings, sensors, motors, manipulator arms, power generators, and computers. These components may then be assembled, for example, into a complex molecular machine system that consists of many components. A complex micron-size medical nanorobot such as a microbivore [44] constructed of such atomically precise components may possess many tens of thousands of individual components, millions of primitive parts, and many billions of atoms in its structure. The conceptual dividing line between fabrication and assembly may sometimes be blurred because in many cases it might be possible, even preferable, to fabricate nominally multipart components as a single part—allowing, for example, two meshed gears and their housing to be manufactured as a single sealed unit.

The process of positional assembly, as with DMS, can be automated via computer control as has been demonstrated experimentally in the case of individual atoms in the Autonomous Atom Assembly project sponsored by NIST and ONR [79] and in the case of microscale parts in automated microelectromechanical systems (MEMS) assembly [80, 81]. This allows the design of positional assembly stations which receive inputs of primitive parts and assemble them in programmed sequences of steps into finished complex components. These components can then be transported to secondary assembly lines which use them as inputs to manufacture still larger and more complex components, or completed systems, again analogous to automobile assembly lines.

6.6 Massively Parallel Positional Assembly

To be practical, molecular manufacturing must also be able to assemble very large numbers of medical nanorobots very quickly. It is not enough to be able to build just one molecularly precise part, component, or medical nanorobot. For nanofactories to be economically viable, we must be able to assemble complex nanostructures in vast numbers—in billions or trillions of finished units (product objects). Approaches under consideration include using replicative manufacturing systems or massively parallel fabrication, employing large arrays of scanning probe tips all building similar diamondoid product structures in unison, as in nanofactories [47–49].

This will require massively parallel manufacturing systems with millions of assembly lines operating simultaneously and in parallel, not just one or a few of them at a time as with the assembly lines in modern-day car factories. Fortunately, each nanoassembly production line in a nanofactory can in principle be very small. Many millions of them should easily fit into a very small volume. Massively parallel manufacture of DMS tools, handles, and related nanoscale fabrication and assembly equipment will also be required, perhaps involving the use of massively parallel manipulator arrays or some other type of replicative system [48].

Reliability is an important design issue. The assembly lines of massively parallel manufacturing systems might have numerous redundant smaller assembly lines feeding components into larger assembly lines so that the failure of any one smaller line cannot cripple the larger one. Arranging parallel production lines for maximum efficiency and reliability to manufacture a wide variety of products (possibly including error detection, error correction, and removal of defective parts) is a major requirement in nanofactory design.

6.7 Nanomechanical Design

Computational tools for molecular machine modeling, simulation, and manufacturing process control must be created to enable the development of designs for diamondoid nanoscale parts, components, and nanorobotic systems. These designs

can then be rigorously tested and refined in simulation before undertaking more expensive experimental efforts to build them. Basic molecular machine design and simulation software has been available for several years [82], and libraries of predesigned nanoparts are slowly being assembled. More effort must be devoted to large-scale simulations of complex nanoscale machine components, design and simulation of assembly sequences and manufacturing process control, and general nanofactory design and simulation.

6.8 Nanofactory Collaboration

The NMAB/NRC Review Committee, in their congressionally mandated review [57] of the NNI, called for proponents of "site-specific chemistry for large-scale manufacturing" to (1) delineate desirable research directions not already being pursued by the biochemistry community; (2) define and focus on some basic experimental steps that are critical to advancing long-term goals; and (3) outline some "proof-of-principle" studies that, if successful, would provide knowledge or engineering demonstrations of key principles or components with immediate value.

In direct response to these requirements, the Nanofactory Collaboration is coordinating a combined experimental and theoretical effort to explore the feasibility of positionally controlled mechanosynthesis of diamondoid structures using simple molecular feedstock. The precursor to the Nanofactory Collaboration was informally initiated by Robert Freitas and Ralph Merkle in the Fall of 2000 during their time at Zyvex. Their continuing efforts, and those of others, have now grown into direct collaborations among 25 researchers or other participants (including 18 PhDs or PhD candidates) at 13 institutions in 4 countries (USA, UK, Russia, and Belgium), as of late 2011. The Collaboration website is at http://www.MolecularAssembler.com/Nanofactory.

At present, the Collaboration is a loose-knit community of scientists and others who are working together as time and resources permit in various team efforts with these teams producing numerous coauthored publications, though with disparate funding sources not necessarily tied to the Collaboration. While not all participants may currently envision a nanofactory as the end goal of their present research (or other) efforts in connection with the Collaboration, many *do* envision this, and even those who do not currently envision this end goal have nonetheless agreed to do research in collaboration with other participants that we believe will contribute important advances along the pathway to diamondoid nanofactory development, starting with the direct development of DMS. While some work has been done on each of the four primary capabilities thought necessary to design and build a functioning nanofactory, for now the greatest research attention is being concentrated on the first key area: proving the feasibility, both theoretical and experimental, of achieving diamond mechanosynthesis.

We welcome new participants who would like to help us address the many remaining technical challenges [83] to the realization of a working diamondoid nanofactory that would permit the fabrication of medical nanorobots.

References

1. Freitas RA Jr (1999) Nanomedicine, Vol. I: Basic Capabilities, Landes Bioscience, Georgetown, TX. http://www.nanomedicine.com/NMI.htm
2. Ding B, Seeman NC (2006) Operation of a DNA robot arm inserted into a 2D DNA crystalline substrate. Science 314:1583–1585
3. Garibotti AV, Liao S, Seeman NC (2007) A simple DNA-based translation system. Nano Lett 7:480–483
4. Goodman RP, Heilemann M, Doose S, Erben CM, Kapanidis AN, Turberfield AJ (2008) Reconfigurable, braced, three-dimensional DNA nanostructures. Nat Nanotechnol 3:93–96
5. Gu H, Chao J, Xiao SJ, Seeman NC (2010) A proximity-based programmable DNA nanoscale assembly line. Nature 465:202–205
6. Sahu S, LaBean TH, Reif JH (2008) A DNA nanotransport device powered by polymerase phi29. Nano Lett 8:3870–3878
7. Hamdi M (2009) Computational design and multiscale modeling of a nanoactuator using DNA actuation. Nanotechnology 20:485501
8. Sharma G, Rege K, Budil D, Yarmush M, Mavroidis C (2009) Computational studies of a protein based nanoactuator for nanogripping applications. Int J Robot Res 28:421–435, http://www.coe.neu.edu/Research/robots/papers/IJRR_Nanorob.pdf
9. Kaur H, Kumar S, Kukkar D, Kaur I, Singh K, Bharadwaj LM (2010) Transportation of drug-(polystyrene bead) conjugate by actomyosin motor system. J Biomed Nanotechnol 6:279–286
10. Hamdi M, Ferreira A, Sharma G, Mavroidis C (2008) Prototyping bio-nanorobots using molecular dynamics simulation and virtual reality. Microelectronics J 30:190–201, http://www.coe.neu.edu/Research/robots/papers/MEJ.pdf
11. Watari M, Ndieyira JW, McKendry RA (2010) Chemically programmed nanomechanical motion of multiple cantilever arrays. Langmuir 26:4623–4626
12. Hill C, Amodeo A, Joseph JV, Patel HR (2008) Nano- and microrobotics: how far is the reality? Expert Rev Anticancer Ther 8:1891–1897
13. Jain KK (2008) Nanomedicine: application of nanobiotechnology in medical practice. Med Princ Pract 17:89–101
14. Mallouk TE, Sen A (2009) Powering nanorobots. Sci Am 300:72–77
15. Sánchez S, Pumera M (2009) Nanorobots: the ultimate wireless self-propelled sensing and actuating devices. Chem Asian J 4:1402–1410
16. Hogg T, Freitas RA Jr (2010) Chemical power for microscopic robots in capillaries. Nanomedicine 6:298–317, http://www.nanomedicine.com/Papers/NanoPowerModel2010.pdf
17. Freitas RA Jr (2010) Comprehensive nanorobotic control of human morbidity and aging. In: Fahy GM, West MD, Coles LS, Harris SB (eds) The future of aging: pathways to human life extension. Springer, New York, NY, pp 685–805, http://www.nanomedicine.com/Papers/Aging.pdf
18. Ishiyama K, Sendoh M, Arai KI (2002) Magnetic micromachines for medical applications. J Magn Magn Mater 242–245:1163–1165
19. Mathieu JB, Martel S, Yahia L et al (2005) MRI systems as a mean of propulsion for a microdevice in blood vessels. Biomed Mater Eng 15:367–374
20. Martel S, Mathieu JB, Felfoul O et al (2007) Automatic navigation of an untethered device in the artery of a living animal using a conventional clinical magnetic resonance imaging system. Appl Phys Lett 90:114105, http://wiki.polymtl.ca/nano/fr/images/1/14/J-2007-MRSUB-APL-Sylvain2.pdf

21. Martel S (2010) Microrobotic navigable entities for magnetic resonance targeting. Conf Proc IEEE Eng Med Biol Soc 1:1942–1945
22. Pouponneau P, Savadogo O, Napporn T, Yahia L, Martel S (2010) Corrosion study of iron-cobalt alloys for MRI-based propulsion embedded in untethered microdevices operating in the vascular network. J Biomed Mater Res B Appl Biomater 93:203–211
23. Yesin KB, Exner P, Vollmers K et al (2005) Biomedical micro-robotic system. 8th International conference on medical image computing and computer assisted intervention (MICCAI 2005/http://www.miccai2005.org), Palm Springs, CA, 26–29 October 2005, p 819
24. Ergeneman O, Chatzipirpiridis G, Gelderblom FB, Pokki J, Pane S, Marin Suarez Del Toro M, Fernandez Sanchez JF, Sotiriou GA, Nelson BJ (2010) Oxygen sensing using microrobots. Conf Proc IEEE Eng Med Biol Soc 1:1958–1961
25. Zhang L, Peyer KE, Nelson BJ (2010) Artificial bacterial flagella for micromanipulation. Lab Chip 10:2203–2215
26. Nelson BJ, Kaliakatsos IK, Abbott JJ (2010) Microrobots for minimally invasive medicine. Annu Rev Biomed Eng 12:55–85
27. Vartholomeos P, Mavroidis C (2010) Simulation platform for self-assembly structures in MRI-based nanorobotic drug delivery systems. In: Proceedings of 2010 IEEE international conference on robotics and automation (ICRA2010), Anchorage, Alaska, 3–8 May, pp 5594–5600. http://www.coe.neu.edu/Research/robots/papers/ICRA2010_3.pdf
28. Behkam B, Sitti M (2007) Bacterial flagella-based propulsion and on/off motion control of microscale objects. Appl Phys Lett 90:1–3, http://nanolab.me.cmu.edu/publications/papers/Behkam-APL2007.pdf
29. Sitti M (2009) Miniature devices: voyage of the microrobots. Nature 458:1121–1122
30. Monash University (2006) Micro-robots take off as ARC announces funding. Press release, 11 October 2006. http://www.monash.edu.au/news/newsline/story/1038
31. Cole E (2007) Fantastic voyage: departure 2009. Wired Mag, 18 Jan 2007. http://www.wired.com/medtech/health/news/2007/01/72448
32. Friend J, Yan B, Yeo L et al (2008) A microrobot for three-dimensional navigation of neural vasculature for enabling treatment of stroke, arteriovenous formations, and other neural disorders. CASS Foundation Grant SM/07/1616
33. Sacconi L, Tolic-Norrelykke IM, Antolini R et al (2005) Combined intracellular three-dimensional imaging and selective nanosurgery by a nonlinear microscope. J Biomed Opt 10:14002
34. Colombelli J, Reynaud EG, Rietdorf J et al (2005) In vivo selective cytoskeleton dynamics quantification in interphase cells induced by pulsed ultraviolet laser nanosurgery. Traffic 6:1093–1102
35. Colombelli J, Reynaud EG, Stelzer EH (2007) Investigating relaxation processes in cells and developing organisms: from cell ablation to cytoskeleton nanosurgery. Methods Cell Biol 82:267–291
36. Heisterkamp A, Maxwell IZ, Mazur E et al (2005) Pulse energy dependence of subcellular dissection by femtosecond laser pulses. Opt Express 13:3690–3696
37. Wakida NM, Lee CS, Botvinick ET et al (2007) Laser nanosurgery of single microtubules reveals location-dependent depolymerization rates. J Biomed Opt 12:024022
38. Mascaro AL, Sacconi L, Pavone FS (2010) Multi-photon nanosurgery in live brain. Front Neuroenergetics 2:21
39. Shen N, Datta D, Schaffer CB et al (2005) Ablation of cytoskeletal filaments and mitochondria in live cells using a femtosecond laser nanoscissor. Mech Chem Biosyst 2:17–25
40. Tirlapur UK, Konig K (2002) Femtosecond near-infrared laser pulses as a versatile non-invasive tool for intra-tissue nanoprocessing in plants without compromising viability. Plant J 31:365–374
41. Konig K, Riemann I, Fischer P et al (1999) Intracellular nanosurgery with near infrared femtosecond laser pulses. Cell Mol Biol 45:195–201
42. Chen X, Kis A, Zettl A et al (2007) A cell nanoinjector based on carbon nanotubes. Proc Natl Acad Sci USA 104:8218–8222

43. Freitas RA Jr (2003) Nanomedicine. In: Biocompatibility, vol IIA, Landes Bioscience, Georgetown, TX, 2003. http://www.nanomedicine.com/NMIIA.htm
44. Freitas RA Jr (2005) Microbivores: artificial mechanical phagocytes using digest and discharge protocol. J Evol Technol 14:1–52, http://jetpress.org/volume14/Microbivores.pdf
45. Johnson ET, Baron DB, Naranjo B, Bond DR, Schmidt-Dannert C, Gralnick JA (2010) Enhancement of survival and electricity production in an engineered bacterium by light-driven proton pumping. Appl Environ Microbiol 76:4123–4129
46. Ellis T, Adie T, Baldwin GS (2011) DNA assembly for synthetic biology: from parts to pathways and beyond. Integr Biol (Camb) 3:109–118
47. Drexler KE (1992) Nanosystems: molecular machinery, manufacturing, and computation. Wiley, New York, NY
48. Freitas RA Jr, Merkle RC (2004) Kinematic self-replicating machines. Landes Bioscience, Georgetown, TX, http://www.MolecularAssembler.com/KSRM.htm
49. Nanofactory collaboration website (2011) http://www.MolecularAssembler.com/Nanofactory
50. Freitas RA Jr (1998) Exploratory design in medical nanotechnology: a mechanical artificial red cell. Artif Cells Blood Substit Immobil Biotechnol 26:411–430, http://www.foresight.org/Nanomedicine/Respirocytes.html
51. Freitas RA Jr (2000) Nanodentistry. J Am Dent Assoc 131:1559–1566, http://www.rfreitas.com/Nano/Nanodentistry.htm
52. Freitas RA Jr (2006) Pharmacytes: an ideal vehicle for targeted drug delivery. J Nanosci Nanotechnol 6:2769–2775, http://www.nanomedicine.com/Papers/JNNPharm06.pdf
53. Freitas RA Jr (2007) The ideal gene delivery vector: chromallocytes, cell repair nanorobots for chromosome replacement therapy. J Evol Technol 16:1–97, http://jetpress.org/v16/freitas.pdf
54. Freitas RA Jr (2005) Nanotechnology, nanomedicine and nanosurgery. Intl J Surgery 3:1–4, http://www.nanomedicine.com/Papers/IntlJSurgDec05.pdf
55. Freitas RA Jr (2000) Clottocytes: artificial mechanical platelets. IMM Report No. 18, Foresight Update No. 41, pp 9–11. http://www.imm.org/Reports/Rep018.html
56. Freitas RA Jr, Phoenix CJ (2002) Vasculoid: a personal nanomedical appliance to replace human blood. J Evol Technol 11:1–139, http://www.jetpress.org/volume11/vasculoid.pdf
57. Committee to Review the NNI (National Nanotechnology Initiative), National Materials Advisory Board (NMAB), National Research Council (NRC) (2006) A matter of size: triennial review of the national nanotechnology initiative. The National Academies Press, Washington, DC, http://www.nap.edu/catalog/11752.html#toc
58. Kenny T (2007) Tip-Based Nanofabrication (TBN). Defense Advanced Research Projects Agency (DARPA)/Microsystems Technology Office (MTO), Broad Agency Announcement BAA 07-59. http://www.fbo.gov/spg/ODA/DARPA/CMO/BAA07-59/listing.html
59. Cohen JD, Sadowski JP, Dervan PB (2007) Addressing single molecules on DNA nanostructures. Angew Chem Int Ed 46:7956–7959
60. Lee JH, Wernette DP, Yigit MV, Liu J, Wang Z, Lu Y (2007) Site-specific control of distances between gold nanoparticles using phosphorothioate anchors on DNA and a short bifunctional molecular fastener. Angew Chem Int Ed Engl 46:9006–9010
61. Freitas RA Jr (2005) Current status of nanomedicine and medical nanorobotics. J Comput Theor Nanosci 2:1–25, http://www.nanomedicine.com/Papers/NMRevMar05.pdf
62. Merkle RC (1997) A proposed 'metabolism' for a hydrocarbon assembler. Nanotechnology 8:149–162, http://www.zyvex.com/nanotech/hydroCarbonMetabolism.html
63. Merkle RC, Freitas RA Jr (2003) Theoretical analysis of a carbon-carbon dimer placement tool for diamond mechanosynthesis. J Nanosci Nanotechnol 3:319–324, http://www.rfreitas.com/Nano/JNNDimerTool.pdf
64. Mann DJ, Peng J, Freitas RA Jr, Merkle RC (2004) Theoretical analysis of diamond mechanosynthesis. Part II. C_2 mediated growth of diamond C(110) surface via Si/Ge-triadamantane dimer placement tools. J Comput Theor Nanosci 1:71–80, http://www.MolecularAssembler.com/JCTNMannMar04.pdf
65. Allis DG, Drexler KE (2005) Design and analysis of a molecular tool for carbon transfer in mechanosynthesis. J Comput Theor Nanosci 2:45–55, http://e-drexler.com/d/05/00/DC10C-mechanosynthesis.pdf

66. Freitas RA Jr (2005) A simple tool for positional diamond mechanosynthesis, and its method of manufacture. US Provisional Patent Application No. 60/543,802, filed 11 Feb 2004; US Patent 7,687,146, 30 Mar 2010. http://www.freepatentsonline.com/7687146.pdf
67. Peng J, Freitas RA Jr, Merkle RC, von Ehr JR, Randall JN, Skidmore GD (2006) Theoretical analysis of diamond mechanosynthesis. Part III. Positional C_2 deposition on diamond C(110) surface using Si/Ge/Sn-based dimer placement tools. J Comput Theor Nanosci 3:28–41, http://www.MolecularAssembler.com/Papers/JCTNPengFeb06.pdf
68. Temelso B, Sherrill CD, Merkle RC, Freitas RA Jr (2006) High-level ab initio studies of hydrogen abstraction from prototype hydrocarbon systems. J Phys Chem A 110:11160–11173, http://www.MolecularAssembler.com/Papers/TemelsoHAbst.pdf
69. Freitas RA Jr, Allis DG, Merkle RC (2007) Horizontal Ge-substituted polymantane-based C_2 dimer placement tooltip motifs for diamond mechanosynthesis. J Comput Theor Nanosci 4:433–442, http://www.MolecularAssembler.com/Papers/DPTMotifs.pdf
70. Temelso B, Sherrill CD, Merkle RC, Freitas RA Jr (2007) Ab initio thermochemistry of the hydrogenation of hydrocarbon radicals using silicon, germanium, tin and lead substituted methane and isobutane. J Phys Chem A 111:8677–8688, http://www.MolecularAssembler.com/Papers/TemelsoHDon.pdf
71. Freitas RA Jr, Merkle RC (2008) A minimal toolset for positional diamond mechanosynthesis. J Comput Theor Nanosci 5:760–861
72. Tarasov D, Akberova N, Izotova E, Alisheva D, Astafiev M, Freitas RA Jr (2010) Optimal tooltip trajectories in a hydrogen abstraction tool recharge reaction sequence for positionally controlled diamond mechanosynthesis. J Comput Theor Nanosci 7:325–353, http://www.molecularassembler.com/Papers/TarasovFeb2010.pdf
73. Lee HJ, Ho W (1999) Single bond formation and characterization with a scanning tunneling microscope. Science 286:1719–1722, http://www.physics.uci.edu/%7Ewilsonho/stm-iets.html
74. Oyabu N, Custance O, Yi I, Sugawara Y, Morita S (2003) Mechanical vertical manipulation of selected single atoms by soft nanoindentation using near contact atomic force microscopy. Phys Rev Lett 90:176102, http://link.aps.org/abstract/PRL/v90/e176102
75. Oyabu N, Custance O, Abe M, Moritabe S (2004) Mechanical vertical manipulation of single atoms on the Ge(111)-c(2x8) surface by noncontact atomic force microscopy. In: Abstracts of seventh international conference on non-contact atomic force microscopy, Seattle, Washington, USA, 12–15 September 2004, p 34. http://www.engr.washington.edu/epp/afm/abstracts/15Oyabu2.pdf
76. Sugimoto Y, Pou P, Custance O, Jelinek P, Abe M, Perez R, Morita S (2008) Complex patterning by vertical interchange atom manipulation using atomic force microscopy. Science 322:413–417, http://www.sciencemag.org/cgi/content/full/322/5900/413
77. Nanofactory Collaboration (2008). Nanofactory Collaboration Colleague Awarded $3M to Conduct First Diamond Mechanosynthesis Experiments. Nanofactory Collaboration press release, 11 Aug 2008. http://www.MolecularAssembler.com/Nanofactory/Media/PressReleaseAug08.htm
78. Tarasov D, Izotova E, Alisheva D, Akberova N, Freitas RA Jr (2011) Structural stability of clean, passivated, and partially dehydrogenated cuboid and octahedral nanodiamonds up to 2 nanometers in size. J Comput Theor Nanosci 8:147–167
79. NIST (2004) Autonomous atom assembly. http://cnst.nist.gov/epg/Projects/STM/aaa_proj.html
80. Tsui K, Geisberger AA, Ellis M, Skidmore GD (2004) Micromachined end-effector and techniques for directed MEMS assembly. J Micromech Microeng 14:542–549, http://dx.doi.org/10.1088/0960-1317/14/4/015
81. Popa DO, Stephanou HE (2004) Micro- and meso-scale robotic assembly. SME J Manuf Proc 6:52–71
82. Sims M (2006) Molecular modeling in CAD. Mach Des 78:108–113
83. Freitas RA Jr, Merkle RC (2007) Remaining technical challenges for achieving positional diamondoid molecular manufacturing and diamondoid nanofactories. Nanofactory Collaboration website. http://www.MolecularAssembler.com/Nanofactory/Challenges.htm

Part II
Nano-Manipulation and Industrial Nanorobotics

Chapter 7
Virtual Tooling for Nanoassembly and Nanomanipulations

Zhidong Wang, Lianqing Liu, Jing Huo, Zhiyu Wang, Ning Xi, and Zaili Dong

Abstract Atomic force microscopy (AFM) (Binning et al., Phys Rev Lett 56:930–933, 1986) has been used as a nanomanipulation tool recently because it not only has high resolution scanning ability but also can be controlled as an end-effector in the nanoenvironment (Junno et al., Appl Phys Lett 66:3627–3629, 1995). There are several challenging problems including controller design with relatively large thermal drift and other uncertainties, real-time positioning and manipulation control with sensor feedback, and nanosensing and manipulation planning. In the last decade, many researchers are working on these problems and some methods have been proposed that solved these problems partially (Chen et al., IEEE Trans Autom Sci Eng 3:208–217, 2006; Li et al., IEEE Trans Nanotechnol 4:605–614, 2005; Resch et al., Langmuir 14:6613–6616, 1998; Hansen et al., Nanotechnology 9:337–342, 1998; Sitti, IEEE ASME Trans Mechatron 9:343–348, 2004). However, the problem caused by single tip interaction is still hindering its efficiency especially in handling nanoparticles/nano-objects to form patterns or nanostructures.

Z. Wang (✉)
Department of Advanced Robotics, Chiba Institute of Technology, Tsudanuma 2-17-1, Narashino, Chiba, Japan
e-mail: zhidong.wang@it-chiba.ac.jp

L. Liu • Z. Wang • Z. Dong
State Key Laboratory of Robotics, Shenyang Institute of Automation, CAS, 114 Nanta Street, Shenhe District, Shenyang 110016, China
e-mail: lqliu@sia.cn; zywang@sia.cn; dzl@sia.cn

J. Huo
College of Information Science and Engineering, Northeastern University, Shenyang 110004, China
e-mail: bluerainhj@163.com

N. Xi
Department of Electrical and Computer Engineering, Michigan State University, 2120 Engineering Building, East Lansing, MI 48824-1226, USA
e-mail: xin@egr.msu.edu

C. Mavroidis and A. Ferreira (eds.), *Nanorobotics*, DOI 10.1007/978-1-4614-2119-1_7,
© Springer Science+Business Media New York 2013

Tools are usually designed and used for object handling or other tasks especially for having higher efficiency and accuracy or coping with various uncertainties on task performing. We proposed a concept of *virtual nanohand* which mimicking multi-fingered hand and controlling an AFM tip to form a virtual tool for achieving stable nano manipulation and nanoassembly. The nanohand strategy is implemented by moving the AFM tip to a set of predefined trajectories in relative high frequency. It allows us easily to design and apply various virtual tools for coping with requirements in nanomanipulation. This virtual tooling strategy is a solution with good potential on realizing high efficiency nanoassembly and nanomanipulation.

7.1 Background

It is well known that nanoparticle is an important nanomaterial and widely used for many research areas to study new phenomenon at nanoscale. With the nanoparticles, Maier et al. proved the diffusion effect of the electromagnetic energy transport [1]. Liu et al. studied the surface-enhanced Raman scattering phenomenon [2]. Makaliwe and Requicha developed an automatic path planning method for nanoparticle assembly [3]. Li et al. successfully demonstrated nanoparticles manipulation through the developed augmented reality system which can provide the real-time visual and force feedback [4]. Chen et al. developed a CAD-guided automatic nanoassembly system to handle nanoparticles and nanorods [5].

However, current commercial AFM only has one single sharp tip for nano-object manipulation. In the conventional manipulation process, the nano-object is imaged with the feedback engaged in the first. Then we need to turn off the feedback in z direction and move the AFM tip to contact and push the nano-object. The contacting area between AFM tip and the nano-object is very small and, a nano-object is usually lost from contact with the AFM tip. Two reasons are mainly considered. One reason is that the AFM tip slips over the nano-object in case that resistance force from the object is relatively large during the manipulation. Another and major reason is that the nano-object may slip away from the AFM tip when the tip is not exactly pushing on the central point of the nano-object. When the object is lost, a new image scan is necessary for relocating the lost nano-object. In [6], an active probe control method is proposed to prevent the tip from slipping over the object. By actively control the rigidity of the cantilever, the cantilever becomes rigid during manipulation and a high-sensitive interaction force is calculated from the control signal. This method also can detect if the object is lost through the force feedback. But it is difficult to know the exact position of the lost object in this situation and a new scanning procedure is still necessary to find the missed object. A local scan method is proposed in [7] to relocate the missed particle in real time, but it is only a remedial method. If the particle is lost quite often, the time consumed by local scan may be a new bottleneck for high efficiency manipulation. Thus, the fundamental approach is that the nano-object can be real-time stably controlled by the AFM tip with losing during the whole process of nanomanipulation.

In this chapter, a nanohand strategy which mimics multi-tip object pushing is introduced to achieve stable nano-object handling with a single AFM tip. Kinematics and statics models of nanoparticles and nanorods pushed by an AFM tip are developed for estimating the possible location of the nano-object center in real time and for determining properties of the nanohand. Some simulation and experiment results are provided for illustrating the validity of the proposed nanohand strategy on performing stable and controllable nano-object manipulation.

7.2 Uncertainty in Nanomanipulation

As a basic nanomanipulation task, we focus on moving a nanoparticle from one place to another by using a single-tip AFM. The simple and effective strategy is pushing the particle center by the AFM tip. In this process, the AFM is used either as a manipulation tool or an imaging tool, but not both at the same time. As pushing a ball in macro world, the nanoparticle will rotate away from the direction of pushing in case that the end-effector is not exactly pushing on the particle center. This phenomenon is significant in performing a nanomanipulation/assembly task than macro world manipulation, because the uncertainty of AFM tip position from various reasons such as temperature drift, creep, etc, is relatively large comparing with the size of nano-objects. Additionally, the uncertainty of resistant force between the supporting surface and the target object cannot be ignorable and be another reason to make the particle deviate from the target direction even lost.

Figure 7.1 shows two results of nanoparticle pushing experiments which is under the same experiment setting. The nanoparticle P_1 is the target object. Other two particles in the upper part of scan images are used as references for canceling relative position error between two scan images. By overlapping images scanned before and after the pushing, movement of particle P_1 can be observed. In the two manipulation processes, the pushing point is set to the center of the particle and the pushing distance is 500nm. Both horizontal and vertical displacements of two experiments are different, because positioning error of the AFM tip exists. Furthermore, the AFM tip as an end-effector can only apply a point contacting force on the nano-object. Both of these reasons result a wide range area of possible positions of the particle center after manipulation (Fig. 7.2). In other words, the manipulation accuracy is poor especially when the pushing distance increases.

Nanorod is also a common nano-object used to construct nanostructures in nanomanipulation. When a rod is pushed by an AFM tip, both translational and rotational motion occurs during manipulation, and the rod rotates around an instantaneous center of rotation depending on the position of pushing contact point.

In Fig. 7.3, experimental results show that the instantaneous center of rotation is different under different pushing points. If the pushing point is choose inappropriately, the rod can easily slip away from the tip and the manipulation would fail. Usually, a user can only have the result of manipulation after taking the second scan image. This lets manipulation of nanorods over long distances be very

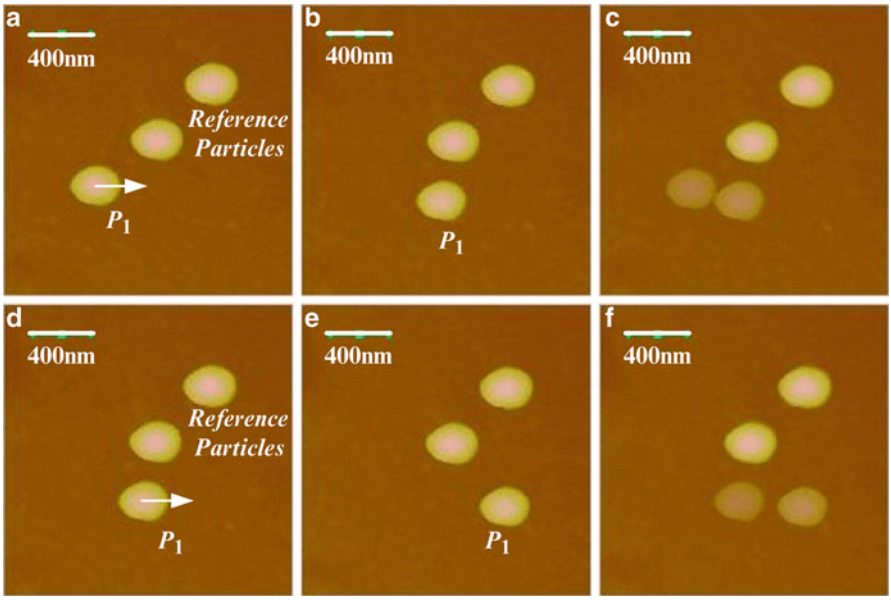

Fig. 7.1 The pushing experiment results under the same initial conditions. The particle P_1 is pushed 500nm horizontally by AFM tip. The first experiment: (**a**) Initial position (**b**) Resultant position (**c**) Overlapping image of (**a**) and (**b**) for showing particle's movement. The second experiment: (**d**) Initial position (**e**) Resultant position (**f**) Overlapping image of (**d**) and (**e**). It is clear that the results are different in the *horizontal* and *vertical* displacements both

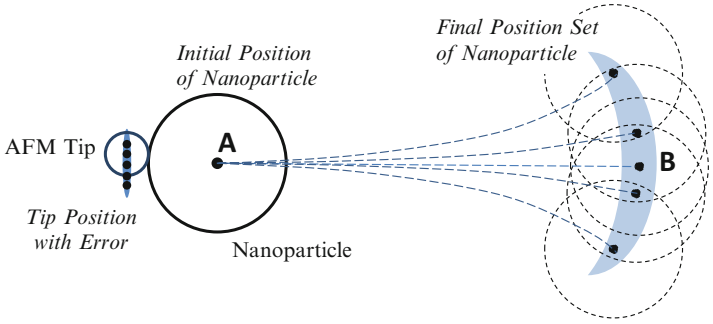

Fig. 7.2 A nanoparticle may be pushed from initial position A to a wide range area B because of AFM tip position error

time-consuming. In addition, the contact between the AFM tip and the nano-object is too small to realize posture control during manipulation. Tip position error makes the manipulation unstable and uncontrollable. Figure 7.4 shows the possible positions after the nanorod is pushed by the single AFM tip. Range of possible positions of the rod is a relative wide area, and the posture will be different with the initial in general. Then, stable pushing strategy is important for efficient nanomanipulation.

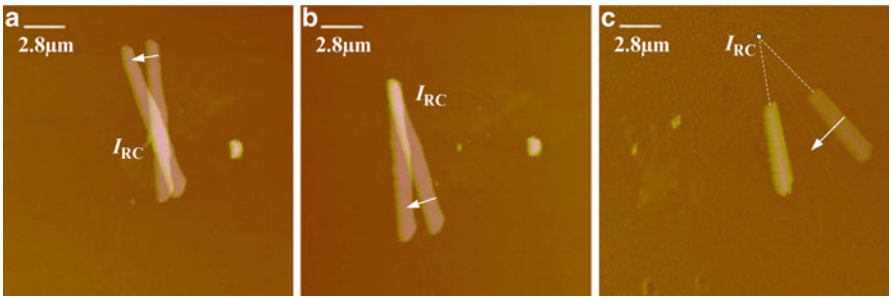

Fig. 7.3 The experimental results that the instantaneous center of rotation is (**a**) inside the rod, (**b**) at the end of the rod and (**c**) out of the rod while the nanorod is pushed on different contacting point by AFM tip

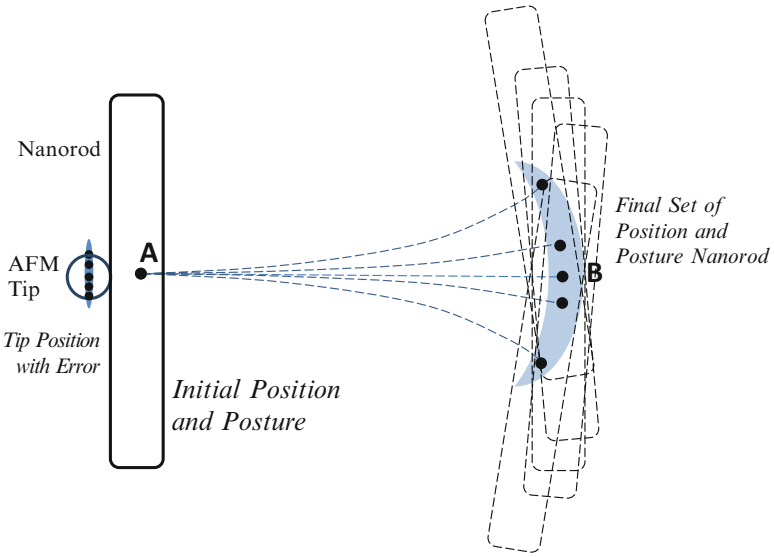

Fig. 7.4 The rod is pushed to a wide range area around the target position and posture because of the inaccuracy of the AFM tip position

7.3 Nanohand Strategy for Stable Manipulation and Assembly

In multi-robot object transportation, concepts of object closure [8] and conditional closure are proposed to solve the problem of position error of mobile robots during manipulation. Based on the concept of conditional closure, we proposed a nano-object transportation strategy a strategy to mimic multi-fingered hand with single AFM tip [9, 10]. We name it *virtual nanohand*. The nanohand strategy is implemented by moving the AFM tip to a set of predefined positions and generating

a short pushing action to the target object from those positions in relative high frequency. It can achieve the effect of multi-tip manipulation for stable pushing only with a single AFM tip. By incorporating this strategy, the problem of pushing position error with a single end-effector can be resolved.

The concept of the nanohand based manipulation is shown in Fig. 7.5. The AFM tip is moved to a set of predefined positions with coverture shape Fig. 7.5(a), and pushes the particle in each position a small step sequentially. By repeating this kind of multiple pushing on two sides of the particle center in proper length of pushing step, the particle can be *controlled* within the nanohand while it is pushed. By modeling of the nanoparticle pushing by a single AFM tip and analyzing maximum errors of the pushing, the pushing points, pushing step-length and pushing speed of the nanohand can be designed for limiting the possible positions of particle center within an up-bonded range. Then, the nanoparticle can be controlled in real time by a single AFM tip without losing during manipulation.

Figure 7.5(b) shows the manipulation process using nanohand strategy to push a nanorod. By planning and controlling trajectory of the nanohand set, the rod can be moved forward in predefined distance first and then be rotated to its target posture even with certain position errors of the AFM tip. By using the nanohand strategy,

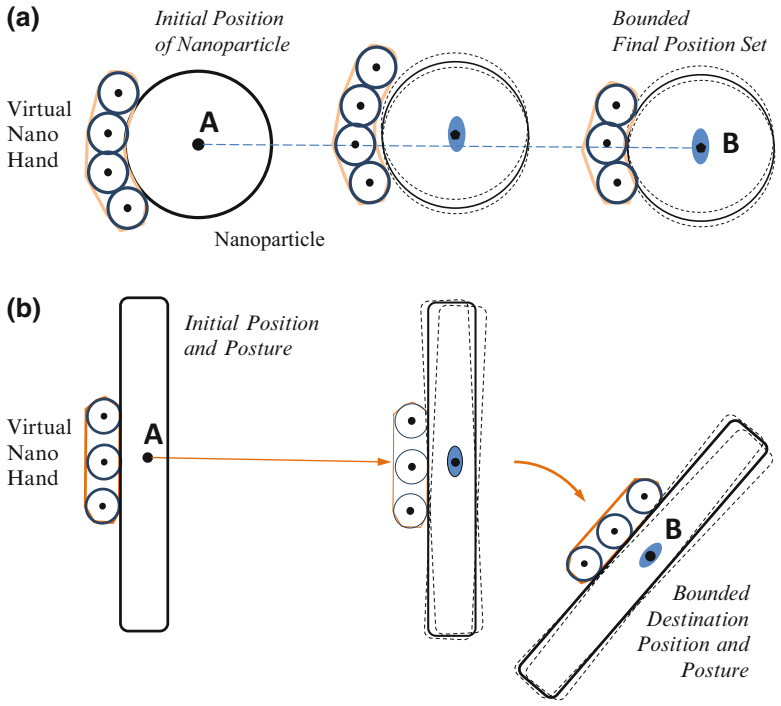

Fig. 7.5 By using nanohand strategy, the nanorod can be handled to the target position and orientation stably with upper-bounded error, even the error of the AFM tip cannot be ignored in nanomanipulation. (**a**) The particle can be pushed to a small and up-bounded area B by using nanohand strategy. (**b**) The effect of errors of AFM tip position can be reduced and stable pushing is realized by using nanohand strategy

real-time position and posture control can be achieved as manipulation performed by multiple AFM tips.

7.4 Models of Nano-object Manipulation

The nanohand strategy imitates multi-tip manipulation by planning pushing point set and pushing step-length. In determining these two parameters, kinematics and statics model of the nano-object in the manipulation are used. In discussing properties of mesoscopic objects, friction is no longer proportional to the normal load [11] and the acceleration is not the decisive factor which affects the movement of nano-object. On the other hand, in nanoscale, all the objects and substrates are covered by water. Viscous friction must be considered in modeling motion of nano-objects. Experiment results also show that different pushing velocities have different PSD voltage deflections while a nanoparticle or nanorod is pushed by using an AFM tip. Figure 7.6 shows the results that under the same pushing conditions, the PSD voltages change in lateral direction when the AFM tip pushes a nanorod with different velocities. The viscous friction effect is significant comparing with object manipulation in macro environments.

When the tip of AFM pushes the nanoparticle in contact mode, the force would make the particle deformed. Then a contact area will be formed between the substrate and the nanoparticle, and it could be modeled as a circular area with radius R (Fig. 7.7). The radius of the contacting area can be calculated by using the Johnson–Kendall–Roberts (JKR) model [12, 13]. Assuming, the tip contacts the particle all the time during the manipulation, the pushing velocity is a constant, and the substrate is flat. Owing to adopt contact mode, the pushing force acting surface would be the plane which is parallel to the substrate where contact area is on. So the particle can be simplified as a disk. It means that the contact area

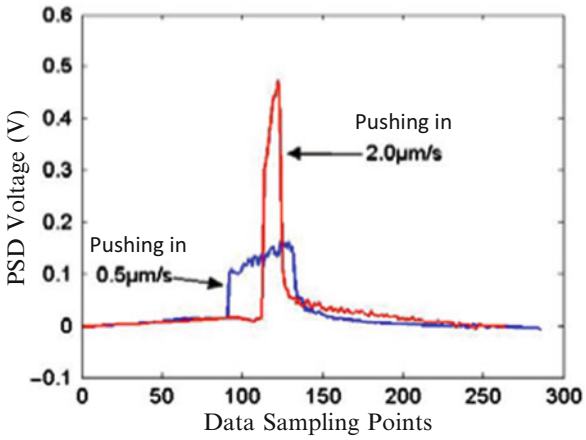

Fig. 7.6 Lateral PSD signal with different pushing velocities on pushing a nanorod

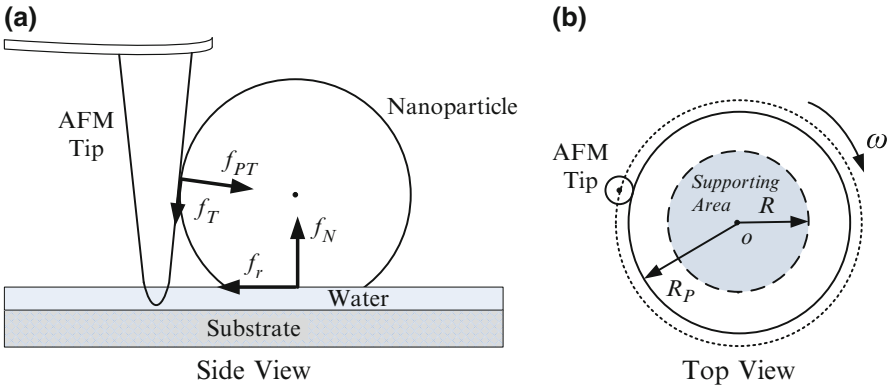

Fig. 7.7 The model of nanoparticle pushing. (**a**) Side view (**b**) Top view

center's movement can reflect the particle center's movement, and then we can discuss the motion of the particle in 2D model (Fig. 7.7). Figure 7.7a is the side view that indicates the relationship of the forces. Figure 7.7b is the top view that indicates the relationship between the contact plane and the pushing plane. When a constant velocity is applied to a nanoparticle, the nanoparticle starts to rotation around an instantaneous center of rotation. If the substrate is a homogeneous media, the movement of the disk can be regarded as uniform circular motion.

f_{PT} is the pushing force applied to the nanoparticle from the AFM tip, f_{T} is the friction between the tip and the particle. F_{N} is the particle–substrate normal forces in contact area. f_{r} is the resistance force including particle–substrate friction and surface effect force. Because the surface of the substrate is covered with water, the viscous friction must be considered in f_{r}. Additionally, vertical components of the contacting forces (f_{PT} and f_{T}) applied from the tip could be considered becoming large while pushing velocity increases. This will also lead the resistance friction and we also can model it as part of viscos friction. R_{P} is the radius of the pushing plane, and it can be calculated according to the shape of the tip and diameter of the particle. R is the equivalent radius of particle–surface interface. ω is the angler velocity of the rotation of the nanoparticle.

Experimental results have shown that the nanorod under pushing may have different kinds of behavior, which depends on its own geometry property. The aspect ratio of a nanorod is defined as $\sigma = L/d$, where L is the length of the rod and d is the width. As mentioned in [14], a rod with aspect ratio of $\sigma < 15$ could be considered as rigid one and its rotation behavior can be observed. This conclusion is also verified in our experiments shown as in Fig. 7.3. It is easy to prove that the instant center of rotation of the nanorod must be on the axis of the rod. Then as shown in Fig. 7.8, the rod can be simplified as a rigid line segment and motion of manipulated rod can be modeled as nanoparticle manipulation. Accordingly, that the rotation of the rod is the uniform circular motion can be assumed.

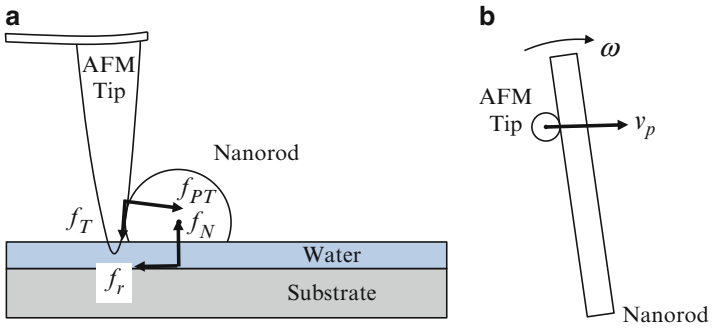

Fig. 7.8 The model of nanorod pushing. (**a**) Side view (**b**) Top view

Considering the effect of pushing speed on the friction between the nano-object and the flat substrate, the distributed friction force f_r of small element on object's support area consists of two components, coulomb friction and viscous friction:

$$f_{\mathrm{r}} = f_{\mathrm{c}} + f_{\mathrm{v}} \tag{7.1}$$

$$f_{\mathrm{c}} = \mu N_{\mathrm{r}} \tag{7.2}$$

$$f_{\mathrm{v}} = c v_{\mathrm{r}} = c r \omega \tag{7.3}$$

where, f_{c} is the dynamic coulomb friction force at a small element and is a constant. μ is the coefficient of dynamic friction, and N_{r} is the pressure of the element on the normal direction of the substrate. f_{v} is the viscous friction force, c is the viscous friction coefficient, and v_{r} is the velocity of the element. r is the length from contacting point of the AFM tip to the instant center of rotation of the nano-object. ω is the angular velocity of the object pushed and is the function of both the velocity at pushing point P and the position of the instant center of rotation.

7.5 Kinematics and Statics of Nano-object Pushing

Different from object handling in the macro world, the effect of mass on motion can be ignored in nanoscale, and only balance of the static forces applied on the object should be considered. We discuss the static model of a nanorod first, because supporting area of a nanoparticle can be modeled as set of multiple line elements which are with the same kinematic and static properties of nanorods.

The external forces applied on the rod in the substrate surface plane can be modeled as shown in Figs. 7.9 and 7.10 for representing cases that the instant center of rotation I_{RC} is at outside the rod and inside the rod respectively. L denotes the

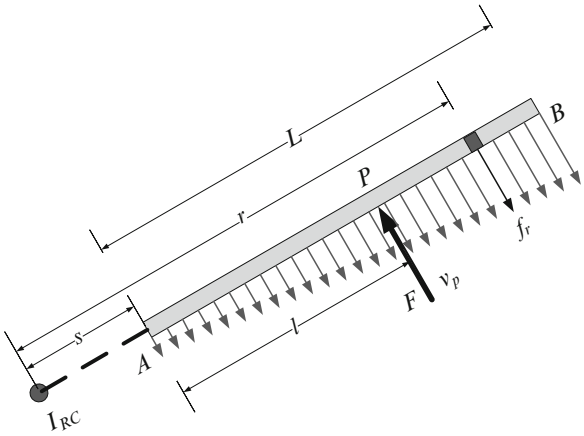

Fig. 7.9 The static model while the instantaneous center of rotation is at the outside of the rod when the contacting point is near the center of the rod

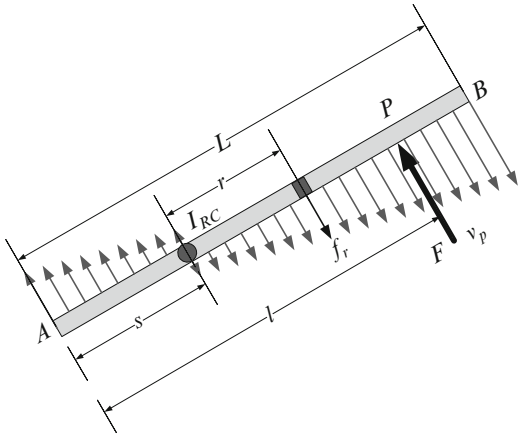

Fig. 7.10 The static model of nanorod while the instantaneous center of rotation is at the inside the rod when the contacting point is far from the rod center

length of the rod, l denotes the distance between the pushing point and the reference end A, s denotes the distance between the instantaneous center of rotation and the reference end, r denotes the distance between a small element of the rod and the reference end A, f_r is the distributed friction force on the small element, and F is the pushing force from the tip. We assume that the rod is pushed in perpendicular to the rod and there is not motion on the direction of rod.

When the pushing point is near the center of the nanorod, the instantaneous center of rotation maybe outside the rod (Fig. 7.9). The angular velocity of the rod is with the following relation to pushing velocity.

$$\omega = \frac{v_p}{l + s} \tag{7.4}$$

where, v_p is the velocity of the pushing point. All torques around I_{RC} are self-balanced during manipulation. The static equation can be written as:

$$
\begin{aligned}
F(l+s) &= \int_{s}^{L+s} (f_c + f_v) \cdot r \mathrm{d}r \\
&= \int_{s}^{L+s} (f_c \cdot r + c\omega \cdot r^2) \mathrm{d}r \\
&= f_c L \left(\frac{L}{2} + s \right) + c \frac{v_p}{l+s} \frac{1}{3} \left[(L+s)^3 - s^3 \right]
\end{aligned} \tag{7.5}
$$

where, left side of the equation denotes the moment applied by the AFM tip, and right side represents the friction resistance consisting of dynamic coulomb friction and viscous friction force which are calculated by integrating friction forces applied on small elements of the rod.

Figure 7.10 shows the model that the instantaneous center of rotation is inside the rod when the pushing point is relatively far from the center of the nanorod.

In this case, the angular velocity of rotation is expressed as following equation:

$$
\omega = \frac{v_p}{l-s} \tag{7.6}
$$

All the torques around I_{RC} are self-balanced during smooth movement, so we can get following expression:

$$
\begin{aligned}
F(l-s) &= \int_{0}^{L-s} (f_c + f_v) \cdot r \, \mathrm{d}r + \int_{0}^{s} (f_c + f_v) \cdot r \, \mathrm{d}r \\
&= \frac{1}{2} f_c (L-s)^2 + \frac{1}{2} f_c S^2 + \int_{0}^{L-s} c\omega \cdot r^2 d + \int_{0}^{s} c\omega \cdot r^2 \, \mathrm{d}r \\
&= \frac{1}{2} f_c (L-s)^2 + \frac{1}{2} f_c s^2 + \frac{v_p}{l-s} \frac{1}{3} \left[(L-s)^3 + s^3 \right]
\end{aligned} \tag{7.7}
$$

There must be an s which can minimize F, in which the rod begins to rotate once the pushing force F reaches this minimum force F_{min}. Therefore, the static point I_{RC} can be determined by following equation with (7.5) and (7.7).

$$
\frac{\mathrm{d}F}{\mathrm{d}s} = 0 \tag{7.8}
$$

When the instant center of rotation at each moment is derived, motion of the nanorod can be obtained numerically while initial conditions are given. Then under a certain pushing velocity and a certain pushing angle, the instantaneous center of the nanorod can be calculated and the pushing points can be determined based on that result to form the virtual nanohand.

Similar with nanorod pushing, the statics model of nanoparticle pushing can be derived by integrating friction resistance on all elements of the support area.

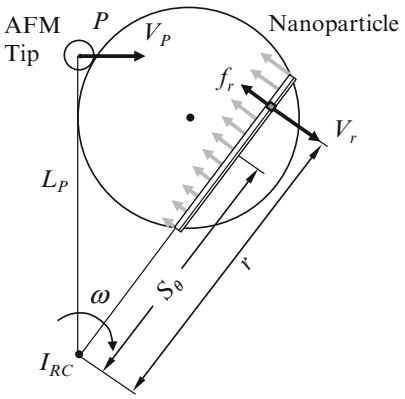

Fig. 7.11 The surface resistance force on a line segment in the support area

Since both translational and rotational motion in general, velocities of elements are different from each other.

For convenience of study, we represent the contact area by a series of straight lines passing through the instant center of rotation, as shown in Fig. 7.11. For each line, distributed friction can be modeled as the model of a nanorod.

V_r is the velocity of element r and is given by $V_\mathrm{r} = r\omega$, where ω is the angular velocity and is invariant, r is the distance between the small element and the instant center of rotation I_RC. Additionally, we have the following condition for ω:

$$\omega = \frac{V_\mathrm{p}}{L_\mathrm{p}} \tag{7.9}$$

where, V_p denotes the pushing velocity of the AFM tip, and L_p is the distance from the pushing point P to the instant center of rotation I_RC. Here, we only discuss case that I_RC is located outside of the support area since the main purpose on handling a nanoparticle is moving it to a target position.

The friction and the torque exerted on the line element are derived by the following equations (Fig. 7.12(a)):

$$f_\theta = \int_{S_\theta - \frac{L}{2}}^{S_\theta + \frac{L}{2}} f_\mathrm{r}\,\mathrm{d}r \tag{7.10}$$

$$M_\theta = \int_{S_\theta - \frac{L}{2}}^{S_\theta + \frac{L}{2}} f_\mathrm{r} \cdot r\,\mathrm{d}r \tag{7.11}$$

where S_θ denotes the distance from the center of the straight line to the instant center of rotation, L is the length of the straight line. S_θ and L in Fig. 7.12(a) can be written

$$S_\theta = S \cdot \sin\theta \tag{7.12}$$

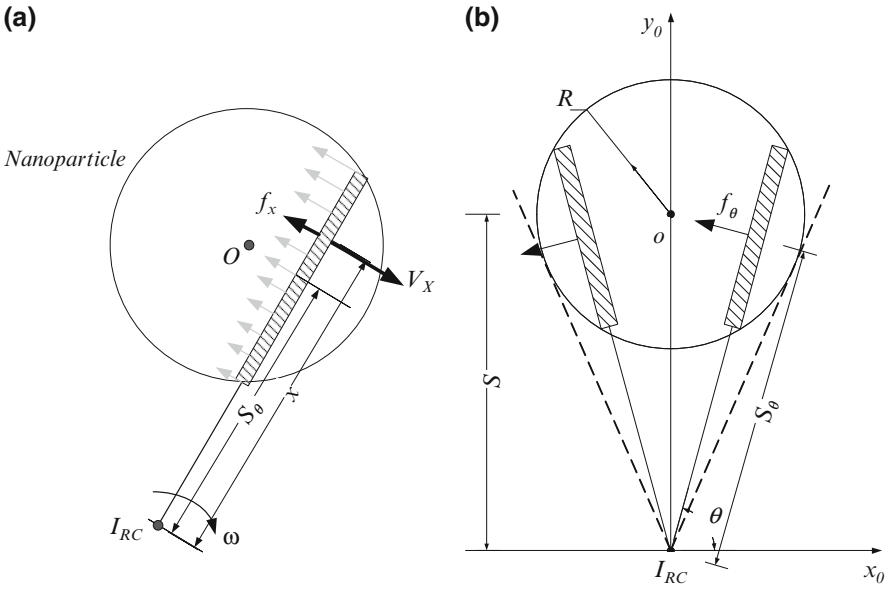

Fig. 7.12 (**a**) The equivalent resistance force and moment on the line segment (**b**) The equivalent resistance forces from two symmetric line segments

$$L = 2 \cdot \sqrt{R^2 - (S \cdot \cos\theta)^2} \tag{7.13}$$

with S is the distance from the center of the contact area O to the instant center of rotation I_{RC}, R is the radius of the contact area, θ is the angle between x_0 axis and the straight line, and the range is $0 < \theta \leqslant \frac{\pi}{2} + \arcsin\frac{R}{S}$.

Then f_θ can be resolved into $f_{\theta x_0}$ and $f_{\theta y_0}$.

$$f_{\theta x_0} = f_\theta \cdot \sin\theta \tag{7.14}$$

$$f_{\theta y_0} = f_\theta \cdot \cos\theta \tag{7.15}$$

Because the straight line elements are symmetrical about the coordinate axis, the vertical component $f_{\theta y_0}$ can be cancelation. Then the friction force f_{fr} and the friction torque M which exert on the nanoparticle can be obtained.

$$f_{\text{fr}} = \int_{\frac{\pi}{2} - \arcsin\frac{R}{S}}^{\frac{\pi}{2} + \arcsin\frac{R}{S}} f_\theta \cdot \sin\theta \cdot \mathrm{d}\theta \tag{7.16}$$

$$M = \int_{\frac{\pi}{2} - \arcsin\frac{R}{S}}^{\frac{\pi}{2} + \arcsin\frac{R}{S}} M_\theta \cdot \mathrm{d}\theta \tag{7.17}$$

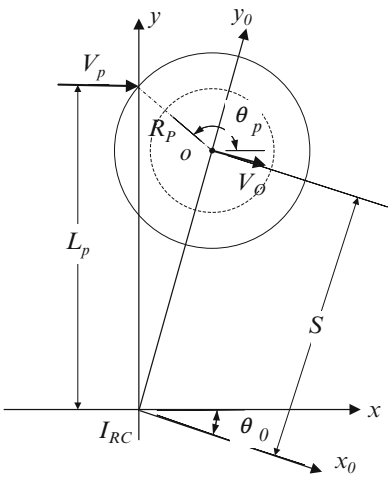

Fig. 7.13 The relation between velocity of AFM tip and velocity of particle pushed

For the nanoparticle the forces and the torques are both balanced, so we can get following expressions

$$M_{\mathrm{P}} = M \tag{7.18}$$

$$f_{\mathrm{P}} = f_{\mathrm{fr}} \tag{7.19}$$

where f_{P} is the component of pushing force and M_{P} is the torque of it. In order to be convenient to analyze and solve problems, transformation of coordinates is done, shown as in Fig. 7.13. θ_0 is the angle of the transformation and can be determined from the equation

$$S \cdot \sin\theta_0 = R_{\mathrm{P}} \cdot \cos(\pi - \theta_{\mathrm{P}}) = -R_{\mathrm{P}} \cdot \cos\theta_{\mathrm{P}} \tag{7.20}$$

where θ_{P} is the angle between the pushing point and the center. According to the balance relationship between the force f_{P} and the torque M_{P}, the equation can be obtained

$$f_{\mathrm{P}} \cdot L_{\mathrm{P}} \cdot \cos\theta_0 = M_{\mathrm{P}} \tag{7.21}$$

where, $L_{\mathrm{P}} = S \cdot \cos\theta_0 + R_{\mathrm{P}} \cdot \sin\theta_{\mathrm{P}}$.

From (7.16) to (7.21), we can get the following equation.

$$\int_{\frac{\pi}{2}-\arcsin\frac{R}{S}}^{\frac{\pi}{2}+\arcsin\frac{R}{S}} (f_\theta \cdot \sin\theta \cdot L_\mathrm{P} \cdot \cos\theta_0 - M_\theta) \cdot \mathrm{d}\theta = 0 \tag{7.22}$$

Ultimately, by solving integral and setup parameters, (7.18) can be written as an expression of S. Using means of numerical integration, we can get the S which is the distance from the center of the contact area to the instant center of rotation.

According to the characteristic of rigid body motion, we can get the following constraint condition:

$$\frac{V_\mathrm{P}}{L_\mathrm{P}} = \frac{V_O}{S} \tag{7.23}$$

where V_O is the velocity of the particle center.

Then under a certain pushing velocity and a certain pushing angle, the deflection of the center can be calculated and the pushing points can be determined based on that result. During the manipulation, according to the location of the center change the pushing points and the pushing step-length to form the nanohand, then the nanoparticle is real-time controllable. Applying the nanohand strategy would resolve the problems of nanoparticle losing and inefficient positioning.

7.6 Experiments and Numerical Analysis

7.6.1 Nanoparticle Pushing Experiments and Numerical Analysis

In this simulation, a radius of 100nm nanoparticle is manipulated on the CD substrate. The experimental tip is NSC15/AIBS which is product by MikroMasch. For getting variable S in the statics model of nanoparticle, the constant parameters f_c and c must be determined. First, measuring the deflection sensitivity γ of the AFM tip by means of force curve by experiments, we have $\gamma = 60\mathrm{nm/V}$. Second, using the same pushing angle and the same pushing step-length, push the nanoparticle five times with a certain velocity, record the PSD voltage deflection δ_v, and calculate the average value. The process is repeated six times with six different velocities. The spring coefficient of the AFM cantilever is relevant with the characteristic of AFM, it is a constant, here the coefficient $k = 40\mathrm{N/m}$. Assume that the contact angle of the tip and the particle isn't changed when the tip pushes the particle, so based on the formulas $x = \delta_\mathrm{V} \times \gamma$ and $f = kx$, the pushing force exerted on the nanoparticle can be calculated. Figure 7.14 shows the relationship between the pushing velocity and the force, the line shown in this figure is fitted by the method of least squares. The Y-intercept is the parameters f_c and the slope is the viscous friction coefficient c.

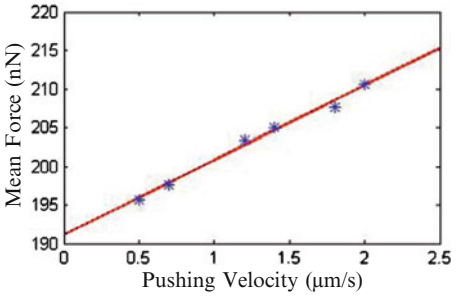

Fig. 7.14 Pushing velocity vs. mean pushing force exerted on the nanoparticle

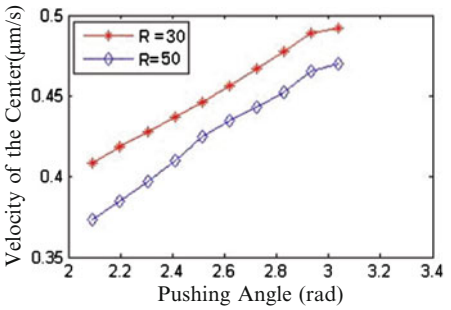

Fig. 7.15 The velocity of the center with two different radius of the contact area

With these calibrated parameters, we can obtain the distance S between the particle center and the instant center of rotation by using numerical integration in Matlab, and then the velocity of the particle center can be calculated. In the nanoscale, contact deformations must be considered. Figure 7.15 shows the simulation results of the velocity of the particle center in different pushing angle. Under the same pushing velocity of the AFM tip, the velocity of the particle center will increase for all pushing angle while the equivalent radius of particle–surface interface increases.

When a nanoparticle is pushed by AFM tip, and the initial pushing angle $\theta_P = 13\pi/12$, pushing velocity $V_P = 0.5\mu m/s$, the equivalent radius of the AFM tip $R_T = 40nm$, the pushing length is 500nm, then the experiment result is shown in Fig. 7.16. From Fig. 7.16(c), we can calculate that the horizontal displacement of the nanoparticle is about 422nm and the vertical deflection is about 71nm.

The simulation is done with the conditions of the Fig. 7.16 experiment. It is assumed that the pushing angle θ_P and the instant center of rotation I_{RC} are invariable in the condition of <100nm pushing length. The velocity and the location of the particle center pushed are calculated, and the trajectory of the particle center is estimated as shown in Fig. 7.17 based on calculated particle motion. In Fig. 7.17, the big cross dots are the start and target position of the nanoparticle center in the experiment. The dash line is the simulation curve and the final position of the simulation is with about 1nm errors. This simulation result illustrates the validity of the static model proposed, and the accuracy may increase when parameters are calibrated precisely and calculation step is set shorter in the simulation.

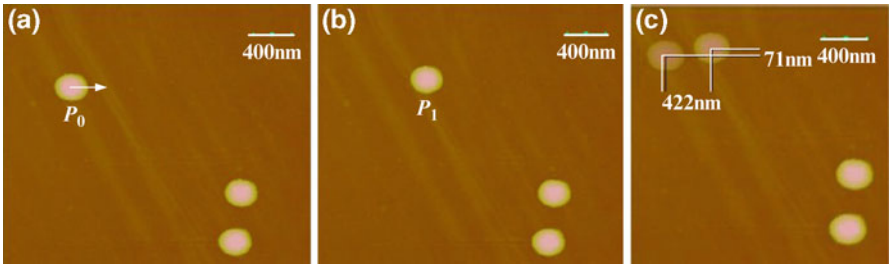

Fig. 7.16 The result of a 500nm pushing experiment. (**a**) Initial position (**b**) Resultant position (**c**) Overlapping image of (**a**) and (**b**) for obtaining the displacement of the particle pushed

Fig. 7.17 The simulation result of the center trajectory of the particle pushed and experiment result. The *big cross dots* show initial position (50nm, 60nm) and final position (473.1nm, 130.9nm) in the experiment. The *dotted line* shows the simulated trajectory of the particle where the initial pushing angle θ_P is $13\pi/12$

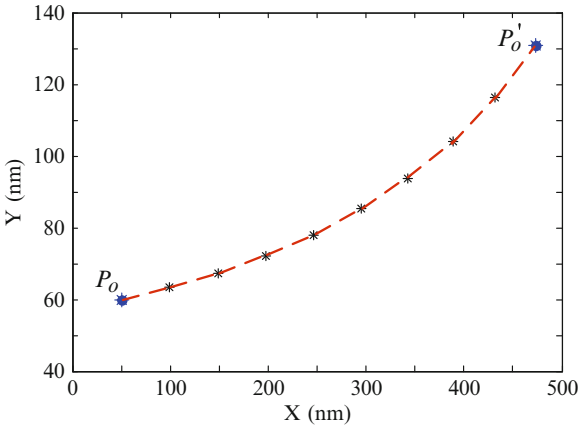

7.6.2 Nanorod Pushing Experiments and Numerical Analysis

Several experiments have been done for verifying the validity of the static model of nanorod manipulation. In the experiments, a ZnO nanorod is used as the target object. Figure 7.18 shows three experimental results. In these experimental processes, the nanorod is pushed by AFM tip under the same conditions, including that the initial pushing direction is perpendicular to the rod, the pushing velocity is 2.0μm/s, the pushing length is about 1μm, and the parameters of the rod are $L = 5.686\mu m$ and $l = 4.186\mu m$. In these three experiments, the initial posture of the rod is different. But the mica surface is flat, and we can assume that surface friction is the same in the all directions of the 2D coordinates. In another word, the initial pushing angle does not affect the manipulation results if the pushing direction is perpendicular to the rod.

Figure 7.18(a–c) are the overlapping scanning images generated from initial and resultant scanning. Figure 7.18(d–f) shows the same overlapping images but the initial position and posture of the rod is set in the x direction, by rotating the images. Even the rod is pushed at the same point in the manipulation planning procedure,

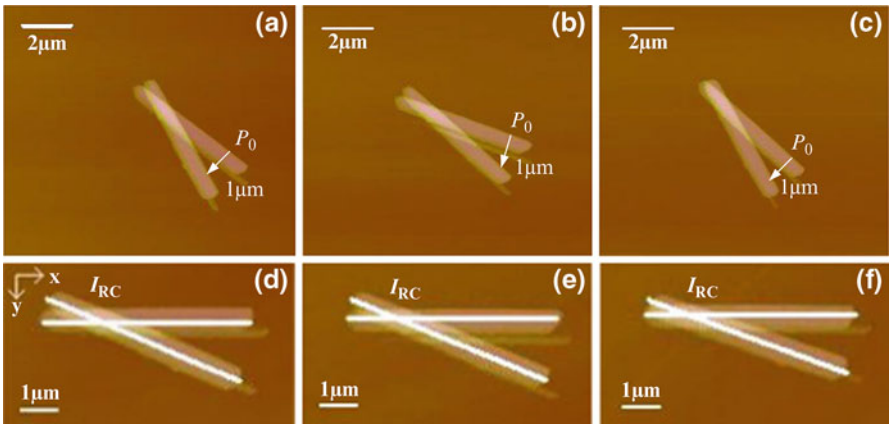

Fig. 7.18 Three experimental results which the instantaneous center of rotation is inside the rod under the same pushing conditions (**a**–**c**). The rotated images of the overlapping image (**a**–**c**) respectively for calculating the displacement of the center of the rod and orientation on three experiments

Table 7.1 Results of three nanorod pushing experiments

	Exp. 1	Exp. 2	Exp. 3
Δx (nm)	−117	−103	−94
Δy (nm)	634	587	564
$\Delta\theta$ (°)	−25.4	−24.8	−19.4

the results of pushing are with some difference. Table 7.1 shows the displacements of the center point of the rod after three pushing experiments. Δx is the horizontal displacement of the rod center, Δy is the vertical displacement of the rod center, and the angle $\Delta\theta$ is the rotation angle of the rod.

From Table 7.1, we can confirm that even under the condition that all the pushing parameters and experimental circumstances the same, the manipulation results were different by each operation. We consider that the main reason for these is that position error of the AFM tip contacting with the rod causes the difference of rod's motion. By using the static model of the nanorod mentioned above, the motion of the rod can be calculated not only for the planned contacting point of the AFM tip but also for the position contacting point including the error. Then this kind of numerical calculation will be essential tool to design the nanohand structure. Here the numerical calculations for the above-mentioned experiments are included for illustrating the validity of the proposed mode. We implement the static model of rod in the Matlab program. It is assumed that changes of the pushing angle and the instantaneous center of rotation can be ignored in a small pushing step. In the following calculation, the whole pushing action is divided into eight parts, where the motion of rod is generated in every 125nm each calculation step. Then the location of the instantaneous center of rotation is calculated, and the displacemnt of the rod

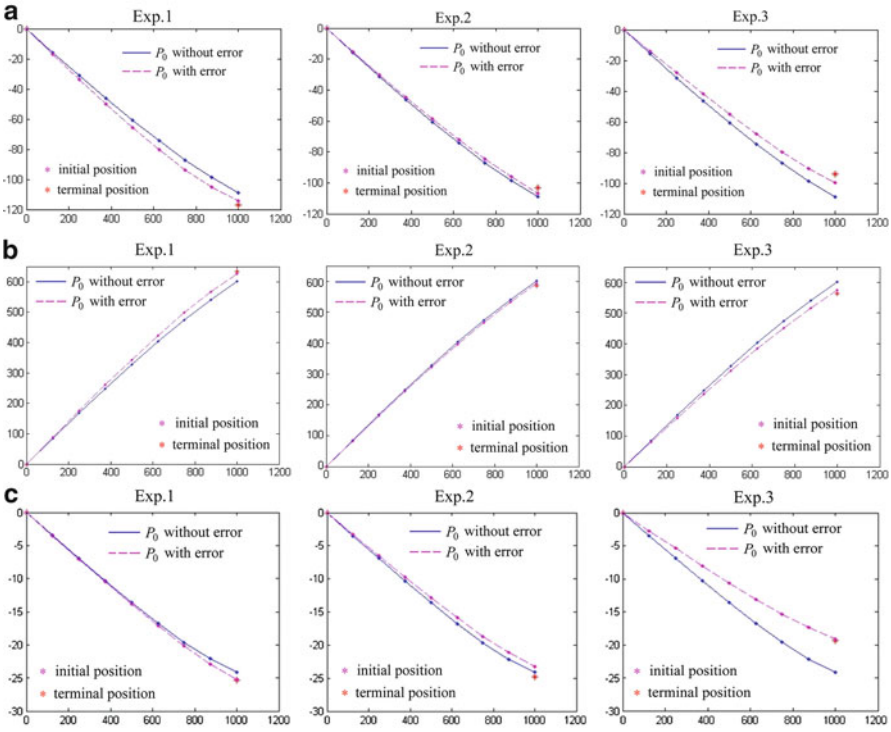

Fig. 7.19 Numerical simulation results with and without thinking about the position error of the AFM tip. In these figures, the *crosses* show the experimental result, the *solid line* with *dots* are the numerical simulation results not considering the position error of AFM tip and the *dash line* with *dots* are the simulation results considering the error. (**a**) Center displacement in *X* direction in Exp. 1, Exp. 2 and Exp. 3. (**b**) Center displacement in *Y* direction in Exp. 1, Exp. 2 and Exp. 3. (**c**) Change of rotation angle in Exp. 1, Exp. 2 and Exp. 3

center in both *X* and *Y* direction, rotational angle can be obtained. The numerical simulation results are shown as Fig. 7.19.

From the numerical simulation and experimental results, we can conclude that though the experimental conditions are the same, the results may be different with each other. Solid lines in Fig. 7.19 show the displacement of the center in both *X*, *Y* direction and orientation angle of the rod. Also by considering position errors, the numerical simulation results will be improved. The dash lines in Fig. 7.19 are calculation results by adding some errors to planned contacting position, and show more near to the experiment result comparing with the blue ones which is calculated from planned contacting position only. In three simulation experiments, for getting better results, the value of the position error is different. For Exp. 1 the value is −18nm that is the pushing point moved 18nm near to the pivot direction, in Exp. 2 the value is 16nm that is the pushing point moved 16nm far away from the pivot

direction, in Exp. 3 the value is 46nm. From the numerical simulation results we can conclude that the position error must be one of the factors which are considered in process of modeling.

7.7 Conclusion

Almost all the existing AFM only has one single tip as the end effector, thus during nanoparticle manipulation, the interaction force between the nanoparticle and the tip can but be applied through a single point, which often leads the AFM tip to slip-away from the particle or split the particle due to their small contact area. This is one of the main bottlenecks for AFM-based high efficiency nanoparticle manipulation. To solve this problem, we proposed a nanohand strategy. Based on the self-balance conditions of the forces and the torques, the kinematics model of nanoparticle is developed, and the location of the center can be predicted at the each moment of manipulation, according to which the pushing points, pushing step-length and pushing speed can be planned artfully to form, a virtual nanohand. In this way, the manipulation effect as multi-tip does can be achieved with a single AFM tip. The simulation shows a stable and controllable nanoparticle pushing can be obtained. This method gives a feasible solution to compensate the shortcomings of single-tip based nanomanipulation and nanoassembly.

References

1. Maier SA, Kik PG, Atwater HA, Meltzer S, Harel E, Koel BE, Requicha AA (2003) Local detection of electromagnetic energy transport below the diffraction limit in metal nanoparticle plasmon waveguides. Nat Mater 2:229–232
2. Tong L, Zhu T, Liu Z (2008) Atomic force microscope manipulation of gold nanoparticles for controlled Raman enhancement. Appl Phys Lett 92:023109
3. Makaliwe JH, Requicha AA (2001) Automatic planning of nanoparticle assembly tasks. In: Proceedings of the 2001 IEEE international symposium on assembly and task planning (ISATP2001), pp 288–293
4. Li GY, Xi N, Yu MM, Fung WK (2004) Development of augmented reality system for AFM-based nanomanipulation. IEEE ASME Trans Mechatron 9:358–363
5. Chen HP, Xi N, Li GY (2006) CAD-guided automated nanoassembly using atomic force microscopy-based nonrobotics. IEEE Trans Autom Sci Eng 3:208–217
6. Zhang JB, Xi N, Li GY, Chan HY, Wejinya UC (2006) Adaptable end effector for atomic force microscopy based nanomanipulation. IEEE Trans Nanotechnol 5:628–642
7. Liu LQ, Luo YL, Xi N, Wang YC, Zhang JB, Li GY (2008) Sensor referenced real-time videolization of atomis force microscopy for nanomanipulations. IEEE ASME Trans Mechatron 13:76–85
8. Wang ZD, Hirata Y, Kosuge K (2003) Control multiple mobile robots for object caging and manipulation. In: Proceedings of the 2003 IEEE/RSJ international conference on intelligent robots and systems, pp 1751–1756

9. Hou J, Wang ZD, Liu LQ, Yang YL, Dong ZL, Wu CD (2010) Modeling and analyzing nanoparticle pushing with an AFM by using nano-hand strategy. In: Proceedings of the 2010 5th IEEE international conference on nano/micro engineered and molecular systems NEMS, pp 518–523.
10. Hou J, Wu CD, Liu LQ, Wang ZD, Dong ZL (2010) Modeling and analyzing nano-rod pushing with an AFM. In: Proceedings of the 10th IEEE conference on nanotechnology IEEE-NANO 2010, pp 329–334
11. Kim S, Ratchford DC, Li XQ (2009) Atomic force microscope nanomanipulation with simultaneous visual guidance. ACS Nano 3:2989–2994
12. Resch R, Baur C, Bugacov A, Koel BE, Madhukar A, Requicha AA, Will P (1998) Building and manipulating three-dimensional and linked two-dimensional structures of nanoparticles using scanning forcemicroscopy. Langmuir 14:6613–6616
13. Tafazzoli A, Sitti M (2004) Dynamic behavior and simulation of nanoparticle sliding during nanoprobe-based positioning. In: Proceedings of the IMECE'04 2004 ASME international mechanical engineering congress, pp 1–8
14. Li GY, Xi N, Chen HP, Pomeroy C, Prokos M (2005) Videolized atomic force microscopy for interactive nanomanipulation and nanoassembly. IEEE Trans Nanotechnol 4:605–614
15. Binning G, Quate CF, Gerber C (1986) Atomic force microscope. Phys Rev Lett 56:930–933
16. Junno T, Deppert K, Montelius L, Samuelson L (1995) Controlled manipulation of nanoparticles with an atomic force microscope. Appl Phys Lett 66:3627–3629
17. Hansen LT, Kuhle A, Sorensen AH, Bohr J, Lindelof PE (1998) A technique for positioning nanoparticles using an atomic force microscope. Nanotechnology 9:337–342
18. Sitti M (2004) Atomic force microscope probe based contrlled pushing for nanotribological characterization. IEEE ASME Trans Mechatron 9:343–348

Chapter 8
Nanorobotic Mass Transport

Lixin Dong, Xinyong Tao, Zheng Fan, Li Zhang, Xiaobin Zhang, Bradley J. Nelson, Mustapha Hamdi, and Antoine Ferreira

Abstract Mass transport at attogram (10^{-18} g) level within, from, and between nanochannels is of growing interest from both fundamental and application perspectives. Mass transport systems at this scale provide a platform for the investigation of nanofluidics and can serve as components for nanomanufacturing systems that feed atoms and connect them into molecules, supramolecules, and, ultimately, super-precision nanostructured products. Such systems will, in turn, enable other nanosystems such as electronic, electromechanical, photonic, and biomedical ones for circuit spot welding, sensing and actuation, single-molecule detection, targeted drug delivery, etc. Nanorobotics enables these nanometer-scale systems through its ability to position and assemble pipes, to deliver the mass in a controlled way,

L. Dong (✉) • Z. Fan
Department of Electrical and Computer Engineering, Michigan State University, East Lansing, MI 48824-1226, USA
e-mail: ldong@egr.msu.edu; fanzheng@egr.msu.edu

X. Tao
College of Chemical Engineering and Materials Science, Zhejiang University of Technology, Hangzhou 310032, China
e-mail: xinyongtao@gmail.com

L. Zhang • B.J. Nelson
Department of Mechanical and Automation Engineering, The Chinese University of Hong Kong, Shatin NT, Hong Kong SAR, China
e-mail: lizhang@mae.cuhk.edu.hk; bnelson@ethz.ch

X. Zhang
Department of Materials Science and Engineering, Zhejiang University, Hangzhou 310027, China
e-mail: zhangxb@zju.edu.cn

M. Hamdi • A. Ferreira
Ecole Nationale Supérieure d'Ingénieurs, Laboratoire PRISME, de Bourges, 88 Boulevard Lahitolle, 18000, Bourges, France
e-mail: mfhamdi@gmail.com; antoine.ferreira@ensi-bourges.fr

C. Mavroidis and A. Ferreira (eds.), *Nanorobotics*, DOI 10.1007/978-1-4614-2119-1_8,
© Springer Science+Business Media New York 2013

and to tune and characterize these systems in situ. We can now envision a mass network that will one day process material atom by atom just as the Internet processes information byte by byte. This science fiction-like dream is becoming an engineering reality, and the intermediate achievements have shown potential applications for near-term applications.

8.1 Introduction

Just over 50 years ago, Richard Feynman predicted that one day people would be able to manipulate the world, atom by atom. By creating material atom by atom, things can be made more accurately, molecules that have yet been synthesized chemically can be assembled mechanically, and no waste will be generated during the production process. To realize this dream, three fundamental nanotechnologies are needed: feeding, positioning, and connection. Key specifications associated with these technologies include (1) feeding atoms in controllable small quantities—ideally individually, (2) atomically precise positioning, (3) chemical connection, and (4) high-speed processing, at least millions of operations per second, but probably much more.

The past two decades have witnessed two major breakthroughs: positioning individual atoms with atomic precision [1] and formation/breaking of individual chemical bonds [2]. However, the state of the art of the feeding and operation rates remains a grand challenge. Current processing rates are about a billionth of what is required, and the feeding method is still primitive: atoms are either sparsely distributed on a surface and individually manipulated, or they are manipulated in relatively large groups.

Mass transport within, from, and between nanochannels is a promising approach for continuously feeding small numbers of atoms in a controllable fashion, and it does not appear that a theoretical limit exists that keeps this from being extended to individual atoms. Combining this feeding technique with a positioning mechanism, e.g., nanorobotic manipulators [3], deposited atoms can be positioned from a continuous source. A fluidic system with multiple channels can serve as a mass network to provide a variety of atoms for positioning and connection. An example of a manufacturing system is schematically shown in Fig. 8.1 where the mass network resembles the Internet for information. Nanofluidic mass networks connect the sources of various atoms to the clients.

Carbon nanotubes (CNTs), with their extremely strong mechanical strength and nanometer-sized hollow cores, are ideal candidates for nanochannels. Controlled melting, evaporation, and flowing of mass within and between these nanochannels are of great interest, both fundamentally and from an application perspective [4–12]. Nanorobotics enables these nanometer-scale systems through its ability to position and assemble these CNT pipes, to deliver the mass in a controlled way, and to tune and characterize these systems in situ.

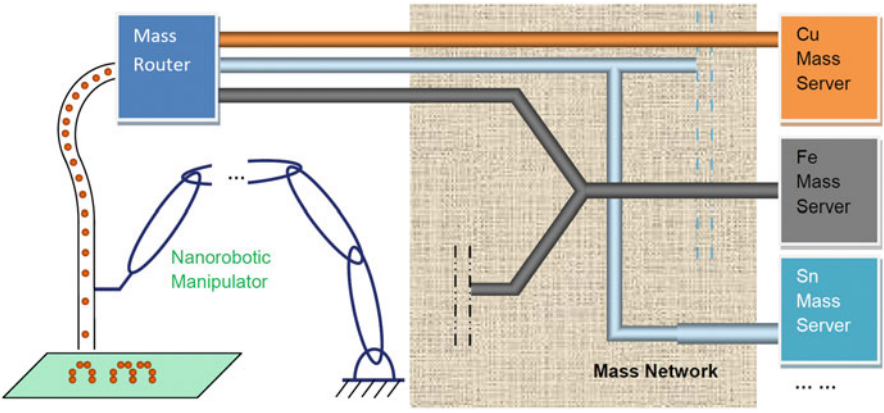

Fig. 8.1 Mass transport for nanomanufacturing

8.2 Filling of Nanotubes and Building Blocks of Mass Transport Systems

Almost immediately after the discovery of CNTs, people started to fill them, first for doping and then for storage. This first demonstration can be traced back to 1993 [13]. As-grown nanotubes typically have their ends caped. To perform capillary filling or use these tubes as pipes in a fluidic network, modifications of their caps and sidewalls are needed. A variety of materials have been encapsulated by CNTs such as metals and their compounds [13–15], water [16], and fullerenes [17]. Two primary approaches, capillary filling and growth, have been developed for filling tubes after or during growth. The difficulty of capillary filling of CNTs with liquid metals is due to high surface tension. A recent investigation showed that by applying a bias during capillary action, a process known as electrowetting [18], this barrier can be overcome. CNTs can also be filled while growing them from catalysts [19], where the materials to be encapsulated either serve as or are mixed with the catalysts.

By tailoring and assembling as-grown CNTs, a variety of functional elements of a nanofluidic system can be built (Table 8.1). Nanotube intermolecular and intramolecular junctions were originally of interest for nanoelectronic circuits, nanomechanical devices, nanoelectromechanical systems, and other nanosystems. For nanofluidic systems, the idea is more straightforward; tubes become pipes.

The primary challenge of building these types of nanofluidic systems is how to make connections for both the internal holes and external walls and to scale the systems up. Oxidation, acid etching, and sonication can be used to open the caps. Using these techniques, CNTs caps can be removed in batches, but with a low controllability of the process. The basic concept behind these technologies is that the caps (which consist of pentagons) are more reactive than the sidewalls (which are made of hexagons). However, after the caps have been removed, the ends of the CNTs become activated, which makes their controllability poor.

Table 8.1 Nanotube-based building blocks for mass transport

Building blocks	Schematics	Images
Cap-opened tubes		[13]
Tubes with holes on the sidewalls		[20]
Kinked tubes		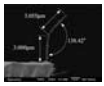 [21]
Bent tubes		[22]
Y-junction		[23]
T-junction [24]		[25]
Prolonged tubes (telescoping)		[21]
Prolonged tubes (connecting)		[26]

Thanks to the advancement of microscopy and nanorobotic technologies, we now have ultrasmall cutters and fingers to make local features on a nanotube. An electron beam can now be focused so small that it can remove a single atom at one time from the sidewall of a nanotube [20]. Table 8.1 shows building blocks based on CNTs. Nanomanipulation of CNTs extends the list. Kink pipes have been made by bending a CNT above its elastic strength. A recoverable bent tube [22] can serve as an elastic joint. Three-way tubes (Y-junctions) can be grown in batches [23], which are more effective than mechanically assembled three ways, e.g., the T-junction formed by connecting two tubes in an end-to-sidewall configuration.

As-grown Y-junctions have the internal channels [25], though residual catalysts may remain inside. It can be imagined that the residual catalyst might not be a problem if it can be melted to flow out. Electron beams and focused ion beams (FIBs) have been used to fuse CNTs together and create internal connections. These have been realized based on surface reconstruction with the energy from the beams; therefore, the sidewalls do not have to be opened. For long distance transport, tubes with centimeter lengths are now available. Interlayer sliding in a CNT [21] makes it possible to create a linear elastic joint. Tube-to-tube connection can also be performed by activating the ends [26, 27].

8.3 Methods for Mass Transport Using a Nanotube

Several approaches have been developed for transporting materials inside or on a nanotube (Table 8.2). CNT-based solid mass transport began with a demonstration of the axial thermal expansion of gallium inside a CNT [26]. Thermal deformation cannot be used for transport in radial directions, whereas evaporation at a higher temperature can separate and/or ionize atoms for further transport both radially and

Table 8.2 Mass transport methods

Mechanism	Schematics
Thermal expansion [4]	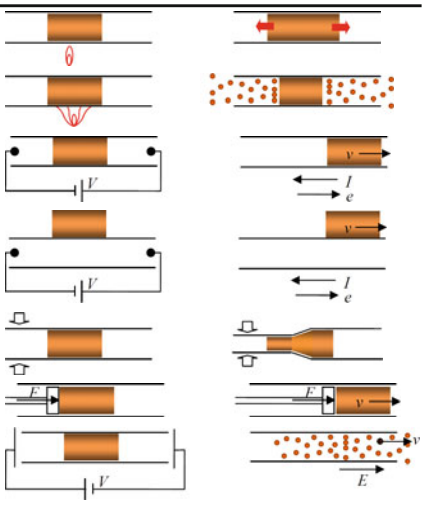
Thermal evaporation [28]	
Electromigration (channel) [5, 29]	
Electromigration (conveyor) [30]	
Electron-beam-induced squeezing [7]	
Mechanical pushing	
Ionization + electrostatic [28]	

Fig. 8.2 Experimental setup for investigating the mechanisms of mass delivery. Two Cu-filled CNTs supported on a sample holder and a probe provide three different cases to investigate: $CNT_{1,A}$, $CNT_{1,B}$, and CNT_2, subjected to electric current, thermal transport, and charges, respectively

axially. Directions of transport can be determined with an electric current or field [30]. The driving force has been attributed to electromigration, so the flow coincides with the carrier flow (electrons in metals and n-type semiconductors or holes in p-type semiconductors). Electron-beam-induced shrinking [7] of the shells provides an interesting way to "squeeze out" encapsulated materials from nanotubes. The shortcomings are obvious; the tubes cannot be reused. Although not yet realized, directly pushing with a piston might also be feasible.

To understand the mechanisms and efficiency of these approaches, experimental investigations have been performed using the setup shown in Fig. 8.2, where two

metal-filled CNTs supported on a common sample holder and a probe provide four different experimental modes: (1) The upper section of the left nanotube, $CNT_{1,A}$, has electric current passing through, and, accordingly, Joule heating will occur. (2) The lower section of the left nanotube, $CNT_{1,B}$, has no current and will experience only thermal transport. The right tube, CNT_2, has no electric current but can be either (3) negatively charged or (4) positively ionized. Thermal transport also occurs from the common sample holder, but not as directly as $CNT_{1,B}$ due to the superior heat conduction ability of CNTs (thermal conductivity: 3,320 W/m K; c.f. Ag: 429 W/m K, Cu: 386 W/m K, Au: 318 W/m K) [31].

The samples used were Cu-filled CNTs. The Cu-tipped CNT samples were synthesized using an alkali-doped Cu catalyst by a thermal chemical vapor deposition method [19]. The CNTs are up to 5 μm long with outer diameters in a range of 40–80nm. The single-crystalline Cu nanoneedles are encapsulated in graphite walls ∼4–6nm thick at the tips of the CNTs. The graphite layers were not parallel to the tube axis.

The experiments were performed in a transmission electron microscope (TEM) equipped with a scanning tunneling microscope (STM) built in a TEM holder (Nanofactory Instruments AB, ST-1000) serving as a manipulator [5, 9, 32]. The sample consisted of a CNT bundle attached to a 0.35-mm-thick Au wire using silver paint, and the wire is held in the sample holder (Fig. 8.2). An etched 10-μm-thick tungsten wire with a tip radius of ∼100nm is used as the probe. The probe can be positioned in a millimeter-scale workspace with subnanometer resolution with the STM unit actuated by a 3°-of-freedom piezotube, making it possible to select a specific CNT and pick it up. Physical contact can be made between the probe and the tip of a nanotube or between two nanotubes. Applying a voltage between the probe and the sample holder establishes an electrical circuit through a CNT and injects thermal energy into the system via Joule heating. By increasing the applied voltage, the local temperature can be increased past the melting point of the material encapsulated in a tube. The process is recorded by TEM images, a multimeter, and a nanoampere meter.

Figure 8.3 includes a series of TEM images recording the evaporation of Cu. The first two frames in Fig. 8.3a show the evaporation driven by current and Joule heating inside two single CNTs when the probe is positively biased (7 V). It can be seen that the length of the copper core inside the CNT on the left side (both $CNT_{1,A}$ and $CNT_{1,B}$) decreases continuously. The time interval 0–120 s in Fig. 8.3a is a series of TEM images recording the transport of Cu inside two single CNTs when the probe is negatively biased (−3.5 V). It can be seen that the length of the copper core inside the CNT on the left side ($CNT_{1,B}$) also decreases continuously. Because the copper core is not between the electrodes, the polarity of the electrodes does not matter; copper will transport toward one of them.

Surprisingly, it can be seen from Fig. 8.3a (170–240 s) that the length of the copper core inside the CNT on the right side (CNT_2) also decreases continuously. A closer inspection of the insets of Fig. 8.3 (0–120 s) reveals that the same phenomena occurred when the probe is positively biased. This implies the possibility that charge-induced transport is more significant than current-induced Joule heating and

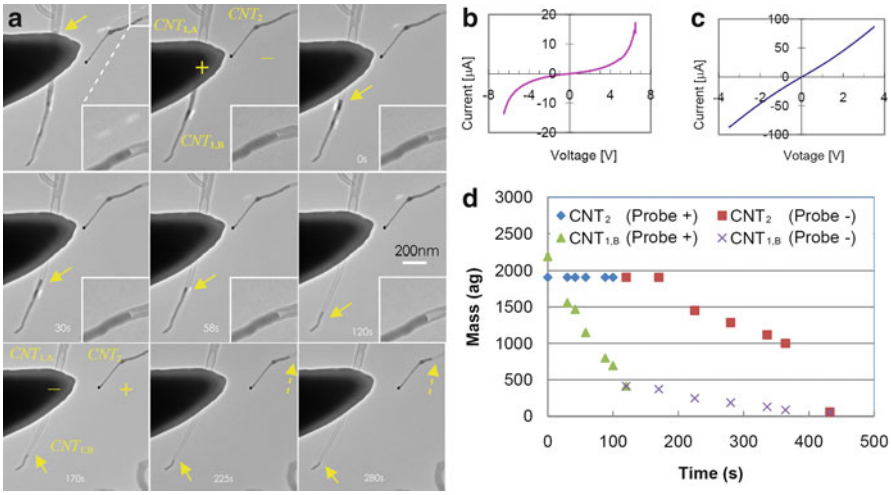

Fig. 8.3 Mechanisms of evaporation. (**a**) 0–120 s shows the electric current and Joule-heating-driven Cu evaporation. A series of TEM images recorded the transport of Cu inside two single CNTs when the probe is positively biased (7 V). It can be seen that the length of the copper core inside the CNT on the left side continuously decreases.170–280 s shows thermal transport and positive charges induced Cu evaporation. A series of TEM images recorded the transport of Cu inside two single CNTs when the probe is negatively biased (−3.5 V). It can be seen that the length of the copper core inside the CNT on the left side also continuously decreases. (**b**) and (**c**) are I–V curves before the threshold on positive and negative biases is reached. It can be seen by comparing (**b**) and (**c**) that conductance improved after copper transport (the minimum resistance changed from (**b**) 377 kW to (**c**) 40 kW). (**d**) Mass evaporation rate

thermal transport. The obvious difference of the evaporation rate for Cu inside CNT_2 suggests that, as the Cu is positively ionized (170–240 s), the repulsive forces between Cu ions are larger than negatively charged case (0–120 s).

Figure 8.3b, c shows I–V curves before the positive and negative threshold biases are reached. It can be seen by comparing Fig. 8.3b, c that the conductance improved after the copper was transported [the minimum resistance changed from 377 to 40 kΩ (Fig. 8.3b, c, respectively)]. This suggests copper deposited on the probe in the case of Fig. 8.3b changed the contact from a Schottky-type to ohmic. The decrease of resistance from 477 kΩ (−6.5 V) to 377 kΩ (6.5 V) in the case of Fig. 8.3b indicates the transport/deposition on the probe occurred during the bias sweeps from −6.5 to 6.5 V.

Figure 8.3d indicates the estimated mass evaporation rate according to the apparent geometries and the density of copper (8.92 g/cm^3). Using linear fitting, the average mass evaporation rate has been found to be 14.3 ag/s and 1.2 ag/s for $CNT_{1,B}$ as the probe is positively (0–120 s) and negatively (170–240 s) biased, respectively. The difference (∼12 times) between the rates of $CNT_{1,B}$ is due to the competition between electrostatic forces and Joule-heating-induced evaporation. The latter is mainly caused by the different absolute values of the bias V (7 V and −3.5 V) and

the resistance R (377–40 kΩ). Considering that thermal power scales with V^2/R, the bias differences translate into a factor of 2.4, but the evaporation rate as the probe is negatively biased should be larger. This is contrary to the experimental observation. Hence, it can be concluded that electrostatic forces dominate evaporation.

The growing distance from the heated section also has contribution but less due to the excellent thermal conductivity of CNTs. Similarly, using linear fitting, the average mass evaporation rate has been found to be 0.1 and 6.1 ag/s for CNT_2 as the probe is positively (0–120 s) and negatively biased (170–240 s), respectively. This suggests that, when Cu is ionized, the repulsive interaction between Cu^+ is much larger than electron charges.

8.4 Mass Transport Inside a Nanotube

Figure 8.4 shows mass transport within a nanotube and its applications. The expansion of the gallium inside a nanotube is used as a thermometer (Fig. 8.4a, [4]) to indicate the surrounding temperature. Gallium's macroscopic expansion properties are retained at the nanometer scale. By associating the end-to-end nanotube resistance with the temperature, a sensor with a readout device independent to the microscopy images was invented (Fig. 8.4b, [33]). The resistance of the Ga-filled nanotube changes when the gallium expands. Figure 8.4c [29] is a nanoshuttle memory device, where an iron nanoparticle shuttle is controllably positioned within a hollow nanotube channel. Different positions of the nanoparticles are used to represent information. The information density can be as high as 10^{12} bits/in^2 and thermodynamic stability in excess of one billion years.

Because of the fluidic pressure on the sidewalls of a CNT, metal flowing in a kink junction of a CNT can induce deformation of the junction. Figure 8.5 shows experimental investigation of this phenomenon. To keep the nanotube freestanding, electron-beam-induced flow is applied instead of current-driven flow. A Sn-filled CNT was exposed to a high-intensity e-beam (30 kV) for 1-min intervals. After each exposure, an image (Fig. 8.5a–d) was taken at ordinary e-beam intensity. During the process, a 12° deflection of the junction was observed which induced a 35-nm displacement at the freestanding tip of the nanotube (the arm length of the horizontal tube is ∼110nm). With its ultracompact sizes, such nanotube-based fluidic junctions might be used as actuators for creating nanorelays, grippers, or

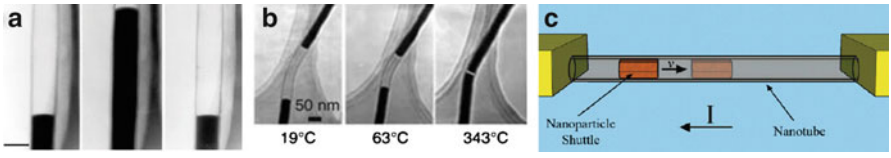

Fig. 8.4 Mass transport within a nanotube and their applications. (**a**) Thermometer, (**b**) temperature sensor, and (**c**) nanoshuttle memory device

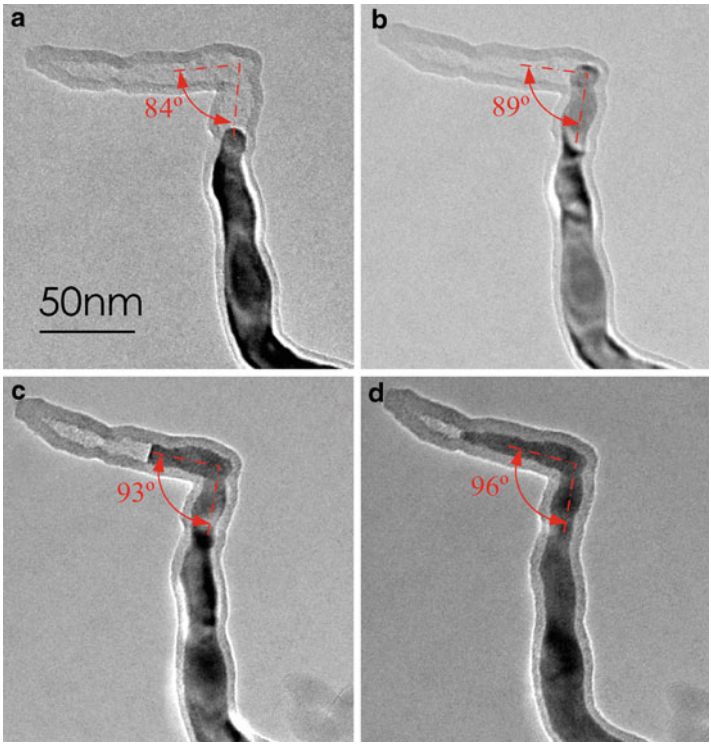

Fig. 8.5 Electron-beam-induced flowing straightens a kinked Sn-filled CNT like what happens in a soft water pipe. After exposing under the e-beam with higher intensity for 1 min, images (**a**) to (**d**) were taken at ordinary intensity

manipulators. This flow-induced deformation can find potential applications as a switch or clamp. Further investigations for improving the controllability using current-driven mechanisms are ongoing.

8.5 Mass Transport from a Nanotube to a Surface

In the semiconductor industry, copper has increasingly replaced aluminum because of its superior electrical conductivity. Growing interest in using it as electrodes and functional elements for the next generation of integrated circuits has been stimulated by the discovery of CNTs, nanowires, and other building blocks and enabled by bottom-up nanotechnologies such as self-assembly [34], robotic assembly [25, 26], and welding [9, 35]. With the possibility of delivering attogram copper from conduits [9, 10], copper-filled CNTs [19] are ideal for self-welding of self-assembled nanotubes [34] onto electrodes, as well as other potential nanofluidic applications [12, 16, 36, 37].

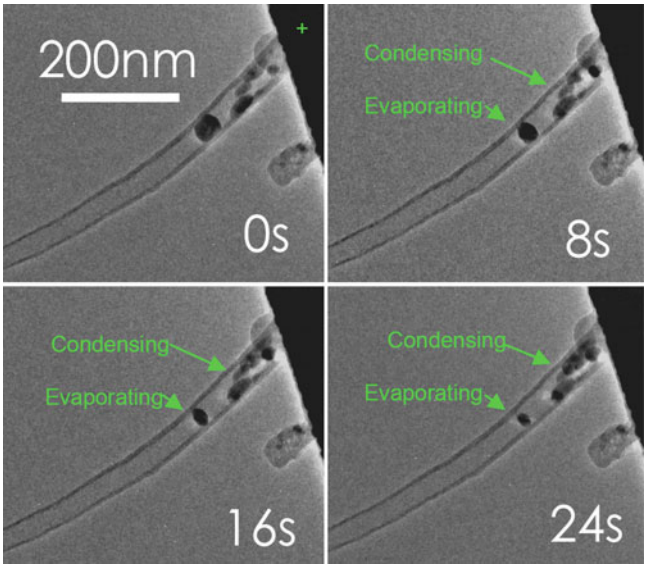

Fig. 8.6 Evaporation and condensation of copper inside a CNT

Previous experimental investigations of controlled melting and flowing of single-crystalline copper from individual CNTs [9, 10] have shown that very low current induces melting and drives the flow, which is much more efficient than irradiation-based techniques involving high-energy electron beams [38–41], FIBs [42], or lasers [36]. Furthermore, conservation of the material is facilitated by its encapsulation as opposed to conveying mass on the external surface of nanotubes [30]. Because both the rate and direction of mass transport depend on the external electrical drive, precise control and delivery of minute amounts of material is possible. However, because of the coupling of electronic and thermal effects, the mechanisms are not well understood. Figure 8.6 reveals the flowing of the copper (bias 2.1 V) from a cap-opened CNT to the electrode (a Pt-coated atomic force microscope (AFM) cantilever). During the process, the contact resistance was improved when copper diffused onto the AFM cantilever (as anode). A detailed observation showed that the process involved the evaporation and condensation of the copper. The volume of the copper decreases at the site indicated by "evaporation" and increases at the site close to the probe (the anode), suggesting the condensation of the material.

Current-driven flowing of copper from nanotubes has been used to demonstrate nanorobotic spot welding [9] (Fig. 8.7).

It is very interesting to note the impact of cooling speed on the final shape of the deposit (Fig. 8.8). While instant cooling will generate a crystal-like polyhedral structure (Fig. 8.8a, b), a sudden cooling will form a real sphere (Fig. 8.8c).

With a combination of self-assembly, self-soldering of nanotubes onto nano-electrodes may be possible. As schematically shown in Fig. 8.9, a self-assembled

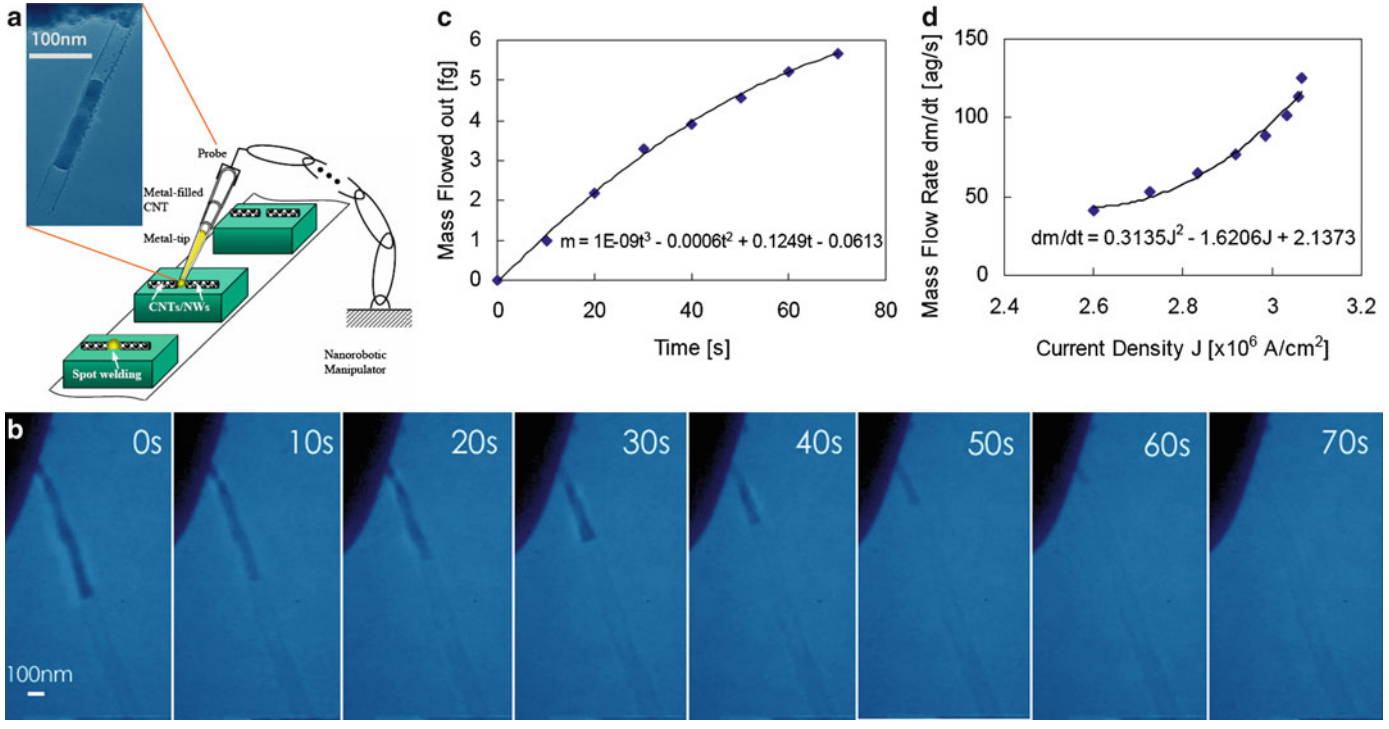

Fig. 8.7 Attogram mass delivery from a CNT. (**a**) Schematic of nanorobotic spot welding. (**b**) Time-resolved TEM images from video frames showing the flowing process. The copper core started to flow inside the carbon shells from the root to the tip as the bias voltage reaches up to 2.5 V. The whole process has continued for about 70 s. (**c**) The mass changes along the time. The mass flow rate can be then drawn out from the fitting curve as ~120 ag/s. (**d**) Correlation of the current density and the mass flow rate shows that the driven mechanism is electromigration

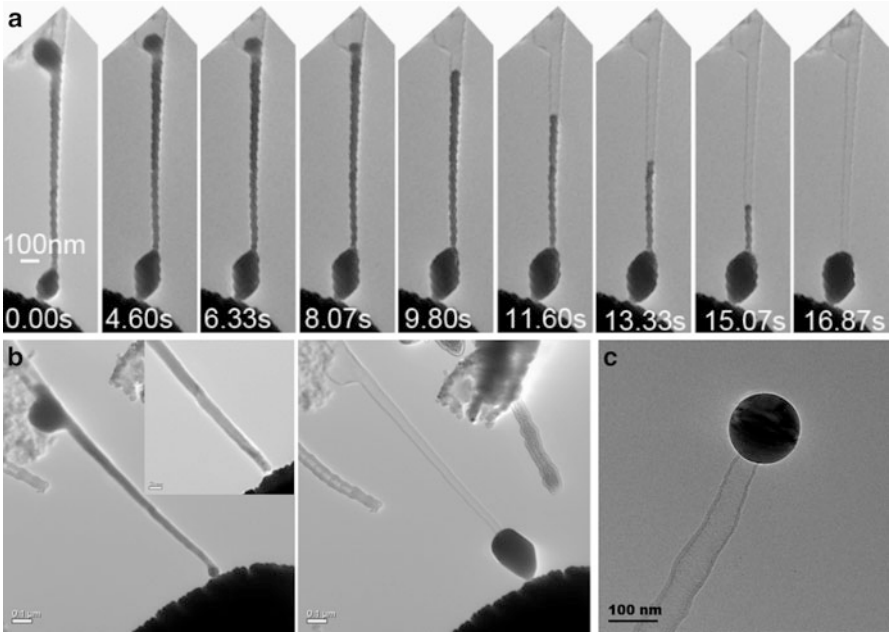

Fig. 8.8 The impact of cooling speed on the shape of deposits. (**a**) A time-resolved crystal-like deposit from a copper-filled CNT due to instant cooling. (**b**) The initial and final shapes. (**c**) A sphere formed on a nanotube by sudden departure of a nanotube from the probe

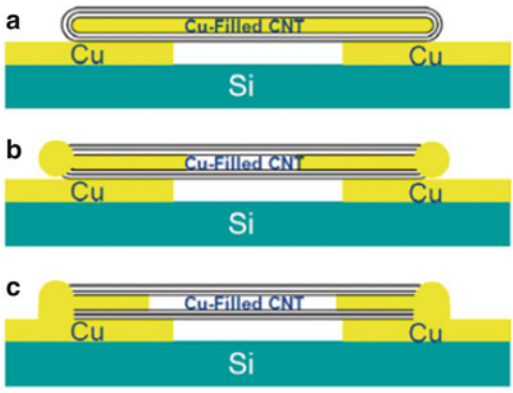

Fig. 8.9 Self-soldering a nanotube onto electrodes

nanotube can be heated by an AC current passing through it, then the encapsulated materials can flow out based on the above mechanism, and the nanotube can be soldered onto the electrodes.

Ionization can induce multiple Cu needles in neighboring tube tips to simultaneously disappear leaving large hollow spaces inside the tubes. Because this process can be done in a noncontact fashion by either heating or ionization, and because the ratio between the inner diameters to the wall thickness can be larger than with non-filled nanotubes, they can potentially serve as containers for hydrogen storage.

8.6 Mass Transport Between Nanotubes

Figure 8.10 presents internanotube mass (Cu) transport. Figure 8.10a shows a junction that is formed when a Cu-tipped CNT attached to an empty tube. Figure 8.10b details the process of internanotube transport due to evaporation, and Fig. 8.10c shows the process after evaporation. Figure 8.10d shows I–V curves before and after evaporation (probe as cathode). Figure 8.10e shows the mass lost from the Cu-tipped CNT and the mass flow rate as determined by line fitting. According to the apparent volume and the density of Cu, the original mass is approximately 2,804 ag (Fig. 8.10a), whereas the received mass by the lower tube is 746 ag (Fig. 8.10c), i.e., 26.6 % of the original mass is transported from the upper tube to the lower one, which is less than half of the transport for the cap-to-wall configuration. Nevertheless, considering that the opened area of the lower tube is only a very small portion (6 %) of the entire surface area of the upper tube that allows Cu atoms to escape, the effect of the electric field is obvious. This implies that without opening a hole on the sidewall, Cu atoms can pass through it. Simulation using molecular dynamics verified that the Cu atoms have passed through the center of the hexagons on the sidewalls.

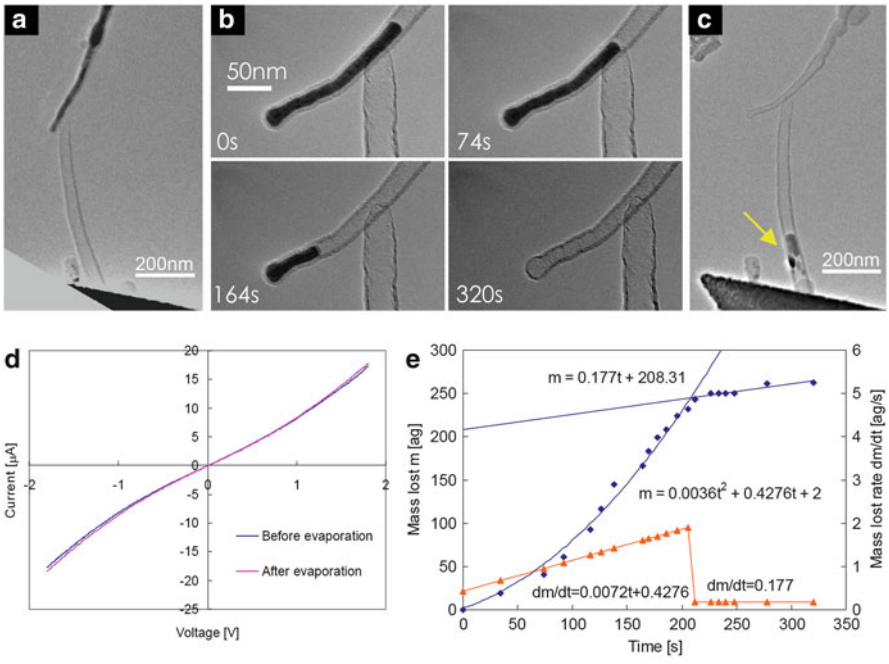

Fig. 8.10 Internanotube mass (Cu) transport. (**a**) A Cu-filled CNT is attaching to an empty CNT. (**b**) The Cu is evaporating. (**c**) After the evaporation. (**d**) I–V curves before and after evaporation (probe as cathode). (**e**) Mass lost from the Cu-tipped CNT and the mass flow rate

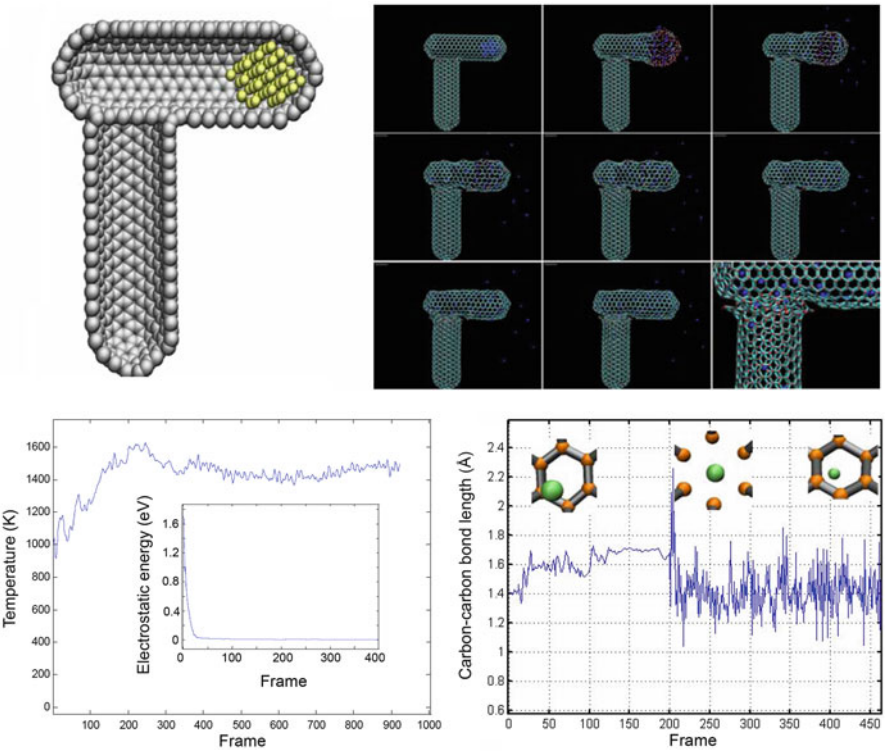

Fig. 8.11 Molecular dynamics simulation of inter-tube mass (Cu) transport. (**a**) Initial configuration of the simulated system with a cut view. Copper cluster is represented as nanoparticle aggegates. (**b**) Frames of melting and inter-tube diffusion of the Cu cluster using molecular dynamics simulation. (**c**) Melting temperature of copper crystal during simulation. The inset shows the electrostatic repulsive energy between copper ions during melting. (**d**) Carbon–carbon bond length during copper diffusion. At frame 200, the copper ions pass through the hexagonal rings, which correspond to the maximum opening of the carbon rings

As having been discussed in the previous investigation on current-driven intrananotube flow, the most possible mechanism for the observed flow in the fluidic junctions is electromigration [5, 9]. Other possible mechanisms such as capillary forces, thermal expansion, and shell-shrinkage-induced flow can be excluded. To understand how the mass have passed through the walls, we numerically investigated inter-tube mass (Cu) transport using molecular dynamics simulation (MDS) (Fig. 8.11). Figure 8.11a shows the initial atomic configuration of the simulated wall-to-cap transport system. The potential energy of the wall-to-cap transport system with a cluster of Cu inside was minimized at an internal pressure of 1 atm using the conjugate gradient method. To investigate copper diffusion, the system was simulated at temperatures between 700 and 1,800 K using molecular dynamics. The position of the copper ions as shown in the frames in Fig. 8.11b indicates that

the copper has melted and diffused. The system temperature during diffusion is shown by the curve in Fig. 8.11c. An analysis of the repulsive electrostatic energy between copper ions is given in the inset of Fig. 8.11c. It can be seen that a peak temperature was reached at frame 200. Accordingly, as shown in Fig. 8.11d, the carbon–carbon bond length obtained a maximum value at frame 200. The simulation indicates that electric energy is responsible for heating and that the repulsive charges increase the distances between copper ions and induce their transport. It can be seen from Fig. 8.11d that with a large enough charge, copper ions can pass through the walls of CNTs without necessarily breaking the bonds. Images clearly show that the hexagon carbon rings stretch during diffusion. Simulation also revealed that electrostatic forces guide the motion of the copper ions, causing the ions to collect in the original empty tube. It can be deduced that by increasing the number of shells, mass lost through the walls can be decreased. On the other hand, to realize internanotube transport, thinner shells are critical for keeping the mobility of the ions. Hence, an optimization of the number of shells will be needed for designing a fluidic system for a specific application.

8.7 Conclusions and Perspectives

Nanofluidic systems are still in their infancy. Although feasibility studies have shown that basic elements for such systems can be built with a combination of chemical synthesis, electron beams, FIBs, and tubes that can be connected together with the assistance of nanomanipulation, the scaling up of these systems remains a grand challenge. The mechanisms for filling and transport have been demonstrated and explained, but significant developments are required for complete system construction. On the plus side, efforts to develop fluidic systems will most probably contribute to the creation of many other types of nanosystems, including fluidic systems themselves. While a mass network remains a future target, a variety of applications of mass delivery have already been demonstrated such as sensing, memory, deposition, spot welding, and self-soldering. Potential applications in drug delivery and mass storage are also under investigation.

References

1. Eigler DM, Schweizer EK (1990) Positioning single atoms with a scanning tunneling microscope. Nature 344(6266):524–526
2. Lee HJ, Ho W (1999) Single-bond formation and characterization with a scanning tunneling microscope. Science 286(5445):1719–1722
3. Dong LX, Nelson BJ (2007) Robotics in the small, part ii: nanorobotics. IEEE Robot Autom Mag 14(3):111–121
4. Gao YH, Bando Y (2002) Carbon nanothermometer containing gallium - gallium's macroscopic properties are retained on a miniature scale in this nanodevice. Nature 415(6872):599

5. Svensson K, Olin H, Olsson E (2004) Nanopipettes for metal transport. Phys Rev Lett 93(14):145901
6. Schaper AK, Phillipp F, Hou HQ (2005) Melting behavior of copper nanocrystals encapsulated in onion-like carbon cages. J Mater Res 20(7):1844–1850
7. Sun L, Banhart F, Krasheninnikov AV, Rodriguez-Manzo JA, Terrones M, Ajayan PM (2006) Carbon nanotubes as high-pressure cylinders and nanoextruders. Science 312(5777): 1199–1202
8. Majumder M, Chopra N, Andrews R, Hinds BJ (2005) Nanoscale hydrodynamics – enhanced flow in carbon nanotubes. Nature 438(7064):44
9. Dong LX, Tao XY, Zhang L, Zhang XB, Nelson BJ (2007) Nanorobotic spot welding: controlled metal deposition with attogram precision from copper-filled carbon nanotubes. Nano Lett 7(1):58–63
10. Golberg D, Costa P, Mitome M, Hampel S, Haase D, Mueller C, Leonhardt A, Bando Y (2007) Copper-filled carbon nanotubes: rheostatlike behavior and femtogram copper mass transport. Adv Mater 19(15):1937–1942
11. Costa PMFJ, Golberg D, Mitome M, Hampel S, Leonhardt A, Buchner B, Bando Y (2008) Stepwise current-driven release of attogram quantities of copper iodide encapsulated in carbon nanotubes. Nano Lett 8(10):3120–3125
12. Dong LX, Tao XY, Hamdi M, Zhang L, Zhang XB, Ferreira A, Nelson BJ (2009) Nanotube fluidic junctions: inter-nanotube attogram mass transport through walls. Nano Lett 9(1): 210–214
13. Ajayan PM, Ebbesen TW, Ichihashi T, Iijima S, Tanigaki K, Hiura H (1993) Opening carbon nanotubes with oxygen and implications for filling. Nature 362(6420):522–525
14. Ajayan PM, Colliex C, Lambert JM, Bernier P, Barbedette L, Tence M, Stephan O (1994) Growth of manganese filled carbon nanofibers in the vapor phase. Phys Rev Lett 72(11): 1722–1725
15. Tsang SC, Chen YK, Harris PJF, Green MLH (1994) A simple chemical method of opening and filling carbon nanotubes. Nature 372(6502):159–162
16. Supple S, Quirke N (2003) Rapid imbibition of fluids in carbon nanotubes. Phys Rev Lett 90(21):214501
17. Smith BW, Monthioux M, Luzzi DE (1998) Encapsulated c-60 in carbon nanotubes. Nature 396(6709):323–324
18. Chen JY, Kutana A, Collier CP, Giapis KP (2005) Electrowetting in carbon nanotubes. Science 310(5753):1480–1483
19. Tao XY, Zhang XB, Cheng JP, Luo ZQ, Zhou SM, Liu F (2006) Thermal cvd synthesis of carbon nanotubes filled with single-crystalline cu nanoneedles at tips. Diamond Relat Mater 15(9):1271–1275
20. Rodriguez-Manzo JA, Banhart F (2009) Creation of individual vacancies in carbon nanotubes by using an electron beam of 1 angstrom diameter. Nano Lett 9(6):2285–2289
21. Dong LX, Arai F, Fukuda T (2004) Destructive constructions of nanostructures with carbon nanotubes through nanorobotic manipulation. IEEE ASME Trans Mechatron 9(2):350–357
22. Poncharal P, Wang ZL, Ugarte D, de Heer WA (1999) Electrostatic deflections and electromechanical resonances of carbon nanotubes. Science 283(5407):1513–1516
23. Li WZ, Wen JG, Ren ZF (2001) Straight carbon nanotube y junctions. Appl Phys Lett 79(12):1879–1881
24. Menon M, Srivastava D (1997) Carbon nanotube “t junctions”: nanoscale metal–semiconductor-metal contact devices. Phys Rev Lett 79(22):4453–4456
25. Dong LX, Subramanian A, Nelson BJ (2007) Carbon nanotubes for nanorobotics. Nano Today 2(6):12–21
26. Dong LX, Arai F, Fukuda T (2003) Nanoassembly of carbon nanotubes through mechanochemical nanorobotic manipulations. Jpn J Appl Phys Pt 1 42(1):295–298

27. Jin CH, Suenaga K, Iijima S (2008) Plumbing carbon nanotubes. Nat Nanotechnol 3(1):17–21
28. Dong LX, Tao XY, Hamdi M, Zhang L, Zhang XB, Ferreira A, Nelson BJ (2009) Nanotube boiler: attogram copper evaporation driven by electric current, joule heating, charge, and ionization. IEEE Trans Nanotechnol 8(5):565–568
29. Begtrup GE, Gannett W, Yuzvinsky TD, Crespi VH, Zettl A (2009) Nanoscale reversible mass transport for archival memory. Nano Lett 9(5):1835–1838
30. Regan BC, Aloni S, Ritchie RO, Dahmen U, Zettl A (2004) Carbon nanotubes as nanoscale mass conveyors. Nature 428(6986):924–927
31. Collins PG, Avouris P (2000) Nanotubes for electronics. Sci Am 283(6):62–69
32. Dong LX, Shou KY, Frutiger DR, Subramanian A, Zhang L, Nelson BJ, Tao XY, Zhang XB (2008) Engineering multiwalled carbon nanotubes inside a transmission electron microscope using nanorobotic manipulation. IEEE Trans Nanotechnol 7(4):508–517
33. Dorozhkin PS, Tovstonog SV, Golberg D, Zhan JH, Ishikawa Y, Shiozawa M, Nakanishi H, Nakata K, Bando Y (2005) A liquid-ga-fitted carbon nanotube: a miniaturized temperature sensor and electrical switch. Small 1(11):1088–1093
34. Subramanian A, Dong LX, Tharian J, Sennhauser U, Nelson BJ (2007) Batch fabrication of carbon nanotube bearings. Nanotechnology 18(7):075703
35. Hirayama H, Kawamoto Y, Ohshima Y, Takayanagi K (2001) Nanospot welding of carbon nanotubes. Appl Phys Lett 79(8):1169–1171
36. Kral P, Tomanek D (1999) Laser-driven atomic pump. Phys Rev Lett 82(26):5373–5376
37. Whitby M, Quirke N (2007) Fluid flow in carbon nanotubes and nanopipes. Nat Nanotechnol 2(2):87–94
38. Dong LX, Arai F, Fukuda T (2002) Electron-beam-induced deposition with carbon nanotube emitters. Appl Phys Lett 81(10):1919–1921
39. Yokota T, Murayama M, Howe JM (2003) In situ transmission-electron-microscopy investigation of melting in submicron al-si alloy particles under electron-beam irradiation. Phys Rev Lett 91(26):265504
40. Xu SY, Tian ML, Wang JG, Xu H, Redwing JM, Chan MHW (2005) Nanometer-scale modification and welding of silicon and metallic nanowires with a high-intensity electron beam. Small 1(12):1221–1229
41. Xie GQ, Song MH, Furuya K, Louzguine DV, Inoue A (2006) Compound nanostructures formed by metal nanoparticles dispersed on nanodendrites grown on insulator substrates. Appl Phys Lett 88(26):263120
42. Kometani R, Kanda K, Haruyama Y, Kaito T, Matsui S (2006) Evaluation of field electron emitter fabricated using focused-ion-beam chemical vapor deposition. Jpn J Appl Phys Pt 2 Lett 45(24–28):L711–L713

Chapter 9
Nanorobotic Manipulation of 1D Nanomaterials in Scanning Electron Microscopes

Yan Liang Zhang, Yong Zhang, Changhai Ru, Jason Li, and Yu Sun

Abstract Nanorobotic manipulation inside a scanning electron microscope (SEM) has been used for maneuvering nanomaterials and nanostructures, charactering material properties, and assembling nanoscaled devices. Teleoperation with joysticks is most often used for controlling motions of nanomanipulators. Progress is being made toward automated nanomanipulation using SEM as a vision sensor. This chapter reviews systems, techniques, and applications of SEM nanomanipulation of 1D nanomaterials.

9.1 Overview

Advances in nanomaterial synthesis have resulted in a plethora of novel materials possessing unique properties (electrical, photonic, mechanical, etc.). Efficiently maneuvering individual nanomaterials into predefined positions and accurately characterizing their properties are important for building high-performance devices and guiding nanomaterial synthesis. Taking 1D nanomaterials as an example,

Y.L. Zhang • J. Li • Y. Sun
Department of Mechanical and Industrial Engineering, University of Toronto, 5 King's College Road, M5S 3G8, Toronto, ON, Canada
e-mail: yanliang.zhang@utoronto.ca; jason.li@utoronto.ca; sun@mie.utoronto.ca

Y. Zhang
Department of Electrical and Computer Engineering, University of Toronto, 5 King's College Road, M5S 3G8, Toronto, ON, Canada
e-mail: yzhang@mie.utoronto.ca

C. Ru
Robotics and Microsystems Center, Soochow University, Suzhou 215021, China
e-mail: changhai.ru@utoronto.ca

Y. Sun (✉)
Advanced Micro and Nanosystems Laboratory, University of Toronto, Toronto, ON, Canada

C. Mavroidis and A. Ferreira (eds.), *Nanorobotics*, DOI 10.1007/978-1-4614-2119-1_9,
© Springer Science+Business Media New York 2013

nanowires/nanotubes must be positioned between source and drain electrodes for building nano-FETs (field effect transistors). A number of large-scale (parallel) methods have been developed, which permit the integration of nanomaterials for device construction in relatively large areas, such as in situ growth of nanowires/nanotubes in predefined locations [1] and approaches for controlling presynthesized nanomaterials (e.g., directed assembly [2], contact printing [3], and dielectrophoresis [4]).

By contrast, mechanical nanomanipulation, despite being slower compared to the aforementioned methods, can enable the manipulation and characterization of individual nanomaterials due to its specificity and precision. Mechanical nanomanipulation typically leverages atomic force microscopy (AFM, or more generally, the family of scanning probe microscopy) or electron microscopy (scanning/transmission electron microscopes—SEM and TEM) as imaging tools. AFM-based nanomanipulation can be conducted either in a vacuum environment, an ambient environment, or an aqueous environment, making the technique applicable to the manipulation of both engineering and biological materials. Nonetheless, since AFM uses the same microcantilever tip for both imaging and manipulation (e.g., pushing or pulling) [5–7], performing truly simultaneous imaging and manipulation is a challenge.

SEM uses focused electron beams to image specimens with a high spatial resolution down to nanometers. It serves as an imaging platform that provides visual feedback at video rates (e.g., 15 Hz) as nanomanipulation occurs. Inside SEM, piezoelectric nanomanipulators with multiple degrees of freedom provide nanometer motion resolution suitable for precisely manipulating nano-objects [8, 9]. This system architecture is powerful in that imaging and manipulation tools are separated and operate coordinately. Additionally, many types of end effectors can be mounted onto nanomanipulators, such as nanoprobes and nanogrippers, for performing a variety of nanomanipulation tasks.

9.2 Nanomanipulation Systems

A number of nanomanipulators have been developed by companies, such as Zyvex, Kleindiek, SmarAct, and attocube, as well as by academic laboratories (e.g., [10–13]). Most of the systems are designed to be mounted on the specimen stage of an SEM or on the chamber wall. The nanomanipulators use piezoelectric motors and actuators to produce accurate motion without interfering with SEM imaging.

Figure 9.1 shows examples of commercially available nanomanipulators. The Zyvex system is composed of four quadrants of 3-DOF nanomanipulators, each of which is composed of a coarse-positioning stage and a fine-positioning unit. The coarse-positioning stage contains three identical piezoelectric slip–stick motors, each of which has a travel of 12 mm with 100-nm resolution. The fine-positioning unit contains a piezoelectric tube having travel ranges of 10 μm along the axis of the tube and 100 μm along each of the two transverse directions with 5-nm nominal resolution.

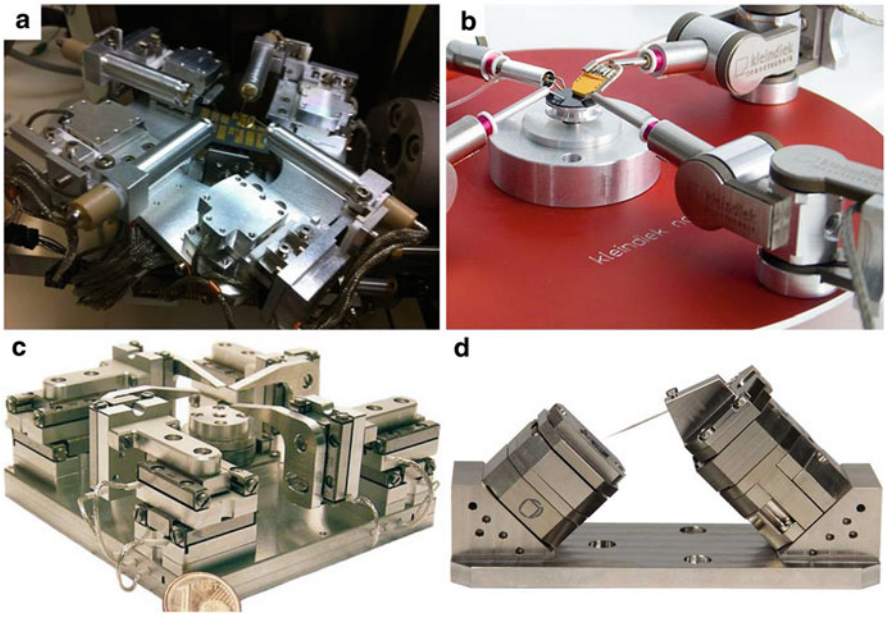

Fig. 9.1 Commercial nanomanipulation systems. (**a**) Zyvex S100, (**b**) Kleindiek NanoWorkstation, (**c**) SmarAct system, and (**d**) Attocube system

The Zyvex system uses separate piezoelectric elements for coarse and fine modes, which has the advantage of a large fine motion range. Different from this configuration, when a system uses a single piezoelectric element to realize both coarse and fine positioning, the footprint of the system is smaller. The single piezoelectric element can either operate as a stick-slip motor for achieving a large motion range (e.g., millimeters) or operate in the fine mode as a piezoelectric actuator to produce fine motion of nanometers with a travel range typically limited to a few micrometers. For example, Fig. 9.1b–d shows a Kleindiek system, a SmarAct system, and an Attocube system, all of which use one drive for both coarse and fine positioning.

9.3 Teleoperated Nanomanipulation

Commercial nanomanipulators are controlled via a keypad/joystick by an operator, while the operator carefully monitors image feedback shown on the SEM screen. This teleoperation approach was used by a number of groups to manipulate nanomaterials and nanostructures for material characterization and device construction. We review only a few examples as follows.

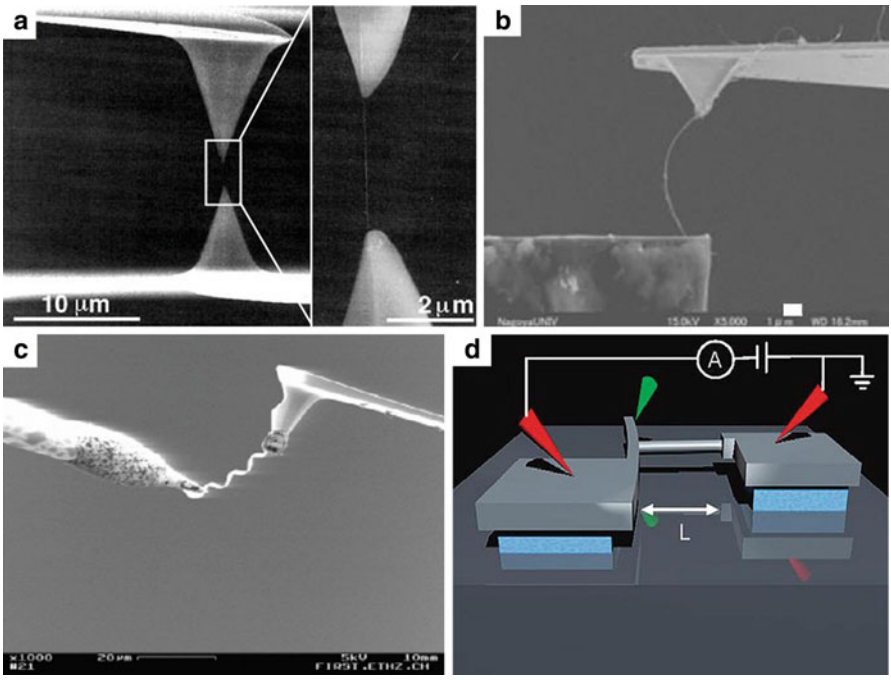

Fig. 9.2 Manipulation of nanomaterials for mechanical and electrical characterization. (**a**) A MWCNT was tensile tested by two AFM cantilevers [14]. (**b**) A bundle of MWCNTs was buckled by an AFM cantilever [15]. (**c**) An InGaAs/GaAs nanospring was stretched between a probe and an AFM cantilever [16]. (**d**) A silicon nanowire was stretched for piezoresistivity characterization [17]

9.3.1 Nanomaterial Characterization

The characterization of nanomaterials is important for understanding their properties and exploring their applications. The mechanical and electrical properties of a range of one-dimensional nanomaterials have been characterized using nanomanipulation. Figure 9.2a shows that two AFM cantilevers stretch a multiwalled carbon nanotube (MWCNT) for tensile testing. Individual MWCNTs were first picked up by one cantilever and attached to the second cantilever. In Fig. 9.2b, an AFM cantilever buckles a bundle of MWCNTs for mechanical characterization. An InGaAs/GaAs nanospring was tensile tested between a probe and an AFM cantilever, as shown in Fig. 9.2c. Figure 9.2d schematically illustrates that a silicon nanowire is stretched for the characterization of its piezoresistivity. The green-colored probe is used to push the freestanding cantilever and stretch the suspended silicon nanowire. The red probes form electrical connections for measuring the resistance changes of the nanowire during straining.

Besides nanomaterial characterization using AFM cantilevers, MEMS (micro-electromechanical systems) devices were also developed for mechanical characteri-

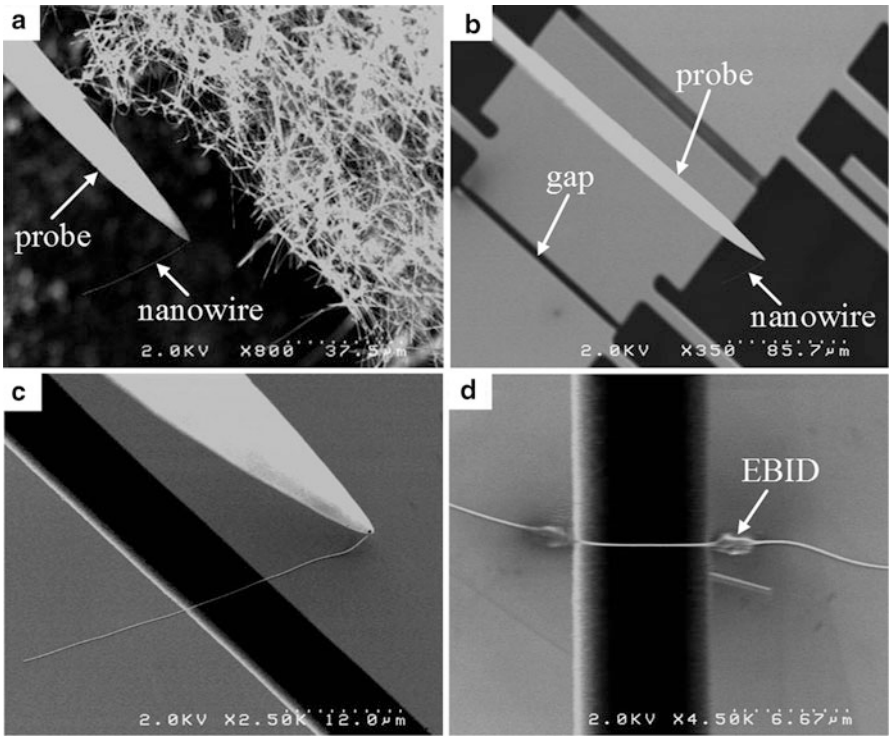

Fig. 9.3 A nanowire is transferred from its growth substrate to a tensile-testing MEMS device via nanomanipulation. (**a**) A nanowire is soldered to a probe tip using EBID and is pulled off from the growth substrate. (**b**) The nanomanipulator transfers the nanowire to the MEMS device. (**c**) The nanowire is placed across the gap of the device. (**d**) The nanowire is EBID fixed to the gap edges, followed by probe retraction

zation of nanomaterials. A critical step for the MEMS-based approach is the transfer of a nanowire/nanotube from its growth substrate to the MEMS device. We experimentally developed the following procedure for the nanowire transfer (Fig. 9.3) without requiring instruments such as focused ion beam (FIB). A nanomanipulator first approaches an edge of the nanowire substrate and establishes contact with a single nanowire near its root. Following the contact, the nanowire is soldered to the probe tip using electron beam-induced deposition (EBID). The deposited material from EBID without injecting precursors is carbonaceous material, which is from the decomposition of contaminants inside the SEM chamber [18–20]. The probe then retracts and pulls the nanowire off from the growth substrate, as shown in Fig. 9.3a. A detached nanowire typically fractures near its root, so the upper section of the nanowire to be used for testing does not experience tension and remains intact.

The nanomanipulator subsequently transfers the nanowire to above the MEMS device (Fig. 9.3b) and lowers the nanowire to place it across the gap of the device (Fig. 9.3c). The first bond between the nanowire and one edge of the gap

is formed again via EBID. The nanomanipulator then orients the nanowire to make it perpendicular to the gap, followed by EBID soldering the nanowire to the second gap edge (Fig. 9.3d). The purpose of fixing the nanowire to the very edges of the gap, rather than some distance away from the edges, is to prevent static friction between the nanowire and the device surface when the nanowire is stretched. Finally, the probe is retracted from the MEMS device, during which the nanowire breaks between the second EBID bond on the device and the EBID bond on the probe. The nanowire is then ready for the tensile test or electromechanical characterization [21].

9.3.2 Device Prototyping

Nanomanipulation has also been used for assembling devices and structures for prototyping purposes. Figure 9.4a1 shows that a probe was picking up a photonic plate. The plates were stacked together to build a 3D photonic crystal (Fig. 9.4a2). In Fig. 9.4b, gold nanowires were picked and placed by a probe to form a pattern. Figure 9.4c shows that a microgripper assembles a nanostructure to an AFM cantilever. The assembly was used for AFM imaging of deep trenches.

9.4 Automated Nanomanipulation

Teleoperated nanomanipulation is time-consuming, skill dependent, and often damages end effectors since it is a trial–error process. As nanomanipulation becomes increasingly relevant for material testing and device construction, the nanomanipulation community is making progress toward automated operation in order to achieve reliability, efficiency, and repeatability. Because of creep, drift, and hysteresis of piezoelectric actuators, open-loop control cannot suffice in precision for automatic nanomanipulation tasks, necessitating feedback control. Integrating position sensors (e.g., optical encoders or capacitive sensors) can be useful. However, the integration of high-resolution encoders increases the cost significantly; furthermore, sensor drift can be significant at the nanometer scale. Thus, visual feedback from SEM stays as the most important form of sensing modality for closed-loop control of nanomanipulators with/without encoders.

9.4.1 Visual Tracking

To visually obtain the *XY* position of an end effector, visual tracking of an end effector in a sequence of SEM images has been achieved using feature-based methods [25, 26] and correlation-based methods [25, 27]. For example, a rigid-

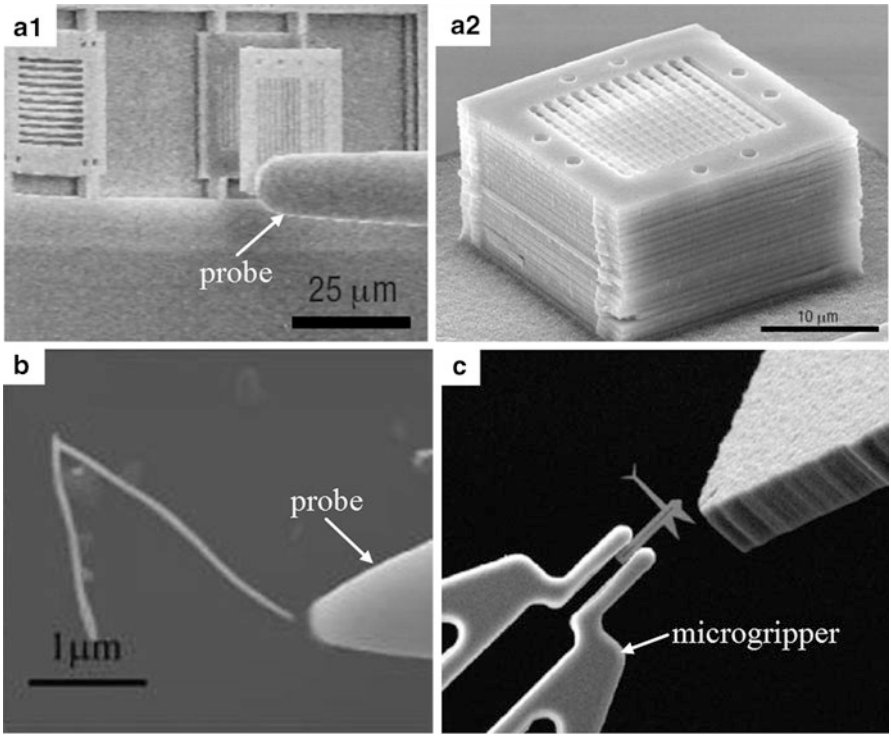

Fig. 9.4 Nanomanipulation for device construction. (**a**) Photonic plates were picked up and stacked to build a 3D photonic crystal [22]. (**b**) Gold nanowires were assembled to form a pattern [23]. (**c**) A microgripper was assembling a nanostructure to an AFM cantilever [24]

model-based visual-tracking method was reported, which applied domain-specific constraints and was evaluated by tracking a microgripper inside an SEM [27]. Based on SEM visual tracking, visual servo control can be realized to control the in-plane position of a nanomanipulator.

9.4.2 Depth Detection

Besides position control along *XY*, precise positioning along the *Z* direction is also essential but more challenging since it is difficult to extract depth information from SEM visual feedback. To address this issue, several techniques were proposed. The depth-from-focus method widely used under optical microscopes was extended to SEM for coarse estimate of the *Z* position of an end effector [18]. A touch sensor using piezoelectric ceramics [18] and a shadow-based depth-detection method [28, 29] were demonstrated for fine estimate of the *Z* position. MEMS sensors for contact

detection under optical microscopes [30] can also be used inside SEM. However, the precision and accuracy of these methods have not been quantified.

In addition, stereoscopic SEM images can be generated by tilting the electron beam [31], which requires the installation of specialized hardware. Tilting the specimen (vs. electron beam) can also be used for SEM stereoscopy [32] but has not been evaluated for nanomanipulation purposes.

We have developed a vision-based contact detection method for micromanipulation under optical microscopy and recently extended this method to SEM nanomanipulation. The method makes use of the phenomenon that a downward-moving probe slides on the surface of the substrate after contact. When a nanomanipulator moves a probe along its z-axis to approach a substrate, the position of the probe in the image frame also moves along a certain direction, due to the perspective projection model of the SEM [27]. When the probe contacts the substrate and begins to slide, an abrupt shift in the moving direction of the probe in the image frame is recognized as the contact point. Therefore, by monitoring the occurrence of this phenomenon, visually tracking a downward-moving probe is capable of detecting the contact between the probe and substrate.

9.4.3 Demonstration: Automated Four-Point Probing of Nanowires

We demonstrated automated nanomanipulation for a well-structured task—four-point probe measurement of individual nanowires [33]. For nanowire sample preparation, nanowires are scratch removed from their growth substrate and placed on a SiO_2-covered silicon substrate. Consequently, the nanowires lie directly on the substrate surface. A Zyvex S100 nanomanipulation system (Fig. 9.1a) was used along with a Hitachi S-4000 SEM for this task.

The four probes were first brought into the field of view under a proper magnification using the coarse-positioning stages, after which only the fine-positioning units were controlled to move the probes. The probes and nanowires were visually recognized by the automated system. A nanowire was selected for testing, and four target positions on the nanowire were determined. The system moved the four probes downward to establish their contact with the substrate via vision-based contact detection. After contact detection, the probes were positioned at a certain height (e.g., 200nm) above the substrate, ready for in-plane movement.

The four piezoelectric tubes were actuated in their respective x- and y-axes for the system to obtain parameters for their mathematical models to be used in feedforward controllers. Through visual servo control with a feedforward controller, the probes were simultaneously moved toward their target positions on the nanowire (Fig. 9.5a). The probes then moved downward to land on the nanowire for measurements. The separation distance between the inner pair of probes can be automatically adjusted by repositioning the probes for measuring the electrical properties of different lengths of the nanowire.

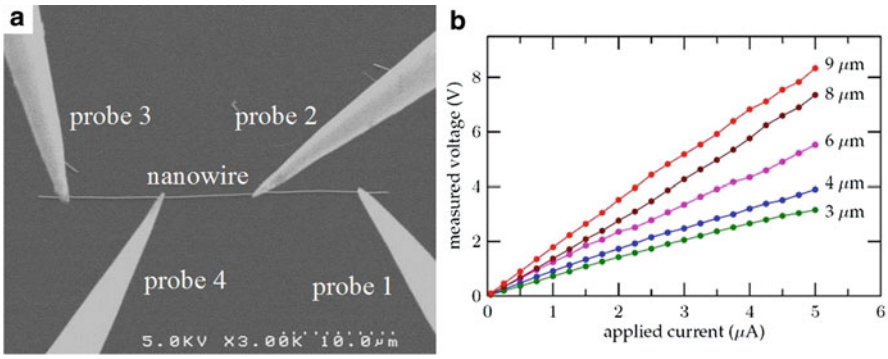

Fig. 9.5 Automated four-point probe measurement of a nanowire [30]. (**a**) The four probes land on target positions on a nanowire. (**b**) *I–V* characteristics of the nanowire with regard to different separations between the two inner probes

I–V data from a nanowire (83nm in width) are shown in Fig. 9.5b. The five data curves correspond to five different separations between the two inner probes. The five corresponding resistance values are proportional to the separations (i.e., the portions of the nanowires between two inner probe tips), as shown in Fig. 9.5b. Assuming the nanowire has a circular cross section, the resistivity was determined to be $9.88 \times 10^{-4} \Omega$m. When a higher current was applied, the nanowire finally failed when the current reached 7.4 μA. The breakdown current density of the nanowire was calculated to be 1.36×10^9 A/m^2.

9.5 Conclusion

Nanorobotic manipulation in SEM enabled precise maneuvering of individual nanomaterials. As many new nanomaterials emerge, nanorobotic manipulation will continue to be a unique technique for characterizing material properties and assembling nanomaterials into nanodevice prototypes. Further technical developments such as SEM vision-based control techniques using visual tracking and visual servoing will be made to automate specific nanomanipulation tasks for enhanced efficiency and reproducibility.

References

1. Rurali R (2010) Colloquium: structural, electronic, and transport properties of silicon nanowires. Rev Mod Phys 82:427–449
2. Rao SG, Huang L, Setyawan W, Hong S (2003) Nanotube electronics: large-scale assembly of carbon nanotubes. Nature 425:36–37

3. Fan Z, Ho JC, Jacobson ZA, Yerushalmi R, Alley RL, Razavi H, Javey A (2008) Wafer-scale assembly of highly ordered semiconductor nanowire arrays by contact printing. Nano Lett 8:20–25
4. Vijayaraghavan A, Blatt S, Weissenberger D, Oron-Carl M, Hennrich F, Gerthsen D, Hahn H, Krupke R (2007) Ultra-large-scale directed assembly of single-walled carbon nanotube devices. Nano Lett 7:1556–1560
5. Requicha AAG, Arbuckle DJ, Mokaberi B, Yun J (2009) Algorithms and software for nanomanipulation with atomic force microscopes. Int J Robot Res 28:512–522
6. Rubio-Sierra FJ, Heckl WM, Stark RW (2005) Nanomanipulation by atomic force microscopy. Adv Eng Mater 7:193–196
7. Hsieh S, Meltzer S, Wang CRC, Requicha AAG, Thompson ME, Koel BE (2002) Imaging and manipulation of gold nanorods with an atomic force microscope. J Phys Chem B 106:231–234
8. Yu MF, Dyer MJ, Skidmore GD, Rohrs HW, Lu X, Ausman KD, Her JRV, Ruoff RS (1999) Three-dimensional manipulation of carbon nanotubes under a scanning electron microscope. Nanotechnology 10:244–252
9. Fukuda T, Nakajima M, Liu P, ElShimy H (2009) Nanofabrication, nanoinstrumentation and nanoassembly by nanorobotic manipulation. Int J Robot Res 28:537–547
10. Dong L, Arai F, Fukuda T (2004) Destructive constructions of nanostructures with carbon nanotubes through nanorobotic manipulation. IEEE ASME Trans Mechatron 9:350–357
11. Fatikow S, Wich T, Hulsen H, Sievers T, Jahnisch M (2007) Microrobot system for automatic nanohandling inside a scanning electron microscope. IEEE ASME Trans Mechatron 12:244–252
12. Heeres EC, Katan AJ, van Es MH, Beker AF, Hesselberth M, van der Zalm DJ, Oosterkamp TH (2010) A compact multipurpose nanomanipulator for use inside a scanning electron microscope. Rev Sci Instrum 81:023704
13. Zhang YL, Zhang Y, Ru C, Chen BK, Sun Y (2013) A load-lock compatible nanomanipulation system for scanning electron microscope. IEEE/ASME Trans Mechatron 18:230–237
14. Yu MF, Lourie O, Dyer MJ, Moloni K, Kelly TF, Ruoff RS (2000) Strength and breaking mechanism of multiwalled carbon nanotubes under tensile load. Science 287:637–640
15. Fukuda T, Arai F, Dong L (2003) Assembly of nanodevices with carbon nanotubes through nanorobotic manipulations. Proc IEEE 91:1803–1818
16. Bell DJ, Dong L, Nelson BJ, Golling M, Zhang L, Grutzmacher D (2006) Fabrication and characterization of three-dimensional InGaAs/GaAs nanosprings. Nano Lett 6:725–729
17. Lugstein A, Steinmair M, Steiger A, Kosina H, Bertagnolli E (2010) Anomalous piezoresistance effect in ultrastrained silicon nanowires. Nano Lett 10:3204–3208
18. Eichhorn V, Fatikow S, Wich T, Dahmen C, Sievers T, Andersen KN, Carlson K, Boggild P (2008) Depth-detection methods for microgripper based CNT manipulation in a scanning electron microscope. J Micro Nano Mech 4:27–36
19. Kratochvil BE, Dong L, Nelson BJ (2009) Real-time rigid-body visual tracking in a scanning electron microscope. Int J Robot Res 28:498–511
20. Kasaya T, Miyazaki HT, Saito S, Koyano K, Yamaura T, Sato T (2004) Image-based autonomous micromanipulation system for arrangement of spheres in a scanning electron microscope. Rev Sci Instrum 75:2033–2042
21. Zhang Y, Liu X, Ru C, Zhang YL, Dong L, Sun Y (2011) Piezoresistivity characterization of synthetic silicon nanowires using a MEMS device. J Microelectromech 20:959–967
22. Aoki K, Miyazaki HT, Hirayama H, Inoshita K, Baba T, Sakoda K, Shinya N, Aoyagi Y (2003) Microassembly of semiconductor three dimensional photonic crystals. Nat Mater 2:117–121
23. Peng Y, Cullis T, Inkson B (2009) Bottom-up nanoconstruction by the welding of individual metallic nanoobjects using nanoscale solder. Nano Lett 9:91–96
24. Kumar RTR, Hassan SU, Sukas OS, Eichhorn V, Krohs F, Fatikow S, Boggild P (2009) Nanobits: customizable scanning probe tips. Nanotechnology 20:395703
25. Kim TH, Zhang XG, Nicholson DM, Evans BM, Kulkarni NS, Radhakrishnan B, Kenik EA, Li AP (2010) Large discrete resistance jump at grain boundary in copper nanowire. Nano Lett 10:3096–3100

26. Lin R, Banmmerlin M, Hansen O, Schlittler RR, Boggild P (2004) Micro-four-point-probe characterization of nanowires fabricated using the nanostencil technique. Nanotechnology 15:1363–1367
27. Dohn S, Molhave K, Boggild P (2005) Direct measurement of resistance of multiwalled carbon nanotubes using micro four-point probes. Sens Lett 3:1–4
28. Eichhorn V, Fatikow S, Sukas OS, Hansen TM, Boggild P, Occhipinti LG (2010) Novel four-point-probe design and nanorobotic dual end effector strategy for electrical characterization of as-grown SWCNT bundles. In Proc IEEE Int Conf Robot Autom, Anchorage, Alaska, pp 4100–4105
29. Chen BK, Zhang Y, Perovic D, Sun Y (2011) MEMS microgrippers with thin gripping tips. J Micromech Microeng 21:105004
30. Kim K, Liu X, Zhang Y, Sun Y (2008) Nanonewton force-controlled manipulation of biological cells using a monolithic MEMS microgripper with two-axis force feedback. J Micromech Microeng 18:055013
31. Jahnisch M, Fatikow S (2007) 3-D vision feedback for nanohandling monitoring in a scanning electron microscope. Int J Optomechatron 1:4–26
32. Ribeiro E, Shah M (2006) Computer vision for nanoscale imaging. Mach Vis Appl 17:147–162
33. Ru C, Zhang Y, Sun Y, Zhong Y, Sun X, Hoyle D, Cotton I (2011) Automated four-point probe measurement of nanowires inside a scanning electron microscope. IEEE Trans Nanotechnol 10:674–681

Part III
Nano-Manipulation in Biomedical Applications

Chapter 10
Nanorobotic Manipulation and Sensing for Biomedical Applications

Fumihito Arai and Hisataka Maruyama

Abstract We developed a method for manipulating a single virus (size: 100nm) that employs optical tweezers in conjunction with dielectrophoretic (DEP) concentration of viruses on a microfluidic chip. The DEP force in the sample chamber concentrates the virus and prevents it from adhering to the glass substrate. The concentrated virus is transported to the sample selection section where it is trapped by optical tweezers. We demonstrated concentration of the virus using the DEP force, transported a single virus, and made it contact to a specific H292 cell. We also developed local measurement with functional gel-microtool for cell measurement. Gel-microtool was impregnated with indicators. In this chapter, bromothymol blue (BTB) and bromocresol green (BCG) were employed as pH indicators. Rhodamine B is temperature-sensitive fluorescent dye and is used for temperature measurement. Gel-microtool is manipulated by optical tweezers. Measurement is performed by detecting the color and the fluorescence intensity of each gel-microtool. We succeeded in pH measurement and temperature measurement using the gel-microtools.

10.1 Introduction

Nanomanipulation and local sensing are important topics in nano-biotechnology in these days [1]. For example, manipulation for virus has become one of the most important topics in recent years [2]. The ability to manipulate a single virus

F. Arai (✉)
Department of Micro-Nano Systems Engineering, Nagoya University, Furo-cho, Chikusa-ku, Nagoya 464-8603, Japan
e-mail: arai@mech.nagoya-u.ac.jp

H. Maruyama
Department of Micro-Nano Systems Engineering, Nagoya University, Furo-cho, Chikusa-ku, Nagoya 464-8603, Japan
e-mail: hisataka@mech.nagoya-u.ac.jp

C. Mavroidis and A. Ferreira (eds.), *Nanorobotics*, DOI 10.1007/978-1-4614-2119-1_10,
© Springer Science+Business Media New York 2013

is necessary to analyze the functions of influenza virus such as cell infection and incubation in a cell. Cultured cells have conventionally been used to analyze viral functions [3]. Although this method can acquire average information from many cells, the properties of individual infected cells vary depending on their physiological states and cell cycle. The efficiency of viral infection also varies between cells. Moreover, viral proliferation depends on the function of the nucleus of the infected cell. To perform quantitative analysis of a virus, single virus infection of a specific cell is required. Moreover, measurement of physiological conditions such as pH and temperature of cells is important for quantitative analysis [4, 5].

Methods for manipulating biomaterials on an optical microscope, an atomic force microscope, and a scanning electron microscope have been developed [6]. It is desirable to manipulate biomaterials in a wet condition to maintain their activity. Moreover, manipulation in a closed space such as a microfluidic chip is also desirable to prevent environmental disturbances. Measurement in the chip is also suitable for stable measurement. In recent years, microfluidic chips have been used to manipulate and measure biomaterials [7]. Noncontact manipulation and sensing are required for on-chip analysis because it is quite difficult to insert mechanical manipulators in the chips.

Various forms of noncontact manipulation including fluidic force, magnetic force, electrical force, and optical tweezers have been developed for on-chip manipulation in microfluidic chips. Hydrodynamic force has several advantages including low cost, low power consumption, and the potential for parallel operation [8]. However, it is difficult to use hydrodynamic force to perform selective manipulation of a single target. Magnetic force is considered to be safe for biomaterials [9]. However, to manipulate a single target, it is necessary to modify it by incorporating a magnetic material because most biomaterials are nonmagnetic. Although it is possible to concentrate biomaterials, concentrated samples can be modified by magnetic materials. Electrophoresis and dielectrophoresis are important means for performing bio-manipulation [10]. They are suitable for manipulating many samples, but it is difficult to use them to manipulate a single sample. Optical tweezers have been used in biology, and they have been employed to manipulate biomaterials such as cell, virus, and DNA [11]. They are capable of manipulating single targets, but they have low throughputs. Thus, to concentrate and perform stable manipulation of biomaterials, a combination of some of the above methods is required.

Several techniques for measurement of the environment inside a microchip have been developed. Conventionally, fluorescence observation was the major approach for environmental measurements [12–14]. A three-dimensional pH measurement with optically manipulated fluorescent particles has also been developed [15]. A microbead modified with a pH-sensitive fluorescent dye was prepared and positioned three-dimensionally using optical tweezers. This method enables three-dimensional, noncontact, and nondestructive measurement with high spatial resolution. Moreover, simultaneous measurement of different conditions such as O_2 and CO_2 is possible by using several fluorescence dyes with different excitation wavelength [16]. However, fluorescent methods have major problems

with absorption, quenching, and photodegradation. Thus, microbead modified with a pH indicator was developed [17]. Such microbead can be used for longtime measurements because of the absence of photodegradation.

We have proposed "On-Chip Robotics" for integrating micro- and nanomanipulation and performing measurements on a microfluidic chip [18–21]. A Robochip is a microfluidic chip in which micro/nanorobots are installed and which can perform single cell measurements and analysis, dispense droplets, cloning, and anatomical manipulation for on-chip micromanipulation such as cell sorting [22]. Robochips have many advantages such as being rapid, highly accurate, and disposable, enabling local environmental control, and being robust against disturbances [23].

In the present study, we infected a specific cell with a single virus by manipulating the virus using optical tweezers in conjunction with dielectrophoretic (DEP) concentration of the virus in a microfluidic chip. Viruses were concentrated by DEP force in the chip. The virus selected from the concentrated group was trapped and transported to the analysis chamber by optical tweezers. We also study about on-chip fabrication of environment measurement gel-microtool. Arbitrary shape gel-microtool is fabricated by connecting the gel-microbead impregnated with indicators. Circular pH measurement gel-microtool and local pH measurement around a yeast cell were demonstrated. Multiple measurements such as a wide-range pH measurement and the simultaneous measurement of the pH and temperature were also demonstrated.

10.2 Nanomanipulation of Single Influenza Virus Using Dielectrophoretic Concentration and Optical Tweezers

10.2.1 Microfluidic Chip for Infecting a Specific Cell with a Single Virus Using DEP Concentration

Figure 10.1 shows a schematic of on-chip infection of a specific cell with a single virus. The microfluidic chip consists of a sample chamber, electrodes for concentrating viruses, an analysis chamber, and microchannels for buffer flow (Fig. 10.1a). Viruses were stained with a fluorescent dye to enable them to be observed. The surfaces of the microchannels and chambers were pretreated with bovine serum albumin (BSA) to prevent viruses adhering to the chip. Each inlet port was connected to the syringe pump through the solution reservoir. The top of the analysis chamber was sealed by a self-adhesive material such as polydimethylsiloxane (PDMS). After single virus infection had been performed, the cell could be extracted by opening the analysis chamber.

Figure 10.1b–e depicts the process of single virus infection using DEP concentration and optical tweezers. The virus solution was first loaded into the sample chamber, and the buffer was simultaneously injected as sheath flow. The viruses were concentrated on the electrodes by DEP force. Viruses were concentrated by

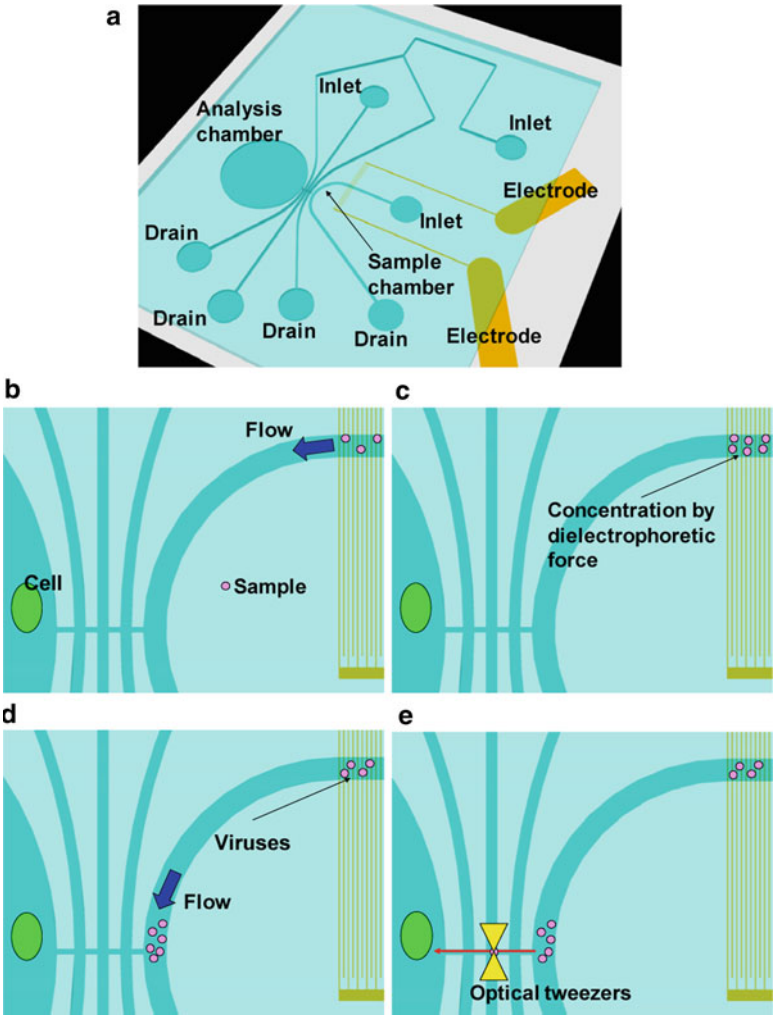

Fig. 10.1 Schematic of single cell infection of a specific cell using DEP concentration and optical tweezers in a chip. (**a**) Schematic of microfluidic chip. (**b**) Virus injection into sample chamber. (**c**) Virus concentration by DEP force. (**d**) Flow of concentrated viruses to selection region. (**e**) Transport of single virus to analysis region and contact with a specific cell for infection

generating a negative DEP force through adjusting the conductivity of the solution and the frequency of the voltage. The DEP force also prevents the viruses from adhering to the chip. A single virus was selected from the concentrated group, and it was trapped and transported to the analysis chamber using optical tweezers. This virus-loading method reduces the consumption of the scarce sample because it is difficult to detect viruses at low concentrations. The transported virus was brought into contact with the target cell to infect it. After infection by the required number of

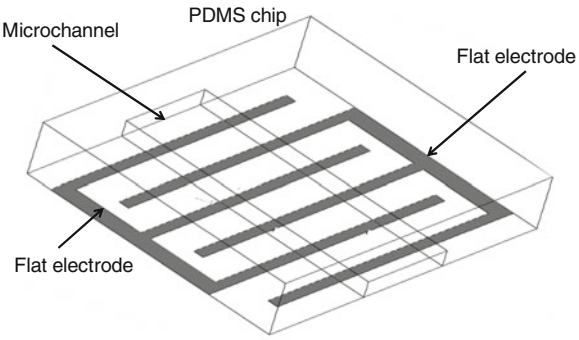

Fig. 10.2 Analytical model

viruses, these chambers can be isolated by stacking using a photo-crosslinkable resin to prevent other viruses from entering the analysis chamber [24]. Viruses outside the analysis chamber cannot enter the chamber due to physical blocking by the polymerized resin.

10.2.2 DEP Concentration of Viruses in Microfluidic Chip

We used DEP force for virus concentration because the virus was present in a low concentration. Figure 10.2 shows a schematic diagram of the electrodes. The electrodes are 10 μm wide, and the gap between them is 30 μm. The concentration of the virus in the solution was 1×10^6 viruses/μl; this low virus concentration made it difficult to observe the virus in the sample chamber since on average, there were <0.1 viruses in the field of view. A high-frequency voltage was applied to the electrodes to generate the DEP force. The effect of the DEP force on the viruses depends on the electric field gradient between the electrodes. The DEP force is given by the following equations:

$$F_{\mathrm{DEP}} = 2\pi\varepsilon_{\mathrm{m}} r^3 \mathrm{Re}\left[\frac{\varepsilon'_{\mathrm{p}} - \varepsilon'_{\mathrm{m}}}{\varepsilon'_{\mathrm{p}} + 2\varepsilon'_{\mathrm{m}}}\right] \nabla |E|^2 \tag{10.1}$$

$$\varepsilon'_{\mathrm{p}} = \varepsilon'_{\mathrm{p}} - j\frac{\sigma_{\mathrm{p}}}{\omega} \tag{10.2}$$

$$\varepsilon'_{\mathrm{m}} = \varepsilon'_{\mathrm{m}} - j\frac{\sigma_{\mathrm{m}}}{\omega} \tag{10.3}$$

where E is the electric field strength; r is the particle radius; $\varepsilon'_{\mathrm{p}}$ and $\varepsilon'_{\mathrm{m}}$ are, respectively, the complex permittivity of the particle and the solution; ε_{p} and ε_{m} are, respectively, the permittivity of the particle and the solution; σ_{p} and σ_{m} are, respectively, the conductivities of the particle and the solution; and ω is the angular frequency of the voltage. If $\varepsilon'_{\mathrm{p}}$ is smaller (larger) than $\varepsilon'_{\mathrm{m}}$, the negative (positive)

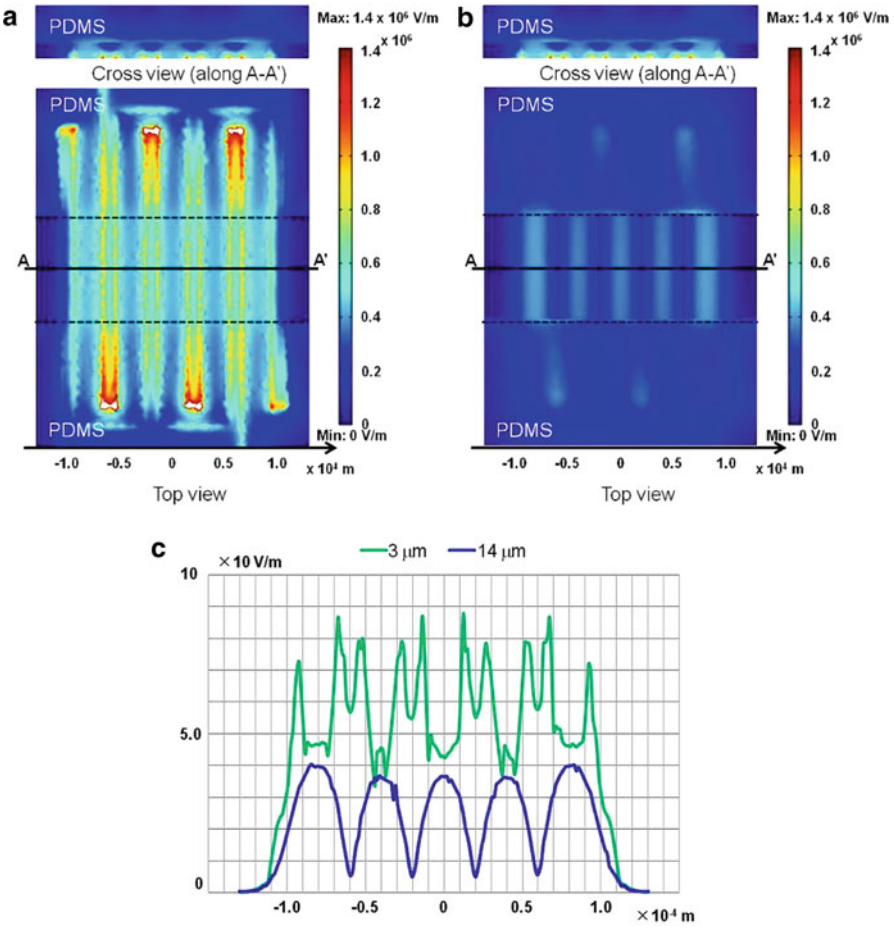

Fig. 10.3 FEM results for the electric field distribution. Electric field distributions at (**a**) 3 μm and (**b**) 14 μm from electrodes. (**c**) Comparison of electric field distributions at two different heights

DEP force causes the particles to move in the direction of decreasing (increasing) gradient. ε'_p and ε'_m depend on the frequency ω.

We analyzed the electric field distribution by the finite element method (FEM) using commercial software (COMSOL Multiphysics, COMSOL AB). In this analysis, the electric field distribution in water was analyzed. The microchannel was 200 μm wide and 15 μm high. The electrodes were 10 μm wide and 600 μm long, and there was a 30-μm gap between them. The permittivity of PDMS and water was 2.67 and 81.0, respectively. Figure 10.3a shows the FEM results for the electric field distribution, and Fig. 10.3b shows the electric field distributions along the center of the microchannel (i.e., line AA′) at two different heights. For both heights, the electric field gradient was high at the edge of the electrode. In contrast, it was low

between the electrodes and at the center of the electrodes. A positive DEP force may cause thermal damage to the sample due to the heat generated by the electrode. To prevent this, we adjusted the frequency to generate a negative DEP force so as to concentrate the viruses between the electrodes.

A high frequency (3 MHz) was employed for DEP manipulation of a virus according to the previous study [24]. We assumed that the virus was spherical with a diameter of 100nm [25]. The permittivity of the virus was taken to be two, and its conductivity was taken to be the same as that of the solution. The solution conductivity was adjusted to 10 mS/m to prevent thermal damage to the sample and electrodes. Under these conditions, the virus experienced a negative DEP force because $\mathrm{Re}\{(\varepsilon'_{\mathrm{p}} - \varepsilon'_{\mathrm{m}})/(\varepsilon'_{\mathrm{p}} + 2\varepsilon'_{\mathrm{m}})\}$ was negative (−0.47).

A negative DEP force also prevents the viruses adhering to the glass surfaces since it operates upward from the glass substrate. The virus moves by Brownian motion. The virus will not adhere to the glass surface if the DEP force exceeds the Brownian force. The Brownian force is given by

$$F_{\mathrm{B}} = m_{\mathrm{v}} \times < x >= \frac{4}{3}\rho_{\mathrm{v}}\pi a^3 \times \sqrt{\frac{RT}{3\pi\eta a N_{\mathrm{A}}}} \tag{10.4}$$

where F_{B} is the Brownian force, ρ_{v} is the virus density, a is the virus radius, R is the molar gas constant (8.31447 J K^{-1} mol^{-1}), T is the temperature, η is the viscosity of the solution (1.004×10^{-6} m^2/s), and N_{A} is the Avogadro constant. We compared the two forces at a height of 50nm above the glass substrate. We assumed that the virus density was 1 g/cm^3. From (10.2), the minimum F_{DEP} is 6.69×10^{-6} N. From (10.3), F_{B} was 1.53×10^{-24} N. Therefore, we concluded that the virus will not adhere to the glass surface since the negative DEP force exceeds the Brownian force.

10.2.3 Fabrication of Microfluidic Chip

Figure 10.4 depicts the process used to fabricate the microfluidic chip. A PDMS chip was fabricated by photolithography and replica molding. Chip molds were fabricated by multi-exposures to fabricate chips that have areas with different heights. A Cr/Au layer was sputtered on a Si wafer. A positive photoresist (OFPR, Tokyo Ohka Kogyo Co. Ltd.) was spin coated and patterned to fabricate an alignment pattern for multi-exposure of a negative resist (SU-8, Kayaku Microchem). After removing the developed OFPR, the Cr/Au layer was etched. The SU-8 sheet was then coated and patterned. This mold has two areas with different heights: one area was 15 μm thick, and it was for the sample chamber, while the other area was 115 μm thick, and it was for microchannels and the analysis chamber. The sample chamber was 200 μm wide. The microchannels were 100 μm wide. The analysis chamber was 5 mm in diameter. The top of the analysis chamber was sealed with a PDMS membrane to allow the sample chamber to be opened for inserting and removing cells.

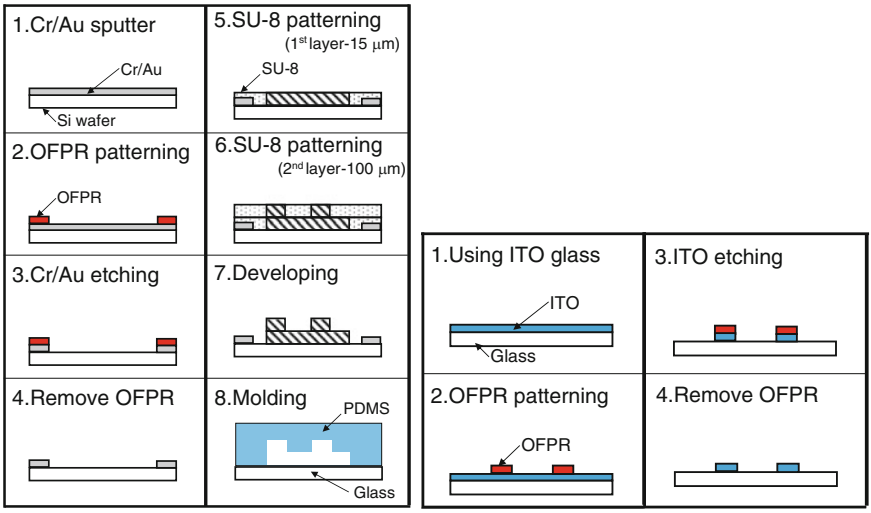

Fig. 10.4 Fabrication process of microfluidic chip. Fabrication processes of (**a**) microchannel and (**b**) glass substrate with electrodes

Figure 10.4b shows the fabrication process for the electrodes. A Cr/Au layer was sputtered on the Si wafer. A positive-photoresist OFPR was then spin coated and patterned to fabricate the pattern for the electrodes. The photoresist was removed after the Cr/Au layer had been etched by $FeCl_3$ solution. Figure 10.5 shows photographs of the sample chamber; it has a sample concentration region and a sample selection region. We could culture H292 cells in the analysis chamber.

10.2.4 Experimental Setup

We used an inverted microscope (IX71, Olympus) equipped with an epifluorescence system. Fluorescent polystyrene (PS) beads (excitation wavelength: 491nm; emission wavelength: 515nm) were injected into the sample chamber using a syringe pump (KDS120, KD Scientific Inc.) to confirm DEP concentration. The flow rate was 0.10 μl/h. A high-frequency voltage was applied to the electrodes by a function generator (WF1974, NF Corporation). The fluorescence intensity of the PS beads was monitored using a color CCD camera (WAT-221, Watec Co. Ltd.) and recorded using a computer. We used a laser confocal microscope (A1R, Nikon Corporation) equipped with a laser manipulation system (maximum power: 1 W; output wavelength: 1,064nm) to perform DEP virus concentration and single virus infection of a specific cell.

Influenza viruses stained with a fluorescent dye (DiI; excitation wavelength: 549nm; emission wavelength 565nm) were used. DiI stains the virus membrane. 1 ml of DiI was mixed with 500 ml PBS(−). PBS(−) consists of 137 mmol/l

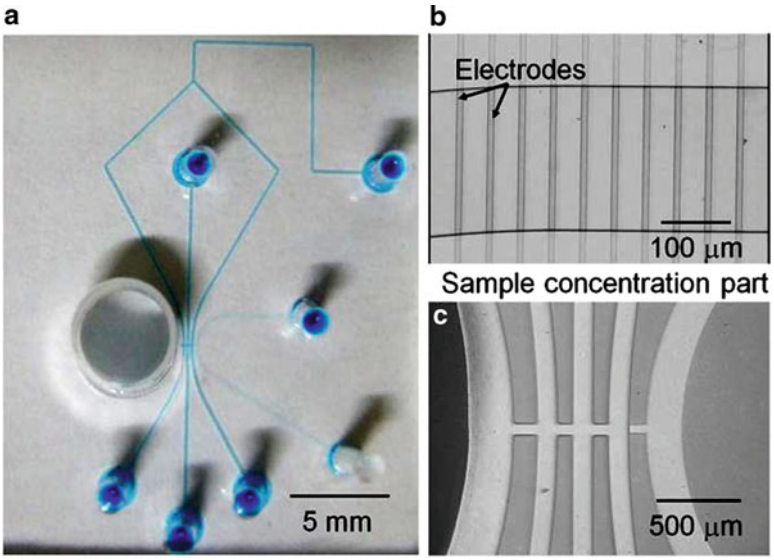

Fig. 10.5 Photographs of microfluidic chip. (**a**) Microfluidic chip (channels are filled by colored water). (**b**) Sample collection region. (**c**) Sample chamber and analysis chamber

NaCl, 2.68 mmol/l KCl, 8.1 mmol/l Na_2HPO_4, and 1.47 mmol/l KH_2PO_4. It has a pH of 7.4. The mixture is mixed with the virus suspension (DiI solution: virus suspension = 1:1). The viruses were incubated in the dark for 30 min. Finally, the virus solution was diluted by adding distilled water to adjust its conductivity to 10 mS/m. The virus concentration was 1×10^6 viruses/μl.

We used a photo-crosslinkable resin, polyethylene glycol methacrylate (PEGMA), to isolate the sample chamber from the analysis chamber after viral infection had occurred. PEGMA is polymerized by ultraviolet light; ultraviolet light was generated by a mercury lamp in the microscope and controlled using a mechanical shutter.

10.2.5 Manipulation of Single Influenza Virus on a Chip

Figure 10.6 shows the experimental results for DEP concentration of influenza viruses using the microfluidic chip. The viruses were injected into the chip by a syringe pump. The flow rate was 0.10 μl/h. A square wave was applied to the electrodes with amplitude of 20 V_{p-p} and a frequency of 3 MHz. Figure 10.6b shows that the viruses were concentrated from 1×10^6 to 1×10^9 viruses/μl. After 5 min of DEP concentration, we released the viruses by turning of the voltage. We then confirmed that no viruses had adhered to the glass substrate in the concentration area. Virus adhered to the glass surface when no DEP force was generated. This

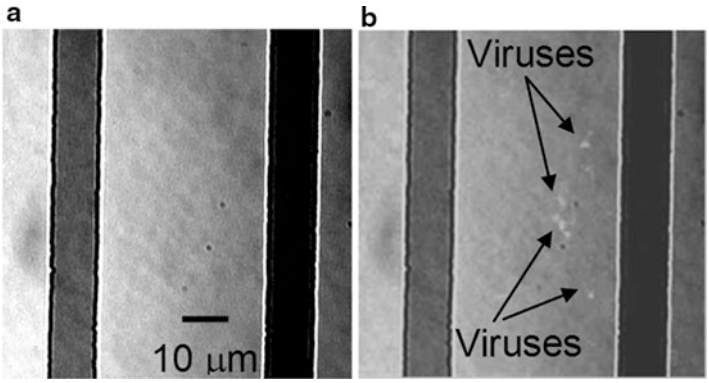

Fig. 10.6 Concentration of influenza viruses by DEP force. (**a**) Before and (**b**) after concentration (20 V_{p-p}, 3 MHz, square wave, 5 min)

result demonstrates that DEP force is effective for concentrating viruses. After releasing the viruses, we transported them to the sample selection region.

Figure 10.7 shows the experimental results for the manipulation of a single virus by direct laser manipulation in the sample chamber using a laser micromanipulator (Sigma Koki). The laser power was set to 0.5 W to avoid photobleaching. Flow was stopped inside the chip. We succeeded in manipulating a single virus using optical tweezers. The maximum transport speed was 10 μm/s. We transported the virus to the analysis chamber and caused it to make contact with a selected H292 cell to infect it.

From this result, we estimated the force for transporting the virus by optical tweezers using Stokes' law:

$$F_v = 6\pi\mu r_v V_v \tag{10.5}$$

where F_v is driving force of the virus, μ(= 1.002 mPa s) is the viscosity at 20 °C, r_v is the radius of the virus, and V_v is the speed of the virus. The size of influenza viruses is considered to be in the range 80–120nm [25]; based on this, we estimated the size of the virus to be about 100nm. For these conditions, F_v was calculated to be 9.4 fN. The angle between the virus transport direction and the flow direction in the microfluidic chip was 90°. The trapping force of the optical tweezers is isotropic. Thus, the flow rate must be kept below 10 μm/s to be able to manipulate the virus when the laser power is 0.5 W.

Finally, the analysis chamber was isolated from the virus chamber by local photopolymerization of PEGMA to prevent other viruses from entering the cell chamber (see Fig. 10.8). These results demonstrate the effectiveness of our proposed system for biomedical analysis.

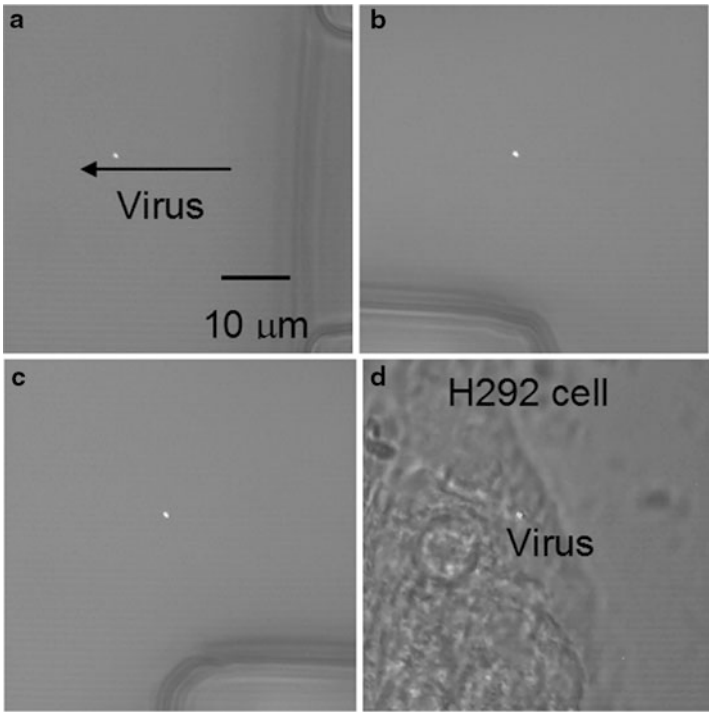

Fig. 10.7 Manipulation of single influenza virus and contact with an H292 cell using optical tweezers. (**a**) Manipulation of single influenza virus by optical tweezers (10 μm/s). (**b**) Transport in microchannel. (**c**) Transport to analysis chamber. (**d**) Contact with a specific H292 cell

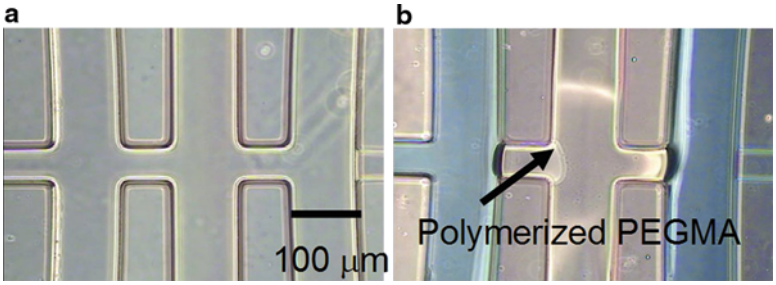

Fig. 10.8 Isolation of chambers by local polymerization. (**a**) Before and (**b**) after isolation by in situ photopolymerization of photo-crosslinkable resin

10.3 Local Sensing Using Functional Gel-Microtool Manipulated by Optical Tweezers

10.3.1 Functional Gel-Microtool for Environment Sensing

An environment measurement gel-microtool is composed of the gel-microbead and an indicator. Measurement is performed by detecting the color of the indicator inside the microbead. The gel-microbead was made by salting out of a photo-crosslinkable resin (ENT–3400, Kansai Paint, Japan), which was used for immobilizing cells and enzymes [20]. This resin consists primarily of polyethyleneglycol (PEG) prepolymer and is hydrophilic. This gel-microbead is manipulated by optical tweezers in an aqueous solution because the relative refractive index of PEG (1.4) is higher than that of water (1.3). The resin can be polymerized by irradiation of near-ultraviolet rays around 366nm. The gel-microbead is used as a carrier of the indicator.

Figure 10.9 shows photographs of the gel-microbead. The concentrations for salting out depend on the Hofmeister series [26]. Concentrations for generating gel-microbeads were confirmed visually in four different electrolytes. All electrolytes exhibited the expected concentration according to the Hofmeister series as shown in Table 10.1. When the electrolyte concentrations were below the limit concentration for salting out, the unpolymerized gel-microbead melted into the solution. However, the polymerized gel-microbead swelled at a lower concentration than the limit concentration for salting out. 0.5 M phosphate dipotassium salt required the lowest concentration for making the gel-microbeads.

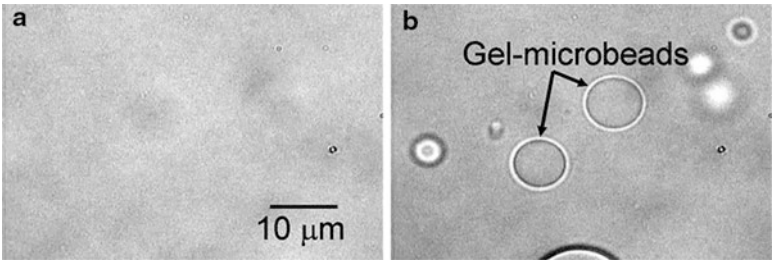

Fig. 10.9 Photographs of the gel-microbeads. (**a**) Gel in 0 M salt solution. (**b**) Gel bead is generated in 0.5 M phosphate dipotassium salt solution

Table 10.1 Low limit concentrations of electrolytes for salting out of the photo-crosslinkable resin

	mol/l
Sodium chloride	5.0
Potassium acetate	1.9
Sodium acetate	1.5
Phosphate dipotassium salt	0.5

All value was determined under 10% photo-crosslinkable resin in each electrolyte solution

Table 10.2 Low limit concentrations of electrolytes for fabrication of the gel-microbead using UV-ray illumination

	mol/l
Sodium chloride	1.9
Potassium acetate	0.5
Sodium acetate	0.3
Phosphate dipotassium salt	0.1

All value was determined under 10% photo-crosslinkable resin in each electrolyte solution

In this paper, BTB (Wako Pure Chemical Industries, Ltd., Japan) and BCG (Wako Pure Chemical Industries, Ltd., Japan) were used as pH indicators. BTB and BCG have different indicator range. BTB is expressed as yellow in an acidic solution (pH < 6), green in a neutral solution, and blue in an alkaline solution (pH > 8). BCG is expressed as yellow in an acidic solution (pH < 4) and blue in a neutral solution (pH < 6). For temperature measurement, Rhodamine B (0.5 mg/l) was used because Rhodamine B is a temperature-sensitive fluorescence dye. The fluorescence intensity of Rhodamine B decreases according to increase of temperature.

10.3.2 In Situ Fabrication of Functional Gel-Microtool

The gel-microbead formed in this study has useful characteristic for fabricating environment measurement gel-microtool. The gel-microbead is connected to other gel-microbead under an electrolyte solution. In purified water, this gel-microbead does not adhere to other objects nonspecifically because PEG is an uncharged polymer. However, the gel-microbead adheres to other gel-microbead in the electrolyte solution shown in Table 10.1. This adhesion is weak because the gel-microbead adheres only by contact. The adhered gel-microbeads often separate in the purified water. Moreover, undesired gel-microbeads may adhere to target gel-microbead because the adhesion arises by contact of the gel-microbeads. To solve problem, we achieved firm connection of the desired gel-microbeads by using UV illumination. The process of connection of the gel-microbeads and fabrication of the four gel-microbeads are described in below. First, the gel-microbeads are manipulated and contacted to each other in an electrolyte solution of concentration lower than the concentration required for adhesion of gel-microbead. After contact of the gel-microbead to target gel-microbead, they are connected by UV illumination. The unilluminated gel-microbeads are not connected. Connection of four gel-microbeads was performed. These gel-microbeads were manipulated by optical tweezers and connected by UV illumination <1 s. The concentrations for connection of the gel-microbeads with UV illumination were confirmed in four electrolytes as shown in Table 10.2. The 0.1 M phosphate dipotassium salt was required the lowest concentration for immobilization.

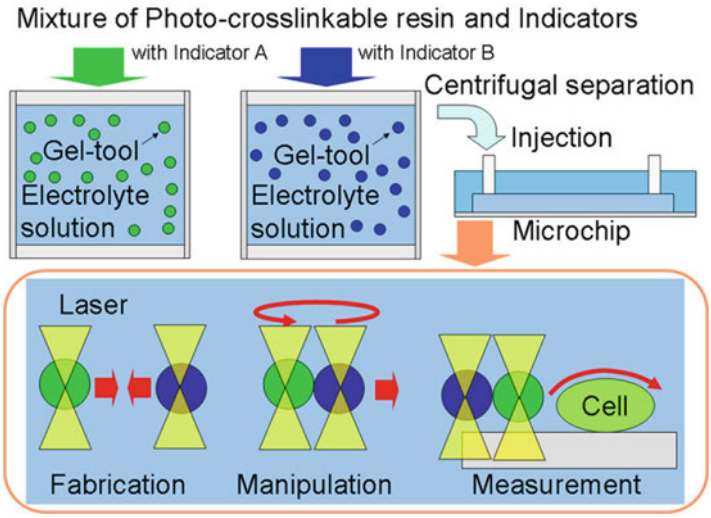

Fig. 10.10 A schematic of fabrication of environment measurement gel-microtool

A schematic of the fabrication process of the environment measurement gel-microtool is shown in Fig. 10.10. Gel-microbead impregnated with an indicator was generated by stirring the mixture of 0.9 g ENT-3400, 0.3 g indicator, and 2.4 g electrolyte solution. Then the gel-microbead was polymerized by UV illumination. Size control of the gel-microbeads is very difficult because gel-microbeads are produced by stirring. The size distribution of gel-microbeads after production was from 1 μm to tens of μm. We collect the gel-microbeads of proposed size by centrifugal separation. In this chapter, the size distribution of gel-microbeads was from 5 to 15 μm. Collected gel-microbeads are injected into the microchip.

The gel-microtool was fabricated by connecting gel-microbead impregnated with desired indicators. The connection of gel-microbeads is carried out by contact of the gel-microbeads manipulated with optical tweezers. When there is no interference between indicators, different indicators can be introduced into the same gel-microbead. Introduction of pH indicators to gel-microbeads of which the size is more than 5 μm was confirmed. We did not check the smaller gel-microbeads because the color change on the gel-microbeads could not be observed. Therefore, we employed gel-microbead larger than 5 μm as pH-sensing gel-microbead. In the proposed process, success rate of impregnating pH indicators to gel-microbeads was almost 100%. Introduction of Rhodamine B to gel-microbeads was also confirmed. We could observe the fluorescence from the gel-microbeads even if the size is smaller than 1 μm. In the proposed process, success rate of impregnating Rhodamine B to gel-microbeads was also almost 100%. Leakage of indicators from the gel-microbeads was checked in microchannel. In case flow rate is lower than 10 mm s^{-1}, we did not observe the leakage of the indicators from the gel-microbeads. In case gel-microbeads were stored in static fluid, we confirmed

indicators were kept in the gel-microbeads more than 1 month. This fabrication process is simple and takes much less time than the chemical surface modification of the microbeads with several indicators.

10.3.3 Calibration of Functional Gel-Microbead

First, calibration of both pH and temperature with the color of the environment measurement gel-microtool was performed. The color of the gel-microbead is obtained as RGB information by the color CCD. RGB values are influenced by brightness which is included in each RGB value. To reduce the influence of brightness, the RGB information was converted to YCrCb information using (10.6) [27, 28]:

$$\begin{aligned} Y &= 0.299\mathrm{R} + 0.587\mathrm{G} + 0.114\mathrm{B} \\ \mathrm{Cr} &= 0.500\mathrm{R} - 0.419\mathrm{G} - 0.081\mathrm{B} \\ \mathrm{Cb} &= -0.169\mathrm{R} = 0.419\mathrm{G} + 0.500\mathrm{B} \end{aligned} \tag{10.6}$$

The Y shows brightness, the Cr shows the color difference for red, and the Cb shows the color difference for blue. The color of both BCG and BTB changes from yellow to blue with increasing pH. Therefore, the Cr value decreases with increasing pH. However, the Cb value increases with increasing pH. In this research, the pH value was calculated using calibrated Cr value because the dispersion of Cr was smaller than that of Cb in our system. Temperature was calibrated with fluorescence intensity. The fluorescence intensity was calculated from the CCD image by (10.1) as Y value. $F_{\mathrm{Intensity}}$ is represented by the relative fluorescence intensity based on the brightness of the brightness at 25°.

Sizes of the sample gel-microbead ranged from 5 to 15 μmϕ. The white balance of the CCD was adjusted manually. Light intensity was adjusted to 2,000 lux. The color of the gel-microbead was obtained in the state where the focus was adjusted in the equatorial plane. The pH values of the sample buffer were measured by a commercial pH meter (pHep5, HANNA). Temperature of the solution was controlled by using thermal robo (TR-1AR, As one corp.).

The calibration results are shown in Fig. 10.11a–c. Six data points were taken in each pH. In Fig. 10.11a, b, the pH value decreased with increasing Cr. There were proportional relationships between the pH and Cr. Equations (10.7) and (10.8) show the linear approximation formulas for the plots in Fig. 10.11a, b. Precision of the pH measurement was about 0.4 because the maximum standard deviations of Cr were about 0.4. In Fig. 10.11c, $F_{\mathrm{Intensity}}$ represents relative fluorescence intensity based on the intensity at 25°. There was also proportional relation between temperature and $F_{\mathrm{Intensity}}$ and the linear approximation formula was shown in (10.9):

$$\mathrm{pH} = -4.8 \times 10^{-1} \times \mathrm{Cr} + 7.7 \tag{10.7}$$

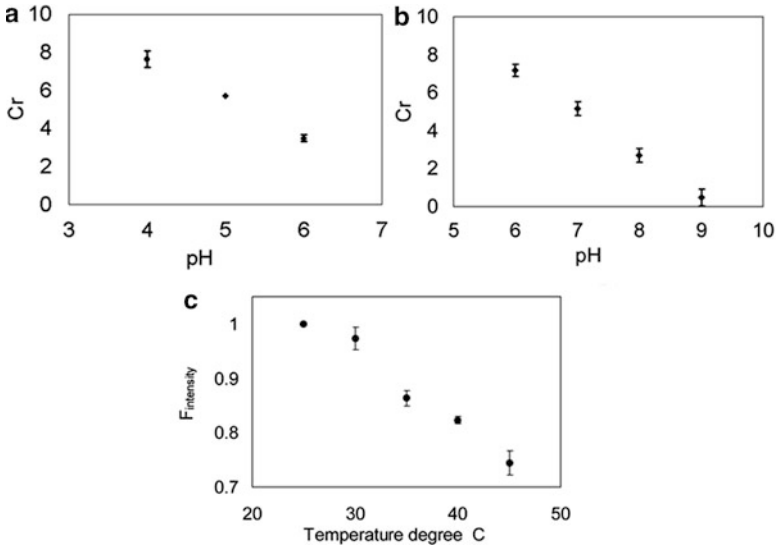

Fig. 10.11 Calibration results. (**a**) Calibration result of pH with BCG. (**b**) Calibration result of pH with BTB. (**c**) Calibration result of temperature

$$\mathrm{pH} = -4.3 \times 10^{-1} \times \mathrm{Cr} + 9.2 \tag{10.8}$$

$$\text{Temperature} = -7.6 \times 10 \times F_{\text{intensity}} + 1.0^2 \tag{10.9}$$

In our experiment system, detection of color and fluorescence was performed by CCD at the video rate of 30 frames/s (1/33 s). We confirmed that time responsibilities of pH measurement using BTB and BCG were about 1 pH/s experimentally. In previous work, time responsibility of temperature measurement using Rhodamine B was <1/33 s [29].

10.3.4 Fabrication of Circle Gel-Microtool and Local pH Measurement Around a Yeast Cell

Figure 10.12a shows a schematic of the fabrication of circular gel-microtool impregnated with BTB and local pH measurement around a yeast cell. Gel-microbeads-impregnated BTB was manipulated and connected. Fabricated gel-microtool was manipulated in the microchip, and a yeast cell was set inside the circle gel-microtool. The pH value around the yeast cell is measured. Figure 10.12b–g

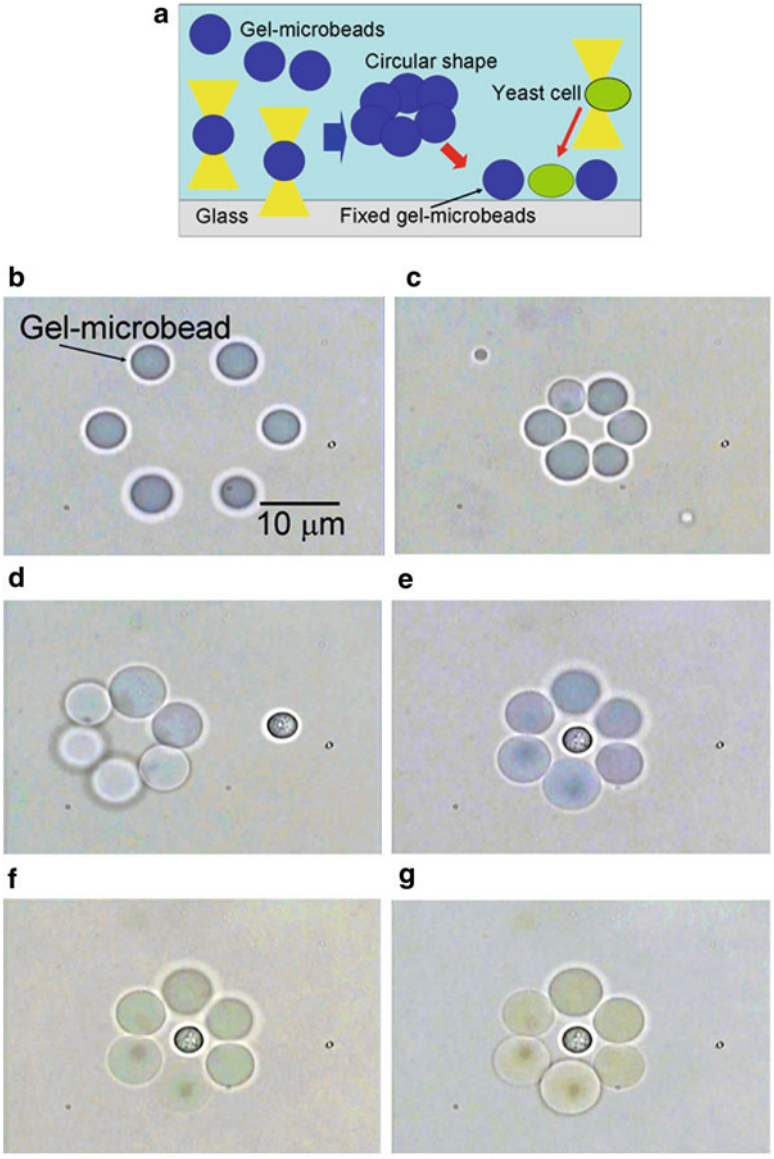

Fig. 10.12 In situ fabrication of circular pH measurement gel-microtool and local pH measurement around a yeast cell. (**a**) A schematic of fabrication of measurement gel-microtool. (**b**) Six pH-sensing gel-microbeads were trapped by optical tweezers. (**c**) Circular pH-sensing gel-microbeads were fabricated. (**d**) A yeast cell was positioned to the center of the circular gel-microbeads. (**e**) pH value was pH 8.9 and (**f**) pH was changed to pH 7.5. (**g**) pH was changed to pH 5.0

shows the experimental result. Six pH-sensing gel-microbeads were connected to circular shape in alkaline solution. Then the fabricated microbeads were fixed on the glass surface. Yeast cell was positioned at the center of the gel-microtool using optical tweezers. The pH value around the yeast cell was measured by detecting the color change of the gel-microtool. The shape of the gel-microtool can be selected at the measurement according to the purpose and situation.

10.3.5 Fabrication of Multiple Measurement Gel-Microtool

In this chapter, two types of the gel-microtool for multiple local environment measurement were demonstrated. One is binding-type gel-microtool. This gel-microtool is used for the wide-range pH measurement and is composed of two gel-microbeads impregnated different pH indicators. BCG and BTB were used for this gel-microtool. Another is coexistence-type gel-microtool. This gel-microtool includes the pH indicator and temperature-sensitive fluorescent dye in a single gel-microbead. BTB and Rhodamine B were used.

Figure 10.13a shows a schematic of the wide pH measurement gel-microtool. Gel-microbead impregnated with BCG was manipulated and contacted to the gel-microbead-impregnated BTB. These gel-microbeads were connected by UV illumination. Figure 10.13, *P* shows the experimental results of the in situ fabrication of the gel-microtool and wide-range pH measurement. The gel-microtool was fabricated in pH 9 solution. Then we introduced pH 4 solution and observed the color change of each gel-microbead.

Figure 10.14a shows a schematic of the pH and temperature measurement gel-microtool. Figure 10.14b–e shows the experimental result of the pH and temperature measurements by single gel-microbead. BCG and BTB are not excited by the wavelength for exciting Rhodamine B. 0.5 mg/l Rhodamine B does not show the color. Therefore, BCG and BTB can coexist with Rhodamine B in the same gel-microbead.

10.4 Conclusions

We have developed a nanorobotic manipulation and sensing such as single virus manipulation for infection of the virus to a specific cell, and gel-microtool modified with indicators for local environment measurement.

In single virus manipulation, we concentrated viruses from 10^6 to 10^9 viruses/μl. The negative DEP force also prevents viruses from adhering to the glass walls as well as being effective for on-chip virus manipulation. The concentrated viruses were manipulated by optical tweezers. We succeeded in infecting a specific H292

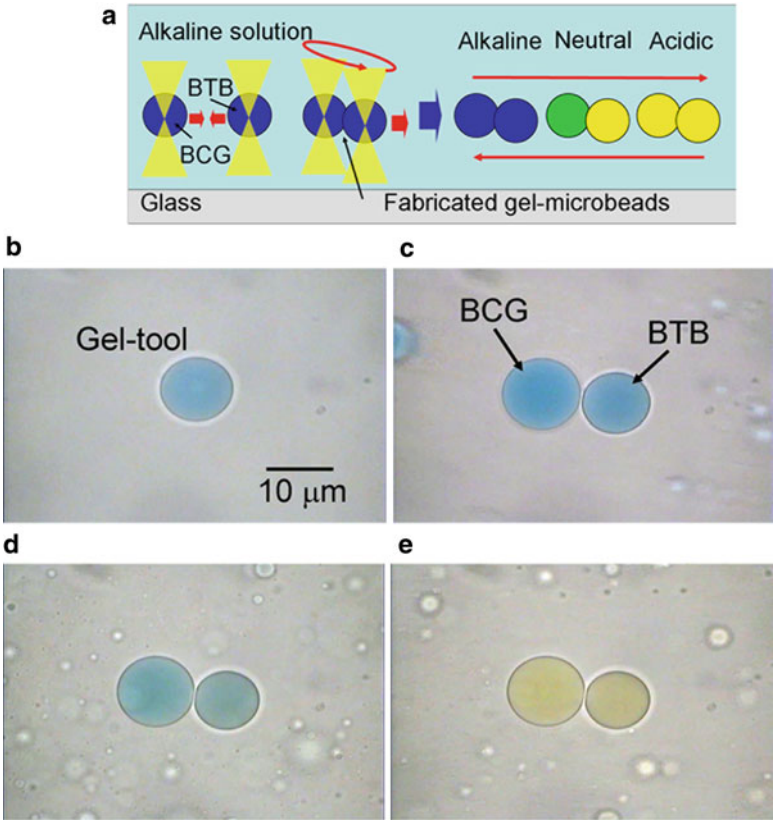

Fig. 10.13 Wide-range pH measurement with fabricated gel-microbeads impregnated with different pH indicators. (**a**) Schematics of wide-range pH measurement gel-microtool. (**b**) Gel-microbead impregnated with BTB. (**c**) Fabrication of gel-microbead impregnated with BTB to gel-microbead impregnated with BCG in pH 9 solution. (**d**) pH was changed to pH 8.1. (**e**) pH was changed to pH 4.6

cell with a single virus. The transport speed of the virus was about 10 μm/s by optical tweezers. This indicates that automation of single virus infection of a specific cell is possible by system integration on the microfluidic chip. Single virus infection is an essential technique for quantitative analysis of the functions of influenza viruses before and after infection of a cell [30].

In local sensing using gel-microbead, we have developed an on-chip environment measurement method using functional gel-microbead impregnated with indicators and have demonstrated on-chip fabrication of the gel-microtool and local pH measurement around single yeast cell. Gel-microbeads impregnated with the indicators were obtained using a simple and short process. The gel-microbeads could be

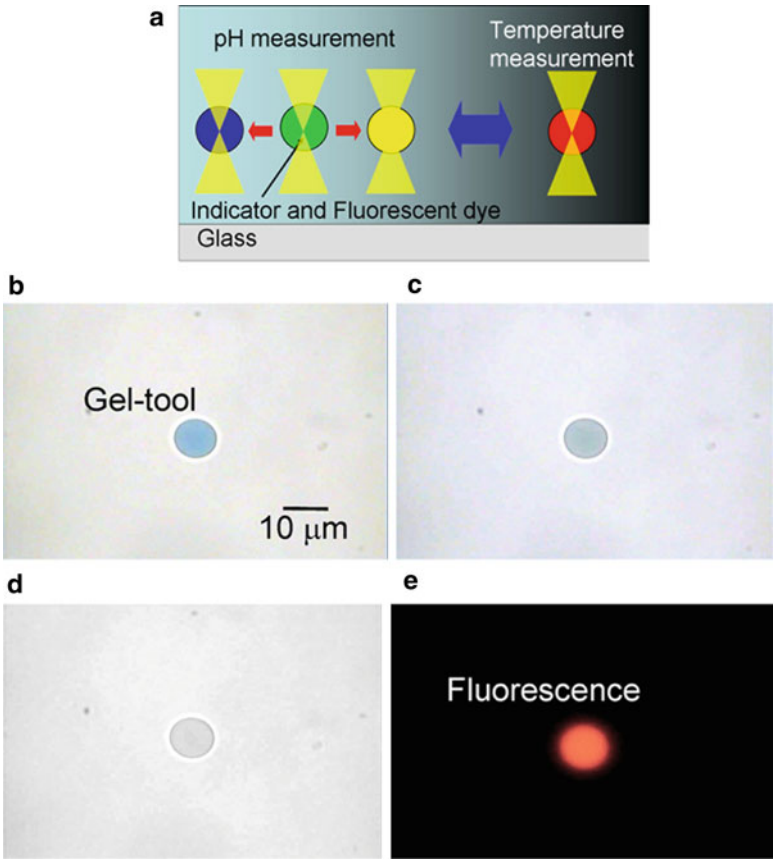

Fig. 10.14 pH and temperature measurement using gel-microbead impregnated with BTB and Rhodamine B. (**a**) Schematics of pH and temperature measurement using gel-microtool. (**b**) pH value was measured by detecting the color of gel-microtool (pH 8.8). (**c**) pH was changed to pH 8.8. (**d**) pH was changed to pH 4.6. (**e**) Temperature was measured by detecting the fluorescence intensity from gel-microbead (25 °C)

manipulated by optical tweezers. The connection of arbitrary gel-microbeads was realized by using UV illumination in the solution that adjusted the electrolytic concentration. The connection of the gel-microbeads impregnated different indicators prevents the interference between the indicators. Type of the gel-microtool can be chosen depending on a purpose such as the number of the measurement condition and the characteristics of the indicators. Moreover, we can achieve the gel-microtool, which can measure a large number of environmental conditions, by combination of these two types of gel-microtools.

These nanorobotic manipulation and sensing techniques will make great contributions to cell biology in the future.

References

1. Inoue I, Wakamoto Y, Moriguchi H, Okano K, Yasuda K (2001) On-chip culture system for observation of isolated individual cells. Lab Chip 1:50–55
2. Amato I (2005) Nanotechnologists seek biological niches. Cell 123:967–970
3. Parvin DJ, Palese P, Honda A, Ishihama A, Krystal M (1989) Promoter analysis of influenza virus RNA polymerase. J Virol 63:5142–5152
4. Bright RG, Fisher WG, Rogowska J, Taylor LD (1987) Fluorescence ratio imaging microscopy: temporal and spatial measurements of cytoplasmic pH. J Cell Biol 104:1019–1033
5. Suzuki M, Tseeb V, Oyama K, Ishiwata S (2007) Microscopic detection of thermogenesis in a single HeLa cell. Biophys J 92:L46–L48
6. Castillo J, Dimaki M, Svendsen EW (2009) Manipulation of biological samples using micro and nano techniques. Integr Biol 1:30–42
7. Arai F, Ichikawa A, Ogawa M, Fukuda T, Horio K, Itoigawa K (2001) High-speed separation system of randomly suspended single living cells by laser trap and dielectrophoresis. Electrophoresis 22:283–288
8. Kim MS, Lee HS, Suh KY (2008) Cell research with physically modified microfluidic channels: a review. Lab Chip 8:1015–1023
9. Kuhara M, Takeyama H, Tanaka T, Matsunaga T (2004) Magnetic cell separation using antibody binding with protein a expressed on bacterial magnetic particles. Anal Chem 76:6207–6213
10. Schnelle T, Müller T, Gradl G, Shirly GS, Fuhr G (2000) Dielectrophoretic manipulation of suspended submicron particles. Electrophoresis 21:66–73
11. Arthur A, Dziedzic JM, Bjorkholm JE, Chu S (1986) Observation of a single beam gradient force optical trap for dielectric particles. Opt Lett 11:288–290
12. Zhang Z, Achilefu S (2005) Design, synthesis and evaluation of near-infrared fluorescent pH indicators in a physiologically relevant range. Chem Commun 47:5887–5889
13. Shinohara K, Sugii Y et al (2004) Measurement of pH field of chemically reacting flow in microfluidic devices by laser-induced fluorescence. Meas Sci Technol 15:955–960
14. Nishimura G, Shiraishi Y, Hirai T (2005) A fluorescent chemosensor for wide-range pH detection. Chem Commun 42:13–5315
15. Kopelman R, Masuhara H, Sakaki K, Zhong-Yon S (1996) Three-dimensional pH microprobing with an optically-manipulated fluorescent particle. Chem Lett 25:141–142
16. Nagl S, Wolfbeis OS (2007) Optical multiple chemical sensing: status and current challenges. Analyst 132:507–511
17. Cho JK, Wong LS et al (2004) PH Indicating resins. Chem Commun 13:1470–1471
18. Arai F, Ichikawa A, Fukuda T, Katsuragi T (2003) Isolation and extraction of target microbes using thermal sol–gel transformation. Analyst 128:547–551
19. Ichikawa A, Arai F, Yoshikawa K, Uchida T, Fukuda T (2005) In situ formation of a gel microbead for indirect laser micromanipulation of microorganisms. Appl Phys Lett 87:191108-1–191108-3
20. Maruyama H, Arai F, Fukuda T, Katsuragi T (2005) Immobilization of individual cells by local photo-polymerization on a chip. Analyst 130:304–310
21. Maruyama H, Arai F, Fukuda T (2008) On-chip pH measurement using functionalized gel-microbeads positioned by optical tweezers. Lab Chip 8:346–351
22. Yamanishi Y, Sakuma S, Onda K, Arai F (2008) Biocompatible polymeric magnetically driven microtool for particle sorting. J Micro Nano Mechatron 4:49–57
23. Ichikawa A, Honda A, Ejima M, Tanikawa T, Arai F, Fukuda T (2007) In-situ formation of a gel microbead for laser micromanipulation of microorganisms, DNA, and viruses. J Robot Mechatron 19:569–576
24. Müller T, Fiedler S, Schnelle T, Ludwig K, Jung H, Fuhr G (1996) High frequency electric fields for trapping of viruses. Biotechnol Tech 10:221–226

25. Stanley MW (1944) The size of influenza virus. J Exp Med 79:267–283
26. Kunz W, Henle J, Ninham WB (2004) 'Zur Lehre von der Wirkung der Salze' (about the science of the effect of salts): Franz Hofmeister's historical papers. Curr Opin Colloid Interface Sci 9:19–37
27. Stern H, Efros B (2005) Adaptive color space switching for tracking under varying illumination. Image Vis Comput 23:353–364
28. Garcia C, Tziritas G (1999) Face detection using quantized skin color regions merging and wavelet packet analysis. IEEE Trans Multimedia 1:264–277
29. Kato H, Nishizawa T, Iga T, Kinoshita K, Ishiwata S (1999) Imaging of thermal activation of actomyosin motors. Proc Natl Acad Sci USA 96:9602–9606
30. Arai F, Kotani K, Maruyama H (2009) On-chip robotics for biomedical innovation: manipulation of single virus on a chip. Proc IEEE NANO 2009:571–574

Chapter 11
Nanohandling of Biomaterials

Michael Weigel-Jech and Sergej Fatikow

Abstract Currently, there is an increasing interest in handling, understanding, and integrating biological systems important for biomedicine, process industry, pharmacy, and biomaterial research. Besides this interest, the demand for adequate, nondestructive, automatable, and fully controllable handling, manipulation, and characterization techniques increases as well. Thanks to the advancements in micro- and nanofabrication and in the robotics area, several approaches and techniques offer us the ability to set up robotic systems, which are able to handle biomaterials down to the nanoscale. In this chapter, some of the most applicable techniques for a robotic and automated use are shown, including advantages and disadvantages as well as current applications and the necessary biological backgrounds for the most common biomaterials a researcher will handle today. So the state of the art for the nanohandling of biomaterials, applicable in current robotic systems and possibly applicable in future robotic systems, is shown as well as our own work on this special field of research.

11.1 Introduction

Current research areas in molecular and cell biology, medicine, and process sensor technology (sensor systems monitoring various processes in industry and science) often require advances in the nano-engineering technologies to look for molecular phenomena with highest possible resolution in order to enlighten the "black box" which still shades most metabolic reactions. The aim of this work, starting from current medical problems, is to propose novel studies especially in molecular and cellular microbiology as well as virology with direct applications in medicine

M. Weigel-Jech (✉) • S. Fatikow
Division Microrobotics and Control Engineering (AMiR), University of Oldenburg,
Uhlhornsweg 84, 26129 Oldenburg, Germany
e-mail: michael.weigel.jech@uni-oldenburg.de; fatikow@uni-oldenburg.de

C. Mavroidis and A. Ferreira (eds.), *Nanorobotics*, DOI 10.1007/978-1-4614-2119-1_11,
© Springer Science+Business Media New York 2013

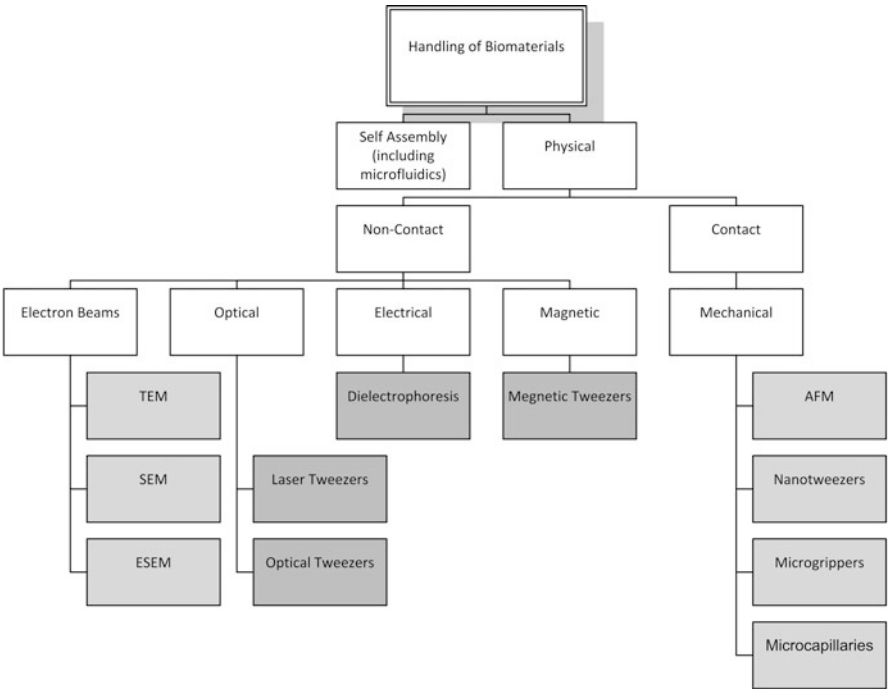

Fig. 11.1 Commonly used methods for the handling, manipulation, and characterization of biomaterials (*light gray*—currently used for nanorobotic approaches, *dark gray*—possible use for feasible robotic approaches in the near and middle future)

and industry, closing the bottom-up cycle. Thanks to the advances in micro- and nanofabrication and micro- and nanorobotics over the last decades, robotic systems which offer the possibility of characterizing and manipulating biological objects can be developed today. The use of such systems enables new studies of single cell phenomena with nanometer resolution (e.g., studying the local mechanical and electrical properties of single bacteria for characterization and evaluation of the resistance to antibiotics or to the spread of infections) up to complete cell compounds (e.g., studying the mechanical properties of bacterial biofilms) and deepens the appreciation of the processes at the nanoscale. According to this, the following chapter will give an overview of biological objects which can be used for the design of micro- and nanorobotic systems as well as their handling. Thus, the use of AFM-based approaches and cell injection approaches will be described as well as the use of SEM and ESEM for biohandling. Information about contactless methods for the handling of biological objects which can be integrated in micro- and nanorobotic systems (e.g., dielectrophoresis, optical tweezers) will be given. The following sections contain most of the relevant information on this topic, including the work of AMiR in this field of research. However, additional methods for nanohandling of biomaterials are known (Fig. 11.1). Among them, the use

of acoustic forces, direct self-assembly, magnetic forces, and many others can be found, but currently as well as in the near future, no combination with nanorobotics seems feasible.

11.2 Commonly Used Biomaterials

When it comes to the handling and characterization of biological objects or biomaterials, it is important to know the molecules' relevant orders of magnitude and the most important properties of biomolecules. This also includes a view at general characteristics of cells and the relevant biomolecules. Furthermore, a view at the possible sizes and powers that one can find is necessary. This section will introduce some of the key points to understand the most important problems for biohandling and the characterization of biomaterials.

11.2.1 Characteristic Sizes

The sizes of some cell types and dimensions of typical biological objects are listed in Table 11.1 to give an overview of the dimensions of the biomaterials mainly handled and characterized today. Additionally, in the following, some values for the force ranges in handling and characterization of biomaterials are given.

Table 11.1 Dimensions of sizes and forces of biomaterials and handling of biomaterials

Description	Size
DNA	nm to m (length)
Frog egg	3 mm
Typical plant cell	10–100 μm
Trypanosoma (protozoan)	12 μm (length)
Human red blood cell	7–8 μm (diameter)
Chlamydomonas (green algae)	5–6 μm
Escherichia coli (bacterium)	1–5 μm (length)
T4 bacteriophage	225nm (length)
Tobacco mosaic virus	300nm (length)
HIV virus	100nm
Poliovirus	30nm
DNA	2nm (diameter)
Force range of a molecular motor	5 pN
Forces of the attraction between proteins and membranes	10–100 pN
Force to deform a cell membrane about 5 μm	215 nN–12 μN

11.2.2 Biological Cells

The cell, discovered by Robert Hooke, is the functional unit of all known living organisms. It is the smallest unit of life that is classified as a living thing and is often called the building block of life. Some organisms, such as most bacteria, are unicellular (consisting of a single cell). Other organisms, such as humans or animals, are multicellular.

There are two types of cells: eukaryotic and prokaryotic. Prokaryotic cells are usually independent, while eukaryotic cells are often found in multicellular organisms. The prokaryote cell is simpler, and therefore smaller, than a eukaryote cell, lacking a nucleus and most of the other organelles of eukaryotes. A prokaryotic cell has three architectural regions:

- On the outside, flagella and pili project from the cell's surface. These are structures (not present in all prokaryotes) made of proteins that facilitate movement and communication between cells.
- Enclosing the cell is the cell envelope—generally consisting of a cell wall covering a plasma membrane, even though some bacteria also have a further covering layer called a capsule. The envelope gives rigidity to the cell and separates the interior of the cell from its environment, serving as a protective filter. The cell wall consists of peptidoglycan in bacteria and acts as an additional barrier against exterior forces. It also prevents the cell from expanding and finally bursting (cytolysis) from osmotic pressure against a hypotonic environment.
- Inside the cell is the cytoplasmic region that contains the cell genome deoxyribonucleic acid (DNA) and ribosomes and various sorts of inclusions. Though not forming a nucleus, the DNA is condensed in a nucleoid. Prokaryotes can carry extrachromosomal DNA elements called plasmids, which are usually circular. Plasmids enable additional functions, such as antibiotic resistance.

Eukaryotic cells are about 15 times wider than a typical prokaryote and can be as much as 1,000 times greater in volume. The major difference between prokaryotes and eukaryotes is that eukaryotic cells contain membrane-bound compartments in which specific metabolic activities take place. Most important among these is the presence of a cell nucleus, a membrane-delineated compartment that houses the eukaryotic cell's DNA. Other differences include:

- The plasma membrane resembles that of prokaryotes in function, with minor differences in the setup. Cell walls may or may not be present.
- The eukaryotic DNA is organized in one or more linear molecules, called chromosomes, which are associated with histone proteins. All chromosomal DNA is stored in the cell nucleus, separated from the cytoplasm by a membrane. Some eukaryotic organelles such as mitochondria also contain some DNA.
- Many eukaryotic cells are ciliated with primary cilia. Primary cilia play important roles in chemosensation, mechanosensation, and thermosensation. Cilia may thus be viewed as sensory cellular antennae that coordinate a large number of

cellular signaling pathways, sometimes coupling the signaling to ciliary motility or alternatively to cell division and differentiation.
- Eukaryotes can move using motile cilia or flagella. The flagella are more complex than those of prokaryotes.

For a list of the main differences of these two cell types also have a look at Table 11.2. Furthermore, for a detailed introduction to cell biology, the book "Molecular Microbiology of the Cell" [1], latest edition January (2008), can be recommended for further readings.

Table 11.2 Comparison of features of prokaryotic and eukaryotic cells

	Prokaryotes	Eukaryotes
Typical organisms	Bacteria, archaea	Protists, fungi, plants, animals
Typical size	1–10 μm	10–100 μm
Type of nucleus	Nucleoid region; no real nucleus	Real nucleus with double membrane
DNA	Circular (usually)	Linear molecules (chromosomes)
RNA/protein synthesis	Coupled in cytoplasm	RNA synthesis inside the nucleus protein synthesis in cytoplasm
Cytoplasmatic structure	Very few structures	Highly structured by endomembranes and a cytoskeleton
Cell movement	Flagella made of flagellin	Flagella and cilia containing microtubules, lamellipodia and filopodia containing actin
Mitochondria	None	One to several thousand (though some lack mitochondria)
Chloroplasts	None	In algae and plants
Organization	Usually single cells	Single cells, colonies, higher multicellular organisms with specialized cells
Cell division	Binary fission (simple division)	Mitosis (fission or budding), meiosis

11.2.3 Escherichia coli Bacteria

E. coli is a rod-shaped bacterium that is commonly found in the lower intestine of warm-blooded organisms (endotherms). Most *E. coli* strains are harmless, but some can cause serious food poisoning in humans, and are occasionally responsible for product recalls. *E. coli* are not always confined to the intestine, and their ability to survive for brief periods outside the body makes them an ideal indicator organism to test environmental samples for fecal contamination. The bacteria can also be grown easily, and its genetics are comparatively simple and easily manipulated or duplicated through a process of metagenics, making it one of the best-studied prokaryotic model organisms and an important species in biotechnology and microbiology.

E. coli cells propel themselves with flagella (long, thin structures) arranged as bundles that rotate counterclockwise, generating torque to rotate the bacterium clockwise. Cells are typically rod shaped and are about 2 μm long and 0.5 μm in diameter. It can live on a wide variety of substrates. Optimal growth of *E. coli* occurs at 37 °C, but some laboratory strains can multiply at temperatures of up to 49 °C. Strains that possess flagella can swim and are motile.

E. coli and related bacteria possess the ability to transfer DNA via bacterial conjugation, transduction, or transformation, which allows genetic material to spread horizontally through an existing population. *E. coli* normally colonizes an infant's gastrointestinal tract within 40 h of birth, arriving with food or water or with the individuals handling the child. As long as these bacteria do not acquire genetic elements encoding for virulence factors, they remain benign commensals. Nonpathogenic *E. coli* strains are used as a probiotic agent in medicine, mainly for the treatment of various gastroenterological diseases. Virulent strains of *E. coli* can cause illnesses, such as gastroenteritis, urinary tract infections, and neonatal meningitis.

11.2.4 Ion Channels

Ion channels are pore-forming proteins that help establish and control the small voltage gradient across the plasma membrane of all living cells (see cell potential) by allowing the flow of ions down their electrochemical gradient. They are present in the membranes that surround all biological cells. Such "multi-subunit" assemblies usually involve a circular arrangement of identical or homologous proteins closely packed around a water-filled pore through the plane of the membrane or lipid bilayer. Some channels permit the passage of ions based solely on their charge of positive (cation) or negative (anion). However, the archetypal channel pore is just one or two atoms wide at its narrowest point and is selective for specific species of ion, such as sodium or potassium. These ions move through the channel pore single file nearly as quickly as the ions move through free fluid. In some ion channels, passage through the pore is governed by a "gate," which may be opened or closed by chemical or electrical signals, temperature, or mechanical force, depending on the variety of channel.

Because "voltage-activated" channels underlie the nerve impulse and because "transmitter-activated" channels mediate conduction across the synapses, channels are especially prominent components of the nervous system. Indeed, most of the offensive and defensive toxins that organisms have evolved for shutting down the nervous systems of predators and prey (e.g., the venoms produced by spiders, scorpions, snakes, fish, bees, sea snails, and others) work by modulating ion channel conductance and/or kinetics. In addition, ion channels are key components in a wide variety of biological processes that involve rapid changes in cells, such as cardiac, skeletal, and smooth muscle contraction, epithelial transport of nutrients and ions, T cell activation, and pancreatic beta-cell insulin release. In the search for new drugs, ion channels are a frequent target.

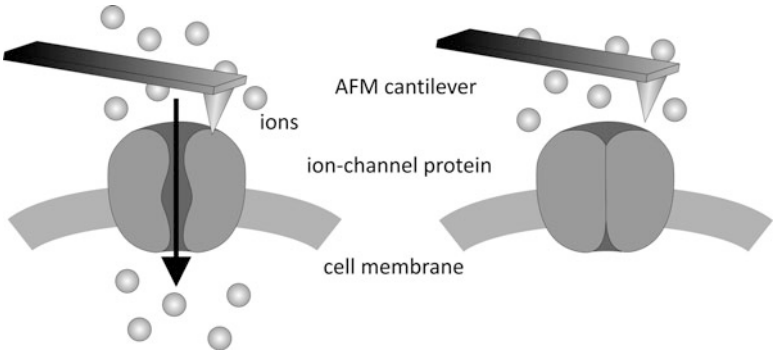

Fig. 11.2 Schematic diagram of a mechanosensitive gated ion channel. The ions flow through the ion channel due to a mechanical stimulation. If the stimulation ends, the channel closes and the ion concentration exchange ends

Ion channels may be classified by the nature of their gating, the species of ions (e.g., sodium, calcium, potassium) passing through those gates, and the number of gates (pores). Voltage-gated ion channels open or close depending on the voltage gradient across the plasma membrane, while ligand-gated ion channels open or close depending on binding of ligands to the channel. Other gating include activation/inactivation by, for example, second messengers from the inside of the cell membrane, rather as from outside, as in the case for ligands. Mechanosensitive ion channels are opening under the influence of stretch, pressure (Fig. 11.2), shear, or displacement.

11.2.5 Deoxyribonucleic Acid

DNA is a nucleic acid that contains the genetic instructions used in the development and functioning of all known living organisms and some viruses. The main role of DNA molecules is the long-term storage of information. DNA is often compared to a set of blueprints or a recipe, or a code, since it contains the instructions needed to construct other components of cells, such as proteins and RNA molecules. The DNA segments that carry this genetic information are called genes, but other DNA sequences have structural purposes or are involved in regulating the use of this genetic information.

Chemically, DNA consists of two long polymers of simple units called nucleotides, with negatively charged backbones made of sugars and phosphate groups joined by ester bonds. These two strands run in opposite directions to each other and are therefore antiparallel. Attached to each sugar is one of four types of molecules called bases. It is the sequence of these four bases along the backbone that encodes information. This information is read using the genetic code, which specifies the sequence of the amino acids within proteins. The code is read by copying stretches of DNA into the related nucleic acid RNA, in a process called transcription.

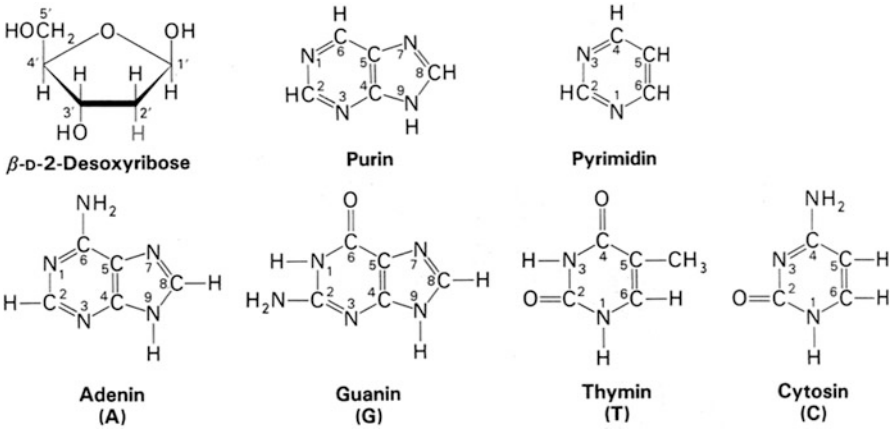

Fig. 11.3 Parts of the nucleosides—λ-D-2-deoxyribose, a purine or pyrimidine base (purine—adenine and guanine, pyrimidine—thymine and cytosine)

DNA is a long polymer made from repeating units called nucleotides. The DNA chain is 22–26 Å wide (2.2–2.6nm), and one nucleotide unit is 3.3 Å (0.33nm) long. Although each individual repeating unit is very small, DNA polymers can be very large molecules containing millions of nucleotides. For instance, the largest human chromosome, chromosome number 1, is a 220 million base pairs long, while the plasmids of an *E. coli* are about 48 k base pairs long. In living organisms, DNA usually does not exist as a single molecule but as a pair of molecules that are held tightly together instead. These two long strands entwine like vines, in the shape of a double helix. The nucleotide repeats contain both the segment of the backbone of the molecule, which holds the chain together, and a base, which interacts with the other DNA strand in the helix. A base linked to a sugar is called a nucleoside (Fig. 11.3) and a base linked to a sugar and one or more phosphate groups is called a nucleotide. If multiple nucleotides are linked together, as in DNA, this polymer is called a polynucleotide.

The backbone of the DNA strand is made from alternating phosphate and sugar residues. The sugar in DNA is 2-deoxyribose, which is a pentose (five-carbon) sugar. The sugars are joined together by phosphate groups that form phosphodiester bonds between the third and fifth carbon atoms of adjacent sugar rings. These asymmetric bonds give a direction to the DNA strand. In a double helix the direction of the nucleotides in one strand is opposite to their direction in the other strand: the strands are antiparallel. The asymmetric ends of DNA strands are called the 5′ (five prime) and 3′ (three prime) ends, with the 5′ end having a terminal phosphate group and the 3′ end, a terminal hydroxyl group. The DNA double helix is stabilized by hydrogen bonds between the bases attached to the two strands. The four bases found in DNA are adenine (A), cytosine (C), guanine (G), and thymine (T). These four bases are attached to the sugar/phosphate to form the complete nucleotide.

Twin helical strands form the DNA backbone. Another double helix may be found by tracing the spaces, or grooves, between the strands. These voids are adjacent to the base pairs and may provide a binding site. As the strands are not directly opposite each other, the grooves are unequally sized. One groove, the major groove, is 22 Å wide and the other, the minor groove, is 12 Å wide. Each type of base on one strand forms a bond with just one type of base on the other strand. This is called complementary base pairing. Here, purines form hydrogen bonds to pyrimidines, with A bonding only to T, and C bonding only to G. This arrangement of two nucleotides binding together across the double helix is called a base pair. As hydrogen bonds are not covalent, they can be broken and rejoined easily. The two strands of DNA in a double helix can therefore be pulled apart like a zipper, either by a mechanical force or high temperature. As a result of this complementarity, all the information in the double-stranded sequence of a DNA helix is duplicated on each strand, which is vital in DNA replication. Indeed, this reversible and specific interaction between complementary base pairs is critical for all the functions of DNA in living organisms. The two types of base pairs form different numbers of hydrogen bonds, AT forming two hydrogen bonds and GC forming three hydrogen bonds. DNA with high GC content is more stable than DNA with low GC content.

DNA exists in many possible conformations that include A-DNA, B-DNA, and Z-DNA forms, although only B-DNA and Z-DNA have been directly observed in functional organisms. The conformation that DNA adopts depends on the hydration level, DNA sequence, the amount and direction of supercoiling, chemical modifications of the bases, the type and concentration of metal ions, as well as the presence of polyamines in solution.

11.3 Handling, Manipulation, and Characterization of Biomaterials

11.3.1 SEM and ESEM

Besides the possibility to manipulate and image nonbiological nanoscopic objects by using a SEM or TEM, special systems have been developed to manipulate and characterize biological objects, for example, manipulation of collagen fibers [1]. One can see the necessary ultrahigh vacuum and low temperatures as a critical problem for the use in case of biological samples [2]. Moreover, the preparation of the biological samples is more complicated and a little bit harsh (biological objects need to be fixed, dehydrated, critical point dried, and coated). With an environmental scanning electron microscope (ESEM), an imaging and manipulation of biological samples is possible without special treatments [3]. Some difficulties when using ESEM in wet samples have been reported [4, 5] so that it seems necessary to use SEM in addition to ESEM to provide a real image of the sample and resolve finer structures in detail [6].

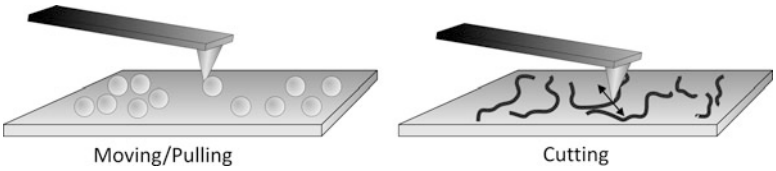

Fig. 11.4 Schematically view of two manipulation tasks done by AFM-based robotic systems. The *left image* shows a movement of nanoparticles using an AFM. The *right image* shows a cutting procedure of DNA via the cantilever, as it is necessary for the design of nanobonding wires

11.3.2 Atomic Force Microscopy

Since the development of the AFM by Binnig, Quate, and Gerber [7], the potential of the AFM for characterization and manipulation of biological objects and materials has quickly been perceived. The main advantages of the AFM are:

- A high resolution down to the sub-nanometer range
- A possibility to work under physiological conditions as well as under vacuum conditions or in a liquid environment, depending on the examined object

Furthermore, in addition to the visualization possibilities, an AFM can measure different properties (mechanical and electrical properties) and manipulate biological objects. For example, one of the greatest advantages in the field of biomaterial characterization and manipulation is the possibility to examine the samples in a liquid environment under nearly lifelike conditions [8, 9]. The AFM also enables the monitoring of the forces exerted during manipulation to provide important information on the interactions between cantilever tip, biological object, and surface.

Currently, the AFM fulfills two tasks—the imaging and the manipulation of the samples. Therefore, a first step always is an imaging step, followed by a manipulation step with the same cantilever. These two steps have to be repeated until the manipulation is done. Unfortunately, it is not possible to get a real-time view of the manipulation process with this method, because the AFM-based imaging process currently needs several minutes depending on the quality of the picture. Such control scheme can be described as “look and move” scheme and requires the use of a scanning electron microscope for the observation of the manipulated object and the AFM probe under real time [10]. For a manipulation, the samples have to be immobilized on the substrates via a reversible method such as electrostatic interactions or low covalent bindings. However, compared to other methods and instruments, the use of AFM-based manipulation and characterization opens the widest field of applications in this area of research. Thus, a high number of different applications, concerning imaging, characterization, and manipulation of biological objects, can be found. In case of the manipulation of biological samples with the AFM, a pushing, cutting, pulling, touching, indenting, and structuring of a broad range of materials (biological and nonbiological) are possible (Fig. 11.4).

Independent of these wide application ranges and the suitability for the imaging, characterization, and manipulation of biological objects, some disadvantages of the AFM-based handling of biological object exist. First of all, the separation of imaging and manipulation, followed by the restriction to small working areas of about $100 \times 100\ \mu m^2$ (e.g., JPK Nanowizard, Nanotec AFM) and the limited working speed efficiency [11], leads to a difficult handling of this method. However, the principle of the method, imaging, characterization, and manipulation by using a small cantilever, is important for the usage in micro- and nanorobotic systems. By using piezoresistive cantilevers, swarms of mobile platforms [12], which will lead to a highly automated and paralleled work, are also possible. With such systems, the limitations concerning the working time efficiency and the small working areas can be circumvented. New methods to build high-speed AFMs are also being developed and published [13].

The AFM can further be used for combined robotic systems to suppress the disadvantages by using additional video microscopy systems and by adding non-contact ablation by ultraviolet (UV) microbeam laser for large scale manipulation of biological objects such as chromosomes [14]. However, AFM-based robotic systems are also used for the imaging, characterization, and handling of all possible materials besides biological objects.

11.3.2.1 Sample Preparation

For characterization or manipulation, the samples have to be immobilized on a substrate or something adequate. Depending on the type of functionalization, the preparation effort can be significantly complicated. One common method is to measure the sample on freshly cleaved mica. Mica has a hydrophilic, charged surface to bind the proteins and other biomolecules easily. Occasionally, mica is treated with buffer systems, which also change the charging of the surface. Additional coating of the mica with gelatin has been found in the mapping of bacterial components. Gold substrates can also be used if coated with protein reactive monolayer. With this method intermolecular bonding forces can be exploited. More restrictive methods are the integration of the sample in agar-agar or other porous media.

11.3.2.2 Cantilever

The characteristics of a cantilever are determined by material, tip shape, and mechanical parameters such as spring constant, resonant frequency, and Q factor. For biological applications, cantilevers are usually made of silicon or silicon nitride. These materials are chemically inert and can be doped to derive electrical charges. In addition, they allow a high Q factor for high sensitivity. Normally very soft cantilevers are used for the contact mode and hard cantilevers are used for the tapping mode.

If measured in liquids, the pH value and the kind of electrolytes influence the forces between tip and sample. Some methods, such as plasma treatment and silane treatment, can change the surface properties (charges) of the substrates, inducing additional effect on the cantilever–surface interactions. Additional coatings can be used for the characterization of bonds between receptors and ligands, cells and molecules, or different cells. Working in liquid, a buffer system can influence the reflection of the laser beam at the backside of the cantilever. Some different reflective coatings can be beneficial to increase the intensity of the reflected laser beam of the positioning system. The cantilever tip is also important for measuring quality. Although a smaller tip radius, however, results in more accurate images, it may be advantageous for soft biological samples to use a duller tip, reducing the risk of damaging the sample. For elasticity measurements, spherical tips can be used since they allow a lower indentation and a well-defined contact area. Using such tips, the mechanical properties of the surface are a medium value compared to the contact site of the cantilever.

11.3.2.3 Advantages and Limits of AFM-Based Handling and Characterization

Compared to the other described methods in the sections above, the AFM has some major advantages for the handling and characterization of biomaterials. The most important points are as follows:

- The AFM can be used in liquids, in vacuum, and at ambient conditions. Meaning that biological samples can be characterized and manipulated at their necessary physiological conditions. Furthermore, living samples and their reaction of mechanical stimulation can be studied.
- The AFM can be used for imaging as well as for manipulation at the same time.
- The possible resolution lies in the nm range.
- Three-dimensional topological information can be obtained.
- No special preparation methods are necessary (no structural changes).
- Different characteristics of a cell can be measured, such as elasticity, conductivity, and adhesion.

However, compared to the other methods, there are also some major drawbacks or limitations of the AFM. Knowing them gives us the possibility to choose the right method or tool to handle or characterize the sample. The most important limitations are given below:

- A 3D-force measurement is not possible until now.
- Another disadvantage is the scanning speed, which is generally too low for real-time mapping. The scanning range for high-speed AFMs is still very low (about $3\ \mu m \times 3\ \mu m$) today.

- The possibility of nanomanipulation can also be a disadvantage—soft materials can be pressed, making the measured height information useless, damaged, or removed from their original location.

11.3.2.4 Applications of AFM for Biomaterials

Among the applications are the manipulation as well as structural and mechanical characterization of various viruses and virus shells [15]; the force mapping of the elastic properties of synaptic vesicles [16]; the mechanical, structural, and electrical characterization of DNA molecules [17, 18]; the manipulation of single-stranded DNA to form simple nanoelectric circuits [19]; the characterization of the mechanical properties of lactate oxidase [20] and other proteins; the dissection of human chromosomes [12, 21]; the mechanical properties (pretransition and progressive softening, depending on mechanical stress) of surface-immobilized antibodies [22]; and the characterization of the mechanical properties of microtubules [23] as well as physicochemical and mechanical properties of bacteria such as *Pseudomonas putida* by using single force spectroscopy [24]. In the following sections, some examples are described in greater detail.

Visualization

An important area of application related to the AFM is the imaging of biological objects. The ability to measure surfaces of non-static samples with nm resolution in liquids enables very interesting experiments and provides information for researchers. These abilities can also provide insight into molecular processes.

Thus, for example, the effect of venom on cell membranes was examined. The venom contains an enzyme which can degrade the cell membranes. This enzyme docks at defects in the membrane, whereby it starts the degradation. The resulting trenches gaping in the membrane are 10nm wide, the holes about 100nm. This process can be perfectly imaged with the AFM. As a result, the researchers discover the behavior of the acting of enzymes, thus being essential for future drug development.

Other investigations deal with the visualization of the reaction of proteins for intercellular communication. These proteins build so-called connexines, important for the cell-to-cell communication in every living organism. Connexines are structured like a pore which, for example, closes under the presence of Ca^{2+} ions. Rare earth metal ions are found in fertilizers for agricultural use. To investigate the influence of these ions on living organisms, *E. coli* has been exposed to La^{3+} ions. The reaction was investigated using AFM and SEM images [25]. The surface analysis of the bacteria has shown that the surface roughness and permeability was increased after the treatment with La^{3+} ions. Furthermore, the experiments have shown that structural changes occur in presence of La^{3+}.

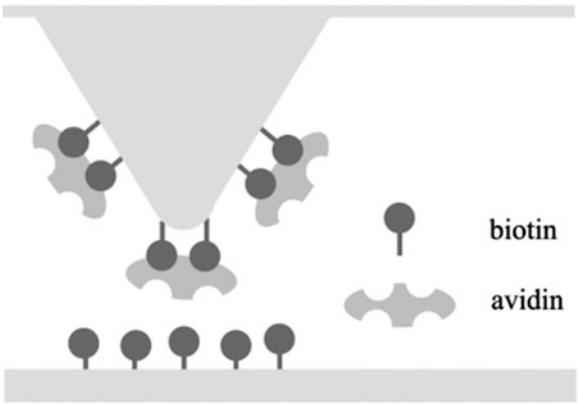

Fig. 11.5 Measurement of ligand–receptor binding forces using a biomolecules coated cantilever

Force Spectroscopy

On the basis of functionalized cantilevers, the chemical structure of a sample or intermolecular bonding forces can be measured. The tip of the cantilever is coated with ligands or antibodies (Fig. 11.5). On the surface of the sample there are corresponding partner molecules. By approaching the cantilever to the sample surface, a direct bond is established between the molecules on the surface and the ones on the cantilever. The breaking of the intermolecular bonds can be calculated using the snapback points in the force–displacement curves, after having retreated the cantilever from the surface.

MRFM can be performed, for example, for the chemical analysis of biomaterials. Using a cantilever, functionalized with a cross-linker and an antibody, the binding forces of single bonds are detectable. Simultaneously topographical images can be recorded. By using this method, the now well-researched avidin–biotin bond was examined [26].

Another area for the analysis of intermolecular forces is biosensors. There are a large number of different biosensors, which are all based on the principle that an analyte binds to a receptor. This analysis of the bonding forces is relevant for the development of new sensors. However, there are possible receptors changing their mechanical properties when docked to a specific analyte. With the help of AFM measurements, these changes can be measured. Based on the resulting data, biosensors can be optimized or new biosensor can be developed [27].

This method can further be improved by using a DNA strand attached to the cantilever (Fig. 11.6). By using this design, the measurement of the hydrogen bonds of DNA is possible. For this the cantilever will be driven near the sample. On the sample complementary single-stranded DNA fragments are immobilized. By moving the cantilever near the single strand on the substrate, a hybridization procedure will start. After the complete hybridization, the cantilever will be pulled away and the bending of the cantilever will be registered. This bending of the cantilever directly depends on the force necessary to break the hydrogen bonds.

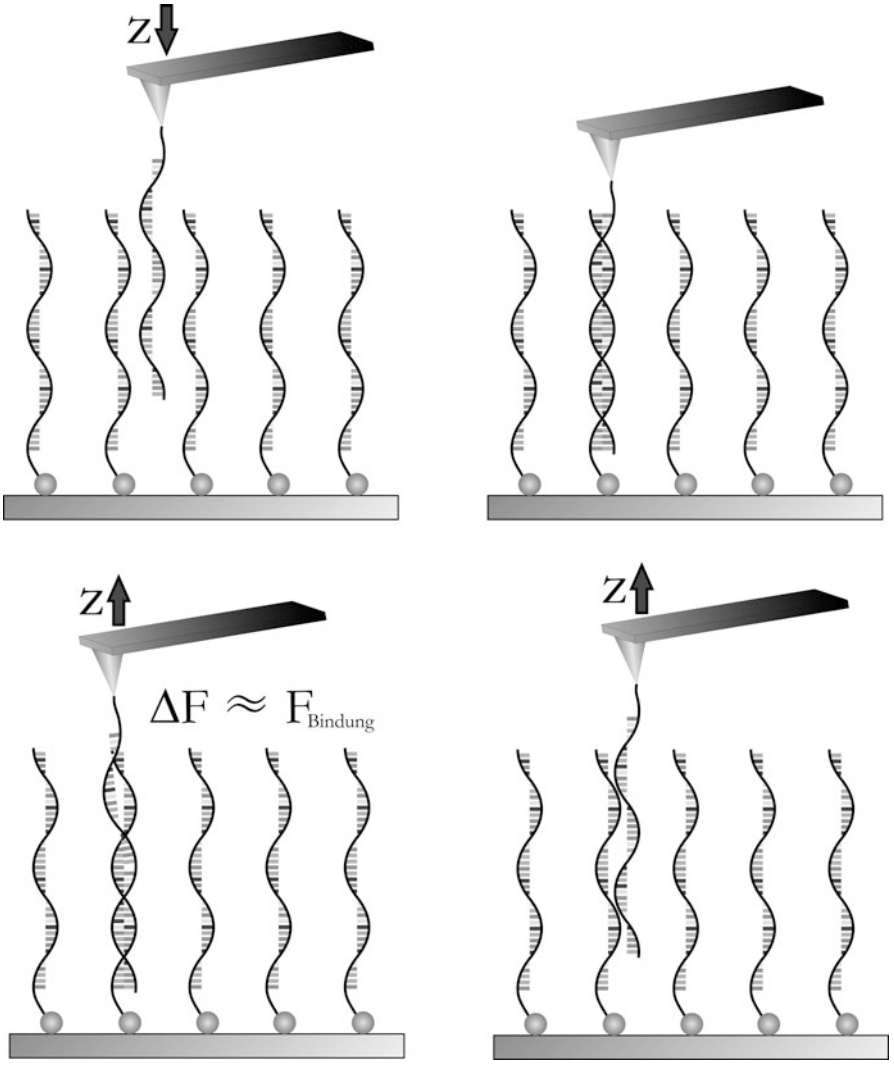

Fig. 11.6 Schematically image of the measurement of the hydrogen bonding strength between two complementary DNA strands

By analyzing the force–distance curves, the sum of all the hydrogen bonds can be calculated. This procedure can be done fully automated and will give information of the interactions between DNA, necessary for the design of future building blocks for electrical circuits.

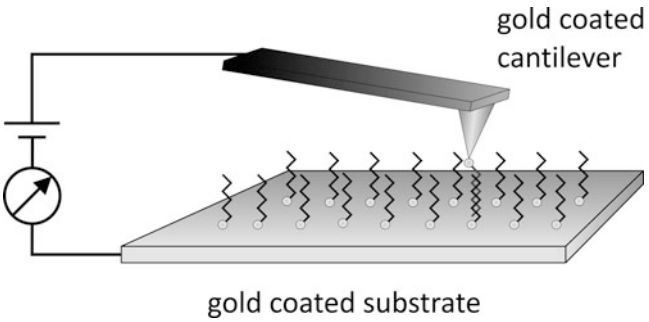

Fig. 11.7 Schematic diagram of the experimental setup for the measurement of the electrical properties of DNA

Stability Measurements of Virus Shells

By using the AFM, force measurements and structural studies of virus shells are also possible [28]. Virus shells are not only used to protect the viral DNA but to enable a selective packaging and enable the possibility to infect host organisms or cells. For structural and topological measurements, a series of jumping mode images were taken. So a number of force–distance curves were recorded at the top point of each shell. As one example the researchers found a nonhomogeneous distribution of the capsule structure of each virus. Information about the stability was obtained through sequences of force–displacement curves, leading to the result that every shell regains its original structure after a few seconds. The results of these experiments have shown that the virus shells also afford mechanical and chemical protecting as well as new ideas for design techniques in nanotechnology.

Measurement of the Electrical Properties of DNA

In accordance to the progressing miniaturization of electric circuits, new ways to realize smaller channel widths are needed. To overcome the limitations of silicon-based processing, the use of objects like CNTs or biomolecules like DNA can be a solution. Today, it is known that the electrical properties of nanoscopic materials and biomolecules are highly different from the electrical properties of macroscopic objects. For this reason, it has become increasingly relevant to investigate the electrical properties of these materials.

In the last years, the conductivity of DNA has been investigated and widely discussed. For example, volatile electron transport properties were observed, covering the complete range from insulating and conducting properties. It is now known that the sample preparation and measurement techniques have a high influence. New measurements confirm the conductivity of dsDNA, whereas ssDNA appears to be an insulator [29]. For this (Fig. 11.7) different types of DNA were bound to

a gold substrate via a thiol group. Also the strands were tied to a 10nm in diameter gold ball via another thiol group. Furthermore, the gold particle was contacted by a gold-coated cantilever, and the measured voltage curves were recorded. Other measurements were carried out without an additional gold particle.

Meanwhile, it appears that the measurements can be successfully reproduced in many research groups, thus leading to a better understanding of the electrical conductivity of DNA.

11.3.2.5 Current Research Work in AMiR

In the following sections, the work of our division on the field of handling, characterization, and manipulation of biomaterials will be described. Our research focus mainly deals with the development of fully automated solutions for handling and manipulation of DNA, for solving of packaging problems in the future of nanoelectronics and for structuring of biosensors for medical and forensic use.

Handling and Manipulation of DNA

In accordance to the progressing miniaturization of electric circuits, new ways to realize smaller channel widths are needed. To overcome the limitations of silicon-based processing, the use of objects like CNTs or biomolecules like DNA can be a solution. Nanowires produced via the metallization of DNA are promising candidates for nanoelectronic devices of future generations. DNA can be considered a basic building block for nanostructure fabrication because it provides unique self-recognition properties. DNA constitutes an ideal template for the organization of metallic and semiconductor particles into wirelike assemblies. Nanoscopic (thickness below 10nm) and regular wirelike metallic structures can be efficiently produced, because DNA molecules have a diameter of only two nanometers and a length in the μm range. Moreover, both the ends of DNA molecules and the surface of solid substrates can be functionalized through a variety of methods to create specific links between DNA and substrate, allowing the integration of DNA molecules into specific, predefined sites of microstructured electronic circuits. By exploiting the specific recognition of complementary nucleotide sequences, complex structures made of DNA can be fabricated and metalized at a later stage. Packaging problems of next-generation nanoelectronic technologies (e.g., single-electron transistors, quantum automata, molecular electronics, etc.) might also be addressed by using DNA strands.

Recently, many researchers have proven the feasibility of DNA manipulation by an AFM tip, primarily in liquid conditions. The next step toward high throughput fabrication is automation of DNA handling. Figure 11.8 shows a manipulation procedure of DNA, which will offer the potential of automated DNA manipulation in dry ambient working conditions. Figure 11.8 (left) shows a topographic scan of a DNA strand. The height of the DNA strand is about 1.5nm. Figure 11.8 (right)

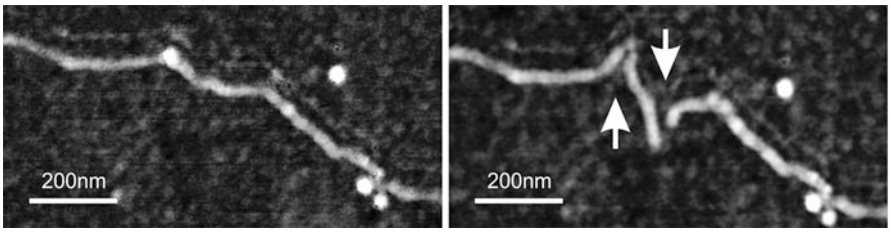

Fig. 11.8 DNA immobilized on silicon without surface modifications (*left*) and the same DNA after the manipulation process (*right*). On the *left side* of the strand, two short distance movements from *bottom* to *top* were implemented. As a result, the corresponding DNA parts have been pushed for about 25nm. On the *right side*, two long distance movements, from *bottom* to *top* and from *top* to *bottom*, were implemented, resulting in DNA displacement by 100nm. Additionally, two cuts across the strand were inflicted to handle the immobilized DNA strand in a controlled way

shows the same DNA strand after several manipulations by the AFM cantilever tip. The DNA was manipulated and successfully moved about 25–100nm. By using this and similar procedures, a fine and coarse positioning of DNA is possible.

These first experiments demonstrate that defined DNA wires can be prepared by AFM cutting, and they can be moved on substrate surface to different locations. These results will be used for the development of automated methods to construct nanoelectric parts or solve packaging purposes on the nanoscale. The experiments show that a DNA manipulation can also be performed in dry ambient conditions.

Automated Structuring of Biological Materials for Biosensors

Biosensors consist of a sensitive biological component, transducer or detector element, and associated electronics or signal processors. An accurate and well-defined preparation of the sensitive components made, for example, of microorganisms, cell receptors, proteins, enzymes, antibodies, or nucleic acids is crucial part of the sensor design. Commonly used methods are microstamping and microprinting, both not able to decrease the structures of the biological component down to the nanometer range. However, higher density is necessary to increase the measurement accuracy and the number of different, simultaneously useable biocomponents. In this section, our current work on automated design of high-density sensitive components using AFM-based lithography is introduced.

The compensation of spatial uncertainties plays an important role for automation of AFM-based handling. While the effects of hysteresis and creep of the PZT-based scanner can be reduced by closed-loop control, spatial uncertainties caused by thermal drift are crucial and less straightforward to deal with. Especially in life science applications, where the AFM is often operated in humid environments, the effect becomes strong and often prevents successful nanohandling, let alone automation of this handling task. To achieve reliable results, the recently developed

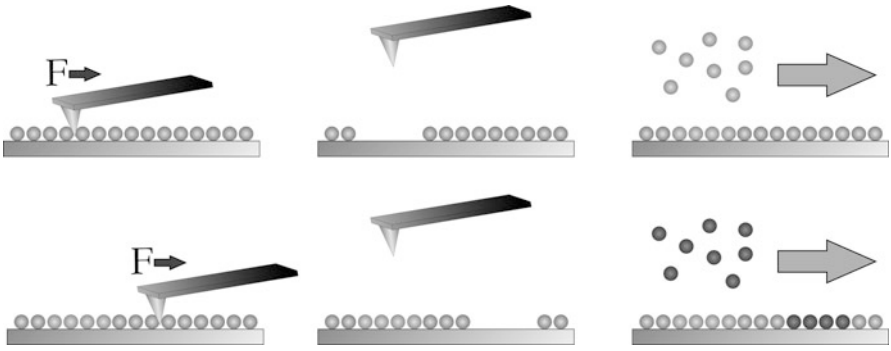

Fig. 11.9 Schematical drawing of the structuring of biosensors with different biomarkers using AFM-based structuring techniques

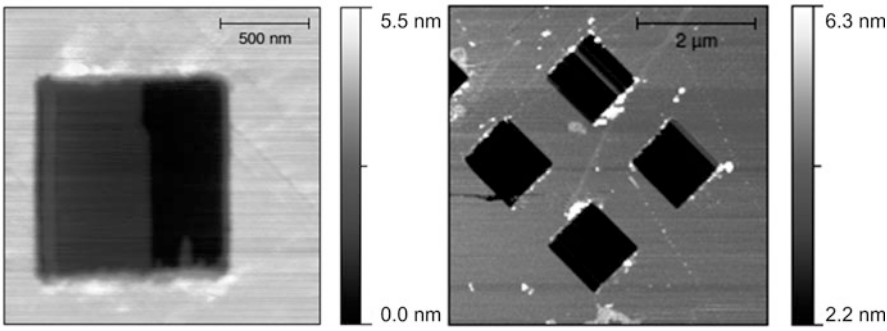

Fig. 11.10 Height image of 1 × 1-µm area scratched into APTES monolayer by AFM machining. The two visible machining depths arise from different force set points used during the processing (*left*) and AFM height image of a series of 1 × 1-µm-sized scratched areas (*right*)

method for real-time drift compensation was applied, both for the presented manipulation of DNA as well as for the AFM-based nanotooling described below.

As a first step toward the automated fabrication of biosensor components (Fig. 11.9), rectangular areas were successfully structured into an APTES monolayer on mica (Fig. 11.10). To further investigate the correlation between the forces applied during manipulation and the resulting machining depths, a series of experiments were performed to scratch multiple areas. This process was automated using the built-in Jython software interface of the utilized AFM, which allows full, customizable control of the AFM procedures.

Nanopackaging Using Biomaterials

Based on their properties, DNA can be considered as a basic building block for nanoelectronic devices as well as for nanoscale bonding wires. Compared to

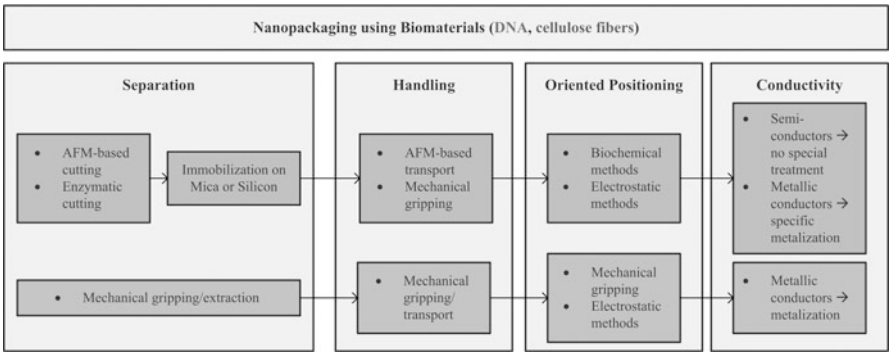

Fig. 11.11 Working routes for the use of biomaterials (DNA—*upper row*; cellulose fibers—*lower row*) as bonding wires for nanopackaging

DNA other organic materials such as microfibrils from wood fibers came recently into focus of international research. First, successful metallization experiments of structures made from organic cellulose make them a possible successor for the pure metallic bonds in micro- to nanosystem technology, which are about 20 μm in diameter or bigger. These cellulose-based building blocks can be obtained from very different sources: certain bacteria produce strands of cellulose, whereas other sources are, for example, algae or wood fibers. In textile industry, technically produced cellulose fibers are also available. The different size ranges from about 20nm from bacterial cellulose up to several hundreds of nanometers for bundles of fibrils from wood fibers. Industrial fibers are some hundreds of μm in size. All sources can be easily purchased.

Toward Nanopackaging Using Biomaterials

As described above and shown in Fig. 11.11, two different biomaterials are used for our work. On the one hand, we use DNA to build flexible nanowires, which have a semiconducting behavior but are also hard to handle with a mechanical manipulation like gripping or AFM-based approaches. On the other hand, we use cellulose fibrils out of wooden fibers that are more robust than DNA but have no usable electric properties. To use them as nanowires, a metallization is necessary. In addition, there are some differences in the raw form of the used materials. While DNA is a long macromolecule which is coiled in liquid solutions, the fibrils are ordered in wooden fibers and have to be separated before they can be used. In the following sections, we describe the necessary steps to use these two different biomaterials in order to realize the use as bonding wires for nanopackaging. Figure 11.12 gives an idea of the ratios between contact pads and wood fibers.

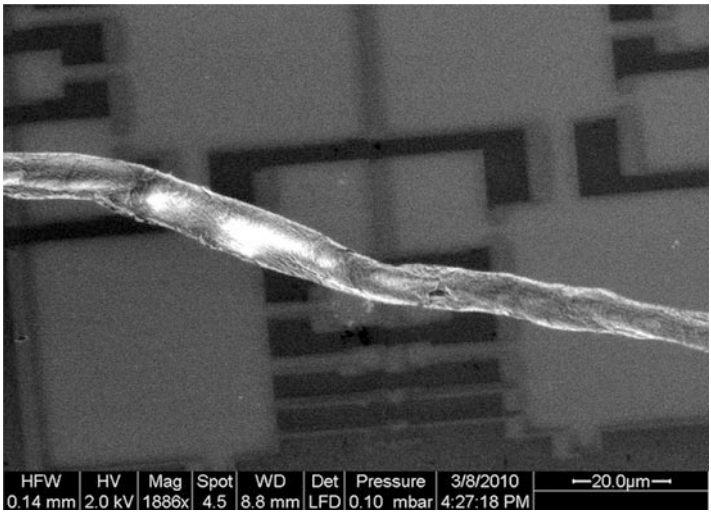

Fig. 11.12 Low-vacuum SEM image of a softwood kraft fiber in front of arbitrary contact pads. The biggest pads have a size of 50 μm × 50 μm and the diameter of the fibers is around 8 μm

Nanopackaging Using DNA Nanowires

As discussed earlier, one of the potential materials for bonding and packaging at the nanoscale is DNA. The physical and electrical properties of DNA enable us to handle and use these biomolecules like classical bonding wires. For this, some crucial steps have to be performed to realize a packaging. Firstly, the DNA has to be immobilized in a way so that the strands can be used properly. For this, the following steps are necessary (1) stretching, (2) immobilization, and (3) preparation of DNA wires with defined lengths. Once the wires are immobilized and ready to use, the handling steps can follow using AFM-based approaches at dry conditions. For this, the tips of the AFM cantilever will be functionalized to remove the DNA from the surface. The next step will be the transport to the first contact or bonding pad, where an additional functionalization with special proteins is used for the binding of the DNA to these sites. With the AFM the nanowire will be stretched to the other, similar functionalized, contact pad. There the DNA will be placed onto the binding sites. A necessary condition for this method is the presence of different binding forces of the used functionalization proteins for the contact pads and the cantilever tip. To support the removing of the DNA from the cantilever, additional negative voltages on the cantilever can be used. Depending on the nature of the electric circuit, the DNA can be metalized or used as a semiconductor.

Nanopackaging Using Cellulose Fibrils

The use of fibrils from wood fibers for packaging purposes requires some similar steps as for DNA. First, (1) the usable part needs to be separated from the fiber (separation step). From our first experiments, it became obvious that because of the high bonding forces specialized methods are necessary. One solution to this will be the use of metal tips to hold the fiber in place while using different pulling angles. Second, if the fibril is separated, it has to be transported and placed on both contact pads, which shall be connected (handling and positioning steps). For this (2) handling procedure, different properties of the fibril need to be considered. Fibrils are not as regular as any other organic material. In turn, their mechanical properties, like bending stiffness, are anisotropic. A possible automation system needs a calculation model to perform the planned actions automatically. This requires characterization steps of fibrils during the first development stages for this type of nanopackaging. It is likely that during the (3) oriented positioning a fixation step is necessary, which could be solved by electrostatic means, until the fibril can be metalized. The last step to turn the fibril into a nanowire is the (4) metallization.

First experimental work on fibrils has been performed inside the SEM in high vacuum with pressures around 2×10^{-6} mbar. Selecting, gripping, and bending of the fibril bundle could be carried out easily.

The presented methods for the handling of biomaterials show the potential for different usage scenarios in industry and scientific research. In case of the handling of DNA, the experiments demonstrate that a DNA manipulation can be performed in dry ambient conditions. Concerning the work with cellulose fibers, the results motivate a more extensive investigation of the fiber–fibril structure in order to achieve a better understanding of the subject for possible future applications. At this stage, it is obvious that the use of cellulose fibers from wood and other sources depends on preceding characterization and manipulation tests to conclude needed changes of the manipulating tools and systems.

11.3.3 Optical Tweezers

Since the demonstration of the use of strongly focused laser beams to manipulate various objects at the micro- and nanoscale by Arthur Ashkin in 1970 [30], the contactless measurement of forces and the contactless handling of biological objects have been revolutionized.

Optical tweezers are capable of manipulating nanometer and micrometer-sized dielectric particles by exerting extremely small forces via a highly focused laser beam. The beam is highly focused by using a microscope objective with a high numerical aperture (Fig. 11.13a). The narrowest point of the focused beam, known as the beam waist, contains a very strong electric field gradient. It turns out that dielectric particles are attracted along the gradient to the region of strongest electric field, which is the center of the beam. The laser light also tends to apply a force on

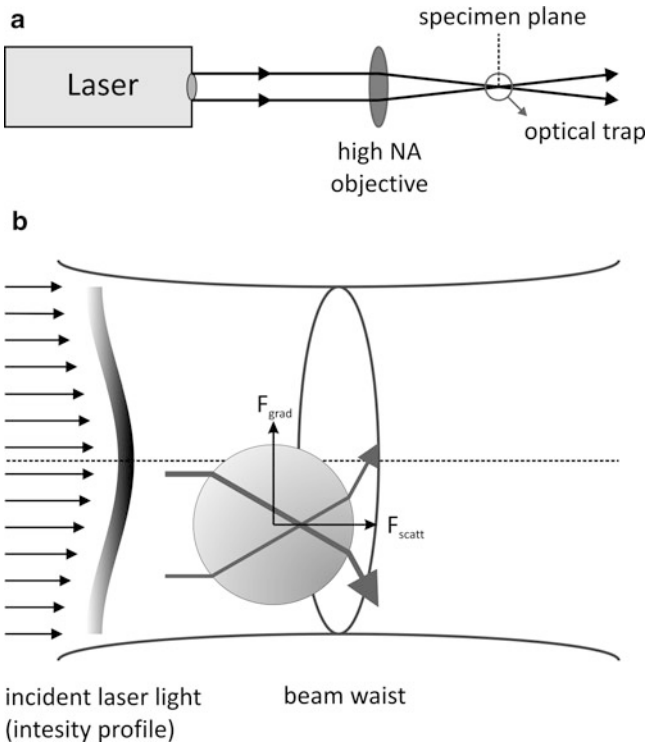

Fig. 11.13 The principles of the work of optical tweezers. (**a**) A laser beam (TEM00 mode) is focused by a high-quality microscope objective to a spot in the specimen plane. (**b**) This spot creates an "optical trap" which is able to hold a small particle at its center. The forces felt by this particle consist of the light scattering and gradient forces due to the interaction of the particle with the light

particles in the beam along the direction of beam propagation. If one considers light to be a group of particles (photons), each impinging on the tiny dielectric particle in its path (radiation pressure of light), it is easy to understand why light can exert a pressure on these nanoscopic or microscopic objects. The resulting force is known as the scattering force (F_{scatt}) and results in the particle being displaced slightly downstream from the exact position of the beam waist, as seen in the Fig. 11.13b.

$$F_{\text{scatt}} = n_m \frac{\text{S}\sigma}{c}$$

with

$$\sigma = \frac{8}{3}\pi (k_{\text{L}} r)^4 r^2 \left(\frac{m^2 - 1}{m^2 + 2} \right)^2 .$$

$\langle S \rangle$ represents the Poynting vector, r the radius of the particle, n_m the refractive index of the surrounding media, m the relative refractive index between media and particle, and k_L the wave number of the light.

Optical tweezers owe their trapping abilities to the gradient force (F_{grad}), which is proportional to the spatial gradient in light intensity and acts in the direction of the gradient.

$$F_{grad} = \frac{\alpha}{2} \nabla E^2$$

with

$$\alpha = n_m^2 r^2 \left(\frac{m^2 - 1}{m^2 + 2} \right).$$

In this case, α represents the polarizability of the trapped microparticle.

The gradient force used by optical tweezers arises from fluctuating electric dipoles that are induced when light passes through transparent objects [31]. When a dielectric sphere is placed in a light gradient, the sum of all rays passing through generates an imbalance in force. This force pushes the sphere toward the brighter region of the light. So a focus functions as a trap because the strong light gradients in its neighborhood point toward the center. With these conditions, trapping is stable if $F_{grad} > F_{scatt}$. Such optical traps are only with high numerical aperture objectives possible in practice.

For quantitative scientific measurements, most optical traps are operated in such a way that the dielectric particle rarely moves far from the trap center. The reason for this is that the force applied to the particle is linear with respect to its displacement from the center of the trap as long as the displacement is small. In this way, an optical trap can be compared to a simple spring, which follows Hooke's law (Fig. 11.14).

The most basic optical tweezer setup (Fig. 11.15) will likely include the following components:

- A laser (usually Nd: YAG with 1,064nm wavelength for working with biological material)
- A beam expander, some optics used to steer the beam location in the sample plane
- A microscope objective (NA between 1.2 and 1.4) to create the trap in the sample plane
- A position detector (e.g., quadrant photodiode) to measure beam displacements
- A microscope illumination source coupled to a CCD camera

With these optical tweezers, it is possible to get the basic information and the interactions of the laser beam and small nanoparticles of silicon and various organic polymers [32] as well as on the resulting forces and the modeling of these interactions [31, 33]. Experiments are conducted to determine the speed of bacteria in various flow schemes [34], to manipulate chromosomes and sperm cells [31],

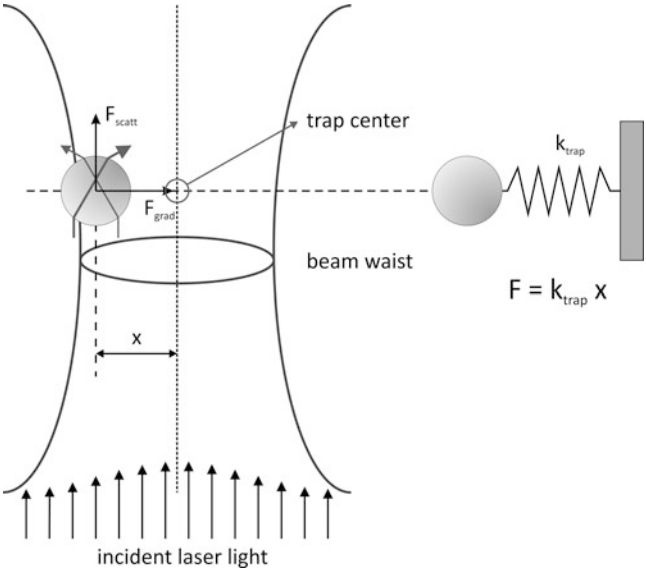

Fig. 11.14 Dielectric objects are attracted to the center of the beam, slightly above the beam waist, as described in the text. The force applied on the object depends linearly on its displacement from the trap center just as with a simple spring system

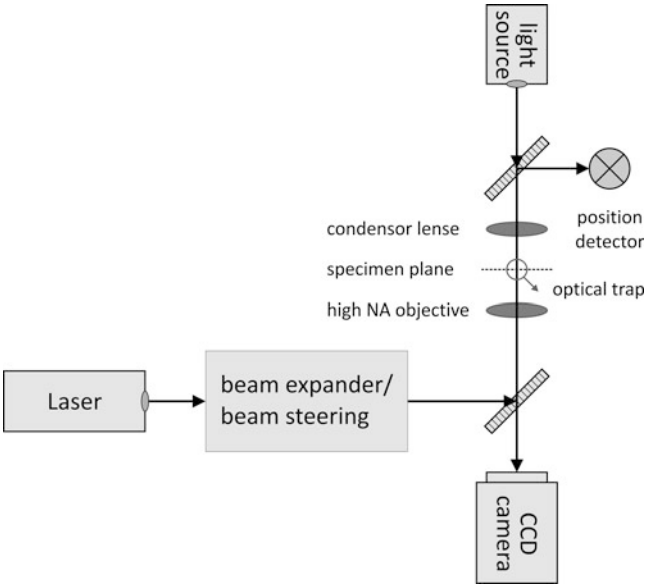

Fig. 11.15 A generic optical tweezer diagram with only the most basic components

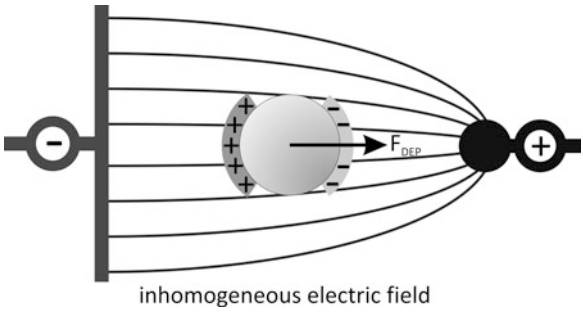

Fig. 11.16 Schematic diagram of the interactions exerts on a particle in a nonuniform electric field

to manipulate cell organelles [35], and to determine the deformation effects on erythrocytes and fibroblasts [36]. With the optical tweezers, it is also possible to characterize DNA in order to provide information on the mechanical, elastic, and entropic properties [34, 37, 38]. Also, the direct manipulation of actin filaments has been demonstrated by using optical tweezers [39].

Compared to other contactless methods for the manipulation of biological objects, the optical tweezers technique also offers the possibility of including in microrobotic and nanorobotic systems to handle biological objects fully automatedly, using current micro-optics advances.

11.3.4 Dielectrophoresis

Among the various manipulation techniques, the electric field-based approach is well suited for miniaturization because of the relative ease of microscale generation and structuring of an electric field on microchips. Dielectrophoresis (DEP, Fig. 11.16) can be described as a phenomenon in which a force is exerted on a dielectric particle subjected to an asymmetric electric field. Due to the fact that all particles exhibit dielectrophoretic activity in the presence of electric fields, the resulting dielectric force does not require the charging of the particle. However, the strength of the force strongly depends on the properties of the surrounding medium, the electrical properties of the surrounding electric field, and on the electrical properties of the particles. This leads to a highly selective manipulation of particles by using an electric field of a particular frequency so that this method can be used for the manipulation, transport, separation, and sorting of different types of biological objects.

First publications on DEP go as far back as to the 1950s. Recently, DEP has been revived due to its potential in the manipulation of microparticles, nanoparticles, and cells. In these first publications DEP was defined as the translational motion of neutral matter caused by polarization effects in a nonuniform electric field. The phenomenological bases are shown below:

- The DEP force can only be seen when particles are in nonuniform electric fields.

- Since the DEP force does not depend on the polarity of the electric field, the phenomenon can be observed either with AC or DC excitation.
- Particles are attracted to regions of stronger electric fields when their permittivity exceeds that of the suspension medium.
- If the permittivity of the medium is greater than that of the particles, the resulting motion of the particles directs to lesser electric field gradient.
- DEP is most readily observed for particles with diameters ranging from 1 to 1,000 μm. Above 1,000 μm, gravity overwhelms DEP; below 1 μm, Brownian motion overwhelms the DEP forces.

For a field-aligned ellipsoid of radius r and length l $(r > l)$ with complex dielectric constant ε_p^* in a medium with complex dielectric constant, ε_m^* the time-dependent dielectrophoretic force is given by:

$$F_{\text{DEP}} = \frac{\pi r^2 l}{3} \varepsilon_m \text{Re}\left(\frac{\varepsilon_p^* - \varepsilon_m^*}{\varepsilon_m^*}\right) \nabla |\mathbf{E}|^2.$$

The complex dielectric constant is $\varepsilon^* = \varepsilon + \frac{\sigma}{j\omega}$, where ε is the dielectric constant, σ is the electrical conductivity, ω is the field frequency, and j is the imaginary number.

This equation is accurate for highly elongated ellipsoids when the electric field gradients are not very large (e.g., close to electrode edges). The equation only takes into account the dipole formed and not higher order polarization. When the electric field gradients are large, higher order terms become relevant and result in higher forces. To be precise, the time-dependent equation only applies to lossless particles because loss creates a lag between the field and the induced dipole. When averaged, the effect cancels out and the equation holds true for lossy particles as well.

It appears that in current literature about DEP on biological structures, the treatment and handling of cells is examined more frequently than other biological objects such as DNA. The described applications start with cell sorting of living and dead cells [40], sorting of healthy and cancer cells [41, 42], and sorting of other different cell types [43, 44]. Few applications for the use of DEP with DNA are described [45, 46].

Compared to other contactless methods for the manipulation of biological objects, the DEP technique also offers the possibility of easily including in micro-robotic and nanorobotic systems to handle biological objects fully automatedly.

11.3.5 Microcapillaries

To understand the fundamental elements of biological systems, the need to analyze individual cells is of great importance. Even in the identification of genes, in gene therapy, and also in the bacterial synthesis of specific DNA sequences, the full knowledge of the reactions and mechanisms of single cells has to be examined.

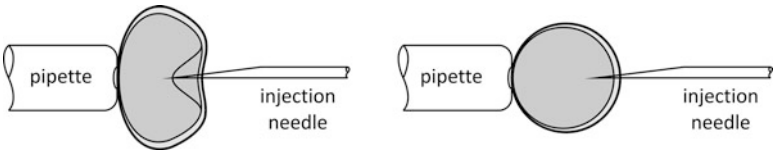

Fig. 11.17 *Left*: classical microinjection (highly deformed cells). *Right*: piezo-driven microinjection (much lesser deformation of the cells)

One approach is the infiltration of known DNA sequences into single cells by using single cell injection (Fig. 11.17). For this, a gripper, an optical trap, or a micropipette is used to hold the cell while another micropipette performs an injection process. Currently, this cell injection is conducted manually and needs well-trained scientists. However, even with fully trained scientists, the success rate is extremely small. A reason for this is the dependence of the injection on the injection speed and trajectory.

To overcome these problems of a manual cell injection and to suppress the contamination and destruction of cells, automated solutions are necessary. Furthermore, automated cell injection can be highly reproducible with precision and control of pipette motion [47]. By using automated cell injection, the risk of contamination can be decreased and the reproducibility can be increased, leading to significantly increased success rates of the cell injection process.

This is, for example, shown by the work of Sun and Nelson which describes a completely automated robotic cell injection system to conduct autonomous pronuclei DNA injection of mouse embryos with a success rate of 100% [47].

11.3.6 Microgrippers and Nanotweezers

Another way of handling biological objects is microgrippers and nanotweezers, which use small and variable forces to pick and place cells or other biological objects. The main advantages of such grippers are a better control of the applied forces and a well-defined mechanical grip effect on the object. Thus, they are more effective in gripping experiments than cantilever-based structures of AFM- and STM-based microrobotic systems. A microgripper also gives the possibility to make direct electrical and mechanical measurements on the grabbed objects if the gripper jaws are conductive or can provide a force feedback signal. Most of these grippers work using electrostatic, thermal, or piezoelectric effects to control the gripping forces. In case of the thermal gripper, the effect of heat-induced material expansion is used. In the case of the piezoelectric gripper, the effect, that piezoelectric ceramics can be expanded and contracted by the use of specific electric fields, is used. Another major advantage of these grippers is their use as a tool for mobile platforms and micro- and nanorobotic systems in combination with linear and rotary positioners (e.g., linear axes of SmarAct GmbH) for fine positioning.

Currently, there are some groups and vendors, which sell various types of microgrippers and nanotweezers for micro- and nanorobotic systems. The group of Peter Bøggild at the Technical University of Denmark has developed silicon microgrippers, nanotweezers, and nanostructured nonstick coatings to avoid adhesive effects during nanomanipulation tasks [48–50]. Also exist nanotube nanotweezers for the manipulation of GaAs nanowires and polystyrene nanoclusters [51]. They are manufactured by Kim and Lieber. Similar nanotweezers have also been used for the successful manipulation of nanowires [52] and DNA [53]. Other companies which produce sorts of microgrippers and nanotweezers are SmarAct GmbH, Nascatec, and Zyvex Instruments. Some of these grippers can operate at UHV conditions as well as in a standard atmosphere. There are differences in the opening widths and the accuracy of the grippers and tweezers, so that it is possible to choose the best gripper with respect to the biological objects which shall be manipulated.

Some of these biological objects, on which microgrippers and nanotweezers were used for manipulation tasks, are cancer cells, for example, the aggressive HeLa cells [54, 55], porcine aortic valve interstitial cells [56], and a wide spectrum of other biological cells [56, 57].

Unfortunately, the working principles of such microgrippers and nanotweezers are also the main disadvantages for its usage with biological objects. The thermal gradients or electric fields to open the grippers can destroy some of the biological samples. To overcome these problems, the development of mechanically actuated grippers has shown an alternative approach, but there is still a risk of damaging and contaminating the biological samples [59, 60].

11.4 Future Trends

Today, micro- and nanotools enable researchers to manipulate and handle microscopic down to nanoscopic biological objects. Many of these techniques can be used to handle biomaterials in a nonautomated way. Some of these techniques are already used in semiautomated robotic systems, to support the researchers during these sophisticated tasks and to enable the control of the processes at the nanoscale. However, still very few techniques can be used fully automated or are integrated in automated working nanorobotic systems. This will be a goal for the near and middle future—the integration of all the handling techniques, shown in this chapter. For the long future, also the integration of some of the other handling methods needs to be done, combined with techniques such as microfluidics and self-assembling, to set up sophisticated robotic systems, which will be able to support the researchers, allowing them the unlimited control over the examined biomaterials without damaging or changing their natural structures.

References

1. Alberts B et al (2002) Molecular biology of the cell. Taylor & Francis, New York
2. Layton BE et al (2005) Nanomanipulation and aggregation limitations of self-assembling structural proteins. Microelectron J 36:644–649
3. Fahlbusch S, Mazerolle S, Breguet JM (2005) Nanomanipulation in a scanning electron microscope. J Mater Proc Technol 167:371–382
4. Tai SSW, Tang XM (2001) Manipulating biological samples for environmental scanning electron microscopy observation. Scanning 23:267–272
5. Mestres P, Pütz N, Laue M (2007) Consequences of tilting of biological specimens in wet mode ESEM imaging. Microsc Microanal 13:244–245
6. Stokes D (2003) Low vacuum & ESEM imaging of biological specimens. Microsc Microanal 9:190–191
7. Muscariello L, Rosso F, Marino G (2005) A critical overview of ESEM applications in the biological field. J Cell Physiol 205:328–334
8. Quate G, Gerber CF, Binnig C (1986) Atomic force microscope. Phys Rev Lett 56:930–933
9. Castillo J, Dimaki M, Svendsen WE (2009) Manipulation of biological samples using micro and nano techniques. Integr Biol 1:30–42
10. Lal R, John SA (1994) Biological applications of atomic force microscopy. Am J Physiol Cell Physiol 266:c1–c21
11. Sitti M (2007) Microscale and nanoscale robotics systems [grand challenges of robotics]. IEEE Robot Autom Mag 14:53–60
12. Rubio-Sierra J, Heckl W, Stark RW (2005) Nanomanipulation by atomic force microscopy. Adv Eng Mater 7:193–196
13. Brufau J, Puig-Vidal M, López-Sánchez J (2005) Micron: small autonomous robot for cell manipulation applications. In: International conference on Robotics and Automation, Barcelona, Spain, 856–861
14. Ando T, Uchihashi T, Kodera N (2008) High-speed AFM and nano-visualization of biomolecular processes. Eur J Physiol 456:211–225
15. Kuznetsov Y, Gershon PD, McPherson A (2008) Atomic force microscopy investigation of vaccinia virus structure. J Virol 82:7551–7566
16. Laney DE, Garcia RA, Parsons SM, Hansma HG (1997) Changes in the elastic properties of cholinergic synaptic vesicles as measured by atomic force microscopy. Biophys J 72:806–813
17. Seidel R, Colombi Ciacchi L, Weigel M, Pompe W, Mertig M (2004) Synthesis of platinum cluster chains on DNA templates: conditions for a template-controlled cluster growth. J Phys Chem B 108:10801–10811
18. de Pablo PJ, Moreno-Herrero F, Colchero J (2000) Absence of dc-conductivity in λ-DNA. Phys Rev Lett 85:4992–4995
19. Kufer SK, Puchner EM, Gumpp H, Liedl T, Gaub HE (2008) Single-molecule cut-and-paste surface assembly. Science 319:594–596
20. Parra A, Casero E, Lorenzo E, Pariente F, Vázquez L (2007) Nanomechanical properties of globular proteins: lactate oxidase. Langmuir 27:2747–2754
21. Stark RW, Rubio-Sierra J, Thalhammer S, Heckl W (2003) Combined nanomanipulation by atomic force microscopy and UV-laser ablation for chromosomal dissection. Eur Biophys J 32:33–39
22. Afrin R, Alam MT, Ikai A (2005) Pretransition and progressive softening of bovine carbonic anhydrase II as probed by single molecule atomic force microscopy. Protein Sci 14:1447–1457
23. Schaap I, Carrasco C, de Pablo PJ, MacKintosh FC, Schmidt CF (2006) Elastic response, buckling, and instability of microtubules under radial indentation. Biophys J 91:1521–1531
24. Abu-Lail NI, Camesano TA (2003) Polysaccharide properties probed with atomic force microscopy. J Microsc 212:217–238
25. Peng L et al (2004) Study on biological effect of la3+ on *Escherichia coli* by atomic force microscopy. J Inorg Biochem 98:68–72

26. Ebner A et al (2005) Localization of single avidin-biotin interactions using simultaneous topography and molecular recognition imaging. Chem Phys Chem 6:897–900
27. Oberleithner H et al (2004) Human endothelium: target for aldosterone. Hypertension 43: 952–956
28. Ivanovska IL et al (2004) Bacteriophage capsids: tough nanoshells with complex elastic properties. Proc Natl Acad Sci 101:7600–7605
29. Cohen H et al (2006) Electrical characterization of self-assembled single- and double-stranded DNA monolayers using conductive afm. Faraday Discuss 131:367–376
30. Wright WH, Sonek GJ, Berns MW (1993) Radiation trapping forces on microspheres with optical tweezers. Appl Phys Lett 63:715–717
31. Ashkin A (1997) Optical trapping and manipulation of neutral particles using lasers. Proc Natl Acad Sci USA 94:4853–4860
32. Wright WH, Sonek GJ, Tadir Y, Berns MW (1990) Laser trapping in cell biology. IEEE J Quantum Electron 26:2148–2157
33. Barton JP, Alexander DR (1989) Fifth order corrected electromagnetic field components for a fundamental Gaussian beam. J Appl Phys 66:2800–2802
34. Svoboda K, Block SM (1994) Biological applications of optical forces. Annu Rev Biophys Biomol Struct 23:247–285
35. Ruiz I, Wang P, Schaffer C, Kleinfeld D, (2003) Optical trapping and ablation. Neurophysics laboratory final report PHYS 173/BGGN 266 Lab. Uiversity of California, San Diego, CA
36. Guck J et al (2001) The optical stretcher: a novel laser tool to micromanipulate cells. Biophys J 181:767–784
37. Baumann CG, Smith SB, Bloomfield VA, Bustamante C (1997) Ionic effects on the elasticity of single DNA molecules. Proc Natl Acad Sci USA 94:6185–6190
38. Yu Y (2003) Introduction to probing DNA with optical tweezers. Introduction to Biophysics - Term Paper
39. Arai Y, Yasuda R, Akashi K (1999) Tying a molecular knot with optical tweezers. Lett Nat 399:446–448
40. Tai CH, Hsiung SK, Chen CY, Tsai ML, Lee GB (2007) Automatic microfluidic platform for cell separation and nucleus collection. Biomed Microdevices 9:533–545
41. Yang J, Huang Y, Wang XB, Becker FF, Gascoyne PRC (1999) Cell separation on microfabricated electrodes using dielectrophoretic/gravitational field-flow fractionation. Anal Chem 71:911–918
42. An J, Lee J, Kim Y, Kim B, Lee S (2008) Analysis of cell separation efficiency in dielectrophoresis-activated cell sorter. In: 3rd International IEEE conference on nano/micro engineered and molecular systems, 965–969
43. Yang J, Huang Y, Wang XB, Becker FF, Gascoyne PRC (2000) Differential analysis of human leukocytes by dielectrophoretic field-flow-fractionation. Biophys J 78:2680–2689
44. Wang XB et al (2000) Cell separation by dielectrophoretic field-flow-fractionation. Anal Chem 72:832–839
45. Regtmeier J, Duong TT, Eichhorn R, Anselmetti D, Ros A (2007) Dielectrophoretic manipulation of DNA: separation and polarizability. Anal Chem 79:3925–3932
46. Tuukkanen S, Kuzyk A, Toppari JJ (2007) Trapping of 27 bp-8 kbp DNA and immobilization of thiol-modified DNA using dielectrophoresis. Nanotechnology 18:295204–295214
47. Sun Y, Nelson BJ (2002) Biological cell injection using an autonomous microrobotic system. Int J Robot Res 21:861–868
48. Mølhave K, Wich T, Kortschack A, Bøggild P (2006) Pick-and-place nanomanipulation using microfabricated grippers. Nanotechnology 17:2434–2441
49. Carlson K, Andersen KN, Eichhorn V (2007) A carbon nanofibre scanning probe assembled using an electrothermal microgripper. Nanotechnology 18:345501–345508
50. Sardan O et al (2007) Microgrippers: a case study for batch-compatible integration of MEMS with nanostructures. Nanotechnology 18:375501–375512
51. Kim P, Lieber CM (1999) Nanotube nanotweezers. Science 286:2148–2150

52. Bøggild P, Hansen TM, Tanasa C, Grey F (2001) Fabrication and actuation of customized nanotweezers with a 25 nm gap. Nanotechnology 12:331–335
53. Hashiguchi G, Goda T, Hosogi M (2003) DNA manipulation and retrieval from an aqueous solution with micromachined nanotweezers. Anal Chem 75:4347–4350
54. Beyeler F, Neild A, Oberti S (2007) Monolithically fabricated microgripper with integrated force sensor for manipulating microobjects and biological cells aligned in an ultrasonic field. J Microelectromech Syst 16:7–15
55. Chronis N, Lee LP (2005) Electrothermally activated SU-8 microgripper for single cell manipulation in solution. J Microelectromech Syst 14:857–863
56. Kim K, Liu X, Zhang Y, Sun Y (2008) Nanonewton force-controlled manipulation of biological cells using a monolithic MEMS microgripper with two-axis force feedback. J Micromech Microeng 18:55013–55021
57. Solano B, Wood D (2007) Design and testing of a polymeric microgripper for cell manipulation. Microelectron Eng 84:1219–1222
58. Blideran MM, Bertsche G, Henschel W, Kern DP (2006) A mechanically actuated silicon microgripper for handling micro- and nanoparticles. Microelectron Eng 83:1382–1385
59. Sokolov I, Subba-Rao V, Luck LA (2006) Change in rigidity in the activated form of the glucose/galactose receptor from *Escherichia coli*: a phenomenon that will be key to the development of biosensors. Biophys J 90:1055–1063
60. Blideran MM, Fleischer M, Henschel W (2006) Characterization and operation of a mechanically actuated silicon microgripper. J Vac Sci Technol B 24:3239–3243

Chapter 12
Apply Robot-Tweezers Manipulation to Cell Stretching for Biomechanical Characterization

Youhua Tan and Dong Sun

Abstract Robotic manipulation of living cells offers us an ability to study biological cells at single cell level, which has received increasing attention in recent years. Optical tweezers technology is such a powerful tool that can apply force and deformation on a cell with resolution at piconewton and nanometer, respectively. In this chapter, we present an approach to integrating optical tweezers into robotic manipulation for cell stretching, and further, for characterizing biomechanical properties of cells. To extract cell properties from the mechanical responses of cells, a theoretical model is developed to reveal cell deformation behaviors. By comparing simulation results to experimental data, the mechanical properties of cells can be characterized. Further, we apply this established modeling and characterization approach to human blood cells for biomechanics study. Our latest results indicate that the mechanical stiffness of human red blood cells increases with elevation in tonicity of suspended solutions, and myeloblasts from acute myeloid leukemia patients with different immunophenotypes exhibit distinct mechanical properties.

12.1 Introduction

Manipulation of living cells provides an ability to study biological cells at single cell level and has become increasingly important in both engineering and biological fields. This technology offers us an opportunity to precisely position cells with good flexibility, which has been widely applied in many biomedical aspects, such as cell transportation [1], isolation [2], microinjection [3], in vitro fertilization [4], stretching [5, 6], and fusion [7].

Y. Tan • D. Sun (✉)
Department of Mechanical and Biomedical Engineering, City University of Hong Kong, 83 Tat Chee Avenue, Kowloon, Hong Kong, China
e-mail: medsun@cityu.edu.hk

C. Mavroidis and A. Ferreira (eds.), *Nanorobotics: Current Approaches and Techniques*, DOI 10.1007/978-1-4614-2119-1_12,
© Springer Science+Business Media New York 2013

Cell manipulation technology has been demonstrated to be effective in studies of cell mechanism and functions. One of the earliest methods was micropipette aspiration [8], which applied a negative pressure to partially or wholly suck a single cell into a micropipette. The relation between cell elongation into the pipette and the suction pressure provided information about mechanical properties of cells [9]. Nanoindentation using atomic force microscopy (AFM) has been extensively used to study various biophysical properties of adherent cells, such as elasticity [10] and adhesion [11]. Magnetic twisting cytometry (MTC) method applied a tiny force to a cell via a magnetic bead linked to the membrane. The time-dependent cell responses to the twisting force revealed the viscoelastic properties of the cell [12, 13]. Optical stretcher, which consists of two counter-propagating divergent laser beams, exerted optical stress, but no net force on the cell membrane [14]. Cell elasticity could be acquired from the imposed force and the induced cell deformation [15]. Optical tweezers technique utilized a highly focused laser beam to trap and move objects of micrometer size. By manipulating micro-beads attached to the cell surface, cells could be stretched or cell tethers were formed [16–18]. The cell deformation or the tether length reflected the intrinsic properties of the cell.

Cell mechanics determines how a cell senses and responds to external or internal mechanical stimuli and plays an important role in regulating cellular functions. Cell mechanics, especially mechanical properties, can be used as a sensitive marker for cell state [19–23]. Recent studies on the pathophysiology of human diseases have suggested that their pathogenesis might result from deviation in the structural and mechanical properties of cells [21, 24]. Accumulating evidence has implicated that abnormity of mechanical properties of cells may be associated with the onset and progression of diseases. For example, osteoarthritic chondrocytes exhibited significantly higher viscoelastic properties such as equilibrium modulus, instantaneous modulus, and apparent viscosity compared to normal ones [25]. Young's modulus of cancerous human epithelial cells was one order of magnitude lower than normal cells [26]. Young's moduli of prostate cancer cells with different metastatic potentials were distinct [27].

Over the past decades, robotics has been demonstrated as a promising tool in control, vision, and system intelligence for macro-object manipulations and has been extended to microscale by using MEMS. Benefiting from great advances of robotics in visual servoing [28], micro-force sensing [29], and motion control [30], microrobotic manipulation of biological objects has attracted substantial attention. In recent years, optical tweezers technology was incorporated into robotic manipulation for handling nonadherent biological cells at micro/nano level precision, where optical tweezers function as special robot end effectors. Such robot-tweezers manipulation provided an ability to apply force and deformation on a microscaled object on piconewton and nanometer and could manipulate biological objects in a noncontact and noninvasive manner. The integration of robotics with optical tweezers into a manipulation system will open up a new dimension of cellular biology that has substantial clinical and biological relevance.

In this chapter, we introduce our recent approach to stretching biological cells with a robot-tweezers manipulation system, for characterization of biomechanics

property of cells. In the manipulation, micro-beads were attached to cell surfaces serving as handles that were handled by optical traps. The cell was stretched by progressively increasing the distance between the beads. The deformation responses were recorded on each cell for analysis. To model the deformation behavior of cells during optical stretching, we developed a computational approach to interpret the mechanical responses and based on which the mechanical properties of cells were characterized. The developed method was further applied to study biomechanics of human blood cells, such as human red blood cells (RBC) under different osmotic conditions and acute myeloid leukemia (AML) cells with different phenotypes.

12.2 Robotic Manipulation with Optical Tweezers

12.2.1 Robot-Tweezers Manipulation System

A robot-tweezers manipulation system has been established in our laboratory, which mainly includes three modules: an executive module, a control module, and a sensory module (Fig. 12.1). The executive module contains a holographic optical tweezer system and an X–Y–Z motorized stage (ProScan, Prior Scientific) with microscopic objectives and a holographic optical trapping device (HOT) mounted on the z-axis. A single laser beam with wavelength of 1,064nm emitted by a continuous laser source (YLM-3-1064-LP-AX1, IPG Photonics) is transmitted via an optical

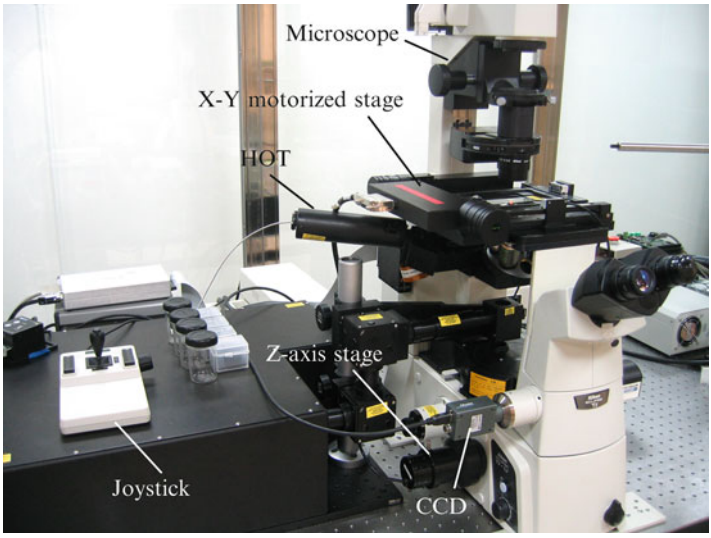

Fig. 12.1 Nanorobotic manipulation system with optical tweezers. Reprinted with permission from [46]

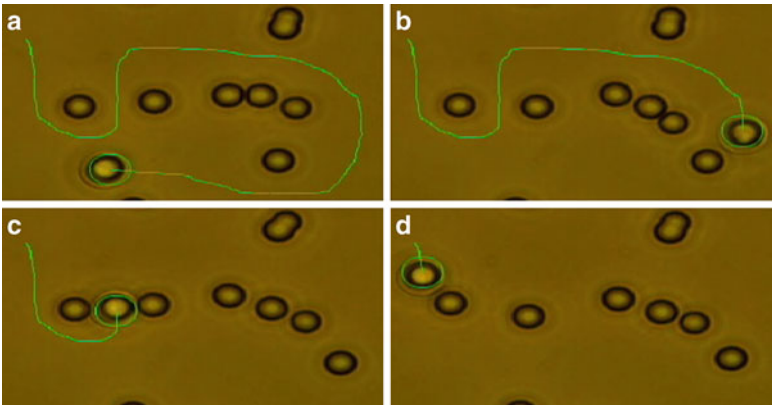

Fig. 12.2 Robotic manipulation of a micro-bead along a designed trajectory with a single optical trap. The *green circle* denotes the optical trap, while the *green line* represents the randomly designed path. The diameter of the bead is about 3.2 μm. Note that all the beads are suspended and fluctuate in the fluid

fiber and sculpted into multiple laser beams by a HOT device. Optical traps are then created on the focal plane when focused by an objective. Positions of these traps can be controlled individually and independently in three dimensions by the HOT device through modulating the phase distribution of a spatial light modulator (SLM). The experimental sample is contained in a home-built chamber, which is assembled with usual microscopic coverslips and slides and placed on the motorized stage with a positioning accuracy of 40nm. The control module comprises a motion controller for the X–Y–Z motorized stage, a programmable phase modulator for the HOT device, and a host computer. The sensory module includes an inverted microscope (Nikon TE2000, Japan), a CCD camera (FO124SC, Foculus), and a PCI image capture and processing card. The positions of biological objects can be obtained through image processing, which serve as visual feedback to guide the manipulation process. All of the mechanical components were supported upon an anti-vibration table.

12.2.2 Robotic Manipulation of Microscaled Objects

Because of the transfer of momentum from the scattering of incident photons, a dielectric object in an optical trap experiences a gradient force, which pushes this particle toward the focal region and then establishes stable trapping near the focus. First of all, we demonstrated the efficiency of optical tweezers in manipulation of microscaled objects, as shown in Fig. 12.2. A bead was trapped by a single optical trap and then moved along a randomly designed trajectory. The position of the optical trap was controlled in three dimensions by programming the phase distribution of the SLM. Under appropriate condition, such as at a proper laser

power, the optical trap could tightly hold the object. In this way, the trapped object could be then well handled. Note that the optical force on the trapped bead was distributed within a certain range. When an untrapped bead was close enough to the trap, it would fall into this trap. Therefore, the distance between the optical trap and other particles should be well controlled to avoid the interference of the environment, such as in Fig. 12.2c.

12.3 Optical Stretching of Biological Cells

Instead of using optical traps to manipulate living cells directly, we coupled microbeads to cell surfaces and then used optical traps to handle these beads to stretch the cell. This manipulation manner mainly had two advantages: (1) it could diminish the potential optical damage to cells, and (2) it could attain relatively large optical force because of the large refraction index of silica or polystyrene beads.

12.3.1 Cell Preparation and Treatment

It was necessary to couple spherical beads to cell surfaces. In brief, biological cells were obtained according to corresponding procedures and suspended in the phosphate-buffered saline (PBS, Sigma). The cells were then washed several times by centrifugation. In parallel, streptavidin-coated beads (Bangs Lab., Fishers, IN) were centrifuged three times. The washed beads were incubated with 1 mg/ml biotin conjugated concanavalin A (Con A, Sigma). The beads were then rinsed and stored in 0.1 mg/ml PBS-BSA solution. The prepared beads were proportionally added to the cell suspension and incubated at 25°C for 1 h to allow the adhesion between beads and cells (generally, two beads for one cell). For cell stretching experiments, the mixture was needed to be diluted into appropriate concentration.

12.3.2 Force Calibration

The viscous-drag-force calibration method was used to calibrate the optical force under a certain laser power [5, 31, 32]. When a bead was trapped and driven by an optical trap, the fluid flow exerted a viscous drag force on the trapped bead. When the velocity of the bead increased up to a critical value V_{crit} beyond which the bead just escaped the laser trap, the bead achieved equilibrium, i.e., the trapping force was equal to the viscous drag force. According to Stokes' law [33], the viscous drag force was expressed as

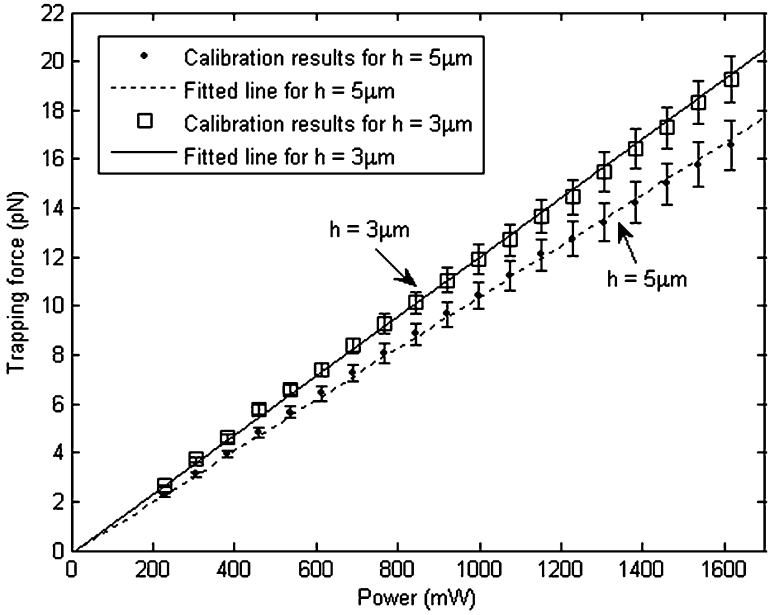

Fig. 12.3 Calibration results of the trapping force versus laser power by trapping a polystyrene bead with radius of 1.55 μm at two different separation depths from the coverslip. The *square* and *dot marks* denote the calibration results of $h = 3$ μm and $h = 5$ μm, respectively. The *error bar* represents the standard deviation of the trapping force. Reprinted with permission from [6]

$$F = \frac{6\pi R\eta_0 V_{\text{crit}}}{1 - 9/16(R/h) + 1/8(R/h)^3 - 45/256(R/h)^4 - 1/16(R/h)^5}, \quad (12.1)$$

where R is the radius of the trapped bead, η_0 is the fluid viscosity (1.01×10^{-3} Pa s for water at 25°C), and h is the separation distance of the bead from the chamber surface.

Figure 12.3 shows the force calibration results, where ten separated measurements were performed to get the average results at each laser power. The relationship between the trapping force and the laser power was close to be linear, which was consistent with the reported results [31, 33]. For a given laser power, the trapping force increases as the separation depth decreases.

12.3.3 Cell Stretching

The cell with two beads attached to the opposite sides in the diameter or with one side coupled to a bead and the other side bound to the chamber was chosen for experiments. One bead was held in place with one trap, while the other was

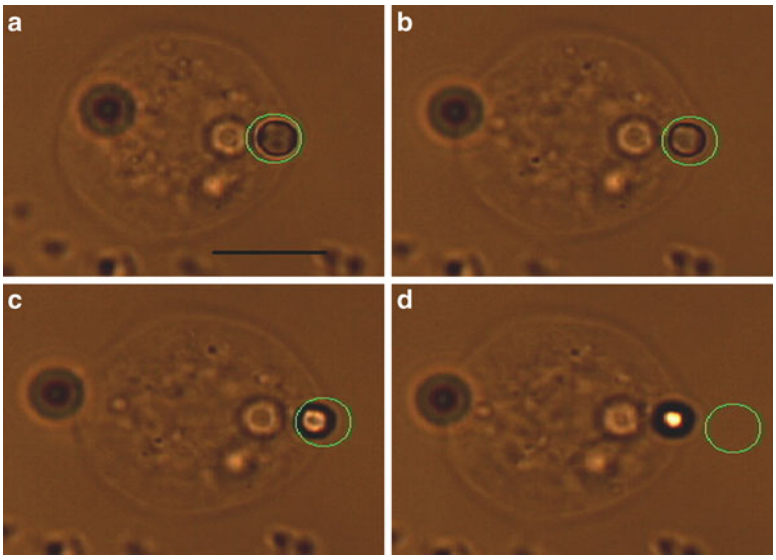

Fig. 12.4 Cell stretching process. (**a**) Before stretching, (**b**) during stretching, (**c**) stretched to the maximum deformation, (**d**) the bead escapes the trap. The *scale bar* is 10 μm

moved by a second trap along the joint line of centroids of these two beads. An increasing membrane tension was exerted on the cell by progressively extending the distance between the beads. If one side of the cell or one of the beads was bound to the chamber, only a single trap was needed to manipulate the unfixed bead. The cell was stretched until one of the beads escaped the trap when the bead achieved equilibrium. At that moment, the cell was stretched to the maximum extent at a given laser power. During cell stretching, the velocity of the moving optical trap was regulated to be slow enough (e.g., <10 μm/s) so that the viscous drag force exerted on the bead could be neglected during cell stretching. Then the trapping force was equal to the cell restoration force due to elongation. The whole stretching process included pre-stretch phase, stretch phase, and post-stretch or cell recovery phase, as shown in Fig. 12.4. After release of the optical force, the cell would then gradually restore its original shape if it was elastic.

During cell stretching, the cell deformation could be measured through image processing. First, the image extracted at the moment when the bead escaped the trap was smoothed with Gaussian filter to suppress the noise. An improved Zernike moment operator was then adopted to detect the edges [34]. The beads were located by using an area criterion to filter the labeled connected components in the binary image. Finally, their centroids could be calculated, as shown in Fig. 12.5. Cell deformation was equal to the elongation of the distance between the two beads after cell stretching. The accuracy of this approach could achieve as high as 0.1 pixels, i.e., 11nm in our system. Moreover, the optical force could be assessed from force calibration. Therefore, the relationship between the cell deformation and the stretching force was established.

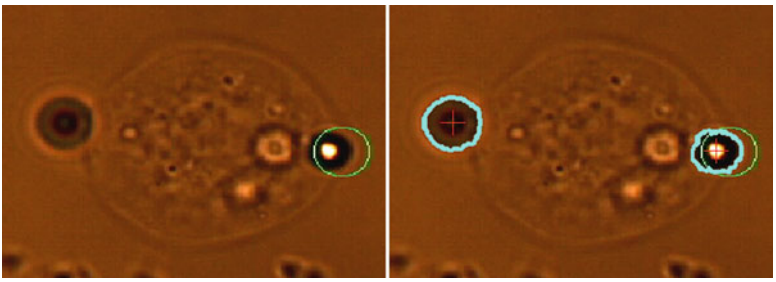

Fig. 12.5 A cell image before (*left panel*) and after (*right panel*) image processing, where *bright blue line* denotes the edges of the beads and the *red cross* represents their centroids

12.4 Mechanical Modeling of Biological Cells in Optical Stretching

To extract the mechanical properties of cells from the deformation responses, a theoretical approach should be developed. The stretching operations of biological cells meet the inherent restrictions in the mechanical model developed previously [35–37]. The deformation behavior of a cell is mainly determined by its membrane and the underlying cytoskeleton network, which can be represented by a thin membrane. According to membrane theory, the quasi-static equilibrium equations can be used to describe the force balance of a cell membrane, expressed by

$$\frac{\partial T_m}{\partial \lambda_m}\lambda_m' + \frac{\partial T_m}{\partial \lambda_c}\lambda_c' = \frac{r'}{r}(T_c - T_m) \tag{12.2}$$

$$K_m T_m + K_c T_c = \sigma_n, \tag{12.3}$$

where λ_m and λ_c, T_m and T_c, and K_m and K_c are the principal stretch ratios, tensions, and curvatures, respectively [35]. σ_n is the membrane stress applied in the normal direction of the deformed cell surface. The prime denotes the derivative with respect to the angle ψ. The indices m and c refer to the corresponding component in the meridian and circumferential directions of the deformed membrane, respectively. According to the coordinate definition (Fig. 12.6), the equilibrium equations could be further developed as follows.

In the contact region, the governing equations are as follows:

$$\lambda_m' = \frac{\lambda_m}{\lambda_c \sin\psi}\left(\frac{f_3}{f_1}\right) - \left(\frac{\lambda_m - \lambda_c \cos\psi}{\sin\psi}\right)\left(\frac{f_2}{f_1}\right), \tag{12.4}$$

$$\lambda_c' = \frac{\lambda_m - \lambda_c \cos\psi}{\sin\psi}. \tag{12.5}$$

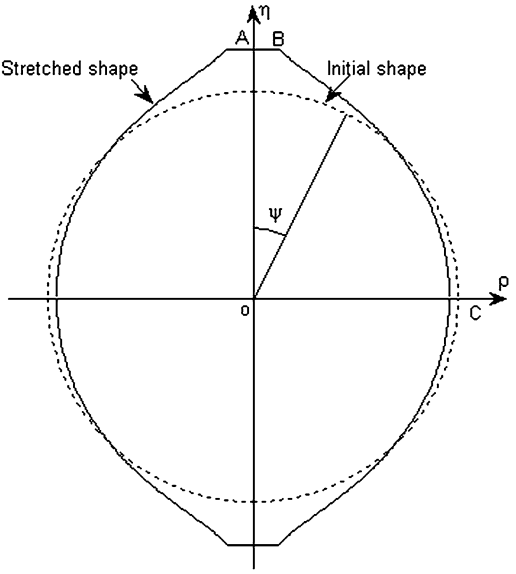

Fig. 12.6 Coordinate definition before and after optical stretching. Reprinted with permission from [6]

In the noncontact region, the governing equations are as follows:

$$\lambda'_m = \left(\frac{\delta\cos\psi - \omega\sin\psi}{\sin^2\psi}\right)\left(\frac{f_2}{f_1}\right) + \left(\frac{\omega}{\delta}\right)\left(\frac{f_3}{f_1}\right), \tag{12.6}$$

$$\delta' = \omega, \tag{12.7}$$

$$\omega' = \frac{\lambda'_m\omega}{\lambda_m} + \frac{({\lambda_m}^2 - \omega^2)}{\delta}\left(\frac{T_c}{T_m}\right) - \frac{\lambda_m({\lambda_m}^2 - \omega^2)^{1/2}\sigma_n r_0}{T_m}, \tag{12.8}$$

where $\delta = \lambda_c \sin\psi$, $\omega = \delta'$, $f_1 = \frac{\partial T_m}{\partial \lambda_m}$, $f_2 = \frac{\partial T_m}{\partial \lambda_c}$, $f_3 = T_c - T_m$, and r_0 is the initial cell radius.

The principal tensions T_m and T_c could be expressed as functions of the principal stretch ratios and the mechanical properties of the cell. Mooney–Rivlin material was adopted to describe the characteristics of membranes. The principal tensions were expressed as follows:

$$\begin{cases} T_m = 2h_0C\left(\dfrac{\lambda_m}{\lambda_c} - \dfrac{1}{(\lambda_m\lambda_c)^3}\right)\left(1 + \alpha\lambda_c^2\right) \\ T_c = 2h_0C\left(\dfrac{\lambda_c}{\lambda_m} - \dfrac{1}{(\lambda_m\lambda_c)^3}\right)\left(1 + \alpha\lambda_m^2\right) \end{cases}, \tag{12.9}$$

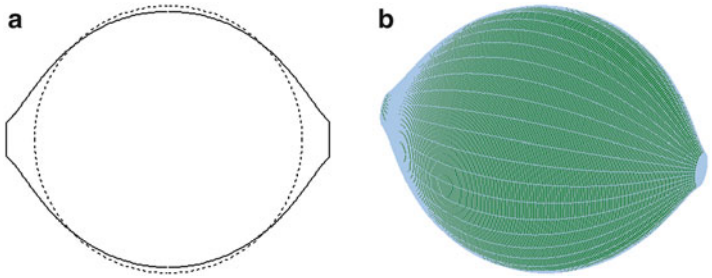

Fig. 12.7 Calculated cell shapes after optical stretching. (**a**) Two-dimensional shape, (**b**) three-dimensional shape. The *dotted line* in (**a**) denotes the initial cell shape. Reprinted with permission from [6]

where C and α are material constants and h_0 is the initial thickness of cell membrane. For homogeneous, isotropic, and incompressible elastic material, $C = E/6(1+\alpha)$, where E is the elastic modulus.

It was assumed that the interactions in the two contact areas were similar, which made the deformed cell shape axisymmetric. Because of dual symmetry, only a quarter of the cell shape was needed to be analyzed. During cell stretching, the cell volume kept constant, i.e., $4/3\pi {r_0}^3 = 2\pi {r_0}^3 \int_{\psi_B}^{\psi_C} \sqrt{{\lambda_m}^2 - \delta'^2}\delta^2 \mathrm{d}\psi$, where the left and right terms denote the cell volume before and after deformation. By using the boundary conditions, the governing equations could be solved through the standard 4-order Runge–Kutta method [38]. The deformed cell shapes, T_m and T_c, were then acquired. The cell deformation was subsequently obtained. According to the force balance in the equatorial plane, the stretching force could also be expressed as follows:

$$F = 2\pi T_{mC}\rho_C - \pi\sigma_n {\rho_C}^2 \tag{12.10}$$

$$d = 2\eta_B - 2r_0, \tag{12.11}$$

where the subscripts B and C denote the actual positions as shown in Fig. 12.6, respectively.

Figure 12.7 illustrates the calculated cell shape after stretching. Given the material constants C and α, the relationship between the stretching force and the induced axial deformation was unique and determinate. Force–deformation curves with different slopes indicated different cell stiffness.

12.5 Biomechanical Characterization and Biomedical Applications

12.5.1 Mechanical Characterization of Biological Cells

According to the theoretical model described above, the relationship between stretching force and cell deformation was established if the mechanical properties were known. By comparing the modeling results to the experimental data, the mechanical properties of cells could be characterized. Here, we adopted a deviation parameter δ to measure the fitness between the mechanical modeling and the experimental data, which was defined as [39]

$$\delta = \frac{1}{n}\sum_{i=1}^{n}\left[\frac{F_{\mathrm{e}}(i) - F_{\mathrm{s}}(i)}{F_{\mathrm{e}}(i)}\right]^2, \tag{12.12}$$

where n is the number of the sampled experimental results, $F_{\mathrm{e}}(i)$ is the ith experimental force value, and $F_{\mathrm{s}}(i)$ is the corresponding modeling force. Given the material parameters, the value of δ could be known. The best fitness was realized when δ was minimized and then the mechanical properties of biological cells could be identified.

12.5.2 Characterizing the Mechanical Properties of Human Red Blood Cells Under Different Osmotic Conditions

Human RBC are responsible for the transport of oxygen and carbon dioxide. We first adopted optical tweezers technology to study the cell mechanics of human RBC under various osmotic conditions [6]. RBC exhibited distinct morphologies when suspended in these solutions with different tonicities, as shown in Fig. 12.8. The cell radii were measured as 3.3 μm, 3.65 μm, and 3.75 μm for RBC in hypotonic, isotonic, and hypertonic solutions, respectively. The modeling relationship between the stretching forces and the induced axial deformations could be obtained based on the cell modeling method for spherical RBC in hypotonic condition. Note that finite element method was used to model the deformation of biconcave RBC in isotonic and hypertonic solutions, because the complex biconcave shape did not fulfill the requirement of the cell model developed above. When the deviation parameter δ between the experiments and the cell modeling was minimized, the most appropriate values of C and α were obtained. The elastic modulus E was then calculated by the relation $E = 6C(1 + \alpha)$.

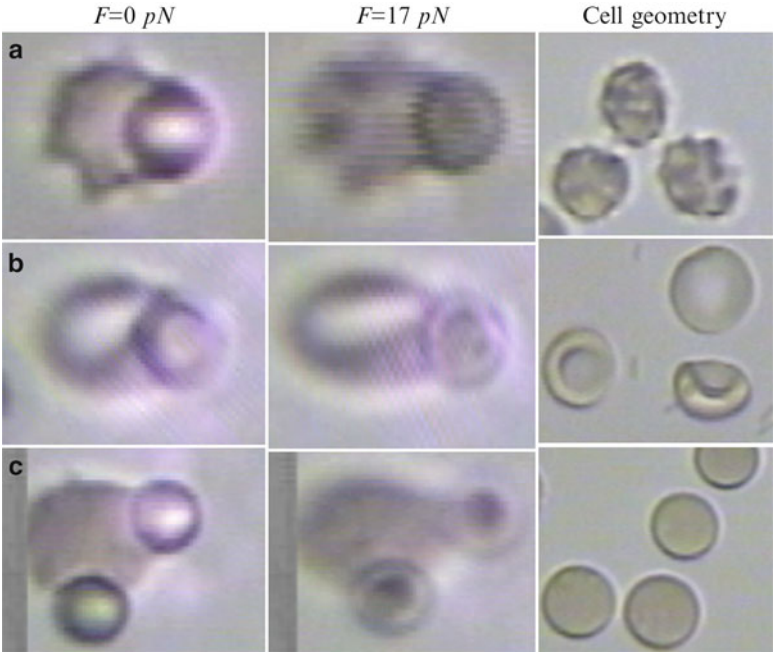

Fig. 12.8 Comparisons of the deformation behaviors of human RBC in different osmotic conditions. (**a**), (**b**), and (**c**) represents the deformation behavior and the stretched cell shape in hypertonic, isotonic, and hypotonic solutions, respectively. The stretching force F is 0 and 17 pN for the *left* and *middle columns*, respectively. The *right column* shows the cell contours in different osmotic conditions. Reprinted with permission from [6]

Figure 12.9 illustrates both the experimental data and the modeling results for RBC. When the elastic moduli E were given as 1.58 ± 0.4 kPa, 2.6 ± 0.3 kPa, and 4.8 ± 0.6 kPa, the values of δ were minimized and the modeling results agreed well with the experimental data in hypotonic, isotonic, and hypertonic conditions, respectively. By using the relation $\mu = Eh_0/2(1 + \nu)$ (the value of the Poisson ratio ν is 0.5), the shear modulus μ was calculated as 10.5 ± 2.7 μN/m, 17.3 ± 2.0 μN/m, and 32.0 ± 4.0 μN/m, respectively. The results in this study agree with previous reports. For example, the shear modulus of RBC in hypotonic condition was in the range of $2.5 \sim 10$ μN/m [5, 9, 18, 40, 41] and on the order of 13 μN/m in isotonic condition [16, 31]. The results also indicate that the shear modulus of human RBC increases as the osmolarity of the solution increases, which is consistent with some other researches. For example, the area dilation modulus and shear modulus of RBC in the isotonic buffer were higher than in the hypotonic buffer [40]. Various osmotic conditions led to great difference in the stiffness of RBC [42]. Moreover, osmotic stress exhibited significant effect on other types of cells, such as articular chondrocytes [43], MDCK cells [44], and neutrophils [45].

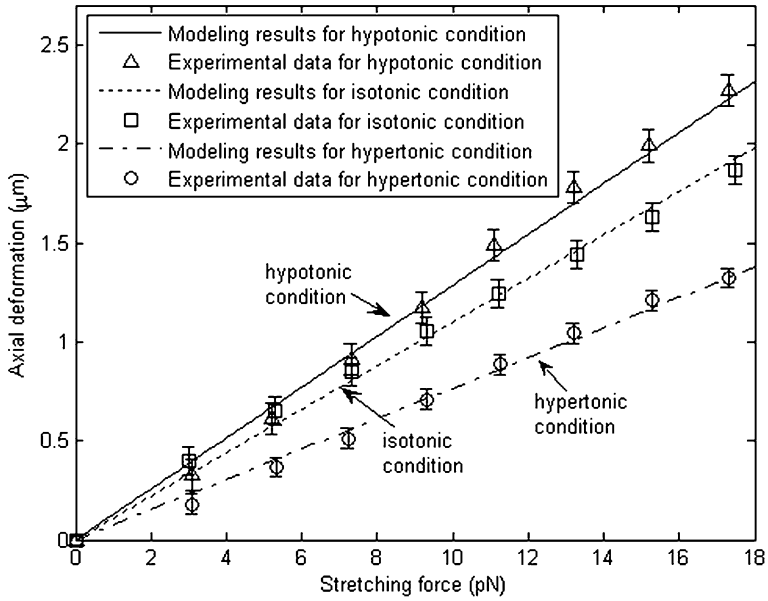

Fig. 12.9 Comparisons of the experimental data and the modeling results for human RBC in different osmotic conditions. The *solid*, *dotted*, and *dash–dot lines* denote the modeling results, while the *triangle*, *square*, and *circle* denote the experimental data. Reprinted with permission from [6]

12.5.3 Studying Cell Mechanics of Myeloblasts from Patients with Acute Myeloid Leukemia

AML is characterized by the abnormal increase of myeloblasts in blood and bone marrow. We now report our study on cell mechanics of myeloblasts from AML patients [46]. The elasticity of myeloblasts was measured separately in terms of $CD34^+$ expression. The experiments were repeated three times, where $62 \sim 71$ $CD33^+CD34^+$ cells and $57 \sim 63$ $CD33^+CD34^-$ cells were tested in total during the stretching experiments. No significant difference was found in cell sizes of these two populations, i.e., 10.1 ± 1.0 μm and 10.6 ± 1.4 μm for the diameter of $CD33^+CD34^+$ and $CD33^+CD34^-$ cells, respectively. Typical deformation responses of $CD33^+CD34^+$ and $CD33^+CD34^-$ cells are shown in Fig. 12.10. Cells are deformed more severely as the stretching force increases. It can be seen that the deformation of AML $CD33^+CD34^+$ cells is much larger than that of $CD33^+CD34^-$ cells, which suggests that there exists significant difference in the deformability of AML cell population.

Figure 12.11 shows the quantitative analysis of the deformation behaviors of AML $CD33^+CD34^+$ and $CD33^+CD34^-$ cells. It can be seen that the deformation of $CD33^+CD34^+$ cells varies over a relatively wide range compared to that of

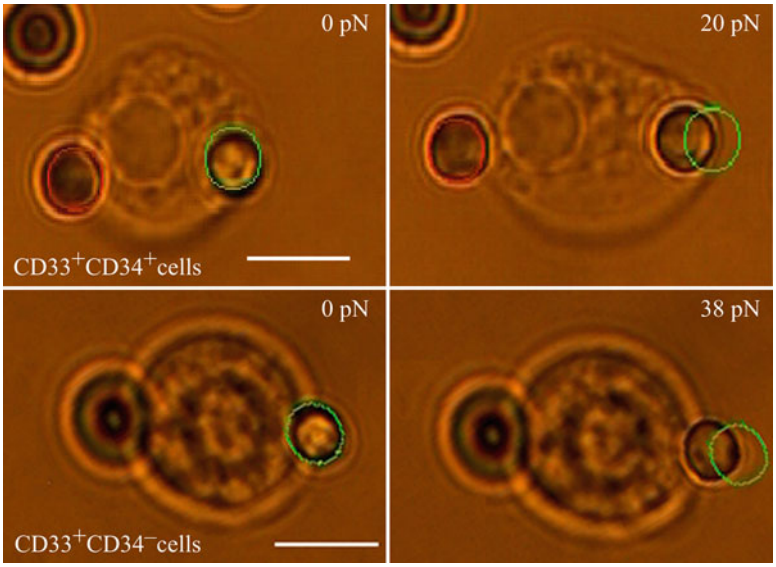

Fig. 12.10 Different deformation behaviors of $CD33^+CD34^+$ (*top panel*) and $CD33^+CD34^-$ cells (*low panel*) from patients with AML. The *scale bar* is 5 μm

$CD33^+CD34^-$ cells. This finding may suggest that AML $CD34^+$ fraction may contain several cell subpopulations, which are heterogeneous from the perspective of cell mechanics, in particular cell deformability. Nevertheless, all the measurement results show that the induced deformation of $CD33^+CD34^+$ cells is greater than $CD33^+CD34^-$ cells under the same stretching force, indicating that the primitive $CD33^+CD34^+$ cells are significantly softer, i.e., $CD34^+$ cells exhibit much higher deformability. Additionally, both $CD33^+CD34^+$ and $CD33^+CD34^-$ cells displayed two-phase deformation behavior. In the first phase, AML cells responded quasi-linearly to the small optical force. When the force increased to some extent, AML myeloblasts exhibited "saturated" mechanical characteristics, i.e., the cell deformation entered into a plateau and the growth of the deformation lowered down. To evaluate the biomechanical properties of AML myeloblasts, the cell mechanical model described above was applied. The membrane tension was expressed as a linear function of the area dilation ratio γ, i.e., $T_m = T_c = k\gamma$, where k is the area compressibility modulus. The modeling deformation behaviors in cell stretching are also shown in Fig. 12.11. Based on this model, the elastic area compressibility modulus was characterized as 0.25 ± 0.15 N/m and 1.40 ± 0.71 N/m for $CD33^+CD34^+$ and $CD33^+CD34^-$ myeloblasts, respectively. This finding indicates that AML $CD33^+CD34^-$ cells are significantly stiffer than $CD33^+CD34^+$ cells.

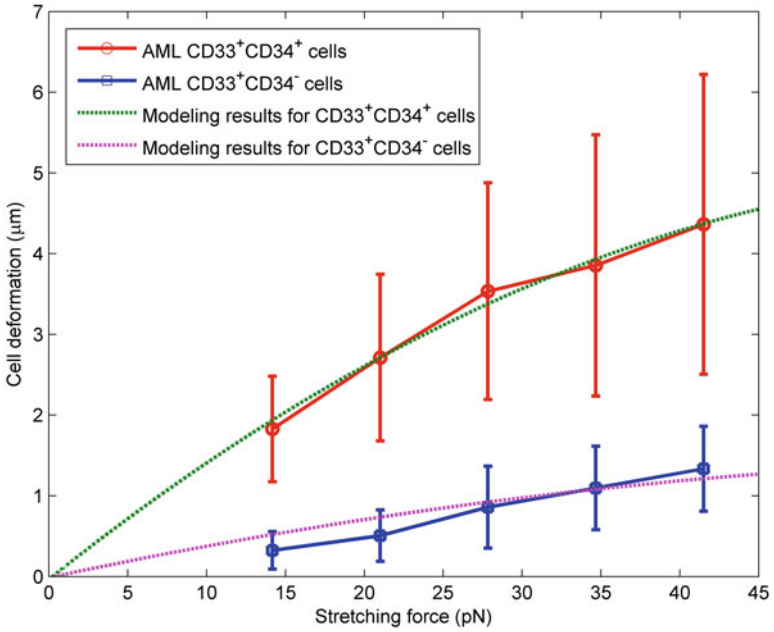

Fig. 12.11 Quantitative analysis of the cell stretching results of $CD33^{+}CD34^{+}$ and $CD33^{+}CD34^{-}$ cells from AML patients. The *error bar* denotes the standard deviation of the experimental results

12.6 Conclusions

In summary, this chapter introduces an approach to integrating optical tweezers technology into robotics manipulation for stretching single biological cells at micro/nano-precision level. To characterize the mechanical properties of cells from the mechanical responses, a theoretical approach was developed to model the deformation behavior of cells during manipulation. By minimizing the deviation between the mechanical modeling results and the experimental data, the mechanical properties could be identified. Further, we applied the proposed method to study the cell mechanics of RBC and myeloblasts. The results show that human RBC exhibit higher mechanical stiffness in solutions with higher tonicity. Also, the myeloblasts from AML patients with different immunophenotypes display distinct mechanical properties. Taken together, the study in this chapter demonstrates that robot-tweezers manipulation can be successfully utilized for cell mechanics study, in particular for biomechanical characterization.

References

1. Li PCH, Harrison DJ (1997) Transport, manipulation, and reaction of biological cells on-chip using electrokinetic effects. Anal Chem 69:1564–1568
2. Arai F, Ichikawa A, Ogawa M, Fukuda T, Horio K, Itoogawa K (2001) High-speed separation system of randomly suspended single living cells by laser trap and dielectrophoresis. Electrophoresis 22:283–288
3. Huang H, Sun D, Mills JK, Cheng SH (2009) Robotic cell injection system with vision and force control: towards automatic batch biomanipulation. IEEE Trans Robot 25:727–737
4. Iritani A (1991) Micromanipulation of gametes for in vitro assisted fertilization. Mol Reprod Dev 28:199–207
5. Henon S, Lenormand G, Richert A, Gallet F (1999) A new determination of the shear modulus of the human erythrocyte membrane using optical tweezers. Biophys J 76:1145–1151
6. Tan Y, Sun D, Wang J, Huang W (2010) Mechanical characterization of human red blood cells under different osmotic conditions by robotic manipulation with optical tweezers. IEEE Trans Biomed Eng 57:1816–1825
7. Stromberg A, Ryttsen F, Chiu DT et al (2000) Manipulating the genetic identity and biochemical surface properties of individual cells with electric-field-induced fusion. Proc Natl Acad Sci USA 97:7–11
8. Hochmuth RM (2000) Micropipette aspiration of living cells. J Biomech 33:15–22
9. Evans EA (1973) New membrane concept applied to the analysis of fluid shear- and micropipette-deformed red blood cells. Biophys J 13:941–954
10. Dimitriadis EK, Horkay F, Maresca J, Kachar B, Chadwick RS (2002) Determination of elastic moduli of thin layers of soft material using the atomic force microscope. Biophys J 82: 2798–2810
11. Sen S, Subramanian S, Discher DE (2005) Indentation and adhesive probing of a cell membrane with AFM: theoretical model and experiments. Biophys J 89:3203–3213
12. Puig-de-Morales-Marinkovic M, Turner KT, Butler JP, Fredberg JJ, Suresh S (2007) Viscoelasticity of the human red blood cells. Am J Physiol Cell Physiol 293:C597–C605
13. Ziemann F, Radler J, Sackmann E (1994) Local measurements of viscoelastic moduli of entangled actin networks using an oscillating magnetic bead micro-rheometer. Biophys J 66:2210–2222
14. Guck J, Ananthakrishnan R, Mahmood H, Moon TJ, Cunningham CC, Kas J (2001) The optical stretcher: a novel laser tool to micromanipulate cells. Biophys J 81:767–784
15. Guck J, Schinkinger S, Lincoln B, Wottawah F, Ebert S, Romeyke M, Lenz D, Erickson HM, Ananthakrishnan R, Mitchell D, Kas J, Ulvick S, Bilby C (2005) Optical deformability as an inherent cell marker for testing malignant transformation and metastatic competence. Biophys J 88:3689–3698
16. Dao M, Lim CT, Suresh S (2003) Mechanics of the human red blood cell deformed by optical tweezers. J Mech Phys Solids 51:2259–2280
17. Jauffred L, Callisen TH, Oddershede LB (2007) Visco-elastic membrane tethers extracted from *Escherichia coli* by optical tweezers. Biophys J 93:4068–4075
18. Sleep J, Wilson D, Simmons R, Gratzer W (1999) Elasticity of the red cell membrane and its relation to hemolytic disorders: an optical tweezers study. Biophys J 77:3085–3095
19. Cross SE, Jin YS, Rao J, Gimzewski JK (2007) Nanomechanical analysis of cells from cancer patients. Nat Nanotechnol 2:780–783
20. Darling EM, Zauscher S, Block JA, Guilak F (2007) A thin-layer model for viscoelastic, stress-relaxation testing of cells using atomic force microscopy: do cell properties reflect metastatic potential? Biophys J 92:1784–1791
21. Ingber DE (2003) Mechanobiology and diseases of mechanotransduction. Ann Med 35: 564–577
22. Mills JP, Diez-Silva M, Quinn DJ et al (2007) Effect of plasmodial RESA protein on deformability of human red blood cells harboring Plasmodium falciparum. Proc Natl Acad Sci USA 104:9213–9217

23. Suresh S, Spatz J, Mills JP, Micoulet A, Dao M, Lim CT, Beil M, Seufferlein T (2005) Connections between single-cell biomechanics and human disease states: gastrointestinal cancer and malaria. Acta Biomater 1:15–30
24. Lee GYH, Lim CT (2007) Biomechanics approaches to studying human diseases. Trends Biotechnol 25:111–118
25. Trickey WR, Lee GM, Guilak F (2000) Viscoelastic properties of chondrocytes from normal and osteoarthritic human cartilage. J Orthop Res 18:891–898
26. Lekka M, Laidler P, Gil D, Lekki J, Stachura Z, Hrynkiewicz AZ (1999) Elasticity of normal and cancerous human bladder cells studied by scanning force microscopy. Eur Biophys J 28:312–316
27. Faria EC, Ma N, Gazi E, Gardner P, Brown M, Clarke NW, Snook RD (2008) Measurement of elastic properties of prostate cancer cells using AFM. Analyst 133:1498–1500
28. Ralis SJ, Vikramaditya B, Nelson BJ (1998) Visual servoing frameworks for microassembly of hybrid MEMS. Proc SPIE 3519:70–79
29. Menciassi A, Eisinberg A, Carrozza MC, Dario P (2003) Force sensing microinstrument for measuring tissue properties and pulse in microsurgery. IEEE ASME Trans Mechatron 8:10–17
30. Sun Y, Nelson BJ (2002) Biological cell injection using an autonomous microrobotic system. Int J Robotic Res 21:861–868
31. Mills JP, Qie L, Dao M, Lim CT, Suresh S (2004) Nonlinear elastic and viscoelastic deformation of the human red blood cell with optical tweezers. Mech Chem Biosyst 1: 169–180
32. Wu Y, Sun D, Huang W (2011) Mechanical force characterization in manipulating living cells with optical tweezers. J Biomech 44:741–746
33. Svoboda K, Block SM (1994) Biological applications of optical forces. Annu Rev Biophys Biomol Struct 23:247–285
34. Qu Y, Cui C, Chen S, Li J (2005) A fast subpixel edge detection method using Sobel-Zernike moments operator. Image Vis Comput 23:11–17
35. Tan Y, Sun D, Huang W, Cheng SH (2008) Mechanical modeling of biological cells in microinjection. IEEE Trans Nanobiosci 7:257–266
36. Tan Y, Sun D, Huang W (2010) Mechanical modeling of red blood cells during optical stretching. J Biomech Eng Trans ASME 132:044504
37. Tan Y, Sun D, Huang W, Cheng SH (2010) Characterizing mechanical properties of biological cells by microinjection. IEEE Trans NanoBioSci 9:171–180
38. Fausett L (2003) Numerical methods: algorithms and applications. Prentice Hall, Upper Saddle River, NJ
39. Schmidt CE, Chen T, Lauffenburger DA (1994) Simulation of integrin-cytoskeletal interactions in migrating fibroblasts. Biophys J 67:461–474
40. Lenormand G, Henon S, Richert A, Simeon J, Gallet F (2001) Direct measurement of the area expansion and shear moduli of the human red blood cell membrane skeleton. Biophys J 81:43–56
41. Hochmuth RM, Waugh RE (1987) Erythrocyte membrane elasticity and viscosity. Annu Rev Physiol 49:209–219
42. Daily B, Elson EL (1984) Cell poking: determination of the elastic area compressibility modulus of the erythrocyte membrane. Biophys J 45:671–682
43. Guilak F, Erichson GR, Ting-Beall HP (2002) The effects of osmotic stress on the viscoelastic and physical properties of articular chondrocytes. Biophys J 82:720–727
44. Steltenkamp S, Rommel C, Wegener J, Janshoff A (2006) Membrane stiffness of animal cells challenged by osmotic stress. Small 2:1016–1020
45. Sung KL, Schmid-Schonbein GW, Skalak R, Schuessler GB, Usami S, Chien S (1982) Influence of physicochemical factors on rheology of human neutrophils. Biophys J 39: 101–106
46. Tan Y, Leung AYH, Wang K, Fung TK, Sun D (2011) Nanomechanical characterization of myeloblasts from cancer patients with optical tweezers. IEEE Nanotechnol Mag 3:17–21

Part IV
Inside the Body Nanorobotic Applications

Chapter 13
Propulsion and Navigation Control of MRI-Guided Drug Delivery Nanorobots

Laurent Arcese, Matthieu Fruchard, and Antoine Ferreira

Abstract The present chapter discusses the control design of MRI-guided robots in the vasculature to achieve targeted therapy through precise drug delivery. Such robots consist of a polymer-binded aggregate of nanosized ferromagnetic and drug particles that can be propelled by the gradient coils of an MRI device. The feasibility of the concept has been largely studied in the literature, but few works address the nonlinear control issues related to a fine modeling of the forces acting on the robot. Different solutions have been proposed for the design of a microrobot, and the principal ones are here exposed. In this chapter, a fine modeling is developed with concerns about the constraints of the application. The notion of optimal trajectory derived from the nonlinear model is presented and shows that one can exploit the complexity of such a model to optimize the tracking performances. The design of a Lyapunov controller is addressed, with the synthesis of an adaptive backstepping law that ensures a fine tracking despite some modeling errors and estimates some key uncertain physiological parameters. The design of a nonlinear observer for reconstructing the robot's unmeasured velocity is also exposed. The benefits of this fine modeling and the use of advanced control law and observer are illustrated by simulations. Finally, perspectives and open problems in the field of MRI-guided robots' control are discussed.

L. Arcese • M. Fruchard
Laboratoire PRISME, University of Orleans, 63 Av de Lattre de Tassigny,
18020, Bourges cedex, France
e-mail: laurent.arcese@bourges.univ-orleans.fr; matthieu.fruchard@bourges.univ-orleans.fr

A. Ferreira (✉)
Laboratoire PRISME, University of Orleans, ENSI de Bourges, 88 Bd Lahitolle,
18000, Bourges, France
e-mail: antoine.ferreira@ensi-bourges.fr

C. Mavroidis and A. Ferreira (eds.), *Nanorobotics*, DOI 10.1007/978-1-4614-2119-1_13,
© Springer Science+Business Media New York 2013

13.1 Introduction

Minimally invasive cancer therapy is currently an active research area since related techniques can both reach remote places without operating and reduce drug or radiation dose. Thereby, they result in lessened medical side effects and a better therapeutic efficiency and safety. Among these approaches, cathetered embolization, focused ultrasound, or radiotherapy [1] is commonly used, though restricted to accessible places or limited by the non-ability to target precisely tumor cells. These drawbacks can be avoided by targeted chemotherapy, which relies on a selective delivery using either drugs linked to antibodies specific for tumor-associated antigenes [2], or drugs carried by autonomous untethered microrobots controlled so as to reach the tumor. However, it proves difficult to embed actuators sufficiently powerful to propel such robots in the cardiovascular system, especially when swimming against the blood flow. The first propulsion scheme is referred to as magnetic bead: Thrust is ensured by pulling the magnetic bead using the magnetic force related to gradients of the external field. This concept was first studied in the eighties using magnets [3] and after by [4, 5] or superconducting magnets [6, 7].

The last innovation in this domain has been provided by the Ecole Polytechnique de Montreal, Canada, where the basic idea is the use of magnetic gradients provided by a clinical MRI device to pull the beads [8, 9]. Such a system combines several advantages: The MRI device provides both fine observation of the scene (thanks to the MRI imager) and actuation of the bead; besides, it makes the implementation easier, since MRI devices are widely implanted in hospitals. This approach is well developed at millimeter scale, since low-level multiplexed controllers and observers have been developed [10], and in vivo experiments have been leaded on a living animal [11] (though the blood flow had been stopped using a balloon catheter).

The main drawback of this approach results from strong limitations on the magnetic gradient amplitude in available MRI devices. As magnetic forces used for propelling are volumetric, whereas the drag force is—at best—dependent on the bead's area, the smaller the bead, the higher the required control forces with respect to hydrodynamic perturbations. Consequently, this approach is well-conditioned for beads whose radius is up to a few dozen micrometers with actual MRI devices. At lower scales, it is necessary either to use additional coils to supply higher gradients [12] or to consider other approaches. MRI system upgraded with additional gradient steering coils in order to increase standard MRI gradient amplitudes (100–500 mT) is currently investigated by the authors in [13]. Spatial resolution of current medical imagers is also an important limitation, especially within real-time constraints [14, 15]. It has been demonstrated in [11] that clinical MRI devices are compatible with real-time control loops, at least for millimeter-scaled robots, since the authors implement the tracking routine within 20 ms. However, real-time imaging limitations induced by clinical MRI is far more challenging for smaller robots.

Another issue is referred to as biomimetic robots using flagella. Two main designs can be distinguished depending on the flagellum design: elastic- or helical-

flagellated robot. The former is illustrated a bead fixed either to a paramagnetic beating flagellum [16], either to an elastic tail [17, 18], thus imitating the motion of eukariotic bacteria. In the first case, the flagella is an elastic rod consisting of magnetic particles that a periodic transverse magnetic field causes to bend and pivot, inducing a backward motion. In the second case, an oscillating magnetic field induces a motion of the flagellum anchor point on the bead: The flagellum thus induces thrust thanks to elastohydrodynamical hyperdiffusion dynamics. The latter design exploits the corkskrew effect induced by rotating a bead fixed to a helical coil [19], like prokariotic bacteria. In this case, the coil is not subjected to any deformation: Propulsion is provided by the torque induced by a rotating magnetic field on the bead. In a Stokes flow, swimming is thus obtained through a corkscrew effect in the fluid [20]: The higher the rotation frequency of the magnetic field, the higher the thrust. Even if these two swimming methods result from different motions, they are both based on converting mechanical power from the magnetic torque to produce the motion. These techniques are well suited for nanorobots since they move at low Reynolds number and are proved more efficient than bead pulling for robots whose radius is down to a few micrometers [21], but prove difficult to implement on classical MRI devices because of timevarying external field. In [22], the flagella of magnetotactic bacteria have been exploited to provide propulsion, while steering has been achieved by inducing a torque on a chain of magnetic nanoparticles—called magnetosomes—embedded in the bacterium. Despite promising, since velocities reached by such systems are about ten times higher than velocities of biomimetic robots of similar dimensions, this recent design faces some unsolved problems leading to a reduced efficiency as reported in [22]. In fact, some problems are not solved yet [23], such as side effects of the fixation of the magnetic material on or in the bacteria or Joule heating that reduces the bacteria's efficiency and velocity. This technique can also be used in addition to the classic magnetic pulling.

In [5], the authors suggest that, under a given size, helical propelling is better than pulling at low Reynold's number. The comparison is still at the benefit of biomimetic robots as the distance to the magnetic coils increases, which is likely to occur when navigating in the body. However, the assumption of navigating at low Reynold's number can be violated if the rotation frequency becomes too high. Reversing direction can also get complicated because of the rigid rod. Furthermore, this actuation approach is limited in practice due to the difficulty of using it within an MRI device. In fact, additional coils providing a rotational magnetic field in an MRI device are a delicate matter, since the precision of an MRI scanner relies on a constant magnetic field. This implies the need for an additional imaging system so as to estimate the nanocapsule's pose; otherwise, no closed-loop control will be achievable.

As the smallest capillaries are under a half-dozen micrometers large, the size of the robot should not exceed 100 nm [24] to avoid embolization hazards and to drive the drugs as close as possible to the tumor. However, forces induced by clinical MRI coils are not strong enough to steer nanorobots in larger vessels. Besides, hydrodynamic wall effects show that a partial vessel occlusion by the robot results

in an optimal ratio between the robot's and the vessel's radii [8, 25]. A natural way of overcoming the MRI limitations is thus to make the radius of the robot decrease as it enters smaller vessels, for example, with a microrobot made of a degradable polymer-binded aggregate of magnetic particles. The micro-aggregates resulting from such a controlled disintegration are too small to be directly visible by the MRI scanner; however, the local magnetic perturbation caused by a swarm of small magnetic particles can be used to locate them, provided that their concentration is sufficient. This raises a crucial issue: the need to control a cloud of robots in order to keep the system observable, which is more difficult than controlling a single robot, since interactions between parts of this multiagent system have to be modeled [25].

This chapter is organized as follows. Section 13.2 introduces the advantages and constraints inherent to the use of a clinical MRI device for propelling a therapeutic robot in the human vasculature. Section 13.3 provides the core of the chapter: a precise modeling of the forces acting on the robot, which includes wall effects (parabolic profile of blood flow, pulsatile arterial walls and effect of the ratio of robot's on vessel's radii), wall interactions (van der Waals and electrostatic forces), and non-Newtonian behavior of blood. The confrontation between the modeling and the constraints introduced in Sect. 13.2 is then discussed to pinpoint sizing and design issues. An optimal trajectory is then derived from the model so as to address some sizing problems and especially to minimize the control effort so as to avoid reaching the MRI actuators saturation. Then Sect. 13.4 is devoted to the design of an adaptive backstepping controller whose aim is to ensure a null error between the robot's trajectory and an optimal reference trajectory deduced from the nonlinear model. This control design based on the backstepping approach recently developed in [26] ensures Lyapunov stability. In Sect. 13.5, the high-gain observer used to reconstruct the state is synthesized. Since the imager measures only the position of the robot, an observer is needed to rebuild the unmeasured robot's velocity that is required to implement the backstepping control law developed in the previous section. Section 13.6 provides simulation experiments that illustrate the performances of the controller-observer pair in a small artery with minor bifurcations. In particular, the high-gain observer, designed so as to ensure robustness to noise measurement, greatly smoothes the output and in turn improves the overall tracking efficiency. Finally, Sect. 13.7 concludes the chapter by summarizing the main aspects of the studied MRI-based nanorobotic drug delivery system, the challenges encountered, and further perspectives.

13.2 Constraints on MRI-Guided Devices in the Vasculature

The relevance of using clinical MRI devices is twofold: The machines are widely spread in hospitals, and their imaging ability yields fine observation of the robot's position in the cardiovascular system. However, using these devices dedicated to observation for control purpose induces some constraints that we present here together with physiological constraints, since the design of a controllable robot is related to this set of limitations.

13.2.1 MRI Constraints

Hydrogen atoms, as the main component of water, are widely spread in the human body, and various tissues can be identified with respect to their hydrogen's density and stability. MRI imaging is based on exciting these atoms, and let them relax to equilibrium to obtain a map of their repartition and properties and thus to get an image of the body tissues in the observed slice. More precisely, clinical MRI imaging can be broken into four major steps. First, the permanent magnet generates a strong and uniform magnetic field in order to align the spin magnetic moment of hydrogen nuclei (protons) along this field. Once polarized, protons are excited by a pulsing RF coil at Larmor frequency to induce a resonance absorption, which modifies the precession motion of the spin. Third, RF excitation is stopped and protons relax to their equilibrium state, producing a free induction decay signal (FID) in the RF coil after some relaxing times. Meanwhile, gradient coils are used first to select the slice to be observed during the polarization step and secondly to perform a phase shift/frequency encoding during the readout step, performing a 2D position encoding within the slice. Finally, the slice image is obtained thanks to inverse Fourier transforms applied on the measured FID. Precision of an MRI imaging system is strongly related to the uniformity and strength of the main magnet on the one hand, since they decrease the signal to noise ratio. On the other hand, speed and strength of the gradient coils (set by their duty cycle) also affect precision and scanning speed of the imager.

The use of MRI as imaging modality for 3D image guidance of endovascular procedures is of great interest. As aforementioned, endovascular navigation is made possible by integrating propulsion and tracking events using time multiplexing. As stated previously, we have seen how the clinical MRI can be utilized to provide microrobots with locomotion capabilities. The same equipment can be utilized for localization by combining imaging/tracking procedures for precise navigation of an untethered interventional robot [10]. The main drawback of MRI localization is that the choice of material for fabrication of the microrobot is limited. Ferromagnetic objects cause image artifacts that are sometimes larger than the object itself to be localized, even though information contained in spatial gradients can overcome this limitation [27]. Efforts to increase MRI sensitivity have focused on development of new magnetic core materials or in the improvement in nanoparticle size or clustering. An emerging theme in nanoparticle research is to control biological behavior and/or electromagnetic properties by controlling shape. Swarms of nanoparticles were localized in an MRI using contrast agents [28] and swarms of magnetotatic bacteria as a single object in [22]. In [29], the authors found that a nanostructure with an elongated assembly of nanoparticles (referred to as nanoworms) influences their efficacy both in vitro and in vivo by enhancing their magnetic relaxivity in the MRI device. In addition to the trade-off between refresh rate and duty cycle of the propulsion gradients, the repetition time of the tracking sequence is another constraint to be taken into account during imaging and tracking sequences [10].

Table 13.1 Properties of ferromagnetic materials

Material	Magnetization at saturation ($A\,m^{-1}$)	Density ($kg\,m^{-3}$)
Permendur	$1.95 \quad 10^6$	8,200
Carbon steel 1,010/1,020	$1.72 \quad 10^6$	7,874
97Fe-3Si	$1.60 \quad 10^6$	7,700
NdFeB-35	$1.23 \quad 10^6$	7,500
Alfenol	$0.63 \quad 10^6$	6,500
Supermalloy	$0.79 \quad 10^6$	8,800
$Fe_3\,O_4$	$0.35 \quad 10^6$	5,200

Magnetization values issued from [30, 31]

Using a clinical MRI device thus induces some constraints. Firstly, the uniform magnetic field produced by the permanent magnet of the MRI device is so high that the spin of magnetic particles is aligned with it. Working on clinical standard MRI devices, where this uniform field is static, thus makes it difficult the use of beating flagellated structures; hence, the choice of robot's propelling design like bead pulling or magnetotactic bacteria is more adequate. Secondly, to combine imaging and control, it is necessary to develop a multiplexing approach. Thirdly, real-time imaging abilities of clinical MRI have been proven compatible with a 1.5 mm radius bead within a 1.5 T clinical MRI [11], using a gradient echo scan, with a 20 ms tracking routine. However, imaging at one order of magnitude smaller, that is, some hundreds micrometers radius bead, is still a challenging issue within real-time constraints, since devoted closed-loop approaches are no more stable if the tracking routine exceeds 40 ms. At the present time, such a spatial resolution requires some seconds on clinical MRI, but the next generation of MRI devices, together with signal processing and computational progress in this area, will greatly improve the MRI real-time performances. Lastly, these clinical MRI are equipped with gradient coils that are not designed for propulsion, but for imaging purpose: The latest MRI devices limitation on magnetic gradient coils is around $80\,mT\,m^{-1}$. Since magnetic force is volumetric, whereas forces to be counterbalanced (drag, electrostatic, etc.) are at best dependent on the area, this limitation on actuators induces a lower bound on the radius of the agglomerate to be controlled: Below this bound, the robot could no more resist external forces and is thus conveyed by the flow. As this lower bound is strongly dependent on the magnetization at saturation of the magnetic material embedded by the robot (the higher, the better), Table 13.1 gives some values for different magnetic materials that can be used in the agglomerate.

13.2.2 Physiological Constraints

Therapeutic nanorobots can access any remote part of the human body by navigating in the human vasculature. It is thus necessary to avoid any embolization that could injure the patient. That implies the use of nanoscaled robots. However, limitation on

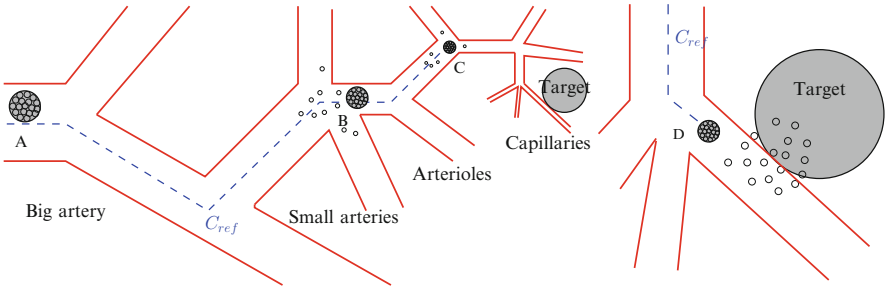

Fig. 13.1 A biodegradable polymer-binded aggregate in the vasculature: The size of the agglomerate goes smaller as the robot enters smaller vessels to avoid embolization and to optimize the propelling force

Table 13.2 Human blood vessel characteristics: from aorta to vena cava, from [32, 33]

Type of blood vessel	Vessels's radius (mm)	Average flow's velocity (min to max) (mm s^{-1})
Aorta	12.5	400 (−200 to 1, 200)
Artery	5	100–400 (−50 to 500)
Large arteriole	0.5	1–100
Small arteriole	0.05	<50
Capillary	0.003	<1
Small veinule	0.01	<2
Large veinule	0.5	<3
Vein	2.5	3–50
Vena cava	15	50–200

Negative values of the flow stand for the flow back values in arterial vessels

the MRI actuators suggests, to the contrary, the design of microrobots. Hence, the idea of using microscaled robots made up of an agglomerate of magnetic nanoparticles. This agglomerate can be binded either by a biodegradable ligand or by self-assembly properties (local magnetic and surfacic forces) [25]. In large vessels, where the blood flow is the highest, the robot could thus benefit from an important propelling force so as to resist the blood drag; whereas, in small vessels where the flow is lower, it would avoid any injury caused by embolism or thrombosis. Finally, in the smaller vessels, the volumetric forces cannot counterbalance the drag, even if the flow velocity is low, and the drug release is thus helped by the disintegration of the agglomerate (see Fig. 13.1). The precision of the controlled targeting is mainly limitated by the spatial resolution of MRI devices, respectively, around point B for clinical MRI devices and until point C for μ-MRI devices on Fig. 13.1.

Since the control of such robots generically requires to resist the drag, Table 13.2 classifies different types of vessels and lists their size and average blood flow velocity.

Controlling such microrobots in the vasculature also raises safety concerns. The two main limitations are inadequate embolization and magnetic hazards. Designing the microrobot as a degradable polymer aggregate keeping an optimal ratio is an answer to the first issue. The second issue is mainly related to neurostimulation induced by using time-varying magnetic fields. At the present time, there are no worldwide regulations for time-varying magnetic gradients. Our works consequently deal with standard slew rates available on clinical MRI devices, but this point should be further investigated for future medical applications.

13.3 Modeling

The robot is a polymer-binded aggregate of ferromagnetic particles immersed in blood vessels. A 2D nonlinear model of the robot will be established. This model encompasses the different forces that affect the robot's motion as well as its electric interaction with the vessel's walls.

The translational and rotational motions of the robot are expressed by:

$$\begin{cases} m\dfrac{\mathrm{d}\mathbf{v}}{\mathrm{d}t} = \mathbf{F}_\mathrm{m} + \mathbf{F}_\mathrm{d} + \mathbf{W}_\mathrm{a} + \mathbf{F}_\mathrm{c} + \mathbf{F}_\mathrm{vdw} + \mathbf{F}_\mathrm{el}, \\ J\dfrac{\mathrm{d}\mathbf{w}}{\mathrm{d}t} = \mathbf{T}_\mathrm{m} + \mathbf{T}_\mathrm{d} + \mathbf{M}_\mathrm{c}, \end{cases} \tag{13.1}$$

where $\mathbf{v}$ and $\mathbf{w}$ are, respectively, the translational and rotational velocity of the robot and m and J its mass and moment of inertia. $\mathbf{F}_\mathrm{m}$, $\mathbf{F}_\mathrm{d}$, $\mathbf{W}_\mathrm{a}$, $\mathbf{F}_\mathrm{c}$, $\mathbf{F}_\mathrm{vdw}$, and $\mathbf{F}_\mathrm{el}$, respectively, denote the magnetic force produced by the MRI gradient coils ($\mathbf{F}_\mathrm{m}$), blood hydrodynamic drag force ($\mathbf{F}_\mathrm{d}$), apparent weight ($\mathbf{W}_\mathrm{a}$), the robot-to-wall contact force ($\mathbf{F}_\mathrm{c}$), the van der Waals force ($\mathbf{F}_\mathrm{vdw}$), and the electrostatic force ($\mathbf{F}_\mathrm{el}$). $\mathbf{T}_\mathrm{m}$, $\mathbf{T}_\mathrm{d}$, and $\mathbf{M}_\mathrm{c}$ denote, respectively, the magnetic torque, hydrodynamic drag torque, and the robot-to-wall contact moment.

In the rest of this chapter, we assume that the orientation of the robot does not change due to the magnetic torque which tends to align the magnetization of the robot along the external field since $\mathbf{T}_\mathrm{d}$ and $\mathbf{M}_\mathrm{c}$ are much smaller order than $\mathbf{T}_\mathrm{m}$.

To determine whether statistical mechanics or continuum mechanics formulations of fluid dynamics should be used, we refer to the dimensionless Knudsen number:

$$K_\mathrm{n} = \frac{k_\mathrm{b}T}{P\pi r^3 2^{5/2}}, \tag{13.2}$$

where T, k_b, and P, respectively, denote temperature, the Boltzmann constant, and pressure. In our case, the low value $K_\mathrm{n} \approx 10^{-13}$ ($\ll 10^{-3}$) ensures that the robot is large enough to neglect the effect of Brownian motion: The robot's motion is subjected to generic Navier-Stokes equations.

13.3.1 Forces Balance

13.3.1.1 Hydrodynamic Drag Force

Navier-Stokes equations are not well-suited for real-time applications. Under the assumption that the robot does not navigate in the heart or in the aorta, that is, if the fluid is dominated by laminar flow dynamics, a drag force modeling may be conveniently used as an approximation of hydrodynamic forces. Note that, even at low Reynolds numbers, the ruggedness of the blood vessel walls can generate local areas of turbulence that we will consider as disturbances on the blood flow velocity. The hydrodynamic drag force $\mathbf{F}_\mathrm{d}$ exerting on a spherical body is thus expressed as

$$\mathbf{F}_\mathrm{d} = -\frac{1}{2}\rho_\mathrm{f}\left[\frac{\|(\mathbf{v}-\mathbf{v}_\mathrm{f})\|}{\beta}\right]^2 AC_\mathrm{d}\frac{(\mathbf{v}-\mathbf{v}_\mathrm{f})}{\|(\mathbf{v}-\mathbf{v}_\mathrm{f})\|}, \tag{13.3}$$

where $\mathbf{v}-\mathbf{v}_\mathrm{f}$ denotes the relative velocity of the robot with respect to the fluid, A is the frontal area of the core, ρ_f is the density of the fluid, and β a dimensionless ratio related to wall effect caused by the vessel's occlusion by the robot [34]:

$$\beta = \frac{1-\lambda^{\alpha_0}}{1+\left(\frac{\lambda}{\lambda_0}\right)^{\alpha_0}}$$

with ratio $\lambda = 2r/D$ and D denoting the vessel's diameter (in meter). Parameters α_0 and λ_0 are functions of the Reynolds number but are commonly set to 1.5 and 0.29, respectively. The drag coefficient C_d, which is a function of the Reynolds number $\mathrm{Re} = \frac{2r\rho_\mathrm{f}|\mathbf{v}-\mathbf{v}_\mathrm{f}|}{\beta\eta}$, is given by [35]

$$C_\mathrm{d} = \frac{24}{\mathrm{Re}} + \frac{6}{1+\sqrt{\mathrm{Re}}} + 0.4.$$

In the case of blood, which exhibits a non-newtonian behavior, the fluid's viscosity η is a function of vessel's diameter d (in micron) and hematocrit rate h_d according to the following empirical relations [36]:

$$\eta = \frac{\eta_\mathrm{plasma}d^2}{(d-1.1)^2}\left[1+\frac{(\eta_{0.45}-1)d^2}{(d-1.1)^2}\frac{(1-h_d)^c-1}{(1-0.45)^c-1}\right]$$

with parameters η_plasma and $\eta_{0.45}$ denoting, respectively, the plasma's viscosity and the relative apparent blood's viscosity for a fixed discharge hematocrit of 0.45, given by

$$\eta_{0.45} = 6\,\mathrm{e}^{-0.085d} + 3.2 - 2.44\,\mathrm{e}^{-0.06d^{0.645}}.$$

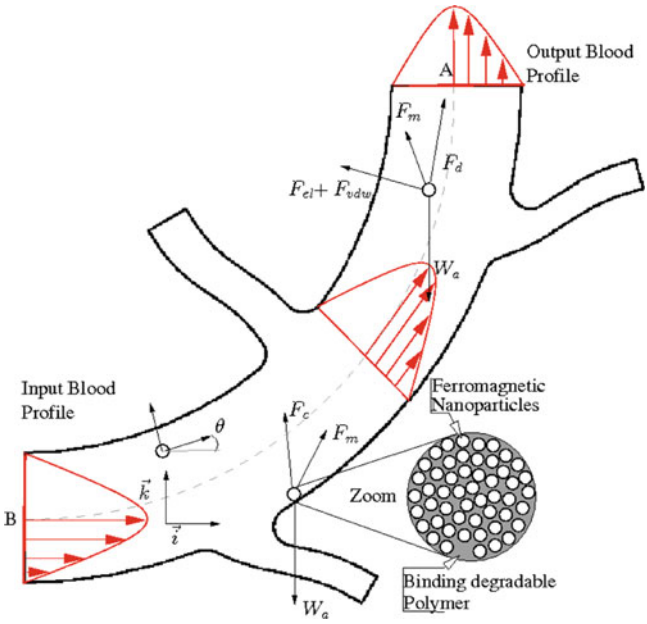

Fig. 13.2 Scheme of a blood vessel with minor bifurcations

The shape of the viscosity dependance on hematocrit is

$$c = \frac{10^{11}}{d^{12}} - (0.8 + \mathrm{e}^{-0.075d}) \left(\frac{d^{12}}{d^{12} + 10^{11}} \right).$$

Wall effects on the fluid in a vessel traditionally result in a parabolic profile of blood flow (see Fig. 13.2) in a cylinder. The pulsative blood's velocity is modeled by an affine combination of a time-varying periodic flow with a spatial parabolic shape. So as to simplify the analytical expression, but with no loss of generality, we only consider the first terms in the time-varying Fourier series of the physiological pulse. In the case of an artery, such an approximation leads to

$$v_f(t) = V_f \left(1 + a_f \sin\left(w_f t + \phi_f\right)\right) \times \left[1 - \left(\frac{D/2 - h - r}{R}\right)^2\right].$$

To fully take into account pulsatile flow in arteries caused by cardiac pumping, one must consider a periodic 10% deformation of the vessel's diameter $D(t)$, synchronized with the pulsative blood's velocity $v_f(t)$. Our studies assume the presence of minor bifurcations (see Fig. 13.2). The developed controller must be sufficiently robust to compensate this effect which could be considered as a disturbance. Minor and major bifurcations can strongly affect the parabolic blood velocity profile. This specific issue is addressed in [37].

13.3.1.2 Apparent Weight

In addition to the hydrodynamic force, apparent weight (combined action of weight and buoyancy) is acting on the spherical robot:

$$\mathbf{W}_{\mathrm{a}} = V(\rho - \rho_{\mathrm{f}})\mathbf{g}, \tag{13.4}$$

where V is the robot's total volume, $\rho = \tau_{\mathrm{m}}\rho_{\mathrm{m}} + (1 - \tau_{\mathrm{m}})\rho_{\mathrm{poly}}$ with ρ_{m} and ρ_{poly} the magnetic material's and polymer's densities, and $\tau_{\mathrm{m}} = \frac{V_{\mathrm{m}}}{V}$ with V_{m} the ferromagnetic volume.

13.3.1.3 Contact Force

The determination of the contact force is important in case of impact between the robot and the wall. Since the robot moves in low velocity, the duration of the impact occurs within a few milliseconds. Hence, the contact force is expressed by a modified Hertzian contact law [38] and under the assumption of no friction between the robot and the wall during the impact period:

$$\mathbf{F}_{\mathrm{c}} = k\delta^{3/2}H(\delta)\mathbf{n} : \text{ loading}, \tag{13.5}$$

where δ is the elastic deformation of the wall at the contact point, H the Heaviside function, $\mathbf{n}$ the normal unit vector pointing from the robot to the contact surface, and k the stiffness given by

$$k = \frac{\frac{4\sqrt{r}}{3}}{\frac{1-\sigma_{\mathrm{p}}^2}{E_{\mathrm{p}}} + \frac{1-\sigma_{\mathrm{w}}^2}{E_{\mathrm{w}}}},$$

where E_{p} (E_{w}) is the Young's modulus of robot (wall) and σ_{p} (σ_{w}) is the Poisson's ratios of robot (wall).

The contact force during unloading is different from the one during loading:

$$\mathbf{F}_{\mathrm{c}} = F_{\mathrm{cm}}\left(\frac{\delta - \delta_0}{\delta_m - \delta_0}\right)^q H(\delta)\mathbf{n} : \text{ unloading}, \tag{13.6}$$

where F_{cm} and δ_{m} are the maximum contact force and corresponding maximum deformation of the wall during the impact. δ_0 is the permanent wall's deformation from loading/unloading cycle, and exponent q varies between 1.5 and 2.5.

13.3.1.4 Van der Waals and Electrostatic Forces

The robot and the wall interact each other through van der Waals and electrostatic forces. The van der Waals potential between the spherical robot and the wall is given by [39]:

$$\mathbf{V}_{\mathrm{vdw}} = -\frac{A_{\mathrm{h}}}{6}\left(\frac{1}{\bar{h}} + \frac{1}{2+\bar{h}} + \ln\frac{\bar{h}}{2+\bar{h}}\right).\mathbf{n}, \tag{13.7}$$

where A_h is the Hamaker constant and $\bar{h} = h/r$ is normalized distance h between the robot and the wall. Then, the van der Waals interaction force is given by differentiating (13.7): $\mathbf{F}_{vdw} = -\nabla \mathbf{V}_{vdw}\, H(h)$.

The electrostatic force between the robot and the wall considered as an uncharged surface is given by [40]

$$\mathbf{F}_{el} = \frac{q^2}{4\pi\epsilon\epsilon_0(r+h)^2}\, H(h)\mathbf{n} \tag{13.8}$$

with q the robot's charge, ϵ the dielectric density of the medium in which the interaction occurs, and ϵ_0 the vacuum permittivity. Hays [41] gives the expression of the maximum allowable charge for a spherical body of radius r:

$$q(\mu C) = S \times Q = 4\pi r^2 \times 30(100r)^{-0.3}.$$

13.3.1.5 Magnetic Force

The gradient coils of the MRI system provide magnetic gradients which produce a magnetic force F_m on the robot:

$$\mathbf{F}_m = \tau_m V(\mathbf{M}.\nabla)\mathbf{B}, \tag{13.9}$$

where $\mathbf{M}$ is the magnetization of the material, μ_0 is the permeability of free space, and $\nabla\mathbf{B}$ is the magnetic field gradient. Note that the static field B_0 of an MRI device is sufficient to ensure a saturation magnetization M_{sat} of the bead.

13.3.2 Discussion

Constraints rising from the use of MRI device for navigating in blood vessels (cf. Sect. 13.2) impact seriously the modeling. We here focus on two major issues related to MRI-guided therapeutic robots: levitation and resisting drag. The former is connected to MRI-constraints and especially to the actuator limitations, while the latter is related both to MRI and physiological constraints.

13.3.2.1 Levitating

On most powerful clinical MRI devices, magnetic gradient coils can deliver at best 80 mT m^{-1}. Table 13.3 clearly shows that few materials can provide levitation, even for a robot without embedded material: Carbon steel, permendur, NdFeB alloys, and FeSi are the best fitted types of ferromagnetic material to use for manufacturing the

Table 13.3 Effect of apparent weight of a ferromagnetic core on the magnetic force required for displacement: magnetic gradient required for levitating assuming that the embedded material has a density $\rho_{poly} = 1{,}500\,kg\,m^{-3}$ for different values of ratio τ_m

Material	$\tau_m = 1$	$\tau_m = 0.8$	$\tau_m = 0.5$
Permendur ($mT\,m^{-1}$)	35.78	36.08	36.98
Carbon steel ($mT\,m^{-1}$)	38.88	39.23	40.20
97Fe-3Si ($mT\,m^{-1}$)	40.72	41.09	42.19
NdFeB-35 ($mT\,m^{-1}$)	64.54	65.65	68.95
Alfenol ($mT\,m^{-1}$)	83.83	84.75	87.53
Supermalloy ($mT\,m^{-1}$)	120.78	122.49	127.64
$Fe_3\,O_4$ ($mT\,m^{-1}$)	113.40	115.06	119.99

propulsion core of the robot; permendur, since its high density is counterbalanced by the highest magnetization saturation value reached at ambient temperature, and FeSi-alloy because its low magnetization at saturation is counterbalanced by a low density (cf. Table 13.1). However, the magnetic force with a FeSi core is about 1.33 times lower than the one with a Permendur core, for a same applied gradient: that is why iron/cobalt or carbon steel alloys are more likely to be used for propulsion purpose. Alloys like Alfenol, Supermalloy, or Ferrite are excluded since, even with no embedded material, the gradients required for levitating are beyond the actuator's limitation. It should be noticed that, in case the robot has to resist the drag while performing levitation, the required gradient can temporarily reach the actuator saturation.

13.3.2.2 Resisting Drag

Effects of the robot's size and wall correcting factor β are here illustrated for two microrobots (radius $r = 250\,\mu m$ in Fig. 13.3 and radius $r = 3\,\mu m$ in Fig. 13.4) navigating, respectively, in macro- and micro-vessels of the circulatory system. These simulations results are given without levitating consideration: That is the reason why required gradients tend to zero along with the flow velocity. In order to infer results, taking levitation into account merely requires a vertical translation (see Table 13.3). Values for the velocities of the blood flow inside different vessels are based on Table 13.2. These figures illustrate the required magnetic gradient to reach the equilibrium between magnetic and drag forces, with consideration of the wall effects, that is, the magnetic gradient needed to generate a magnetic force able to resist the flow. The considered robot is supposed to be made of Permendur.

Figure 13.3 shows the feasibility, for a $250\,\mu m$ radius permendur core, of resisting the flow inside almost all of the macro-vasculature, within the constraints of current MRI devices (black thick line gives the $80\,mT\,m^{-1}$ limitation for actuators). If there is no problem in venous macro-system, required magnetic gradients are a bit too high for maximal values of the flows velocity inside arterial macro-system.

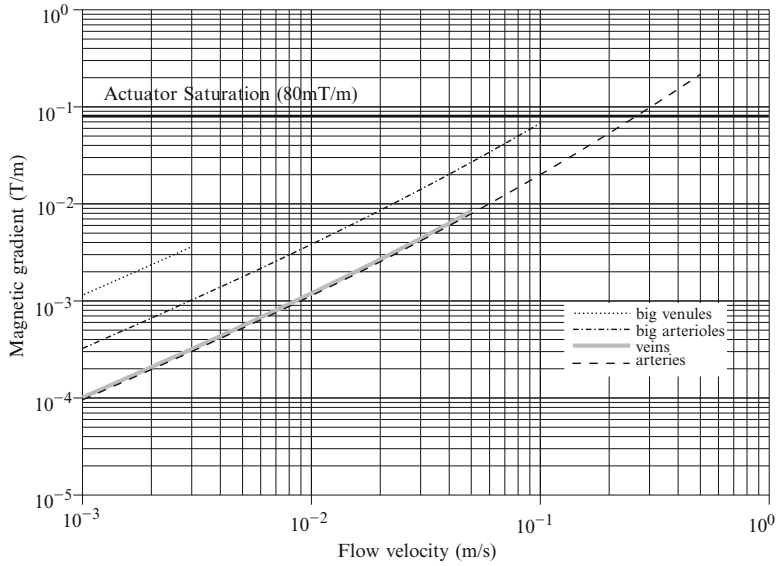

Fig. 13.3 Magnetic gradient of propulsion required for resisting the blood flow inside different big vessels for a 250 μm-radius robot (see Table 13.2 for physiological constraints)

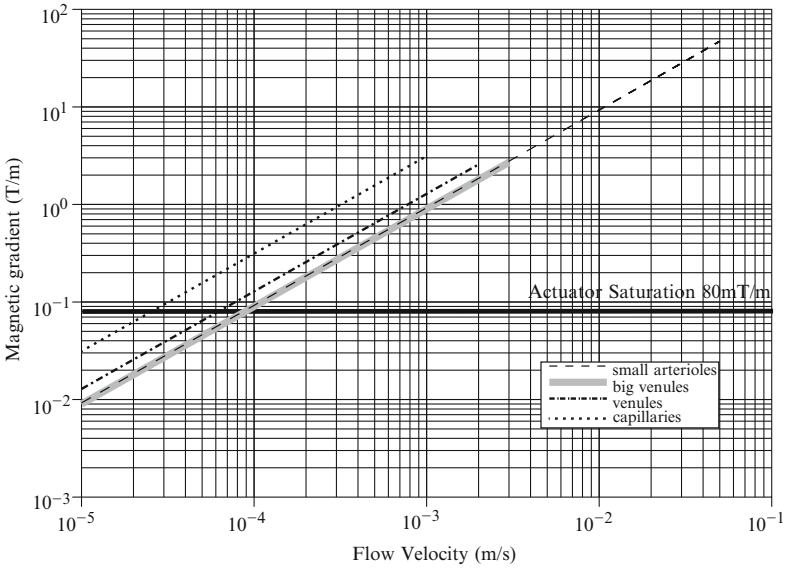

Fig. 13.4 Magnetic gradient of propulsion required for resisting the blood flow inside different small vessels for a 3 μm-radius robot (see Table 13.2 for physiological constraints)

Since maximal velocity values of the flow inside arterial system are related to heart pumping effects, Fig. 13.3 suggests it will be possible to resist the flow in arteries, except at ejection instants during the ventricular systole. As a consequence, it should be able for the control, in good configurations, to guide the robot, even against the tide (for instance, if the robot had followed a wrong path). At the opposite, in microvasculature, a 3 μm-radius permendur core cannot generically resist the flow, unless the flow velocity is really low, as illustrated in Fig. 13.4. In this case, the control objective has to be relaxed into steering the robot toward either side of a bifurcation.

Besides, Figs. 13.3 and 13.4 underline the importance of the radius ratio in wall effects on the drag force (cf Sect. 13.3.1.1). For instance, let us compare results for a capillary and for a venule in Fig. 13.4: For a given magnetic gradient, the same robot can resist to a blood flow whose velocity is 2 times higher in a venule than in a capillary.

13.3.3 Optimal Trajectory

Microrobots are inserted into the human body from an injection point and have to reach a target point. This raises the problem of the reference trajectory that the microrobot has to follow from the start point to the end point where the drug must be delivered. This reference trajectory depends obviously on the map of the human vasculature. A data processing is necessary to know which path is the shorter, that is, to solve the pathplanning issue. This domain has been largely explored in the literature, and several methods have been proposed to find a reference trajectory from a set of medical imaging [42–44]. A first natural idea is to use an algorithm as "shortest path" such as Voronoï method. This type of algorithm provides a reference trajectory centered in the middle of the blood vessels (Fig. 13.5). Unfortunately, the actuators are not powerful enough to counterbalance the numerous forces acting on the microrobot and especially the drag force that is maximal at the center of the vessel because of the parabolic profile of the blood velocity (cf. Sect. 13.3.1.1). Such a reference trajectory is thus difficult—or even impossible—to track and would lead to a tracking and therapeutic failure. Another approach is to exploit the nonlinearities of the proposed model so as to define points where these forces tend to annulate, thus resulting in an optimal trajectory that minimizes the control efforts and makes the tracking feasible despite unfavorable conditions.

First, a series of anchor points is defined for different positions in the blood vessel (Points A^*, B^*, and C^* on Fig. 13.6). At these points, the electrostatic and van der Waals forces counterbalance perfectly the robot's apparent weight. These points indicate the direction that the trajectory should follow. A B-spline trajectory is then build by joining the different open paths between the points (Fig. 13.6). Each path is naturally continuous, and chosen $\mathcal{C}^2$, with its neighbors. The resulting reference trajectory is closed to the vessel's wall since the drag force decreases due to the parabolic profile (see Fig. 13.2).

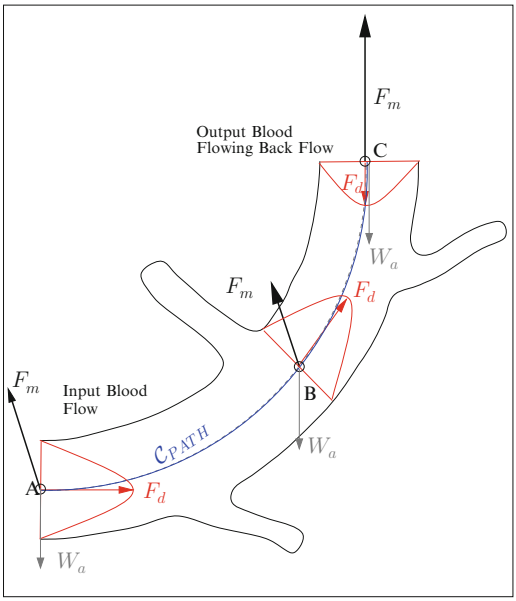

Fig. 13.5 Command $\mathbf{F}_m$ without optimal trajectory: The control effort required to track the reference is too high for the MRI actuators

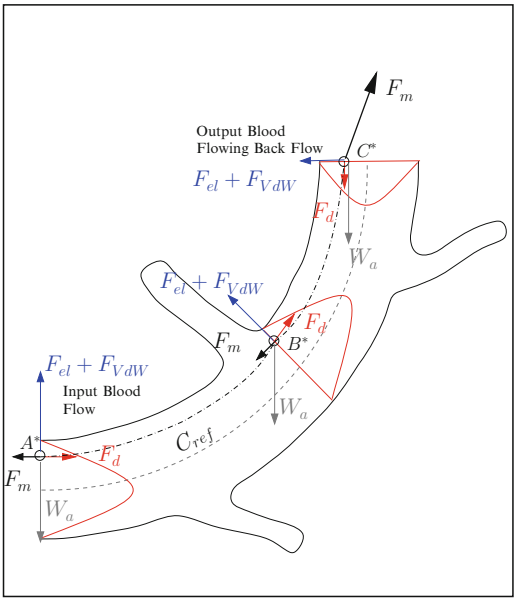

Fig. 13.6 Command $\mathbf{F}_m$ with optimal trajectory: External forces tend to annulate each others, resulting in a feasible tracking

13.3.4 State Space Representation

Let (x, z) denote the position of the robot in the vessel with respect to a given frame $\mathcal{F}(O, \mathbf{i}, \mathbf{k})$. The state model is established from differential equation (13.1) defining the robot's dynamic behavior, projected on **i** and **k** axes:

$$\begin{cases} m\ddot{x} = F_{d_x} + F_{vdw_x} + F_{el_x} + F_{c_x} + F_{m_x} \\ m\ddot{z} = F_{d_z} + F_{vdw_z} + F_{el_z} + F_{c_z} + W_a + F_{m_z} \end{cases}, \tag{13.10}$$

where indexes x (respectively, z) denote projections on **i** (**k**).

Let x_1, x_2, (x_3, x_4) denote respectively the particle's position and velocity along **i** axis (respectively, along **k** axis). Assuming that positions x_1 and x_3 can be measured thanks to the MRI imaging system, let y denote the state's measure. Using expressions of forces given by (13.9), (13.3), (13.4), (13.8) and van der Waals interaction derived from potential (13.7) and adequate projection of the local frame and of the relative velocity along the geometry of the vessel (angles ψ and ϕ, respectively), system (13.10) can be written in the form

$$(\mathcal{S}) \begin{cases} \dot{x}_1 = x_2 \\ \dot{x}_2 = f_2(x) + au_1 \\ \dot{x}_3 = x_4 \\ \dot{x}_4 = f_4(x) + au_2 \\ y = (x_1, x_3)^T \end{cases}, \tag{13.11}$$

where control inputs $u_1 = \nabla B_x$ and $u_2 = \nabla B_z$ are the magnetic gradients, parameter $a = \frac{\tau_m M}{\rho}$, and functions f_i are given by

$$\begin{cases} f_2(.) = F_{dn_x} + F_{eln_x} + F_{vdwn_x} + F_{cn_x} \\ f_4(.) = F_{dn_z} + F_{eln_z} + F_{vdwn_z} + F_{cn_z} + W_{an} \end{cases}.$$

The index n indicates that the forces are normalized with respect to the robot's mass m. These forces are expressed as

$$\begin{cases} F_{dn_x} = \dfrac{9\eta\cos(\phi)}{2r^2\beta\rho}\|v - v_f\| + \dfrac{3\rho_f\cos(\phi)}{20r\beta^2\rho}\|v - v_f\|^2 + \dfrac{9\rho_f\cos(\phi)}{4r\beta^2\rho}\dfrac{\|v - v_f\|^2}{1 + \sqrt{\frac{2\rho_f r}{\beta\eta}\|v - v_f\|}} \\ F_{eln_x} = \dfrac{3q^2\sin(\psi)}{16\pi^2 r^3\rho\epsilon\epsilon_0}\left[\dfrac{H(h_1)}{(r+h_1)^2} - \dfrac{H(h_2)}{(r+h_2)^2}\right] \\ F_{vdwn_x} = \dfrac{A_h\sin(\psi)}{8\pi r^2\rho}\left[\left(\dfrac{1}{h_1^2} + \dfrac{1}{(2r+h_1)^2} - \dfrac{2}{h_1(2r+h_1)}\right)H(h_1)\right. \\ \qquad \left. - \left(\dfrac{1}{h_2^2} + \dfrac{1}{(2r+h_2)^2} - \dfrac{2}{h_2(2r+h_2)}\right)H(h_2)\right] \\ F_{cn_x} = \dfrac{3k\sin\psi}{4\pi r^3\rho}\delta^{3/2}H(\delta) \end{cases},$$

where h_1 and h_2 are the distances from the robot to the upper and lower walls. The above expressions are similar along the z axis.

13.4 Control Approach

A control law Lyapunov-stabilizing trajectories for system $(\mathcal{S})$ is now presented. The determination of Lyapunov functions is generically a challenging issue. According to [45,46], it is preferable to use control Lyapunov functions (CLFs) in a backstepping control approach. Since this design requires a triangular form for the control system, we propose the following change of variables:

$$\left\{ X = \begin{pmatrix} x_1 \\ x_3 \end{pmatrix}; Z = \begin{pmatrix} x_2 \\ x_4 \end{pmatrix}; u = \begin{pmatrix} u_1 \\ u_2 \end{pmatrix}; U = au. \right. \tag{13.12}$$

As shown in the force balance, the model has many parameters that are highly variable from one person to another. An adaptive nonlinear control [47] based on a backstepping approach can be developed so as to online estimate some uncertain parameters (see Fig. 13.7). The update law must ensure convergence of the estimated parameter to its real value, while the control inputs must stabilize the tracking error between the actual and reference trajectory to zero. Assuming that the parameter $\frac{q^2}{\varepsilon}$ is uncertain, we set the new system from (13.11) and (13.12) to apply the adaptive control approach:

$$(\mathcal{S}') \begin{cases} \dot{X} = Z \\ \dot{Z} = F_0(X, Z) + \varphi(X)\theta + U, \\ Y = X \end{cases} \tag{13.13}$$

where $\varphi(X)$ is the electrostatic force without the parameter $\frac{q^2}{\varepsilon}$, θ the vector of unknown constant parameter, and with

$$F_0(X, Z) = \begin{pmatrix} F_{dn_x} + F_{cn_x} + F_{vdwn_x} \\ F_{dn_z} + W_{an} + F_{cn_z} + F_{vdwn_z} \end{pmatrix}. \tag{13.14}$$

Using the change of variables given in (13.12), we construct the control law in two steps.

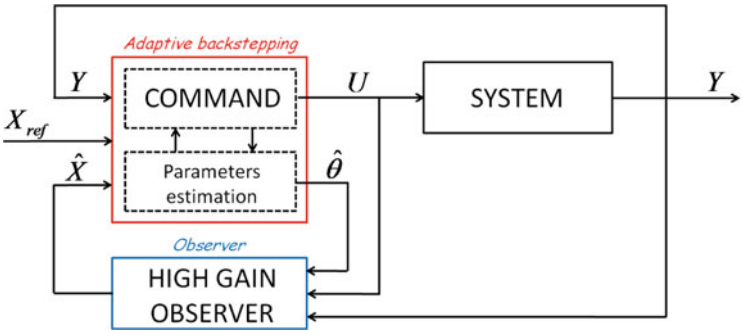

Fig. 13.7 Closed-loop system overview

Step 1: Let

$$\begin{cases} \tilde{X} = X - X_r \\ \tilde{Z} = Z - Z_r - \alpha \end{cases} \tag{13.15}$$

denote the position and velocity error, respectively. X_r, $\dot{X}_r = Z_r$, and $\ddot{X}_r$ are the desired reference trajectory, velocity, and acceleration, respectively. α is a stabilizing function.
A CLF candidate is

$$V_1 = \frac{1}{2}\tilde{X}^T\tilde{X} + \frac{1}{2}(\hat{\theta} - \theta)^T\Gamma^{-1}(\hat{\theta} - \theta) \quad \geq 0, \tag{13.16}$$

where $\hat{\theta}$ is the estimated parameter and Γ a positive-definite matrix.
Calculating the derivative of V_1 along system (13.13) and setting $\alpha = -k_1\tilde{X}$, we obtain:

$$\dot{V}_1 = -k_1\tilde{X}^T\tilde{X} + \tilde{X}^T\tilde{Z} + (\hat{\theta} - \theta)^T\Gamma^{-1}\dot{\hat{\theta}}. \tag{13.17}$$

The second term $\tilde{X}^T\tilde{Z}$ will be canceled at the next step. One can notice from the previous expressions that

$$\dot{\tilde{X}} = \dot{X} - \dot{X}_r = \tilde{Z} + \alpha = \tilde{Z} - k_1\tilde{X}. \tag{13.18}$$

Step 2: From (13.15) and (13.18), we have

$$\dot{\tilde{Z}} = \underbrace{F_0 + \varphi\theta + U}_{\dot{Z}} - \dot{Z}_r \underbrace{+k_1(\tilde{Z} - k_1\tilde{X})}_{-\dot{\alpha}}. \tag{13.19}$$

In this step, the CLF is given by

$$V_2 = V_1 + \frac{1}{2}\tilde{Z}^T\tilde{Z} \quad \geq 0. \tag{13.20}$$

The derivative of V_2 along system (13.13) is expressed as

$$\begin{aligned} \dot{V}_2 = &-k_1\tilde{X}^T\tilde{X} + \tilde{Z}^T[(1 - k_1^2)\tilde{X} + k_1\tilde{Z} - \dot{Z}_r + F_0 + \varphi\theta + U] \\ &+(\hat{\theta} - \theta)^T\Gamma^{-1}\dot{\hat{\theta}}. \end{aligned} \tag{13.21}$$

Since we have $\theta = \hat{\theta} + (\theta - \hat{\theta})$, the derivative of V_2 along system (13.13) is expressed as

$$\begin{aligned} \dot{V}_2 = &-k_1\tilde{X}^T\tilde{X} + \tilde{Z}^T[(1 - k_1^2)\tilde{X} + k_1\tilde{Z} - \dot{Z}_r + F_0 + \varphi\hat{\theta} + U] \\ &+(\hat{\theta} - \theta)^T\Gamma^{-1}(\dot{\hat{\theta}} - \Gamma\varphi^T\tilde{Z}). \end{aligned} \tag{13.22}$$

To cancel the last term in (13.22), we set

$$\dot{\hat{\theta}} = \Gamma\varphi^T\tilde{Z} \tag{13.23}$$

and to ensure $\dot{V}_2$ is negative definite, we set

$$(1-k_1^2)\tilde{X}+k_1\tilde{Z}-\dot{Z}_r+F_0+\varphi\hat{\theta}+U=-k_2\tilde{Z}. \tag{13.24}$$

To summarize, from (13.18), (13.23), and (13.24), the control law U and the update law for the parameter estimate $\hat{\theta}$ can be expressed as

$$\begin{cases} U &= \ddot{X}_r-(k_1+k_2)(Z-\dot{X}_r)-(1+k_1k_2)(X-X_r)-F_0-\varphi\hat{\theta} \\ \dot{\hat{\theta}} &= \Gamma\varphi^T[Z-\dot{X}_r+k_1(X-X_r)] \end{cases}. \tag{13.25}$$

Considering the magnetization M to be unknown, the control law and the update law $\dot{\hat{\theta}}$ are given by

$$\begin{cases} u = \varphi^{-1}\left[\ddot{X}_r-(k_1+k_2)(Z-\dot{X}_r)-(1+k_1k_2)(X-X_r)-F_0\right]\frac{1}{\hat{\theta}} \\ \dot{\hat{\theta}} = \Gamma u^T\varphi^T[Z-\dot{X}_r+k_1(X-X_r)] \end{cases}. \tag{13.26}$$

13.5 State Estimation

The backstepping control laws (13.25) and (13.26) require the knowledge of the robot's velocity in addition to its position, measured by the MRI system.

Among the different observers cited in the literature, our attention was drawn to the high-gain observer. Unlike other observers, locally Lipschitzian state's functions ensure the convergence of the observer. This one requires the system to have canonical form which can be obtained using the change of variables of (13.12). From the forces expressions of Sect. 13.3, one can notice that only the drag force depends on the robot's position and velocity. Hence, only drag force has to be locally Lipschitzian to ensure the convergence of the observer given for the backstepping control law by [48]

$$\begin{cases} \dot{\hat{X}} = \hat{Z}+LG_x(\hat{X}-Y) \\ \dot{\hat{Z}} = F_0(\hat{X},\hat{Z})+\varphi(\hat{X})\theta+U+L^2G_z(\hat{X}-Y) \end{cases}, \tag{13.27}$$

where L is the high gain and $G_x=\begin{pmatrix} g_1 & 0 \\ 0 & g_3 \end{pmatrix}$ and $G_z=\begin{pmatrix} g_2 & 0 \\ 0 & g_4 \end{pmatrix}$ are defined from the Hurwitz matrix H_u:

$$H_u=\begin{pmatrix} g_1 & 0 & 1 & 0 \\ 0 & g_3 & 0 & 1 \\ g_2 & 0 & 0 & 0 \\ 0 & g_4 & 0 & 0 \end{pmatrix}.$$

13.6 Simulations

Simulations are performed by taking into account the limitations of a clinical MRI system. The magnetic field of $3T$ is strong enough to assume that the particles reach their saturation magnetization. The magnetic field gradients are used to control the microrobot's motion in the human body. As stated in Sect. 13.2, these MRI devices can provide a maximum magnetic field gradient of $80\,\mathrm{mT\,m^{-1}}$. In order not to exceed the capacity of MRI systems, the applied control law is now corrected as:

$$U_a(t) = \frac{U(t)}{k(t)} \quad \text{with} \quad k(t) = \max\left[1, \frac{U(t)}{U_{\text{sat}}}\right]. \tag{13.28}$$

Performances and stability of the controller with respect to noise measurement, parameters variations, and uncertainties are now illustrated by simulations, whose nominal parameters are given in Table 13.4.

13.6.1 Error on the Electrostatic Force

This first simulation is performed assuming an error of 20% from the nominal blood's dielectric and maximum allowable charge for a spherical body ratio. The motivation for estimating the uncertain parameter on-line is twofold. First, among

Table 13.4 Simulations data

Plasma viscosity	η_{plasma}	5×10^{-3} [Pa s]
Blood density	ρ_{f}	1,060 [kg m^{-3}]
Magnetic material density	ρ_{m}	7,500 [kg m^{-3}]
Robot radius	r	250 [μm]
Young's moduli	$E_{\text{p}},\ E_{\text{w}}$	$10^9,\ 10^6$ [Pa]
Poisson's ratio	$\sigma_p,\ \sigma_w$	0.27, 0.2 [Pa]
Vessel diameter	D	3 [mm]
Polymer density	ρ_{poly}	1, 500 [kg m^{-3}]
Ferromagnetic ratio	τ_{m}	0.8
Magnetization	M	1.23×10^6 [A m^{-1}]
Hematocrit rate	h_d	0.45
Hamaker constant	A_{h}	4×10^{-19} [J]
Blood dielectric density	ε	77 [C^2 N^{-1} m^{-2}]
Blood velocity	V_f	0.025 [m s^{-1}]
parameters	$a_f,\ w_f,\ \phi_f$	$1.15,\ 2\pi,\ \pi/2$
Initial condition on X, Z	X_0, Z_0	$(0,0)^T, (0,0)^T$
Initial condition on $\hat{X}, \hat{Z}$	$\hat{X}_0, \hat{Z}_0$	$(0.001,0)^T, (0,0)^T$
Inputs saturations	U_{sat}	80 [mT m^{-1}]
ontroller gains	k_1, k_2	7, 14
Observer gains	L	19
	g_1, g_2, g_3, g_4	$-6, -13, -12, -4$

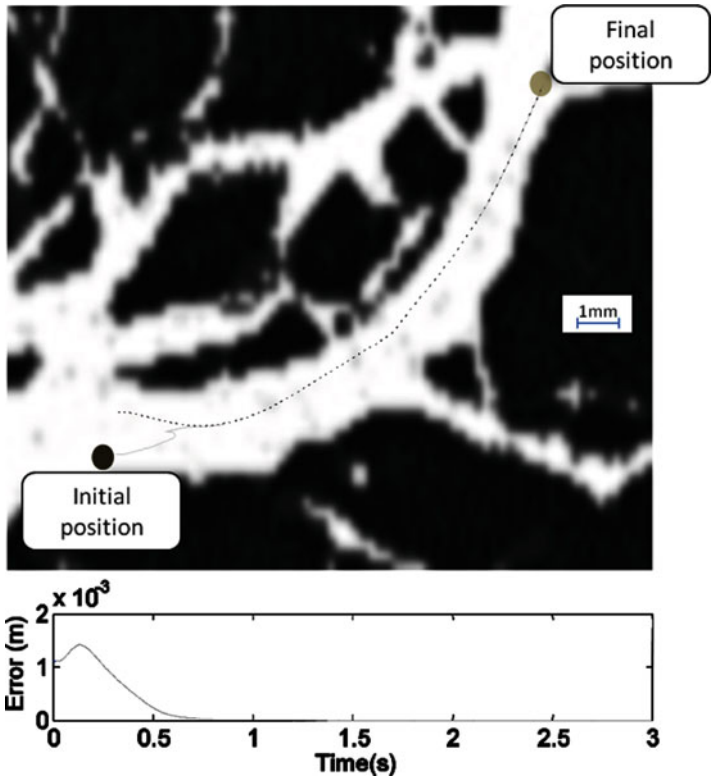

Fig. 13.8 (**a**) Reference (*black dash line*) and simulated (*gray solid line*) trajectories. (**b**) Tracking error

the physiological parameters of the model, which are the most difficult to measure and are very variable from one patient to another, sensitivity is the highest for $\frac{q^2}{\epsilon}$ and, to a lesser extent, for η and A_{h}. Second, adaptive backstepping cannot effectively deal with nonlinear parameters such as viscosity η.

The simulation demonstrates the relative stability of the proposed controller-observer. It shows that the parametric error affects neither the stability of the closed-loop system (Fig. 13.8a) nor the convergence of the observer (Fig. 13.9). Nevertheless, we note an important tracking error between $t = 0\,\mathrm{s}$ and $t = 0.6\,\mathrm{s}$. This phase is critical since the control inputs (Fig. 13.10) reach the actuator saturation in the range $t \in [0\ 0.2]\,\mathrm{s}$ and the parameter is not updated. Then, from $t = 0.2\,\mathrm{s}$ to $t = 1.3\,\mathrm{s}$, the estimated parameter is updated and converged to the nominal value. The tracking error as well as the microrobot's velocity estimation error (Fig. 13.11b) is affected by the parametric error because the model-based controller and observer are quite sensitive to this uncertainty. However, as the update law gradually stabilizes the parametric error to zero (Fig. 13.12), we observe a noticeable improvement of both tracking and estimation efficiency. The adaptive backstepping

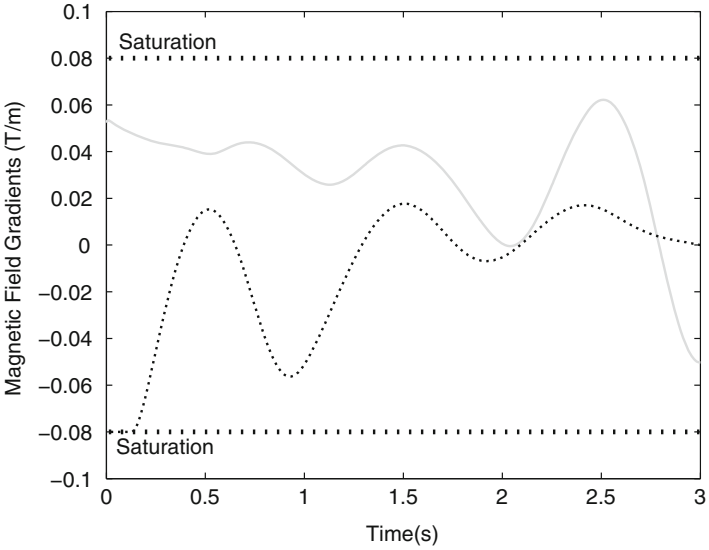

Fig. 13.9 Control input : magnetic field gradients on **i**-axis (*black dash line*) and on **k**-axis (*gray solid line*)

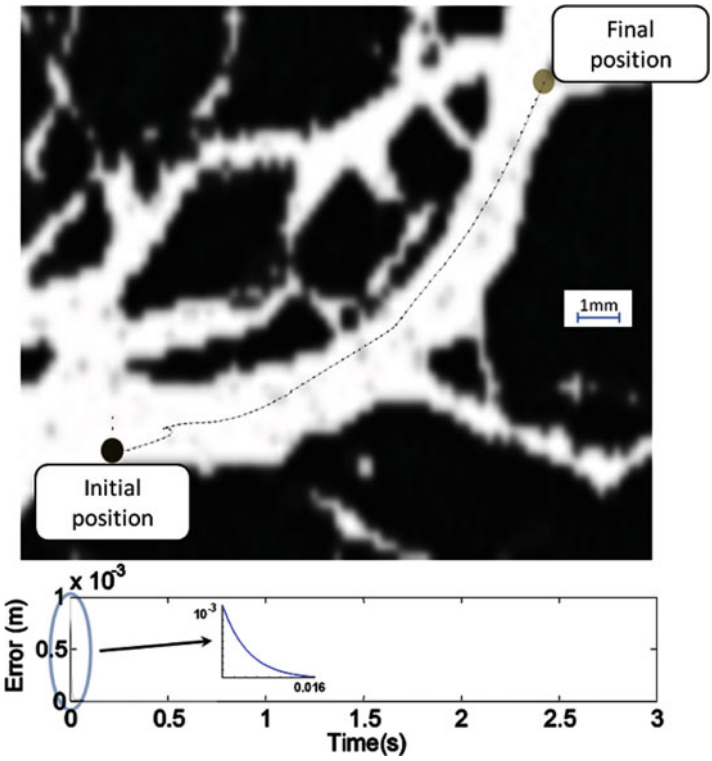

Fig. 13.10 (**a**) Simulated (*gray solid line*) and estimated (*black dash line*) trajectories. (**b**) Estimation error

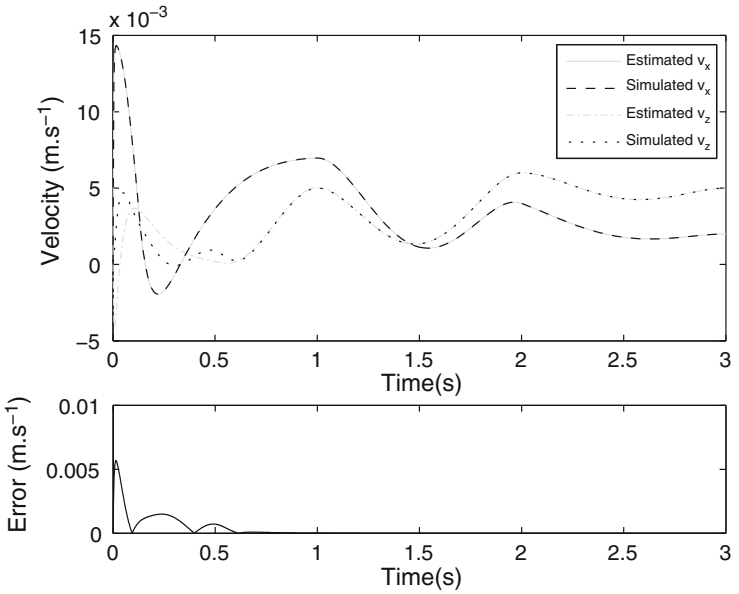

Fig. 13.11 (**a**) Simulated and estimated velocities along **i** and **k** axes. (**b**) Velocity estimation error

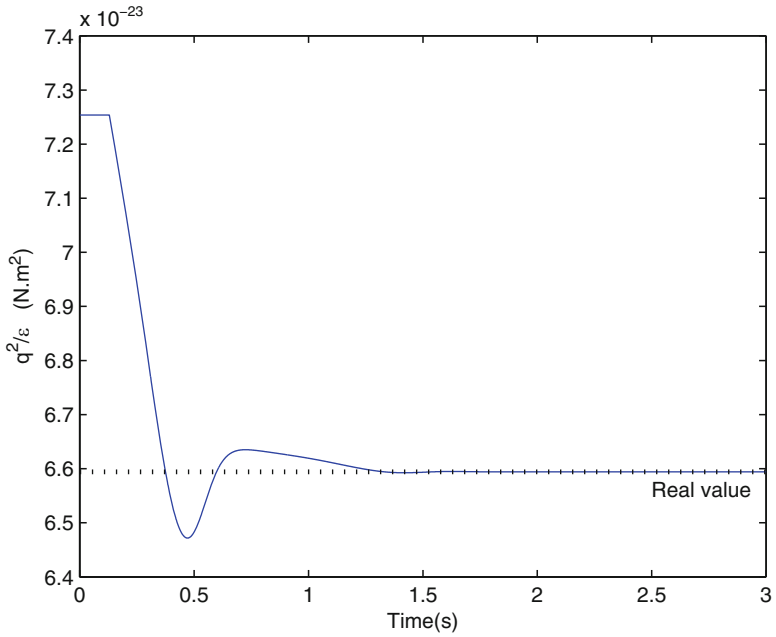

Fig. 13.12 On-line estimation of parameter $\frac{q2}{\varepsilon}$

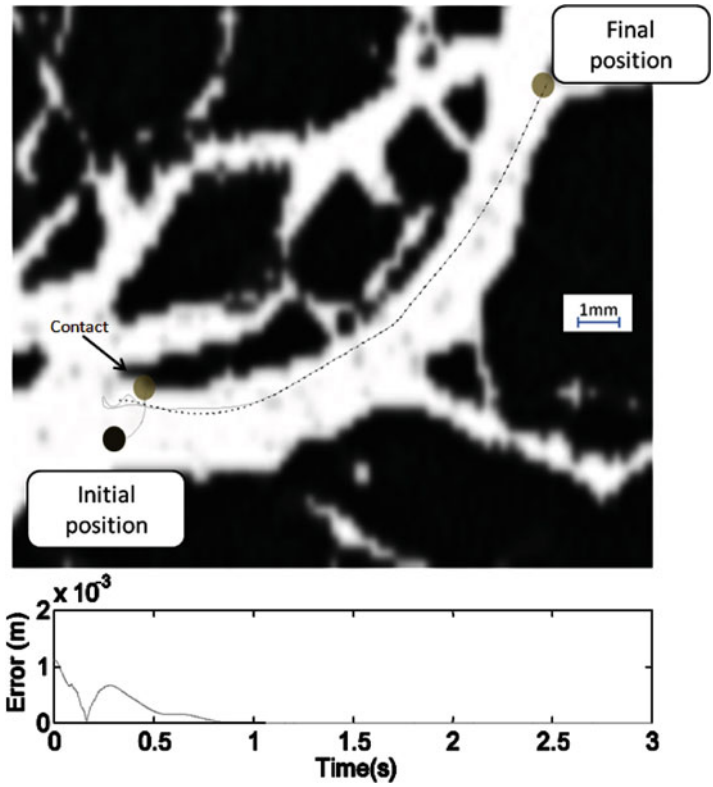

Fig. 13.13 (**a**) Reference (*black dash line*) and simulated (*gray solid line*) trajectories. (**b**) Tracking error

approach applied in this simulation thus fulfills two goals. During the transient phase, when estimated parameter has not yet converged, the controller/observer pair ensures a degraded but good tracking and estimation of velocity, thus demonstrating robustness to parametric uncertainties. After the estimated parameter has converged to its nominal value, the controller ensures an essentially perfect stabilization of the microrobot along the reference trajectory.

13.6.2 Error on the Magnetic Force

The magnetization of the NdFeB microrobot is one of the most sensitive parameters, as it appears in factor of the control inputs. This second simulation is performed assuming an error of 5% from the nominal magnetization value. Figure 13.13a illustrates that the closed-loop system is stable and the tracking is efficient. The magnetization of the microrobot is underestimated, so the control inputs will be higher during this transient phase. This phase is critical since the control inputs

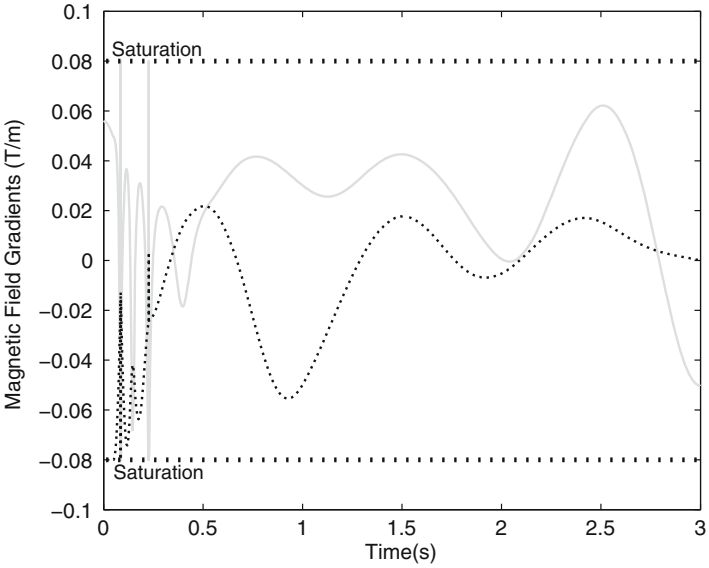

Fig. 13.14 Control input : magnetic field gradients on **i**-axis (*black dash line*) and on **k**-axis (*gray solid line*)

(Fig. 13.14) reach the actuator saturation and the parameter is not updated. One can notice that the microrobot is moving rapidly toward the reference trajectory and the collision with the blood vessel's wall is inevitable by twice. The estimated position of the microrobot (Fig. 13.15) and the estimated velocity (Fig. 13.16) are highly disturbed during this phase. The estimation of the parameter (Fig. 13.17) drops after the collision before converging. At time $t = 1\,\mathrm{s}$, the parameter has converged to zero, and the robot is progressively stabilized along the reference trajectory.

13.7 Conclusion

This chapter focuses on an innovative method to perform targeted therapy by navigating in the cardiovascular system using an MRI system. The idea is the use of the magnetic gradients coils of a clinical MRI to pull a therapeutic microrobot to a desired area as well as providing fine observation of its motion in the vasculature. To perform this task, a precise nonlinear model is presented for an MRI guided microrobot in blood vessels. The microrobot is a polymer-binded aggregate of nanoscaled ferromagnetic particles which is subjected to numerous external forces. This model takes into account the non-Newtonian behavior of blood and the properties of blood vessels such as electrostatic, van der Waals, and contact forces. An optimal trajectory is then derived from this precise model so as to minimize the control efforts. Since the modeling describes both physical and physiological forces,

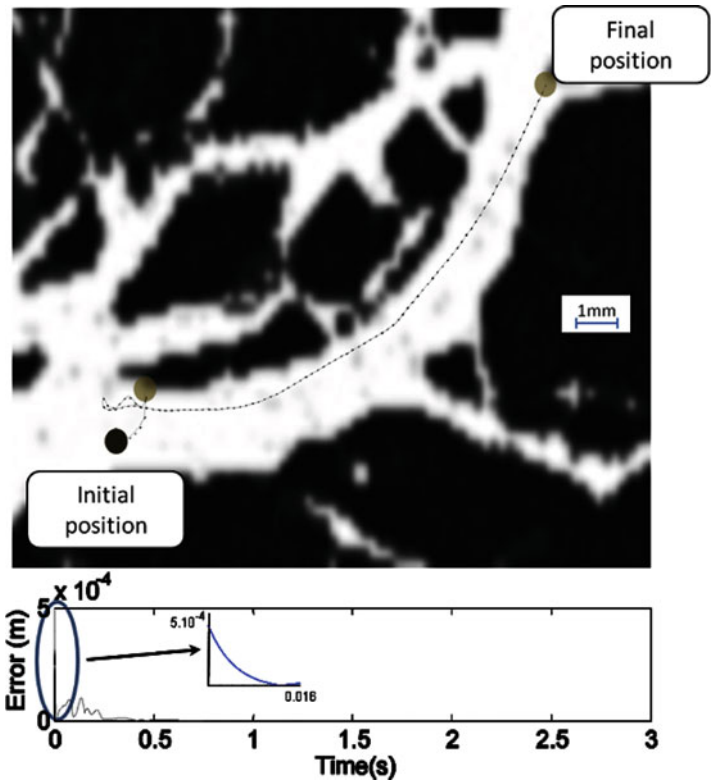

Fig. 13.15 (**a**) Simulated (*gray solid line*) and estimated (*black dash line*) trajectories. (**b**) Estimation error

it is affected by many biological parameters uncertainties. To robustify the tracking with respect to these uncertainties, an adaptive backstepping law has been developed and exposed in this chapter. The aim of this controller is twofold. First, this one is based on a Lyapunov function which ensures the stability of the system. Secondly, this controller performs an on-line estimation of some key uncertain parameters. As this control design requires the velocity of the microrobot, which cannot be measured by the MRI system, a high-gain observer is also synthesized to reconstruct the full state. To validate this approach and the stability of the controller/observer pair, simulations have been performed with assuming important modeling errors on two significant parameters that affect the dynamics of the aggregate.

This sensitivity to matched uncertainties is a challenging issue: If biological parameters are very variable among patients, the pumping blood is also very difficult to estimate (amplitude, mean value, and frequency). If some parameters can be estimated using adaptative backstepping, it will not be as simple for parameters like the blood's viscosity. In fact, drag force is a nonlinear function of viscosity, thus breaking classical adaptive approaches' assumptions, and this problem remains

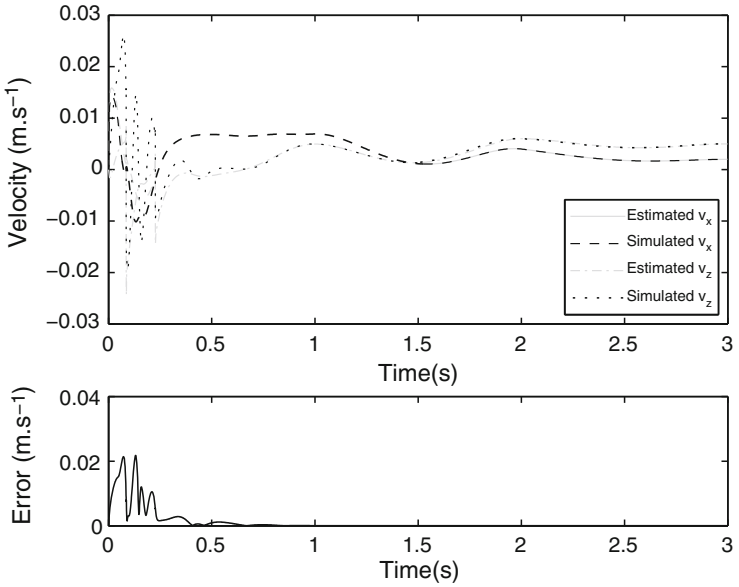

Fig. 13.16 (**a**) Simulated and estimated velocities along **i** and **k** axes. (**b**) Velocity estimation error

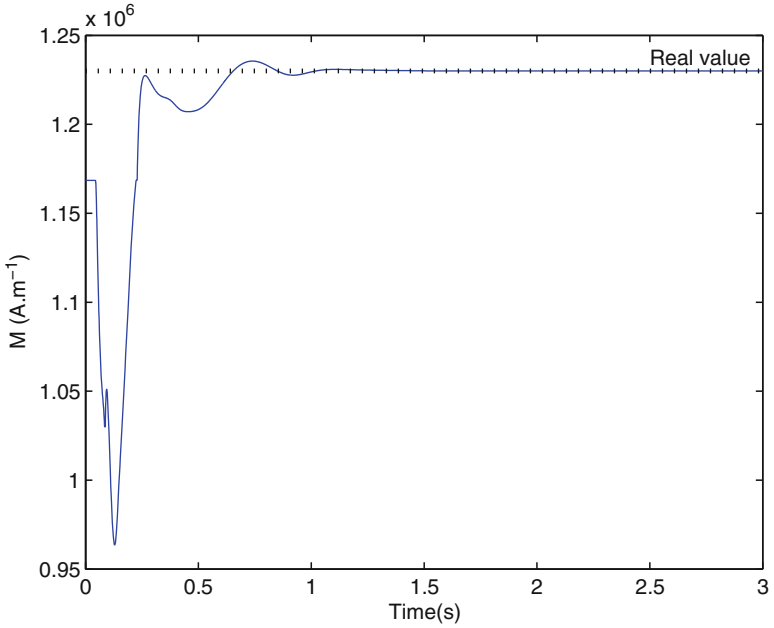

Fig. 13.17 On-line estimation of parameter M

open. The blood flow velocity is supposed to be measured in this chapter, whereas it is a tricky issue, in practice, to measure it accurately, especially in deep vessels and inside an MRI device. To solve the difficult problem of estimating the blood velocity, a promising approach relies on the synthesis of a Kazantzis-Kazantzis Luenberger observer [49]. Modeling of the impact of major bifurcations on the blood's velocity profile should also be investigated. These improvements should robustify the presented approach and widen the range of application of targeted chemotherapy. Nevertheless, any model-based approach is intrinsically sensitive to assumption violations that may occur especially in experimental setups, namely the respect of the static field uniformity assumption and the precision of the gradient field actuators.

The challenges related to targeted therapy through MRI-guided nanorobots are numerous, and this chapter cannot address all the connected research topics: experimental setup designs, increased precision of the aggregate's position using its magnetic properties, MRI real-time imaging, physical properties of self-assembly structures, pathplanning, etc. For a focus on the multiplexing issues, the interested reader can refer to [10]. A crucial hindrance of MRI-based navigation stems from the strong limitations on the magnetic gradient coils in clinical MRI devices. Since propulsion is provided by the volumetric magnetic forces, whereas the drag force is surfacic, the smaller the aggregate, the higher the required control forces with respect to hydrodynamic perturbations. At the nanoscale, magnetic forces induced by available MRI devices are not sufficient to steer the aggregate within the smallest blood vessels, which reduces the accuracy of the drug delivery. Current research aims to overcome this limitation by upgrading the MRI systems with additional gradient steering coils in order to increase their amplitude and, in turn, provide a more precise delivery of the drugs in the vicinity of the diseased cells.

Acknowledgements This work was supported by European Union's 7th Framework Program and its research area ICT-2007.3.6 Micro/nanosystems under the project NANOMA (Nano-Actuactors and Nano-Sensors for Medical Applications).

References

1. Kraus-Tiefenbacher U et al (2005) Intraoperative radiotherapy for breast cancer using intrabeam system. Tumori 91(4):339–345
2. Sievers E et al (1999) Selective ablation of acute myeloid leukemia using antibody-targeted chemotherapy: a phase 1 study of an anti-cd33 calicheamicin immunoconjugate. Blood 97(11):3678–3684
3. Gillies GT, Ritter RC, Broaddus WC, Grady MS, Howard MA, McNeil RG (1994) Magnetic manipulation instrumentation for medical physics research. Review of Scientific Instruments 65(3):533–562
4. Honda T, Arai KI, Ishiyama K (1996) Micro swimming mechanisms propelled by external magnetic fields. IEEE Trans Magn 32(5):5085–5087
5. Abbott J, Nagy Z, Beyeler F, Nelson B (2007) Robotics in the small: part 1 microrobotics. IEEE Robot Autom Mag 14(2):92–103

6. Quate EG, Wika KG, Lawson MA, Gillies GT, Ritter RC, Grady MS, and MAH (1991) Goniometric motion controller for the superconducting coil in amagnetic stereoaxis system. IEEE Trans Biomed Eng 38(9):899–905
7. Takeda SI, Mishima F, Fujimoto S, Izumi Y, Nishijima S (2006) Development of magnetically targeted drug delivery system using superconducting magnet. J Magn Magn Mater 311(1):367–371
8. Mathieu JB, Beaudoin G, Martel S (2006) Method of propulsion of a ferromagnetic core in the cardiovascular system through magnetic gradients generated by an mri system. IEEE Trans Biomed Eng. 53(2):292–299
9. Mathieu J, Martel S (2007) In-vivo validation of a propulsion method for untethered medical microrobots using a clinical magnetic resonance imaging system. In: IEEE International Conference on Intelligent Robots and Systems, pp 502–508
10. Tamaz S, Gourdeau R, Chanu A, Mathieu JB, Martel S (2008) Real-time mri-based control of a ferromagnetic core for endovascular navigation. IEEE Trans Biomed Eng 55(7):1854–1863
11. Martel S, Mathieu JB, Felfoul O, Chanu A, Aboussouan E, Tamaz S, Pouponneau P, Yahia H, Beaudoin G, Soulez G, Mankiewicz M (2007) Automatic navigation of an untethered device in the artery of a living animal using a conventional clinical magnetic resonance imaging system. Appl Phys Lett 90(11):114105(3p)
12. Yelin KB, Vollmers K, Nelson BJ (2006) Modeling and control of untethered biomicrorobots in a fuidic environment using electromagnetic fields. Int J Rob Res 25(5–6):527–536
13. Jun YW, Seo JW, Cheon J (2008) Nanoscaling laws of magnetic nanoparticles and their applicabilities in biomedical sciences. Accounts Chem Res 41(2):179–189
14. Uecker M, Zhang S, Voit D, Karaus A, Merboldt KD, Frahm J (2010) Real-time mri at resolution of 20 ms. NMR Biomed 23:986–994
15. Zhang S, Gersdorff N, Frahm J (2011) Real-time magnetic resonance imaging of temporomandibular joint dynamics. Open Med Imaging J 5:1–7
16. Dreyfus R, Beaudry J, Roper ML, Fermigier M, Stone HA, Bibette J (2005) Microscopic artificial swimmers. Nature 437:862–865
17. Wiggins CH, Goldstein RE (1998) Flexive and propulsive dynamics of elastica at low reynolds number. Phys Rev Lett 80(17):3879–3882
18. Evans AA, Lauga E (2010) Propulsion by passive filaments and active flagella near boundaries. Phys Rev E 82(4):041,915
19. Behkam B, Sitti M (2006) Design methodology for biomimetic propulsion of miniature swimming robots. ASME J Dyn Syst Meas Control 128(1)
20. Yesin KB, Vollmers K, Nelson BJ (2004) Analysis and design of wireless magnetically guided microrobots in body fluids 2:1333–1338
21. Abbott JJ, Peyer KE, Lagomarsino MC, Zhang L, Dong L, Kaliakatsos IK, Nelson BJ (2007) How should microrobots swim? Int J Rob Res 28(11-12):1434–1447
22. Martel S, Mohammadi M, Felfoul O, Lu Z, Pouponneau P (2009) Flagellated magnetotactic bacteria as controlled mri-trackable propulsion and steering systems for medical nanorobots operating in the human microvasculature. Int J Rob Res 28:571–582
23. Martel S, Tremblay CC, Ngakeng S, Langlois G (2006) Controlled manipulation and actuation of micro-objects with magnetotactic bacteria. Appl Phys Lett 89(23):233904(3p)
24. Bawa R (2008) Nanoparticle-based therapeutics in humans: a survey. Nanotechnol Law Bus 5(2):135–155
25. Vartholomeos P, Mavroidis C (2010) Simulation platform for self-assembly structures in mri-based nanorobotic drug delivery systems. In: IEEE international conference on robotics and automation, pp 5594–5600
26. Arcese L, Fruchard M, Ferreira A (2009) Nonlinear modeling and robust controller-observer for a magnetic microrobot in a fluidic environment using mri gradients. In: IEEE international conference on intelligent robots and systems, pp 534–539
27. Sun C, Lee JS, Zhang M (2008) Magnetic nanoparticles in mr imaging and drug delivery. Adv Drug Deliv Rev 60(11):1252–1265

28. Xu T, Wong J, Shikhaliev P, Ducote J, Molloi MAGS (2006) Real-time tumor tracking using implanted positron emission markers: concept and simulation study. Med Phys 33:2598–2609
29. Park JH, von Maltzahn G, Zhang L, Schwartz MP, Ruoslahti E, Bhatia SN, Sailor MJ (2008) Magnetic iron oxide nanoworms for tumor targeting and imaging. Adv Mater 20:1630–1635
30. McCurrie RA (1994) Structures and properties of ferromagnetic materials. Academic, London
31. Gray DE (1972) American institute of physics handbook. McGraw Hill, New York
32. Plowman S, Smith D (1997) Exercise Physiology. Needham Heights, MA Allyn and Bacon
33. Schmidt-Nielsen K (1984) Scaling: why is animal size so important? Cambridge University Press, Cambridge
34. Kehlenbeck R, Felice RD (1999) Empirical relationships for the terminal settling velocity of spheres un cylindrical columns. Chem Eng Technol 21:303–308
35. White F (1991) Viscous fluid flow. McGraw Hill, New York
36. Pries AR, Secomb TW, Gaehtgens P (1996) Biophysical aspects of blood flow in the microvasculature. Cardiovasc Res 32(4):654–667
37. Arcese L, Fruchard M, Ferreira A (2012) Endovascular magnetically-guided robots: navigation modeling and optimization. IEEE Trans Biomed Eng. To be published 59(4):977–987
38. Choi I, Lim C (2004) Low-velocity impact analysis of composite laminates using linearized contact law. Compos Struct 66:125–132
39. Iimura K, Watanabe S, Suzuki M, Hirota M, Higashitani K (2009) Simulation of entrainment of agglomerates from plate surfaces by shear flows. Chem Eng Sci 64:1455–1461
40. Hays D (1991) Electrostatic adhesion of non-uniformly charged dielectric sphere. J Phys Conf Ser 118:223–228
41. Hays D (1991) Role of Electrostatics in Adhesion, in Fundamentals of Adhesion. Plenum Press, New York
42. Kirbas C, Quek F (2004) A review of vessel extraction techniques and algorithms. ACM Comput Surv 36:81–121
43. Reuzé P, Coatrieux J, Luo L, Dillenseger J (1993) A 3d moment based approach for blood vessel detection and quantification in mra. Technol Health Care 1:181–188
44. Tokuda J, Fischer G, DiMaio S, Gobbi D, Csoma C, Mewes P, Fichtinger G, Tempany C, Hata N (2010) Integrated navigation and control software system for mri-guided robotic prostate interventions. Comput Med Imaging Graph 34:3–8
45. Krstić M, Kanellakopoulos I, Kokotović P (1995) Nonlinear and Adaptive Control Design. Wiley, New York
46. Kanellakopoulos I, Kokotović P, Morse A (1992) A toolkit for nonlinear feedback design. Syst Control Lett 18:83–92
47. Krstić M, Kanellakopoulos I, Kokotović P (1992) Adaptive nonlinear control without over-parametrization. Syst Control Lett 19:177–185
48. Gauthier J, Hammouri H, Othman S (1992) A simple observer for nonlinear systems. application to bioreactors. IEEE Trans Autom Control 37(6):875–880
49. Andrieu V, Praly L (2006) On the existence of a kazantis-kravaris / luenberger observer. Society for Industrial and Applied Mathematics: J Control Optim 45(2):432–456

Chapter 14
Generating Magnetic Fields for Controlling Nanorobots in Medical Applications

Simone Schürle, Bradley E. Kratochvil, Salvador Pané, Mohammad Arif Zeeshan, and Bradley J. Nelson

Abstract During the past decade, significant progress has been shown in nanoscale drug delivery systems, systems for in vitro-testing such as lab-on-chip devices, endoscopic capsules, and robotics for minimally invasive medicine. Advances in nanofabrication technology yielded many new approaches for the batch fabrication process of nanoscale drug carriers including nanotubes, nanowires, and nanoparticles. A major issue is the powering and steering control of these untethered devices in order to allow in vivo interaction with the human body. Several approaches have been suggested that can be categorized as energy storage, energy harvesting, and energy transmission. One promising technique in the class of power transmission is magnetism. Magnetic forces and torques can be applied directly to magnetic material and enable navigation in bodily fluids. In this chapter, we focus on wireless magnetic control of nano drug delivery systems and, in particular, the generation of the required magnetic fields.

14.1 Introduction

Micro- and nanorobots have the potential to revolutionize many aspects of medicine. These untethered, wireless controlled and powered devices will make existing therapeutic and diagnostic procedures less invasive and will enable new procedures never before possible. Miniaturization of functional devices down to nanoscale dimensions has been enabled through the advancement and new development of both bottom up and top down approaches in nanotechnology. This paves the way for many life science applications such as in vitro molecular diagnosis and

S. Schürle • B.E. Kratochvil • S. Pané • M.A. Zeeshan • B.J. Nelson (✉)
Institute of Robotics and Intelligent Systems, CLA H 17.1, Tannenstrasse 3, 8092 ETH Zurich, Switzerland
e-mail: schuesim@ethz.ch; kratochvil@iris.mavt.ethz.ch; vidalp@ethz.ch; marifzee@ethz.ch; bnelson@ethz.ch

C. Mavroidis and A. Ferreira (eds.), *Nanorobotics: Current Approaches and Techniques*, DOI 10.1007/978-1-4614-2119-1_14,
© Springer Science+Business Media New York 2013

biochemical analysis as well as in vivo interaction with the human body [1]. However, when scaling down the physics that predominates changes, for example, imagine a microrobot in the circulatory system. The fluid dynamics change and inertia becomes irrelevant. Instead surface forces that result in significant viscous drag dominate.

A major point to consider is powering the devices. Powering techniques can be classified into three main categories: onboard, scavenged, and transmitted power [2]. Although batteries offer an inexpensive power source, they are not promising candidates since the total deliverable energy scales with volume. Microelectromechanical system (MEMS)-based power generators provide higher energy densities and several approaches to convert various types of energy into electrical energy have been proposed [3, 4]. A desirable way for powering would be to harvest chemical energy directly from the environment such as biofuel cells. Alternatively, power can be instead transmitted wirelessly.

One approach to wireless transmission is the use of magnetic fields. Here it can be further distinguished by induction or by direct application of magnetic forces and torques. From a medical point of view, the magnetic permeability of the human body is approximately the same as that of air, so there are no significant interactions of tissue with low-frequency magnetic fields, as opposed to electric fields. The basic principle of transmitting electrical power with magnetic fields is based on Faraday's law of induction. When current flows in a circuit (primary), a magnetic field is generated in its surroundings. An effective voltage source develops in any nearby circuit (secondary) [5]. Many mesoscale devices incorporate this principle [6–8]. Large coils outside the body generate a varying field that is captured by small coils embedded in capsules. However, at the microscale the challenge is in designing the receiver coils, because they are constrained by planar microfabrication processes. Additionally, the efficiency of voltage rectification on the receiver side becomes increasingly important as the device scales down because the induced voltage amplitude decreases as well.

For microrobots made of a ferromagnetic material, energy can be transmitted directly by an externally applied magnetic field. A magnetic body subjected to an external magnetic field will experience a torque related to the field strength and the magnitude of its own magnetization as well as a magnetic force that is related to the field gradient and the body's magnetization and volume [9].

There is a large body of work describing different possible drug carriers based on magnetic nanospheres or nanowires and nanotubes that are manipulated by externally applied magnetic fields. Ideas to combine these manipulation methods with existent MRI technology have been proposed [10].

In this chapter, we discuss the approach and theory of direct magnetic manipulation of magnetic nanomaterial and explain in detail a system for generating fields for 5-DOF control of nonspherical magnetic bodies. We also give a brief review of current batch fabrication methods of magnetic nanoagents suitable for in vivo medical applications.

14.2 Manipulation of Magnetic Bodies in Fluids

14.2.1 Swimming Behavior at Low Reynolds Numbers

Consider an object of characteristic dimension a which is moving through a liquid at velocity ϑ. The viscosity of the fluid is expressed by η and the density by ρ. Introduced by Osborne Reynolds, the ratio of the inertial force to the viscous force is called the Reynolds number and can be expressed as

$$\mathrm{Re} = \frac{a\vartheta\rho}{\eta} \text{ or } \mathrm{Re} = \frac{a\vartheta}{\nu}, \tag{14.1}$$

where ν is the kinematic viscosity of the fluid. From the equation we can understand that for low Re we are in a world that is either very viscous, very slow, or very small. Low Re flow around a body is referred to as creeping flow or Stokes flow. Further, the flow pattern does not change appreciably whether it is slow or fast, and the flow is effectively reversible. Consequently, reciprocal motion results in negligible net movement [11].

For a better understanding of how different physics are in this world of low Re, consider the locomotion principles of microorganisms in nature. We distinguish between three different basic methodologies of how microorganisms swim [12, 13], as illustrated in Fig. 14.1. For example, cilia are active organelles that are held perpendicular to the flow during the power stroke and parallel to the flow during the recovery stroke. Many cilia are used simultaneously. Another kind of active organelles are eukaryotic flagella. They deform to create paddling motions, such as traveling waves or circular translating movements. Bacterial (prokaryotic) flagella work differently and use instead a molecular motor to turn the base of a passive flagellum [11].

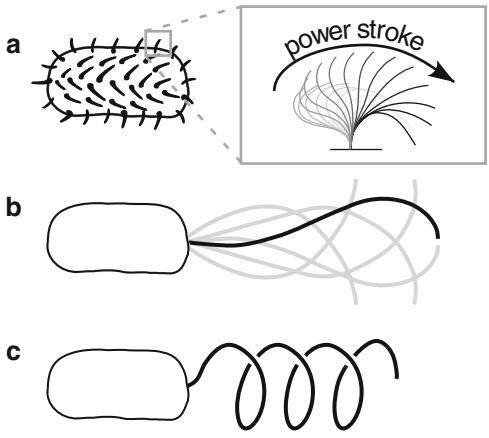

Fig. 14.1 *Locomotion of microorganisms*. (**a**) Cilia move across the flow during the power stroke, and fold near the body during the recovery stroke. (**b**) Eukaryotic flagella create patterns such as traveling waves. (**c**) A molecular motor spins a passive bacterial flagella (reprinted with permission from [11])

A number of bio-inspired robotic swimming methods have been published that try to mimic the locomotion principle for an effective way of transportation. However, many of these techniques require mechatronic components that present challenges in microfabrication and wireless power and control [14, 15]. Almost all these methods use magnetic fields. As discussed above, this actuation principle is attractive since no other method offers the ability to transfer such large amounts of power wirelessly over relatively large distances. Also, a variety of control strategies have been proposed for navigating wireless microrobots such as gradient magnetic fields, stick–slip actuation based on rocking magnetic fields, or by exploiting resonating structures. Bio-inspired magnetically driven propulsion techniques of helical shaped microagents that mimic a bacteria flagellum have been suggested. A rotating magnetic field can be used to rotate a helical propeller [16, 17], eliminating the need to replicate a molecular motor in a microrobot.

A controllable external pulling source is not available for microorganisms; however, we can generate such a source and utilize gradients in magnetic fields to apply forces and torques directly on untethered microrobots; a strategy that obviously could not have evolved through natural selection.

14.2.2 Modeling the Magnetization of Soft Magnetic Bodies

Direct-gradient propulsion is a noncontact manipulation method that can be realized by the use of either permanent or soft magnetic materials. In the first case, the magnetization of the object does effectively not depend on the applied magnetic field, and the object can be modeled as a simple magnetic dipole. The resulting equations for the torque and the force acting on the object are easily determined [18].

If we consider a soft magnetic material, we face easier fabrication methods as well as different issues in control. Additionally, soft magnetic materials can reach levels of magnetization as high as the remanence magnetization of permanent magnets [4, 19, 20]. However, with soft magnetic materials, the magnetization of the body is a nonlinear function of the applied magnetic field. Hence, the relationship between the applied field and the resulting torque and force is nontrivial [18].

The control of soft magnetic beads has been studied widely [10, 21, 22]. Here, a spherical shape simplifies the control problem since there is no preferred direction of magnetization. However, let us now consider a soft magnetic body with a unique axis of symmetry, as shown in Fig. 14.2. We choose ellipsoids as it has been shown that many simple geometries can be accurately modeled magnetically as ellipsoids [23, 24]. Regarding the shape of nanowires as potential drug carriers, we then model the magnetization of a cylindrical body based on its ellipsoidal equivalent.

As illustrated in Fig. 14.2, the body coordinate frame is located at the center of mass and the x-axis is aligned with the axis of symmetry. The body is magnetized to a magnetization $\mathbf{M}$ in units ampere per meter (A/m) by an external magnetic field $\mathbf{H}$ (A/m) at the body's center of mass. Because of the symmetry of the body, the field $\mathbf{H}$, the magnetization $\mathbf{M}$, and the axis of symmetry are coplanar. The applied magnetic field can be also expressed as an applied magnetic flux density $\mathbf{B}$ with the

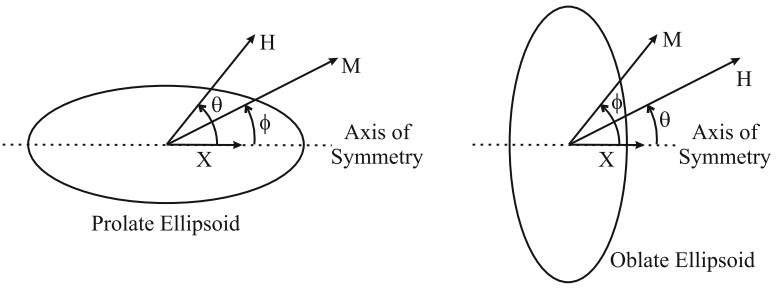

Fig. 14.2 *Axially symmetric bodies in an external magnetic field*. The x-axis of the body frame is aligned with the axis of symmetry. The field $\mathbf{H}$, the magnetization $\mathbf{M}$, and the axis of symmetry are coplanar. $\theta \in [0°, 90°]$ is the angle between $\mathbf{H}$ and the axis of symmetry, and $\varphi \in [0°, 90°]$ is the angle between $\mathbf{M}$ and the axis of symmetry (reprinted with permission from [18])

unit tesla (T). They are related as $\mathbf{B} = \mu_0\, \mathbf{H}$, where $\mu_0 = 4\pi \times 10^{-7}$ T/Am, is the permeability of free space [18]. At low applied fields, the magnetization grows linearly with the applied field until it reaches a saturation magnitude. As the field strength increases, the constant-magnitude saturated magnetization vector rotates toward the applied field.

Let us first consider the linear magnetization region for relatively low applied fields. As stated in [18], the magnetization is related to the internal field by the susceptibility of the material $\mathcal{X}$ as

$$\mathbf{M} = \mathcal{X} \cdot \mathbf{H}_\mathrm{i}. \tag{14.2}$$

The internal field $\mathbf{H}_\mathrm{i}$ can be described as linear superposition of the applied field $\mathbf{H}_\mathrm{d}$ and a demagnetizing field

$$\mathbf{H}_\mathrm{i} = \mathbf{H} + \mathbf{H}_\mathrm{d}. \tag{14.3}$$

The demagnetizing field $\mathbf{H}_\mathrm{d}$ is related to the magnetization by a tensor N of demagnetization factors based on the body geometry as $\mathbf{H}_\mathrm{d} = -N\mathbf{M}$. The matrix N is diagonal if the body coordinate frame is defined such that it aligns with the principle axes of the body: $N = \mathrm{diag}(n_x, n_y, n_z)$. Combining the earlier assumptions, we can relate the magnetization to the applied field by a susceptibility tensor

$$\mathbf{M} = \mathcal{X}_\mathrm{a} \cdot \mathbf{H}_\mathrm{i} \tag{14.4}$$

with a tensor of the form

$$\mathcal{X}_a = \mathrm{diag}\left(\frac{\mathcal{X}}{1 + n_x\mathcal{X}}, \frac{\mathcal{X}}{1 + n_y\mathcal{X}}, \frac{\mathcal{X}}{1 + n_z\mathcal{X}}\right). \tag{14.5}$$

$\mathbf{M}$, $\mathbf{H}$ and $\mathcal{X}_a$ are all written with respect to the body frame. Because of symmetry of the elliptical body, we need only to consider two demagnetization factors—the factor along the axis of symmetry n_a, and the factor in all radial directions

perpendicular to the axis of symmetry n_r. For relatively large susceptibility values, as they are typical for soft magnetic materials on the order of 10^3–10^6, and if we assume the demagnetization factors are not too close to zero, we can approximate (14.5) with

$$\mathcal{X}_a = \mathrm{diag}\left(\frac{1}{n_a}, \frac{1}{n_r}, \frac{1}{n_r}\right). \tag{14.6}$$

From (14.5) we can see that magnetization is insensitive to changes in susceptibility if the susceptibility is relatively high. And in turn, the susceptibility is dominated by the body geometry, since it is determined by the demagnetization factor, which is a geometry-dependent value. The demagnetization factors for general ellipsoid bodies are part of the well-understood results of magnetostatics and were first computed in 1945 [25]. Generally, they are related by the constraint $n_x+n_y+n_z = 1$. We can rewrite this for an axially symmetric body as $n_a+2n_r = 1$. To understand the influence of the geometry on the magnetization vector, we need to look at the magnetization angle ϕ that describes the offset between the magnetization vector and the body symmetry axis. The longer the axis of the body, at constant radial dimension, the smaller the angle will become, since the demagnetization factor n_a along the body's symmetry axis will get smaller and, hence, the magnetization along this axis stronger. This can be understood from the following expressions:

$$n_a = \frac{1}{R^2-1}\left(\frac{R}{2\sqrt{R^2-1}}\ln\left(\frac{R\sqrt{R^2-1}}{R-\sqrt{R^2-1}}\right)-1\right) \quad \text{(prolate ellipsoid)} \tag{14.7}$$

$$n_a = \frac{R^2}{R^2-1}\left(1-\frac{R}{\sqrt{R^2-1}}\sin\left(\frac{R+\sqrt{R^2-1}}{R-\sqrt{R^2-1}}\right)\right) \quad \text{(oblate ellipsoid)}, \tag{14.8}$$

where $R \geq 1$ is the ratio of the long and short dimensions of the body. We can compute the magnetization angle ϕ directly, assuming (14.5), as

$$\phi = \tan^{-1}\left(\frac{n_a}{n_r}\tan\theta\right), \tag{14.9}$$

Thus, the larger R gets, the smaller n_a, and hence the smaller the angle ϕ. The offset angle between ϕ and θ determines how much the body is turning in order to align its magnetization axis with the vector of the applied field which is known as the torque. For a uniform magnetization throughout the body, we assume the volume contributes linearly to the torque and force that the body experiences in an applied external field. This assumption is fairly reasonable for small shapes with high aspect ratios. Hence, we can express the magnetic torque acting on the body in an applied external field as

$$T = \mu_0 v \mathbf{M} \times \mathbf{H}, \tag{14.10}$$

where v is the volume of magnetic material in m^3. The torque, in Newton meters, acts on the magnetic moment of the body such that $\mathbf{M}$ aligns with the direction of the magnetic field. A soft magnetic material in a magnetic field will become magnetized along its long axis, also called its easy axis and the torque tends to align the longest axis of the body with the field.

From (14.9) we can already see that for a soft magnetic sphere, where $n_x = n_y = n_z$ or $n_a/n_r = 1$ applies, there will be no torque acting on the body, since the magnetization vector and the field vector are always aligned which each other. This assumes the absence of any remanent magnetization. However, when taking hysteresis effects into account, the magnetization along the field vector will always be dominant and almost no rotational movement can be translated. This is why, if rotary motion of magnetic beads is required, a permanent magnetic material is generally used.

If the magnetization vector computed in (14.4) results for a certain applied field $\mathbf{H}$ in a smaller magnitude than the saturation magnetization m_s of the material, then we take $\mathbf{M}$ and ϕ as accurate. However, for $|\mathbf{M}| > m_s$, we move into the saturated-magnetization region. We set $|\mathbf{M}| = m_s$ and compute the rotation of $\mathbf{M}$ by minimizing the magnetic energy with respect to ϕ

$$e = \frac{1}{2}\mu_0 v(n_r - n_a)m_s^2 \sin^2\phi - \mu_0\, v m_s |\mathbf{H}| \cos(\theta - \phi), \tag{14.11}$$

where e is the energy in units of Joule. This equation is typically applied as a model for single magnetic-domain samples, but it is a good approximation of a multidomain body once saturation has been reached. To minimize e in (14.10), we get the derivative of e and equalize it to zero

$$(n_r - n_a)m_s \sin(2\phi) = 2|\mathbf{H}| \sin(\theta - \phi). \tag{14.12}$$

$\mathbf{M}$ will rotate such that ϕ satisfies (14.11). Within that model the magnetization vector $\mathbf{M}$ changes continuously with changes in the applied field $\mathbf{H}$, as proven in [18].

Due to the dominant magnetic shape anisotropy, it is in general more appropriate to use bodies with a preferred magnetization axis, the easy axis. For example, this applies for a cylindrical nanowire. We can apply the same constraints to any shape by equating them to ellipsoids. Improving these approximations has been the object of numerous studies, especially for cylinders [26, 27]. From [24] we can extract the demagnetization factor along a cylinder axis based on the model of an equivalent ellipsoid. For a cylinder of length l and radius r with aspect ratio $\tau = l/2r$ the following expression for the demagnetization factor along the cylinder's axis applies:

$$n_a^{\mathrm{cyl}}(\tau) = 1 + \frac{4}{3\pi\tau} - F\left(-\frac{1}{\tau^2}\right), \tag{14.13}$$

with $F(x) \equiv {}_2F_1\left[-\frac{1}{2},\ \frac{1}{2},\ 2,\ x\right]$, which is defined by the Gaussian hypergeometric function ${}_2F_1(a,\ b,\ c,\ z)$.

Let us consider ferromagnetically filled carbon nanotubes to be magnetized. We assume common design parameters such as a length $l = 1\ \mu\text{m}$ and a radius $r = 50\text{nm}$. Computing (14.13) with these values, where a piecewise polynomial approximation of ${}_2F_1$ is created, we get $n_a = 0.0412$, and therefore $n_r = 0.4794$, and the cylinder long axis is the easy axis. For precise and fast alignment performance, we try to maximize the magnetic torque T in (14.10) and look for the external field needed to fully magnetize the body for a maximum $\mathbf{M}$. For a soft magnetic body this means reaching the saturation magnetization m_s. The resulting magnetization dependent on the externally applied magnetic field is given by combining (14.3) and (14.4) as

$$\mathbf{M} = \frac{\mathcal{X}}{1 + \mathcal{X}N}\mathbf{H}, \tag{14.14}$$

which can be approximated as $\mathbf{M} = \frac{1}{N}\mathbf{H}$ for high $\mathcal{X}$, as for nickel ($\mathcal{X} = \mu_r - 1 = 599$).

If we apply a field parallel to the body's long axis, which we set to be coplanar with the x-axis of the coordinate frame, and we set $\mathbf{M} \equiv m_\text{s}$ for the desired reach of the saturation magnetization, we get $|\mathbf{H}_\text{sat}| = n_a \cdot m_\text{s}$ for the field required to fully magnetize the body. This, however, involves the assumption that the body is fully, uniformly magnetized along its long axis.

With the magnetic moment, we can now apply a torque and orient the object as desired. In addition, we can apply a force on the magnetized body and pull the object along its long axis, which is the topic of the next subchapter.

14.2.3 Pulling Through Fluids by Applied Magnetic Gradients

When a magnetic body is subjected to an externally applied magnetic field, it will experience a torque aligning its long axis with the direction of the applied field. Let us set the field vector coplanar with the x-axis of the coordinate frame. Now, if we apply a magnetic gradient that is coplanar with the x-axis, the object will experience a force and is pulled along its long axis. More generally, the magnetic force that body experiences can be expressed as

$$\mathbf{F} = \mu_0 v(\mathbf{M} \cdot \nabla)\mathbf{H}. \tag{14.15}$$

When pulling a magnetic object through Newtonian fluid at low Re, the object nearly instantaneously reaches its terminal velocity ϑ where the viscous drag force, which is linearly related to velocity through a drag coefficient, exactly balances the applied magnetic force $\mathbf{F}$.

We can approximate the magnitude of the required magnetic field gradient needed to accelerate the body until drag force and magnetic force are in equilibrium and a certain body velocity, such as one body length per second, is reached. Since no electric current is flowing through the region occupied by the body, Maxwell equations provide the constraint $\nabla \times \mathbf{B} = 0$. This allows us to express (14.15) in the more intuitive form

$$\mathbf{F} = v(\nabla \cdot \mathbf{B})^{\mathrm{T}}\mathbf{M}. \tag{14.16}$$

If we consider that the field gradient is a vector coplanar with the x-axis of the coordinate frame and the body is uniformly and fully magnetized along its long axis, which is coplanar with the x-axis, we get

$$\begin{pmatrix} F_x \\ F_y \\ F_z \end{pmatrix} = v \begin{pmatrix} \frac{\partial B_x}{\partial x} & 0 & 0 \\ 0 & 0 & 0 \\ 0 & 0 & 0 \end{pmatrix}^{\mathrm{T}} \cdot \begin{pmatrix} m_{\mathrm{s}} \\ 0 \\ 0 \end{pmatrix}. \tag{14.17}$$

We assume only an axial contribution of the field gradient in x-direction and no field and field gradient applied along the y- and z-axis. From classical hydrodynamics we know that drag force can be expressed as

$$\mathbf{F}_{\mathrm{drag}} = D \cdot \vartheta, \tag{14.18}$$

where ϑ is the velocity of the object and D is the fluid and object dependent drag coefficient. For a spherical bead of diameter d, the translational drag coefficient is described as Stokes flow as [28]

$$D_{\mathrm{sphere}} = 3\pi\eta d. \tag{14.19}$$

For slender bodies, such as very thin cylindrical objects, resistive force coefficients (RFC) can be used [29], and the drag coefficient can be approximated as

$$D_{\mathrm{cylinder}} = \frac{2\pi\eta l}{\ln\left(\frac{l}{r}\right) - 0.807}. \tag{14.20}$$

The required gradient $\partial B_x/\partial x$ can be determined when the magnetic force $\overrightarrow{F}$ is identified with the drag force $\mathbf{F}_{\mathrm{drag}}$ and by defining a desired velocity vector along the x-axis.

14.3 Generating Magnetic Fields and Gradients

14.3.1 State of the Art

Controlled magnetic fields can be generated by stationary current-controlled electromagnets [17], as shown in Fig. 14.3, by electromagnets that are position and current controlled [30], by position-controlled permanent magnets, or even by a commercial magnetic resonance imaging (MRI) systems [31]. In any case, the rapid decay of magnetic field strength with distance from its source creates a major challenge for magnetic control.

Permanent magnets generate strong fields on a per volume basis, however, obstacles such as the interaction between adjacent magnets and the requirement of a certain shielding mechanism in order to "turn off" the magnetic field must be considered. In order to control the field strength the magnets need to be externally actuated. In comparison, air-core solenoids have rather weak fields compared to permanent magnets, but field contributions superpose linearly, so current controls the field strength and the field can be switched off instantly.

A common approach to the generation of homogenous fields is the use of Helmholtz coil configurations. By positioning three pairs orthogonal to each other a 3-degree-of-freedom system is achieved. The magnetic propulsion methods discussed above use Helmholtz coils, Maxwell coils, or various combinations thereof, that entirely surround the workspace to generate the desired field strength and orientation. Figure 14.3 shows a typical Helmholtz configuration.

In such a 3 DOF system, the direction of the magnetic field and the magnetic gradient are dependent on each other, meaning that a nonspherical object cannot be freely navigated. This system is consequently nonholonomic, i.e., there exist constraints that prevent the object from moving instantaneously in some directions.

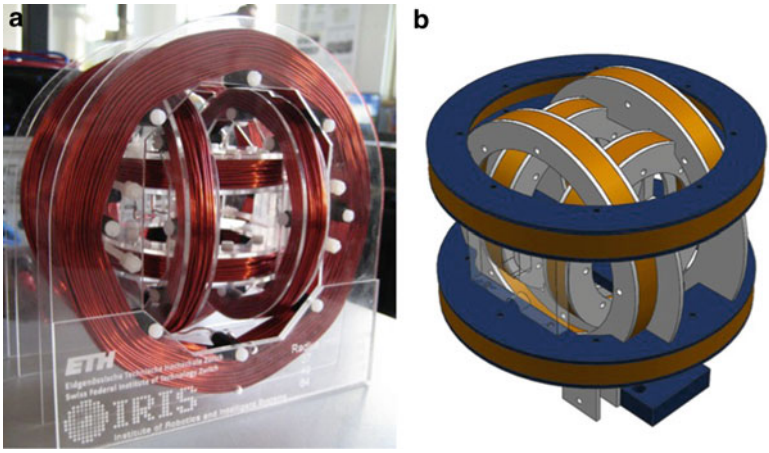

Fig. 14.3 Example of a Helmholtz coil configuration. (**a**) real configuration, (**b**) model

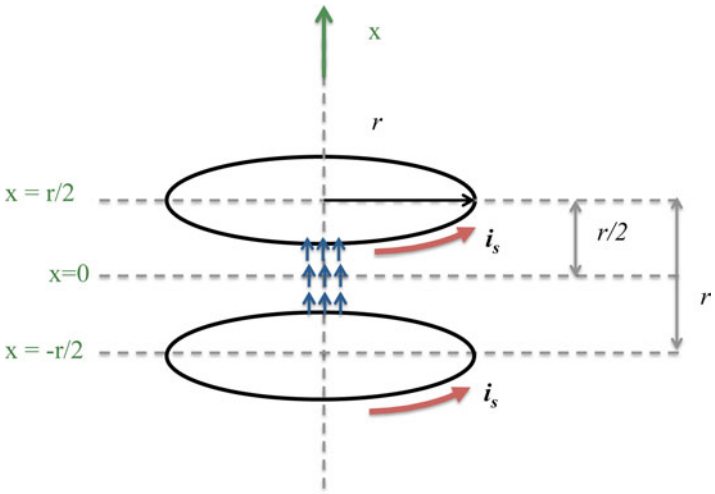

Fig. 14.4 Electromagnetic coils in Helmholtz configuration as field-generation hardware for microrobot propulsion. Uniform magnetic fields in the center of the workspace are generated by current flowing in the same direction

14.3.1.1 Calculating Magnetic Fields and Gradients Generated by Solenoids

Consider a single current loop l at a distance $r/2$ from the origin of the axis. We can express the magnetic field B_x^l along its axis (off-axis field is not considered) generated by a current i_s flowing through the conductor. From the Biot–Savart rule we get

$$B_x^l(x,i_s) = \mu_0 \frac{i_s r^2}{2\left(r^2 + \left(\frac{r}{2} - x\right)^2\right)^{3/2}}, \tag{14.21}$$

where x is the distance along the axis of the coil from its center, and r is the radius of the current loop. For generating higher fields, we can extend the current loop to a solenoid s consisting of n wire turns. A total current $I = n \cdot i_s$ flows then through the coil and the generated field can be expressed as

$$B_x^s(x,i_s) = \mu_0 n \frac{i_s r^2}{2\left(r^2 + \left(\frac{r}{2} - x\right)^2\right)^{3/2}}. \tag{14.22}$$

Now, if we would like to generate a homogenous field over a larger volume of space, we add another solenoid at a distance r from the first solenoid plane, at the position $x = -r/2$, as shown in Fig. 14.4.

We can linearly superpose the two fields generated by the same current i_s flowing through both coils as

$$\begin{aligned} B_x(x,i_s) &= B_x^1(x,i_s) + B_x^2(x,i_s) \\ &= \frac{\mu_0 n}{2}\left(\frac{i_s r^2}{\left(r^2+\left(\frac{r}{2}-x\right)^2\right)^{3/2}} + \frac{i_s r^2}{\left(r^2+\left(\frac{r}{2}+x\right)^2\right)^{3/2}}\right). \end{aligned} \tag{14.23}$$

At the center point of the two coils we get now the axial component of the field in x-direction as

$$B_x(0,i_s) = \left(\frac{4}{5}\right)^{3/2}\frac{\mu_0 n i_s}{r}. \tag{14.24}$$

Note that this is an accurate expression for on-axis field computation and does not cover the off-axis field. The off-axis field calculation is nontrivial and in most cases there is no closed-form analytic solution. It is reasonable, though, to assume a homogenous field for a certain small workspace around the center point at $x = 0$. For Helmholtz coils this can usually be stated for a volume around the center point as large as 5 % of the distance between the coil planes. Another assumption is that the thickness of the wire is considered infinitesimally small and, hence, the coil is considered a plane with no expansion along the x-axis. For long solenoids with many wire turns or with thick wire, the expression in (14.23) must be integrated over the length a of the coil from $x = r/2$ to $x = r/2 + a$.

In order to obtain 3-DOF control, we add two more pairs of coils in an orthogonal arrangement as previously mentioned and shown in Fig. 14.3. We can now build up the field vector $\mathbf{B}(\mathbf{P}) = \left[B_x(\mathbf{P}), B_y(\mathbf{P}), B_z(\mathbf{P})\right]$ at a point $\mathbf{P} = [x, y, z]^{\mathrm{T}}$ of the workspace consisting of the three axial contributions of each coil pair.

To generate a gradient an additional coil pair for each axis can be added. The current in the gradient pair is of same magnitude, but in the opposite direction (Fig. 14.5).

The magnitude of the field gradient at a certain point along the axis can be obtained by the derivative of $B_x'(x,i_s) = B_x^1(x,i_s) - B_x^2(x,i_s)$, where the contributions of the two coils are subtracted according to the inverse current flow. The system consists of 12 solenoids but only 6 current inputs.

An alternative is to work with a single coil pair in each direction for both the generation of field and gradient, resulting in a system of 6 solenoids but controlling each current independently. In other words, a gradient can also be generated with a classic Helmholtz configuration by applying a higher current in one coil of the pair than in the other, with the result of a constant gradient and homogenous field in the center of the two coils.

Depending on the design constraints other variations, such as Maxwell coils, can be employed through a similar derivation.

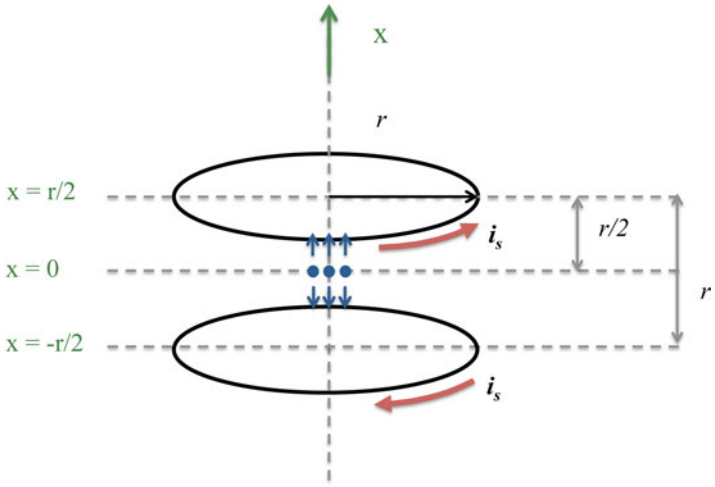

Fig. 14.5 Maxwell coil configuration. Gradient fields can be generated by running the current in opposite directions

14.3.1.2 General Control System

Within a given set of air-core electromagnets, each electromagnet creates a magnetic field throughout the workspace that can be computed for any point **P** of the workspace and any given electromagnet e. We express this field as a vector $\mathbf{B}_e(\mathbf{P})$ From (14.21), the field created by of a solenoid, we know that the field depends linearly on the current i_s through the air-core electromagnet. Hence, we can express $\mathbf{B}_e(\mathbf{P})$ for each electromagnet as a unit-current vector in units T/A multiplied by a current value i_e in units A [32, 33] as

$$\mathbf{B}_e(\mathbf{P}) = \overrightarrow{\widetilde{B}}_e(\mathbf{P}) i_e. \tag{14.25}$$

Since the field contributions of the individual currents superimpose linearly, this can be denoted by the $3 \times n$ unit-field contribution matrix $\mathcal{B}(\mathbf{P})$

$$\mathbf{B}(\mathbf{P}) = \left[\tilde{\mathbf{B}}_1(\mathbf{P}) \ldots \tilde{\mathbf{B}}_n(\mathbf{P})\right] \begin{bmatrix} i_1 \\ \vdots \\ i_n \end{bmatrix} = \mathcal{B}(\mathbf{P})\mathbf{I}. \tag{14.26}$$

This also applies for electromagnets with soft magnetic cores, if the material used resembles an ideal soft magnetic material with negligible hysteresis and the cores are kept within their linear regions.

Furthermore, we can express the gradient of the field in a given direction in a specific frame, e.g., the x direction, as the contributions from each of the currents

$$\frac{\partial \mathbf{B}(\mathbf{P})}{\partial x} = \begin{bmatrix} \frac{\partial \tilde{\mathbf{B}}_1(\mathbf{P})}{\partial x} \cdots \frac{\partial \tilde{\mathbf{B}}_n(\mathbf{P})}{\partial x} \end{bmatrix} \begin{bmatrix} i_1 \\ \vdots \\ i_n \end{bmatrix} = \mathcal{B}_x(\mathbf{P})\mathbf{I}. \tag{14.27}$$

To control a nonspherical magnetic body, we need to precompute the magnitude of the magnetic field (to apply a desired torque to orient the body) and the magnetic gradient **G** (to apply a desired force to move the body) at a certain point **P**. This can be combined as

$$\begin{bmatrix} \mathbf{B} \\ \mathbf{G} \end{bmatrix} = \begin{bmatrix} B(\mathbf{P}) \\ \hat{\mathbf{B}}^{\mathrm{T}} B_x(\mathbf{P}) \\ \hat{\mathbf{B}}^{\mathrm{T}} B_y(\mathbf{P}) \\ \hat{\mathbf{B}}^{\mathrm{T}} B_z(\mathbf{P}) \end{bmatrix} \begin{bmatrix} i_1 \\ \vdots \\ i_n \end{bmatrix} = \mathcal{A}(\hat{\mathbf{B}}, \mathbf{P})\mathbf{I}. \tag{14.28}$$

The n electromagnet currents are mapped to a field and gradient through an $6 \times n$ actuation matrix $\mathcal{A}(\hat{\mathbf{B}}, \mathbf{P})$ which depends on the orientation of the magnetic field and the set point. For a desired field/gradient vector, the currents required can be found using the pseudoinverse

$$\mathbf{I} = \mathcal{A}(\hat{\mathbf{B}}, \mathbf{P})\dagger \begin{bmatrix} \mathbf{B} \\ \mathbf{G} \end{bmatrix}. \tag{14.29}$$

If there are multiple solutions to achieve the desired field and gradient, the pseudoinverse finds the solution that minimizes the two-norm of the current vector, which is desirable for the minimization of both power consumption and heat generation. The pseudoinverse of $\mathcal{A}$ is of rank 5 corresponding to the no-torque generation about the magnetization axis, which is never possible. More details on this can be found in [32]. In order now to use (14.29), a unit-current field map must be constructed for each of the electromagnets. This can be done by analytical models, finite-element-method (FEM) data or system measurements.

14.3.2 A Hemispherical Electromagnetic System for 5-DOF Wireless Micromanipulation

The use of a Helmholtz coil configuration does not allow the generation of fields and gradients independently of one another; we are thus limited to nonholonomic manipulation performance for any full state control in 3D. To create a holonomic system with 5-DOF (3-DOF positioning and 2-DOF pointing orientation) wireless

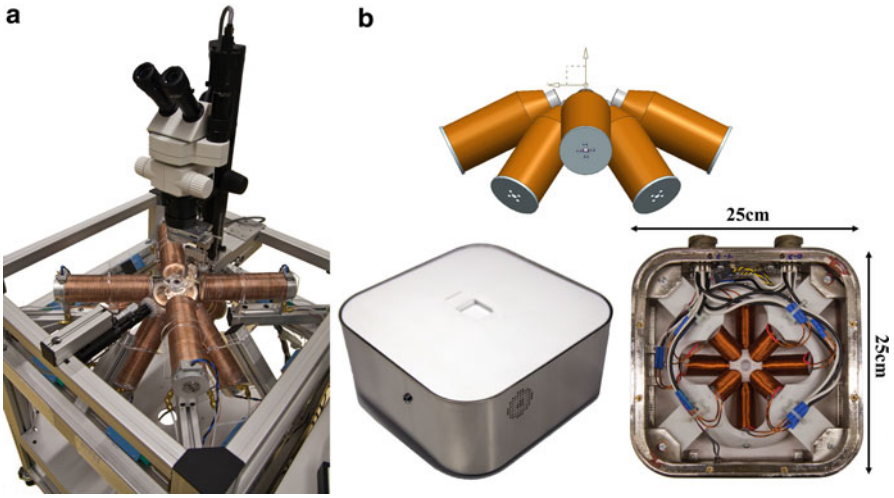

Fig. 14.6 (**a**) OctoMag system constructed at ETH Zurich [31] (**b**) *top* and *bottom right*: electromagnetic core arrangement as model and from *bottom view*; *bottom left*: *top view* of the system, a 30 mm × 30 mm area is available for sample placement [32]

control of a magnetic microrobot a different electromagnet configuration is needed. Stationary electromagnets are selected instead of permanent magnets that must be mechanically actuated. Air-core electromagnets are advantageous due to the linear superposition of the generated fields, but the fields are very weak unless superconducting coils are used. However, superconductors have slow slew rates. Alternatively, soft magnetic cores can be used to enlarge the field by a factor μ_r, which depends on the magnetic permeability of the core material. However, analytical modeling becomes more complicated, since the fields do not superimpose linearly. Though, if kept in their linear regions, this presents only a minor constraint on modeling and still offers a relatively large region of control.

So far, we have considered microrobotic control that relies on systems that fully surround the workspace. A technical difficulty lies in scaling the system to create an interior volume that is relatively large. Based on the control system explained in Sect. 14.3.1 and by leaving the number of electromagnets open, an optimization problem can be created that results in a new system with a unique coil configuration. The system enables the control of a microrobot through a large workspace while being completely unrestrained in rotational DOFs. The system is called the OctoMag (see Fig. 14.6a) and is discussed in detail in [32].

In a modification of the OctoMag, the location of the electromagnets is restricted to a single hemisphere. This allows more physical freedom in the workspace and allows the system to be compatible with an inverted microscope. This system, called the MiniMag, is shown in Fig. 14.6b [33]. With its much smaller size it also fits under conventional tabletop microscopes and is easily transportable.

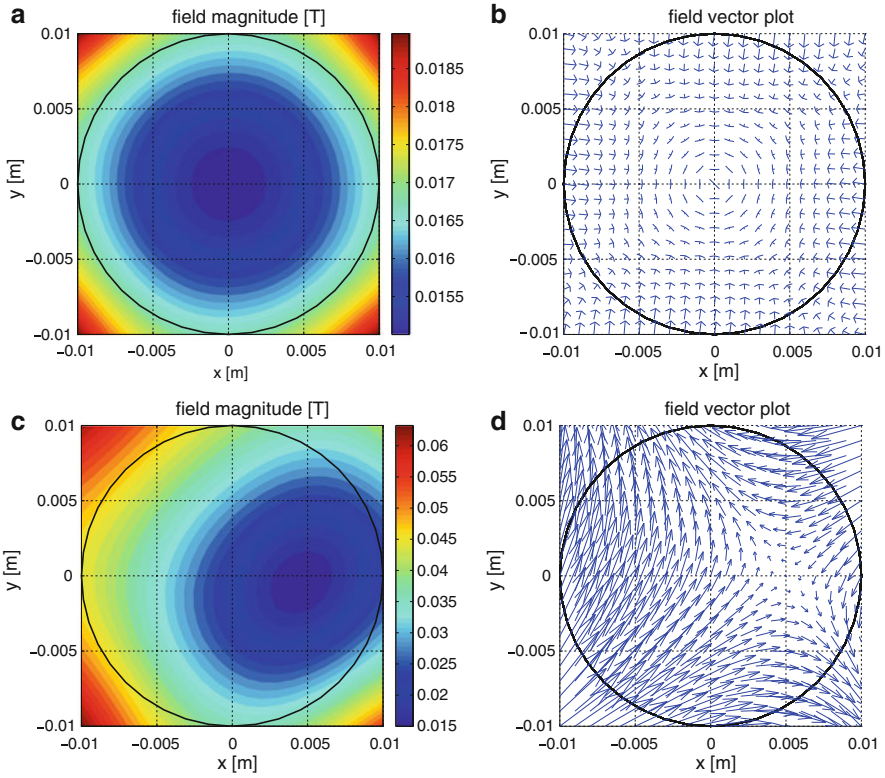

Fig. 14.7 Theoretical field magnitude (**a**, **c**) and orientation (**b**, **d**) at $z = 0$ of the workspace when the system is commanded to a 15 mT field along the positive z-axis at [0.000, 0.000, 0.000] (**a**, **b**) and at [0.005, 0.000, 0.000] (**c**, **d**). The figure illustrates a more homogeneous region when the set point is at the center of the workspace than toward the extremities, which reduces the need for position feedback when working within a small workspace (reprinted with permission from [32])

14.3.2.1 System Design

An optimal magnetic manipulation system can be designed using n electromagnets [32]. Given a design criteria of an isotropic task space, a configuration with eight electromagnets, arranged as illustrated in Fig. 14.6, results in the best performance. Intuition might lead one to believe that electromagnets must uniformly surround the workspace in order to create the desired isotropic behavior, but this is not the case. With the configuration shown in Fig. 14.6, pushing, pulling, and lateral forces can be exerted while maintaining any desired microrobot orientation.

Using (14.29) for control requires knowledge of the microrobot's pose. Figure 14.7 depicts the contour plots of a magnetic field of 15 mT along positive z, set for the position **P** at the origin of the magnetic workspace (a, b) and for a position 5 mm off center (c, d). The generated field is inhomogeneous and increases towards

the extremities. The set point of the magnetic field defines an unstable equilibrium position from where the field magnitude increases equally in all directions. The instability of this equilibrium causes magnetic agents to drift, as dictated in theory by Earnshaw's theorem. For drift minimization, the magnetic agent needs to be kept in the unstable equilibrium state by setting the magnetic field at its updated location.

For open-loop control experiments, the set point can be left at the origin of the system if we limit the physical workspace. Then, we can assume that the magnetic field does not significantly vary across that area (Fig. 14.7a, b) and the drift is minimal. Hence, we can eliminate the need for any localization of the micro/nanorobot. This assumption is reasonable in the case of objects ranging on the order of nanometers or tens of micrometers that use workspaces smaller than $500\ \mu m^3 \times 500\ \mu m^3 \times 500\ \mu m^3$. For applications that require a larger workspace, the set point needs to be updated through vision-based agent localization (Fig. 14.7c, d). However, as the set point approaches the boundaries of the workspace, higher inhomogeneities are appearing.

Closed-loop servoing requires an additional control loop, wherein the error between the desired and the current position of the object is used as input to a PID controller that calculates the desired magnetic field strength and gradient. With closed-loop position control the drift is compensated for.

There are a number of methods to generate the current field maps that are required for the control system. One can either explicitly measure the magnetic field of the final, constructed system at a grid of points, or one can compute the field values at a grid of points using FEM models. For every single electromagnet a unit-current field map must be calculated as shown in (14.25). In the event that a given electromagnet configuration exhibits geometrical symmetry, it is possible to calculate fewer maps and then rotate them during run time using homogeneous transformations. The point dipole model is chosen as analytical model for fast computational reasons. This approximation is suitable for solenoids and cylindrical magnets, also derived in [34].

14.3.2.2 System Performance

MiniMag is capable of producing magnetic fields in excess of 20 mT and field gradients of 2 T/m up to 2 kHz and with OctoMag fields up to 50 mT and gradients of 2 T/m up to 10 Hz can be reached. The frequency response is in latter case slower, since the coils have higher inductance and higher voltages need to be applied to drive the system. Although MiniMag was originally designed for gradient control of microobjects, a variety of different control methods are possible, e.g., stepping or rotational modes. Figure 14.8 demonstrates a microrobot moving on a circle trajectory while levitating in a plane under closed-loop servo control. The servo control was performed with a simple proportional controller to the target point. The tilt visible in the trace is due to the fact that the drift in the system varies slightly across the workspace due to calibration and modeling inaccuracies, which are not taken into consideration in the controller causing it to be biased.

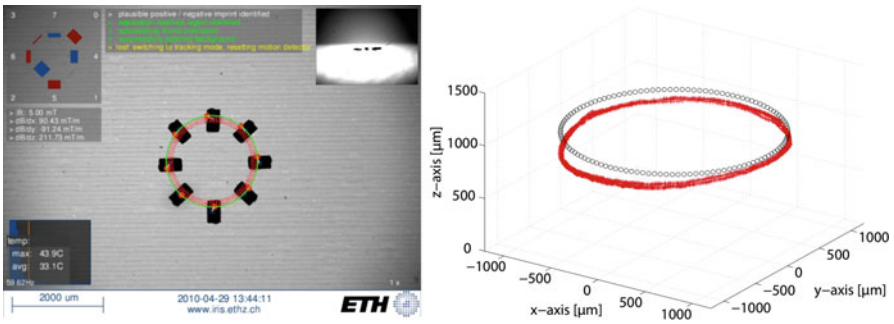

Fig. 14.8 Time-lapse image of a permanent magnetic agent being servoed along a circular trajectory in the MiniMag. The image shows a *top view* of the experiment, while the picture-in-picture inset shows a *side view*. The trace on the *right image* shows tracked data for the duration of the experiment. The *circles* indicate the target way points while the *pluses* show the tracked position. The average trajectory completion time is 7.14 s (reprinted with permission from [32])

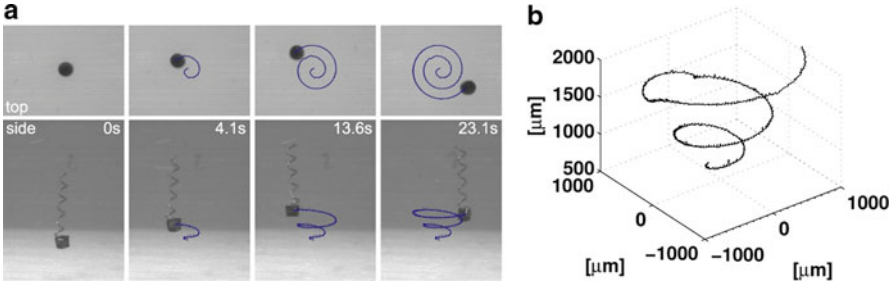

Fig. 14.9 Hybrid swimming/gradient strategy. The agent is rotated at a speed sufficient for gravity compensation and the small gradients on the order of 50–100 mT/m are used to servo the agent through the trajectory [32]

As an alternate propulsion method, swimming strategies can be implemented for microrobotic control through the use of rotating magnetic fields [11]. Figure 14.9 shows results of using the MiniMag for this type of control. In this experiment we first levitate a helical swimmer with a 380 µm large SmCo head and an approximately 2,000 µm long Cu tail into the center of the workspace using gradient control. A rotational magnetic field around the z-axis at different frequencies with no gradient is applied and the corresponding average vertical velocities are recorded. When the rotation frequency is small, the swimmer does not exert as much force as gravity and falls. At 25–50 Hz the agent generates enough force to lift itself, and at frequencies beyond this it moves in the vertical direction.

The system is capable of 5-DOF control while occupying a single hemisphere and providing an open workspace. It provides precise positioning under closed-loop control with computer vision but can also be used with no visual tracking, relying only on visual feedback from the human operator during teleoperation.

14.4 Fabrication of Magnetic Drug Carriers

14.4.1 Overview

In the past 20 years, several synthetic methods for the fabrication of nanostructures such as nanoparticles, nanohelices, nanotubes, and nanowires (NWs) have been proposed. Miniaturization of devices towards the nanoscale is important for many new applications in biotechnology and medicine. In the field of micro- and nanorobotics, these nanostructures provide a potential biomedical platform for controlled, noninvasive medicine. The treatment of cancer is one of the most pursued directions in these fields. Procedures like chemotherapy, radiation therapy, and surgery are applied and succeed in several cases; however, they are far from being efficient. A major drawback is the inability to specifically target cancer cells; hence, healthy regions become traumatized. As an alternative, the use of multifunctional magnetic nanomaterials that specifically target cancer cells has been proposed [35]. These materials can be used for better imaging of tumors, and to locally deliver anticancer drugs simultaneously. Among the variety of magnetic nanostructures available, NWs or nanotubes are advantageous over others due to their high aspect ratio and magnetic shape anisotropy. Carbon nanotubes (CNTs) are probably the most widely studied nanostructure, due to their extraordinary mechanical and physicochemical properties. A wide variety of applications, including biomedical devices for diagnostics and drug delivery, have been proposed. Since carbon nanotubes can be functionalized both endohedrally and exohedrally, they can be used as multifunctional nanocarriers for targeted drug delivery [35].

14.4.2 Magnetic Nanoparticles

Magnetic nanoparticles (MNPs) represent one major class of nanoscale materials and a tremendous amount of work has been carried out to better address clinical needs through specific design, synthesis, and surface functionalization of MNPs. Potential applications can be divided into two major areas, MNPs for MR imaging and for drug delivery. In MRI technology, they can be used for cancer imaging, cardiovascular disease imaging, and molecular imaging. Next-generation MNP-based MRI contrast agents and carriers for drug delivery incorporate novel nanocrystalline cores, coating materials, and functional ligands to improve the detection and specific delivery of these nanoparticles [36].

MNPs can be generally classified into two main groups: ceramics, such as iron oxide and barium ferrite, metallic NPs and alloys, such as cobalt, nickel, iron, and combinations thereof containing at least one ferromagnetic element. Numerous synthetic methods have been developed to synthesize MNPs such as coprecipitation, sol–gel synthesis, microemulsion synthesis, sonochemical reaction, hydrothermal reaction, thermal decomposition, electrospray synthesis, and laser pyrolysis [37].

Methods to fabricate iron oxide NPs vary from classical wet chemistry solution based methods to laser pyrolysis or chemical vapor deposition (CVD) [38]. Iron oxide NPs are particularly attractive due to their biocompatibility and ease of fabrication. Metallic NPs, such as those made of iron or nickel, tend to be chemically unstable. However, since iron nanoparticles are attractive due to their high saturation magnetization, ways to improve stability have been pursued. As a result, core-shell techniques such as the coating with magnetite (Fe_3O_4), gold, or biocompatible silica have been suggested. Concerning metal-alloy NPs, combinations of metals can be synthesized that exhibit superparamagnetic properties or that possess high magnetocrystalline anisotropy such as FePt [37].

There are numerous strategies to functionalize MNPs depending on the type of MNP and purpose of the functionalization. For biocompatibility reasons an additional coating is often required. For the purpose of drug delivery, suitable drug molecules have to be attached, preferably in a manner so that they can also be released. For optical imaging probes, fluorescent dyes are added. With advancements in DNA technology, the delivery of genes attached to MNPs may present a potential application.

14.4.3 Fabrication of Magnetic Nanowires

Most magnetic nanowires for applications in biomedicine are fabricated by the use of nanoporous templates and a subsequent electrodeposition of the required metal [39]. This method of template synthesis has become popular for the preparation of cylindrical materials in a facile, high-throughput and cost-effective way [40]. As described above for nanoparticles, surface functionalization is also pursued for NWs. Among this wide range of nanomaterials, carbon nanotubes are particularly interesting. Their unique electrical, mechanical, and optical properties are already widely exploited; however, they are also superb candidates for various functionalization methods. They offer strong covalent bonds as well as weaker π-π-stacking and hydrophobic wrapping. CNTs combined with magnetic nanowires create a device amenable to magnetic manipulation. Filling CNTs with a ferromagnetic material results in an object that becomes most easily magnetized along its long axis.

Several approaches have been adopted to fill the core of carbon nanotubes with ferromagnetic materials like Ni, Co, and Fe including

1. Pyrolysis, where formation and filling of carbon nanotubes occur simultaneously [41–43].
2. Step-by-step approach, where during the growth process of the CNT their caps are removed and magnetic material diffuses inside the tubule [44, 45].
3. Template-assisted growth of carbon nanotubes followed by electrodeposition of metal catalysts inside the pores of a template [46, 47].

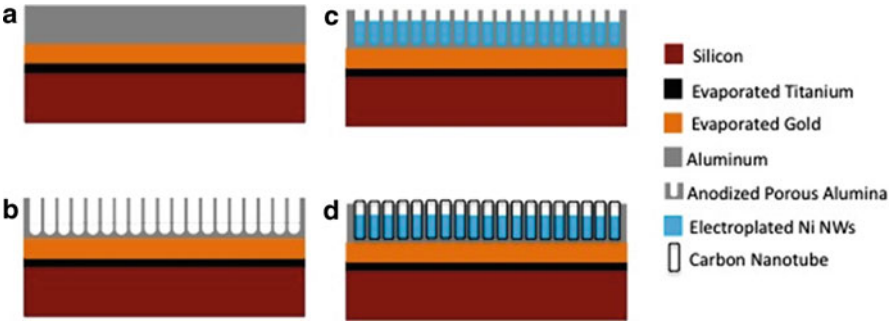

Fig. 14.10 Fabrication steps of the Ni-filled CNTs: (**a**) Silicon wafer with evaporated Al on *top*; (**b**) Anodization process; (**c**) Electrodeposition of Ni NWs (**d**) CNT growth

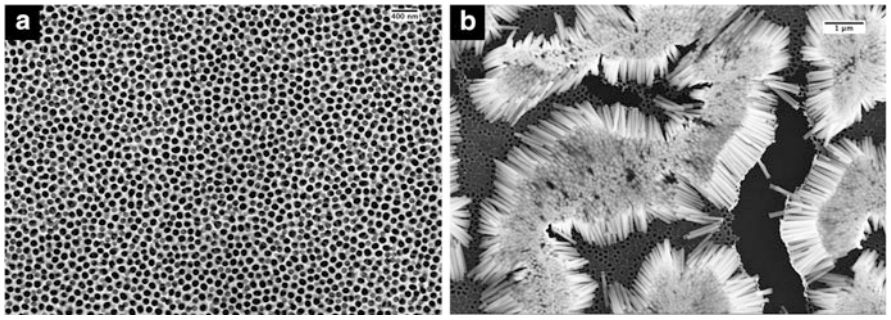

Fig. 14.11 (**a**) SEM image of AAO template. The pore diameter distribution is 110 ± 10nm (**b**) Array of Ni NWs after selective etching of the AAO template

The template-assisted synthesis has become a widely adopted fabrication technique. The process steps to fabricate ferromagnetic nickel nanowire cores encapsulated in a carbon nanotube shell by the use of template-assisted electrodeposition and growth is shown in Fig. 14.10.

The sequence starts with the fabrication of a suitable template for NW synthesis [35]. Aluminum is evaporated on a layer of gold and titanium on a silicon surface and a subsequent anodization process transforms the layer into porous alumina (AAO) (Fig. 14.11a). Anodization of aluminum is tunable with regards to both diameter and length depending on the operating conditions such as anodizing voltage and time. AAO templates also produce arrays of carbon nanotubes of equal dimensions thereby making it possible to have a standardized growth process for large-scale production. An array of uniform pores of e.g., 100nm diameter and 1 μm depth (which is defined by the thickness of the aluminum layer) can be achieved.

Next, nickel is deposited inside the pores by galvanostatic pulse current (PC) electrodeposition. Eletrodeposition is an effective method for growing 1D nanostructures in a controlled way without the implementation of expensive instrumentation, high temperatures or low-vacuum pressures. A result of a batch of Ni NWs after template release is illustrated in Fig. 14.11b.

Fig. 14.12 Hybrid CNT-based magnetic nanostructures arranged on the silicon surface after release of the template

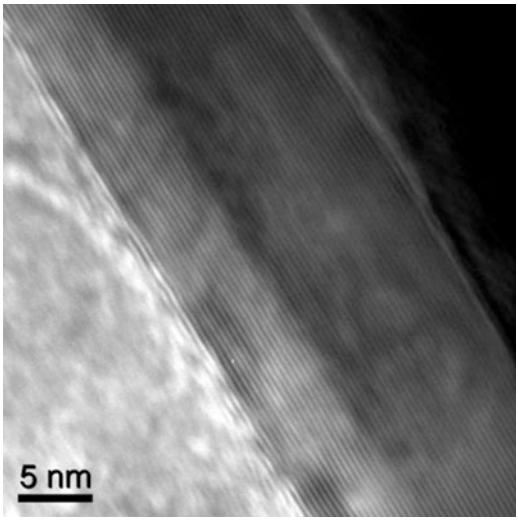

Fig. 14.13 High resolution TEM image demonstrating graphitic shells encapsulating a Ni NW. the thickness of the shells is 17.65nm whereas the interlayer distance is 0.345nm which corresponds to 50 shells

After PC electrodeposition, low-pressure chemical vapor deposition (LPCVD) is utilized to coat nanowires with graphitic as shown in Figs. 14.12 and 14.13.

Finally, the AAO template is dissolved, e.g., by NaOH, and the Ni-filled CNTs can be washed and dispersed in liquid. They are ready then for further exohedral functionalization such as the chemical attachment of fluorescent dyes for tracking and drug molecules for targeted delivery. Considering the manipulation,

the graphitic volume was neglected in the above estimations, which increase the drag force and decrease the actual magnetic volume per drug carrier. However, the thickness of the shell layer varies widely and was not considered due to simplicity.

As mentioned earlier, there are numerous techniques to fabricate cylindrical hybrid magnetic drug carriers. However, the template-assisted technique was described here more in detail, since it is a facile batch-fabrication method that allows a uniform coating of ferromagnetic nanowires with high quality graphene layers for biomedical functionalization.

14.5 Conclusion

This chapter focuses on methods of generating multi degree-of-freedom magnetic fields and gradients to wirelessly control nanorobots with potential applications in targeted drug delivery. Recent developments in fabricating magnetic nanodevices that can be used for biomedical applications indicate this area of research has great potential. The field of nanorobotics requires the expertise of several disciplines including medicine, biology, physics, micro-/nanosystem technology, hardware engineering, and computer science and is pushing research in fabrication of optimal nanostructures for the use as minimally invasive platforms.

References

1. Lymberis A (2010) Micro-nano-biosystems: an overview of European research. Minim Invasive Ther 19:136–143
2. Nelson BJ (2010) Microrobots for minimally invasive medicine. Annu Rev Biomed Eng 12: 55–85
3. DiSalvo FJ (1999) Thermoelectric cooling and power generation. Science 285(5428):703–706
4. Kasap SO (2006) Principles of electronic materials and devices, 3rd edn. McGraw-Hill, New York, NY
5. Popovic M et al (2006) Electromagnetic induction. In: Bansal R (ed) Fundamentals of engineering electromagnetics. Taylor & Francis, Boca Raton, FL
6. Theodoridis MP, Mollov SV (2005) Distant energy transfer for artificial human implants. IEEE Trans Biomed Eng 52(11):1931–1938
7. Lenaerts B, Puers R (2007) An inductive power link for a wireless endoscope. Biosens Bioelectron 22(7):1390–1395
8. Guanying M et al (2007) Power transmission for gastrointestinal microsystems using inductive coupling. Physiol Meas 28(3):N9–N18
9. Furlani EP (2001) Permanent magnet and electromechanical devices: materials, analysis, and applications. Academic, San Diego, CA, p 518
10. Martel S et al (2007) Automatic navigation of an untethered device in the artery of a living animal using a conventional clinical magnetic resonance imaging system. Appl Phys Lett 90(11):114105-1–114105-3
11. Abbott JJ et al (2009) How should microrobots swim? Int J Robot Res 28:1434–1447
12. Brennen C, Winet H (1977) Fluid mechanics of propulsion by cilia and flagella. Annu Rev Fluid Mech 9:339–398

13. Vogel S (2003) Comparative biomechanics: life's physical world. Princeton University Press, Princeton, NJ
14. Behkem B, Sitti M (2006) Design methodology for biomimetic propulsion of miniature swimming robots. ASME J Dyn Syst Meas Control 128:36–43
15. Kósa G, Shoham M, Zaaroor M (2007) Propulsion method for swimming microrobots. IEEE T Robotic Autom 23(1):137–150
16. Honda T, Arai KI, Ishiyama K (1996) Micro swimming mechanisms propelled by external magnetic fields. IEEE T Magn 32(5):5085–5087
17. Zhang L, Abbott JJ, Dong LX, Kratochvil BE, Bell D, Nelson BJ (2009) Artificial bacterial flagella: fabrication and magnetic control. Appl Phys Lett 94:064107
18. Abbott JJ (2007) Modeling magnetique torque and force for controlled manipulation of soft-magnetic bodies. IEEE T Robotic 23(6)
19. Jiles D (1991) Introduction to magnetism and magnetic materials. Chapman and Hall, London
20. O'Handley RC (2000) Modern magnetic materials: principles and applications. Wiley, New York, NY
21. Ergeneman O, Dogangail G, Kummer MP, Abbott JJ, Nazeeruddin MK, Nelson BJ (2008) A magnetically controlled wireless optical oxygen sensor for intraocular measurements. Sens J 8:29–37
22. Amblard F, Yurke B, Pargellis A, Leibler S (1996) A magnetic manipulator for studying local rheology and micromechanical properties of biological systems. Rev Sci Instrum 67(3): 818–827
23. Judy JW (1996) Batch-fabricated ferromagnetic microactuators with silicon flextures. Dissertation, University of California, Berkeley
24. Beleggia M, De Graef M, Millev YT (2006) The equivalent ellipsoid of a magnetized body. J Phys D Appl Phys 39:891–899
25. Osborn JA (1945) Demagnetizing factors of the general ellipsoid. Phys Rev 67(11/12):351–357
26. Joseph RI (1966) Ballistic demagnetizing factor in uniformly magnetized cylinders. J Appl Phys 37:4639
27. Chen DX, Brug JA, Goldfarb RB (1991) Demagnetizing factors for cylinders. IEEE Trans Mag 27(3601)
28. White FM (1991) Viscous fluid flow, 2nd edn. McGraw-Hill, New York, NY
29. Cox RG (1970) The motion of long slender bodies in a viscous fluid part 1. General theory. J Fluid Dyn 44:791–810
30. Yesin KB, Vollmers K, Nelson BJ (2006) Modeling and control of untethered bio-microrobots in a fluidic environment using electromagnetic fields. Int J Robot Res 25(5–6):527–536
31. Mathieu JB, Beaudoin G, Martel S (2006) Method of propulsion of a ferromagnetic core in the cardiovascular system through magnetic gradients generated by an MRI system. IEEE BioMed Eng 53(2):292–299
32. Kummer MP et al (2010) OctoMag: an electromagnetic system for 5-DOF wireless micromanipulation. IEEE T Robotic 26:6
33. Kratochvil BE et al (2010) MiniMag: a hemispherical electromagnetic system for 5-DOF wireless micromanipulation. In: Proceedings of IEEE ISER, New Delhi, India
34. Derby N, Olbert S (2010) Cylindrical magnets and ideal solenoids. Am J Phys 78(3a):229
35. Zeeshan MA et al (2011) Structural and magnetic characterization of batch-fabricated nickel encapsulated multi-walled carbon nanotubes. Nanotechnology 22:275713
36. Sun C, Lee JSH, Zhang M (2008) Magnetic nanoparticles in MR imaging and drug delivery. Adv Drug Deliv Rev., 60(11):1252–65
37. Hao R et al (2010) Synthesis, functionalization, and biomedical applications of multifunctional magnetic nanoparticles. Adv Mater 22:2729–2742
38. Tartaj P et al (2003) The preparation of magnetic nanoparticles for applications in biomedicine. J Phys D Appl Phys 36:182–197
39. Varadan VK, Chen L, Xie J (2008) Nanomedicine: design and application of magnetic nanomaterials, nanosensors and nanosystems. Wiley, Chichester

40. Nagawaka M, Oda H, Kobayashi K (2010) Inorganic and metallic nanotubular materials: recent technologies. Springer, Berlin
41. Leonhardt A et al (2003) Synthesis and properties of filled carbon nanotubes. Diam Relat Mater 12:790–793
42. Watts PCP et al (2002) Fe-filled carbon nanotubes: nano-electromagnetic inductors. Chem Mater 14:4505–4508
43. Kozhuharova R et al (2003) Synthesis and characterization of aligned Fe-filled carbon nanotubes on silicon substrates. J Mater Sci Mater Electron 14:789–791
44. Korneva G et al (2005) Carbon nanotubes loaded with magnetic particles. Nano Lett 5:879–884
45. Pal S, Chandra S, Phan MH, Mukherjee P, Srikanth H (2009) Carbon nanostraws: nanotubes filled with superparamagnetic nanoparticles. Nanotechnology 20:485604–485611
46. Yen JH et al (2005) Effect of nanowire catalyst for carbon nanotubes growth by ICP-CVD. Diam Relat Mater 14:841–845
47. Liu LF (2006) Template synthesis, characterization and magnetic property of Fe nanowires-filled amorphous carbon nanotubes array J. Phys D Appl Phys 39:3939–3944

Chapter 15
Techniques for MRI-Based Nanorobotics

Christian Dahmen, Tim Wortmann, and Sergej Fatikow

Abstract This chapter describes several techniques developed for the use of clinical MRI systems for robotic approaches. At the core are approaches developed for the detection of ferromagnetic object artifacts inside MRI images, the tracking of these and the propulsion sequence. All approaches have been verified in experiments, and tests for the transferability to nanoparticle agglomerations have been made.

15.1 Introduction

Magnetic resonance imaging (MRI) is a powerful medical imaging modality which uses strong magnetic fields and sophisticated signal generation, receiving and field modulation strategies to extract images from biological tissue. Approaches are widely followed on how to use the MRI with additional actuation and robotic components to develop robotic systems with many uses in surgery, diagnostics, and treatment [1]. Though the strong magnetic fields put heavy constraints on useable materials and feasible actuation principles for any kind of actuation technology, the magnetic gradient coils used for imaging themselves offer a possibility for generating forces. Though the achievable gradients are limited in clinical MRI systems, the principal feasibility for certain cases has been shown [2].

This work focuses on the development of techniques to enable the use of this approach in medical applications. All design has been done in a standard MRI

C. Dahmen (✉) • T. Wortmann • S. Fatikow
Division Microrobotics and Control Engineering (AMiR), University of Oldenburg, Uhlhornsweg 84, 26129 Oldenburg, Germany
e-mail: christian.dahmen@uni-oldenburg.de; tim.wortmann@informatik.uni-oldenburg.de; fatikow@uni-oldenburg.de

C. Mavroidis and A. Ferreira (eds.), *Nanorobotics: Current Approaches and Techniques*, DOI 10.1007/978-1-4614-2119-1_15,
© Springer Science+Business Media New York 2013

environment supplied by the MRI manufacturer. Certain attempts have been made to test the scalability of the imaging and propulsion to agglomerations of nanoparticles. All the work presented was part of the European project NANOMA.

15.2 MRI Artifact Imaging

MRI is based on the phenomenon of nuclear magnetic resonance (NMR). Many materials show NMR, but for medical applications the magnetic resonance of hydrogen nuclei is by far the most important. NMR can be explained best using the concept of nuclei spin (Fig. 15.1).

An externally applied magnetic field B_0 causes the nuclei to rotate around the direction of the field ("precession," Fig. 15.2). The frequency of precession ω_0 is directly proportional to the gyromagnetic ratio γ of the nucleus and the applied field strength (Larmor equation).

$$\omega_0 = \gamma \cdot B_0$$

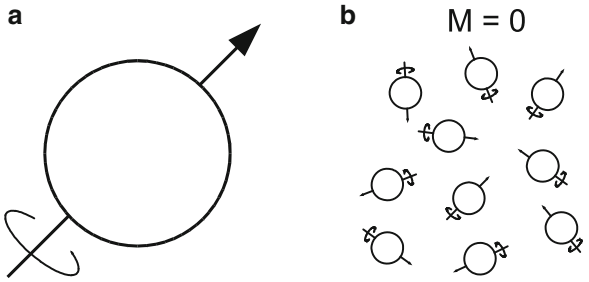

Fig. 15.1 (**a**) Concept of nuclei spin and its magnetic moment vector. (**b**) Without an externally applied magnetic field, nuclear spins are randomly oriented. Therefore the sum of their magnetic moments ("net magnetization") is equal to zero

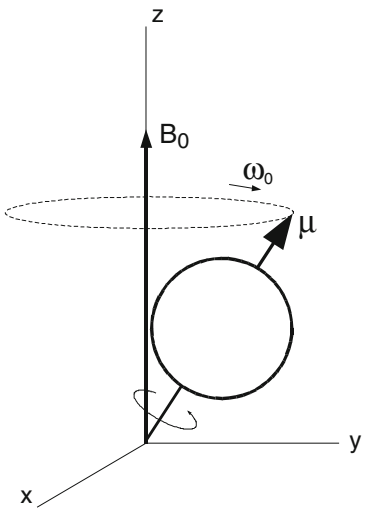

Fig. 15.2 Precession of a nuclear magnetic moment μ around an externally applied magnetic field B_0 along the *dashed line*. The angular frequency of precession is ω_0

If the specimen is exposed to an electromagnetic RF pulse with frequency ω_0, the magnetic moment vector μ can be caused to invert direction and therewith change into a high-energy state ("spin down"). Shortly after this excitation μ will return to its original state ("spin up") and emit the energy difference in the form of another RF signal. This signal response is the NMR. The strength of the NMR signal depends on many conditions but mainly on the density of the excited nuclei in the specimen and on their chemical bondings. These parameters vary between different tissues of the human body and therefore NMR can be exploited to create tomographic images of the human body.

The tissues do not only differ in proton density but also in the time that is needed to recover from the excitation. This "relaxation" can be further subdivided into longitudinal (along B_0) and transverse components which are best described by T1 and T2. By definition T1 is the time needed until 63 % of the original longitudinal net magnetization in thermal equilibrium is restored. After T2, the transverse magnetization has vanished to 37 % of its initial value. This results in three basic forms of image contrast which can be used to form a MR image: proton density, T1-, and T2-weighted intensity images.

By analyzing the spectral composition of a NMR signal conclusions about its constituting materials can be drawn. However this knowledge cannot be used to form an image as there is no information about the spatial origin of the signal. This problem can be overcome by introducing gradient fields $G_{X,Y,Z}$ in all spatial directions, which are applied additionally to the static field B_0. By modulating the gradient strength theoretically a specific point inside the specimen can be chosen in which the resulting Larmor frequency exactly matches the frequency of a very narrow-banded excitation RF-pulse. Successively scanning every volume element (voxel) would provide a three-dimensional image. However this procedure is highly inefficient and not applicable in medical examinations.

Instead, whole slices (2D image) or even volumes (3D image) are excited simultaneously. This becomes feasible if images are acquired not in spatial, but in Fourier domain. In the context of MRI, the discrete Fourier domain is called "*k*-space." The principle of spatial encoding in one direction is depicted in Fig. 15.3. By applying the gradient field after excitation, a dephasing in transverse magnetization is started. In consequence, signals from voxels with opposite phase of the precession cancel each other. This is equivalent to spatial filtering of the image content. As time continues, the phase shift and thus the spatial frequency increases. With this method the spatial frequency components can be recorded separately. If enough *k*-space data is available an image can be reconstructed by inverse transform into the spatial domain.

This encoding principle can be used in all spatial directions. Naturally the *k*-space does not need to be completely filled in order to reconstruct an image.

Two basic types of pulse sequences can be distinguished based on the way the echo is created: spin-echo and gradient-echo. Both types of sequences start with an RF excitation pulse. Spin-echo sequences use a second RF pulse for refocusing of the spins and causing an echo. Gradient-echo sequences cause an echo just by switching of the gradient fields. Signal acquisition is carried out at echo time.

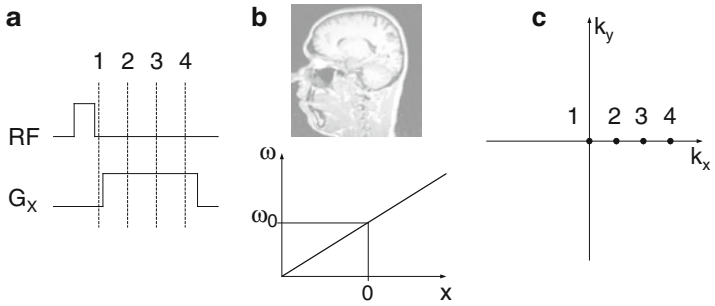

Fig. 15.3 The principle of spatial encoding using a linear magnetic-field gradient. (**a**) After an initial excitation RF-pulse a constant magnetic-field gradient is applied along the x axis. The effect is evaluated at four points of time. (**b**) A linear dependency between position x and angular frequency of precession ω results from the gradient field. This causes a phase shift in transverse magnetization which increases over time. (**c**) The spatial wave in x-direction filters the received RF-signal so that the signal measured at each point of time 1–4 corresponds to one point in k-space

Important for the approach of detecting small ferromagnetic objects in the MRI is that the imaging process is very sensitive to field inhomogeneities. This is one factor influencing device costs and complexity when dealing with high DC field strengths. For detecting ferromagnetic objects, this actually is advantageous. The field distortion caused by the material stretches much further than the object dimensions. In this way it can be thought of a kind of "magnifying glass" effect, though the morphology of the object cannot be extracted. The field distortions lead to several effects which produce artifacts inside the image. The most important are intravoxel dephasing and spatial misregistration. In order to understand the artifact generation process, simulations have been executed.

15.3 Artifact Simulations

The understanding of the effects which lead to the formation of MRI susceptibility artifacts can be supported by simulating the process of MRI. In this section, an implementation of an MRI simulator with a focus on susceptibility artifact generation is presented. Numerical MRI simulators have a large range of applications, including MRI sequence design, hardware development, or education. The computational cost of an MRI simulation is generally high. Due to advances in computational capacity and also simplifications of the simulation process, an increasing number of effects related to MRI image formation can be simulated [3, 4]. Most simulators are based on the evaluation of the Bloch equation [5], which allows the computation of magnetic moments of atomic nuclei (spins). The Bloch equation is in fact a macroscopic equation and does not model quantum mechanical

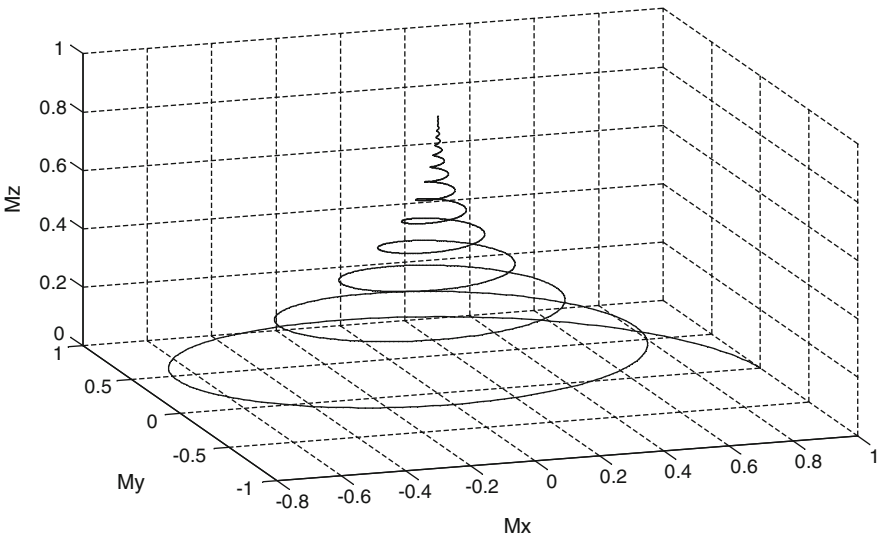

Fig. 15.4 Relaxation trajectory of a nuclear magnetic moment (*spin*) after excitation, computed by evaluation of the Bloch equation

effects. According to the Bloch equation, the magnetization vector $\mathbf{M}(t)$for a given point of time t can be computed from

$$\mathbf{M}(t) = \begin{pmatrix} e^{-\frac{t}{T2}} & 0 & 0 \\ 0 & e^{-\frac{t}{T2}} & 0 \\ 0 & 0 & e^{-\frac{t}{T1}} \end{pmatrix} \cdot \begin{pmatrix} \cos(\gamma B_0 t) & \sin(\gamma B_0 t) & 0 \\ -\sin(\gamma B_0 t) & \cos(\gamma B_0 t) & 0 \\ 0 & 0 & 1 \end{pmatrix} \mathbf{M}(t_0) + \begin{pmatrix} 0 \\ 0 \\ M_0 \cdot \left[1 - e^{-\frac{t}{T1}}\right] \end{pmatrix} \tag{15.1}$$

where M_0 is the core magnetization in thermal equilibrium, $\mathbf{M}(t_0)$is the initial magnetization after excitation, and T1 and T2 are the time constants for the volume of interest. The relaxation is thereby described with the help of an exponential function, whereas the precession movement is expressed by the rotation matrix. Figure 15.4 shows a typical trajectory of the magnetization vector during relaxation. The equations assume a sufficiently small voxel size in which the model inputs, especially the precession frequency and T1 and T2 are constant. In order to model the effect of intravoxel dephasing, the voxel grid used for imaging must be further subdivided. For each resulting subvoxel, the equation is evaluated independently.

Prior to the simulation, a description of the object of interest and its surrounding volume must be specified in the form of two types of input matrices. The relaxation times T1 and T2 are mostly material constants and will typically depend on the

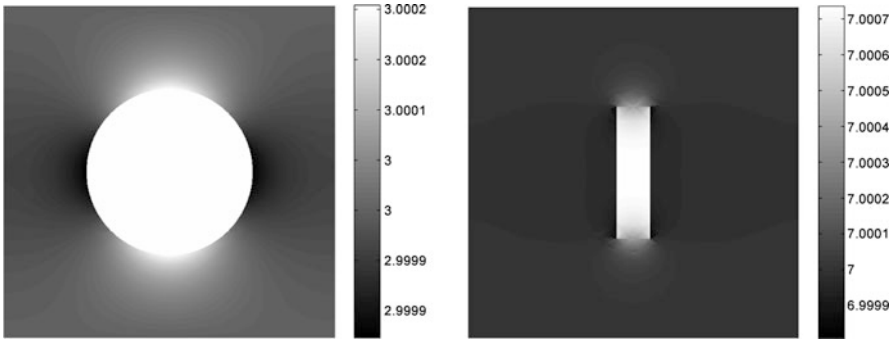

Fig. 15.5 Magnetic flux density in the surrounding plane of a sphere (*left*) and a bar magnet (*right*). The *left plot* has been generated by evaluation of (2) ($B_0 = 3T$). The *right plot* has been generated using the finite element method ($B_0 = 7T$).

surrounding tissue or phantom material. In most cases, the goal of MRI is to recover T1- or T2-weighted images and therefore in the optimal case input and output of the simulation will be identical. However, the focus of this investigation is not on perfect reconstruction of anatomical structure but on the simulation of susceptibility artifacts. The local differences in magnetic properties can be summarized in a matrix of local magnetic flux densities.

Generally, the computation of the magnetic flux density around magnetic objects is nontrivial for arbitrary object shapes. The preferred procedure is the finite elements method. For this investigation, the software COMSOL Multiphysics 3.5 has been used. The most important input parameters are the magnetic susceptibility inside (χ_i) and outside (χ_e) the magnetic body. For some regularly shaped objects, analytical approximations exist [6]. The magnetic flux density in (B_i) and around (B_e) a sphere of radius R can be approximated from

$$B_\mathrm{i} \approx B_0 \left(1 + \frac{\chi_\mathrm{e}}{3}\right)$$

$$B_\mathrm{e} \approx B_0 \left(1 + \frac{\chi_\mathrm{e}}{3} + R^3 \frac{(\chi_\mathrm{e} - \chi_\mathrm{i})(x^2 + y^2 - 2z^2)}{3(x^2 + y^2 + z^2)^{5/2}}\right) \tag{15.2}$$

Figure 15.5 (left) shows the magnetic flux density in the surrounding of a ferromagnetic sphere with $R = 50$ mm, based on evaluation of (15.2). The susceptibilities have been set to $\chi_\mathrm{e} = -9.035 \cdot 10^{-6}$ and $\chi_\mathrm{i} = 10^{-4}$. The results of the COMSOL simulation for a bar magnet can be seen in Fig. 15.1 (right).

The core of the simulation is the application of a pulse sequence and an evaluation of the Bloch equations at discrete points of time during the readout phase of the sequence. All components of a pulse sequence involve an action in the simulation. In MRI sequences, RF pulses are typically named after their expected flip angle and the local magnetization vectors must be updated accordingly.

Gradient fields lead to a local variation of the magnetic flux density and therefore a deviation in the precession frequency and phase. Besides the input matrices containing relaxation times and local flux densities the simulation requires a set of parameters. These are:

- Echo time TE, repetition time TR, and echo type (SE or GRE)
- Receiver bandwidth BW in kHz
- Main magnetic field $\mathbf{B}_0$
- Number of layers
- Number of pixel/voxel per layer Res
- Subvoxel per voxel S_{xy}
- Flip angle (only GRE)

With the help of theses parameters the gradient strengths and acquisition time can be derived. The acquisition time is obtained from

$$\Delta t = 1/BW. \tag{15.3}$$

Frequency- and phase-encoding gradient are computed as follows:

$$G_{\mathrm{f}} = \frac{\pi}{S_{xy} \cdot \Delta t \cdot \gamma/1000}, \tag{15.4}$$

$$G_{\mathrm{p}} = \frac{\Delta\Phi}{S_{xy} \cdot \Delta t \cdot \gamma/1000}. \tag{15.5}$$

The row-dependent difference in phase is

$$\Delta\Phi = \frac{2\pi}{\mathrm{Res} \cdot S_{xy}} \cdot ((k_y - 1) - \mathrm{Res}/2), \tag{15.6}$$

with the actual row in k-space is $k_y = [1 \ldots \mathrm{Res}]$. Signal acquisition is performed by computing the vector sum of the transverse components of $\mathbf{M}(t)$ at each sampling point. The acquired signal is computed by

$$M_{\perp}(t) = \sum_{k=1}^{N} M_{xk}(t) + i\ M_{yk}(t), \tag{15.7}$$

where N is the total number of spins in the system. M_{xk} and M_{yk} are the x- and y-component of (15.1) for spin k. From the acquired signals, the simulation result can be reconstructed using the inverse Fourier transform.

Figure 15.6 shows simulation results for a steel sphere with a diameter of 2 mm in a homogeneous medium and a FOV of 10 cm. The image matrix is 64×64, whereas the spin matrix is $128 \times 128 \times 256$. Scans differ in the type of echo, the orientation of G_{f} and B_0 with respect to each other (parallel $\parallel$ or perpendicular $\perp$) and the relative slice location in the volume (50 % corresponds to the sphere location).

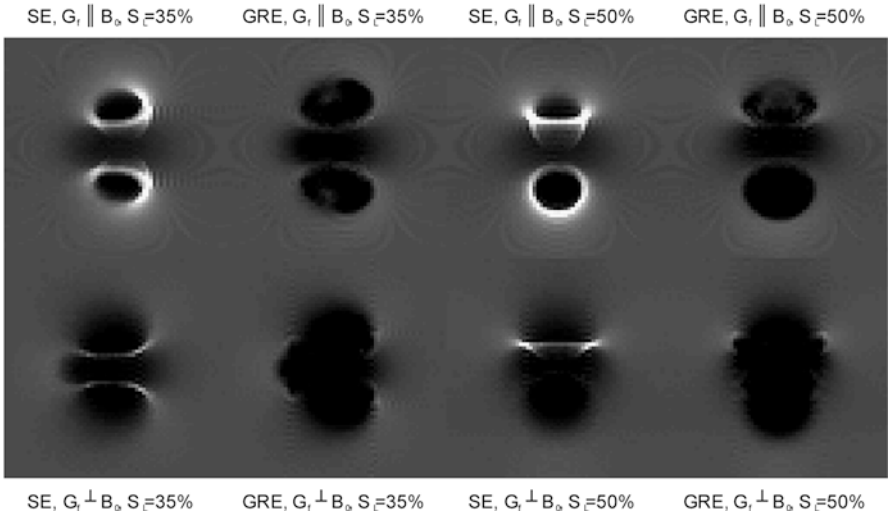

Fig. 15.6 Simulated susceptibility artifacts for steel sphere ($\varnothing = 2$ mm, $\chi_i = 10^5$), FOV = 10 cm, image matrix = 64×64, spin matrix = $128 \times 128 \times 256$

SE artifacts exhibit the characteristic bright fringes caused by spatial misregistration. The GRE artifacts show larger areas of signal loss. The orientation of the frequency encoding gradient has a strong impact on the artifact shape and must be taken into account.

15.4 Artifact Imaging Experiments

In order to test the imaging characteristics of magnetic objects in the MRI, a series of experiments has been carried out. The usage of phantoms allows the isolated investigation of susceptibility artifacts in a well-defined environment. A phantom dedicated for studying magnetic susceptibility artifacts should at least contain two components: a magnetic object and a source of signal. A popular choice of a signal source is water. However, for the targeted application the medium should provide the possibility to fixate an object at a spatial location. Therefore, a phantom filled with agarose gel has been chosen. It emits a signal comparable to gray matter and can be mixed to the desired stiffness. Figure 15.7 shows scans of a phantom equipped with a $\varnothing = 2.5$ mm steel sphere placed in the center. The diameter of the phantom is 145 mm. It can be seen that the dimension of the susceptibility artifact exceeds the size of the sphere by orders of magnitude. The artifacts observed for basic spin-echo and gradient-echo have a correspondence with the simulated scans in Fig. 15.4 (SE, $G_f \parallel B_0$, $S_l = 50$ % and GRE, $G_f \perp B_0$, $S_l = 50$ %). The single-shot sequence allows frame rates $\gg 1$ fps but has not been simulated. Multiple solid object shapes

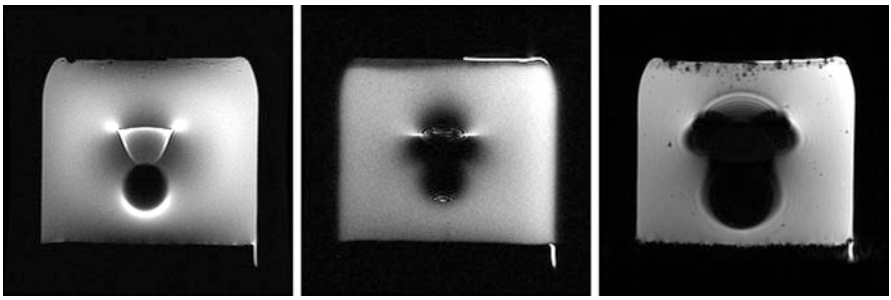

Fig. 15.7 Susceptibility artifacts caused by a $\varnothing = 2.5$ mm steel sphere, embedded into an agarose gel phantom. Sequences are spin-echo, single-shot fast spin-echo, and gradient-echo (*left* to *right*)

have been tested: spheres of varying diameter, cuboids, and a disk. In summary, for objects with small aspect ratios their shape has no impact on the artifact appearance.

Because the agarose gel phantoms show a homogeneous image background, they allow the examination of imaging defects without an interference with the background structure. However, the targeted environment will show anatomical structure. Therefore, some of the imaging experiments have been repeated in an animal tissue environment. Slice views for each plane containing two duck legs with a $\varnothing = 1$ mm steel sphere embedded can be seen in Fig. 15.8. No significant difference in artifact shape as compared to the agarose gel phantoms can be observed.

Additionally to the solid samples, also superparamagnetic nanoparticles in synthetic carrier oil (ferrofluids) have been investigated. Two setups have been built for this purpose. In the first setup, different amounts of ferrofluids have been mixed in containers with agarose gel. Results for a spin-echo sequence can be seen in Fig. 15.9 (left). Increased concentration of the nanoparticles leads to an increased damping of the signal. In the second setup, the ferrofluid has been fixed at a single location near the center of an agarose gel phantom (see Fig. 15.9, right). The high concentration of magnetic material leads to distortions similar to those observed from solid objects.

15.5 Artifact Recognition Algorithms

The recognition of magnetic objects deals with the problem of initially localizing objects in a 3D scan. No prior knowledge is available about the location or number of objects. This problem can be solved by exploiting the imaging characteristics studied in the previous sections. Most susceptibility artifacts observed show a very good contrast in signal intensity between artifact and surrounding tissue or phantom. This property can be used in order to separate between objects and background or in other words perform segmentation. Generally, two forms of segmentation can

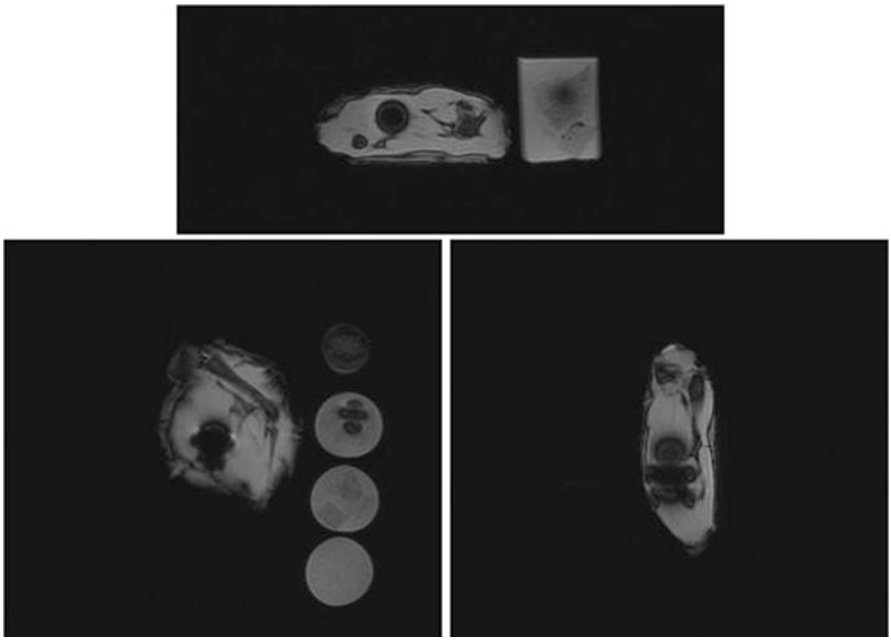

Fig. 15.8 [!t]Slice views of each plane showing animal tissue sample (equipped with $\varnothing = 1$ mm steel sphere) and agarose gel phantoms (one of them equipped with a $\varnothing = 0.6$ mm steel sphere)

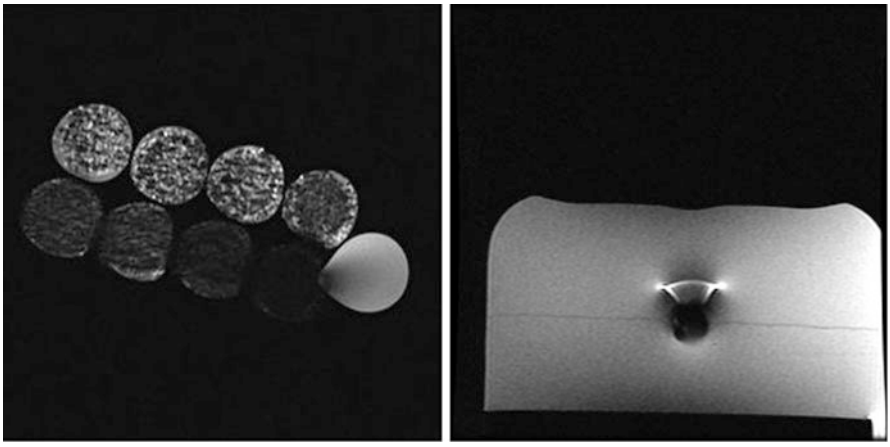

Fig. 15.9 Appearance of Ferrofluids in fast spin-echo sequences. The *left scan* shows nine agarose gel phantoms with different concentrations of ferrofluids distributed over all the volume. The *right scan* shows pure Ferrofluid locally fixed near to the *center* of an agarose gel phantom

be distinguished [7]. The first method is based on the detection of structures of the object borders, such as points, lines, or edges. Initial experiments showed that especially in the presence of structured image background these methods do not lead to reproducible results. Alternatively, regions may be distinguished based on their intensity level. Depending on the object type, imaging sequence and surrounding tissue, the intensity level in MRI scans can vary over a large range. Therefore, image processing in MRI should not rely on the exact reproduction of intensity levels [8].

An adaptive procedure widely used in medical image processing is the expectation maximization (EM) algorithm [9]. The EM algorithm requires a statistical model and aims at iterative estimation of the model parameters. In the context of image segmentation, a Gaussian Mixture Model (GMM) is a common choice of such a model [10]. The model assumes that each segmentation zone in the scan is a random process with a Gaussian characteristic. Image pixel generated by each source must be described by a feature vector $x_{l,}$ which can contain for instance intensity, color, or texture information. For simplicity and due to the lack of color information, only signal intensity has been used here. Using a fixed number of processes K, the GMM is described by

$$F(x_l|\Theta) = \sum_{k=1}^{K} \alpha_k \; G(x_l|\theta_k) \tag{15.8}$$

where Θ is the complete parameter set for all processes and G is a Gaussian distribution parameterized by the vector of mean and standard deviation $\theta_k = [\mu_k, \sigma_k]$. $\alpha_k$is a weighting factor indicating the a-priory probability of a data point originating from process k. The algorithm needs an initial parameter set $\Theta^{(0)}$. In each iteration, two steps are carried out:

- The expectation step computes the a posteriori probabilities of each pixel belonging to each process. For obtaining an intermediate result, each pixel can be assigned to the process with highest a posteriori probability.
- In the maximization step, the parameter vector Θ is updated by pretending, the results from the expectation step were new measurement data.

The result of the EM segmentation is an assignment of each pixel to a segmentation zone. An example can be seen in Fig. 15.10. A big advantage over fixed-level thresholding techniques is the capability to learn the decision boundaries.

Depending on the choice of K, a number of segmentation zones can be grouped in order to form connected objects. For example, the two segmentation zones with lowest mean intensity can be chosen to form candidate objects. Individual objects can be distinguished by incorporating a labeling step which assigns a unique identifier to each connected component. These objects serve as input to the following classification scheme. Figure 15.11 shows segmented artifacts caused by metallic spheres inside agarose gel phantoms.

Intensity levels in MRI scans typically cover a larger range as compared to the usual 8-bit image data. Usually a contrast stretch is performed prior to display. This

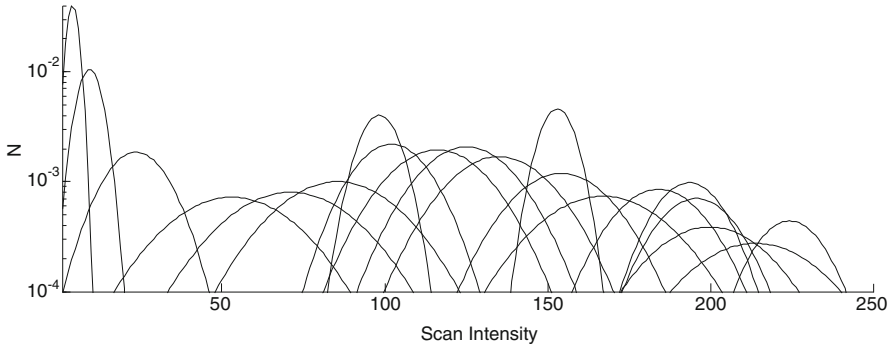

Fig. 15.10 Resulting EM segmentation zones obtained for a $\varnothing = 3$ mm steel sphere imaged using a gradient-echo sequence, where $K = 20$

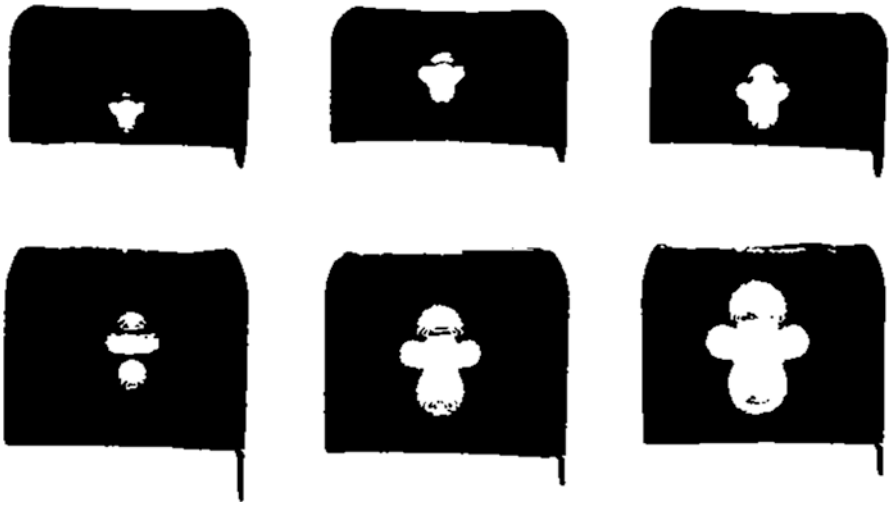

Fig. 15.11 Binary segmentation results for a set of agarose gel phantoms equipped with steel spheres of varying diameter of 1.0 mm, 1.2 mm, 1.5 mm (*upper row*) and 2.0 mm, 2.5 mm, and 3.0 mm (*lower row*). A FSE sequence has been used

covers the fact that volumes perceived as "dark" can correspond to very different intensity levels, depending on the rest of the scan. Figure 15.12 shows the histogram of a HASTE scan, covering a large range of intensity levels. On the other hand, the areas of signal loss caused by a susceptibility artifact reliably produce low signal intensity values.

The output of the segmentation procedure has been studied with the help of a selection of scans from phantom experiments and full 3D head imaging. All scans have been acquired using gradient-echo imaging. Finally, three types of objects have been identified in the output of the segmentation procedure:

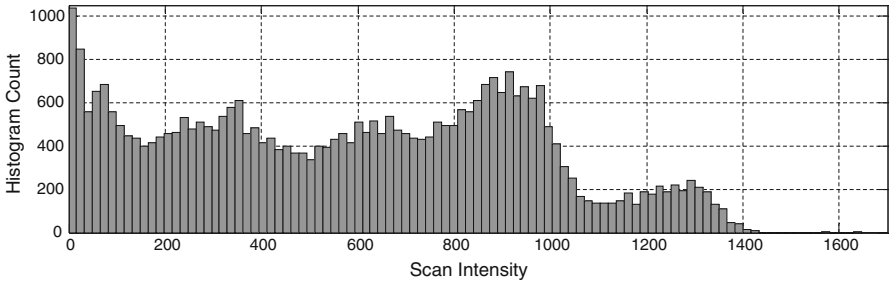

Fig. 15.12 Intensity histogram for a HASTE scan of a water container equipped with two steel spheres

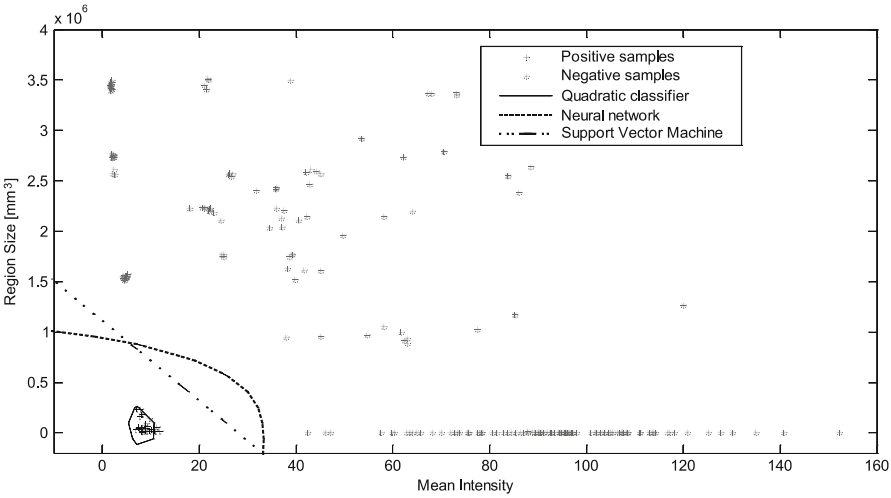

Fig. 15.13 Scatter plot of segmented volumes with respect to size and mean intensity. The decision boundaries of three different classifiers are indicated

- Background: The surrounding air of phantom or patient produces low signal intensities. Typically, the segmented background is the largest object in the volume of interest.
- Susceptibility artifact caused by magnetic object: Exhibits characteristics as studied above.
- Cavities, bones, anatomical structure: Can show object sizes comparable to those of susceptibility artifacts.

A scatter plot of all identified objects can be seen in Fig. 15.13, where positive samples (susceptibility artifacts) have been marked with a+ and a− samples (background and anatomical structure) have been marked with a*. The feature vector for each sample is composed of the segmented object volume and the mean signal intensity inside the object. The plot shows that the EM segmentation can indeed

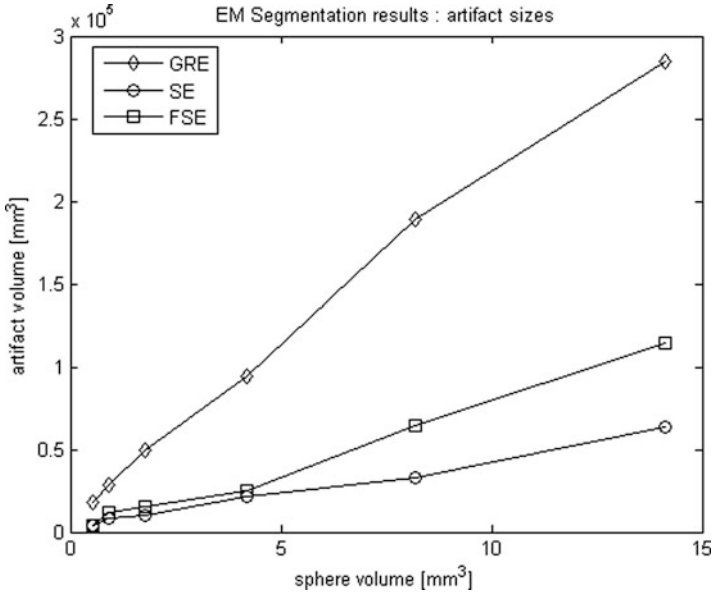

Fig. 15.14 Computed artifact volume after EM segmentation in dependency of imaging sequence and sphere volume

converge towards intensity levels above the mean level found in susceptibility artifacts. Nevertheless, the object classes can be distinguished based on the proposed feature vector and are in fact linearly separable. The decision boundaries of three classifiers have been indicated in the figure: The quadratic Bayes classifier, the back-propagation trained feed-forward neural net classifier and a linear Support Vector Machine. Details about classifier design can be found in [11].

By incorporating prior knowledge about object size and imaging sequence, the classification scheme can be improved. In the initial experiment, all artifact objects in the training dataset had been collectively defined to be positive samples. Alternatively, only the subset corresponding to the expected objects and imaging sequence can be used for classifier training. This will permit sharper decision boundaries. The relationship between artifact volume and sphere volume for gradient-echo, spin-echo, and fast spin-echo is depicted in Fig. 15.14. A further improvement can be achieved by expanding the feature vector by an object shape descriptor. The segmentation and classification procedure allows detecting multiple artifact objects in a volume. Figure 15.15 shows two slice scans of a water-filled phantom equipped with two steel spheres of different diameter. In order to demonstrate the transferability of the results to a real-tissue environment, the procedure has been applied to the animal tissue sample described above. Figure 15.16 shows the segmentation results for a $\varnothing = 1$ mm steel sphere, embedded into an agarose gel phantom and animal tissue, yielding to similar classifier responses.

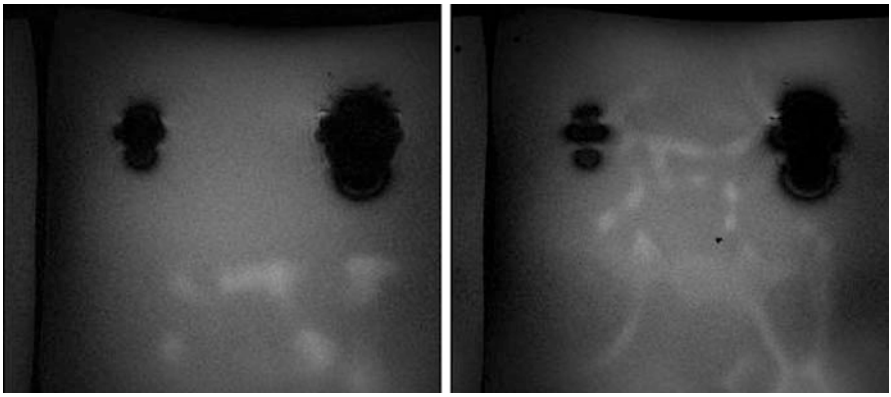

Fig. 15.15 Multiple steel spheres (*left* in each scene: $\varnothing = 1$ mm, *right* in each scene: $\varnothing = 2$ mm) present in the same image scene. The surrounding medium is water. Sequence: FLASH, TE = 4.8 ms, TR = 9.1 ms

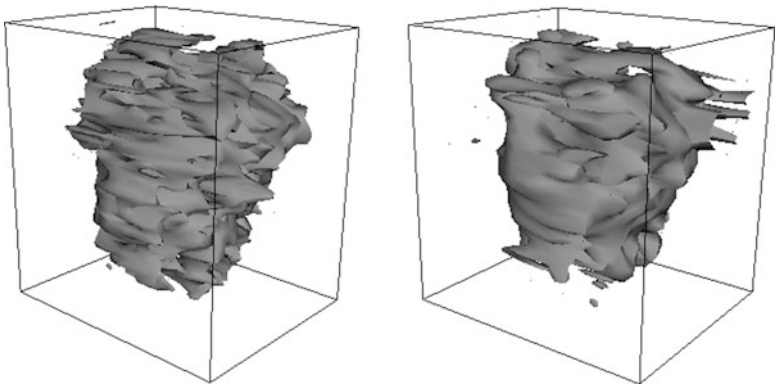

Fig. 15.16 Extracted volumes of susceptibility artifact generated by a $\varnothing = 1$ mm steel sphere in a GRE sequence. The sphere has been embedded into an agarose gel phantom (*left*) and animal tissue (*right*)

15.6 Artifact Tracking Algorithms

For the tracking of the artifacts inside the MRI image slices, different algorithms are used. The algorithms are based on template matching.

When the recognition algorithm has detected the artifact and its initial three-dimensional position, the position and a slice stack of the artifact is transferred to the tracking algorithm, as can be seen in Fig. 15.17.

The tracking algorithm uses the template stack to determine two separate information. First, the best fitting template stack slice is determined. All template stack slices are correlated with the input MRI slice:

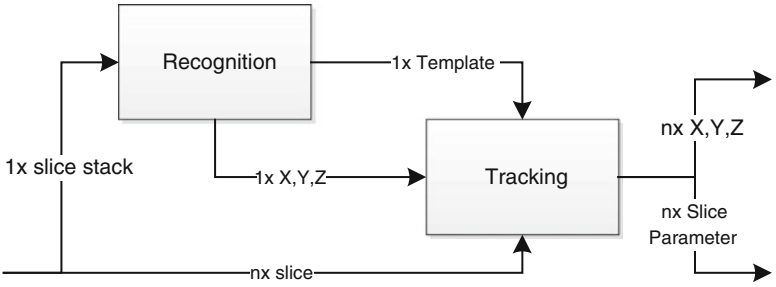

Fig. 15.17 Data flow between recognition and tracking algorithm. MRI image data coming in on the *left*, generated data going out on the *right*

$$C_n(x, y) = I(x, y) * T_n(x, y)$$

The best fit is then chosen and the two-dimensional position of the artifact inside the MRI slice is determined using the selected slice. This is done by calculating the maximal value of the correlation matrix and its position inside the matrix:

$$C_n(x_n, y_n) = \max(C_n(x, y))$$

$$C(x_0, y_0) = \max_{\forall n}(C_n(x_n, y_n))$$

The calculation is done with sub-pixel accuracy using center of gravity calculation of the correlation peak. For this, first a thresholding is executed:

$$T(v) = \begin{cases} v - t & \text{if } v \geq t \\ 0 & \text{else} \end{cases}$$

$$C_{\text{thresh}}(x, y) = T(C(X, y))$$

Afterwards, the center of gravity is calculated:

$$x_0 = \frac{\sum\limits_{x,y} x \cdot C(x,y)}{\sum\limits_{x,y} C(x,y)}, \; y_0 = \frac{\sum\limits_{x,y} y \cdot C(x,y)}{\sum\limits_{x,y} C(x,y)}$$

The best fitting slice is also further refined to enable a more exact z-dimension position. This is also done by center of gravity calculation:

$$z_0 = \frac{\sum\limits_{n} z_n \cdot C_n(x_0, y_0)}{\sum\limits_{n} C_n(x_0, y_0)}$$

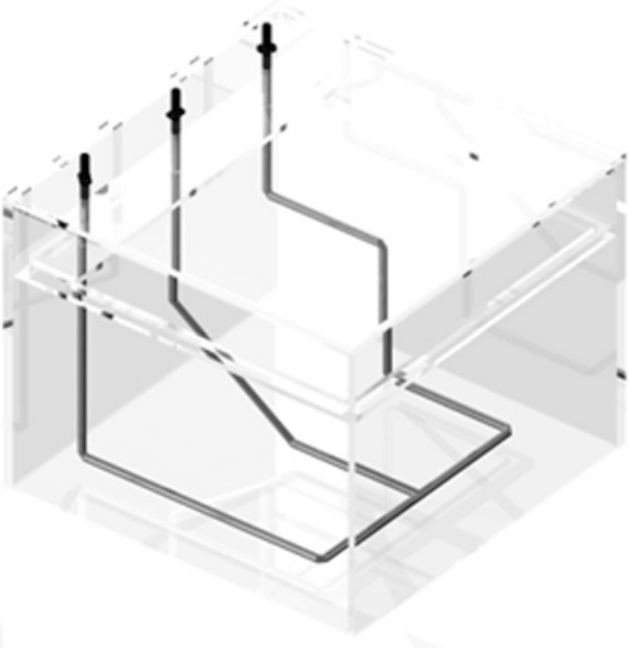

Fig. 15.18 CAD drawing of the setup used. It is an acrylic glass box with dimensions 30 cm in all directions. Inside is a glass pipe system with an inner diameter of 3–5 mm, in which ferromagnetic spheres can be moved. Attached can be external components to generate liquid flow

The determined position (x_0, y_0, z_0) is then stored and made available for later processing steps. Also, a new slice position is calculated which can be used by the gradient controller to update the MRI scanning parameters.

The tracking algorithm has been tested using a HASTE sequence and a ferromagnetic ball inside a glass pipe system. A CAD model of the setup can be seen in Fig. 15.18 and the realized setup in Fig. 15.19.

The HASTE sequence delivers fast images but does not yet enable automatic slice update. For the testing of two-dimensional tracking this is still sufficient. Acquired MRI slices can be seen in Fig. 15.20.

The data in Fig. 15.21 show that the ferromagnetic ball can be tracked reliably while it is not too close to the setup borders. Still, tracking may be lost depending on the signal status and the movement artifacts.

15.7 MRI Based Magnetic Propulsion

MRI-based propulsion exploits the magnetic field generated by the MRI gradient coils to exert a driving force on ferromagnetic materials and objects. The idea was

Fig. 15.19 Picture of the box and pipe setup

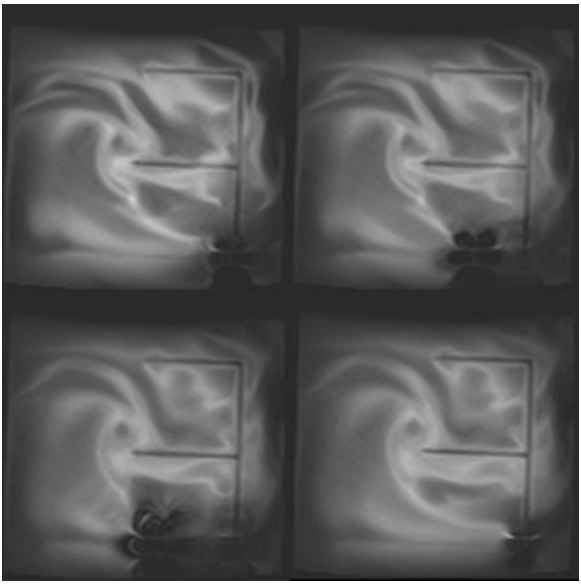

Fig. 15.20 Image slices acquired using a HASTE sequence. The artifact is visible in the *bottom right corner* of the slice and is moving horizontally. *Bottom left* is the slice 56 in which the tracking was lost. Visible is the strong movement artifacts and the lack of artifact shape

already proposed in [2] and subsequently demonstrated in a clinical MRI. The force that can be exerted by the MRI gradients can be expressed as

$$F = \nabla(m \cdot B)$$

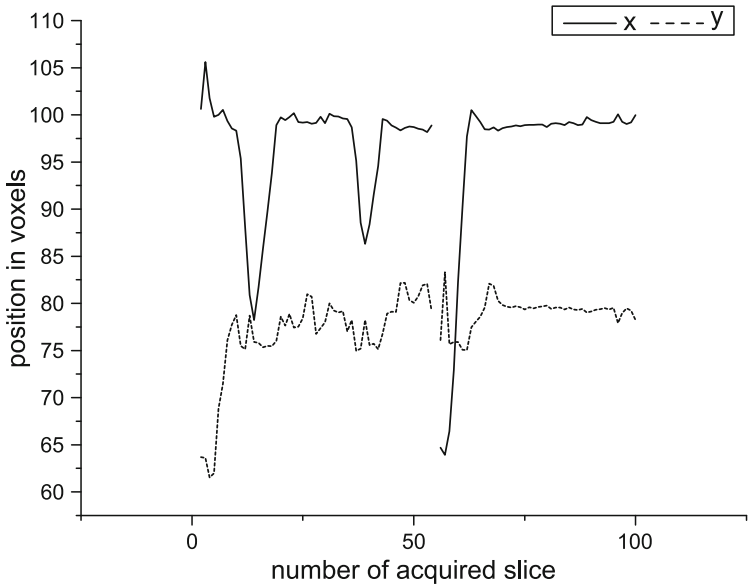

Fig. 15.21 The *x* and *y* positions tracked in the MRI slices acquired by a HASTE sequence. Clearly visible is the error in *x*-position at slice 56. The tracking was lost due to very fast movement and resulting too strong movement artifacts and had to be recovered

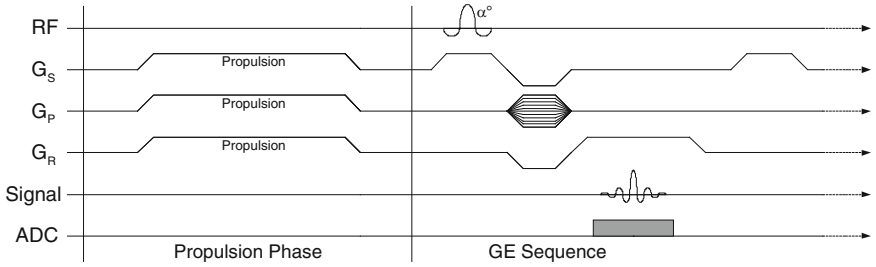

Fig. 15.22 Combined propulsion and imaging sequence. The propulsion phase may be significantly longer than the imaging phase. In this case, a gradient-echo sequence is used for imaging

Using the imaging gradients, only one of the imaging and propulsion functions can be active at any chosen time. Therefore, a time sharing approach has to be taken. The sequence designed consists of an imaging part, which delivers a MRI image slice and a propulsion part, which switches the gradient coils to generate the necessary magnetic field for the wanted force. The principal sequence design is shown in Fig. 15.22.

15.8 Propulsion Experiments

For experiments with the propulsion sequence, the following setup has been used.

The acrylic box was filled with water and a 2.5-mm steel ball was introduced into a special mechanical mechanism which holds the ball in place until the box is completely inside the MRI. This is to prevent movements of the ball due to the high gradients during insertion into the MRI. The setup inside the MRI is depicted in Fig. 15.23.

The steel ball was propelled by the tailored sequence. The movement has been filmed using a high zoom camera. The results of the movement can be seen in Fig. 15.24.

While millimeter-sized objects are interesting, also for certain medical applications, we also verified the force induction on nanoparticle agglomerations. For this, a ferrofluid from FerroTec with iron oxide nanoparticles sized around 10nm was filled into a closed capsule. To enable movement without surface friction, the capsule was additionally filled with air and put into the water filled acrylic box. Therefore, the capsule was swimming on the water surface. The capsule can be seen in Fig. 15.25.

It was possible to move the capsule, though the movement was much slower than the movement of the steel ball. This has three reasons, first the content of ferromagnetic material is lower with the capsule and therefore the magnetic moment of the steel ball is stronger. Second, the mass of the capsule is higher, leading to slower acceleration. The last reason is the damping in water due to the high surface of the capsule.

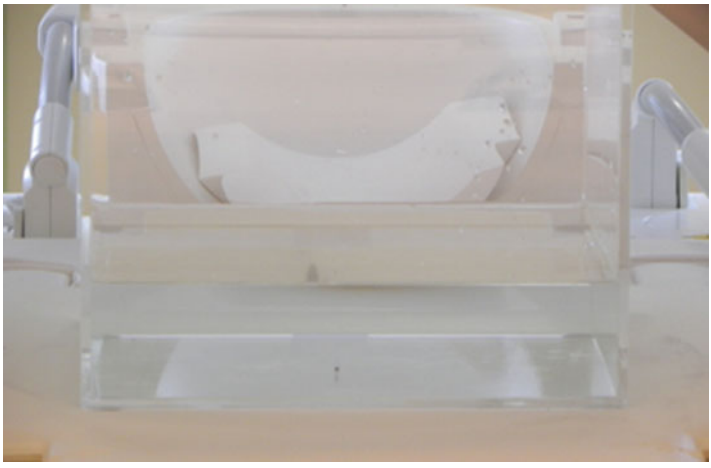

Fig. 15.23 Experimental setup for the propulsion. Visible in the *middle* is the 2.5 mm steel ball. The setup is already introduced into the MRI bore

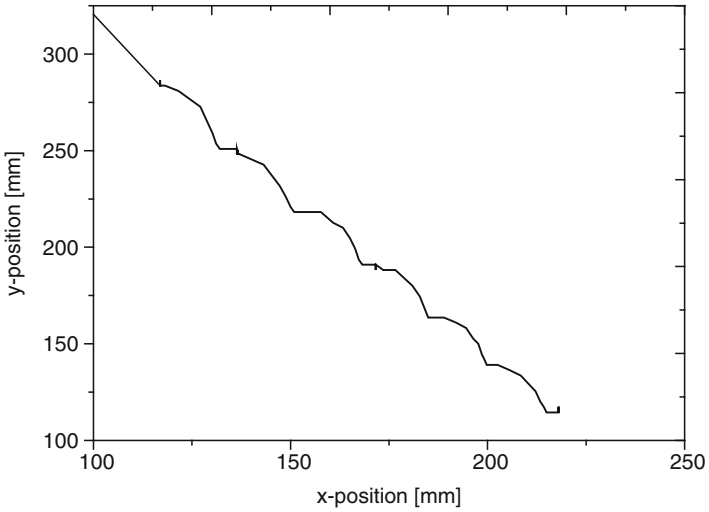

Fig. 15.24 The tracked steel ball from the propulsion experiment. Tracking was executed in video images. Visible is that the movement is not linear. This is due to friction effects

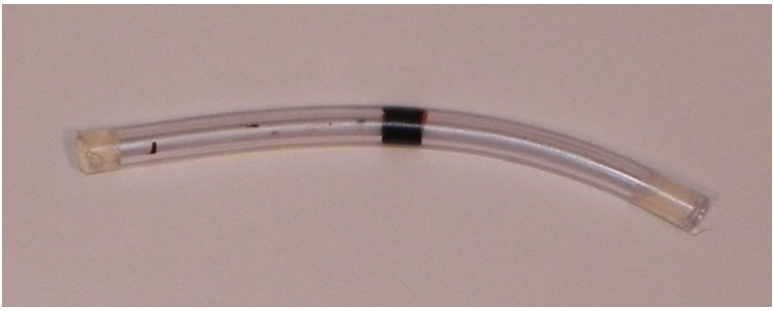

Fig. 15.25 The capsule filled with iron oxide nanoparticles in oil and air

Considering the achievable repetition rate of the tracking-propulsion process, this highly depends on the quality and optimization of the imaging sequence and on the duty cycle needed to propel the object of interest. Technically, when using very fast imaging sequences, a repetition rate of few executions per second could be achieved. An additional increase of the repetition rate would require sequences which are reduced to even less *k*-space line acquisitions. The minimal number of *k*-space lines required for tracking is 3, in which case it may be possible to reach the repetition rate of 20–30 Hz published by [12].

15.9 Conclusion

As shown in this chapter, the MRI combined with additional software and ferromagnetic objects as end-effectors may be a sufficient tool not only for imaging but also for actuation. This makes it feasible to use the MRI to realize robotic systems without the need for additional actuation mechanisms. Though the actuating force is scaling down unfavorably in comparison to drag forces in the cardiovascular system, still the actuation of agglomerated nanoparticles is possible under certain conditions. The conditions necessary are the presence of a significant quantity of ferromagnetic material, a strong agglomeration force and a flow which is sufficiently low to enable steering. When not dealing with strong flow like in the cardiovascular system, even manipulation of micro- and nanoparticles may be feasible. Due to the artifact imaging, even objects far below the MRI resolution can be detected.

The use of the MRI as robotic system has many potential applications in the medical field like targeted drug delivery or supporting diagnosis or even minimal invasive surgery, which should be exploited using technologies like the ones presented here.

References

1. Hempel E, Fischer H, Gumb L, Höhn T, Krause H, Voges U, Breitwieser H, Gutmann B, Durke J, Bock M, Melzer A (2003) An MRI-compatible surgical robot for precise radiological interventions. Comput Aided Surg 8(4):180–191
2. Mathieu J.-B, Beaudoin G, Martel S (2006) Method of propulsion of a ferromagnetic core in the cardiovascular system through magnetic gradients generated by an MRI system. IEEE Transactions on Biomedical Engineering 53(2):292–299
3. Wortmann T, Dahmen C, Geldmann C, Fatikow S (2010) Recognition and tracking of magnetic nanobots using MRI. In: Proceedings of international symposium on optomechatronic technologies (ISOT), 2010
4. Stöcker T, Vahedipour K, Pflugfelder D, Jon Shah N (2010) High-performance computing MRI simulations. Magn Reson Med 64(1):p186–p193
5. Benoit-Cattina H, Collewet G, Belaroussi B, Saint-Jalmes H, Odet C (2005) The simri project: a versatile and interactive mri simulator. J Magn Reson 173:97–115
6. Yodera DA, Zhaob Y, Paschalc CB, Fitzpatrick JM (2004) MRI simulator with object-specific field map calculations. Magn Reson Imaging 22(3):315–328
7. Gonzales RC, Woods RE (2008) Digital image processing, 3rd edn. Prentice Hall, Upper Saddle River, NJ
8. Edelman R, Hesselink J, Zlatkin M, Crues J (2006) Clinical magnetic resonance imaging. Elsevier, New York, NY
9. Moon TK (1996) The expectation-maximization algorithm. IEEE Signal Process Mag 13(11):47–60
10. David A Forsyth, Jean Ponce (2002) Computer vision: a modern approach. Prentice Hall, Upper Saddle River, NJ
11. Duda RO, Hart PE, Stork DG (2001) Pattern classification. Wiley, New York, NY
12. Felfoul O, Mathieu J-B, Beaudoin G, Martel S (2008) In vivo MR-tracking based on magnetic signature selective excitation. IEEE Trans Med Imaging 27(1):28–35

Chapter 16
Therapeutic Bacterial Nanorobots for Targeted Drug Delivery Deep Inside Tumors

Sylvain Martel

Abstract In medical interventions such as in cancer therapy, targeting remote tumors through the human vasculature while avoiding the systemic circulatory network responsible for side effects is a great challenge. Recently, the fundamental principles used in robotics have been considered for the implementations of platforms and microscale entities based on nanoscale components to deliver doses of therapeutics to such targets. To achieve such goal, more conventional and well-known engineering practices must expand beyond known traditional practices and consider a wider range of disciplines. These include the use of synthetic and biological versions with bacterial carriers capable of carrying the therapeutic loads deep into the tumor. Here, the advantages and limitations of both synthetic relying on magnetism and bacterial carriers relying on a self-propelling flagellated system will be described and the advantages of combining both approaches for navigation in the vascular network will be demonstrated.

16.1 Introduction and Motivation

Potential applications of nanorobots capable of assisting in various medical interventions include but are not limited to tumor targeting, and elimination or reduction of arteriosclerosis, blood clots leading to stroke, accumulation of scar tissue, localized pockets of infection, and many more. But so far, nanorobots have been subjected to various speculations trying to describe far-future versions that in most cases resemble the larger and most common counterparts but implemented at

S. Martel (✉)
Nanorobotics Laboratory, Department of Computer and Software Engineering, Institute of Biomedical Engineering, École Polytechnique de Montréal (EPM), Station Centre-Ville, P.O. Box 6079, Montréal, QC, Canada H3C 3A7
e-mail: sylvain.martel@polymtl.ca

C. Mavroidis and A. Ferreira (eds.), *Nanorobotics: Current Approaches and Techniques*, DOI 10.1007/978-1-4614-2119-1_16,
© Springer Science+Business Media New York 2013

a smaller scale. These visions are often wrong since they most often forget scaling effects such as Reynolds numbers and the ones at the nanoscale. Indeed, the physics and the forces involved at the nanoscale differ from the ones at the macroscale. Based on this, the designer of microscale nanorobots can take advantages of nanotechnology combined with the laws of physics at the macroscale to embed more functionality while being more suited for a given application where considering traditional engineering based on macroscale physics becomes insufficient. These designs will eventually use advanced materials and manufacturing techniques, while traditional parts to be assembled will rely more on biology and biochemistry. This design strategy should help in the implementations of miniature systems with embedded capability well beyond the ones relying on only the more traditional technologies. As it will be described in the following sections, such approach has been successfully used for the implementation of microscale devices designed to operate in the human vascular network.

16.2 The Environment

Due to the diameters of the blood vessels, the lack of direct line of sight to track such robots for navigation purpose, and many more obstacles, implementing robots to operate in the human vasculature is indeed not an easy task. But the opportunities for applications and the need to provide new tools in medical target interventions are great.

In general, the human vascular network offer more potential for interventions, especially when we consider that it offers close to 100,000 km of accessibility to various regions inside the human body. The diameter of the various blood vessels in the human vasculature limit the overall diameter of the untethered robots from a few millimeters in larger blood vessels such as the arteries, down to $\sim$4 μm in the narrowest capillaries. The larger diameter for a robot navigating in such vessels should be approximately no more than half the diameter of the vessels being traveled in order to avoid an increase in the drag force caused by the vessel walls and acting against the robot or device.

As such, in order to reach the capillary networks, such robots must travel through the arterioles after being injected typically in one of the larger arteries. Since the diameters of the arterioles may vary from $\sim$150 μm down to $\sim$50 μm, an overall diameter for each robot of no more than $\sim$25 μm is required to reach the entrance of the larger capillaries. But in order to reach deeper in the microvasculature and towards a targeted region located in a tumor for maximum therapeutic efficacy, each microrobotic entities would need an overall diameter not exceeding $\sim$2 μm. This size would allow them to release their therapeutic loads with overall sizes in the nanometer range, allowing them to penetrate further through other mechanisms such as diffusion including transition through the blood–brain barrier (BBB).

16.3 Synthetic Microscale Medical Robots and Carriers

In 2007, the results of a first proof of concept that successfully demonstrated the automatic navigation (i.e., without human intervention) using the magnetic gradient fields of a clinical MRI scanner, of a magnetically saturated untethered object (a 1.5-mm bead) in the blood vessel of a living animal [1–6], were published. The technique known as magnetic resonance navigation (MRN) relied on a clinical magnetic resonance imaging (MRI) scanner where the highly homogeneous field (typically 1.5T or 3T on commercial clinical MRI scanners) was used to fully saturate the ferromagnetic core being navigated, while the 3D magnetic gradients typically used for image slice selection were used to propel the untethered object in any direction. A special MR-tracking algorithm was used to feed positional data to a computer to correct the trajectory along the carotid artery of a living swine, 24 times per second.

Later, the 1.5-mm bead was replaced by biodegradable microcarriers (diameter 50 μm) as depicted in Fig. 16.1, making them the first navigable therapeutic agents. They were called therapeutic magnetic microcarriers (named TMMC) and contained doxorubicin (a cancer drug widely used to treat humans) that was synthesized and navigated successfully through the hepatic artery at 4 cm beneath the skin before reaching predetermined target sites in the liver of live rabbits prior to controlled release of the drug (DOI: 10.1016/j.biomaterials.2010.12.059). This result represents a significant advance compared to all other state-of-the-art

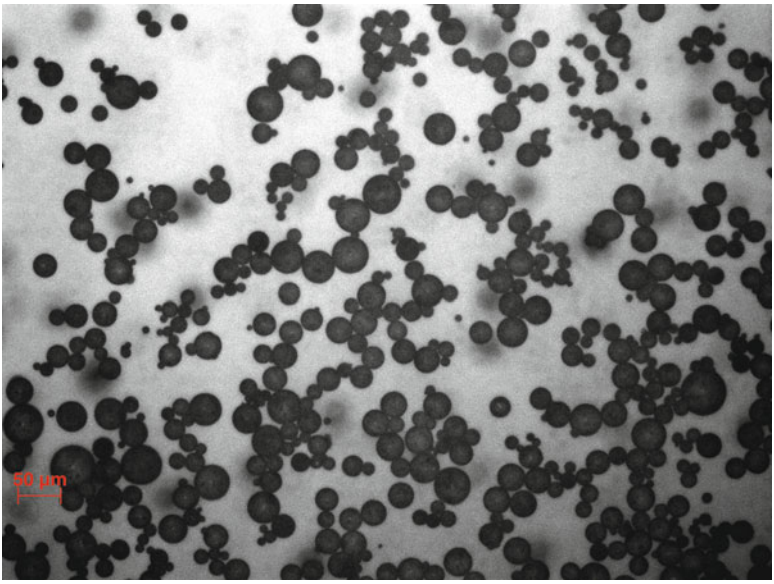

Fig. 16.1 Photograph of the first MR-navigable therapeutic microcarriers

magnetic drug targeting (MDT) approaches since the technique is still the only one allowing not only controlled navigation (to avoid systemic circulation and hence potential secondary effects) but also targeting at any depth in the body. But as predicted, the experimental results concurred with previous calculated estimations in that the minimum diameter using magnetic gradients from a clinical MRI scanner even upgraded with additional gradient coils providing 400 mT/m instead of the typical 40 mT/m was insufficient to induce a propelling force on magnetic therapeutic microcarriers (such as the TMMC) of <50 μm in diameter. Therefore, another approach was needed to go beyond these synthetic microcarriers for efficient navigation in the microvascular network and in order to reach deep inside tumors.

16.4 Therapeutic Self-Propelled Bacterial Carriers

In order to reach deep inside tumors for maximum therapeutic efficacy instead of performing chemoembolization further away from the potential tumor sites as for the previous experiments, calculations based on physiological and technological data indicated that microcarriers with an overall diameter not exceeding 2 μm and with propelling force of at least 4 picoNewtons (pN) would be required. Since these specifications are well beyond today's technological limits, it forces us to consider a self-propelled (hence eliminating the requirement of high gradient fields well above technological limits) micro-entity. Since the fabrication of a synthetic version of such self-propelled entity with an overall diameter of no more than 2 μm (to navigate efficiently in the narrower capillaries) is well beyond technological limits, a biological entity having the proper characteristics was considered instead. This biological entity is the nonpathogenic MC-1 flagellated magnetotactic bacteria (MTB) and initial experimental results confirmed that this particular flagellated bacterium can indeed act like a future synthetic or artificial microrobot or an efficient therapeutic microcarrier when operating in the microvasculature.

The MC-1 bacterium (Fig. 16.2) has a diameter between 1 and 2 μm allowing for the maximum surface available to attach nanoscale components such as drug-loaded liposomes (a real advantage to optimize the amount of drug being delivered per MTB) while optimizing travel speed in the smallest diameter vessels found in humans by avoiding wall retardation effect. The thrust propelling force of each cell is provided by two flagella bundles and has been experimentally measured in human blood ranging from 4.0 to 4.7 pN (a tenfold increase from other typical flagellated species), allowing swimming velocities between 100 and 150 body (cell) lengths per second (200–300 μm/s). A chain of membrane-based single magnetic domain iron-oxide nano-crystals (nanoparticles) called magnetosomes synthesized naturally inside each cell during batch cultivation [7] is used for directional control of the bacteria using a weak (slightly higher than the Earth's geomagnetic field instead of tens to hundreds of thousands times higher for any other MDT approaches which is impossible to produce deeper in the body) directional magnetic field (magnetotaxis control [8, 9]) by inducing a directional torque on the nano-chain (similar to

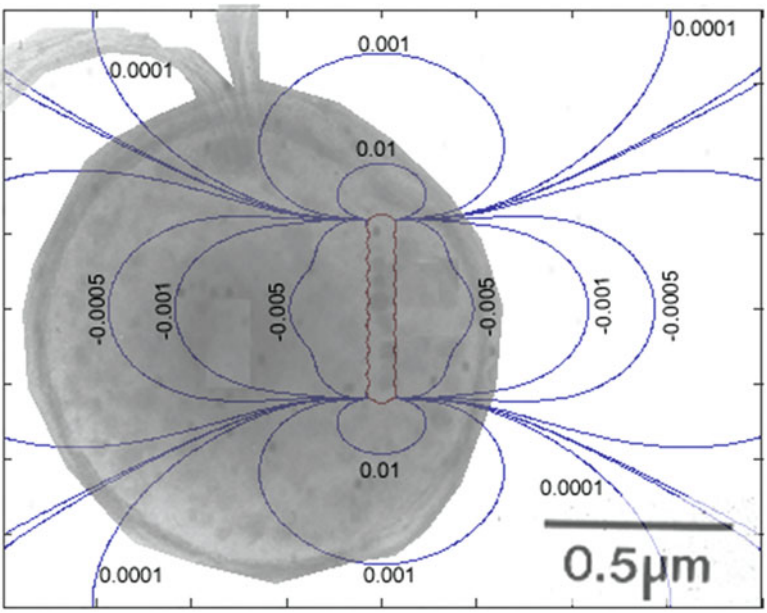

Fig. 16.2 Photograph of the MC-1 magnetotactic bacterium with the two bundles of flagella (*top*) with the distortion of the MRI scanner's homogeneous field being plotted from the chain of magnetosomes used for directional control

rotating a magnetic compass needle towards an artificially generated North pole). The same nanoparticles synthesized in MTB are also well known as being the best biocompatible contrast agents for MRI, allowing us to estimate the amount of drug (if the MTB are used as therapeutic microcarriers) and the distribution of the drug using adequate MRI sequences (this has already been shown by our group).

Other types of bacteria have been considered for fighting tumors by proliferating in the tumor necrotic zone [10–12]. These bacteria would reach tumoral lesions by means (e.g., chemotaxis) that are not compatible with electronic computers or any other tools. Although there are efforts to use chemotaxis-based bacteria to move micro-objects in an aqueous medium [13], preliminary results suggest that the use of bacteria being influenced by magnetotaxis would be more appropriate and efficient for computer-based or tool-based navigation and targeting such as for medical target interventions [14]. Furthermore, as stated earlier, the use of MTB as carriers can not only enhance targeting through flagellated propulsion and directional control from an external system or tool, but can also be tracked for feedback control by MRI due to the chain of magnetosomes in the cell that causes a local field inhomogeneity detectable by MRI. It should be noted that such tracking should be done only for investigating targeting efficacy by evaluating the quantity and distribution of the drug-loaded MTB in the targeted region and not during travel. Since the high

directional homogeneous field inside the bore of a MRI scanner would prevent directional control of the MTB, such directional control is performed by a special platform called a magnetotaxis system located outside the MRI scanner.

Although it appears that the MC-1 cells are the only bacteria known so far that have the ideal specifications to be used as therapeutic microcarriers in the microvasculature and capable of directly targeting deep in the tumor necrotic zone, data acquired during the past years also showed that they have two important limitations.

First, although much more effective in the microvasculature and in the tumors than any other known technologies, they are far less efficient in larger blood vessels (due to higher blood flows) compared to the MRI-based navigation using synthetic microcarriers (TMMC). This nonpathogenic cell will only survive for 30–40 min when exposed to the human body temperature of 37°C (could be extended by lowering the temperature at the zone being targeted). To resolve the above two limitations, work has begun for encapsulating MTB in special 50 μm MRI-navigable liposomal structures or micelles to be injected in an artery prior to being navigated and released closer to the microvasculature where they become more efficient. But although this technology could soon be highly valuable to target many types of tumors, at present, this approach is still not mature enough. Instead, to avoid injection in an artery prior to transport towards the microvasculature surrounding the tumor, these MTB are considered initially as therapeutic navigable microcarriers for colorectal tumors, hence bypassing the artery and larger vessels by performing an injection of the therapeutic-loaded MTB directly and closer to the tumor by accessing the injection site through the rectum.

16.5 Conclusion

The complementary use of synthetic and bacterial nanorobots would typically yield better targeting possibilities when transiting though the human vascular network. Although flagellated magnetotactic bacteria of type MC-1 with thrust exceeding 4 pN are more efficient when transiting through the capillary networks, they are less efficient in larger blood vessels due to a higher flow velocity. Therefore, synthetic microcarriers (e.g., TMMC) and the ones proposed for the transport of these bacteria through the larger blood vessels and towards the release sites at the arteriocapillar network entry would most likely be mandatory for targeting tumors, with one potential exception being colorectal tumors. But by integrating nanotechnology, biology, and modern engineering techniques, promising new robotic platforms and navigable nanorobotic carriers may become real in the next generation of medical interventions.

References

1. Martel S, Mathieu J-B, Felfoul O, Chanu A, Aboussouan E, Tamaz S, Pouponneau P, Beaudoin G, Soulez G, Yahia L'H, Mankiewicz M (2007) Automatic navigation of an untethered device in the artery of a living animal using a conventional clinical magnetic resonance imaging system. Appl Phys Lett 90(11):114105-1–114105-3
2. Mathieu J-B, Martel S (2009) Aggregation of magnetic microparticles in the context of targeted therapies actuated by a magnetic resonance imaging system. J Appl Phys Mater 106:044904-1–044904-7
3. Martel S, Mathieu J-B, Felfoul O, Chanu A, Aboussouan E, Tamaz S, Pouponneau P, Yahia L, Beaudoin G, Soulez G, Mankiewicz M (2008) A computer-assisted protocol for endovascular target interventions using a clinical MRI system for controlling untethered microdevices and future nanorobots. Comput Aided Surg 13(06):340–352
4. Felfoul O, Mathieu J-B, Beaudoin G, Martel S (2008) In vivo MR-tracking based on magnetic signature selective excitation. IEEE Trans Med Imaging 27(1):28–35
5. Tamaz S, Chanu A, Mathieu J-B, Gourdeau R, Martel S (2008) Real-time MRI-based control of a ferromagnetic core for endovascular navigation. IEEE Trans Biomed Eng 55(7):1854–1863
6. Mathieu J-B, Martel S (2007) Magnetic microparticle steering within the constraints of an MRI system: proof of concept of a novel targeting approach. Biomed Microdevices 9, 6:801–808
7. Blakemore RP (1975) Magnetotactic bacteria [in geomagnetic field]. Science 190:377–379
8. Martel S, Tremblay C, Ngakeng S, Langlois G (2006) Controlled manipulation and actuation of micro-objects with magnetotactic bacteria. Appl Phys Lett 89:233804–233806
9. Martel S, Mohammadi M, Felfoul O, Lu Z, Pouponneau P (2009) Flagellated magnetotactic bacteria as controlled MRI-trackable propulsion and steering systems for medical nanorobots operating in the human microvasculature. Int J Robot Res 28(4):571–582 (invited paper for a special edition on current state of the art and future challenges in nanorobotics)
10. Kasinskas RW, Forbes NS (2006) Salmonella typhimurium specifically chemotax and proliferate in heterogeneous tumor tissue in vitro. Biotechnol Bioeng 94(4):710–721
11. Bettegowda C, Dang LH, Abrams R (2003) Overcoming the hypoxic barrier to radiation therapy with anaerobic bacteria. Proc Natl Acad Sci 100(25):15083–15088
12. Forbes NS, Munn LL, Fukumura D, Jain RK (2003) Sparse initial entrapment of systemically injected salmonella typhimurium leads to heterogeneous accumulation within tumor necrosis. Cancer Res 63:5188–5193
13. Behkam B, Sitti M (2007) Bacterial flagella-based propulsion and on/off motion control of microscale objects. Appl Phys Lett 90(2):23902-1–23902-3
14. Martel S, Felfoul O, Mathieu J-B, Chanu A, Tamaz S, Mohammadi M, Mankiewicz M, Tabatabaei N (2009) MRI-based nanorobotic platform for the control of magnetic nanoparticles and flagellated bacteria for target interventions in human capillaries. Int J Robot Res 28(9):1169–1182, Special Issue on Medical Robotics

Chapter 17
Sensing Strategies for Early Diagnosis of Cancer by Swarm of Nanorobots: An Evidential Paradigm

G. F. Cerofolini and P. Amato

As a general rule, the greatest crimes never come to light because the greatest criminals, their perpetrators, are too clever to be caught.
J. Futrelle, The Scarlet Thread [1]

Abstract Precancerous states are necessarily characterized by the simultaneous and persistent occurrence of high temperature, high concentration of pyruvic and lactic acids and low *p*H. These physico-chemical features may thus be viewed as the fingerprint of a growing tumour. A detection strategy based on the use of swarm of nanorobots circulating in the haematic stream is described, together with the basic idea allowing the implementation of the sensing and actuating tools necessary to perform the job.

17.1 Introduction

This chapter is devoted to formulate a conceptual scheme for the identification of cancerous or precancerous states inside the organism.

This work is based on the following assumption: The best way to recognize pathogenic states inside the organism requires a distributed surveillance system

G.F. Cerofolini
Department of Materials Science, University of Milano–Bicocca, via Cozzi 53, 20125 Milano, Italy
e-mail: gianfranco.cerofolini@mater.unimib.it

P. Amato (✉)
Micron, 20041 Agrate Brianza MI, Italy

DISCo, University of Milano–Bicocca, 20125 Milano, Italy
e-mail: pamato@micron.com

C. Mavroidis and A. Ferreira (eds.), *Nanorobotics*, DOI 10.1007/978-1-4614-2119-1_17,
© Springer Science+Business Media New York 2013

mimicking the immune system and making up for its failures in the detection of diseases *generally* manifesting with the exhaustion of the reproduction function, for which there was not selective pressure for their recognition and termination. To be concrete, we have in mind cancer, although Parkinson and Alzheimer diseases satisfy the same condition.

The idea of using a distributed surveillance system formed by a swarm of nanorobots[1] able to navigate, to recognize pathogenic state and to collect and transmit such an information is not new [2]. We have recently reconsidered this idea in the light of current integrated-circuit technology [3]; in this chapter, we reformulate our programme, specializing it to cancer, as an evidential (clue-based) paradigm. In particular, we shall consider the entire organism as the scene of crime, the appearance of the disease as the crime, the tumour as the perpetrator, the swarm as the detecting corpus and each member of swarm as the agent able to collect pieces of evidence of the crime.

17.2 Circulatory System: The Scene of Crime

The surface area A of any body of assigned regular form varies with its volume V as

$$V \propto A^{3/2}, \tag{17.1}$$

the constant of proportionality being characteristic of the shape. Any organism, whose single constituents require a continuous flow of energy[2] not to die, cannot increase its volume indefinitely preserving its shape. In fact, the required energy would increase as V, whereas the energy input increases at most as A, so that if an organism grew continued indefinitely according to (17.1), above a certain volume a part of the organism could not be any longer fed by an adequate energy. The strategy adopted by living organisms to continue their growth in spite of the limits imposed by (17.1) is reproduction.

The growth of single cells is an extremely complicated process with several phases an numerous checkpoints; to some extent, it can however be described as formed by two phases: *growth* G, during which the cell increases its volume, and *mitosis* M, during which modifies its shape increasing its area without large change of volume [4]. At the end of the G phase, the cell attains a volume twice that it had at the beginning of its life; during M, together with important intracellular modification (formation of telomere and separation of the chromosomes), the cell changes its shape eventually assuming an area twice that it had at the beginning of its life. In this way, with the separation of the nucleus in two parts, the cell is in the condition of forming two copies of the parent cell. Figure 17.1 sketches this process.

[1] A robot with overall size on the micrometre length scale, whose constituting devices are on the nanoscale, is referred to as *nanorobot*.

[2] In the case considered here, the energy is chemical in nature, although there are system like the majority of the vegetable kingdom where such an energy is ultimately electromagnetic in character.

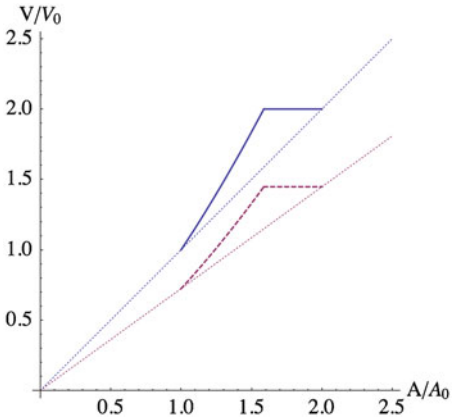

Fig. 17.1 Lin-lin plot of the volume V of a of single cell as a function of its outer area A, calculated assuming that the cell preserves its original shape during the entire G phase while changes continuously shape during the M phase until two new cells are formed. The *solid line* represents spherical organisms, while the *dashed* one represents (hypothetical) cubic organisms. V_0 is the initial volume of the sphere, and A_0 is its area

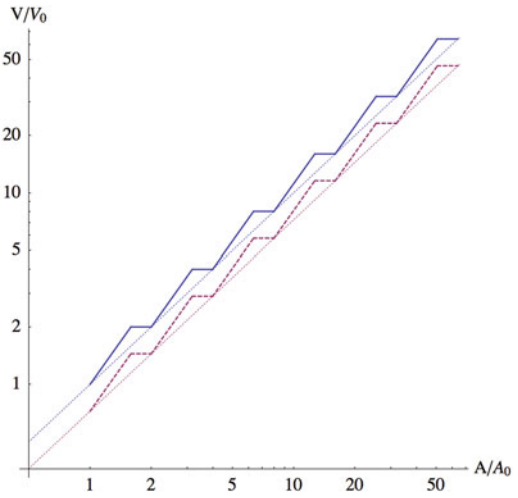

Fig. 17.2 Log-log plot of the volume V of a system composed of single-cell organisms as a function of their total area A, for six generations. The *solid line* represents spherical organisms, while the *dashed* one represents (hypothetical) cubic organisms. V_0 is the initial volume of the sphere, and A_0 is its area

If each newly born cell may be viewed as isolated, the process can be reiterated indefinitely; Fig. 17.2 shows that if the details of the GM cycle are ignored, the cell colony grows over many generations with total volume approximately proportional to the corresponding area,

$$V \propto A, \tag{17.2}$$

a behaviour that allows the functional characteristics of each cell to be preserved during growth [5, 6].

If the cells were homogeneously dispersed in an unbound medium, their number could increase indefinitely. In a limited environment or in the absence of motility, however, the cells cannot be assumed independent of one another, because the required energy increases in proportion to their number while the energy input can increase only with the size of the zone exposed to the medium.

The strategy adopted to overcome this limit by populations of single cells involves the growth of dendritic colonies with fractal-like structure. Much more interesting is the method adopted by higher organisms to solve this problem. The organization of higher organism is based on the specialization of the various organs to specific functions (locomotion, vision, hearing, digestion, reproduction, etc.). This result is obtained specializing the expressome to the task, so that cells with the same genome are expressed in such a way as to generate, for instance, (a) nucleus-free cells (red blood cells) as well as polynucleated cells (muscle cells) in addition of course to mononuclear cells, (b) highly regular lenticular cells (again red blood cells) as well as dendritic cells (nerve cells) and (c) cells undergoing frequent mitosis (epithelial cells) as well as cells not undergoing any reproduction for most of life time (again nerve cells), and certainly, the list is not exhaustive.

All the functions of the organism are supported by organs requiring an adequate input of energy and neg-entropy; their needs are satisfied centralizing the collection of energy and neg-entropy and distributing them to the various organs through the circulatory system.

To some extent, the circulatory system can be described by two trees forming a double canopy inside each organ [7], where the ultimate branches of the canopies are linked by filaments (*capillaries*). The circulatory system is so built that energy-rich substances and O_2 can out diffuse from it (thus feeding nearby cells) only in the capillaries; conversely, the waste materials produced by cell metabolism are eventually collected in nearby capillaries before being eventually delivered to the secretion apparatus. This basin, where the transport of matter is dominated by diffusion, will be referred to as diffusion basin. The union of all diffusion basins must embed all the living parts of the organism.

This structure can work as described, but in higher organisms, it is complicated and, in view of the key role of evolution on structure–function relationship, made more efficient by another distributed system, devoted to increase the collection efficiency catabolites and other wastes—the lymphatic system. Although this system could play a key role in therapy, it will be henceforth ignored, and we shall limit our attention to the blood circulatory system.

A lumped model of animal organism is sketched in Fig. 17.3, where the entire organism is depicted as formed by several (respiratory, digestive, urinary, cardiovascular, lymphatic, immune, etc.) systems linked by two complex space-filling systems (the circulatory and lymphatic systems). The chemicals necessary to the life are taken from the environment through the respiratory system (O_2) and digestive system (food) and distributed to all tissues of the organism through the circulatory system (that in turn must be fed by a subsystem with the same features—*vena venorum*); the circulatory and lymphatic systems are also involved in the elimination of the CO_2 and nitrogen-catabolite wastes by the respiratory and urinary systems, respectively.

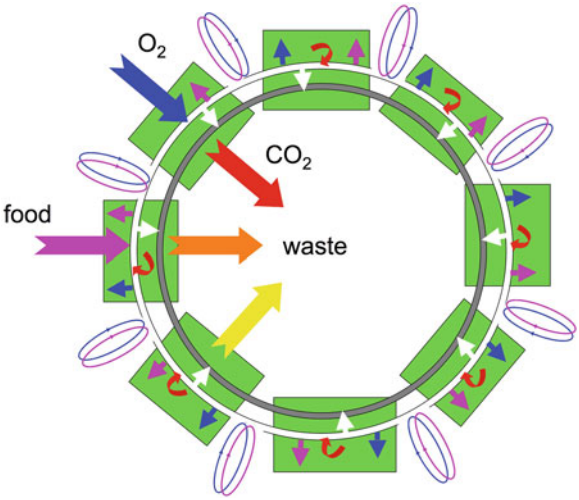

Fig. 17.3 Lumped model of animal organisms emphasizing the distribution of O_2 and nutritive elements by the circulatory system and the collection of CO_2into the circulatory system and the passage of wastes into the lymphatic system

A fractal-tree analysis of the circulatory system is given in appendix; for the present purposes, we limit here to mention the following features that will be used:

- The circulatory system is formed by a double (arterial and venous) tree.
- Each tree has a branching factor of 2 and terminates after a number n of approximately 35 branchings.
- The trunks of the trees are connected (by heart), whereas the canopies are connected by 2^n ($\simeq 3 \times 10^{10}$) capillaries.
- Each capillary feeds on the mean 2×10^3 cells, as follows from the total number of cells of an adult human (6×10^{13} cells).
- The average capillary diameter is in the range 4–8 μm, and its length is 0.5 – 1 mm.
- The mean blood velocity in capillaries is $v_n = 5 \times 10^{-2}$ cm s^{-1} so that the mean time τ_n spent by the any particle flowing along the capillary is around 1–2 s whereas the time required by blood for a complete cycle is about 60 s.

For the purposes of this work, it suffices to emphasize that a hypothetical sensor travelling in the circulatory system as a red blood cell could be used to feel the "chemical state" of the cells belonging to the diffusion basin of the capillary.

17.3 Cancer: The Crime

There are several theories of the origin of cancer. Most of them accept that genetic lesions have a major role in determining tumour phenotype, although evidence is accumulating that cancers of distinct subfamilies may derive from different cells of

origin [8]. Without advocating any theory of tumour genesis (tissue or mesenchymal stem cell undergoing mutation or a hybridization with an oncogenic virus) and without pretending to formulate any theory of tumour growth, we list a few general properties of cancerous cells that by themselves are able to account for some general behaviour of the complex interaction between the tumour and the vascular system.

A cell becomes malign essentially because a sequence of a few (about 5), otherwise unavoidable but unlucky, errors in the replication of its genetic material.[3] In this way, cancer is essentially a disease of the elder.

Cancer is an extremely complex disease whose major features are listed in the following:

C_1 cancerous cells are mutations of tissue cells with unbound Hayflick limit; this fact allows their unlimited reproduction provided that there is adequate room and sufficient amount of nutritive substances.

C_2 cancerous cells are aggressive and destroy their neighbouring cells via the emission of proteolytic enzymes or, more likely, by acidification of their environment.

C_3 the metabolism (and thus the reproduction rate) of cancerous cells is much faster (by approximately a factor of 50) than that of non-malign cells.

C_4 the mutant cancerous cells retain much of the characters of the non-malign tissue cells.

The combination of all these features has dramatic effects: C_2 produces available room to growth thanks to the necrosis of nearby cells; C_3 implies that the faster reproduction rate of cancerous cells allows them to hold actually that room before non-malign cells; C_4 implies the immune response is not effective, and C_1 implies that, in the absence of other factors, the disease extends to the whole organism, at least until the organism is able to feed the cancer.

The capillary system is already optimized to its diffusion basin that cannot tolerate a large increase of O_2 consumption therein: In fact, moving in the frame of the minimum volume model [9] and using physiological data of muscle blood flow and O_2 consumption rate in man during heavy exercise, Kamiya and coworkers calculated the optimum capillary number to be 3.7×10^{10} [10]; since this number agrees well with the morphological data, the vascular-tissue system is constructed so as to attain the highest efficiency in O_2 transport to tissue at its maximum activity.

Since the metabolism of cancer cells is approximately 50 times faster than that of healthy cells [11], for solid tumours (to which the following analysis is restricted), a capillary able to sustain 2×10^3 healthy cells can feed approximately 40 cancerous cells. This fact has important effects on the dynamics of tumour growth in the early stages.

Consider now that each capillary is substantially unable to support any large additional request of O_2 to the diffusion basin—the growth of only ten cancerous

[3] Hence, the first rule for cancer prevention: Avoid abnormal cell replication by reducing inflammation factors and excessive immune response.

cells would impact significantly (approximately by 12%) on the oxygen uptake of healthy cells so that the tissue structure must necessarily undergo heavy changes. The transformation of the entire diffusion basin into a cluster of cancer cells (a *tumourlet*) leaves a lot (approximately 98% of the entire mass supported by the capillary) of necrotic cells and is responsible for heavy tissue hypoxia [12].

The growth of the maximum sustainable amount of cancerous cells is necessarily associated with the migration of the colony first towards the capillary and then, along it, towards the arteriole orifice where the capillary is originated. In so doing, most of the tissue (original healthy cells and older cancerous cells) undergoes necrosis so that one can imagine different scenarios:

- The growth continues without destroying the arteriole–capillary–venule local circulation system.
- The growth proceeds destroying locally the local circulation system in such a way as to produce the necrosis of the entire region (with healthy and malign cells).
- The growth continues destroying the local circulation system but in a way that allows the inner region of the tumour to be fed directly by the arteriole.

The first case might be taken as characteristic of benign tumours, which are able to destroy the entire hosting tissue but do not involve the entire organism (except for the primary damage they produce). The second case may perhaps be viewed as a spontaneous remission (self-healing) of the disease. The third case is responsible for the transformation of a local disease in a systemic disease essentially because of the acceleration of the tumour growth rate produced by the exposure to blood of larger and larger fraction of the tumour.

The development of the tumour occurs in a relatively quiet manner up to the *angiogenic switch* [13], when the tumour promotes a neo-vascularization able to sustain its subsequent explosive growth and its transformation from a local disorder into a systemic diseases [14]. Until the angiogenic shift has occurred (that does not necessarily happens), the tumour is referred to as in a *dormant phase*. The tumour is generally believed to remain in the dormant phase up to a size of 1 mm; the cancerous cells contained in a volume of diameter 1 mm are expectedly 2×10^4 (this amount follows from the maximum number of cells that can be contained in 1 mm^3, about 10^6, assuming that the tumour in the dormant phase is a complex network of tumourlets, each fed by one capillary, where 98% of the biological material is necrotic). More difficult is to estimate the number of cancerous cells after the angiogenic switch; imaging is possible when the tumour has a larger size than 5 mm; a tissue with such a diameter could contain up to 10^8 cells; on another side, assuming that only 2% of the of the whole mass is formed by cancerous cells (as in the dormant phase), the tumour would contain 2×10^6 cells (see Fig. 17.4). We tentatively assume that a tumour at the imaging limit contains 10^7 cancerous cells.

What gives a hope in this picture is that in all stages, the tumour is characterized by a large exposure to the bloodstream so that it can be detected by the agents circulating in the blood. The above argument implies that a nanorobot in a capillary could feel the metabolic pattern of the family of cells fed by the capillary itself, thus surveying the cells contained within a diffusion length.

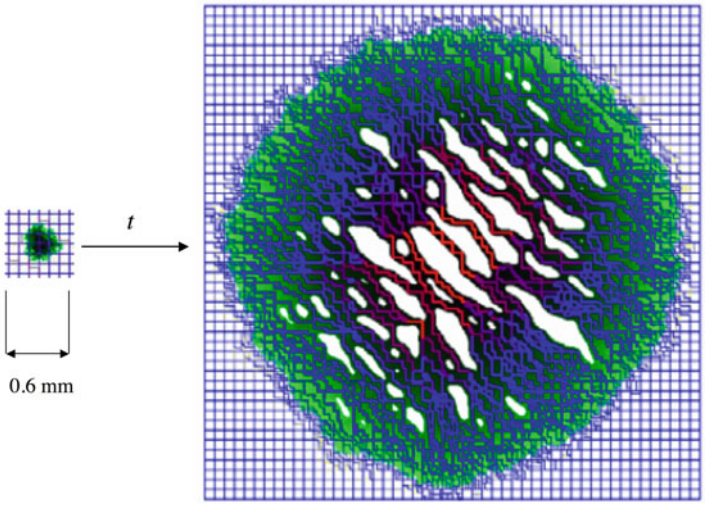

Fig. 17.4 Dramatic morphological change of the solid tumour when its size switches from the submillimetre (*left*) to the centimetre scale length (*right*). According to Bartha and Rieger [15], the capillary network is assumed to form a three-dimensional regular grid with step of 100 μm; all the remaining region is filled with cells. The tumour is characterized by proliferating cells, with the younger ones on its boundary and the oldest ones inside (increasing darkness indicating age). The tumour bulk is characterized by large regions (shown in *white*) of necrotic materials

17.4 General Features of Cancerous Tissues: The Clues

In view of the previous considerations, one fundamental issue of fight on cancer is its early diagnosis. How early it can be may be understood considering the phenomena occurring even in the early stages of cancer growth. Common markers to solid tumours are hyperthermia, hypoxia and acidity. The possibility of determining excess heat and tissue oxygenation maps by swarms of circulating nanorobots was first envisaged by Freitas [2].

17.4.1 Hyperthermia

Needless to say, the faster metabolism of cancerous cells and their accumulation at the arterial orifice generating the capillary is responsible for a local increase of temperature. This effect is so large that it is exploited not only in digital infrared thermal imaging to make diagnostic-quality images for breast cancer screening [16], but also hyperthermia is a type of cancer treatment in which the exposure to high temperatures (up to 45°C) damages and kills cancer cells, usually with minimal injury to normal tissues. Hyperthermia may shrink tumours by killing cancer cells and damaging proteins and structures within cells [17, 18]. Denoting with $\mathscr{C}_k$ a

cluster of k cancerous cells, with a long right arrow a spontaneous and easy process and with a short left arrow a difficult and non-spontaneous process, the tumour growth can be sketched by means of the following quasi-equilibrium "reaction"

$$\mathscr{C}_k \rightleftarrows \mathscr{C}_{k+1} + \text{heat}. \tag{17.3}$$

Irrespective of the detailed hyperthermia mechanism (increase of perfusion, permeability, pH, O_2 partial pressure, metabolic activity or drug uptake), the inhibitory effect of heat on cancer can be understood in terms of Le Chatelier–Braun principle applied to Reaction (17.3)—as far as the disease produces a heat excess, imparting heat to the system depresses the evolution of the disease.

17.4.2 Hypoxia

Human solid tumours are considerably less well oxygenated than normal tissues.[4] Hypoxia is essentially related to the fragility of the circulation system feeding the tumour. The collapse of weak portions of the tumour circulatory apparatus exposes the tissue to even hypoxic conditions, and the tumour can tolerate such conditions only exploiting the glycolytic pathway.[5] In this pathway, energy is produced by the transformation of glucose first to pyruvic acid and then to lactic acid (rather than to CO_2 and H_2O). These acids by themselves are however unable to produce what is perhaps the most important effect on the nearby tissue—the pH reduction.

17.4.3 Acidity

The organism as a whole is a strongly buffered system: Actually, it is able to regulate the pH of the blood to 7.40 ± 0.05. The tumour genesis produces a decrease of pH (as measured by microelectrodes and thus averaged over a distance non-smaller than electrode diameter) by approximately 0.5 units (so that the H_3O^+ concentration increases by a factor of 3) [21].

[4] Hypoxia leads to resistance to radiotherapy and anticancer chemotherapy, as well as predisposing to increased tumour metastases. However, it can be exploited in cancer treatment. One such strategy is to use drugs that are toxic only under hypoxic conditions, and the first drug of this class to enter clinical testing, tirapazamine, is showing considerable promise [19, 20].

[5] Moreover, the character expressing the cell ability to survive in strongly hypoxic conditions can be selected during cancer evolution by the strong competitions among fast-reproducing newly-born malign cells.

Assuming for the increase of tissue acidosis the same mechanism as in muscle during exercise[6] [22], the increased acidity is not due to the anaerobic production of pyruvic and lactic acid, but rather to the vivacious metabolic ATP hydrolysis.

The resulting high H_3O^+ production rate has dramatic effects: Whereas the tumour cell succeeds in regulating the internal *p*H, the lower external *p*H on one side contributes (in combination with the proteolytic enzymes possibly produced by the cancerous cell) to destroy the nearby healthy cells and on the other side facilitates via Bohr's effect the loss of O_2 from the oxyhaemoglobin transported by red blood cells. In this way, the fast metabolism of cancerous cells allows their aggression to the hosting tissue and facilitates oxygen uptake.

17.5 Diagnosis of Cancer: Smoking Gun or Frame Evidence?

We know a lot of cytotoxic substances, either of natural origin or artificially synthesized. From the point of view of human pharmacology, what makes different one from another, distinguishing them in *poison* or *drug*, is their selectivity. In this respect, a drug is nothing but a poison able to destroy selectively guest or deviant organisms (from viruses to tissues or parasites) without excessive perturbation of the hosting organism. Of course, such a total selectivity is impossible (so that any drug has unavoidable side effects), but nonetheless, the recognition of the pathogenic agent is a fundamental issue of any systemic (i.e., nonsurgical) treatment of the disease.

The selective recognition of specific antibodies occurring at the surface of cancer cells (the smoking gun), allowing their terminations using cytotoxic substances conjugated to ligands able to bind selectively to the antibodies, has ever been a *leit motif* of the fight on cancer. The following discussion leads however to conclude that this road is probably a *cul de sac*.

Cancer is certainly a disease of the elder, as confirmed by the power law of the dependence of its occurrence with age [23]. However, it occurs even in children, and in those cases, it is even more aggressive. In the light of evolution, this fact implies that *the advantage for the species, coming from the supposedly possible specialization of the immune system able to recognize and terminate cancer, is so small that the species has not payed the cost for such an evolution*. We see two reasons for that:

Genetic First of all, cancer is a disease characterized by a high heterogeneity, where each phenotype is able to develop autonomously (and often more fast) even when the others are destroyed.

Systemic The common features associated with cancer genesis and growth (hyperthermia, hypoxia and acidification) are the same as those characteristic

[6] We shall return later on this analogy.

of muscle under physical exercise. We propose this similitude as the reason why the immune systems does not recognize the tumour as a pathogenic state to terminate—because it is confused with a physiological state.

Getting success where evolution has failed is certainly a difficult task.

Leaving the mainstream of the fight on cancer, in the following we shall ignore the first case and concentrate on the way to overcome the limits posed by the possible confusion of cancer symptoms with the general features of muscle under exercise.

Before considering the details of our programme, we however observe that the systemic confusion can also explain tumour angiogenesis. Although the detailed mechanisms of this process are not clear yet, taking as a model for angiogenesis the revascularization processes resulting from heavy physical exercise, one can indeed hypothesize that the angiogenesis is ultimately a *physiological* response of the organism to the increased demand of energy and O_2 (in this case by malign cells).[7]

Our programme is thus that of *endowing the immune system with an artificial surveillance system devoted to detecting the simultaneous occurrence of hyperthermia, hypoxia and excessive acidity due to localized cancerous states without confusing it with the similar conditions produced under physiological conditions*.

In the light of our crime detection, the search of the perpetrator is not addressed to the identification of the smoking gun but rather to a frame evidence resulting from the simultaneous occurrence of three events and their persistence in time.

For that, we imagine to use a swarm of agents, wandering through the organism along the bloodstream, devoted to recognize hyperthermia, hypoxia and excessive acidity, resting in the region of detection to form a cluster so numerous to inform the hosting human of the presence of candidates to tumour.

17.6 Swarm of Nanorobots: Detectives

The basic idea for the early detection of tumours is to inject into the circulatory system a swarm of "detectives" able to identify the presence in the organism of malign cells, even if they are just a few or, ideally, just one. The malign cell identification task can be decomposed in two different aims. The first aim is the effective location of the malign cells; the second aim is the reporting of this location outside the body (e.g., to an external unit).

Every living region of the body can become the origin of cancer. This implies that in principle, the agent must be able to explore the entire body. Actually all the living parts of the body are at a distance of a nearby capillary by at most an O_2 decay length; in other words, an agent moving in the body transported by

[7] If this model were correct, cancer would be a source of paradoxes, with self-healing due to necrosis, and cancerogenesis due to physiological response!

blood is in principle able to feel the metabolic field of the body averaged over a distance of about 50 μm. Taking into account that such an agent can explore about one capillary per minute, the time required for exploring the entire organism would be of approximately 2×10^{12} s, exceeding the human lifetime by approximately 3 orders of magnitude. Such an exploration strategy requires thus a swarm of agents, whose population is determined by the mean number of necessary visits per region. Assuming that each region requires one visit per month, the total number of agents would be approximately 7×10^5.

To be transported by the stream along the entire system, the agent must be so small as not to obstruct the capillary. This condition gives a criterion about size, which cannot be much larger than that of a red blood cell: Having already in mind a production technology, we assume that the area of the agent is on the scale of $10^2\ \mu m^2$. Of course, the shape should in a sense be the opposite one to that of the red blood cell (whose lenticular shape is matched just to occlude the capillary and to bend under the stream pressure to undergo striction and to release as much O_2 as possible). The agent should thus have an ellipsoidal shape with major axis much longer than its minor axis.

The agent must perform a lot of sophisticated functions like navigation, recognition, data collection and transmission so that it must be viewed as a robot; on another side, the limited area available to host them implies that the necessary intelligence and sensing elements are implemented in nanoscale devices. The agent must thus be viewed as a nanorobot.

In view of their limited size, nanorobots have necessarily limited computational resources. The maximum density of devices that can be hosted in a *planar* circuit is given by $1/4F^2$ where F is the minimum producible feature size (the so-called $4F^2$ architecture). At the forefront of the technology, $F = 40$ nm, so that a planar surface of area $10^2\ \mu m^2$ could host 1.6×10^4 devices (and thus be endowed with a logic of 16 kbits. At the end of the road map (say, within the next 10 years) [24], F should be reduced to 10 nm, and the logic could be formed by 250 kbits. This value is likely achievable within the frame of the current technological paradigm as well from technological shifts like that based on the crossbar structure [25–27]. The shift to molecular electronics would however facilitate the integration of sensing devices onto the nanorobot [28, 29]. Further increase of density with planar arrangements seems to be in contrast with physical laws; however, if the crossbar structure is built with out-of-plane wire arrays, tera-scale integration seems possible [30, 31] so that the logics hosted in a $10^2\ \mu m^2$ nanorobot could have a megabit complexity.

Just to have an idea of the computational possibility of such a device, we remind that the simplest natural living system that can survive on a well-defined chemical medium is *Mycoplasma genitalium*. Mycoplasma genitalium has the smallest genome of any organism that can be grown in pure culture, and its genomic complexity is just around 1 Mbit [32]. This comparison suggests that the hypothesized nanorobot can likely perform sophisticated jobs provided that it is endowed with suitable hardware for sensing and actuating and sophisticated algorithm to manage them.

In [3], we described a few options for imparting to the nanorobot the minimal required functions (power supply, navigation, recognition, data collection and transmission, etc.). In this work we shall focus our attention on ambient recognition, having in mind the sensing of regions suspected of hosting a developing tumour.

In particular, according to the strategy described in the following, we want that when the nanorobot enters a capillary detects the temperature of the medium and the amount of lactic acid; in the case, the nanorobot feel values that can be considered symptoms of cancer actuates appendages for docking to nearby wall where remains anchored until the local pH is sufficiently low.

First of all, consider the time spent by the nanorobot in the capillary, about 4 s, as follows from the length of capillary, 8×10^{-2} cm, and the blood velocity therein, 2×10^{-2} cm s^{-1}. This time is manifestly long enough to allow sufficiently accurate measurements.

The basic strategy is based on the docking of the nanorobot on nearby capillary walls when it feels an abnormal increase of temperature and the simultaneous presence of pyruvic acid and a high concentration of H_3O^+.

For the detection of the ambient temperature, we hypothesize two possible ways: (1) In the first approach, the nanorobot is triggered by transient increase of temperature as measured by a built-in Seebeck thermocouple, whose sensing junction is exposed to the environment (and thus feeling the capillary temperature) while its reference junction is thermally isolated (and thus close to the temperature in the arteriole generating the capillary); (2) in the second case, the temperature is periodically detected under near equilibrium conditions by measuring the resistance of a semiconducting wire exposed to the environment.

Once allowed by the change of temperature, the nanorobot looks for chemical signatures of the tumour. According to the general idea described in this work, the simultaneous presence of pyruvate and hydronium ions can be assumed an adequate clue. Extracting the information, however, is not easy: The general scheme here proposed involves the gentle derivatization of crossbars (as described in [29]) with nicotinamide dinucleotide (NAD)[8] and the functionalization in its vicinity with lactate dehydrogenase (LDH). In this way, the following redox reactions are expected to occur very efficiently:

$$\bigotimes \cdots \mathrm{NAD} + \mathrm{CH_3COCO_2H} + \mathrm{H^+} \overset{\mathrm{LDH}}{\rightleftharpoons} \bigotimes \cdots \mathrm{NAD} + \mathrm{CH_3CH(OH)CO_2H}, \quad (17.4)$$

where $\bigotimes \cdots \mathrm{NAD}$ denotes the derivatized crossbar. The higher is the concentration of pyruvic acid and the acidity, the larger the reaction shift towards the lhs. The positive charge on the grafted NAD molecule will produce a positive voltage on the upper side of the underlying crossbar, and this signal can be taken as a marker for the simultaneous detection of CH_3COCO_2H and H^+.

[8] "Gentle" means that the derivatization preserves the redox properties of NAD; in particular, the gentle derivatization should not interfere with Reaction (17.4).

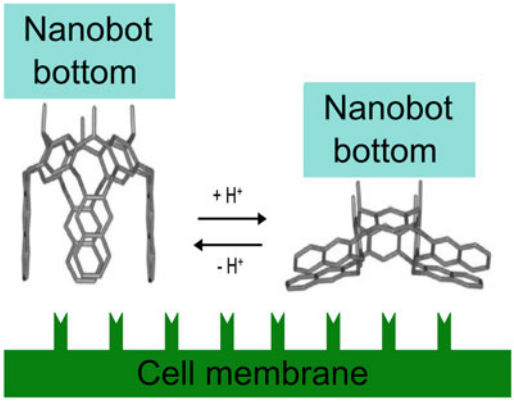

Fig. 17.5 Conformational changes, resulting after proton capture on quinoxaline cavitands, allowing the nanorobot docking on nearby capillary walls in the presence of pyruvic acid and high acidity

Signalling the presence of the pathogenic chemical state requires that the nanorobots behave collectively as a swarm. The collective behaviour, in turn, is started from the docking of the nanorobot to a nearby wall. That is achieved derivatizing the bottom of the nanorobot with quinoxaline cavitands, as discussed in [3] and shown in Fig. 17.5. Due to the hydrophobic character in cave conformation, the termination will prevent the docking to epithelial cells. Imagine, however, that once a marker molecule is detected, the nanorobot produces electrochemically (via electrolysis of water) H^+ and inject them at its bottom. Their capture by the nitrogen atoms will cause the opening of the cavity in the kite position due to the Coulomb repulsion strength among positively charged nitrogen atoms. The protonated nitrogen atoms will then be attracted the negatively charged sites on the cell membrane forming the glue for the attachment of the nanorobot to a nearby cell forming the capillary wall.

After docking, electrolysis is turned off, and the cave–kite conformation is eventually controlled by the ambient *p*H. If the initial low *p*H that produced the nanorobot anchorage was produced by physiological reasons, the *p*H recovery to 7.4 will produce the detachment of the nanorobot, while it will remain anchored to the wall until the low *p*H condition persists; of course, such a behaviour is possible only via an extremely accurate tuning of the basic strength of proton-hosting site.

As already mentioned, nanorobots, due to their size, are necessarily devices with very limited computational and energetic resources and able to have only strictly local interaction with the other nanorobots. Consequently, it is not feasible to fancy that a single nanorobot has on board the components and the energy to transmit a signal outside the body. However, although at first sight, these facts seem to make the challenges really daunting; from nature, we have experiences of tiny living beings (like ants or bees) with very limited resources but nonetheless able to perform complex tasks. In fact a task which cannot be tackled by a single individual can be tackled by a swarm of individuals without the need for a central supervisor. This is the very idea at the base of *swarm intelligence* [33], and its application for the control of swarm of micro and nanobots for medical applications has already been presented in literature [34–36].

To accomplish the identification task, the swarm of nanorobots needs to accomplish the following subtasks: (1) autonomous dispersion in the capillary bed, (2) chemical sensor reading, (3) marking of the region where a positive signal is detected and (4) clustering in the marked region. Once a cluster of a few nanorobots formed around a malign cell, it could be big enough to be imaged via computerised x-ray axial tomography or have enough energy to behave as antenna able to transmit a signal. The authors described a surveillance system together with a strategy to tackle the identification task in [3, 37]; here, we focus on a general description of the most complex of these subtasks—the clustering around malign cells.

In swarm robotics, spatial coordination between robots is often critical. When the robots are macroscopic, usually this coordination is achieved via local relative positioning sensors which are based, for example, on ultrasound or infrared technologies. Thus, by using these sensors, nearby robots can communicate and determine the bearing, orientation and range of their neighbours. When nanorobots are considered, it is possible to exploit the fact that collisions are not an issue at microscopic level. Of course, this is very different from what happens for macroscopic robots, where collision avoidance is a major issue to be taken into account. *Vice versa*, communication between nanorobots can happen through direct physical clashes [3].

It can be hypothesized that when two nanorobots collide in liquid phase (say in blood), they remain paired for a short time. Although this can lead to the random formation of a cluster, it may easily be destroyed by the thermal reservoir. On the other side, clusters may be stabilized when they are formed on the membrane of a cell, so that nanorobots anchoring on unhealthy cells become themselves sites for docking of other nanorobots. This *self-docking* mechanism has also the advantage of accelerating the formation of the cluster.

To illustrate this mechanism, consider a square area of 30×30 (arbitrary units) and that 50 nanorobots are introduced in its lower left corner—at coordinate (0, 0); see Fig. 17.6. Suppose that the target site to be identified is in position (20, 20). The sensing happens trough direct contact, and we assume that each nanorobot can sense a site in a range of radius 1. At each time step, every nanorobot chooses a random direction and moves 3 units along it. When a nanorobot senses the target, it stops moving (anchors to its position); now, the nanorobot becomes itself a target, and since it is much larger than the true objective, it can be sensed in a range of radius 2. Running this simulation 1,000 times (with 60 time steps each) shows that when the anchored nanorobots are not used as new target, the cluster is on average of 2.78 nanorobots, while if they are used as new targets (i.e., new sites for docking), the cluster is on average of 9.91 nanorobots. The left column of Fig. 17.6 shows the result of one of the simulations. This naive strategy for cluster formation seems to be effective only when the concentration of target sites is low, that is, in the early phase of tumour development. In fact, running the same simulation with ten targets randomly distributed in the area shows that on average only three of them are identified, because most of the nanorobots tends to cluster around a few targets. The centre and right column ofFig. 17.6 show the result of simulations performed

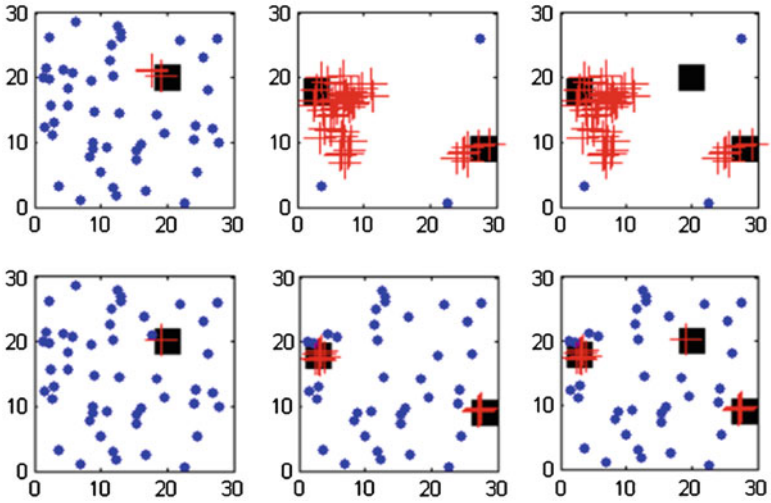

Fig. 17.6 Cluster (+) of nanorobots (·) around the target (■). *Top*: without self-docking. *Bottom*: with self-docking

with two and three targets, respectively. Both the strategies (with or without self-docking) have problems in dealing with them. This means that, at present stage, the self-docking strategy is effective only at the early stage of tumour development.

17.7 Conclusions

The common symptoms of the neoplastic disease (high temperature, low *p*H and hypoxia) are characteristic of a physiological condition (heavy physical exercise)—that perhaps explains why the immune system is poorly effective in recognizing and terminating cancer.

In the light of this analogy, we have developed a strategy, based on the use of nanorobots able to mark the regions where the said symptoms persist with time and to signal them exploiting techniques of swarm intelligence.

The single agents circulate in the blood and have size on the 10-μm length scale; a swarm of 7×10^5 nanorobots guarantees that each capillary is explored on the mean once per month.

Appendix: Fractal-Tree Description of the Circulatory System

Since the work of Mandelbrot, the fractal geometry of biological structures [38] has suggested that fractal methods could be used for modelling of human circulatory

system.[9] In fact, in the recent years, fractal analysis of blood vessel in any different parts of human body has been described. In particular in [40], the application of asymmetrical and symmetrical *fractal trees* has been analysed. A fractal tree can be loosely defined as a trunk and a number of branches that each looks like the tree itself, thus creating a self-similar object. Often, these structures appear strikingly similar to real trees.

To some extent, the circulatory system can be described by two fractal trees forming a double canopy inside each organ [7], where the ultimate branches of the canopies are linked by filaments (*capillaries*). For the sake of simplicity, let us suppose that the two fractals are specular and that each of them is a symmetric tree where at each bifurcation, two new branches are generated. Given this extreme simplification, just three parameters are needed to characterize the fractal tree: the number n of branching (i.e., the depth of the tree), the ratio b between the diameters of parent and children branches and the ratio h between their lengths.

The description of the circulatory system as a double fractal tree whose canopies are linked by capillaries (common boundary of the trees) must satisfy the following five conditions:

$$2^n = N, \tag{17.5}$$

$$\frac{1-(2b^2h)^{n+1}}{1-2b^2h} = \frac{\frac{1}{2}v}{\pi r_0^2 l_0}, \tag{17.6}$$

$$\frac{1-(2b^2h)^{n+1}}{1-2b^2h} = \frac{\tau}{2}\frac{u_0}{l_0}, \tag{17.7}$$

$$(2b^2)^n = \frac{u_0}{u_n}, \tag{17.8}$$

$$h^n = \frac{1}{2}\frac{l_n}{l_0}, \tag{17.9}$$

[9] In particular, Mandelbrot stresses the point that the seminal Harvey work (published in 1628 [7]) led to a view of the circulation of the blood which asserts that both an artery and a vein are found within a (infinitely) small distance of nearly every point of the body. Stated differently, every point in nonvascular tissue should lie on the boundary between the two blood networks. Considering then that blood is expensive, the volume of all the arteries and veins must be a small percentage of the body volume, leaving the bulk to tissue. These criteria are apparently contradictory since the tissue must be a topologically 2-dimensional shape (it is the common boundary of two 3-dimensional shapes) and it must have a non-null volume. However, the two above requirements are perfectly compatible in fractal analysis. In fact, tissues can be described as fractal surfaces whose topological dimension is 2 and whose fractal dimension is close to 3. Examples of this kind of fractals have been introduced by Osgood in 1903 [39].

where N is the number of capillaries, v is the blood volume, r_0 and l_0 the aorta radius and length, τ is the cycle time of the blood, u_0 and u_n are the speed of the blood in the aorta and capillaries and l_n is the length of the capillaries.

In the above five equations, the parameters n, b and h defining the fractal geometry of the tree are on the lhs, whereas the quantities on the rhs can be found in handbooks of anatomy and physiology. In view of the relative variability of these data from one source to another, we list the ones assumed in this work: $N = 3 \times 10^{10}$, $v = 5 \times 10^4\,\mathrm{cm}^3$, $r_0 = 1\,\mathrm{cm}$, $l_0 = 6\,\mathrm{cm}$, $\tau = 60\,\mathrm{s}$, $u_0 = 26.5\,\mathrm{cm\,s}^{-1}$, $u_n = 2 \times 10^{-2}\,\mathrm{cm\,s}^{-1}$ and $l_n = 0.08\,\mathrm{cm}$.

Of course, the above equations are not consistent, so that we should limit to determine the fractal tree describing experimental data with minimum inaccuracy. To improve the accuracy of the search, we add another geometric condition produced by the need that even the organs at the maximum distance from the aorta (hand and foot fingers) must be bathed by the capillary system. This condition reads

$$\frac{1 - h^{n+1}}{1 - h} = \frac{\frac{1}{2} D_\mathrm{V}}{l_0 \cos(\phi)}, \tag{17.10}$$

where D_V is the Vitruvian diameter ($D_\mathrm{V} = 170\,\mathrm{cm}$) and ϕ is the average branching angle[10] ($\phi = 20\,^\circ$). Although the notion of Vitruvian diameter goes back to Da Vinci, to the best of our knowledge, (17.10) has never been used yet. It is immediately understood merging the concept of circulatory system with the famous Da Vinci's drawing generally referred to as Vitruvian Man (hence, the name; see Fig. 17.7). The drawing (a blend of art and science during Renaissance) depicts a male figure in two superimposed positions with his arms and legs apart and simultaneously inscribed in a circle and square and can be interpreted saying that the proportion of man is so done to admit a centre (the heart) able to bathe the farthest organs (hand and foot fingers) irrespective of posture.

Of course, (17.5)–(17.10) are not consistent so that we should limit to determine the fractal tree describing experimental data with minimum inaccuracy. Defining the relative inaccuracies as follows:

$$\begin{aligned}
\epsilon_1(n, b, h) &= \frac{2^n - N}{N} \\
&= \frac{1}{N} 2^n - 1, \\
\epsilon_2(n, b, h) &= \frac{2}{v} \pi r_0^2 l_0 \frac{1 - (2b^2 h)^{n+1}}{1 - 2b^2 h} - 1, \\
\epsilon_3(n, b, h) &= \frac{2}{\tau} \frac{l_0}{u_0} \frac{1 - (2b^2 h)^{n+1}}{1 - 2b^2 h} - 1,
\end{aligned}$$

[10] Since the tree is assumed symmetric, there is only one angle for both branching arteries.

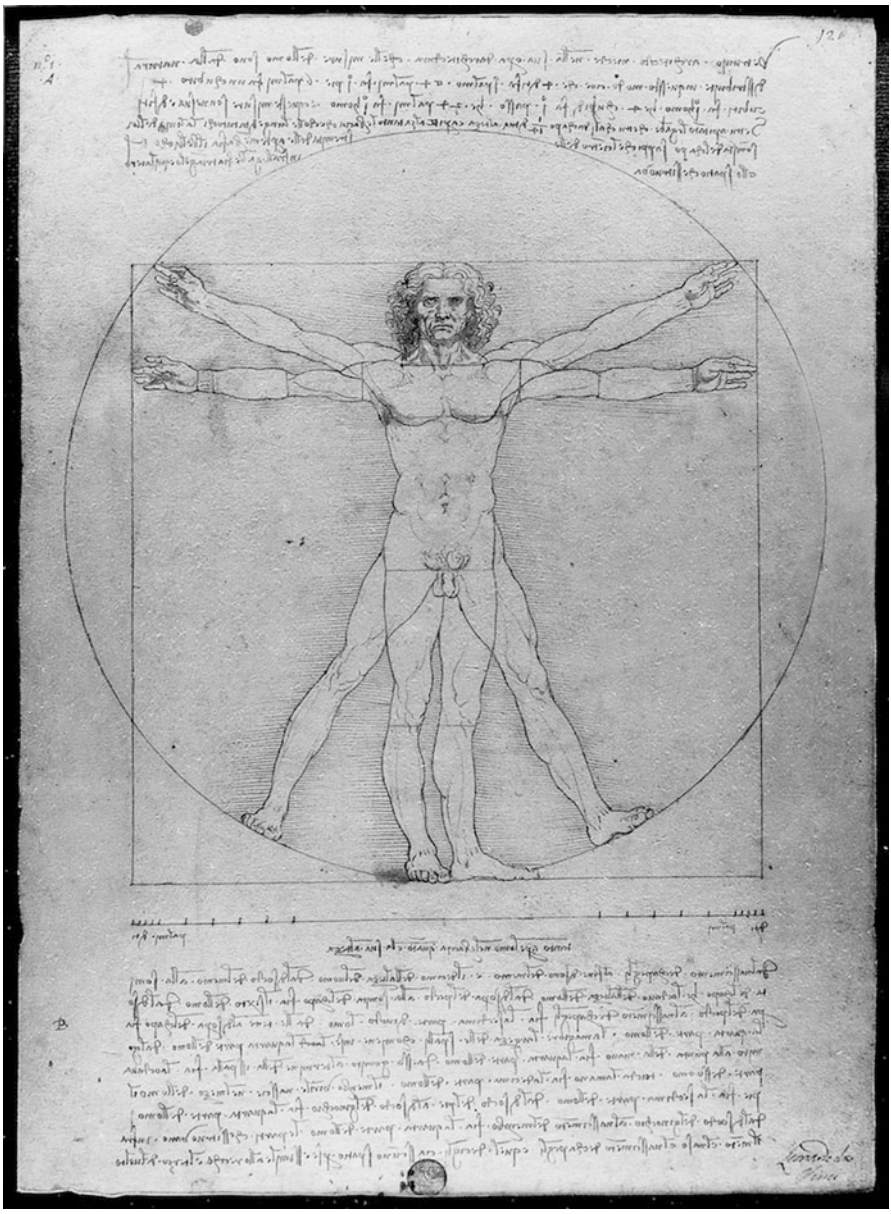

Fig. 17.7 Da Vinci's Vitruvian Man

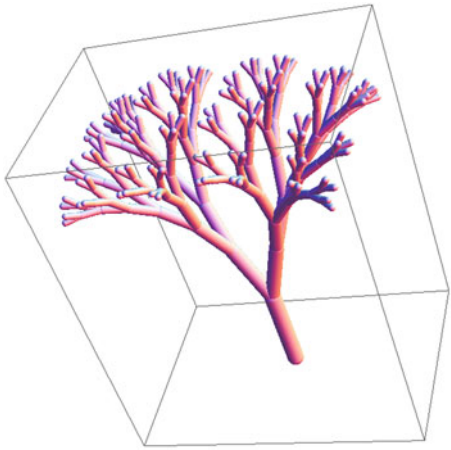

Fig. 17.8 3D geometry of fractal vascular symmetrical tree

$$\epsilon_4(n,b,h) = \frac{u_n}{u_0}(2b^2)^n - 1,$$
$$\epsilon_5(n,b,h) = \frac{2}{l_n} l_0 h^n - 1,$$
$$\epsilon_6(n,b,h) = \frac{2l_0\cos(\phi)}{D_V}\frac{1-h^{n+1}}{1-h} - 1;$$

the condition determining n, b and h is thus given by

$$\sum_{i=1}^{6} \epsilon_i^2(n,b,h) = \min. \tag{17.11}$$

Given as constraints that $25 < n < 40$, $0 < b < 1$ and $0 < h < 1$, the optimal estimates of n, b and h are the following: $\hat{n} = 34.818, \hat{b} = 0.784$ and $\hat{h} = 0.867$. These estimates are coherent with other ones computed with different methods [3, 37]. Figure 17.8 shows a symmetrical fractal tree (whose depth is 9) with the above parameters.

To check the stability of these equations, the same optimization process has been run by excluding, in turn, one of the six equations. The obtained estimates are shown in Table 17.1. On one side, from the table, it is possible to note that the first equation is paramount in defining an accurate value of depth of the tree. In fact, without the condition $2^n = N$, the estimate $\hat{n}$ is set equal to the maximum allowed value (in this case 40). On the other side, the estimates of all the other parameters (and also n in the other conditions) are quite stable regardless of the lack of any single condition.

Table 17.1 Estimates of the parameters n, b and h considering in turn just five out of the six conditions for the description of the circulatory system as a double fractal tree whose canopies are linked by capillaries

Excluded condition	$\hat{n}$	$\hat{b}$	$\hat{h}$
1	40.000	0.773	0.882
2	34.818	0.784	0.867
3	34.805	0.784	0.866
4	34.818	0.784	0.867
5	34.818	0.784	0.867
6	34.814	0.783	0.869

References

1. Futrelle J (1973) The scarlet thread. In: Bleiler EF (ed) Best thinking machine detective stories. Dover, New York, pp 48–76
2. Freitas RA (1999) Nanomedicine, volume I: basic capabilities. Landes Biosciences, Georgetown
3. Cerofolini GF, Amato P, Masserini M, Mauri G (2010) A surveillance system for early-stage diagnosis of endogenous diseases by swarms of nanobots. Adv Sci Lett 3:345–352
4. Aguda BD (2006) Modeling the cell division cycle. Lect Notes Math 1872:1–22
5. Cerofolini GF (1981) Size, shape, growth and reproduction—towards a physical morphology. Thin Solid Films 79:277–299
6. Cerofolini GF (1983) The biomedium. adsorbed water as a model for the aqueous medium supporting life functions. Adv Colloid Interface Sci 19:103–136
7. Harvey W (1910) On the motion of the heart and blood in animals. In: Scientific papers; physiology, medicine, surgery, geology, with introductions, notes and illustrations. The harvard classics, vol 38. P. F. Collier & Son, New York
8. Visvader J (2011) Cells of origin in cancer. Nature 469:314–322
9. Kamiya A, Togawa T (1972) Optimal branching structure of the vascular tree. Bull Math Biol 34:431–438
10. Kamiya A, Takeda S, Shibata M (1987) Optimum capillary number for oxygen delivery to tissue in man. Bull Math Biol 49:351–361
11. Brannon-Peppas L, Blanchette JO (2004) Nanoparticle and targeted systems for cancer therapy. Adv Drug Delivery Rev 56:1649–1659
12. Bauer A, Jackson T, Jiangy Y (2007) A cell-based model exhibiting branching and anastomosis during tumour-induced angiogenesis. Biophys J 92:3105–3121
13. Folkman J (1971) Tumour angiogenesis: therapeutic implication. N Engl J Med 285:1182–1186
14. Welter M, Rieger H (2010) Physical determinants of vascular network remodeling during tumour growth. Eur Phys J E 33:149–163
15. Bartha K, Rieger H (2006) Vascular network remodeling via vessel cooption, regression and growth in tumours. J Theor Biol 241:903–918
16. Kennedy DA, Lee T, Seely D (2009) A comparative review of thermography as a breast cancer screening technique. Integr Cancer Ther 8:9–16
17. Luk KH, Hulse RM, Phillips TL (1980) Hyperthermia in cancer therapy. West J Med 132:179–185
18. Steeves RA (1992) Hyperthermia in cancer therapy: where are we today and where are we going? Bull N Y Acad Med 68:341–350
19. Brown JM (2000) Exploiting the hypoxic cancer cell: mechanisms and therapeutic strategies. Mol Med Today 6:157–162
20. Keith B, Simon MC (2007) Hypoxia-inducible factors, stem cells, and cancer. Cell 129:465–472

21. Tannock IF, Rotin D (1989) Acid *p*H in tumors and its potential for therapeutic exploitation. Cancer Res 49:4373–4384
22. Robergs RA, Ghiasvand F, Parker D (2004) Biochemistry of exercise-induced metabolic acidosis. Am J Physiol Regul Integr Comp Physiol 287:R502–R516
23. Klawansky S, Fox MS (1984) A growth rate distribution model for the age dependence of human cancer incidence: a proposed role for promotion in cancer of the lung and breast. J Theor Biol 111:531–587
24. ITRS: international technology roadmap for semiconductors (2009) http://www.itrs.net/links/2009ITRS/Home2009.htm downloaded on January 15, 2011
25. Heath J, Kuekes P, Snider G, Williams R (1998) A defect-tolerant computer architecture: opportunities for nanotechnology. Science 280:1716–1721
26. Snider GS, Kuekes PJ, Hogg T, Williams RS (2005) Nanoelectronic architectures. Appl Phys A 80:1183–1195
27. Cerofolini GF, Romano E (2008) Molecular electronics *in silico*. Appl Phys A 91:181–210
28. Cerofolini GF (2009) Nanoscale devices: fabrication, functionalization, and accessibility from the macroscopic world. Springer, Berlin
29. Cerofolini GF (2010) Two routes to subcellular sensing. In: Korkin A, Krstić P, Wells J (eds) Nanotechnology for electronics, photonics, and renewable energy. Springer, New York, pp 153–182
30. Cerofolini GF, Ferri M, Romano E, Suriano F, Veronese GP, Solmi S, Narducci D (2010) Tera scale integration via a redesign of the crossbar based on a vertical arrangement of poly-Si nanowires. Semicond Sci Technol 25:095011
31. Cerofolini GF, Ferri M, Romano E, Suriano F, Veronese GP, Solmi S, Narducci D (2011) Crossbar architecture for tera scale integration. Semicond Sci Technol 26:045005
32. Glass JI, Assad-Garcia N, Alperovich N, Yooseph S, Lewis MR, Maruf M, Hutchinson CA 3rd, Smith HO, Venter JC (2006) Essential genes of a minimal bacterium. Proc Nat Acad Sci USA 103:425–430
33. Bonabeau E, Dorigo M, Theraulaz G (1999) Swarm intelligence: from natural to artificial systems. Oxford University Press, New York
34. Martel S, Mohammadi M (2010) Using a swarm of self-propelled natural microrobots in the form of flagellated bacteria to perform complex micro-assembly tasks. In: Proceedings of the 2010 IEEE international conference on robotics and automation (ICRA). Anchorage, Alaska
35. Nagy Z, Harada K, Flickiger M, Susilo E, Kaliakatsos IK, Menciassi A, Hawkes E, Abbott JJ, Dario P, Nelson BJ (2009) Assembling reconfigurable endoluminal surgical systems: opportunities and challenges. Int J Biomechatron Biomed Robot 1(1):3–16
36. Requicha AAG (2003) Nanorobots, NEMS, and nanoassembly. Proc IEEE 91:1922–1933
37. Amato P, Masserini M, Mauri G, Cerofolini G (2011) Early-stage diagnosis of endogenous diseases by swarms of nanobots: an applicative scenario. In: Dorigo M (ed) Swarm intelligence: 7th international conference, ANTS 2010, Brussels, Belgium, September 8–10, 2010. Proceedings, vol. 6234. Springer, Berlin, pp 408–415
38. Mandelbrot BB (1983) The fractal geometry of nature. W. H. Freeman, New York
39. Osgood WF (1903) A Jordan curve of positive area. Trans Am Math Soc 4:107–112
40. Gabrys E, Rybaczuk M, Kedzia A (2005) Fractal models of circulatory system. Symmetrical and asymmetrical approach comparison. Chaos Solitons Fractals 24:707–715

Part V
Bio-Nano Actuators for Nanorobotics

Chapter 18
DNA Nanorobotics

Harish Chandran, Nikhil Gopalkrishnan, and John Reif

Abstract This chapter overviews the current state of the emerging discipline of DNA nanorobotics that make use of synthetic DNA to self-assemble operational molecular-scale devices. Recently there have been a series of quite astonishing experimental results—which have taken the technology from a state of intriguing possibilities into demonstrated capabilities of quickly increasing scale and complexity. We first state the challenges in molecular robotics and discuss why DNA as a nanoconstruction material is ideally suited to overcome these. We then review the design and demonstration of a wide range of molecular-scale devices; from DNA nanomachines that change conformation in response to their environment to DNA walkers that can be programmed to walk along predefined paths on nanostructures while carrying cargo or performing computations, to tweezers that can repeatedly switch states. We conclude by listing major challenges in the field along with some possible future directions.

18.1 Introduction

DNA self-assembly is an emerging scientific discipline that seeks to engineer nanoscale systems created out of DNA strands. The underlying principle of DNA self-assembly is the programmability of DNA strands based on the specific

H. Chandran (✉) • N. Gopalkrishnan
Department of Computer Science, Duke University, L.S.R.C. Building,
Box 90129, Durham, NC 27708-0129, USA
e-mail: harish@cs.duke.edu; nikhil@cs.duke.edu

J. Reif
Department of Computer Science, Duke University, L.S.R.C. Building,
Box 90129, Durham, NC 27708-0129, USA

Computing and Information Technology, King Abdulaziz University, Jeddah, Saudi Arabia
e-mail: reif@cs.duke.edu

C. Mavroidis and A. Ferreira (eds.), *Nanorobotics*, DOI 10.1007/978-1-4614-2119-1_18,
© Springer Science+Business Media New York 2013

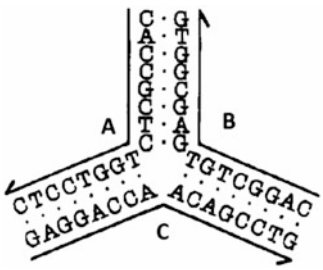

Fig. 18.1 A 3-way junction involving 3 DNA strands

Watson–Crick binding of DNA bases, adenine (abbreviated A), cytosine (C), guanine (G) and thymine (T). Typically, A prefers to pair up with T, while C with G. Hence the sequence ATATC would hybridize to its reverse complement (complement of the molecule written in reverse) GATAT. The sequences for a set of DNA molecules can be designed such that they interact among themselves in specific ways. For example, three molecules A, B, and C can be designed such that first part of A is reverse complementary to the last part of C, last part of A is reverse complementary to first part of B, and last part of B is reverse complementary to first part of C. In the right chemical soup, these molecules can assemble into a three-way DNA junction (see Fig. 18.1).

This basic principle allows us to program nanoscale DNA objects of required geometry and has resulted in a myriad of nanostructures (see [1–10] for some illustrative examples). But more importantly, dynamic behavior of these objects can be controlled via the action of DNA enzymes that act upon specific sequences of DNA strands, competitive DNA hybridization, or environmental changes such as pH or temperature. This chapter reviews some of the recent advances made in this emerging field of DNA nanorobotics. We begin by listing some of the challenges of DNA nanorobotics.

18.1.1 Challenges of DNA Nanorobotics

The aim of DNA nanorobotics is the design and fabrication of dynamic DNA nanostructures that perform specific tasks via a series of state changes. We limit ourselves to tasks that involve some form of robotic motion, such as locomotion or conformational changes. State changes can be viewed at different granularities, from the hybridization/denaturing of a single base to hybridization/denaturing of entire strands. These state changes can be effected autonomously, in which case the system switches state without external intervention, while in other cases precise amounts of specific species, such as DNA strands or enzymes, are introduced to enforce state changes. It should be noted that different copies of the nanostructures might be in different states at the same time and we are generally interested in the overall average behavior system.

Various challenges arise in attempting to create a DNA nanorobot. Design of the DNA robot begins at the domain level where the overall mechanism of action of the robot is developed without actually assigning DNA sequence to the strands. Instead the different interacting segments of the DNA strands that constitute the robot are assigned a domain name which in the next step is assigned to specific DNA sequences. The mapping of domains to DNA sequences is done with care to avoid spurious interaction among the various domains.

Another important consideration at this stage is the fuel that powers the robot. Typically, robots are powered either by enzymes that act upon specific DNA strands of the robot or by the energy of hybridization of freely floating single-stranded fuel DNA with specific strands of the DNA robot. Sometimes entropic effects can be used to power a state change. For example, two DNA strands that are held together by the hybridization of a small domain might denature spontaneously leading to an increase in the entropy of the system.

Other challenges include actual assembly of the DNA nanorobot and its purification, setting up initial operating conditions, and finally designing experiments that validate the proposed mechanism of action of the DNA nanorobot. Since it is very hard to directly observe the operation of the robot, other means of real-time detection, such as froster resonance energy transfer (FRET), are typically used. Each step in the process of creating DNA nanorobots is quite challenging.

We first briefly describe the working of two naturally occurring protein motors that have served as inspirations for various DNA nanorobots and then discuss the properties of DNA that make it an ideal material for mimicking such motors.

18.1.2 Natural Examples: Myosin and Kinesin

Kinesin is a motor protein that moves directionally along a microtubule powered by hydrolysis of ATP to ADP while transporting large cargo. It is a dimer, each component of which has a globular head at one end connected to a tail region via a long, thin stalk (see [11]). The head has binding domains to the microtubule, while the tail binds to the cargo. The common mechanism that accounts for its movement is the hand-over-hand mechanism where one of the kinesin heads remains anchored to the microtubule while the other swings over and beyond it.

Myosins (see [12]) are a class of motor proteins similar to kinesins. They bind to actin filaments via their head domains and push along them using the energy generated by ATP hydrolysis. Many myosin molecules bind to different locations on the actin filament and combine to push it. The power stroke occurs while the myosin is bound to actin. The myosin is detached from the actin at the end of the power stroke. ATP hydrolysis causes rebinding and the cycle repeats.

18.1.3 DNA: An Ideal Material for Molecular Robotics

Below we list some reasons why DNA is a material uniquely suited for building and manipulation at the molecular scale. From the perspective of design, the advantages are as follows:

1. A variety of predictable geometries can be achieved by carefully programming the interaction of DNA sequences.
2. The structure of most complex DNA nanostructures can be reduced to determining the structure of short segments of double-stranded DNA (dsDNA). The basic geometric and thermodynamic properties of dsDNA are well understood and can be predicted by available software systems from key relevant parameters like sequence composition, temperature, and solution composition.
3. Design of DNA nanostructures can be assisted by software. To design a DNA nanostructure or device, one needs to design a library of single-stranded DNA (ssDNA) strands with specific segments that hybridize to (and only to) specific complementary segments on other ssDNA. There are a number of software systems (developed at NYU, Caltech, Harvard, Arizona State, and Duke University) for design of the DNA sequences composing DNA tiles and for optimizing their stability, which employ heuristic optimization procedures for this combinatorial sequence design task.

From the perspective of experiments, the advantages are as follows:

1. The solid-phase chemical synthesis of custom ssDNA is now routine and inexpensive; a test tube of ssDNA consisting of any specified short sequence of bases (<150) can be obtained from commercial sources for modest cost (about half a US dollar per base at this time); it will contain a very large number (typically at least 10^{12}) of identical ssDNA molecules. The synthesized ssDNA can have errors (premature termination of the synthesis is the most frequent error), but can be easily purified by well-known techniques (e.g., electrophoresis as mentioned below).
2. The assembly of DNA nanostructures and devices is a very simple experimental process: in many cases, one simply combines the various component ssDNA into a single test tube with an appropriate buffer solution at an initial temperature above the melting temperature of the target nanostructure, and then slowly cools the test tube below the melting temperature. Various devices can be implemented by simple strand displacement processes.
3. The assembled DNA nanostructures and devices can be characterized by a variety of techniques. Gel electrophoresis provides information about the relative molecular mass of DNA molecules, as well as some information regarding their assembled structures. Other techniques like atomic force microscopy (AFM), transmission electron microscopy (TEM) and cryo-electron microscopy (cyroEM) provide images of the actual assembled DNA nanostructures on 2D surfaces and in 3D. These can be used to study snapshots of the device in its various stages of operation. DNA strands can be coupled to fluorescent

molecules and their corresponding quencher molecules. The fluorescent signal from a fluorescent emitter–quencher pair is sensitive (at nanometer resolution) to the distance between them. These markers can be attached to different moving parts of the nanorobot and a fluorescence spectrophotometer be used to infer the configuration of the DNA robot.

18.1.4 Outline of the Chapter

In this chapter, we classify various efforts in building DNA-based molecular motors and devices under four broad categories. In Sect. 18.2, we describe devices that respond to changes in their environment. The environmental changes can be used to actuate these devices. In Sect. 18.3, we describe DNA-based motors that use enzymes that act upon DNA strands to effect the desired change in state. These enzymes are both protein enzyme and deoxyribozymes (DNAzymes). In Sect. 18.4, we describe DNA devices and motors that are operated only by the competitive hybridization and denaturation of DNA strands. The key to these devices is the process of strand displacement (defined later). Finally in Sect. 18.5, we describe programmable molecular devices that compute specific functions when undergoing state changes. These devices in theory can undergo complex motions based on the program they are executing. In Sect. 18.6. we make concluding remarks and state some open problems.

18.2 DNA Nanomachines That Switch Conformation Based on Their Environment

The earliest demonstration of conformational changes of synthetic DNA induced by changes in salt concentration (sodium and magnesium ions) was achieved by Pohl and Jovin [13]. Mao et al. [14] connected two DX [1] tiles by a short piece of dsDNA and used conformational change between Z and B forms of this DNA segment to reposition the two DX tiles (Fig. 18.2). When the connecting segment is in the B form (right-handed double helix), the DX tiles are on the same side of the connecting segment, while in the Z form (left-handed double helix) they switch to opposite sides. This conformational switching behavior is demonstrated using FRET experiments. The branching point of two homologous double strands that form a Holliday junction [15] can migrate by exchange of their hybridized bases, lengthening one of the double strands while correspondingly shortening the other. This process is called *branch migration*. Yang et al. [16] showed that one can effect branch migration by applying torsional forces to one of the dsDNA of the Holliday junction. The torque is applied by the use of ethidium, which intercalates between the strands of a dsDNA, unwinding it. This induces branch migration.

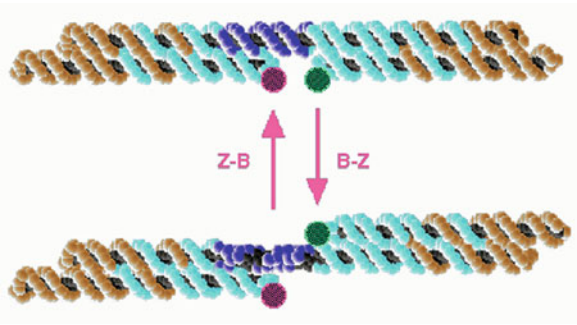

Fig. 18.2 The middle segment of the DNA nanostructure switches from B to Z form based on the solution conditions and this can be detected based on the change in fluorescent activity of the system. Reprinted by permission from Macmillan Publishers Ltd: Nature, [14], © 1999

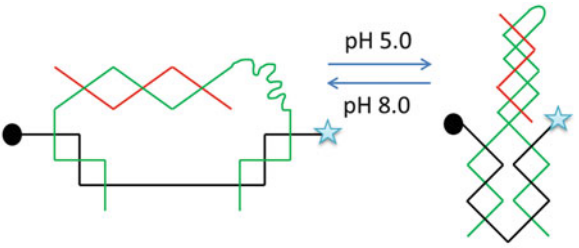

Fig. 18.3 The state of the DNA changes from duplex to triplex based on pH. The change is observed by change in fluorescence as the flurophore (*star*) is separated from the quencher (*dot*)

The i-motif [17] is a single strand of DNA which at pH 5 folds up into a compact three-dimensional single-stranded DNA structure in which two DNA double helices have their base pairs fully intercalated by C–C base pairs. The relative orientation of the double helices is antiparallel so that each base pair faces its neighbors. A conformational switch in the i-motif can be achieved in the presence of a complementary DNA strand by increasing the pH to 8 [18, 19]. A light-sensitive dye can be used [20] to induce reversible pH changes which lead to repeated conformational change of the i-motif. A similar autonomous switching effect can be achieved by using chemical oscillators that regulate pH [21, 22]. Cao et al. [23] demonstrate that a solution of gold nanoparticles conjugated to DNA strands changes color when the gold particles aggregate. The pH-dependent conformational change of the i-motif has been converted into a visual signal by using it to aggregate gold particles [24]. Alternatively, the conformational switch of the i-motif can be detected using a polythiophene derivative (PMNT) which forms an interpolyelectrolyte complex with the i-motif through electrostatic interactions exhibiting a relatively red-shifted absorption wavelength [25]. The i-motif was used to bend and straighten an array of microfabricated silicon cantilevers via electrostatic repulsion [26]. The process, controlled by pH changes, was found to be highly reversible and exerted single motor forces of about 11 pN/m.

Chen et al. [27] (Fig. 18.3) and Brucale et al. [28] show alternate DNA motifs that demonstrate pH sensitive reversible conformation switching based on a DNA duplex–triplex transition.

The first ever in vivo pH sensitive conformation switching DNA nanomachine was demonstrated by Modi et al. [29]. The device switches from an open state

to a closed triangular state in acidic conditions. The change in state is observed via FRET. The nanomachine is delivered inside a fruitfly cell by attaching it to transferrin, a protein absorbed through endocytosis.

18.3 DNA Nanomachines Powered by Enzymatic Actions

Many initial demonstrations of DNA-based nanomachines make extensive use of protein enzymes. Typically, ligase and various restriction enzymes are used. We first give a brief introduction of how these enzymes operate and then survey DNA nanomachines that use them.

18.3.1 Introduction to Enzymes That Manipulate DNA

There are a wide variety of known enzymes and other proteins used for manipulation of DNA nanostructures that have predictable effects. Interestingly, these proteins were discovered in natural bacterial cells and tailored for laboratory use.

DNA restriction (Fig. 18.4) is the cleaving of phosphodiester bonds between the nucleotide subunits at specific locations determined by short (4–8 base) sequences by a class of enzymes called nucleases. Endonucleases cleave the phosphodiester bond within a polynucleotide chain, while exonucleases cleave the phosphodiester bond at the end of a polynucleotide chain. Some nucleases have both these abilities. Some restriction enzymes cut both the strands of a DNA double helix, while others cut only one of the strands (called nicking).

DNA ligation (Fig. 18.5) is the rejoining of nicked double-stranded DNA by repairing the phosphodiester bond between nucleotides by the class of enzymes known as ligases.

DNA polymerases (Fig. 18.6) are a class of enzymes that catalyze the polymerization of nucleoside triphosphates into a DNA strand. The polymerase "reads" an intact DNA strand as a template and uses it to synthesize the new strand. The newly polymerized molecule is complementary to the template strand. DNA polymerases can only add a nucleotide onto a preexisting 3-prime hydroxyl group. Therefore it needs a primer, a DNA strand attached to the template strand, to which it can add

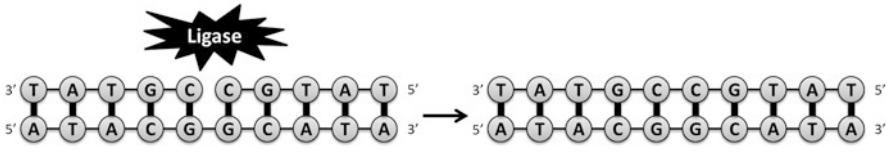

Fig. 18.4 Ligase healing a single-stranded nick. Note that the two parts are bound to the same template

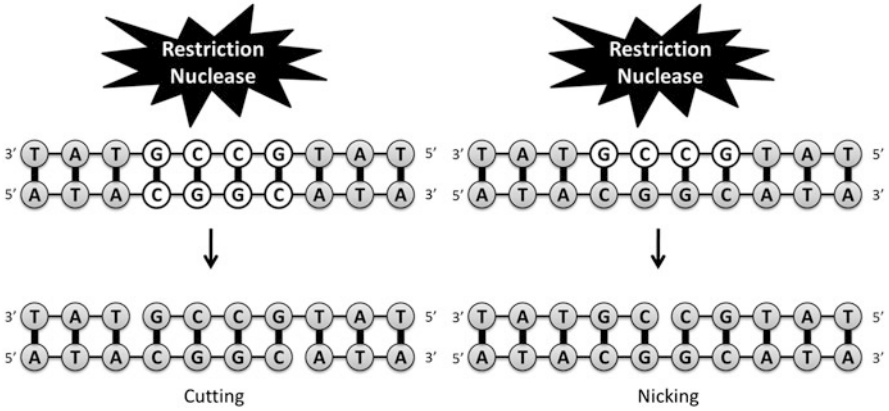

Fig. 18.5 Example of restriction enzyme cut of a single-stranded DNA sequence. The subsequence recognized by the nuclease is *unshaded*

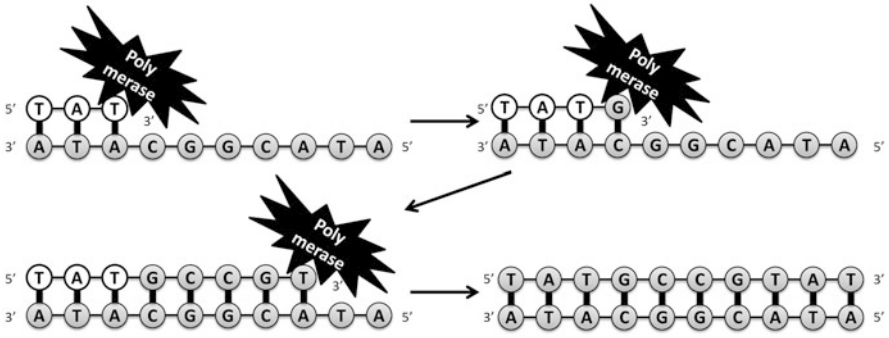

Fig. 18.6 Extension of primer strand (*unshaded*) bound to the template by DNA polymerase

the first nucleotide. Certain polymerase enzymes (e.g., φ-29) can, as a side effect of their polymerization reaction, efficiently displace previously hybridized strands.

In addition, deoxyribozymes (DNAzymes) are a class of nucleic acid molecules that possess enzymatic activity—they can, for example, cleave specific target nucleic acids. Typically, they are discovered by in vivo evolution search and have had some use in DNA computations.

Besides their extensive use in other biotechnology, the above reactions, together with hybridization, are often used to execute and control DNA computations and DNA robotic operations. The restriction enzyme reactions are programmable in the sense that they are site specific, only executed as determined by the appropriate DNA base sequence. Ligation and polymerization require the expenditure of energy via consumption of ATP molecules, and thus can be controlled by ATP concentration.

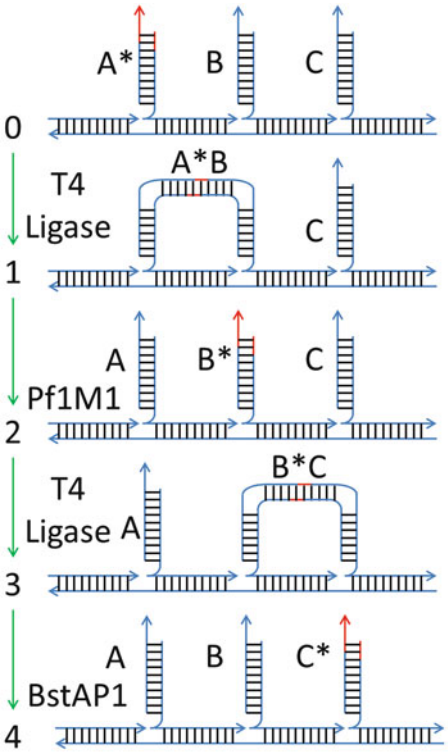

Fig. 18.7 Steps of the walker powered by enzymes

18.3.2 DNA Motors Based on Enzymatic Actions

Yin et al. [30] demonstrate a molecular motor that transports two short DNA segments along a linear track. The two segments are indicated in red (Fig. 18.7) and are passed from A to B to C in a sequence of steps mediated by different enzymes. The double-stranded segments A, B, and C are attached to a linear double-stranded track by flexible single-stranded regions. The ends of A and B can therefore be in proximity, whence they may bind via their complementary sticky ends. Now the DNA ligase T4 seals the nick, joining segments A and B into a single double-stranded segment. The restriction enzyme Pf1M I now cuts at its two recognition sites, allowing the segments A and B to separate, with the red segments now transported to B. Note that the restriction enzyme cuts asymmetrically and hence this step is irreversible. The same process can now take place between B and C, with a different restriction enzyme, BstAP I, recognizing two distinct sites between B and C. Again, the restriction step is asymmetric and prevents the red segment from being passed back along the linear track. The whole process is autonomous, the track setup and the three enzymes are mixed together in one pot, and the reaction is allowed to proceed to completion without external mediation.

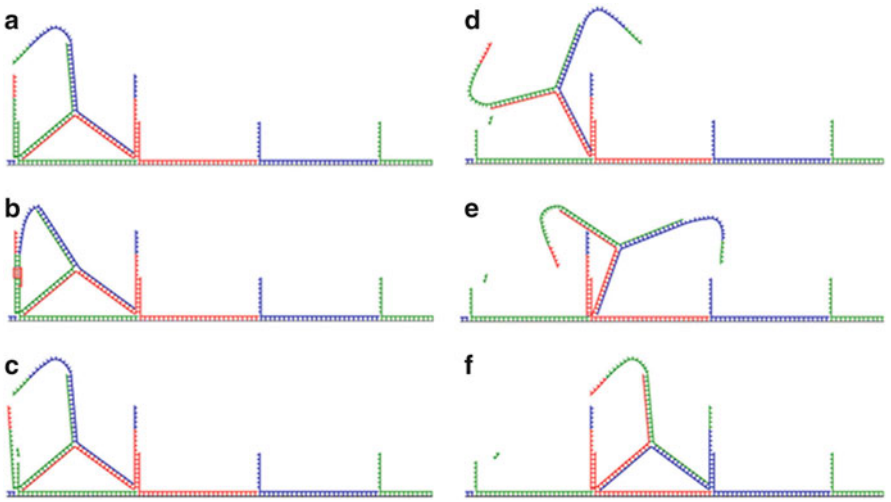

Fig. 18.8 Steps of the walker powered by restriction enzymes

A similar motor was suggested by Sekiguchi et al. [31], with an aim to allow the walker to walk along 2D and 3D paths (Fig. 18.8). They suggest through simulations and initial experimental demonstrations that their design can feasibly walk along pre-programmed paths but full experimental demonstrations are not achieved.

One of the weaknesses of the Yin et al. [30] motor is that the cargo is transported only two steps. Bath et al. [32] demonstrate a very similar DNA motor which walks constantly along longer distances. Their design is also autonomous, with the help of the catalytic action of the restriction enzyme N. BbvC IB (Fig. 18.9). The track is a single strand of DNA, with periodically spaced single-stranded DNA stators hybridized along its length. The cargo is passed unidirectionally along neighboring stators. When the cargo is attached along its full length to a stator, the restriction enzyme cuts the stator at a recognition site. The short segment of the stator attached along the top of the cargo can now float away (driven by entropic effects). The next stator along the track can now bind to the cargo and detach it from the previous stator, thus moving the cargo by one step. The process is repeated till the fuel is exhausted or the cargo reaches the end of the track. The cargo cannot move back since the bridges have been burnt behind—the toehold by which it binds to the stator is no longer present.

A modification of the Bath et al. [32] motor uses DNAzymes (DNA strands with enzymatic RNA restriction activity) instead of using restriction enzymes [33]. The track, as before, is a single strand of DNA. The stators are however identical RNA sequences positioned periodically along the track (Fig. 18.10). The cargo is a DNAzyme that cleaves the RNA stators at a sequence-specific site when hybridized to them. The mechanism of the motor is otherwise identical to the motor of Bath et al. [32] described above.

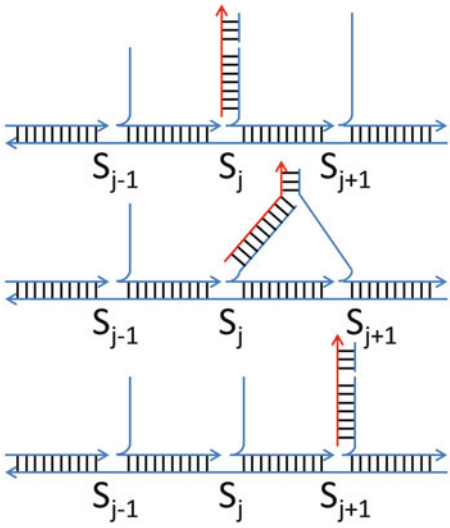

Fig. 18.9 Steps of the unidirectional walker is shown here. The track gets used up as the walker progresses

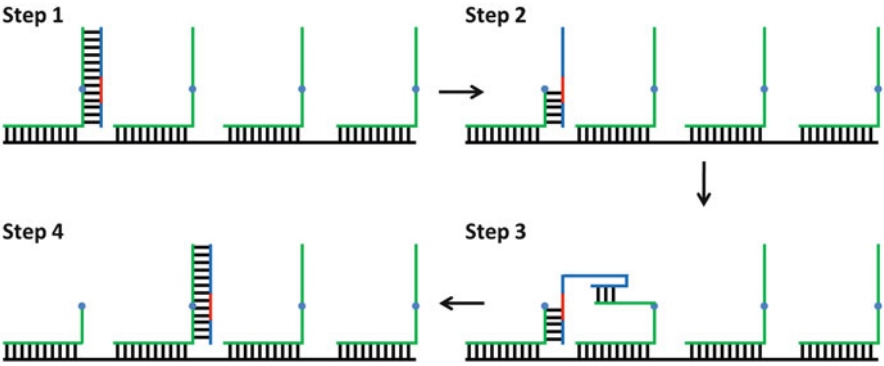

Fig. 18.10 Steps of the walker powered by DNAzymes. The DNAzyme region of the strand is shown in different *shade*

Chen et al. [34] developed an autonomous version of the DNA tweezers of Yurke et al. [35] (see Sect. 18.4) that opens and closes a DNA nanostructure by the catalytic activity of a DNAzyme (Fig. 18.11). The flexible linear DNA nanostructure can either be in an open state where its two ends are held apart by a short double-stranded region or in a compact closed state where the ends are close together because the single-stranded DNAzyme collapses into a coil as a result of entropic forces. The switch from the closed to the open state occurs via the binding of a RNA sequence S, while the reverse switch occurs when the DNAzyme cleaves S and its short substrands float away due to entropic effects. Note that if we throw in an excess of strand S, this cycle would execute many times in an autonomous manner.

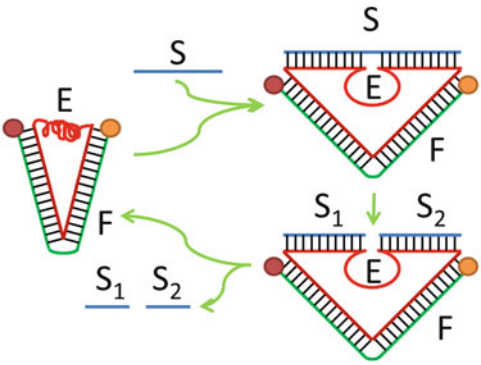

Fig. 18.11 The motor opens and closes based on the concentration of the strand S

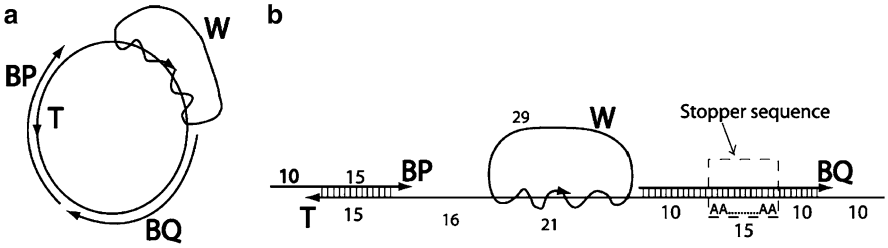

Fig. 18.12 Nano transport device powered by φ-29. Polymerase extends the primer BP, and pushes the wheel W on the track T. Protector strand BQ prevents the wheel from moving on its own but is dislodged by polymerase extension of BP on *left*. Reprinted with permission from Sahu et al. [37]. © 2008 American Chemical Society

Bishop and Klavins [36] describe a chemical reaction network model of the autonomous tweezers of Chen et al. [34] and suggest that certain waste products build up over time that inhibit the switching of the tweezers between its two states. They suggest a modification of the autonomous tweezers in which the waste products are selectively digested using the enzyme ribonuclease H.

Sahu et al. [37] demonstrated transport of a cargo along a circular track powered by a strand displacing DNA polymerase, φ-29. Figure 18.12 shows the circular single-stranded wheel W mounted on the circular track T. The wheel is driven forward by the polymerization of the primer sequence BP, while the protection sequence BQ prevents spontaneous displacement of the wheel in the absence of the polymerase.

18.4 DNA Motors Based on Hybridization Reactions

While protein enzymes are powerful and efficient, they are difficult to predictively modify. Also, the range of environmental conditions in which enzyme-mediated DNA nanomachines operate is restricted as compared to pure nucleic acid systems.

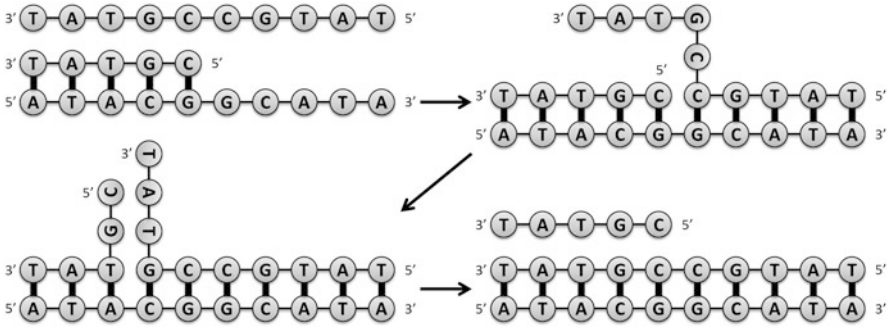

Fig. 18.13 Strand displacement of a DNA strand induced by the hybridization of a longer strand, allowing the structure to reach a lower energy state

There have been attempts to replace enzymes and achieve the same functionality by programming purely nucleic acid systems, with a fair degree of success. In particular, there have been some ingenious enzyme-free nanomachines driven by the energy of hybridization of DNA strands. The key to these devices is the process of strand displacement. We first describe the strand displacement process and then briefly review these devices.

18.4.1 Introduction to DNA Strand Displacement

Strand displacement is the displacement of a single strand of DNA from a double helix by an incoming strand with a longer complementary region to the template strand. The incoming strand has a toehold, an empty single stranded region on the template strand complementary to a subsequence of the incoming strand, to which it binds initially. It eventually displaces the outgoing strand via a kinetic process modeled as a one-dimensional random walk. Strand displacement is a key process in many of the DNA protocols for running DNA autonomous devices. Figure 18.13 illustrates DNA strand displacement via branch migration.

18.4.2 DNA Motors Based on Hybridization Reactions

The first application of strand displacement processes to a DNA nanomachine is the molecular tweezers of Yurke et al. [35]. The tweezers nanostructure consists of two double-stranded DNA arms linked via a flexible single-stranded region (Fig. 18.14). Single-stranded sticky regions extend beyond the ends of the arms. The tweezers can exist in two states, the open state when the sticky ends are unbound and the closed state when the sticky regions are hybridized to a fuel strand F. The tweezers transition from the open to the closed state via the hybridization of the fuel strand F.

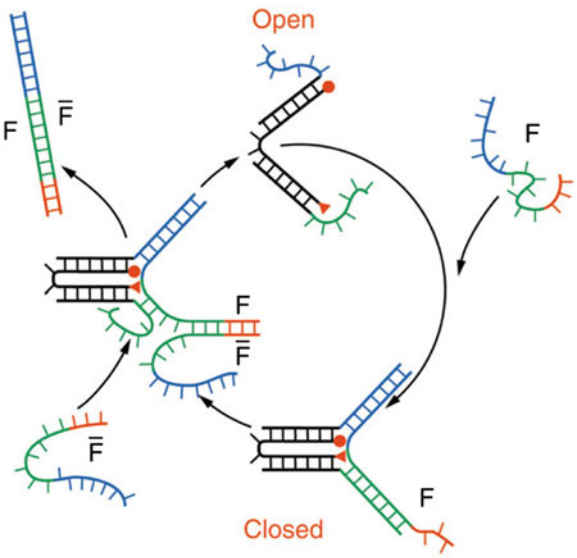

Fig. 18.14 The tweezer cycling between open and closed states. Reprinted by permission from Macmillan Publishers Ltd: Nature [35], © 2000

It transitions from the closed to the open state when the strand $\bar{F}$ binds to F via a toehold and strand displaces it, freeing the sticky regions of the tweezers. The complex $F\bar{F}$ is produced as a waste product of this cycle.

Sherman and Seeman [38] demonstrate a bipedal walker that moves along a linear track, evocative of kinesin and myosin. However, their biped walker moves forward in an inchworm fashion where the relative positions of the leading and trailing leg do not change. The walker system has the following parts (Fig. 18.15): a track (blue), two legs (brown), two feet (pink and orange), and two footholds (green and turquoise). The walker progresses along the track by the binding and unbinding of the feet on the footholds. The binding occurs simply when a single-stranded *set* strand binds a foot to its foothold by forming a bridge across them. The unbinding occurs when this bridge is stripped away via a toehold due to the strand displacement action of *unset* strands.

Shin and Pierce [39] demonstrate another similar bipedal walker but with the difference that their walker moves in a foot–over-foot manner (like kinesin) where each step the trailing foot swings past the leading foot. Their walker W (Fig. 18.16) consists of two single-stranded legs partially hybridized together, leaving single-stranded attachment regions on each. The track is a double-stranded helix with single-strand stators jutting out at periodic intervals. Locomotion is achieved by hybridizing and denaturing the legs of W to the stators in a precise sequence. First, the legs of W are anchored to the first two stators by the use of bridging DNA strands. The trailing leg is then pried loose by using a detachment strand to strand displace away its bridging strand via a toehold. The single-stranded leg then swings over and binds to the next stator, representing a step of the walker. The new trailing leg is now also pried loose in the same manner. Note that the walker may move backwards if the sequence of attachments and detachments is reversed.

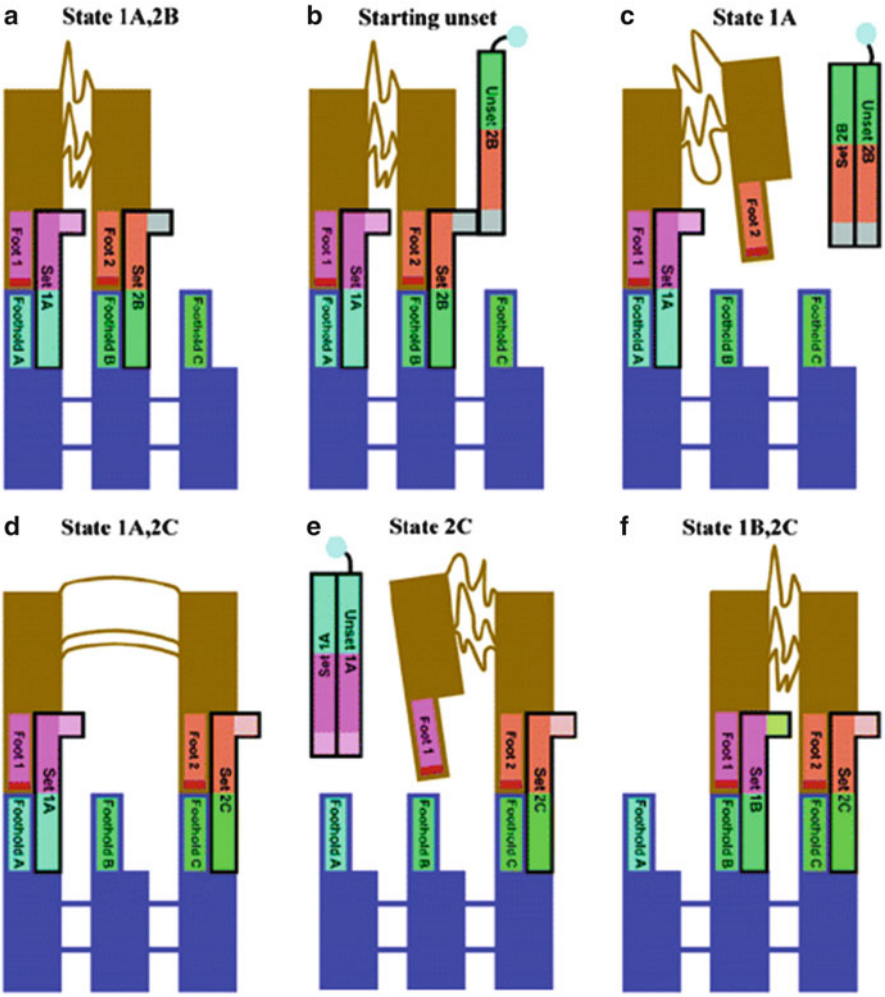

Fig. 18.15 Single step of the inchworm walker. Reprinted with permission from Sherman and Seeman [38]. © 2004 American Chemical Society

The DNA motor of Tian and Mao [40] (Fig. 18.17) operates on the same principle as the walker of Shin and Pierce [39], with the exception that the cargo walks along a circular track and returns to its original position after three steps. Due to the symmetry of the design, the cargo and the track have the same geometric circular structure.

Another similar approach is taken by Yin et al. [41] where a biped walker walks hand over hand along stators attached to a double-stranded linear track. The key difference is that the stators are in the form of hairpins and the process is autonomous because the stators have identical sequence and the two legs of the

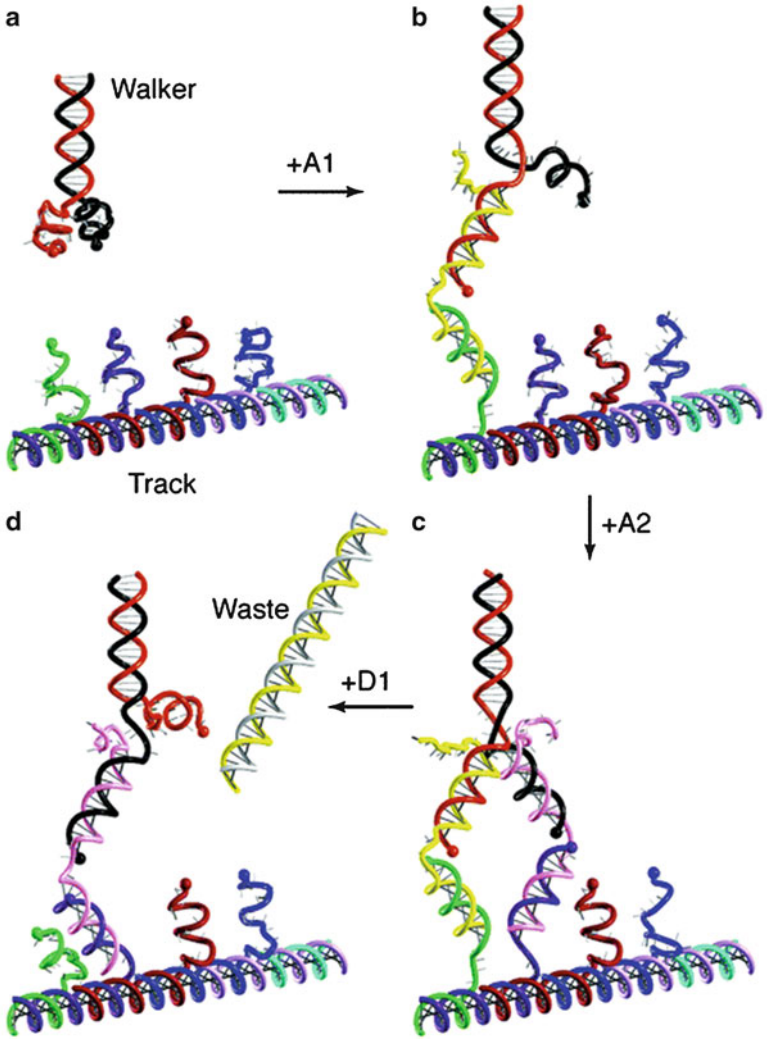

Fig. 18.16 Single step of the foot-over-foot walker. Reprinted with permission from Shin and Pierce [39]. © 2004 American Chemical Society

walkers have the identical complementary sequence (Fig. 18.18). The walker is driven forward when its trailing leg is detached from the stator by the fuel strand B via a toehold-mediated strand displacement process and the leg swings over to the next stator in line. However, there is about a 50% chance at each step that the leading foot is detached from the stator, in which case the walker halts. There is also a slight probability that both the legs of the walker detach from the track.

The walkers we have seen so far are not autonomous and thus it is difficult to run them for many steps. Green et al. [42] have designed an autonomous biped walker

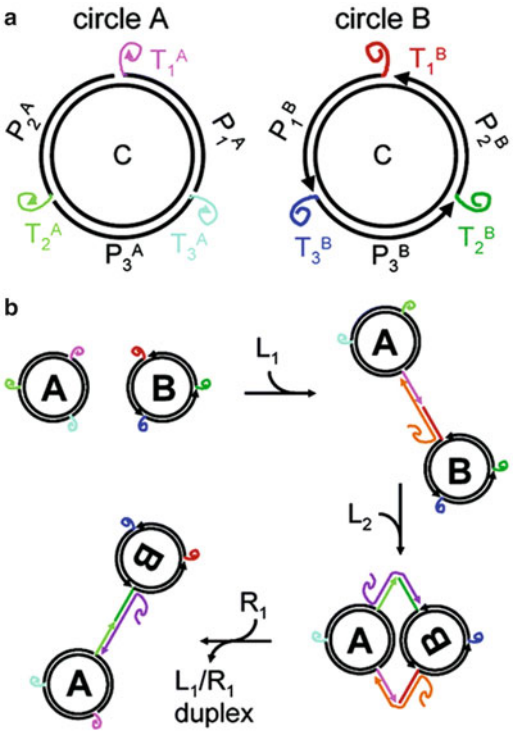

Fig. 18.17 A foot-over-foot walker walks a circular track. Reprinted with permission from Tian and Mao [40]. © 2004 American Chemical Society

that functions as a Brownian ratchet. The walker moves along a linear track with an asymmetric bias towards one end of the track, with the help of fuel supplied by DNA hairpins. The walker moves using the foot-over-foot mode of transport. The trailing foot is much more likely to detach from the track compared to the leading foot. Once detached, the trailing foot may swing forward ahead of the leading foot or may reattach back at its original position, with about equal probability. The net result of this is that the walker is biased towards stepping forward rather than back, and behaves like a Brownian ratchet. The walker assembly is illustrated in Fig. 18.19. Note that the trailing and leading feet are in competition for the same subsequence on the track. When the trailing foot loses, it exposes a toehold by which the fuel strand H1 invades and detaches it. This is the asymmetry that makes the detachment of the trailing foot much more likely. Once detached, a further fuel strand H2 takes away H1 and allows the foot to attach back to the track, either at the same location or further along the track, in which case a forward step is taken.

Venkataraman et al. [43] constructed a DNA motor inspired by bacterial pathogens like *Rickettsia rickettsii*. The motor transports a single-stranded cargo by polymerization, with the cargo always located at the growing end of the polymer. The system consists of two meta-stable hairpins H1 and H2 and an initiator strand (A) which carries the cargo (R) (Fig. 18.20). The hairpins are relatively unreactive in the absence of the initiator, but in its presence a chain reaction occurs which

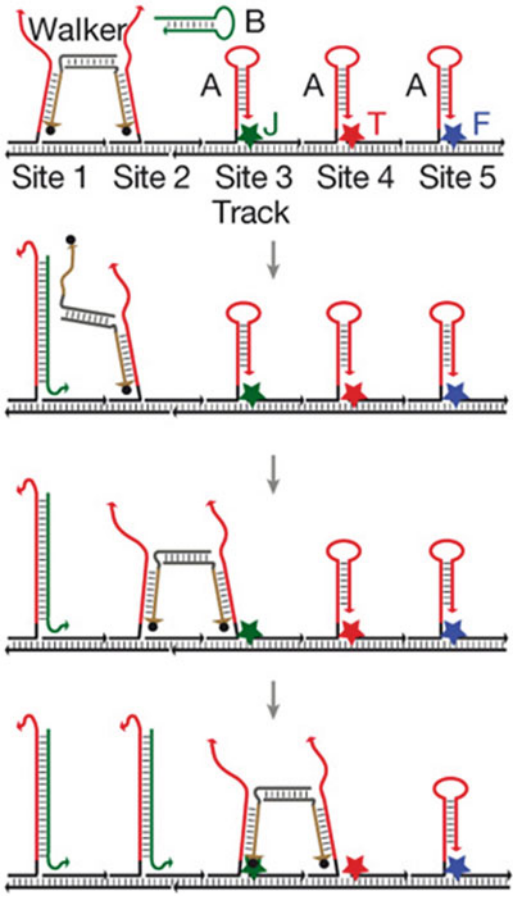

Fig. 18.18 Another foot over foot walker. Reprinted by permission from Macmillan Publishers Ltd: Nature [41], © 2008

builds a linear double-stranded polymer, with each hairpin unfolding to attach as a bridge between two hairpins of the other type. The byproduct of the polymerization is the transport of the cargo relative to the initiator strand. The whole process is autonomous.

18.5 Programmable DNA Nanomachines

So far we have reviewed DNA nanomachines that are highly specialized; they are designed for executing a particular task: transporting cargo, walking along a linear track, or changing the state of a nanostructure. The behavior of these nanomachines cannot be significantly affected without a major redesign. In this section, we examine programmable DNA nanomachines which are capable of a range of programmed behavior.

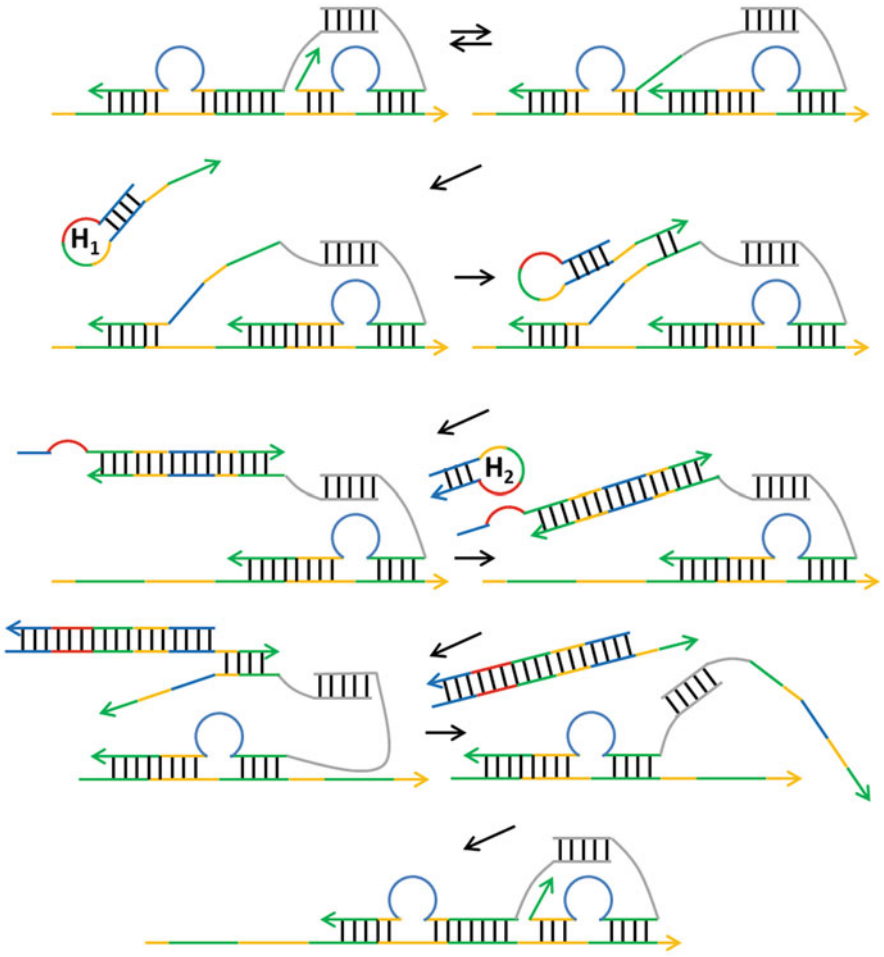

Fig. 18.19 Autonomous Brownian biped walker

Reif and Sahu [44] propose designs for a RNA nanostructure that walks on a 2D addressable DNA surface. A network of DNAzymes is embedded on a 2D plane, and the input nanostructure is routed over it. The path the input nanostructure takes can be programmed by modifying its sequence. The transport of the walker across the surface can be understood as a finite state machine that switches states based on input. The input is encoded as a set of hairpins on the walker which are successively digested by various DNAzymes of the automaton. The DNAzyme that currently binds the walker indicates the state of the automaton. At each stage, the sequence on the walker that corresponds to the next input symbol is consumed by restriction action of the DNAzyme, the walker is transported to the next DNAzyme on the surface, and the next input to be consumed is exposed. Figure 18.21 shows a couple

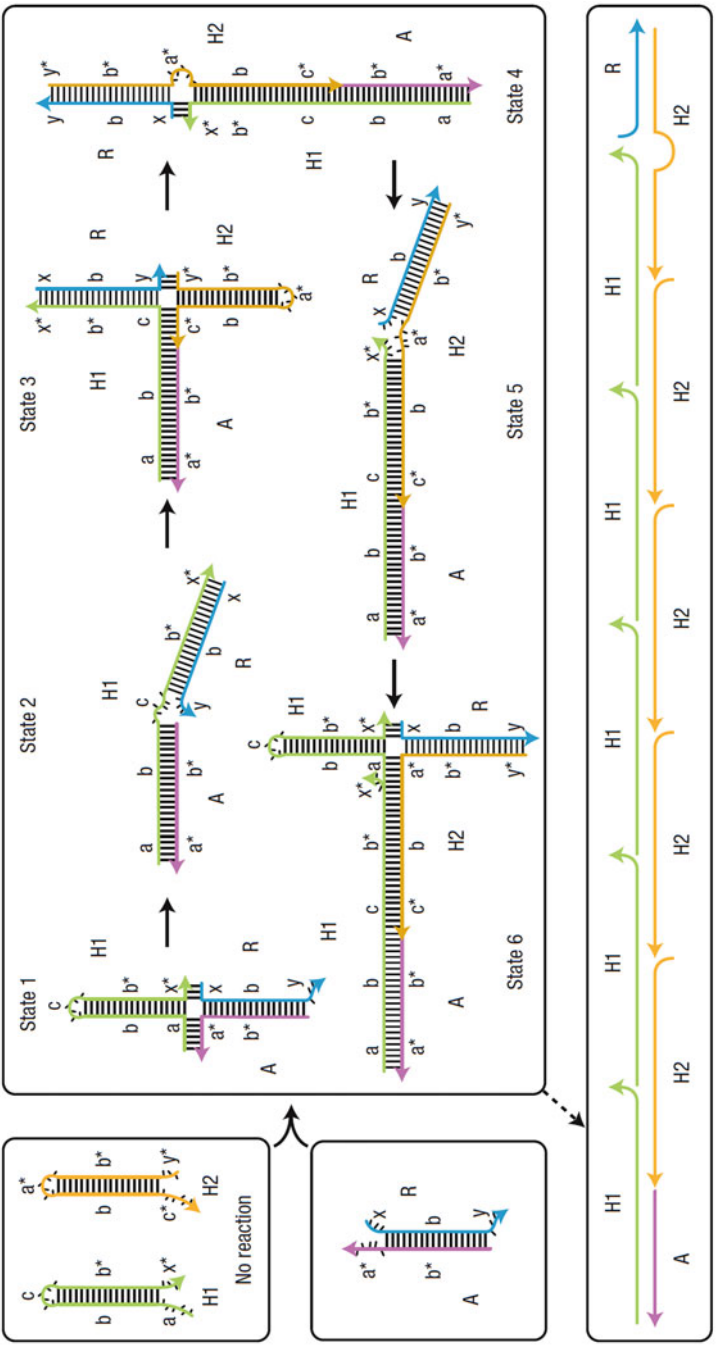

Fig. 18.20 Motor that transports cargo by polymerization. Reprinted by permission from Macmillan Publishers Ltd: Nature [43], © 2007

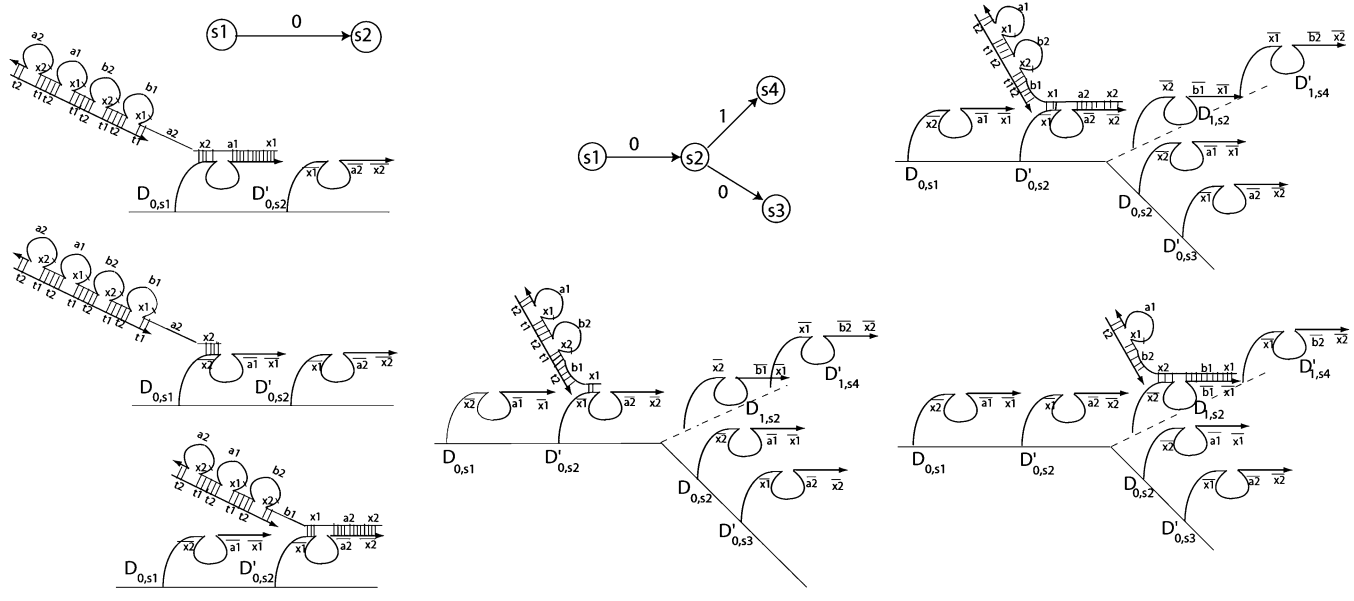

Fig. 18.21 An input RNA nanostructure routed through a DNAzyme network. Reprinted from Reif and Sahu [44], © (2009), with permission from Elsevier

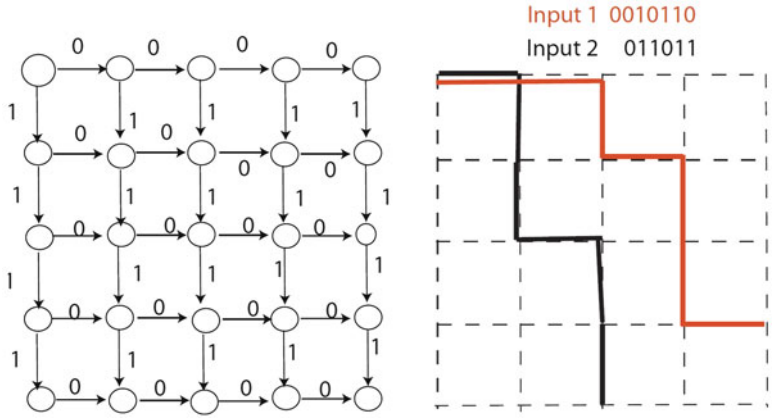

Fig. 18.22 Programming different routes

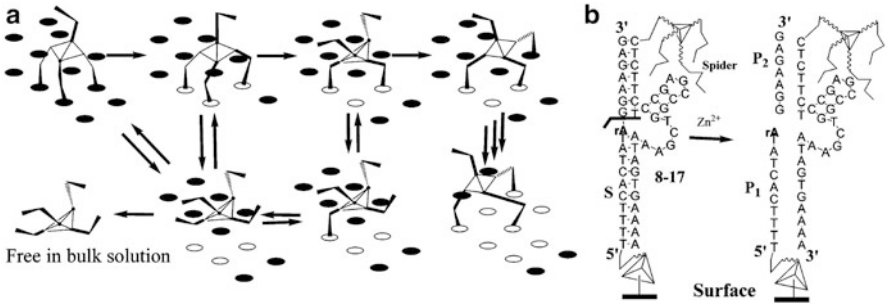

Fig. 18.23 Molecular spider performing biased random walk. Reprinted with permission from Pei et al. [45]. © 2006 American Chemical Society

of example automata transitions. Such a machine can be used to route a walker on a 2D lattice grid, for example, an input of 1 causes the walker to move down while 0 causes it to move to the right (Fig. 18.22). The key advantage of this design is that the surface is not destroyed as the walker is transported over it and thus can be reused. Several walkers can, in theory, independently walk the surface at the same time.

Pei et al. [45] demonstrate diffusion of a multi-pedal DNA walker (henceforth referred to as a spider) on a 2D substrate. In simple terms, their spider crawls a 2D surface in a biased random walk. The body of the spider is a molecule of streptavidin, and its four legs are DNAzyme molecules attached to the body. The spiders crawls a surface by attaching and detaching from RNA substrates (Fig. 18.23). The attachment occurs via DNA–RNA hybridization, while the detachment is via the catalytic restriction of the RNA stator by the DNAzyme followed by spontaneous denaturation from short strands due to entropic effects. Once a leg detaches from

a substrate, it binds (with high probability) to a new substrate and the process continues. Thus, the spider is biased towards binding unvisited substrates.

This work was recently extended in Lund et al. [46] to allow the spider to crawl along a specific programmed pathway on a fully addressable DNA origami substrate [6]. As before the spider has a streptavidin body, three DNAzyme legs, and one DNA leg used to anchor it to its start point (Fig. 18.24). The path the spider must follow is specified by precisely placed RNA substrate strands sticking out of the origami structure. This programmed track can be assembled with high yield in a simple one pot reaction. The spider first attaches to the start site using its anchor leg. The anchor is strand displaced from the start site by an incoming trigger strand, which allows the spider to start crawling. The DNAzyme legs now attach and cleave RNA substrates along their path. The DNAzyme legs have longer complementary sequences to unvisited substrates than to visited ones, and hence stay attached to the former for longer durations, eventually cleaving them. This introduces a motion bias for the spider towards unvisited substrates and results in a biased random crawl. The spider stops when it reaches the end of its path where it encounters special stop substrates which are DNA strands that cannot be cleaved by the DNAzyme legs. The spider operates autonomously once it is displaced from its anchor.

A similar multi-pedal walker was demonstrated in Gu et al. [47]. In addition to walking on a DNA origami substrate, the walker picks up cargo in a programmable manner. This is akin to an assembly line where each component may be added to the already built assembly, or omitted if so desired. The operation of the walker is illustrated in Fig. 18.25. The walker is a triangular DNA nanostructure with single-stranded sticky ends for its three hands (which pick up cargo) and four feet (which help it move along stators on the origami surface). The cargoes are distinguishable gold nanoparticles. Each cargo station can be either in an ON state, donating cargo, or in an OFF state, not donating cargo. As the walker moves by the stations, it picks up cargo from ON stations in one of its hands. Each station corresponds to a specific hand with which it may interact. The details of the walking and cargo pickup are illustrated in Fig. 18.26. The techniques for driving the walker forward and for picking up cargo are similar to the many DNA strand displacement-based walkers we have seen previously. Note that the process is not autonomous and requires addition of appropriate fuel strands at specific time instants.

18.6 Conclusion

The ultimate goal of nanorobotics is the creation of autonomous nanosystems that are capable of carrying out complex tasks. Additionally, we would like these systems to be programmable in the sense that one should not resort to complete redesign of the system to achieve simple changes in target behavior.

The programmability of DNA makes it an ideal construction material at the nanoscale. DNA self-assembly offers a massively parallel method for low cost manufacturing of complex nanosystems. In the past two decades, several ingenious

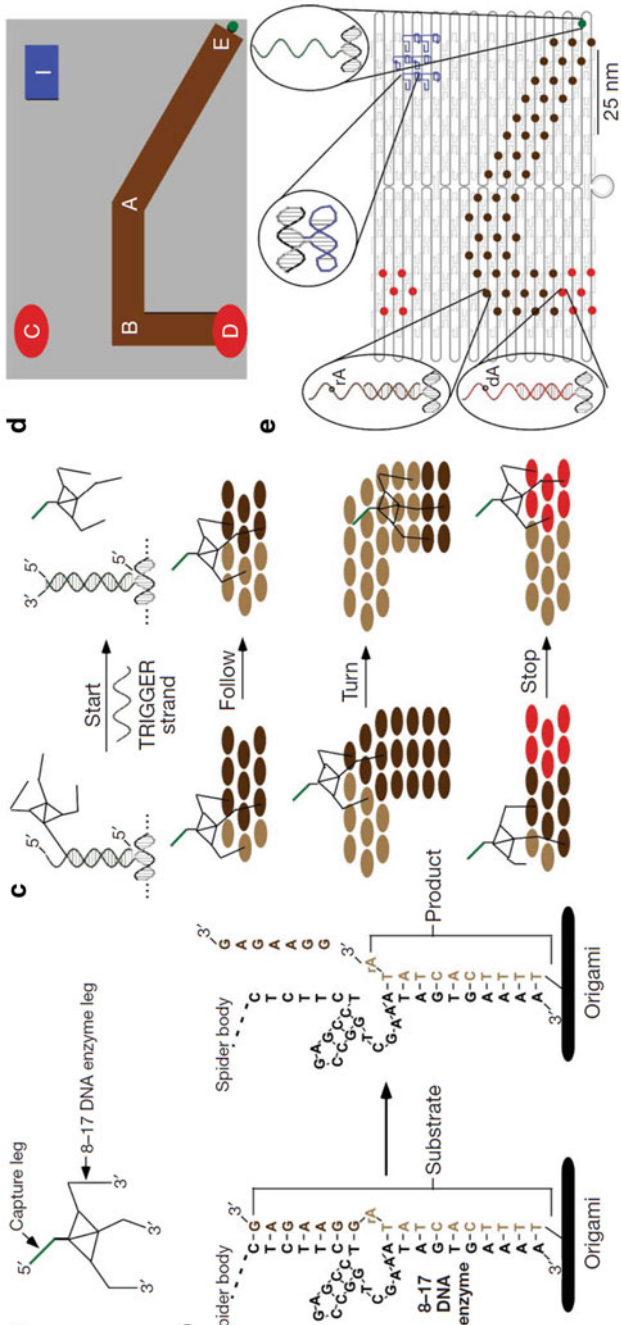

Fig. 18.24 Molecular spider performing a biased Brownian walk along a track. Reprinted by permission from Macmillan Publishers Ltd: Nature [46], © 2010

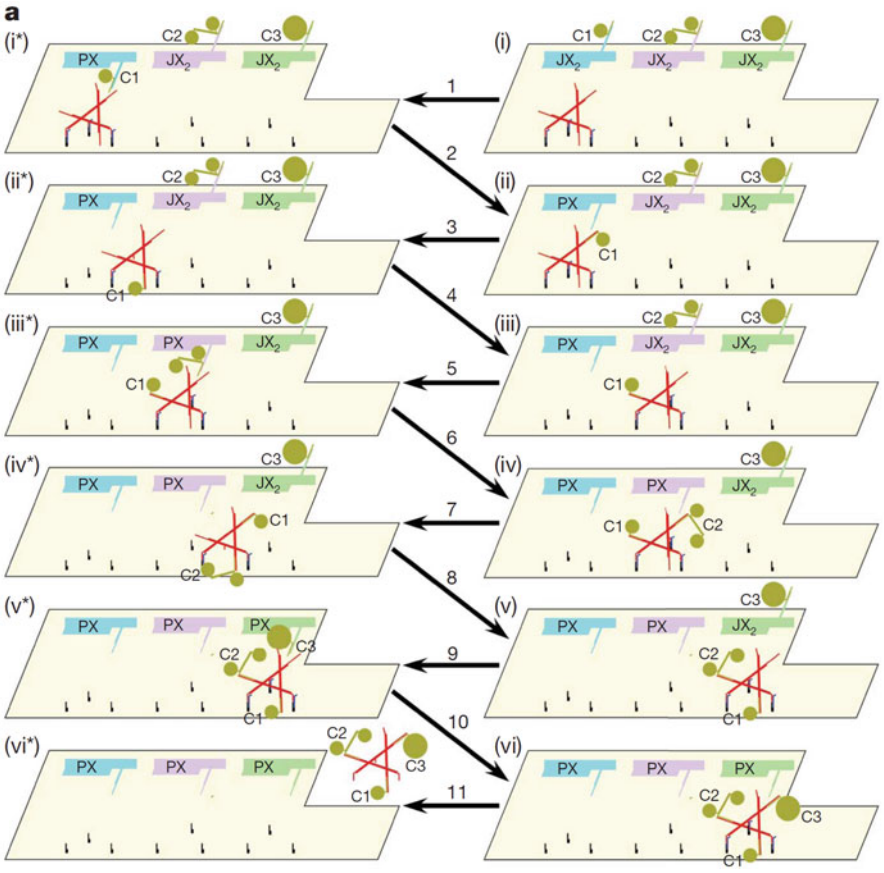

Fig. 18.25 Operation of the molecular assembly line. Reprinted by permission from Macmillan Publishers Ltd: Nature [47], © 2010

DNA nanostructures of increasing complexity have been demonstrated. Encouraged by these results, attempts were made to control the dynamic behavior of DNA nanostructures. This chapter reviewed some of these preliminary efforts.

Early attempts of DNA nanorobotics enforced state changes of complex DNA nanostructures using environmental parameters such as salt and pH levels, while other efforts utilized protein enzymes and DNAzymes to effect state changes. More recently, enzyme-free systems driven by hybridization of fuel DNA strands and entropic effects were achieved. Some of the systems reviewed were autonomous, while others required manual addition of precise amount of various reagents to enforce state change. Some of the systems were programmable, where one can easily modify the behavior of the nanorobots, while others were not programmable and require comprehensive redesign of the nanosystem. Several theoretic designs for complex programmable autonomous DNA nanorobots have been proposed. Simplified versions of these have been demonstrated in the laboratory.

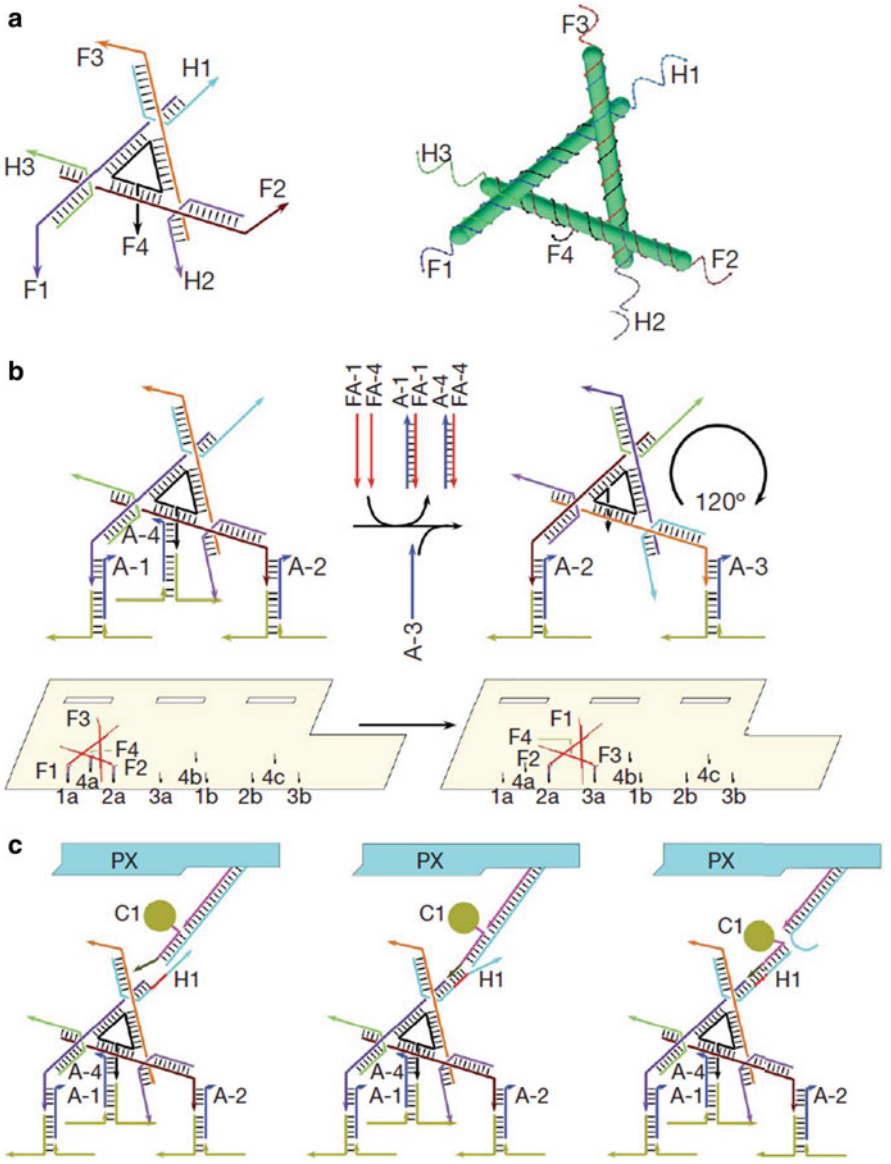

Fig. 18.26 The details of the assembly line. Reprinted by permission from Macmillan Publishers Ltd: Nature [47], © 2010

These pioneering efforts have provided a glimpse into the future of DNA nanorobotics and have demonstrated its enormous potential. Many challenges remain and provide exciting opportunities for research. We have barely begun a long and fascinating journey.

References

1. Winfree E, Liu F, Wenzler L, Seeman N (1998) Design and self-assembly of two-dimensional DNA crystals. Nature 394:539–544
2. LaBean T, Yan H, Kopatsch J, Liu F, Winfree E, Reif J, Seeman N (2000) Construction, analysis, ligation, and self-assembly of DNA triple crossover complexes. J Am Chem Soc 122(9):1848–1860
3. Yan H, Park SH, Finkelstein G, Reif J, LaBean T (2003) DNA-templated self-assembly of protein arrays and highly conductive nanowires. Science 301(5641):1882–1884
4. Shih W, Quispe J, Joyce G (2004) A 1.7-kilobase single-stranded DNA that folds into a nanoscale octahedron. Nature 427(6975):618–621
5. He Y, Chen Y, Liu H, Ribbe A, Mao C (2005) Self-assembly of hexagonal DNA two-dimensional (2D) arrays. J Am Chem Soc 127(35):12202–12203
6. Rothemund P (2006) Folding DNA to create nanoscale shapes and patterns. Nature 440: 297–302
7. He Y, Ye T, Su M, Zhang C, Ribbe A, Jiang W, Mao C (2008) Hierarchical self-assembly of DNA into symmetric supramolecular polyhedra. Nature 452(7184):198–201
8. Douglas S, Dietz H, Liedl T, Hogberg B, Graf F, Shih W (2009) Self-assembly of DNA into nanoscale three-dimensional shapes. Nature 459(7245):414–418
9. Dietz H, Douglas S, Shih W (2009) Folding DNA into twisted and curved nanoscale shapes. Science 325(5941):725–730
10. Zheng J, Birktoft J, Chen Y, Wang T, Sha R, Constantinou P, Ginell S, Mao C, Seeman N (2009) From molecular to macroscopic via the rational design of a self-assembled 3D DNA crystal. Nature 461(7260):74–78
11. Yildiz A, Tomishige M, Vale R, Selvin P (2004) Kinesin walks hand-over-hand. Science 303(5658):676–678
12. Toyoshima YY, Kron S, McNally E, Niebling K, Toyoshima C, Spudich J (1987) Myosin subfragment-1 is sufficient to move actin filaments in vitro. Nature 328(6130):536–539
13. Pohl F, Jovin T (1972) Salt-induced co-operative conformational change of a synthetic DNA: equilibrium and kinetic studies with poly(dG-dC). Angew Chem Int Ed 67(3):375–396
14. Mao C, Sun W, Shen Z, Seeman N (1999) A nanomechanical device based on the B–Z transition of DNA. Nature 397:144–146
15. Duckett D, Murchie A, Diekmann S, Kitzing E, Kemper B, Lilley D (1988) The structure of the holliday junction, and its resolution. Cell 55(1):79–89
16. Yang X, Vologodskii A, Liu B, Kemper B, Seeman N (1998) Torsional control of double-stranded DNA branch migration. Biopolymers 45(1):69–83
17. Gehring K, Leroy J-L, Gueron M, Tetrameric A (1993) DNA structure with protonated cytosine-cytosine base pairs. Nature 363(6429):561–565
18. Liu D, Balasubramanian S, Proton-Fuelled A (2003) DNA nanomachine. Angew Chem Int Ed 42(46):5734–5736
19. Liu D, Bruckbauer A, Abell C, Balasubramanian S, Kang D-J, Klenerman D, Zhou D, Reversible A (2006) pH-driven DNA nanoswitch array. J Am Chem Soc 128(6):2067–2071
20. Liu H, Xu Y, Li F, Yang Y, Wang W, Song Y, Liu D (2007) Light-driven conformational switch of i-motif DNA. Angew Chem Int Ed 46(14):2515–2517
21. Liedl T, Simmel F (2005) Switching the conformation of a DNA molecule with a chemical oscillator. Nano Lett 5(10):1894–1898
22. Liedl T, Olapinski M, Simmel F, Surface-Bound A, Switch DNA (2006) Driven by a chemical oscillator. Angew Chem Int Ed 45(30):5007–5010
23. Cao Y, Jin R, Mirkin C (2002) Nanoparticles with Raman spectroscopic fingerprints for DNA and RNA detection. Science 297(5586):1536–1540
24. Sharma J, Chhabra R, Yan H, Liu Y (2007) pH-driven conformational switch of i-motif DNA for the reversible assembly of gold nanoparticles. Chem Commun 477–479

25. Ren X, He F, Xu Q-H (2010) Direct visualization of conformational switch of i-motif DNA with a cationic conjugated polymer. Chem Asian J 5(5):1094–1098
26. Shu W, Liu D, Watari M, Riener C, Strunz T, Welland M, Balasubramanian S, McKendry R, Molecular DNA (2005) Motor driven micromechanical cantilever arrays. J Am Chem Soc 127(48):17054–17060
27. Chen Y, Lee S-H, Mao C (2004) A DNA nanomachine based on a duplex-triplex transition. Angew Chem Int Ed 43(40):5335–5338
28. Brucale M, Zuccheri G, Samori B (2005) The dynamic properties of an intramolecular transition from DNA duplex to cytosine-thymine motif triplex. Org Biomol Chem 3(4): 575–577
29. Modi S, Swetha MG, Goswami D, Gupta G, Mayor S, Krishnan Y (2009) A DNA nanomachine that maps spatial and temporal pH changes inside living cells. Nat Nanotechnol 4(5):325–330
30. Yin P, Yan H, Daniell X, Turberfield A, Reif J, Unidirectional A, Walker DNA (2004) Moving autonomously along a linear track. Angew Chem Int Ed 116(37):5014–5019
31. Sekiguchi H, Komiya K, Kiga D, Yamamura M (2008) A design and feasibility study of reactions comprising DNA molecular machine that walks autonomously by using a restriction enzyme. Nat Comput 7(3):303–315
32. Bath J, Green S, Turberfield A, Free-Running A, Motor DNA (2005) Powered by a nicking enzyme. Angew Chem Int Ed 44(28):4358–4361
33. Tian Y, He Y, Chen Y, Yin P, Mao C (2005) A DNAzyme that walks processively and autonomously along a one-dimensional track. Angew Chem Int Ed 44(28):4355–4358
34. Chen Y, Wang M, Mao C (2004) An autonomous DNA nanomotor powered by a DNA enzyme. Angew Chem Int Ed 43(27):3554–3557
35. Yurke B, Turberfield A, Mills A, Simmel F, Neumann J (2000) A DNA-fuelled molecular machine made of DNA. Nature 406(6796):605–608
36. Bishop J, Klavins E (2007) An improved autonomous DNA nanomotor. Nano Lett 7(9): 2574–2577
37. Sahu S, LaBean T, Reif J (2008) A DNA nanotransport device powered by polymerase φ. Nano Lett 8(11):3870–3878
38. Sherman W, Seeman N (2004) A precisely controlled DNA biped walking device. Nano Lett 4:1203–1207
39. Shin J-S, Pierce N, Synthetic A (2004) DNA walker for molecular transport. J Am Chem Soc 126(35):10834–10835
40. Tian Y, Mao C (2004) Molecular gears: a pair of DNA circles continuously rolls against each other. J Am Chem Soc 126(37):11410–11411
41. Yin P, Choi H, Calvert C, Pierce N (2008) Programming biomolecular self-assembly pathways. Nature 451(7176):318–322
42. Green S, Bath J, Turberfield A (2008) Coordinated chemomechanical cycles: a mechanism for autonomous molecular motion. Phys Rev Lett 101(23):238101
43. Venkataraman S, Dirks R, Rothemund P, Winfree E, Pierce N (2007) An autonomous polymerization motor powered by DNA hybridization. Nat Nanotechnol 2:490–494
44. Reif J, Sahu S (2009) Autonomous programmable DNA nanorobotic devices using dnazymes. Theor Comput Sci 410:1428–1439
45. Pei R, Taylor S, Stefanovic D, Rudchenko S, Mitchell T, Stojanovic M (2006) Behavior of polycatalytic assemblies in a substrate-displaying matrix. J Am Chem Soc 128(39):12693–12699
46. Lund K, Manzo A, Dabby N, Michelotti N, Johnson-Buck A, Nangreave J, Taylor S, Pei R, Stojanovic M, Walter N, Winfree E, Yan H (2010) Molecular robots guided by prescriptive landscapes. Nature 465(7295):206–210
47. Gu H, Chao J, Xiao S-J, Seeman N, Proximity-based A (2010) Programmable DNA nanoscale assembly line. Nature 465(7295):202–205

Chapter 19
DNA for Self-Assembly

Ahlem Abbaci and Stéphane Régnier

Abstract Biological processes, and in particular DNA hybridization, offer the potential to form the basis for the assembly of nano-devices. DNA and RNA can be used to perform two types of functions: to assemble parts of nano-robot and to transmit information. This chapter focuses on the assembly function of DNA and its optimization. Indeed, these molecules possess computing properties based on the nucleic acid 4-letter alphabet which gives them programmable features. In order to determine the feasibility of such processes, the strength of DNA hybridization is measured and optimized using a method based on atomic force microscopy. The multidisciplinary work presented here targets the selection of DNA, the theoretical study, and the experimental validation.

19.1 Introduction

The choice of biomolecules for bio-nano-robot design is crucial and relies on their specific biological interactions. These biomolecules can be used to perform two types of functions: to assemble parts of nano-robot and to transmit information.

DNA and RNA possess computing properties based on the nucleic acid 4-letter alphabet which gives them programmable features. Moreover, these molecules are provided with physical properties such as electrical conductivity [1] and stable and

A. Abbaci
Université Pierre et Marie Curie - 4 place Jussieu 75252 Paris cedex 05, France
e-mail: ahlem.abbaci@gmail.com

S. Régnier (✉)
Université Pierre et Marie Curie - Institut des Systémes Intelligents et Robotique- Equipe projet MAP, 4 place Jussieu - Boite Courrier 173, 75252 Paris Cedex 05, France
e-mail: stephane.regnier@upmc.fr

C. Mavroidis and A. Ferreira (eds.), *Nanorobotics*, DOI 10.1007/978-1-4614-2119-1_19,
© Springer Science+Business Media New York 2013

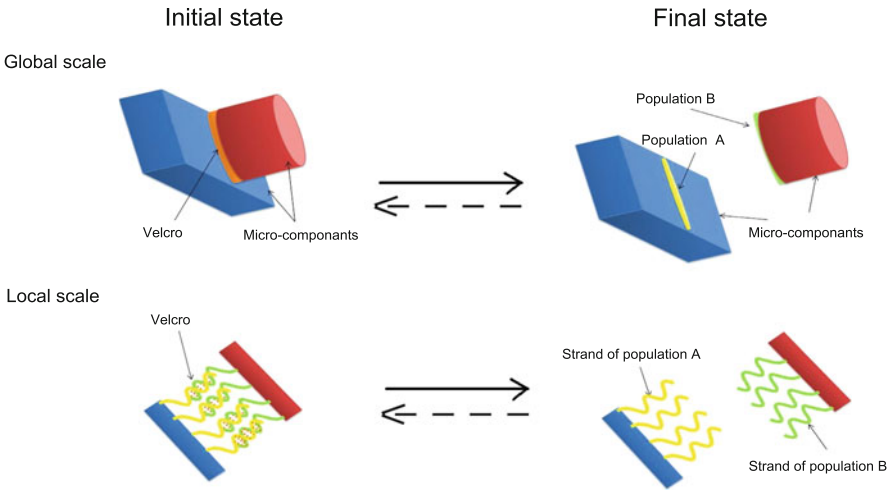

Fig. 19.1 Principle of microscopic self-assembling based on DNA. DNA simple strand populations A and B are complementary

controllable adhesion forces at the origin of complex three-dimensional synthetic structures [2, 3]. These properties make these molecules a real material with both complex and comprehensive properties.

This chapter focuses on the assembly function. From this point of view, two fundamental properties are identified to characterize the biological interaction called *DNA hybridization*:

- **Stability**, which is the ability to keep nanostructures in an assembled state in an unstructured environment over a time period
- **Specificity**, which is the mutual recognition between the structures to be assembled

In the framework of the European project Golem,[1] it is proposed to study the DNA assembly function for micro-component self-assembly. Figure 19.1 illustrates this type of assembly. It consists of setting DNA simple strands on the micro-component surfaces, using the technique of surface functionalization, and achieving self-assembly process through the control of some hybridization parameters such as the temperature. The set of two complementary strands populations fixed on each surface is called *DNA-based bond*. This new bio-bond adhesion is explored by studying the involved force in the separation of self-assembled micro-objects.

The stability study from a theoretical point of view is detailed in the first part. This property can be approached from several angles. If one looks at the interaction between two DNA single strands, the approach can be borrowed from the work in molecular modeling. If one is interested in studying the interaction between

[1] http://www.golem-project.eu/.

two populations of complementary strands fixed on the surfaces to be joined, this geometrically constrained configuration can be studied with a thermodynamic approach.

The second part is dedicated to the experimental characterization of stability. This is to characterize the interaction forces specific to the DNA. Several techniques for characterizing biomolecular interactions have been proposed over the last 20 years. These are mainly based on physical principles and thermodynamics such as X-ray crystallography or magnetic resonance spectroscopy. Atomic force microscopy is one of these techniques that present the most advantages. The abilities to make measurements in aqueous media [4], chemically modify the gripper to measure specific forces [5], and modify dynamic parameters directly involved in the issue of self-assembly, such as approach and retreat velocity, are the main advantages of using atomic force microscope (AFM) to measure interaction forces that characterize the stability of a velcro composed of two populations of complementary DNA strands. In this second part, the AFM experiments are detailed and analyzed.

The third part is dedicated to the study of specificity. Based on the programmability of DNA, an algorithmic approach to sequence generation is proposed. The goal is to have pairs of DNA strand whose properties and stabilities of specifics are optimized. An experimental validation is then undertaken. These experiments validate the design approach of sequences and highlight the influence of key parameters such as the approach velocity and the assembly waiting time.

19.2 Two Approaches for a Theoretical Characterization of Stability

The stability of the DNA-based microscopic self-assembly is carried out through the DNA hybridization process. The study of this property is particularly essential for determination of the environmental parameters for the design of the assembly chamber and requires an ab initio characterization of the hybridization process. Several parameters are now known: temperature, pH, and salt composition of the solvent [6]. The nitrogenous base sequence and its length influence also the molecule's behavior [7].

Stability is definitely biomolecular and can be expressed in terms of energy through several methods. The choice of a method depends on, however, the conceptualization of the system. When the contribution of each DNA strand to stay in the hybridized state is considered from an individual point of view, the first approach is called *local approach*.

When the DNA-based adhesion is considered in its entirety as a thermodynamical and statistical system, the approach used is called *global approach*.

In the following, each of these two approaches is detailed to determine how it can be more adapted to our problem with respect to the studied system, to the proposed experimental study, and to the influence and controlling parameters.

19.2.1 The Local Approach

Several methods exist to estimate the energy of one molecular system at the molecular scale [8]. Molecular modeling is one of these methods where the stability is quantified through the potential energy. This energy depends on the conformation and fundamentally on the structure of the strands in interaction. To estimate the energy, it is preferable to use a force field[2] where each atom's energy is a function of the atom's center position [9]. The three-dimensional structure of a DNA double-stranded molecule can be given by a molecular modeling software directly from its nitrogenous bases sequence. Such software provides different force fields to calculate the interaction energy as a function of one of the force fields proposed (Amber, CHARMM, etc.) [10].

In this work, it is necessary to compare the theoretical calculated values of interaction energy to the experimental measured interaction forces obtained by AFM. Because the micro-component separation is made perpendicular to the functionalized surfaces, a special consideration is given to the double helix hypothetical axis. The force that occurs at this axis can be estimated from the study of energy variation during a displacement.

If the analytical expression of the interaction energy is not accessible through the molecular modeling software, a method of estimating the force is to approximate the interaction energy by an analytic function [11] from a set of points. The derivation of this function gives a direct estimate of the force required to drive the system from binding state to nonbinding state. This is assessed using an extrapolation of a set of values around a fixed position. In this energy approximation, the molecules are assumed rigid as the relative atom positions of each strand are fixed. Indeed, the mass center position of the molecule is the central element in this method.

In reality, DNA strands are elastic [12, 13], and this approach does not take into account this molecule's particularity. Although it is possible to solve the problem of the elasticity using an intermediate model, the local approach remains complex. Indeed, the velcro DNA-based consists of an unknown number of strands attached to the surface of micro-components. Methods for determining the distribution density of the strands attached to surfaces exist such as fluorescence [14]. These methods require specialized equipment and must be a separate study. This question remains important in this approach because each strand's behavior is studied separately. In addition, the population effect, which can be studied through a statistical physics reasoning, must be incorporated in this approach.

Ultimately, the extrapolation of the interaction energetic profile between two strands based on the assumption of a rigid molecule, does not take into account the molecule's elastic behavior. An alternative may be proposed for the study of this

[2] A force field is an ensemble of numerical parameters determined by techniques such as crystallography.

behavior, but several drawbacks make the local approach inappropriate and difficult to implement in the context of the DNA-based velcro. Indeed, in addition to the unknown distribution density parameter, the estimated interaction energy depends on the force field used. Consequently, the derived force value depends on the chosen force field and is not absolute. Finally, environmental parameters such as hydration and the presence of cations, and the populational behavior of DNA strands are too complex to be studied from a molecular point of view.

19.2.2 The Global Approach

In the global approach, stability is characterized by the ability of micro-components to remain in an assembly state. Characterizing the overall stability is therefore necessary to characterize the separation process of two micro-components.

The global approach takes into account both the molecular systems overall behavior and each strand pair individual behavior. Quantification of stability is achieved using tools from thermodynamics. These provide a quantification of the system's energy variation as a whole and the disorder degree due to the different configurations adopted by the strand pairs during hybridization.

From the thermodynamics point of view, the studied system is defined as an open one. Two states are identified. The initial state corresponds to the hybridized state of the molecular system, and the final state is the non-hybridized one.

The transition from the initial to the final state is characterized by an energy variation that reflects the system's ability to remain in its assembled state. It corresponds to the free energy variation of the overall velcro. The studied system may be compared to a bio-microarray molecular system. Thus, the methods used to study these type of systems can be applied here. In that technology, hybridization occurs between the free strands in solution and the strands attached to a surface, usually glass. Several dedicated models to estimate the free energy variation state function based on intrinsic and extrinsic DNA parameters exist. The nearest neighbor model is one of the most used models in this area [15]. In this model, the estimation of this energy variation requires knowledge of the nitrogenous base sequence. The central assumption is to estimate the free energy of one base pair as a function of its two neighboring base pair energies. This energy estimation is valid for a perfect hybridization between two strands. This setting aside, several exceptions are possible. Indeed, two noncomplementary strands can be assembled partially, or the strand may fold on themselves. These exceptions are called *mismatch* (denoted as MM), as opposed to *perfect match* (denoted as PM) for perfect hybridization as a double helix [16].

It is necessary to define the notion of a couple of base pairs that are of ten types. For each type of couple, a numerical energy value ΔG_i is associated. These numerical parameters are the nearest neighbor model parameters [17] determined at a temperature of 37 ° and a salt concentration about 1M (standard parameters).

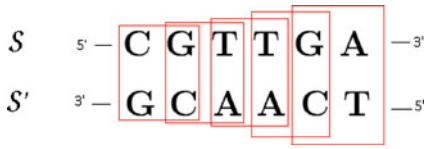

Fig. 19.2 Algorithm for free energy variation ΔG computing. A window of couple of base pair slides along the representation of the two complementary sequences hybridized. These sequences exhibit five couples of base pairs

Two complementary sequences, with chemical orientation 5'-3', S: CGTTGA and S': TCAACG, are illustrated in Fig. 19.2. With a length of 6 bases, S has 5 base pairs: GC, GT, TT, TG, and GA. Similarly, S' has the following 5 base pairs: CG, AC, AA, AC, and CT. Consequently, the double helix formed by hybridization of perfect S and S' has five couples of base pairs: GC/GC, GT/CA, TT/AA, TG/AC, and GA/TC (Fig. 19.2). At standard parameters, the ΔG estimation for a perfect hybridization between the sequences S and S'is the sum of ΔG_i characteristics of the five couples of base pairs. Here, $\Delta G = -5.35$ Kcal/mol at standard parameters. For a given sequence, it is possible to imagine a window framing a couple of a base pairs sliding along the two complementary sequences as shown in Fig. 19.2.

From [17], a general equation (19.1) is obtained taking into account both intrinsic parameters, i.e., n is the number of nitrogenous bases, $\Delta H(i)$ and $\Delta S(i)$ enthalpic and entropic components of ΔG_i characteristic of the ith couple of base pairs, and extrinsic parameters, temperature T and salt concentration $[Na^+]$:

$$\Delta G(T, Na^+) = \sum_i (\Delta H(i) - T\Delta S(i)) - 0.114(n-1)\ln[Na^+]. \tag{19.1}$$

For a known sequence, at fixed environmental parameters, the higher the temperature T and the lower the concentration $[Na^+]$, the higher is the energy variation.

This equation characterizes the transition between the initial and the final states. Converted into force, this energy represents the interaction force involved in the separation process. To correlate the energy values ΔG derived from the nearest neighbor model with experiments, estimating the interaction force F must be made. The conversion of ΔG in F can be expressed as approximated by (19.2):

$$F = -\frac{\mathrm{d}\Delta G}{\mathrm{d}x} \tag{19.2}$$

F is the sum of the forces exerted on the external system, and x the displacement along the axis of the double helix.[3] As this is a variation of energy and not a differential, the estimated force gives an average value and not an instantaneous one. The average interaction force $\bar{F}$ is obtained by

[3]The hypothetical axis of the double helix discussed in the local approach.

$$\bar{F} = -\frac{\Delta G}{\Delta x}. \tag{19.3}$$

For hybridization of the type *perfect match* with that matched all bases along the double helix, the displacement Δx can be approximated by the length of the sequence. Indeed, the energy difference calculated for this type of hybridization corresponds to the separation of n nitrogen bases. Δx can be approximated by (19.4):

$$\Delta x = n\, d_{\text{base}} \tag{19.4}$$

with d_{base} distance between two consecutive bases of one strand. For example, $d_{\text{base}} = 0.34\,\text{nm}$ for a salt concentration of 1 M [18].

For the sequence S_1, one of the sequences proposed in Golem, for the PM hybridization, $\Delta G = -164.42\,\text{kcal/mol}$, and $\bar{F}$ is estimated at 44 pN.

In this global approach, it is possible to take account of both individual and DNA population behaviors in the stability quantification. This quantification is based on an estimate of energy whose two main components are the enthalpy and the entropy. Control settings are easily accessible, and the conversion of energy into force is achieved. This conversion gives a mean value of the interaction force for configurations of type PM.

19.2.3 Conclusion

For several reasons, some among them bring the access control parameters and the elasticity of the molecule, the local approach is highly simplified.

The global approach provides direct access to the intrinsic and the extrinsic DNA parameters. In this approach, the interaction force is estimated at approximately 44 pN (for one of the sequences used in Golem, the sequence S_1 75 bases in length). This estimate is valid for a complete hybridization of the bases along the double helix formed by the two complementary strands. This value is retained as a first approximation and is compared with experimental measurements in the remainder of this chapter.

19.3 Measurement of Stability with Atomic Force Microscope

To characterize the DNA interactions, several techniques exist. The technique of osmotic pressure was first used to measure DNA condensation interactions (the interaction between double helices) [19]. For thinner molecular interactions, in which membership and direction are involved, such as molecular recognition, a direct measurement is needed. Thus, techniques such as magnetic tweezers [20] or

optical tweezers [21] are used to measure the individual elongation properties of a double helix of length 10 μm. Using the technique of flexible microneedles, forces obtained are from 10 to 15 pN [22]. In 2002, Bockelmann et al. [23] confirmed the results obtained by their predecessors, using another technique, optical trapping interferometry, and bringing a new factor in the dependence of the interaction force to the GC content[4] of nucleotide sequences.

Several studies have been conducted to characterize the unwinding initiation between two strands. Information from these studies is great significance in understanding the DNA response to external mechanical disturbance. However, the strand separation by a force applied in the direction of the hypothetical axis of the double helix remains an unexplored phenomenon. Furthermore, in our studied case, the collective behavior of the DNA strands glued on a surface becomes important. This state is an additional challenge to the characterization of stability. Indeed, the process is stochastic because the molecular system contains hundreds of thousands of molecules. Therefore, the characterization of interaction forces requires the use of an instrumental dedicated platform that measures interactions due to a force applied perpendicular to the functionalized surfaces.

Among the existing instruments for measurement of surface forces, the AFM is the most appropriate because of its sensitivity in the measurement of stress (hundreds of piconewtons order). In addition, in the AFM technology, the environmental conditions of microscopic self-assembly can be reproduced in the separation of two functionalized objects, such as electrostatic and hydrodynamic forces, approach and retreat velocities, and the influence of applying external forces.

Experiments using a commercial AFM to quantify the stability of a DNA-based bond composed of two complementary DNA strands populations were performed. The use of AFM for measuring DNA-DNA simple strands is introduced. The technical issues of calibration and optical detection are not addressed. A brief summary is proposed in the second paragraph. Then, special attention is paid to the results obtained for the sequence S_1, one of the sequences studied in Golem.[5]

19.3.1 Using AFM Technique to Measure DNA Force Interactions

An atomic force microscope consists of a cantilever of 100-μm length. It is provided with a tip interacting with the surface. A sensor measures the cantilever deflection, and a control loop controls the parameters such as tip-surface distance or the force applied [5](Fig. 19.3).

Invented by Gerd K. Binnig, Nobel Prize winner in physics [24], the principle of AFM is to scan the surface by the cantilever tip and to reproduce the surface to-

[4]Percentage of nitrogenous bases on a DNA molecule that is either guanine or cytosine.

[5]http://www.golem-project.eu/.

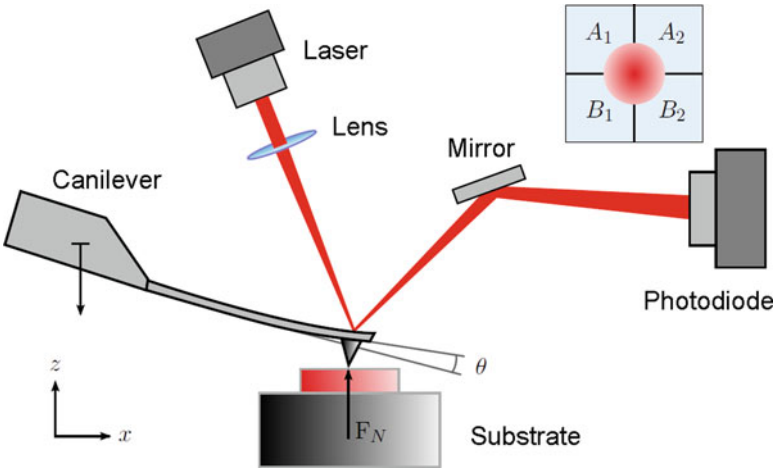

Fig. 19.3 AFM general principle

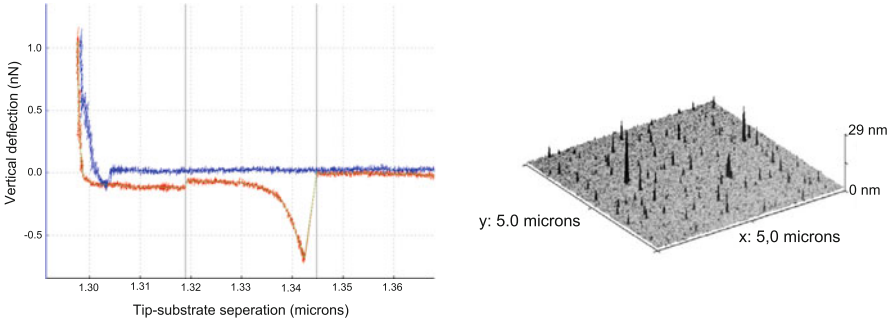

Fig. 19.4 The AFM used for surface characterization. At *left*, the approach/retreat curve for a silicon substrate in a liquid medium. The interaction force is plotted against the beam. The approach phase is shown by the part generally flat of the curve, and the retreat is the part of the curve including a peak. At *right*, the topography of a silicon surface

pography (Fig. 19.3). This is achieved by measuring and representing the cantilever deflection depending on its position.

The AFM can also be used to measure interaction forces needed for determining the physical behavior of objects at scales below the micrometer. Measuring and analyzing physical phenomena at the microscopic scale are of great significance in micro-object handling and assembly. In this experimental context, the AFM is used to measure the interaction forces between the functionalized tip and the micro-object surface. Knowing the cantilever stiffness, denoted as k, efforts can be deducted. Figure 19.4 illustrates an AFM measurement between the cantilever tip and a silicon substrate. Here, the force displacement curve is called *approach/retreat curve* (A/R)

due to the process of approach and the retraction of cantilever (or substrate) during the measurement.

For 10 years, this technology was used by a community of biophysicist experimenters for the characterization of the intramolecular interaction forces. The advantages of AFM for such a use are the ability to make measurements in aqueous media [4] and chemically modifying the gripper to measure the specific forces [5].

In the particular case of functionalization with DNA strands, the A/R curve of one measure of interaction forces, several *jumps* corresponding to different *unbinding events* can occur. The graphical representation of this measure takes the form of an A/R curve with the same shape of the curve shown in Fig. 19.4. These jumps may be due to different hybridized strand pairs or to interactions between certain segments of a given strand pair or to the molecule's elasticity. It is therefore difficult to interpret an A/R curve when a DNA measure is involved. In most of the work encountered in the literature, the hypothesis of an interaction between two individual DNA strands led the authors to interpret the collected data within the meaning of a single molecule [25–27]. Throughout this work, this assumption makes easier data interpretation. In our analysis, this assumption is kept.

Each measured *unbinding event* is characterized by its *rupture force* value, called also *unbinding force* and denoted as F_r. This force can be defined as the necessary and sufficient force to break the barrier energy that characterizes the biomolecular binding intensity also called *activation energy*. This is the amount of energy required to initiate or break a relationship. It can be also defined as the work done by an external force moving in the physical sense of the link.

The energy supplied to a biomolecular system in an A/R process influences directly the physical response of the studied system. This energy is expressed in terms of the A/R velocity denoted as v and the cantilever stiffness k. The product of these two parameters is known as *loading rate*, denoted as T_c. The external force exerted on the molecular system over time can be seen through this parameter.

In the following paragraphs, a brief state of the art is proposed for the rupture force and the loading rate.

19.3.1.1 The Rupture Force

The first AFM measurements of biomolecular interaction forces are from 1994. That first work on the biomolecular biotin-avidin complex [26] generated the most interest and has contributed to the advance in interpretation methods of AFM biochemical interaction measurements [28]. The work on DNA [25] was slowed because of the difficulty of interpretation with regard to molecule's *complex spatiotemporal* behavior. Indeed, during hybridization, the formation of biomolecular unexpected complex structures called *mis-matches* (MM) is largely responsible of this complex behavior.

Early work on interaction forces measured between DNA strands in the axis of the double helix was made on a sequence of 20 bases in length[6] by Lee et al. [25]. The measured forces are between 1520 and 830 pN. A second study performed by Sattin et al. [29] on the same sequence reveals quite different measurements with values between 10 and 80 pN. Both teams, however, show great variability in the measurements. The statistical analysis proposed in the two studies attempts to relate the observed variability with the different configurations adopted by the DNA strands during hybridization. Lee et al. [25] submitted their AFM measurements in the form of three statistical classes with three possible configurations.[7] The statistical classes represent the most probable rupture force values. Sattin et al. [29] show that the number of statistical classes increases with the number of repetitions of measurements. Thus, the authors repeat the measurements with the same cantilever 1,500 times on different blocks functionalized with different sequences. This protocol then makes possible the comparison between measurements of different interactions. The authors show the need to have a large number of measurements for statistical analysis of variability.

Two other major works are selected in this chapter, those of Strunz et al. [27] and Morfill et al. [30]. Both teams make AFM measurements on the DNA strands with different sequences but the same length of 20 bases. They achieve the same order of magnitude as Sattin et al. [29].

The results obtained by Strunz et al. [27], Morfill et al. [30], and Sattin et al. [29] are of the same order of magnitude unlike the work of Lee et al. [25]. These first three works have in common an experimental parameter of the same order of magnitude. This parameter is the loading rate, which could explain this homogeneity. In the following section, the influence of this experimental parameter is introduced.

19.3.1.2 The Loading Rate

The **loading rate**, denoted as T_c, is an experimental parameter that directly influences the rupture force. It is the product of the A/R velocity v and the cantilever stiffness k. This parameter reflects the impact of the energy charged on the molecular system.

The rupture force dependency on the loading rate logarithm is given in [31] through the theory of dynamic force spectroscopy (DFS). This feature is experimentally proven for several protein complexes [32–34] and for DNA [27, 30].

In this theory, the biomolecular binding is characterized by a *lifetime* (or relaxation time) that was introduced by Bell in 1978 [35] in the context of the mechanical characterization. Based on Kramers theory [36] and Bell's model, Evans et al. extended this pioneer model by taking into account the applied force on the molecular system and due to the liquid environment.

[6] The sequence of nitrogenous bases is $[(CAGT)_5]$.

[7] These configurations correspond to 20, 16, and 12 nitrogen bases consecutively hybridized.

Concerning DNA, Strunz's [27], Sattin's [29], and Morfill's [30] measurements are performed with loading rates of the same order of magnitude (10^{-9} N/s). Thus, the measured rupture forces are of the same order of magnitude.

Comparison of the AFM measurements is required to keep this parameter constant. The consideration of the loading rate parameter is therefore crucial in the analysis of rupture forces measurements specific to DNA.

19.3.1.3 Conclusion

The characterization of the DNA-based bond stability using an AFM is based on the measurements of rupture force characteristic of the unbinding events. Variability shown by several experimental works [25, 27, 29, 30] requires a great repetition number to achieve statistical analysis.

Comparison of data requires constant experimental parameters. Indeed, the rupture force depends not only on the sequence of nitrogenous bases and its length but also on an important experimental parameter, the loading rate. Furthermore, characterization of the rupture force values for different loading rates would provide some basic knowledge concerning the microscopic assembly.

Finally, the DNA structure and complexity and the number of experimental statistical classes corresponding to the number of possible configurations seem to be the cause of the observed variability. Nevertheless, the link between these elements is not clearly identified in the literature.

Experiments were performed in Golem with several values of experimental parameters. The next section is dedicated to the measurements for a proposed sequence S_1.[8] In these measurements two methods are proposed. The first mode is called *ponctual*.

19.3.2 Quantification of DNA Interactions

Quantifying the interaction between two populations of DNA strands is done by measuring the final rupture of bonds. This is achieved by measuring the rupture force F_r between a functionalized cantilever tip and a functionalized substrate. For a given measure, F_r is the maximum recorded jumps on the A/R curve. For example, the curve of Fig. 19.4 illustrates the AFM measurement obtained with the following experimental parameters: $v = 1\ \mu$ m/s and $k = 0.1$ N/m with $F_r = 50$ pN.

In our measurements, two modes are proposed. The first one, called *ponctual*, consists of repeating the A/R process 256 times on the same part of substrate.

[8]The sequence S_1 proposed in the European project Golem (5'-3'): CAA ATA CCG TGG GAC GAC ACG CAC CGG CAG TGC GCA GGC AGC GTC GGA CAC AAC ACG CTT ACG GCC CTC AAC ACT.

The second mode called *scan* consists of repeating the A/R process by scanning the substrate surface on different parts that can be described as a regular grid. The ponctual mode experiments the measure repeatability on the same molecular system. The scan mode compares responses of several molecular systems assumed to be identical. During these A/R experiments, the force versus displacement is recorded with known loading rates. The dissociation of the two surfaces during the retreat phase is induced by strand separation of the hybridized structures formed during the approach phase of the experiment. Only experiments in which the measures correspond to molecular responses are used. Indeed, the experiments are sorted through a statistical variance analysis. This analysis identifies invalid experiments where variability is due to a temporal dependency of unbinding events to the experimental setup.

Figure 19.5 shows the rupture forces F_r estimated from the measurements. A homogeneous distribution is observed on all measures. The recorded values are less than 150 pN with high rates (98 %). The average value of these samples is thus representative.

The histograms of Fig. 19.5 show the variability for each experiment. The classification is performed with a cutting constant of 10 pN. Between 13 and 15 statistical classes are observed. This variability is in agreement with the variability described in the literature.

Finally, for the sequence S_1, the rupture force is estimated in the range [36 pN; 44 pN]. Variability described in the literature [29, 30] appears on these measures and complicates the characterization of the S1 sequence stability. The use of a given sequence in our problem of microscopic self-assembly requires the control of this variability. It is therefore necessary to find methods to identify what is possible to control this variability.

19.3.3 Conclusion

Experimental characterization of stability is realized through AFM measurements for a given sequence S_1. From these data, the average value of rupture force is estimated at 39 ± 4 pN. Surface interaction[9] is at 4 nN/μm^2.

The observed variability on the measures is difficult to interpret and makes complex the classification of the DNA-based bond stability in the context of microscopic assembly. To overcome this variability and to obtain a quantitative indication of the bond quality, the design of a dedicated sequence is needed. This is to eliminate MM configurations through the study of the second fundamental property of microscopic self-assembly, the specificity.

[9] According to the manufacturer, the tip of the beam can be likened to a sphere of diameter between 20 and 60 nm.

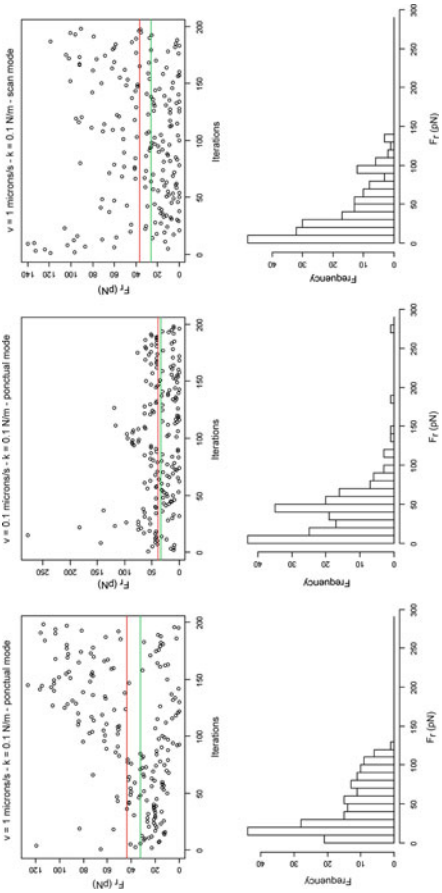
v = 1 microns/s - k = 0.1 N/m - ponctual mode
v = 0.1 microns/s - k = 0.1 N/m - ponctual mode
v = 1 microns/s - k = 0.1 N/m - scan mode
Iterations
Frequency
Fr (pN)

Fig. 19.5 Measured rupture forces for the sequence S_1. At the *top*, the gap between the average (*top line*) and the median (*bottom line*) gives an indication of the average value representativeness for each experiment. *Below*, histograms of rupture forces

19.4 Specificity Analysis

Specificity characterizes the degree of "mutual recognition selectivity" between micro-components during a self-assembly process. It is generated by the WC complementarity[10] between DNA strands belonging to two DNA populations attached to the micro-component surfaces. This selectivity can be encoded by a DNA strand sequence. In this section, an algorithm for generating optimal sequence to achieve this property is proposed.

The study of stability of the sequence S_1 has demonstrated the need to reduce possibilities of *mismatch* (MM) configurations. Minimizing this type of configuration involves the use of an optimized sequence whose most likely configuration is the type *perfect match* (PM).

For a given DNA strand, the nitrogenous base sequence is encoded by its complementary strand sequence. The basis of this coding is the WC complementarity between bases G and C on one hand and A and T on the other. Thus, the DNA molecule specificity consists of the uniqueness of this nitrogenous base composition.

Several algorithmic methods and experimental techniques developed around the area of DNA computing exist. This new discipline is common to both research areas, DNA computers [37] and nucleic nanostructures [38]. The basic principle is similar to machine programming of electronic computers. This is indeed a program to establish design principles for systematic molecular systems with desired properties. Applied to DNA, the main objective is to design unique and dissimilar sequences. These must meet specific conditions that may affect the thermodynamic properties. For example, this may be realized by avoiding stable MM structures through the combinatorial DNA rules. However, the main difficulty concerns the trade-off between maximizing the stability and the specificity.

The developed algorithms in this discipline are numerous and varied. Table 19.1 is a non-exhaustive summary of the state of the art for generating sequence algorithms. Two major families of algorithms exist. The first optimizes these

Table 19.1 Algorithms for sequence generation of state of the art [43]

Approaches	Authors
Exhaustive research	[39]
Random research	[40]
Template-map strategy	[41,42]
Graphs	[43]
Stochastic methods	[44]
Dynamic programming	[45]
Bio-inspired methods	[46]
Evolutionary algorithms	[47]

[10]DNA base pairing: adenine (A) forms a base pair with thymine (T), and guanine (G) forms a base pair with cytosine (C).

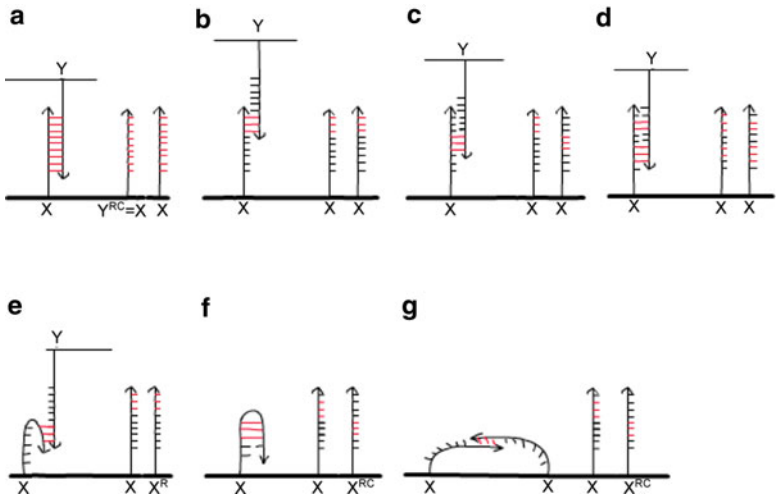

Fig. 19.6 Scenarios of possible configurations between two complementary DNA strands

conditions during construction of the sequence. In the second family, sequences are generated randomly. Afterward, specific conditions, such as thermodynamic properties, are verified using a "filter." This is a set of predefined conditions to maintain the desired sequences. In both types of algorithms, the conditions are set for the requirements of stability and specificity in particular.

19.4.1 Generation of Dedicated Sequence

19.4.1.1 Principle

During hybridization of a strand with its complementary set, multiple configurations are possible. They depend essentially on the nitrogen base sequence and are identified in Fig. 19.6.

The proposed solution to optimize stability is to increase the probability of forming a configuration using PM or reduce the number of MM configurations with low energy. If case A is the perfect hybridization type (PM) between complementary strands X and Y, cases B, C, D, E, F, and G in this figure represent the unwanted MM configurations.

In following sections, the "sequence reference" is attached to the substrate by its 5' end. It is indexed from 1 to n, where n is the number of nitrogenous bases in the 5'-3' orientation.

The ideal filter to address this issue must eliminate these undesirable configurations. The conditions that constitute the filter consist of comparing segment pairs of length β belonging to each of the interacting strands. To compare two words of the same length $m1$ and $m2$, the Hamming function $H(m1, m2)$ is defined as the number of positions for which the symbols are different. If the two words $m1 =$ ATCGAAA

and $m2$ = ATGGAAT, then $H(m1, m2) = 2$. The use of this distance involves six comparisons. An optimization is possible to reduce the number of comparisons considering the definitions of complementary sequence, noted with exponent C, and the reverse sequence noted with exponent R.

Complementary Sequence For each A (C respectively) of the sequence reference, a symbol T (with respect to G) is equivalent to the complementary sequence and vice versa. The resulting strand is oriented 3'-5' for the same index. In the AFM experiments, the complementary sequence is attached to the AFM tip by its 5' end.

Reverse Sequence The reverse sequence is obtained by changing the 5'-3' orientation to 3'-5'.

Property *The reverse complementary sequence of a sequence Y complementary to a sequence X is X itself: $Y^{RC} = X$.*

This property reduces the number of comparisons between strand segments corresponding to six cases of MM. Thus, considering the x_i segments of length β of one sequence X, the comparison of these segments to the segments y_j of the complementary sequence Y is equivalent to the comparison of the x segments to themselves with different indices i and j.

The six MM cases B, C, D, E, F, and G of Fig. 19.6 can be summarized in the following three conditions:

- To avoid cases B, C, and D, each of the two segments x_i and x_j of the generated sequence must be different.
- To avoid cases F and G, each of the two segments x_i^R and x_j^C of the generated sequence must be different.
- To avoid the case E, each of the two segments x_i and x_j^R of the generated sequence must be different.

with i and j indices of different segments in the studied sequence.

These comparisons can be expressed through the function H. The three previous conditions can then be written as follows:

- $H(x_i, x_j) > \alpha$.
- $H(x_i^R, x_j^C) > \alpha$.
- $H(x_i, x_j^R) > \alpha$.

The parameter α is a minimum Hamming distance set by the user. It provides a minimum difference of α bases between the segments. The three rules define the filter of the sequence generation algorithm detailed in the following section.

19.4.1.2 Algorithm

The algorithm for generating specific sequences aims at generating a sequence whose configuration is most likely the PM configuration. To maximize stability, this sequence must also have a value of desired ΔG. This algorithm consists of two

steps. The first one is the generation of a random sequence of nitrogen bases, and the second verifies the specificity of the sequence across the three defined rules.

The defined filter checks only the sequence specificity. Stability is characterized by two parameters ΔG, the Gibbs free energy variation, and l, the length of the unknown sequence. The energy ΔG is calculated from the nearest neighbor model in the global approach discussed later. These two parameters are linked. Indeed, its calculation requires knowledge of the nitrogenous base sequence and thus depends indirectly on the length l. The latter is unknown: it is necessary to fix one of the two parameters. By setting a maximum value of energy, denoted by ΔG_{m}, such that the free energy of the unknown sequence is below this threshold, a frame of the l can also be proposed.

The estimated interval is of the form $[l_{\max}; l_{\min}]$ whose terminals are the lengths of maximum and minimum sequences, respectively. Indeed, the pair (A, T), whose energy is minimal in absolute value, and the pair (G, C), whose energy is maximal, define two characteristic sequences. First, a sequence built successively with (A, T) has a lower energy than a random sequence constructed for the same length. Second, similarly, a sequence built with successively (G, C) has a higher energy than a random sequence constructed for the same length.

The energy of any given sequence is within the range defined by the energies of the two characteristic sequences. At standard environmental parameters, these characteristic energies are given by the following equations:

$$\Delta G_{\min} = 1.2n - 1.1, \tag{19.5}$$

$$\Delta G_{\max} = 3.4n - 3.1. \tag{19.6}$$

From (19.5) and (19.6), $l_{\max}$ and $l_{\min}$ can be estimated as follows:

$$l_{\max} = d_{\mathrm{base}} * \frac{\Delta G_{\mathrm{m}} + 3.1}{3.4}, \tag{19.7}$$

$$l_{\min} = d_{\mathrm{base}} * \frac{\Delta G_{\mathrm{m}} + 1.1}{1.2}. \tag{19.8}$$

The random sequence produced by the algorithm is of length l and with absolute energy higher than the given ΔG_{m}.

The second step is to check the specificity of the sequence through the filter defined by the three rules. This requires the determination of two parameters: α and β. The parameter α is the minimum Hamming distance for defining the three rules, and β is the length of the segments to compare the number of bases.

19.4.2 Theoretical Analysis

The objective of the algorithm is to provide sequences for which the defined configurations in the filter are improbable. The formation probability of configurations is given through the value of ΔG. Thus, configurations in which the Gibbs

Table 19.2 S_1–S_3 theoretical comparison

Properties	S_1	S_3
Hetero configurations	118	41
Hairpin configurations	14	1
Hetero configurations (energy >4 Kcal/mol)	27	0
Hairpin configurations (energy >4 Kcal/mol)	14	0
ΔG (PM)	164 Kcal/mol	51 Kcal/mol

energy variation is less than -4 kcal/mol are considered improbable [25]. Four bases correspond to this energy, and the parameter α is initialized to this value.

Using the Hamming function, segments of length β are compared. This length can be initialized with values close to the persistence length of single-stranded DNA, estimated at 11 bases (for a B form of DNA) [18]. This length characterizes the smallest unit of a strand similar to a rigid segment. The sequences are generated randomly: the optimization of computation time led to an underestimation of the length and initialized to 8 bases. The choice of energy and the length of the sequence are fixed in relation to the specific sequence desired.

The probability of MM configuration formation increases with sequence length. Sequences of small lengths are preferred. On one hand, compared to the sequence S_1, the length of the sequences generated should be less. On the other hand, for reasons of detection, the experimental characterization of sequences requires a choice of length at least greater than 10 nm. A sequence of length 30 bases, denoted by S_3, is thus produced using this algorithm.

Comparison of possible configurations[11] between the specific sequence S_3 and the old sequence S_1 shows one unstable possible configuration of type *hairpin* for the sequence S_3, while configurations of this type are stable in their entirety for the sequence S_1. For configurations of type *hetero*,[12] no stable configuration is possible for the generated sequence.

With an optimal probability for the configuration PM, the sequence S_3 seems more specific than the sequence S_1 initially tested. To validate the specificity of this sequence, experiments were conducted (Table 19.3).

19.4.3 Experimental Analysis

Seven experiments are conducted. The experimental parameters of each experiment are summarized in Table 19.3.

Measurements of interaction forces between S_1 and its complementary strand detailed in the second part of this chapter are different from experiences detailed

[11] mfold.

[12] Complementarity between two segments with different indices from two complementary strands.

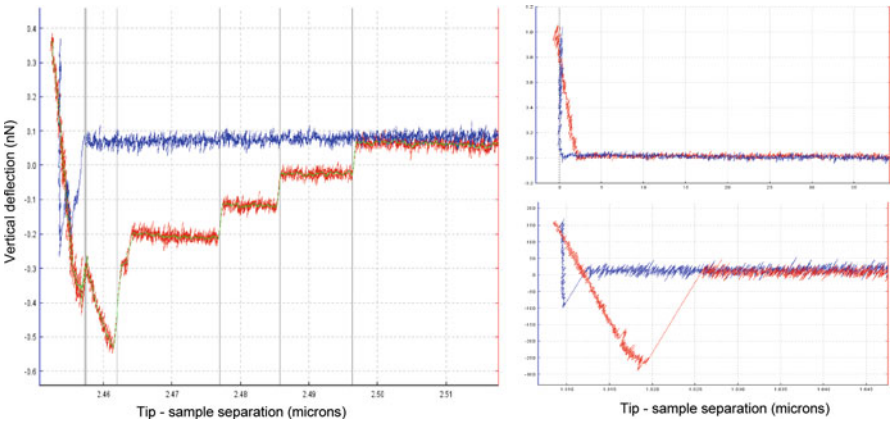

Fig. 19.7 A/R curves in the study of specificity. *Left* Exp14, and *right top* Exp1, *right bottom* Exp10. See Table 19.3

in this part because the material used is disassemblable (AFM, beams, ambient, noise, etc.). The target also appears dissimilar as these experiments are intended to demonstrate the specificity of the new sequence and the influence of two experimental parameters of velocity and latency time. This last corresponds to a time measured in seconds, introduced between the two-stage approach and the retreat of an AFM measurement. The introduction of this parameter in the characterization of interactions between DNA strands is a way to study the influence of time on the stability of specific DNA-based adhesion. In these second series of measurements, two velocities (0.05 and 0.1 μm/s) and two latency times (0 and 60 s) are studied.

The specificity analysis is based on the comparison of specific interactions between the two complementary sequences S_3 and S_4 generated by the algorithm and is nonspecific between S_3 and the initial sequence S_1 proposed in Golem. Thus, for the specific interactions, a homogeneous distribution is expected as only stable configuration is possible, while for nonspecific interactions, heterogeneous distribution is expected.

This analysis consists of two types of comparison, the rupture forces and the rupture distances. The rupture distance corresponds to the distance made by the cantilever during a local rupture event. The rupture distance is not directly represented on the A/R curves (Fig. 19.7). Indeed, the displacement shown in these curves is of the cantilever base and not of the tip. To obtain the rupture distance, it must be subtracted from the measured displacement on the curve, and the cantilever bending that corresponds to the corresponding measured force is divided by the cantilever stiffness [5].

Table 19.3 Experimental parameters for specificity study

Interaction	Non specific	Non specific	Non specific	Specific	Specific	Specific	Specific
Experience	Exp1	Exp5	Exp14	Exp10	Exp16	Exp17	Exp13
Cantilever			S_3	S_4	S_4	S_4	S_4
Substrate		S_3	S_1	S_3	S_3	S_3	S_3
Velocity (μ m/s)	0.1	0.1	0.1	0.1	0.05	0.05	0.1
Distance (μm)	1	1	1	1	1	1	1
Repetition number	10	10	20	20	10	10	10
Points number	1	5	12	8	20	20	16
Environment	PBS (1M)	PBS (1M)	PBS (1M)	PBS (1M)	PBS (1M)	PBS (1M)	PBS (1M)
Stiffness (N/m)	0.28	0.26	0.21	0.043	0.18	0.18	0.14
Loading rate (N/s)	$3\ 10^{-8}$	$3\ 10^{-8}$	$2\ 10^{-8}$	$4\ 10^{-9}$	$1\ 10^{-8}$	$1\ 10^{-8}$	$1.4\ 10^{-8}$
Latency time (s)	0	0	0	0	0	60	60

19.4.3.1 Plateau Phenomenon

A phenomenon of regular plateaus is observed for all experiments except the experiment with a velocity $v = 0.1\,\mu$m/s.

The appearance of these levels involves classifying data by the appearance of each plateau. The study of the values of rupture force and rupture distance homogeneity function of these groups is a way to analyze the phenomena characteristic of each experiment.

The length of the sequence S_3 is 10 nm. When the measured distance is greater than this value, the measured interaction on the plateau corresponds to an interaction of a couple of strands different from the first. However, when the rupture distance is less than this value, it is not possible to deduce the number of pairs of interacting strands.

19.4.3.2 Analysis of Specificity

The mean value of rupture distance is 2 nm for specific interactions (Exp10) and 7 nm for nonspecific ones (Exp14).[13] Consequently, the measured nonspecific interactions may correspond either to one or more S_3-S_1 pairs.

The rupture forces measured in the specific experience are higher than in the nonspecific experience. The highest values correspond to the force recorded during the first plateau group with an average of 793 pN. The values of the second and the third plateaus are higher than the average value estimated at 219 pN for the nonspecific experience. The specific rupture forces are naturally lower as the sequence generated S_3 is smaller. In addition, because of S_1, in the nonspecific experience, complex configurations are set up during the hybridization.

The histograms of Fig. 19.8 show the consistency measures for the specific experience. Indeed, the average value is significant, while the measures of nonspecific experience are much more heterogeneous. Even if the measured forces are weaker in the specific experience, these two experiments show that the sequence S_3 is specific with the repeatability of the phenomenon.

19.4.3.3 The Velocity Influence

From the conducted experiments, we observe:

- The averages of measured rupture force with low velocity (0.05 μm/s) are well above the estimated average for the measures with higher velocity (0.1 μm/s). In addition, the average F_r for different plateau groups is decreasing for experience with low velocity: 1510 pN, 456 pN, and 81 pN. Thus, stronger interactions are measured with lower velocity.

[13] See Table 19.3.

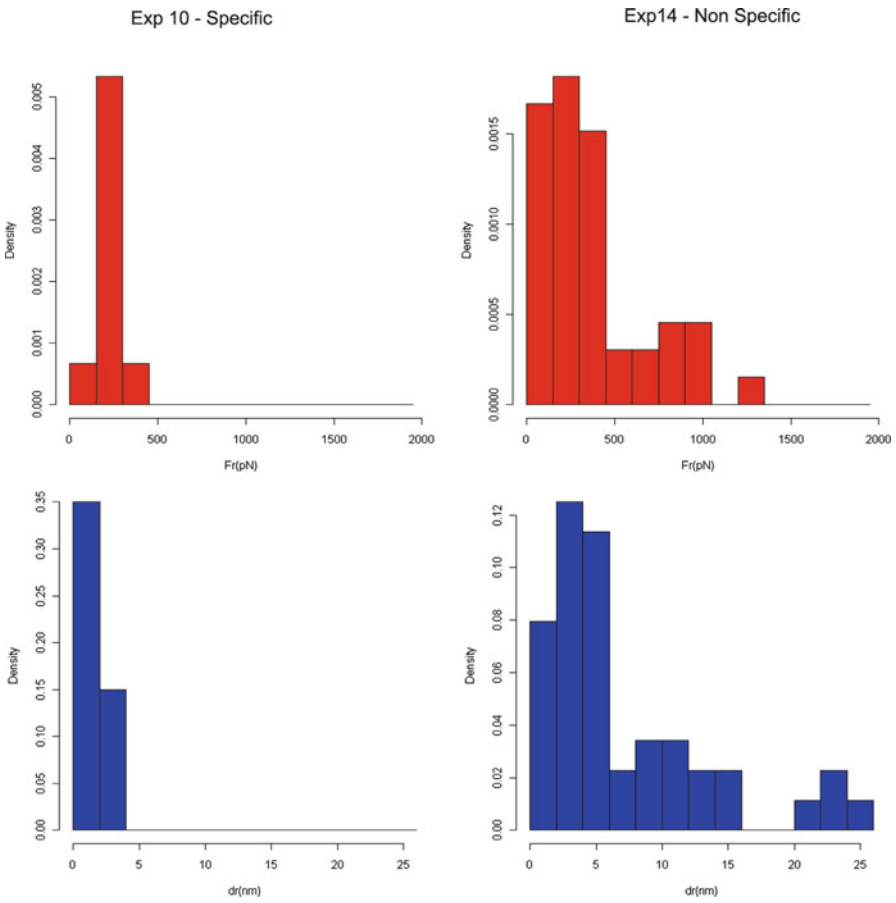

Fig. 19.8 Specificity analysis. Specific and nonspecific (*Top*) rupture force and (*Bottom*) rupture distance distributions. The same experimental parameters are used in both experiences (See Table 19.3)

- The rupture distances measured are much higher and heterogeneous in the experience with lower velocity. The averages of the different plateau groups are 4, 8, and 9 nm. They are growing and are close to the characteristic value 10 nm. It appears that the interactions measured for each plateau with lower velocity introduce match interactions of different couple of strands.

For a low velocity, a larger number of interactions are observed through the phenomenon of plateaus. These interactions correspond to pairs of different strands. It is possible that the decrease of the rupture forces is due to a detachment of successive strands hybridized during the approach.

Low velocity improves the overall stability of the DNA-based adhesion involving a larger number of strands. Indeed, with a lower velocity, the analysis shows that the DNA strands appear to hybridize more often with a stronger adhesion.

19.4.3.4 The Latency Time Influence

Experiments show that the velocity influences the overall adhesion stability involving a larger number of strands. We can assume that hybridization takes some time. To study the influence of time on the specific interaction ($S_3 - S_4$), AFM measurements were performed by introducing a time delay between the two-stage approach and the retreat called *latency time* T_a. This is not to determine the time required for hybridization but to identify whether the influence of this parameter is typical:

- For a velocity $v = 0.1\,\mu$m/s and a latency time of 60 s, the number of plateaus becomes very high, and the values of measured F_r are much larger (averaging 540 pN) than those measured with no latency (219 pN average). The introduction of a wait at this rate implies a larger number of strands in the adhesion between the two populations of complementary strands. This is a gradual separation of the hybridized strands during the approach.
- For a velocity $v = 0.05\,\mu$m/s and a latency time of 60 s, the overall number of plateaus does not vary compared to the experience with zero latency, but the values of measured F_r are much larger when latency is introduced. Here again, the introduction of a waiting time at a constant rate implies a greater number of strands in the adhesion between the two populations of complementary strands. This is a gradual separation of the strands hybridized during the approach.

Finally, when the latency time is 60 s, but the velocity is lower, the number of levels is less important in the experiment at low velocity, but the values of F_r are much higher.

19.4.3.5 Conclusion

The latency significantly influences the overall stability of the DNA-based adhesion. Indeed, the number of pairs of strands increases, and the intensity of the measured rupture forces is optimized by the introduction of this parameter.

Nevertheless, the influence of this parameter depends on the A/R velocity. Indeed, when this parameter is important (0.1 μm/s), the stability is optimized by increasing the number of strands of the interaction, and when it is lower (0.05 μm/s), the stability of the velcro is optimized by increasing the intensity of interactions.

19.5 Conclusion

Self-assembly of components on a microscopic scale is an innovative approach to the widespread use and the industrialization of emerging systems based on micro- and nanotechnology.

The multidisciplinary work presented here is part of the European project Golem objectives and specifically targets the selection of DNA, the theoretical study, and the experimental validation.

The prospects of this work are numerous and go beyond the framework of the microscopic self-assembling. The integration of biological functions on micro- and nano-devices opens a new avenue for the implementation of the properties of actuation, sensing, and interaction control. These functions exist in nature and are complicated to replicate using only inorganic matter, whereas they are part of the fundamental processes of biology. For example, nano-robots for in vivo applications could be provided with capacity to transport biological interaction-controlled drugs or perform diagnostics.

References

1. Fink HW (2001) DNA and conducting electrons. Cell Mol Life Sci 58:1–3
2. Rothemund PWK (2006) Folding DNA to create nanoscale shapes and patterns. Nature 440:297–302, doi:10.1038/nature04586
3. Yu He, Tao Ye, Min Su, Chuan Zhang, Ribbe AE, Wen Jiang, Chengde Mao (2008) Titre. J Nature 452:198–201
4. Marti O, Drake B, Hansma PK (1987) Atomic force microscopy of liquid-covered surfaces: atomic resolution images. Appl Phys Lett 7:484–486
5. Butt H-J, Cappella B, Kappl M (2005) Force measurements with the atomic force microscope: technique, interpretation and applications. Surf Sci Rep 59:1–152
6. Saenger W (1983) Principles of nucleic acid structure. In: Charles RC (ed) Springer, New York
7. Rief M, Clausen-Schaumann H, Gaub HE (1999) Sequence-dependent mechanics of single DNA molecules. Nature Struct Biol 6:346–349, doi:10.1038/7582
8. Brandsdal Bo, Osterberg F, Almlöf F, Feierberg I, Luzhkov Vb, Aqvist J (2003) Free energy calculations and ligand binding. Adv Protein Chem 66:123–158
9. Leach A (2001) Molecular modelling: principles and applications, 2nd edn. Prentice Hall, Englewood Cliffs
10. Guvench O, MacKerell AD Jr (2008) Comparison of protein force fields for molecular dynamics simulations. In: Molecular modeling of proteins, 3rd edn. Humana Press, Springer
11. Daunay B, Micaelli A, Régnier S (2001) Energy-field reconstruction for haptics-based molecular docking using energy minimization processes. In: Actes de IROS'07: IEEE international conference on intelligent robots and systems (ACTI). San Diego, USA
12. Poland D, Scheraga HA (1966) Phase transitions in one dimension and the Helix-Coil transition in polyamino acid. J Chem Phys 45:1456
13. Neukirch S (2004) Extracting DNA twist rigidity from experimental supercoiling data. Phys Rev Lett 93:19
14. Nomura Y, Nakamura T, Feng Z, Kinjo M (2007) Direct Quantification of Gene Expression Using Fluorescence Correlation Spectroscopy. In: Current pharmaceutical biotechnology. Bentham Science Publishers, Japan

15. Glazer M, Fidanza JA, McGall GH et al (2006) Kinetics of oligonucleotide hybridization to photolithographically patterned DNA arrays. Anal Biochem 358:225–238
16. Zuker M (2006) Mfold web server for nucleic acid folding and hybridization prediction. Nucleic Acids Res 31:3406–15
17. SantaLucia Jr (1998) A unified view of polymer, dumbbell, and oligonucleotide DNA nearest-neighbor thermodynamics. PNAS 96:1460–1465
18. Williams MC, Wenner JR, Rouzina I, Bloomfield VA (2001) Effect of pH on the overstretching transition of double-stranded DNA: evidence of force-induced DNA melting. Biophys J 80:874–881
19. Rau DC, Lee B, Parsegian VA (1984) Measurement of the repulsive force between polyelectrolyte molecules in ionic solution: hydration forces between parallel DNA double helices. Proc Natl Acad Sci USA 81:2621–2625
20. Smith SB, Finzi L, Bustamante C (1992) Direct mechanical measurements of the elasticity of single DNA molecules by using magnetic beads. Science 258:1122–1126
21. Perkins TT, Quake SR, Smith DE, Chu S (1994) Relaxation of a single DNA molecule observed by optical microscopy. Science 264:822–826
22. Essevaz-Roulet B, Bockelmann U, Heslot F (1997) Mechanical separation of the complementary strands of DNA. Proc Natl Acad Sci USA 94:22
23. Bockelmann U, Thomen Ph, Essevaz-Roulet B, Viasnoff V, Heslot F (2002) Unzipping DNA with optical tweezers: high sequence sensitivity and force flips. Biophys J 82:1537–1553
24. Binnig G, Quate CF, Gerber Ch (1986) Atomic force microscope. Phys Rev Lett 56:930–933
25. Lee GU, Chrisey LA, Colton RJ (1994) Direct measurement of the forces between complementary strands of DNA. Science 266:771–773
26. Florin EL, Moy VT, Gaub HE (1994) Adhesion forces between individual ligand-receptor pairs. Science 264:415–417
27. Strunz, Torsten et al (1999) Dynamic force spectroscopy of single DNA molecules. Proc Natl Acad Sci USA 96:11277–11282
28. Evans E, Ritchie K (1999) Strength of a weak bond connecting flexible polymer chains. Biophys J 76:2439–2447, doi: 10.1016/S0006-3495(99)77399-6
29. Sattin BD, Pelling AE, Goh CM (2004) DNA base pair resolution by single molecule force spectroscopy. Nucleic Acids Res 32:4876–4883
30. Morfill J, Khner F, Blank K et al (2007) B-S transition in short oligonucleotides. Biophys J 93:2400–2409, doi: 10.1529/biophysj.107.106112
31. Evans E, Ritchie K (1997) Dynamic strength of molecular adhesion bonds. Biophys J 72:1541–1555, doi: 10.1016/S0006-3495(97)78802-7
32. Janovjak H, Sapra KT, Mller DJ (2005) Complex stability of single proteins explored by forced unfolding experiments. Biophys J 88:37–39
33. Odrowaz PM, Czuba P, Targosz M, Burda K, Szymonski M (2006) Dynamic force measurements of avidin-biotin and streptavdin-biotin interactions using AFM. Acta Biochim Pol 53:93–100
34. Liu W et al (2008) Comparative energy measurements in single molecule interactions. Biophys J 95:419–425
35. Bell GI (1978) Models for the specific adhesion of cells to cells. Science 200:618–627
36. Kramers H (1940) Brownian motion in a field of force and the diffusion model of chemical reactions. Physica 7:284–304
37. Adleman LM (1994) Molecular computation of solutions to combinatorial problems. Science 266:1021–1024
38. Seeman NC, Kallenbach NR (1983) Design of immobile nucleic acid junctions. Biophys J 44:201–209
39. Hartemink AJ, Hartemink ErJ, Gifford DK, Khodor J (1998) Automated constraint-based nucleotide sequence selection for DNA computation. In: 4th Int. meeting on DNA-based computing, pp 227–235
40. Penchovsky R, Ackermann J (2003) DNA library design for molecular computation. J Comput Biol 10:215–229

41. Frutos AG, Thiel AJ, Condon AE, Smith LM, Corn RM (1997) DNA computing at surfaces: four base mismatch word design. In: 3rd DIMACS workshop DNA based comput. The rise of modern genomics 238
42. Masanori Arita, Satoshi Kobayashi (2002) DNA sequence design using templates. Ohmsha, Ltd. and Springer-Verlag 20:263–277
43. Feldkamp U, Saghafi S et al (2002) DNA Computing. In: DNASequenceGenerator: a program for the construction of DNA sequences. Springer, Berlin, SpringerLink
44. Tanaka F, Nakatsugawa M, Yamamoto M, Shiba T, Ohuchi A (2001) Developing support system for sequence design in DNA computing. In: 7th Int. workshop DNA based comput, pp 340–349
45. Marathe A, Condon AE, Corn RM (1999) On combinatorial DNA word design. In: 5th DIMACS workshop DNA based comput, pp 75–89
46. Deaton R, Chen J, Bi H, Rose JA (2002) TA software tool for generating noncrosshybridization libraries of DNA oligonucleotides. In: 8th Int. workshop DNA based comput, pp 252–261
47. Shin S, Lee I, Kim D, Zhang B (2005) Multi-objective evolutionary optimization of DNA sequences for reliable DNA computing. IEEE Trans Evol Comput 9:143–158

Chapter 20
Local Environmental Control Technique for Bacterial Flagellar Motor

Toshio Fukuda, Kousuke Nogawa, Masaru Kojima, Masahiro Nakajima, and Michio Homma

Abstract Micro/nanorobots have attracted scientific attention to develop novel technologies such as drug delivery systems. Recently, microorganisms, especially flagellated bacteria, have been used as propulsion for microobjects. To enhance the controllability of bacteria-driven microrobots, it is needed to establish a method to control the bacterial driving force directly. In many cases, the bacterial movements are regulated by the environment. Therefore, local environmental control technique

T. Fukuda (✉)
Department of Micro-Nano Systems Engineering, Nagoya University, Furo-cho, Chikusa-ku, Nagoya 464-8603, Japan
e-mail: fukuda@mein.nagoya-u.ac.jp

Center For Micro-nano Mechatronics, Nagoya University, Furo-cho, Chikusa-ku, Nagoya 464-8603, Japan

K. Nogawa
Institute for Advanced Research, Nagoya University, Furo-cho, Chikusa-ku, Nagoya 464-8601, Japan
e-mail: nogawa@robo.mein.nagoya-u.ac.jp

Department of Micro-Nano Systems Engineering, Nagoya University, Furo-cho, Chikusa-ku, Nagoya 464-8603, Japan

M. Kojima
Department of Systems Innovation, Osaka University, 1-3, Machikaneyama-cho, Toyonaka 560-8531, Osaka, Japan
e-mail: arai-lab.sys.es.osaka-u.ac.jp

M. Nakajima
Center For Micro-nano Mechatronics, Nagoya University, Furo-cho, Chikusa-ku, Nagoya 464-8603, Japan
e-mail: nakajima@mein.nagoya-u.ac.jp

M. Homma
Division of Biological Science, Nagoya University, Furo-cho, Chikusa-ku, Nagoya 464-8602, Japan
e-mail: g44416a@cc.nagoya-u.ac.jp

C. Mavroidis and A. Ferreira (eds.), *Nanorobotics*, DOI 10.1007/978-1-4614-2119-1_20,
© Springer Science+Business Media New York 2013

is desired for bacterial driving force control. In this chapter, we introduce a local environmental control technique based on nano/micro dual pipettes for bacterial flagellar motor control. We show transient-state control of Na^+-driven flagellar motor rotational speed by switching local discharges between Na^+-containing and -free solutions, and steady-state control by simultaneous local discharges of the solutions with controlling discharge velocities independently. We found that rotational torque generated by the flagellar motor could be controlled in 10^2 pN·nm orders using the local environmental control technique based on nano/micro dual pipettes.

20.1 Introduction

Recently, micro/nanorobots have been actively studied. If functional micro/nanorobots are realized, it is expected to lead the developments of novel technologies, especially in the medical robotics domain for drug delivery systems (DDS) and nano/micro-surgery inside the human body [1–5]. The requirements for functional micro/nanorobots are various: sensing, actuation, data transmission, remote control, power supply subsystems, etc., and their embedment or integration into the micro/nanorobots to make it functional [6, 7]. So, all components have to be downsized by improving the manufacturing technique or using novel materials. Here, we focused on the actuation and its power supply subsystem because we think that the actuation is the most fundamental function for all sorts of micro/nanorobots.

To achieve the downsizing of the actuators to micro/nano-meter scale, recently, propulsion for the micro/nanoobjects based on biomolecular motors and microorganisms have been used [3, 4, 8–14]. Such bioactuators are natural actuators in micro/nano-meter scale. Their energy sources are chemical reactions. So, there is a possibility to reduce the size of complete robotic systems to micro/nano-meter scale.

Flagellated bacteria are one of the promising candidates to solve the propulsion challenge for micro/nanoobjects. In the first place, the bacteria self-propagate unlike the biomolecular motors which need reconstitution. Many bacteria, such as *Escherichia coli* (*E. coli*), *Vibrio* and *Salmonella*, can multiply in short time (from few dozen minutes to a few hours depending on the environmental condition, such as temperature and nutrients). This facilitates the mass production of the actuators at low time-cost.

Second, the bacteria have the metabolic function. The micro/nano electro mechanical actuators become easily impaired in a short time due to the friction of the rotational or the sliding motion. Also the biomolecular motors have the same problem [10]. So, the self-repairing function of the actuators is necessary for the actual utilization of the micro/nanorobots. The bacteria can produce the proteins and can replace the old proteins by their metabolic function. Therefore, this self-repairing function is an advantage over other actuators.

Third, the bacteria have the biomolecular motors, bacterial flagellar motors, which convert chemical reactions into mechanical energy for propulsion at high energy conversion efficiencies of up to near 100 %. The internal-combustion engines convert the fuels (thermal energy) into the driving force at low efficiency around

Table 20.1 Methods and prospective features to control bacterial propulsion for microobject

Method	Control		Example	References
	Direction	Speed		
Configuration	− (improved directivity)	−	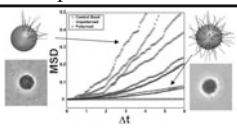	[13]
Magnetotaxis	+	−	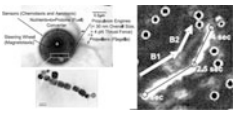	[3, 4]
Phototaxis	+	−	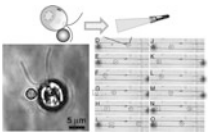	[14]
Chemotaxis	+	−	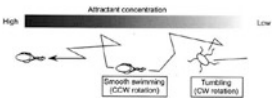	[15, 16]
Energy source	−	+	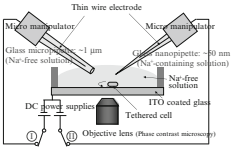	[17–19]

30–40 %. The electric motors convert the electric power into the driving force at efficiencies of up to ∼90 %. However, there is a lot of energy loss in the electric power generation when the thermal energy is converted into the electric energy. Therefore, the biomolecular motors, especially the bacterial flagellar motors, excel in the energy efficiency.

Fourth, most of the bacteria naturally have sensors and systems to regulate the propulsion in response to the environment. Some bacteria do not move randomly but have a taxis system to move toward or away from environmental stimuli [15], such as chemical substances (chemotaxis), temperature (thermotaxis), light (phototaxis), and magnetic field (magnetotaxis). In addition, some of the flagellated bacteria such as *E. coli*, *Vibrio*, and *Salmonella* were genetically and behaviorally studied well. These bacteria can be modified genetically to add or delete some functions depending on the requirements for the micro/nanorobots. As the taxis system is well characterized, it is expected that the taxis system can be utilized to control the bacterial propulsion artificially. Therefore, we focused on the flagellated bacteria as the actuators for the micro/nanorobots.

Since Darnton et al. [12] achieved a random delivery of bacteria-driven microobject using *Serratia marcescens*, various control methods of bacteria-driven microobjects were demonstrated. These methods and prospective features to control

the bacterial propulsion for microobjects are summarized in Table 20.1. A good configuration of the bacteria and microobjects increases the directivity of the bacteria-driven microobjects. Behkam et al. [13] improved the directivity of the bacteria-driven microobject delivery by limiting the bacterial attaching area. It is difficult to control the bacteria-driven microobjects arbitrarily by such configuration, because of the bacterial random propulsion generation. Bacterial taxis systems, such as magnetotaxis and chemotaxis, can be used to control the bacteria-driven microobject [3, 4, 15, 16]. Also an example is given using the phototactic beating type flagellated microbe *Chlamydomonas reinhardtii* [14]. By using these taxis systems, the directions of the continuously moving bacteria-driven microobjects can be controlled.

If the moving speed can be controlled directly by precise and direct control of the bacterial driving force, it is expected to enhance the controllability of the bacteria-driven microobject more. Walter et al. [17] modified *E. coli* genetically and used light to control the flagellar driving force by generating the electrochemical gradient utilizing light-driven proton pumping from inside to outside across the membrane. We developed local environmental control system with nano/micro dual pipettes to control the bacterial driving force by controlling the external ion concentration [18, 19].

In this chapter, we introduce a local environmental control technique based on nano/micro dual pipettes for bacterial flagellar motor control by dynamic and arbitrary changes in the local reagents/ions concentrations. We demonstrate transient-state control of Na^+-driven flagellar motor rotational speed by switching local discharges between Na^+-containing and -free solutions, and steady-state control by simultaneous local discharges of the solutions with controlling discharge velocities independently.

20.2 Bacterial Flagellar Motor

Many bacteria swim actively in liquid by rotating their flagella and migrate toward favorable directions. The bacterial flagellum has a helical filament that acts as a propeller. Each flagellum consists of a helical filament extending from the cell body, a basal body embedded in the cell surface, and a flexible hook that connects them [20–23] (Fig. 20.1). The bacterial flagellar motor is a molecular machine that converts ion-motive force (IMF) into the mechanical force; the energy source of the rotation is the electrochemical gradient of H^+ or Na^+ ion across the cytoplasmic membrane. The rotational speed of the flagellar motor depends on IMF [24, 25]. In most situations, it can be considered that the concentration of the coupling ion inside the membrane is constant, because of the homeostasis of the bacteria. Therefore, the rotational speed of the flagellar motor mainly depends on the ion concentration in the external environment.

While the bacterial cell is swimming at constant speed (v), Magariyama et al. [26] defined the driving force generated by the flagellar motor (F_D) as:

$$F_D = \alpha_f v + \gamma_f \omega_f \tag{20.1}$$

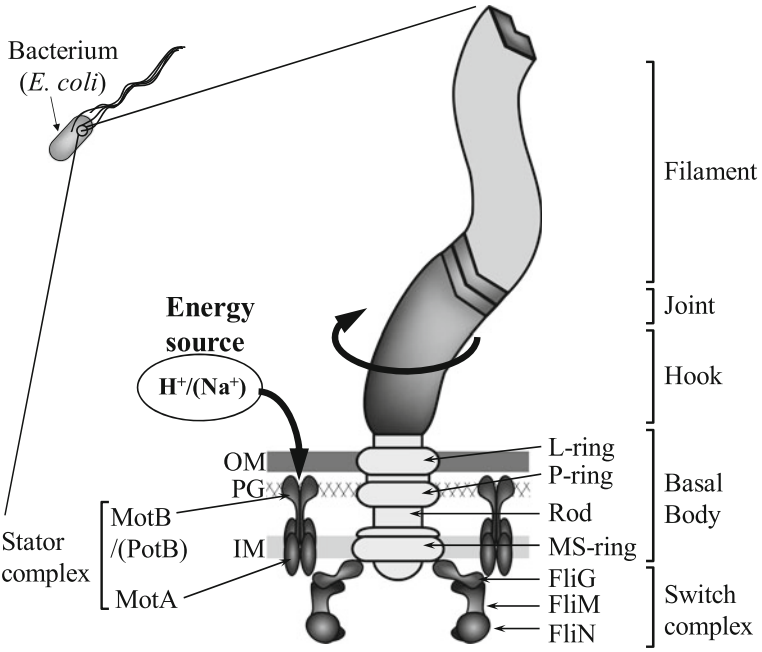

Fig. 20.1 Schematic of the bacterial flagellum. The substructures and components of the flagellum of *E. coli*. H^+/Na^+ influx through the stator complex is believed to generate torque at the interface between the stator component of MotA and the rotor component of FliG. *OM* outer membrane, *PG* peptidoglycan, *IM* inner membrane

with the assumption that the flagellar filament is a helical rigid body and rotates around the axis of the helix (where ω_f is the rotational speed of the flagellum, α_f and γ_f are the drag coefficients depending on the shape of the flagellar filament, the radius and the pitch of the flagellar helix, and the radius and the length of the flagellar filament). Under this assumption, the driving force of the flagellar motor (F_D) depends on the swimming speed of the bacterial cell (v) and the rotational speed of the flagellum (ω_f). Generally, the swimming speed of a bacterial cell (v) is roughly proportional to the rotational speed of its flagellum (ω_f) [26]. So, basically, the driving force generated by the flagellum can be controlled based on the rotational speed of the flagellar motor.

20.3 Local Environmental Control Technique Based on Nano/Micro Dual Pipettes

Conventionally, Piper et al. [27] used a glass nanopipette for local and repeatable delivery of water-soluble reagent in ionic solution to make localized controlled changes in reagent concentration on a surface. Then they applied their method to

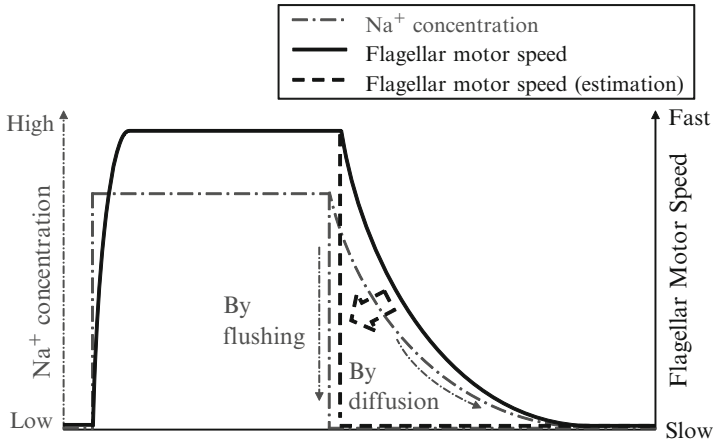

Fig. 20.2 Schematic of the changing aspects of Na^+ ion concentration by diffusion and flushing

control the Na^+-driven flagellar motor in single *E. coli* cell by dosing Na^+ ions. However, their system was not enough to produce an intended dynamic change in the reagents/ions concentrations. When the discharge of Na^+-containing solution is conducted with a single pipette, diffusion of Na^+ ions is the only way to reduce the Na^+ ion concentration. In addition, even if the solution is not being discharged, the Na^+ ions diffuse through the pipette–bath interface and are unintentionally supplied to the flagellar motor. In this case, the flagellar motor rotation is affected by the diffusion rate. In fact, we confirmed that the rotational speed of the flagellar motor was affected by diffusion of Na^+ ions in an experiment with a single pipette [18]. If both drastic increase and decrease in the Na^+ ion concentration can be generated as shown in Fig. 20.2, it will be possible to control the bacterial driving force more arbitrarily by controlling the ion concentration in the external environment. So, we constructed the local environmental control system with nano/micro dual pipettes, as shown in Fig. 20.3 [18, 19].

This system has glass nano/micro pipettes with a ∼50 nm/∼1 μm inner diameter that are used for the discharge of the Na^+-containing/Na^+-free solutions, respectively. Each pipette is fixed to a micromanipulator. So, it is possible to approach the pipettes to an arbitrary cell, and additionally the cell–pipette distance can be controlled independently for each pipette. The bath is filled with the Na^+-free solution. To discharge the solutions, DC voltage is applied between indium tin oxide (ITO)-coated glass at the bottom of the bath and the thin wire electrodes inserted into the pipettes. The discharges of the solutions can be switched or turned on/off independently with changing the discharging velocity by the applied DC voltages.

Through this dual pipettes system, the Na^+ ions are supplied to the flagellar motor of an arbitrary cell by discharge from the nanopipette. The Na^+ ions diffusing from the nanopipette and the Na^+ ions remaining around the cell can be flushed by discharge from the micropipette to immediately stop the feeding of the Na^+ ions to

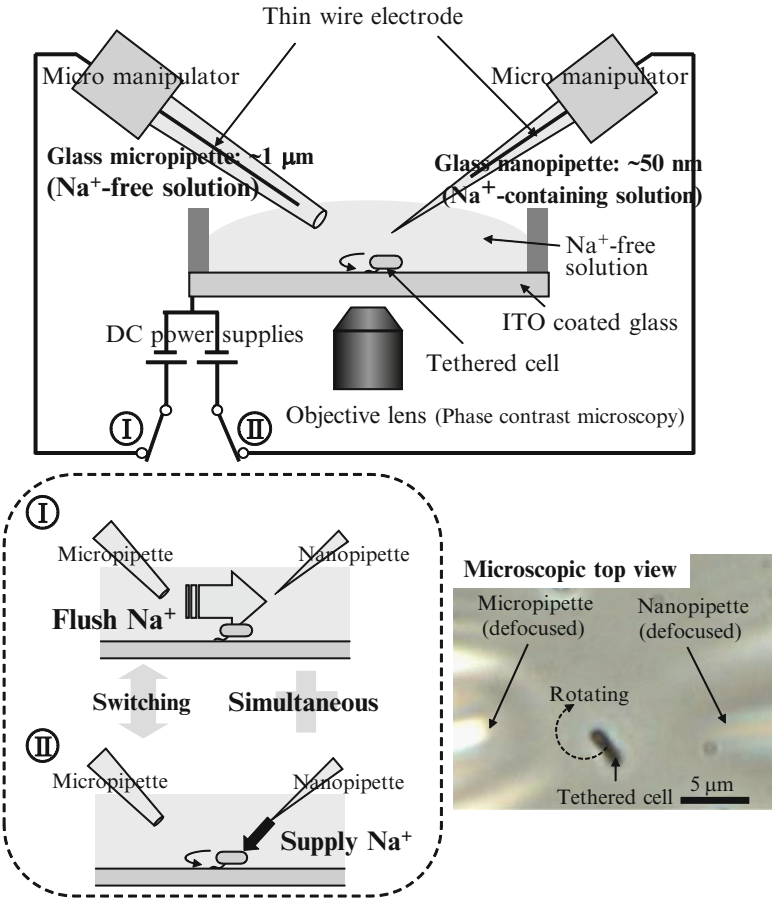

Fig. 20.3 Schematic and experimental appearance of the local environmental control system with nano/micro dual pipettes for the rotational speed control of Na^+-driven flagellar motor

the flagellar motor. So, when the discharge is switched between the Na^+-containing and the Na^+-free solutions, the feeding of the Na^+ ions to the flagellar motor can quickly change between ON and OFF states. Furthermore, the transition rate of speedup and slowdown of the flagellar motor rotational speed can be controlled (transient-state control) by controlling the feeding rate of Na^+ ions with the applied DC voltages.

Meanwhile, for continuous discharge of the Na^+-containing solution for a long period of time, the rotational speeds of flagellar motor get into the same value at any applied DC voltages because of saturation of the local Na^+ ion concentration or the rotational speed of tethered cell [19]. However, when both solutions are discharged simultaneously, the local Na^+ ion concentration is determined by the difference between the discharging velocities of both solutions. Therefore, the

steady-state control of flagellar motor rotational speed can be realized without changing the concentration of the discharging solution by simultaneous discharges of both solutions.

20.4 Rotational Speed Control of Flagellar Motor Using Local Environmental Control Technique Based on Nano/Micro Dual Pipettes

Tethered cells were used for the flagellar motor rotational speed control experiments as shown in Fig. 20.3. Generally, it is difficult to directly observe and measure the rotational speed of the flagellum under the optical microscope because of its ultrathin filament and high-speed rotation. "Tethered cells" means the cells whose flagella are attached onto a substrate [28] as shown in Fig. 20.4. When cells rotate the flagella with attaching onto a substrate, as a result, cell bodies rotate. That is to say, tethered cell is the system with which rotational speed of the flagellum can be easily observed as the rotational speed of the cell body. The rotational speed of the cell body was measured by image processing. (The details of cell strain, culturing condition, fabrication procedure of the tethered cells, and observation and measurement of the rotational speed are shown in [18, 19].)

20.4.1 Transient-State Control of Flagellar Motor Rotational Speed

Figure 20.5 is the time-series data of the transient-state control of the Na^+-driven flagellar motor rotational speed in single *E. coli* cell by the local environmental control technique based on nano/micro dual pipettes. The shaded area in Fig. 20.5 represents the terms for which the Na^+-containing solution was discharged from the nanopipette. This result shows that the rotational speed of Na^+-driven flagellar motor was iteratively increased/decreased in a near-pulse shape, as shown in Fig. 20.2, by switching the local discharge between Na^+-containing and Na^+-free solutions with nano/micro dual pipettes.

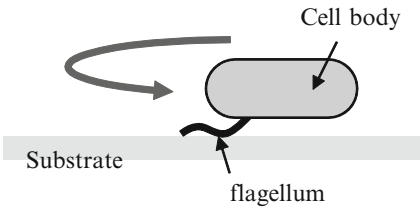

Fig. 20.4 Schematic of the tethered cell

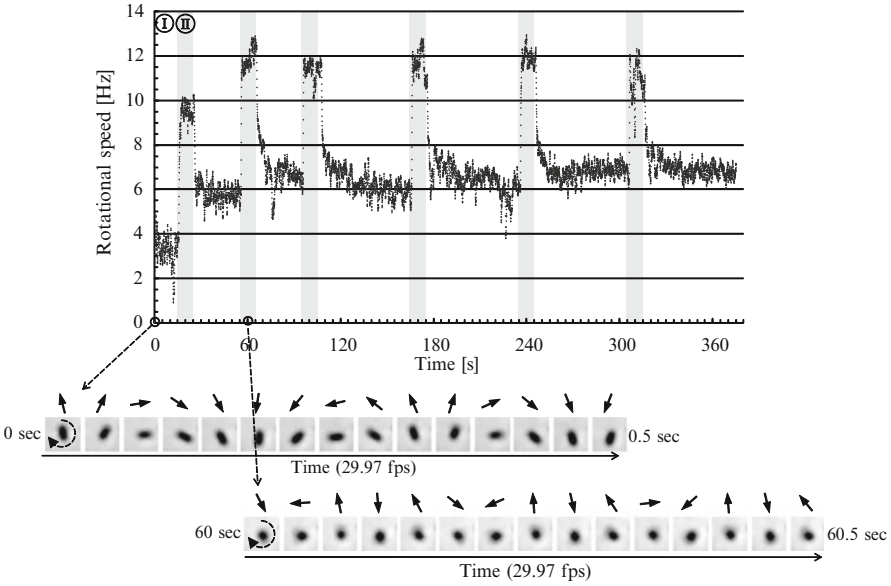

Fig. 20.5 Transient-state control of the Na^+-driven flagellar motor rotational speed by switching the discharges. (I) The terms for which the Na^+-free solution was discharged from the micropipette. (II) The terms for which the Na^+-containing solution was discharged from the nanopipette (reprinted from [18] with permission)

20.4.2 Steady-State Control of Flagellar Motor Rotational Speed

Figure 20.6a/b is the time-series data of the control/steady-state control of the Na^+-driven flagellar motor rotational speed in single *E. coli* cell by the local environmental control technique based on nano/micro dual pipettes. In the control, the discharge of Na^+ ions was continued for a long period at 20 V, and the rotational speed got into ∼6.9 Hz. In Fig. 20.6b, when the Na^+-containing and Na^+-free solutions were discharged simultaneously, the rotational speed was increased from the base level ∼5.0 to ∼6.3 Hz. It was slightly slower than the rotational speed in the control (∼6.9 Hz, in Fig. 20.6a). After multiplying the applied DC voltage of the micropipette, the rotational speed slightly decreased to ∼5.6 Hz. It was still faster than the base level (∼5.0 Hz), because the Na^+-containing solution was still being discharged. This result shows that the steady state of the rotational speed of the Na^+-driven flagellar motor was controlled by simultaneous local discharges of the Na^+-containing and Na^+-free solutions with controlling the discharging velocities independently.

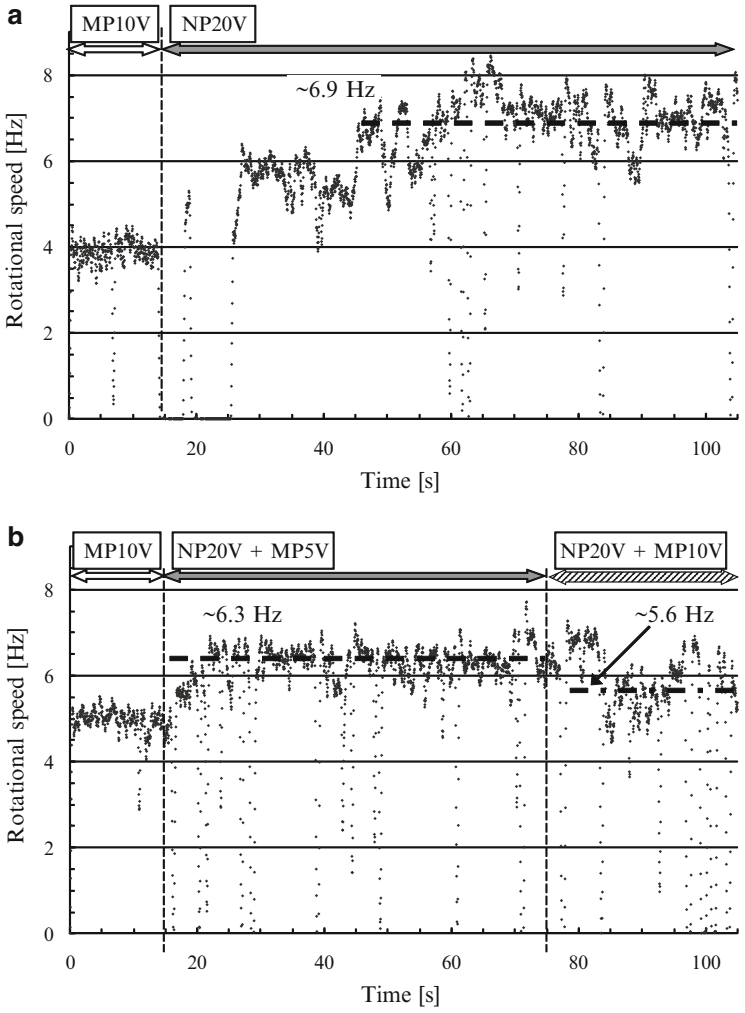

Fig. 20.6 (**a**) Control and (**b**) steady-state control of the rotational speed of Na^+-driven flagellar motor by simultaneous discharges with changing the applied voltages independently. *NP* nanopipette (Na^+-containing), *MP* micropipette (Na^+-free) (reprinted from [19] with permission)

20.5 Evaluation of Control Performance of Local Environmental Control Technique Based on Nano/Micro Dual Pipettes

For the evaluation of the control performance of the local environmental control technique based on nano/micro dual pipettes, the rotational torque generated by the flagellar motor in Fig. 20.6 was estimated as an example. The rotating cell body was

simplified as the rotating cylinder. Under this condition, the rotational torque (T) is calculated by the equations

$$T = \gamma\omega \tag{20.2}$$

and

$$\gamma = \frac{\frac{1}{3}\pi\eta L^3}{\ln(L/2r) - 0.66}, \tag{20.3}$$

where γ is the rotational drag coefficient, ω is the rotational speed, η is the viscosity of the environmental solution, L is the length of the cylinder, and r is the radius of the cylinder [29]. The rotational torque was calculated by (20.2) and (20.3) where η is 0.001 Pa s (pure water), L is 3 μm, and r is 0.5 μm.

The results of the rotational torque calculation were $\sim 2.8 \times 10^3$/$\sim 2.5 \times 10^3$/$\sim 2.3 \times 10^3$ pN·nm at ∼6.9 /∼6.3 /∼5.6 Hz, respectively. This shows that the rotational torque of the flagellar motor could be controlled in 10^2 pN·nm orders by the local environmental control technique based on nano/micro dual pipettes. This value is hundredth part of the maximum rotational torque of the magnetic-actuated artificial flagella reported by Zhang et al. [30]. It can be concluded that the driving force of the flagellar motor can be controlled very finely.

20.6 Conclusions

In this chapter, we introduced the local environmental control technique based on nano/micro dual pipettes for bacterial flagellar motor control by dynamic and arbitrary changes in the local reagents/ions concentrations. We showed the transient-state control of the rotational speed, i.e., the driving force, of the Na^+-driven flagellar motor in single *E. coli* cell by switching local discharges between Na^+-containing and -free solutions. Then we demonstrated steady-state control by simultaneous local discharges of the solutions with controlling discharge velocities independently. And, we found that the rotational torque of the flagellar motor could be controlled in 10^2 pN·nm orders by the local environmental control technique based on nano/micro dual pipettes.

In addition, the local environmental control technique based on nano/micro dual pipettes can be used for any other reagents/ions. The dynamic and arbitrary controlled change in the local reagents/ions concentrations will be useful as a chemical stimulation or a trigger to analyze or control the biological samples, such as DNA [27], ion channel, protein, and neuronal cell [31].

References

1. Cavalcanti A, Shirinzadeh B, Kretly LC (2008) Medical nanorobotics for diabetes control. Nanomedicine 4(2):127–138. doi:10.1016/j.nano.2008.03.001
2. Cavalcanti A, Shirinzadeh B, Fukuda T, Ikeda S (2009) Nanorobot for brain aneurysm. Int J Robot Res 28(4):558–570. doi:10.1177/0278364908097586
3. Martel S, Mohammadi M, Felfoul O, Lu Z, Pouponneau P (2009) Flagellated magnetotactic bacteria as controlled mri-trackable propulsion and steering systems for medical nanorobots operating in the human microvasculature. Int J Robot Res 28(4):571–582. doi:10.1177/0278364908100924
4. Martel S, Felfoul O, Mathieu JB, Chanu A, Tamaz S, Mohammadi M, Mankiewicz M, Tabatabaei N (2009) MRI-based medical nanorobotic platform for the control of magnetic nanoparticles and flagellated bacteria for target interventions in human capillaries. Int J Robot Res 28(9):1169–1182. doi:10.1177/0278364908104855
5. Patel GM, Patel GC, Patel RB, Patel JK, Patel M (2006) Nanorobot: a versatile tool in nanomedicine. J Drug Target 14(2):63–67. doi:10.1080/10611860600612862
6. LaVan DA, McGuire T, Langer R (2003) Small-scale systems for in vivo drug delivery. Nat Biotechnol 21(10):1184–1191. doi:10.1038/nbt876
7. Hede S, Huilgol N (2006) Nano: the new nemesis of cancer. J Cancer Res Ther 2(4):186–195. doi:10.4103/0973-1482.29829
8. Osada Y, Gong JP (2009) Nano-biomachine from actin and myosin gels. Polym Sci A 51(6):689–700. doi:10.1134/S0965545X09060145
9. Hiyama S, Moritani Y, Gojo R, Takeuchi S, Sutoh K (2010) Biomolecular-motor-based autonomous delivery of lipid vesicles as nano- or microscale reactors on a chip. Lab Chip 10(20):2741–2748. doi:10.1039/C004615A
10. Soong RK, Bachand GD, Neves HP, Olkhovets AG, Craighead HG, Montemagno CD (2000) Powering an inorganic nanodevice with a biomolecular motor. Science 290(5496):1555–1558. doi:10.1126/science.290.5496.1555
11. Akiyama Y, Iwabuchi K, Furukawa Y, Morishima K (2009) Long-term and room temperature operable bioactuator powered by insect dorsal vessel tissue. Lab Chip 9(1):140–144. doi:10.1039/B809299K
12. Darnton N, Turner L, Breuer K, Berg HC (2004) Moving fluid with bacterial carpets. Biophys J 86(3):1863–1870. doi:10.1016/S0006-3495(04)74253-8
13. Behkam B, Sitti M (2008) Effect of quantity and configuration of attached bacteria on bacterial propulsion of microbeads. Appl Phys Lett 93:223901. doi:10.1063/1.3040318
14. Weibel DB, Garstecki P, Ryan D, DiLuzio WR, Mayer M, Seto JE, Whitesides GM (2005) Microoxen: microorganisms to move microscale loads. Proc Natl Acad Sci USA 102(34):11963–11967. doi:10.1073/pnas.0505481102
15. Homma M, Oota H, Kojima S, Kawagishi I, Imae Y (1996) Chemotactic responses to an attractant and a repellent by the polar and lateral flagellar systems of Vibrio alginolyticus. Microbiology 142:2777–2783. doi:10.1099/13500872-142-10-2777
16. Hyakutake A, Kawagishi I, Homma M (2004) Motility- and chemotaxis-related genes of *Vibrio* spp. and their involvement in virulence. Jpn J Bacteriol 59(2):403–414 (in Japanese)
17. Walter JM, Greenfield D, Bustamante C, Liphardt J (2007) Light-powering Escherichia coli with proteorhodopsin. Proc Natl Acad Sci USA 104(7):2408–2412. doi:10.1073/pnas.0611035104
18. Nogawa K, Kojima M, Nakajima M, Kojima S, Homma M, Fukuda T (2009) Rotational speed control of Na^{+}-driven flagellar motor by dual pipettes. IEEE Trans Nanobiosci 8(4):341–348. doi:10.1109/TNB.2009.2035281
19. Nogawa K, Kojima M, Nakajima M, Homma M, Fukuda T (2011) Driving force control of flagellar motor by local environmental control system with nano/micro dual pipettes. J Robot Soc Jpn 29(5):463–469 (in Japanese)

20. Macnab R (1996) Flagella and motility. In: Neidhardt FC, Curtiss R, Ingraham JL, Lin ECC, Low KB, Magasanik B, Reznikoff WS, Riley M, Schaechter M, Umbarger HE (eds) Escherichia coli and Salmonella: cellular and molecular. American Society for Microbiology, Washington, DC, pp 123–145
21. Yorimitsu T, Homma M (2001) Na^+-driven flagellar motor of Vibrio. Biochim Biophys Acta 1505(1):82–93. doi:10.1016/S0005-2728(00)00279-6
22. Aldridge P, Hughes KT (2002) Regulation of flagellar assembly. Curr Opin Microbiol 5(2):160–165. doi:10.1016/S1369-5274(02)00302-8
23. Kojima S, Blair DF (2004) The bacterial flagellar motor: structure and function of a complex molecular machine. Int Rev Cytol 233:93–134. doi:10.1016/S0074-7696(04)33003-2
24. Lo CJ, Leake MC, Pilizota T, Berry RM (2007) Nonequivalence of membrane voltage and iongradient as driving forces for the bacterial flagellar motor at low load. Biophys J 93(1):294–302. doi:10.1529/biophysj.106.095265
25. Fung DC, Berg HC (1995) Powering the flagellar motor of Escherichia coli with an external voltage source. Nature 375(6534):809–812. doi:10.1038/375809a0
26. Magariyama Y, Sugiyama S, Muramoto K, Kawagishi I, Imae Y, Kudo S (1995) Simultaneous measurement of bacterial flagellar rotation rate and swimming speed. Biophys J 69(5):2154–2162. doi:10.1016/S0006-3495(95)80089-5
27. Piper JD, Li C, Lo CJ, Berry R, Korchev Y, Ying L, Klenerman D (2008) Characterization and application of controllable local chemical changes produced by reagent delivery from a nanopipet. J Am Chem Soc 130(31):10386–10393. doi:10.1021/ja8022253
28. Silverman M, Simon M (1974) Flagellar rotation and the mechanism of bacterial motility. Nature 249(452):73–74. doi:10.1038/249073a0
29. Howard J (2001) Mechanics of motor proteins and the cytoskeleton. Sinauer Associates, Sunderland, pp 106–107
30. Zhang L, Abbott JJ, Dong L, Peyer KE, Kratochvil BE, Zhang H, Bergeles C, Nelson BJ (2009) Characterizing the swimming properties of artificial bacterial flagella. Nano Lett 9(10):3663–3667. doi:10.1021/nl901869j
31. Sánchez D, Anand U, Gorelik J, Benham CD, Bountra C, Lab M, Klenerman D, Birch R, Anand P, Korchev Y (2007) Localized and non-contact mechanical stimulation of dorsal root ganglion sensory neurons using scanning ion conductance microscopy. J Neurosci Methods 159(1):26–34. doi:10.1016/j.jneumeth.2006.06.018

Chapter 21
Protein-Based Nanoscale Actuation

Gaurav Sharma, Atul Dubey, and Constantinos Mavroidis

Abstract This chapter discusses protein-based nanoscale actuation mechanisms with two illustrative examples, the viral protein linear nanoActuator and the GCN4 peptide nanoActuator. The VPL peptide is based on the conformation change mechanism of envelope glycoprotein of naturally occurring retroviruses. The GCN4 is an artificial design based on two α-helical coils. Structural features, stability, and optimal design considerations are described in detail. Computational methods are applied to gain knowledge about a given molecule and its suitability to function as a nanoActuator.

21.1 Introduction

Many new age engineering applications seek devices that work at the nano scale. Modern day discoveries such as that of carbon nanotubes with their associated applications drive the initiative from macro to nanoscale devices. Nanodevices based on biological systems like proteins promise to be small, fast, and energy efficient [1, 2]. For specific applications, engineers want to develop nano-scale

G. Sharma
Battelle Memorial Institute, 505 King Ave, Columbus, OH 43201, USA
e-mail: sharmag@battelle.org

A. Dubey
Department of Chemical and Biochemical Engineering, Rutgers University,
98 Brett Road, Piscataway, NJ 08854, USA
e-mail: atuldubey@gmail.com

C. Mavroidis (✉)
Department of Mechanical and Industrial Engineering, Northeastern University, 334 Snell Engineering Center, 360 Huntington Avenue, Boston, MA 02115, USA
e-mail: mavro@coe.neu.edu

C. Mavroidis and A. Ferreira (eds.), *Nanorobotics: Current Approaches and Techniques*, DOI 10.1007/978-1-4614-2119-1_21,
© Springer Science+Business Media New York 2013

actuators [3], joints, motors, and other machine components which could either be single-molecule or macromolecular.

With advances in imaging techniques in the recent decades, it has been possible to observe the functioning of subcellular molecular machines in living organisms. These complex machines are optimized to carry out specific tasks such as moving cellular cargo, oxidizing high-energy molecules, etc. Such devices can be used in an artificial environment by applying appropriate stimuli. A bottom-up approach of assembly can also be applied [4–10].

Molecular machines can be protein-based, DNA-based, or chemical machines. They have a different operating environments, force and displacement capabilities, and fuel requirements. Hence all of them figure in a molecular part-list and can be utilized when requirements are specific to them. For example, protein-based ATP motors require protons or high energy molecules, whereas DNA-based machines require DNA strands as fuel. Both these machines can be used to produce rotary motion, although in different environmental circumstances. There is a need to find nanoscale equivalents of robot parts such as actuators, links, end-effectors, sensors, etc. In the first part of this review, a protein-based linear actuator, called the viral protein linear (VPL) actuator, is discussed. The second part presents another molecular actuator which is based on a coiled-coil protein and has been engineered to undergo pH-dependent reversible actuation.

21.2 The VPL nanoActuator

The idea of VPL originates from the modus operandi of a family of retroviruses [11]. The role of envelope glycoproteins (surface proteins) of various retroviruses in the process of membrane fusion has been investigated and understood over the years. Such viruses infect their target cells by the process of membrane fusion. Membrane fusion is necessary for a large number of diverse processes in biology such as protein trafficking, protein secretion, fertilization, viral invasion, and neurotransmission. The mechanism is best understood among enveloped viruses such as the influenza virus [12–15]. Specialized viral proteins are required to promote membrane fusion—a process which is otherwise very slow. In many cases, these membrane-fusion proteins also serve as agents that promote the binding of the virus onto the cell surface receptors. In the influenza virus, a protein called hemagglutinin (HA) mediates both the binding of the virus to the cell surface and the subsequent fusion of viral and cellular membranes. The receptor binding subunit of HA is termed HA1, while the fusogenic subunit is denoted as HA2. Figure 21.1 shows a schematic of the influenza virus.

HA1/HA2 complex consists of the disulfide bonded HA1 and HA2 peptides. Each HA monomer is synthesized as a fusion-incompetent precursor polypeptide known as HA0, which undergoes proteolytic cleavage to give rise to the two chains [16, 17]. The two subunits have different functions. For example, in the case of the human immunodeficiency virus (HIV), HIV 1, the precursor glycoprotein is

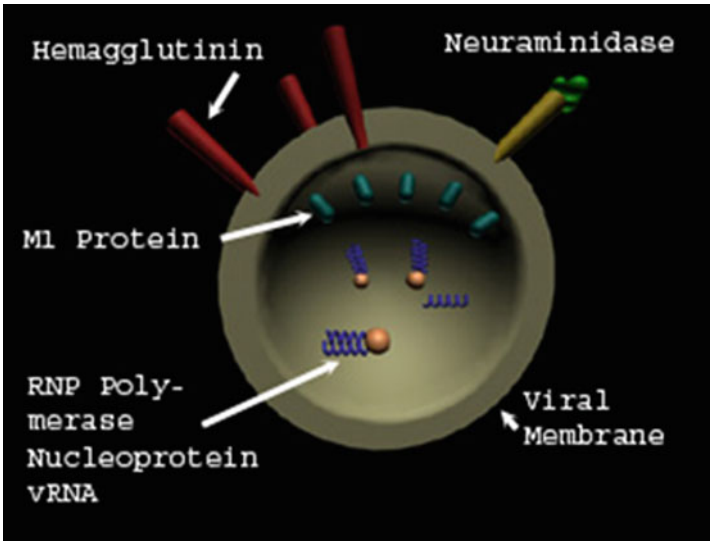

Fig. 21.1 A schematic of the influenza virus. Hemagglutinin (HA) polypeptides lie on the surface of the virus, while viral RNA resides inside. HA has subunits that attach to cells and then facilitate membrane fusion in order to infect the cell (reprinted with permission from Springer Publishers)

gp160, which is proteolytically cleaved into gp120 and gp41 subunits. The gp120 is the surface subunit and the gp41 is the transmembrane (TM) subunit. The surface subunit serves to recognize the cell to be infected when it comes in the vicinity of the virus with the help of receptors located on the cell surface. The gp41 mediates membrane fusion between the viral and cellular membranes. It has been found that gp41 and the corresponding TM subunits in other (above listed) viruses acquire an alpha-helical conformation when the virus is in its active or fusogenic state. The structure is like a hairpin composed of three coils, having one C terminal (carboxy-end) and the other N terminal (amino-end). The carboxy regions pack in an antiparallel manner around the three hydrophobic amino ends as shown in Fig. 21.3.

The native HA1/HA2 complex in the viral envelope is fusion-inactive. The cell-surface receptor needed for the virus to bind onto the cell is known as sialic acid. HA1 binds to this receptor and hence serves the purpose of bringing the virus and cell together. Upon binding with sialic acid, the virus is endocytosed by the cell (Fig. 21.2). HA remains dormant until the endosome begins to mature, and the pH in the HA surroundings drops to a value of about 5.

At this pH, there is a conformational change in HA2 domain of HA that induces the viral membrane to fuse with the cellular, endosomal membrane, thereby permitting the nucleocapsid of the virus to be deposited into the cytoplasm of the cell. Hence it can be inferred that the acidic pH acts as the physiological trigger for the HA conformational change. Since the low pH also activates membrane fusion, the low pH conformation of HA is also known as fusogenic conformation.

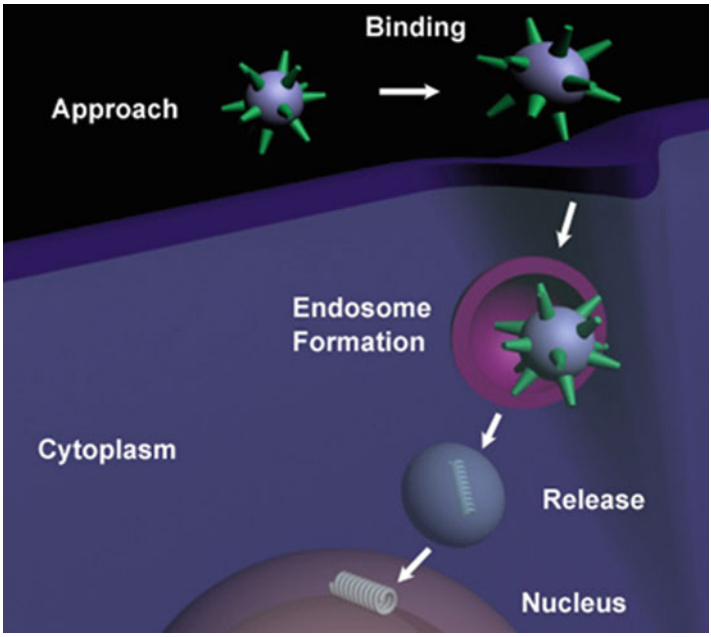

Fig. 21.2 Various stages in influenza virus infection. The virus in endocytosed by the cell and an endosome is formed, wherein a conformational change of interest occurs (reprinted with permission from Springer Publishers)

The crystal structures of HA in both the native and the fusogenic conformations are known [18–21]. As stated above, the HA1 only serves the purpose of cellular recognition and binding to the cell surface receptor and is not of much interest as a nanoActuator. The HA2 subunit, however, is then responsible for the membrane fusion activity. In the native state, the central region of HA2 folds as a helical hairpin-like monomeric structure (Fig. 21.3a). The monomer consists of two segments A and B. At the N-terminal is the fusion peptide contained in segment A (residues 1–25) followed by short antiparallel β-sheet (residues 26–37). The outer arm of the hairpin is a small α-helix (residues 38–53) which is connected to a long α-helix (residues 82–125) by a loop region (residues 54–81). The loop region converts into a relatively more rigid α-helix and forms a continuation of the long α-helix as shown in Fig. 21.3b. The short α-helix is thus translated upward along with the fusion peptide (not shown). Figure 21.3c shows the native state of the HA2 trimer. The remaining structure other than the helices (bottom) is the fusion peptide from the N-terminal and the other smaller secondary structures following the long helices. The helical hairpins open up to form an extended three-stranded coiled-coil structure with the previously loop regions now helical. Such coiled-coil motif is found in many other proteins such as the leucine zipper domain of some transcription factors. The α-helices are wrapped around each other with a left-handed superhelical twist.

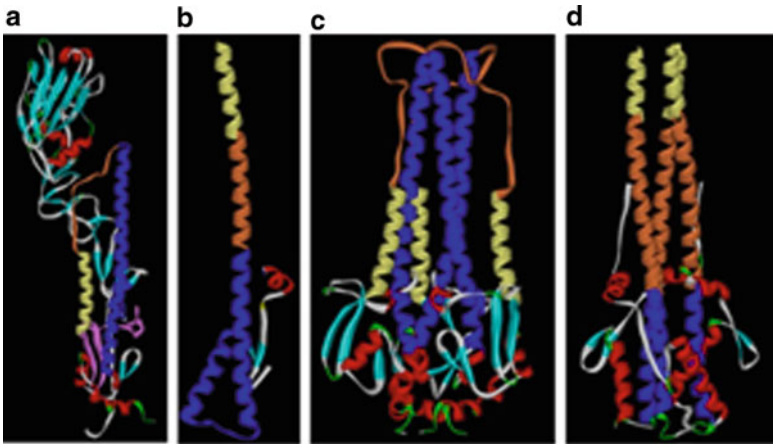

Fig. 21.3 (**a**) Hairpin-like structure of central HA2 native state monomer. (**b**) HA2 chains A and B in fusogenic states. (**c**) The native state of the HA2 trimer. (**d**) Fusogenic state of the HA2 trimer (reprinted with permission from Springer Publishers)

Two more such subunits (consisting of two segments each) are present to form a trimer together. The long α-helices from each subunit in the native state form a well-known structure called the three-stranded coiled-coil system. Coiled coils can be visualized as an intertwined rope of three interacting helices. As is visible in Fig. 21.3c, d, in addition to the helical domains, there are other regions—small helices, β-sheets, turns, and random loop regions. The blue regions in the native stage in Fig. 21.3c are triple-stranded coiled coils wound against each other. They are connected to smaller helices (yellow) in the HA2 domain by loop regions shown in orange. The smaller helices connect to the fusion peptide (residue numbers 1–25). After attachment and pH drop, the orange loop regions convert into extended coiled coils effectively, extending the blue coils and moving the fusion peptide by about 10nm [22].

Coiled-coil motifs contain hydrophobic and hydrophilic amino acids in a repeating heptad pattern (positions a through g) as shown in Figs. 21.4 and 21.5. Looking down the axis of the helix, hydrophobic residues tend to occur at the positions a and d of the heptad repeat and these residues form the interface between the helices. It is believed that HA folds into its thermodynamically most stable state at neutral pH, known as its native state. But at a lower pH, the fusogenic state becomes thermodynamically more feasible and hence the protein changes conformation in order to achieve it [23]. Another model that is widely accepted suggests that the native state is a metastable state that can be disturbed by any agent, not only pH. It has been observed that heat can also produce this conformational change at neutral pH and so does a denaturant such as urea [23].

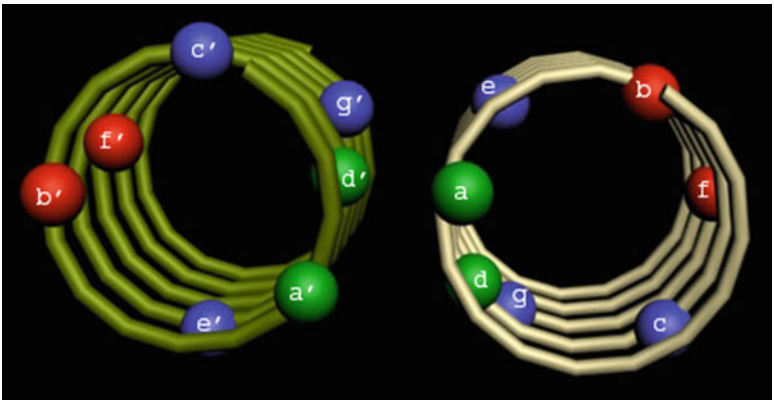

Fig. 21.4 Two helices of a coiled-coil system. The seven positions (*a*–*e*) denote locations of hydrophobic/hydrophilic residues. Hydrophobic residues tend to occur on the inside positions *a* and *d*, whereas the hydrophilic residues reside in other positions (reprinted with permission from Springer Publishers)

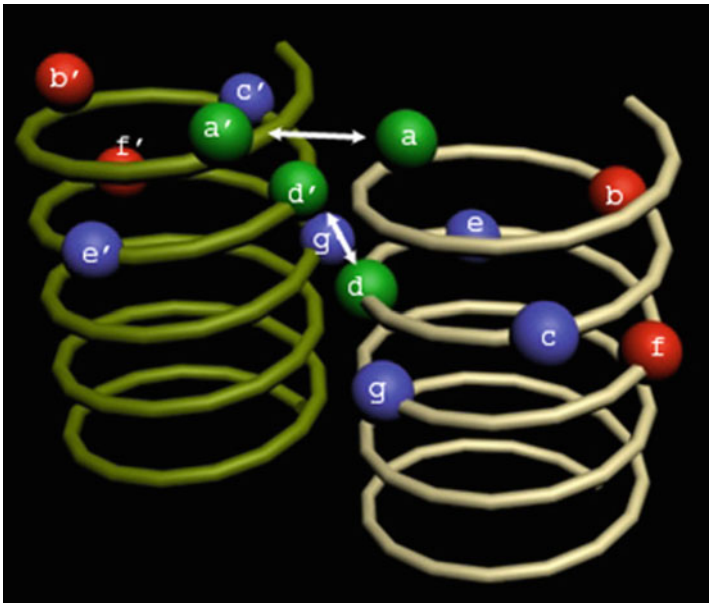

Fig. 21.5 Packing of two helices of a coiled-coil system. The hydrophobic residues in positions a–a′ and d–d′ of each chain interact with each other to stabilize the coiled-coil system (reprinted with permission from Springer Publishers)

In addition to influenza, there are other viruses and their respective peptides that can be candidates for a VPL-like nanoActuator, such as the HIV 1 peptide gp41 [24], the human respiratory syncytial virus (HRSV) protein subunit F1 [25], the simian

immunodeficiency virus (SIV) protein gp41 [26], the Human T-cell leukemia virus type 1, protein gp21 [27], the simian parainfluenza virus peptide unit SV5 [28], and the Ebola virus protein gp2 [29]. Each of these peptides can result in a different actuator that can have different properties such as weight, volume, range of motion, and force generation capabilities. However, the principle of actuation is the same. Studies have shown [15, 30, 31] that the common characteristic in these viruses is the structure of a portion of the envelope glycoprotein and the mode of infection.

21.2.1 Molecular Dynamics Simulations of VPL nanoActuator

For the computational study, a fragment from the VPL segment, the loop36, was chosen due to its established role in the conformational change [22]. The large conformational change was simulated using the targeted molecular dynamics (TMD) technique [32, 33] using implicit solvent calculations. In order to simulate the effect of environmental pH change on the VPL motor protein [34], acidic amino acids were protonated. In the TMD simulations, the protein was allowed to undergo a transition from one known state to another. This is a useful approach to ensure the feasibility of the conformational change and to get an idea of the magnitude of the energy change involved. The VPL nanoActuator works in a solution where there are protons bombarding the protein due to a reduction in the solution pH. This allows acidic amino acids in the protein to accept the protons on their negatively charged sites, and hence get protonated. Protonation changes the energy balance of the solvent–protein system and can create conditions that promote a conformational change. Low pH simulations on the small fragment loop36 were performed to study the effect on the protein conformation and the way it interacts energetically with its surroundings.

In addition to the TMD analyses, classical molecular dynamics approaches were performed to quantify some other aspects such as helicity and free energy of the peptides. In order to be able to perform classical unbiased MD simulations in a realistic time scale, it is important to energize the system by using high temperatures. The open and closed structures were taken from the protein data bank (PDB) with the open state as the target state and the closed state as the starting point [35]. The simulations were performed using an implicit solvation model known as Effective Energy Function for proteins EEF1 [36]. Loop36 is a 36-residue long peptide of the VPL protein that forms a hinge region of the viral protein joining the two α-helical regions of each monomer [21, 22]. An initial state as obtained from PDB [37] file 1HGF at pH of about 7.0, loop36 consists of a 15-residue long α-helical part with the remaining fragment in a random and flabby form (Fig. 21.6). It is located in the segment B of the influenza hemagglutinin protein sequence from residues 54 to 89. It has been recognized as being critical for a pH-dependent conformational change [22, 23]. The loop36 wild-type (naturally occurring) sequence is as follows:

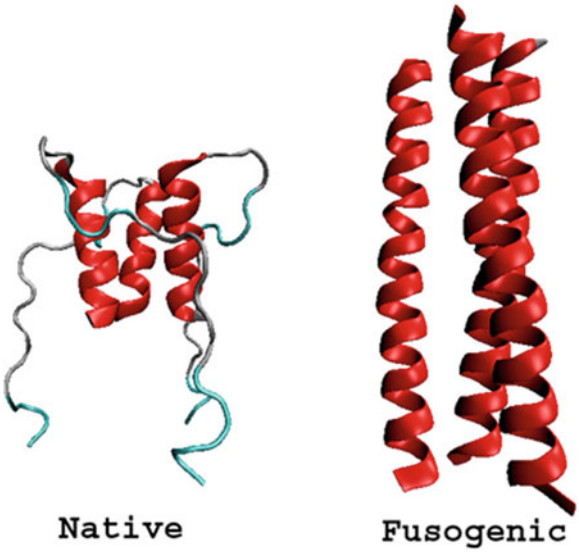

Fig. 21.6 The peptide loop36 in the initial and final states of the conformational change. Coiled coils are helical and the random loop regions are hanging from them. The random loop regions rise and convert into α-helical coiled coils upon activation (reprinted with permission from Springer Publishers)

ARG VAL ILE GLU LYS THR ASN GLU LYS PHE HIS GLN ILE GLU LYS GLU PHE SER GLU VAL GLU GLY ARG ILE GLN ASP LEU GLU LYS TYR VAL GLU ASP THR LYS ILE

The initial and final states of loop36 as obtained by the crystal structures 1HGF (pH ∼7.0) and 1HTM (pH ∼5.0) from PDB are shown in Fig. 21.6.

In order to simulate low pH, the biochemical response of certain amino acids to the acidic conditions was considered. Some amino acids are acidic in nature, some basic, and some neutral; and they get protonated at different pH values. Out of the 20 constituent types of amino acids, glutamic acid (GLU), aspartic acid (ASP), and histidine (HIS) are in their unprotonated states at neutral pH (7.0). There is only one histidine residue in loop36, whereas there are eight glutamic acid residues and two aspartic acid residues which make a large part of loop36. Hence, overall, there were 11 residues out of the 36 that were protonated.

Figure 21.7 shows the visual molecular dynamics (VMD) [38] rendered transition of a loop36 monomer from initial (closed) state to an open (fusogenic) state. The entire transition is achieved in 66 ps when using TMD, while it is not achievable in 30 ns using traditional MD techniques. As seen in the figure, after 20 ps the loop regions of the peptide are halfway open and after 50 ps they are completely opened but have not attained an α-helical conformation.

The deviation of the final state from the initial state of the monomer in Fig. 21.7 can be seen in the root mean square deviation (RMSD) from the open state. Results are depicted in Fig. 21.8 and values of RMSD indicate that the open and close conformation differ by approximately 19 Å. The rate of opening of the monomer can be estimated by the slope of this curve, which in this case is 0.2 Å/ps. It must be kept in mind that to have an estimation of the real rate of opening, this value should

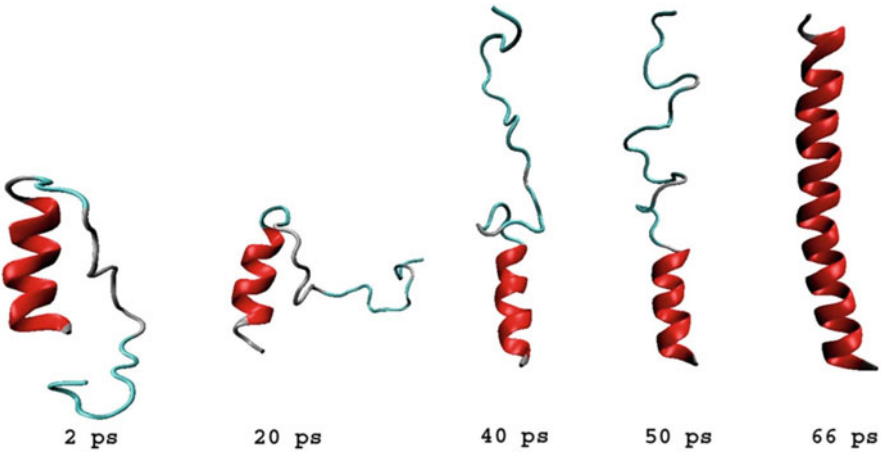

Fig. 21.7 Transition of a loop36 monomer from native to fusogenic state during a TMD simulation (reprinted with permission from Springer Publishers)

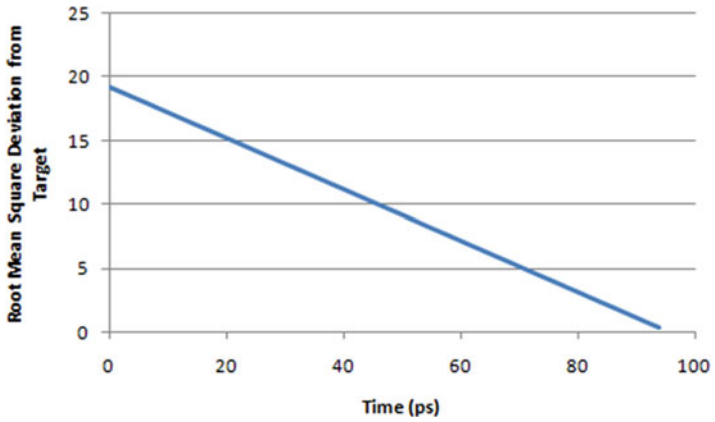

Fig. 21.8 RMSD from the final state is an indicator of the rate of opening of the peptide. In the beginning the RMSD has a maximum value, which decreases linearly with time as the open state is achieved (reprinted with permission from Springer Publishers)

be rescaled to account for the increase in speed of the process given by TMD. Thus, the real rate of opening is approximately 3.5 Å/μs.

21.2.2 Optimal Design of VPL nanoActuator

Mutations in a protein can be made by replacing one or more constituent amino acids with different amino acids. The structure and properties of a protein change when

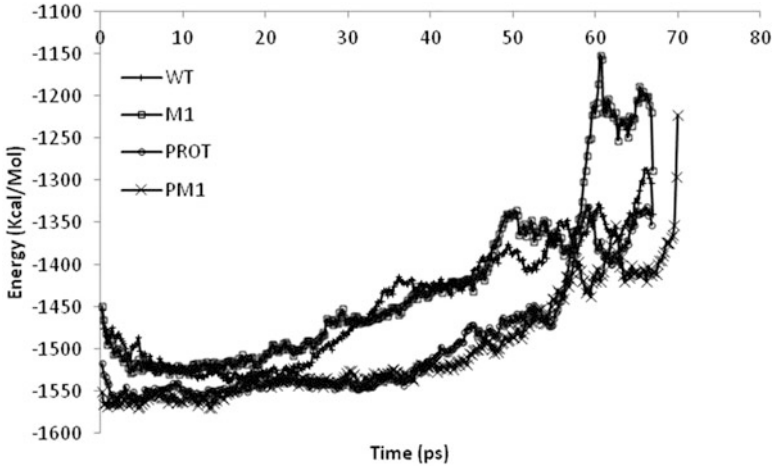

Fig. 21.9 Comparison of potential energy paths of four types of loop36 monomers. (1) Wild type WT (the protein in this state does not have any mutation or protonation), (2) mutated type M1 (in this state), GLY (glycine) is replaced by ALA (alanine), (3) protonated type PROT (GLU (glutamic acid)) is replaced by protonated GLU, ASP (aspartic acid) by protonated ASP, HIS (histidine) replaced by doubly protonated histidine, and (4) protonated and mutated type PM1 (in this state, the protein has both protonation and mutation). The low pH structures follow lower energy pathways than the neutral pH structures, although all structures eventually achieve similar end-state energy values (reprinted with permission from Springer Publishers)

they undergo a mutation. It is therefore possible to design a protein according to specific requirements; for example, if a high hydrophobicity is desired, hydrophobic amino acids should replace some of the residues.

The loop36 peptide contains one glycine (GLY) residue which is known as a helix-breaker amino acid because its side chain is simply one hydrogen atom. In experimental studies, it is observed that replacing this residue by an alanine (ALA) results in better α-helix formation [22]. In line with the experiments, in our simulations the glycine is replaced with the alanine. The GLY residue is the 22nd residue in loop36, and a mutated version of the loop36 with GLY replaced by ALA is called mutation M1. The unmutated version of the peptide is simply called the wild type (WT). GLY contains no side chain and it has no atom attached to the α-carbon (CA). On the other hand, ALA contains a simple side chain (CH3) attached to its CA atom.

The four different cases compared in this study are as follows:

1. The wild type (no mutation or protonation) guided to an open state
2. One mutation M1
3. Protonation of amino acids (with no mutations)
4. Mutation and protonation (PM1). Conformational energies of these simulations are compared in Fig. 21.9.

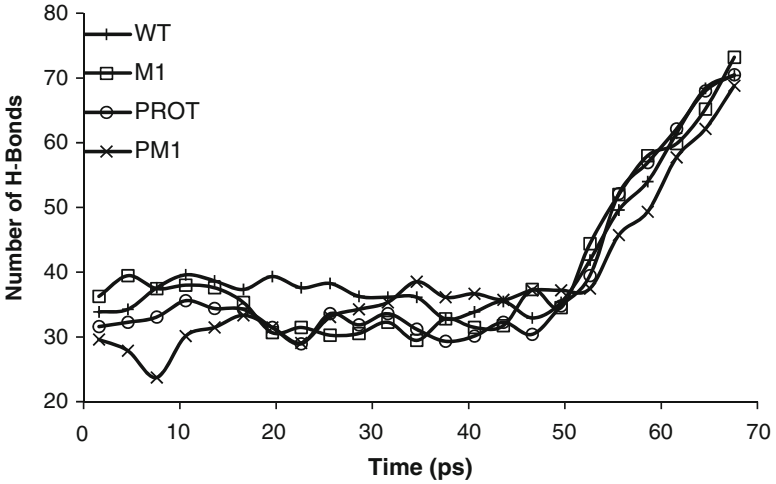

Fig. 21.10 The number of H-bonds in each of the monomer WT, M1, PROT, and PM1 modified structures varies as the open state is achieved. A moving average of 15 points (3 ps) is shown in each *curve*. The H-bonds oscillate around a constant value up to about 50 ps in each of the cases. A steep rise in the number is observed beyond this point. This region corresponds to the helix formation which results in intra-helical H-bond formation (reprinted with permission from Springer Publishers)

The intra-helical H-bonds stabilize α-helical structures. The hydrogen bonds for the loop36 conformational transition (Fig. 21.10) were found to be oscillatory in nature and hence a moving average with a period of 15 time units was chosen. Each observation was made every 0.2 ps, hence 15 points correspond to 3 ps time interval. In the initial stages of the simulation (time < 50 ps), the partial helix of loop36 is the only region with a significant number of H-bonds. The random loop region is converted into α-helix beyond 50 ps and hence a steep increase in the numbers is observed. The variation in the open state contacts, namely, the H-bonds quantitatively describe the achievement of the open state.

Even though classical methods cannot capture a large conformational change such as that exhibited in the VPL nanoActuator, they provide insight into important structural details and properties [39]. Typically higher temperatures are used to accelerate structural events in macromolecule simulations. When the protein is exposed to high temperatures, not only can it fold/unfold but it may also become denatured. Heating a protein corresponds to increasing the kinetic energy of its atoms, and this, in turn causes the molecules to vibrate more, possibly disrupting many of the hydrogen bonds and nonpolar interactions, and hence the secondary structure of the protein. The classical simulations on VPL protein were performed to understand the behavior of the VPL trimer at elevated temperatures. Knowledge of this will also help to ascertain whether there is a range of temperatures in which changes of structure such as folding or α-helix formation were initiated, before the protein denatures [33]. Figure 21.11 shows temperature effects on the VPL trimer

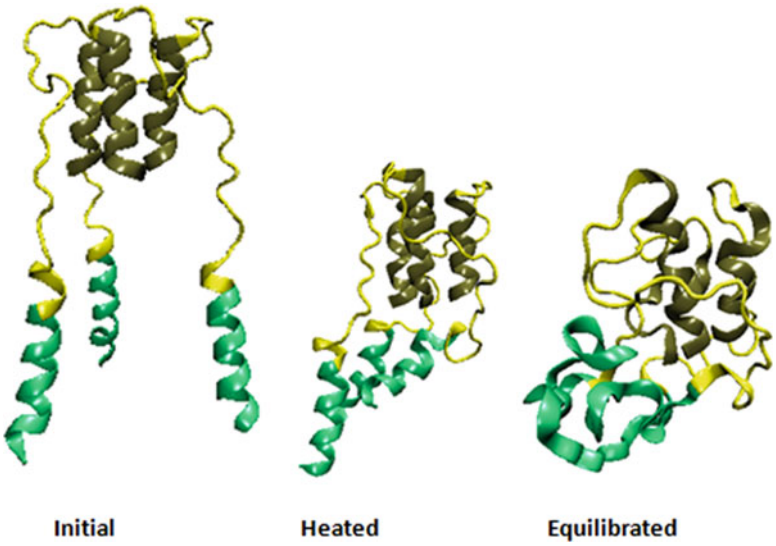

Fig. 21.11 Effect of temperature on VPL peptide. The heated state corresponds to 500°C temperature achieved in 150 ps and the equilibrated state corresponds to a constant temperature equilibration for up to 6 ns. The peptide gets denatured at this point

loop50, which is an extended loop36 trimer. In contrast to the TMD simulations in which the open state was achievable in about 60 ps, the classical simulations need approximately 4 μs to achieve the same results (Fig. 21.12) [40].

It has been shown experimentally [41] that viral membrane fusion in the hemagglutinin of influenza virus occurs at 335 K. The loop50 trimer was subjected to a range of simulated temperatures ranging from 333 to 973 K with an attempt to capture the conformational changes required for fusion and hence the performance of the VPL nanoActuator. The RMSD from the initial equilibrated state at various temperatures is shown in Fig. 21.13. The expected trend would be that increasing temperature increases the RMSD from the initial state as it allows the peptide to jump energy barriers and denatures it. This was observed in simulations at 773 and 973 K. However, the 333 K simulation indicates that the peptide has a larger difference with the initial state (larger RMSD values) in the same time frame than those at 343, 363, and 423 K. This result is in agreement with the experimental observation and suggests that larger conformational changes may take place in the temperature range of 333–343 K [22]. The extremely high temperatures 773 and 973 K result in denaturation of the peptides as seen by the H-bond data in Fig. 21.14.

The VPL undergoes a remarkably large conformational change upon a drop in pH. In order to simulate the motion of the protein, targeted and traditional MD techniques are employed. Structural changes induced by pH variations are studied by protonating a number of amino acids in the peptide sequence. The TMD results showed a clear preference to conformational transition paths at low pH values.

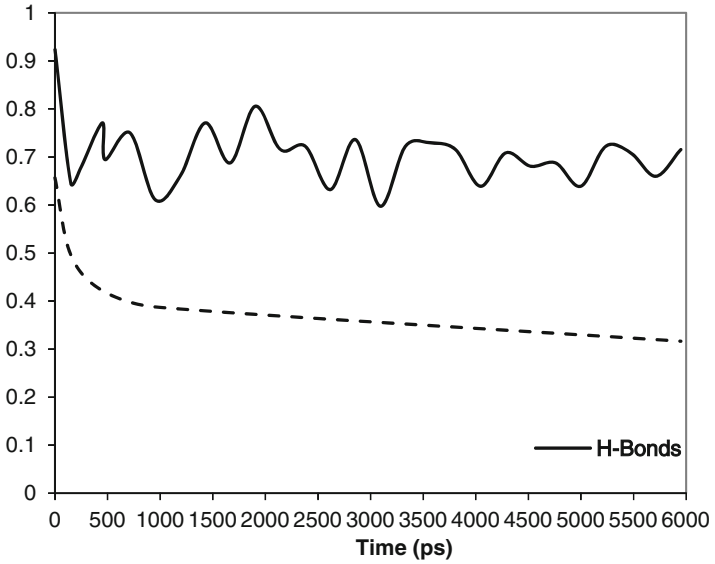

Fig. 21.12 Helicity and fraction of open state contacts for a 6-ns classical high temperature molecular dynamics simulation

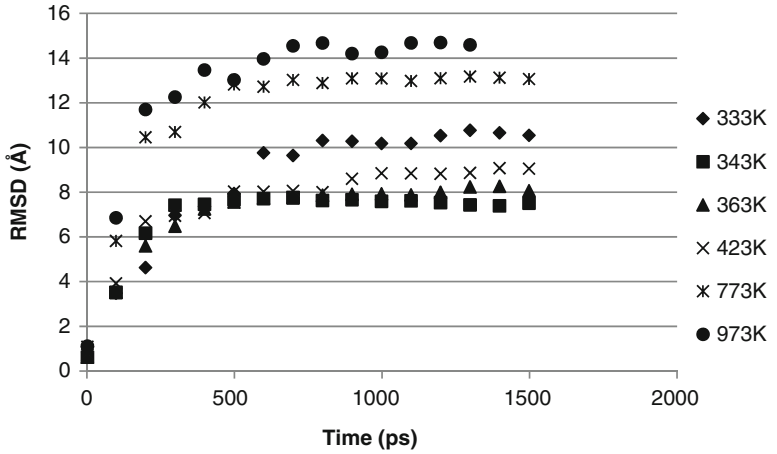

Fig. 21.13 RMSD of the loop50 trimer from its initial state for each of the simulations ranging from 333 to 973 K. Higher temperatures take the peptide further away from the initial state which indicates a larger conformational change. However, there is significant denaturation of the peptide at 773 and 973 K (reprinted with permission from Springer Publishers)

Our findings confirm that the protein forms a helical coil at acidic pH values, but it shows a coiled structure at neutral pH. It is important to mention that high temperature approaches remain a valuable tool for conformational exploration; one

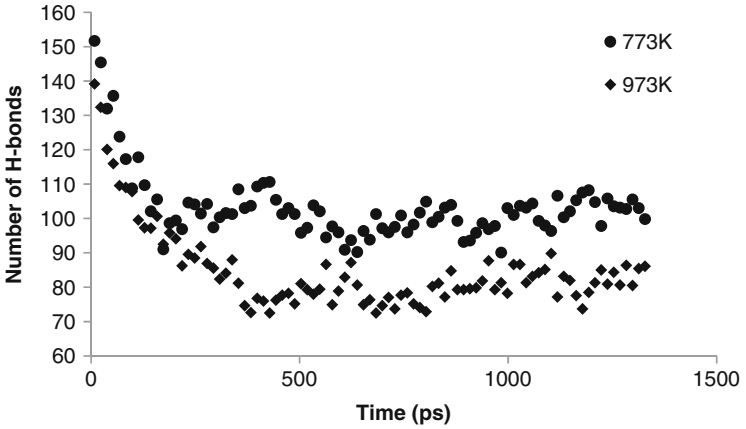

Fig. 21.14 H-bonding data for the conformational changes achieved at 773 and 973 K (reprinted with permission from Springer Publishers)

must understand, however, that torsional transition kinetics are not correct at higher temperatures. Furthermore, rescaling to lower temperatures yields only approximate results. In spite of this, our goal is to present a methodology for studying large conformational changes in nanoscale molecular systems using both targeted and traditional molecular dynamics techniques that can ultimately be extended to much longer time frames using parallel computing.

21.3 The GCN4 Peptide-Based nanoActuator

In this section, we review the molecular dynamics-aided design, biophysical characterization, and potential applications of an engineered peptide-based nanoActuator. A nanoscale length two-stranded parallel α-helical coiled-coil protein/peptide was used to create a robust nanoActuator that can be employed for nanoscale manipulation and sensing. The coiled coil is a ubiquitous protein motif made up of α-helices wrapping around each other forming a supercoil [42]. As discussed previously coiled coils are ideal candidates for protein design studies, as they represent probably the simplest secondary structure with physical properties that make them ideal for both nanoscale manipulation and measurement. The particular coiled-coil model studied here is the one corresponding to the leucine zipper (LZ) of the yeast transcriptional activator GCN4 [43]. From an engineering point of view, GCN4-LZ consists of two identical 33-residue polypeptide chains/helices and is ∼4.5nm long and ∼3nm wide. The helices wrap around each other to form approximately ¼ turn of a left-handed supercoil. The pitch of the supercoil averages 181 Å, and the average distance between the helix axes is 9.3 Å [44]. Figure 21.15 shows the enlarged view of the leucine zipper with the corresponding dimensions.

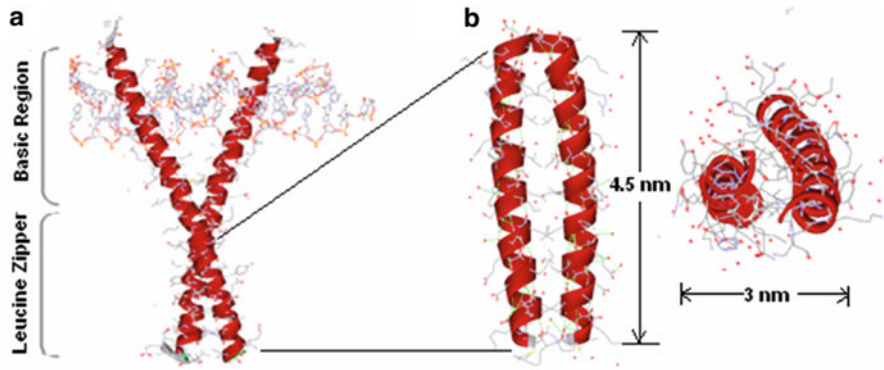

Fig. 21.15 (**a**) Coiled-coil GCN4 bound to DNA showing the basic and the leucine zipper regions; (**b**) enlarged view of the leucine zipper region showing the side (*left*) and top (*right*) views and the corresponding dimensions (reprinted from [66], with permission from Sage Publications)

The GCN4-LZ peptide was engineered to obtain an environmentally responsive nanoActuator involving the reversible movement of helices toward and away from each other. The actuation mechanism depends on the creation of like electrostatic charges along the peptide chain which forces the two coils to repel each other and move apart, thus creating an opening tweezer-like motion of the nanoActuator. This motion can be reversed by neutralizing the charges. Creating electrostatic charges depends on the differences in the ionization states of certain amino acids in the peptide chain, which in turn depends on the pH of the solvent. Of the 20 amino acid residues, histidine, glutamic acid, and asparatic acid ionize at pH range 4–7.4. Glutamic and asparatic acids are initially negatively charged at neutral pH ($\sim$7.4) and become neutral at lower pH due to the addition of a proton. On the other hand, histidine which is neutral at pH $\sim$7.4 becomes positively charged at lower pH ($\sim$4). Thus by introducing different ionizable residues along the peptide chain and varying the pH of the solvent, different nanoActuator architectures with varying degree of motion can be obtained. Figure 21.16 shows the schematic of one such nanoActuator.

21.3.1 Peptide Design and Molecular Dynamic Studies

The X-ray crystallographic structure of the native GCN4 (PDB entry: 1YSA), complexed with AP-1 yeast DNA, was obtained from the Protein Data Bank. The DNA was removed by deleting the coordinates from the PDB structure and the two peptide chains (A and B) were truncated to contain 33 residues each numbered 249–281 corresponding to the coiled-coil portion of the peptide (henceforth referred to as GCN4-LZ). Two different nanoActuator mutants (M1 and M2) were designed using GCN4-LZ as template. First, a pentaglycine tag was added at the N-terminus

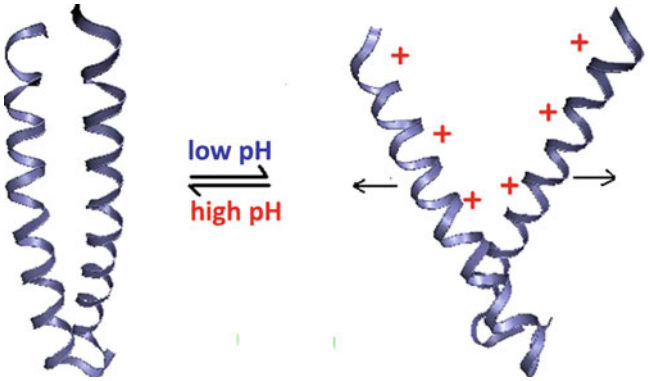

Fig. 21.16 Schematic of a nanoActuator showing the working principle; (*left*) nanoActuator in its initial closed state at neutral pH; (*right*) open configuration of the nanoActuator due to the electrostatic repulsions of the positively charged histidines residues along the chain at low pH (reprinted from [66], with permission from Sage Publications)

of GCN4-LZ; the glycine (Gly) residues were added in order to maintain the same number of residues as those in the nanoActuator mutants described below. The resulting structure is referred to as the wild-type (WT) peptide in subsequent discussions. Mutant M1 consists of a pentahistidine tag (His-tag) aligned with the α-helix at the N-terminus of the GCN4-LZ. Mutant M2 consists of five mutations (L253H, K256H, E259H, L261H, and Y265H) in each of the helical chains in addition to the His-tag. At low pH upon histidine protonation, the His-tags at the N-terminus of the mutants help in generating electrostatic repulsive forces, thereby aiding the motion of the nanoActuator. Figure 21.17 shows the architecture of different nanoActuator mutants with the position of His-tags and histidine residues shown in dark color.

The protonation states of histidine (His), glutamic acid (Glu), and asparatic acid (Asp) residues were modified appropriately to model neutral and low pH. His residues are unprotonated at neutral pH, whereas Glu and Asp are negatively charged. At low pH, His are protonated and therefore positively charged, whereas Asp and Glu are considered neutral. The nanoscale molecular dynamics (NAMD) [45] program was used to perform molecular dynamics (MD) simulations in this study. The protein was modeled with an all-atom CHARMM27 force field [46]. Please see [47, 48] for detailed information on peptide design and MD simulation parameters.

21.3.2 Wild-Type Structure and Mutant M1 Are Stable

Previous experimental [49–51] and computational studies [52–54] have shown that the wild-type GCN4-LZ is stable and does not undergo any conformational

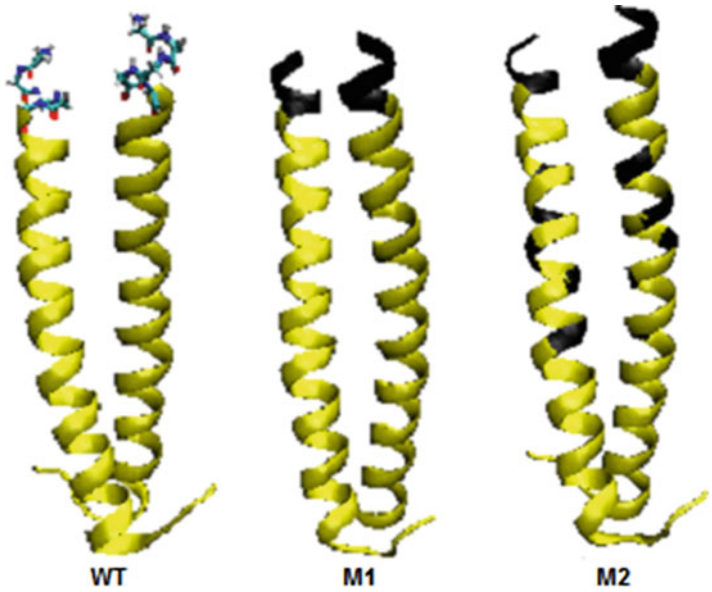

Fig. 21.17 NanoActuator mutants; wild-type (WT), mutants M1 and M2. The position of glycine tag in WT "bond" representation. Position of His-tags and histidine mutations in other mutants is shown in *dark color* (reprinted from [66], with permission from Sage Publications)

change at both neutral and low pH. In our initial setup where simulations were performed starting with the GCN4-LZ crystal structure, the backbone Cα root mean square deviation (RMSD) for residues 248–281 did indeed remain low (1.5 Å) over the course of simulation at neutral and low pH. This value agrees well with the previously reported range of RMSD values from MD simulations [53, 55, 56] of GCN4-LZ. No net opening was observed between the two helices (as measured by the distance between the His247 residues in the corresponding helices) for the WT structure at low pH; the initial and final distance between the two helices was 11 Å and 12 Å respectively (Fig. 21.18a). This behavior was expected since the wild-type GCN4 is in a very stable conformation due to various hydrophobic and electrostatic interactions as explained earlier. Also under normal physiological conditions (pH ∼7), there was no protonation of the residues and hence no extra electrostatic charges strong enough to overcome the stabilizing hydrophobic interactions were generated.

The pH-dependent actuation of mutant M1 which contains a 5-histidine tag at the N-terminus of each helical chain (see Fig. 21.17) was next evaluated at low pH. It was hypothesized that the protonation of histidine residues in the N-terminal tags at pH 4 would result in significant electrostatic repulsive forces and "push" the two helices apart, thus generating the closed-to-open mechanochemical actuation in the mutant peptide. Two atoms (Cα atoms of the His246 residues) were selected near the N-terminal of the individual chains in order to measure the opening

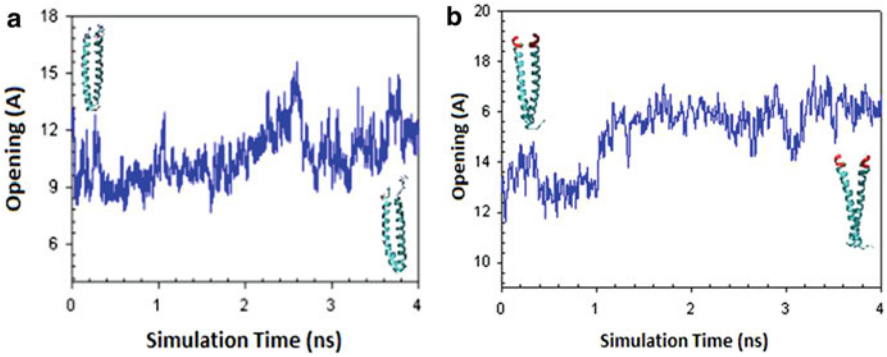

Fig. 21.18 (**a**) Opening dynamics of WT peptide at pH 4. There was no net opening observed between the two helices, the initial and final distance between the two helices was 11 Å and 12 Å, respectively. This is largely due to the hydrophobic binding and the absence of perturbation forces in the WT structure; (**b**) opening dynamics of Mutant M1. The initial separation of 13 Å between the two helices increased to 16 Å over the simulation time, thereby showing a total opening of only 3 Å which is insignificant and can be attributed to thermal fluctuations. The opening was measured between the Cα atoms of His246 residues in peptide chains. Images in *inset* are the simulation snapshots at 0 and 4 ns (reprinted from [66], with permission from Sage Publications)

between the helices and the distance between the two was plotted as a function of simulation time. Figure 21.18b shows the plot of opening dynamics of M1 during the simulation. No significant opening was observed after a 4-ns simulation; the initial distance of 13 Å between the two atoms remained constant during the first nanosecond of simulation after which it increased to 16 Å and remained stable at this separation for the rest of the simulation. The increase of 3 Å is not significant and can be attributed to atomic fluctuations or the perturbation in the histidine residues due to repulsive forces rather than the overall displacement of the two chains. This implies that the electrostatic repulsive forces generated by the positively charged N-terminal histidines are not sufficient to overcome the strong hydrophobic interactions that stabilize the coiled-coil core of M1 mutant.

21.3.3 M2 Shows pH-Dependent Conformational Change

A new mutant M2 was designed to incorporate histidine residues along the length of coiled coil in order to offset the attractive hydrophobic interactions in the core. M2 incorporates the following point mutations in addition to the N-terminal histidine tag: L253H, K256H, E259H, L261H, Y265H. M2, therefore, has a uniform distribution of His residues along the helical chain which resulted in a spatial distribution of electrostatic charges in addition to the concentrated charges from the distal His-tags. Further, the L253H, L261H, and Y265H mutations replace the hydrophobic leucine and tyrosine residues with polar His residues, thereby

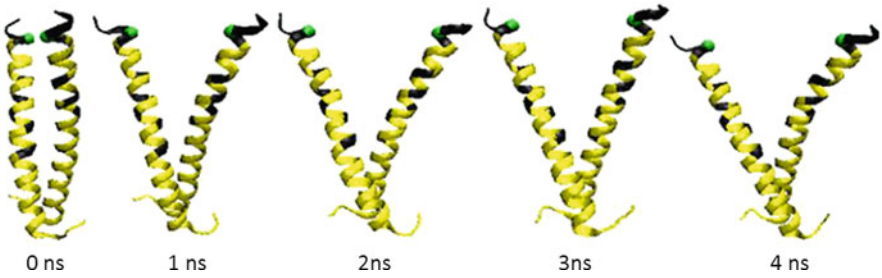

Fig. 21.19 Snapshots of mutant M2 at various time instances during a 4-ns simulation. The position of histidine residues is shown in *dark color*. Location of the His246 residue between which the opening is measured is shown as a *sphere*

significantly reducing the strength of the hydrophobic interactions toward the N-terminal and "middle" regions of the coiled-coil core while maintaining the strong hydrophobic core in the C-terminal region. This evolved design was therefore a balance between repulsive forces that can induce the actuation mechanism at acidic pH and strong hydrophobic interactions that can (1) maintain the coiled-coil structure and (2) serve as the restituting force for the "hinge" action in order to restore the original conformation of the peptide at neutral pH.

Figure 21.19 shows the snapshots of a 4-ns simulation of M2. Large conformational changes were observed in the M2 system leading to a significant net opening between the two helices. The helices rapidly moved apart within the first nanosecond and continued to move apart steadily until three nanoseconds, before adopting a final stable conformation. The distance between the Cα atoms of the His246 residues in both chains was plotted as a function of the simulation time (Fig. 21.20). The initial distance between the two atoms was 11 Å, which gradually increased to 28 Å at the 2.5-ns stage. The distance then fluctuated due to the dynamic nature of the electrostatic forces but stayed near the 27 Å separation during the rest of the simulation (4 ns). Thus, a net opening of 16 Å, which is approximately 150 % of the initial separation, was observed for M2 at low pH. This result verifies the hypothesis that selective mutations can be performed in the native GCN4-LZ that can induce large conformational changes without compromising its structural stability.

21.3.4 Conformational Change in Mutant M2 Is Reversible upon pH Modulation

One of the key design goals of a nanoActuator is reversibility of mechanochemical actuation. It was therefore investigated if the mutant M2 demonstrated a reversible open-to-closed transition when the pH was reverted back to neutral from acidic. The initial structure (the "open" state) for this simulation was taken from the final conformation generated from the previous 4-ns closed-to-open simulation at low

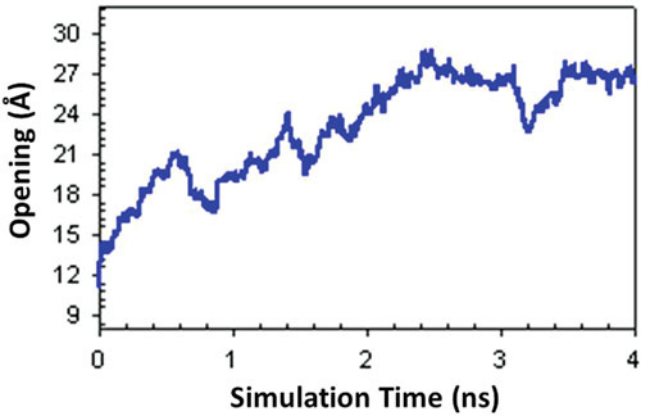

Fig. 21.20 Opening dynamics of M2 at low pH. The initial separation between the two chains was 11 Å which gradually increased to 27 Å at the 2.5-ns stage and then stabilized for the rest of the simulation giving a net opening of 16 Å (reprinted from [66], with permission from Sage Publications)

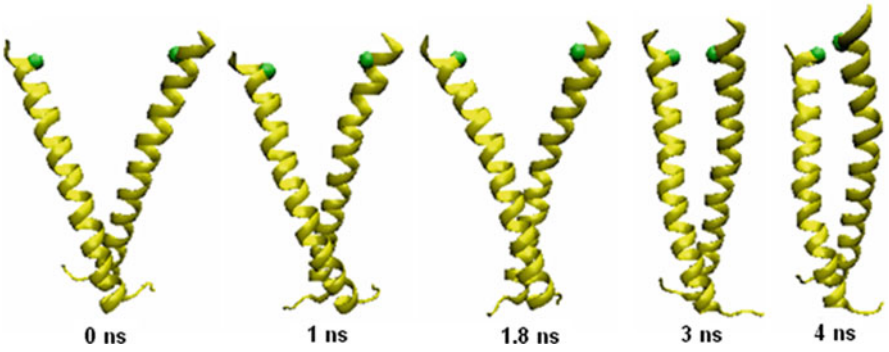

Fig. 21.21 Snapshots of a 5-ns simulation of open-to-close transition to show the reversible motion of mutant M2. Due to lack of ionic repulsions at neutral pH and also due to the attractive hydrophobic interactions, the actuator chains rapidly closed back. The final state closely resembles the initial NMR structure

pH. Histidine, glutamic acid, and aspartic acid residues in M3 were unprotonated to simulate neutral pH. Figure 21.21 shows snapshots of a 5-ns long reversible motion simulation of M2. Increasing the pH back to neutral triggered the reversible transition of the mutant and the final conformation generated by this simulation resembles the initial starting structure from the closed-to-open simulation (Fig. 21.21).

Figure 21.22 shows the dynamics of the reversible motion of M2 over the simulation time. The "open" state generated at the end of the close-to-open simulation of M2 at pH 4 was in a state of dynamic equilibrium. This means that the peptide was in a "tensed" state, wherein the restituting forces due to helices elasticity and the hydrophobic attractions near the C-terminal of the peptide chains

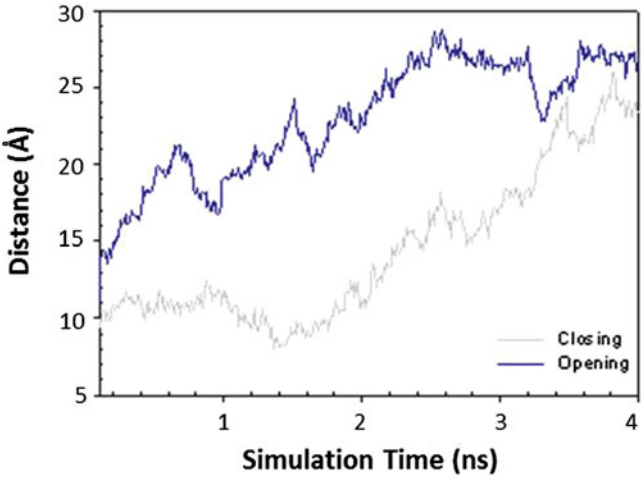

Fig. 21.22 Reversible motion dynamics for mutant M2 at neutral pH. As all elastic systems mutant M2 shows motion hysteresis (reprinted from [66], with permission from Sage Publications)

balanced the repulsive electrostatic forces of the ionized histidine residues. At pH 7, the force generating capability vanished due to histidine neutralization leading to the restitution of the "relaxed" state. The reversible transition of the mutant at pH 7 was exactly as hypothesized and verifies the concept of designing a nanoActuator element whose actuation can be modulated by pH. Figure 21.22 reveals also that the new nanoActuator has some hysteretic behavior which is something very common in nonlinear actuators as the one discussed in this review.

From the results, it is obvious that mutant M2 is the best design for a nanoActuator element. It shows maximum pH-dependent opening while maintaining its structural rigidity. The motion of the M2 mutant also was shown to be reversible upon pH modulation. The next step was to calculate the mechanical force generated by the M2 nanoActuator upon pH actuation.

21.3.5 Mechanical Force Generated by the nanoActuator

In this section, we discuss the results from computational studies employing statistical mechanics principle to investigate the nature and magnitude of the mechanical force generated by the M2 nanoActuator. A modified steered molecular dynamics (SMD) technique was employed within the conventional MD framework. This type of technique has also been previously employed to study the mechanical force generated in G proteins [57]. The closed-to-open transformation model of the nanoActuator at low pH is used as a computational platform to estimate the external force and hence the work done by the system. To measure this force, the

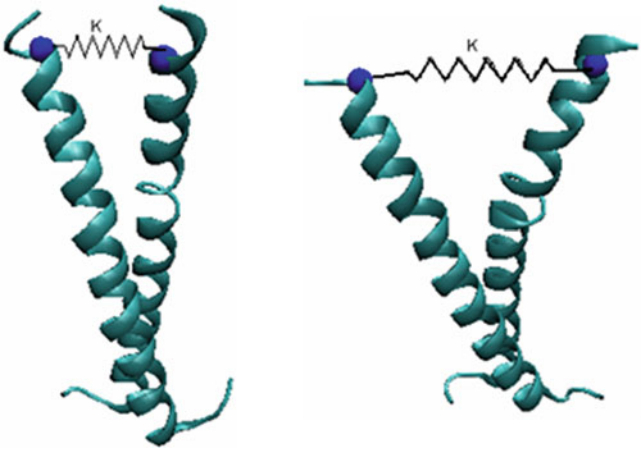

Fig. 21.23 Schematic representation of the structure of the closed (*left*) and open (*right*) states of the nanoActuator. To estimate the force generation capabilities of the nanoActuator, a harmonic spring with a known spring constant was attached to the COM of His-246 residues (shown as *spheres*) near the N-termini of the two chains (reprinted from [66], with permission from Sage Publications)

low pH simulation of M2 mutant was repeated but this time with an applied external constraint to its motion. This constraint was applied in the form of a harmonic spring of known stiffness k, attached to the center-of-mass (COM) of the His-246 backbone atoms in the corresponding chains (Fig. 21.23). Please see [48] for a more detailed discussion on methods used in this study.

The harmonic guiding potential and the corresponding exerted force for this system are of the form

$$U = -k(x - x_0)^2/2; \quad F = k(x - x_0),$$

where x is the distance between the COMs of the two His-246 residues at any given time instance t, and x_0 is the equilibrium value (at $t = 0$) of x. With a known value of the spring stiffness k, the time series of the reaction coordinate x can be obtained from the MD simulations which can then be plugged into the force equation above to obtain the force-time series. A statistical analysis of the force-time series can reveal the nature and magnitude of the force exerted by the nanoActuator. Seven simulations were performed with the value of k varying between 0.2 and 3 kcal/mol/Å^2. Figure 21.24 shows a representative result of a 4-ns SMD simulation of the nanoActuator peptide in the presence of an attached harmonic spring with $k = 0.6$ kcal/mol/Å^2. The time series of force (top curve) exerted by the protein on the spring is calculated using the equation $F(t) = k(x(t) - x_0)$, while the bottom curve shows the corresponding normalized force distribution histogram.

For the most part, the nanoActuator exerts a stretching force on the spring the magnitude of which increases with the applied load (spring stiffness). For

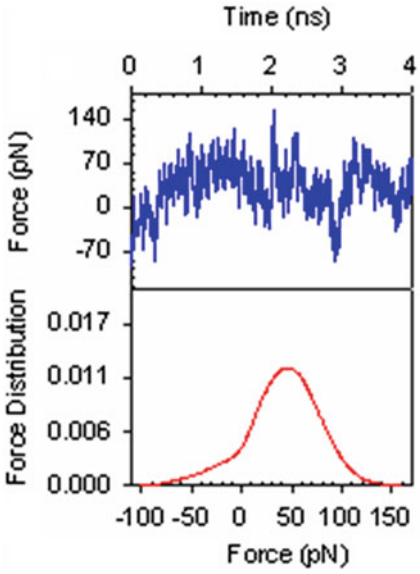

Fig. 21.24 Force–time series (*upper*) and the corresponding force distribution histograms (*lower*) obtained for a 4-ns simulation of mutant M2 at low pH with a harmonic spring attached to the COM of the His-246 backbone of the two chains. The value of k is 0.6 kcal/mol/Å^2 (reprinted from [66], with permission from Sage Publications)

$k = 0.2$ kcal/mol/Å^2, the mean force exerted is 20 pN (results not shown) which increases to 50 pN for $k = 0.6$ (Fig. 21.24). The magnitude of mean force remained in the 40–50 pN range for larger force constants of $k = \{0.8, 1.0, 2.0, 3.0\}$. This force output is comparable to that generated by other protein-based molecular motors such as flagella, ATPase, etc. [58], even though the nanoActuator is smaller in size and does not require any external fuel such as ATP for its functioning.

21.3.6 Applications of the nanoActuator: Modulation of DNA-Binding Activity

The pH-dependent conformational change of the nanoActuator can be employed for modulating the DNA-binding affinity of the parent GCN4 transcription activator protein. The design principle can also be employed to generate proteins with distinct DNA-binding specificities and different physiological targets, thereby having implications in engineering of novel transcription factors and ligand design for DNA purification. To demonstrate the DNA-binding modulation capability of the nanoActuator, a new peptide was designed in which the DNA-binding basic region of the parent GCN4 peptide was grafted at the end of the N-terminus of the nanoActuator based on the M2 mutant design (henceforth called GCN4mT). The residue sequence of the resulting GCN4mT peptide is shown in Fig. 21.25a.

Two simulations were carried out to study the GCN4mT–DNA complex at low and neutral pH, respectively. It was hypothesized that the conformational opening in the GCN4mT and protonation (and hence neutralization) of charges

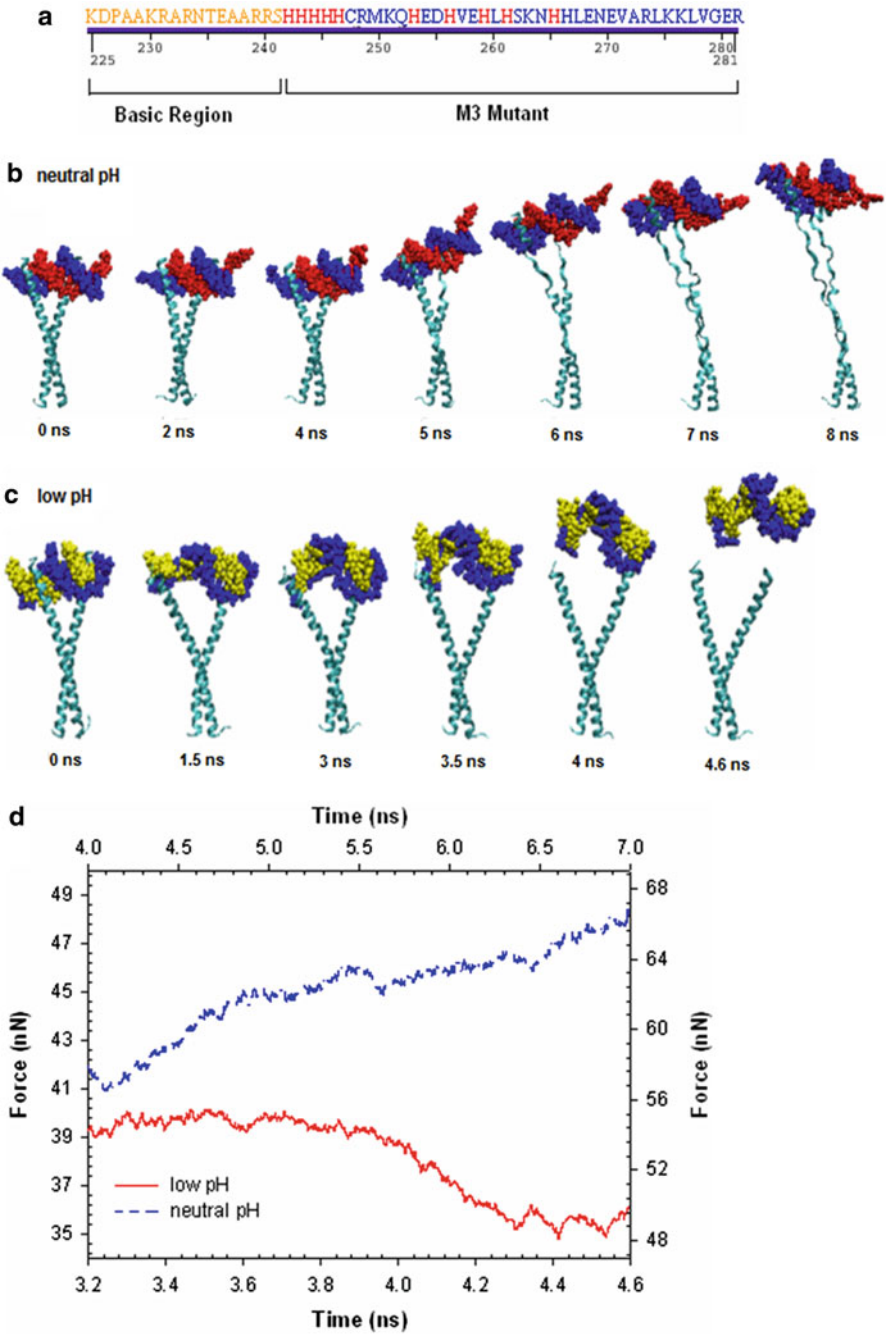

Fig. 21.25 (continued)

on the adenosine nucleotides at low pH [59] would result in the reduction of the GCN4mT–DNA binding activity, in turn resulting in the release and diffusion of DNA molecule away from the GCN4mT binding site. However, diffusion is an extremely slow process governed mostly by random Brownian motions and hence is difficult to simulate in typical MD timescales. In order to "accelerate" the diffusion process and therefore, obtain quantitative data on the strength of GCN4mT–DNA binding, we employed SMD technique. The DNA molecule was pulled out of the GCN4mT-binding site using a constant velocity SMD simulation and the force required for this pull was computed and plotted. Each simulation was further divided into two runs: In the first run, a normal 4-ns MD simulation (without applying SMD) was carried out on the GCN4mT–DNA complex to let the system evolve naturally and change conformation. A second 4-ns long MD simulation was then started from the end point of the first simulation, but this time the C-terminal residues of the peptide were held fixed while the DNA atoms were pulled out with a constant velocity. Please see [47, 60] for a more detailed discussion on methods used in this study.

Figure 21.25b, c shows the simulation snapshots of the GCN4mT–DNA complex at neutral and low pH values. No major conformational changes were observed in the GCN4mT–DNA system at neutral pH during the first 4 ns of simulation (Fig. 21.25b). This was expected, firstly because at neutral pH there are no electrostatic repulsive forces "pushing" the peptide chains since the histidine residues are unionized. Secondly, the DNA bases as well as phosphate backbone is negatively charged at neutral pH and hence binds electrostatically with the positively charged residues in the DNA-binding region of the peptide. For the next 4 ns, the C-terminal residues (Arg281) in both peptide chains were held fixed and the DNA atoms were pulled with a constant velocity in the direction of the vector joining the COM of DNA atoms and the COM of the fixed Arg281 residues in the peptide chains. This effectively pulls out the DNA along the longitudinal axis of the peptide. There was no reduction of the DNA binding capability of the GCN4mT at neutral pH, which is evident from the 4–8-ns simulation snapshots in Fig. 21.25b. The strength of the GCN4mT–DNA binding at neutral pH was such that instead of the DNA molecule being released from the GCN4mT binding pocket, the force applied on the DNA

Fig. 21.25 (**a**) Residue sequence of the GCN4mT peptide. The basic DNA binding region is grafted at the N-terminus of the mutant M3 design; snapshots of the SMD simulation to study DNA-binding modulation; (**b**) at neutral pH the DNA molecule is tightly bound to the peptide chains and cannot break free when pulled using an external force; (**c**) at low pH the conformational changes in the GCN4mT peptide reduces the strength of DNA binding and when pulled the DNA molecule is rapidly released from the peptide-binding cavity; (**d**) force required pulling the DNA out of the GCN4mT-binding cavity. The *left* and *bottom* axis are for data at low pH, while the *top* and *right* axis are for neutral pH data. As hypothesized the force required to pull the DNA is considerably smaller at low pH (reprinted from [47], with permission from Dove Medical Press Ltd.)

atoms was transferred to peptide chains and the α-helices started to unfold under its influence.

At low pH, a significant actuation mechanism was observed in the GCN4mT peptide during the initial 4 ns of simulation; the actuation was a result of the electrostatic repulsive forces in the M2 coiled-coil portion. The average RMSD of the Cα atoms was 4.3 Å at low pH which is significantly higher when compared to 2.2 Å RMSD at neutral pH. At low pH, the system was initially simulated till the Cα RMSD for the peptide stabilized at a constant value (4.3 Å), signifying that the peptide had achieved a stable "open" state. This corresponds to the 3.2 ns mark in the simulation timeline. At this stage, the C-terminal residues (Arg281) were fixed and the DNA molecule was "pulled" using a constant velocity. As can be seen from the simulation snapshots shown in Fig. 21.25c, the DNA molecule was rapidly released from the GCN4mT-binding cavity without destabilizing the protein secondary structure. The force required to pull the DNA was computed using the equation:

$$\mathbf{F} = -\nabla U \quad U = \frac{1}{2}k[vt - (\mathbf{r} - \mathbf{r}_0) \cdot \mathbf{n}]^2.$$

Here, U is the potential energy, k is spring constant, v is the pulling velocity, t is time, $\mathbf{r}$ is the actual position of the pulling atom, $\mathbf{r}_0$ is the initial position of the pulling atom, and $\mathbf{n}$ is the pulling direction. Figure 21.25d shows the plot of this force at both the neutral and low pH values. The force required to pull the DNA from the GCN4mT-binding cavity is much weaker at low pH than at neutral pH. At low pH a 40-nN force was being applied to the DNA molecule to overcome the peptide–DNA interactions. At the 3.9-ns stage, the DNA molecule started to break free from the peptide, which resulted in a weaker "pulling" force from this point on. At the 4.4-ns stage, the DNA molecule is completely free from the peptide-binding cavity and the only force required is the friction force to drag it through the water box which is signified by the flattening of the force curve at a low (35 nN) value. Due to the lack of initial conformational "opening" in the GCN4mT peptide at neutral pH the peptide-DNA interaction remains strong which results in a higher force (58 nN) being applied to pull the DNA. This applied force increases with simulation time due to the additional work being performed upon unfolding of the coiled-coil α-helices.

Taken together, the SMD simulation results (Fig. 21.25b, c) in conjunction with the force profiles (Fig. 21.25d) suggests a reduced DNA binding of the GCN4mT peptide at low pH when compared to neutral pH and confirms our hypothesis that DNA binding activity of the GCN4 peptide can be engineered in order to obtain environmentally responsive mutants as exemplified by the pH-activated nanoActuator in this case. Environmentally responsive DNA-binding protein systems can lead to practical tools for the studying cellular chemistry and controlling transcription process. Several groups have reported techniques for controlling DNA-binding ability of basic zipper domains and cross-linked peptide constructs with applications in drug delivery either independently [61, 62] or in conjunction with cell-penetrating

peptides [63]. Examples of these techniques include the reversible photocontrol of designed GCN4-bZIP proteins using a azobenzene chromophore [64] and the design of a negative vitellogenin promoter-binding protein (VBP) leucine zipper [65]. In a similar fashion, we propose that our nanoActuator construct may also have applications in drug delivery; drug-binding domains may be grafted at the N-terminus of the nanoActuator which can than be employed for releasing the bound drug by inducing repulsions in the helices of the coiled-coil upon pH activation.

21.4 Conclusion

This chapter discusses protein-based nanoscale actuation for bio-nano robotic applications and elaborates upon the research on two systems, the VPL and GCN4. For the study of nanoActuators, molecular simulations provide a very valuable tool. Experiments at the nanoscale may not be simple to perform. Alteration to the protein sequence (mutations) is a good example of a process in which computational studies are much easier to perform than experimental ones due to the complexities involved. One of the challenges is to learn how to control structural mechanisms, behavior, and properties of the basic nanocomponents involved in molecular motors.

In this review, we illustrate how conformational changes in a protein/peptide structure can be induced through its interaction with peptides, mutation of its sequence, and changes in temperature and solution pH. We also illustrated a new method to estimate the mechanical forces generated by biological motors and simulation results to show a potential application of the nanoActuator. From a bio-nanotechnological perspective, the results presented here demonstrate that the mechanical properties of protein-based nanodevices can be controlled by using rational design based on protein engineering principles. The force calculation technique can readily be applied to other bio-molecular systems and has implications in the area of bio-nanotechnology and in particular to study and characterize the mechanical properties of novel protein- and DNA-based nanodevices. In this review we have illustrated the use of molecular dynamics simulations to study some aspects of the response of the VPL motor and the GCN4 nanoActuator to different stimuli.

We are at the dawn of a new era in the development of molecular machinery, and we are just starting to elucidate some of the challenges that these nanoActuators represent. Future studies will involve investigating interfacing with other molecular components such as carbon nanotubes, biological membranes, inorganic substrates, ions, etc. As mentioned earlier, the end-effector of VPL can be designed according to the requirement. Moreover, the composition of the peptide can be varied according to the environment, as long as the rules of having hydrophobic and polar residues to ensure stability of the coiled-coil system are adhered to. The length of the VPL peptides, the role of the solvent (and solvent composition), and binding energies to various target objects are other variables that need to be investigated in order to assess conditions for optimum performance (i.e., for example, maximum force and stability and a given velocity).

The VPL and GCN4 peptides are known to work better with specific mutations [22]. This opens up doors for further mutational analysis of the peptide, again directed toward achieving optimal performance parameters. The goal will be to determine the optimal sequence of the peptide that results in the most stable, quickest, powerful, and robust nanoActuator.

References

1. Mavroidis C, Dubey A (2003) Biomimetics: from pulses to motors. Nat Mater 2(9):573–574
2. Mavroidis C, Dubey A, Yarmush ML (2004) Molecular machines. Annu Rev Biomed Eng 6(1):363–395. doi:10.1146/annurev.bioeng.6.040803.140143
3. Sharma G, Badescu M, Dubey A, Mavroidis C, Tomassone SM, Yarmush ML (2005) Kinematics and workspace analysis of protein based nano-actuators. J Mech Des 127(4): 718–727. doi:10.1115/1.1900751
4. Boyer PD (1998) Energy, life, and ATP. Biosci Rep 18(3):97–117
5. Oster G, Wang H (2003) Rotary protein motors. Trends Cell Biol 13(3):114–121
6. Vale RD, Milligan RA (2000) The way things move: looking under the hood of molecular motor proteins. Science 288(5463):88–95
7. Berg HC (2003) The rotary motor of bacterial flagella. Annu Rev Biochem 72:19–54
8. Seeman NC (2003) DNA in a material world. Nature 421(6921):427–431
9. Yurke B, Turberfield AJ, Mills AP, Simmel FC, Neumann JL (2000) A DNA-fuelled molecular machine made of DNA. Nature 415:62–65
10. Balzani VV, Credi A, Raymo FM, Stoddart JF (2000) Artificial molecular machines. Angew Chem Int Ed Engl 39(19):3348–3391
11. Dubey A, Mavroidis C, Thornton A, Nikitczuk K, Yarmush ML (2003) Viral protein linear (VPL) nano-actuators. In: 2003 Third IEEE conference on nanotechnology, 2003 (IEEE-NANO 2003), 12–14 Aug 2003, vol 142. pp 140–143
12. Skehel JJ, Wiley DC (2000) Receptor binding and membrane fusion in virus entry: the influenza hemagglutinin. Annu Rev Biochem 69:531–569
13. Wiley DC, Skehel JJ (1987) The structure and function of the hemagglutinin membrane glycoprotein of influenza virus. Annu Rev Biochem 56:365–394
14. Schoch C, Blumenthal R, Clague MJ (1992) A long-lived state for influenza virus-erythrocyte complexes committed to fusion at neutral pH. FEBS Lett 311(3):221–225
15. Weissenhorn W, Dessen A, Calder LJ, Harrison SC, Skehel JJ, Wiley DC (1999) Structural basis for membrane fusion by enveloped viruses. Mol Membr Biol 16(1):3–9
16. Lazarowitz SG, Compans RW, Choppin PW (1971) Influenza virus structural and nonstructural proteins in infected cells and their plasma membranes. Virology 46(3):830–843
17. Skehel JJ, Waterfield MD (1975) Studies on the primary structure of the influenza virus hemagglutinin. Proc Natl Acad Sci USA 72(1):93–97
18. Wilson IA, Skehel JJ, Wiley DC (1981) Structure of the haemagglutinin membrane glycoprotein of influenza virus at 3 A resolution. Nature 289(5796):366–373
19. Weis W, Brown JH, Cusack S, Paulson JC, Skehel JJ, Wiley DC (1988) Structure of the influenza virus haemagglutinin complexed with its receptor, sialic acid. Nature 333(6172): 426–431
20. Weis WI, Brunger AT, Skehel JJ, Wiley DC (1990) Refinement of the influenza virus hemagglutinin by simulated annealing. J Mol Biol 212(4):737–761
21. Bullough PA, Hughson FM, Skehel JJ, Wiley DC (1994) Structure of influenza haemagglutinin at the pH of membrane fusion. Nature 371(6492):37–43
22. Carr CM, Kim PS (1993) A spring-loaded mechanism for the conformational change of influenza hemagglutinin. Cell 73(4):823–832

23. Carr CM, Chaudhry C, Kim PS (1997) Influenza hemagglutinin is spring-loaded by a metastable native conformation. Proc Natl Acad Sci USA 94(26):14306–14313
24. Chan DC, Fass D, Berger JM, Kim PS (1997) Core structure of gp41 from the HIV envelope glycoprotein. Cell 89(2):263–273
25. Singh M, Berger B, Kim PS (1999) LearnCoil-VMF: computational evidence for coiled-coil-like motifs in many viral membrane-fusion proteins. J Mol Biol 290(5):1031–1041
26. Caffrey M, Cai M, Kaufman J, Stahl SJ, Wingfield PT, Covell DG, Gronenborn AM, Clore GM (1998) Three-dimensional solution structure of the 44 kDa ectodomain of SIV gp41. EMBO J 17(16):4572–4584
27. Kobe B, Center RJ, Kemp BE, Poumbourios P (1999) Crystal structure of human T cell leukemia virus type 1 gp21 ectodomain crystallized as a maltose-binding protein chimera reveals structural evolution of retroviral transmembrane proteins. Proc Natl Acad Sci USA 96(8):4319–4324
28. Baker KA, Dutch RE, Lamb RA, Jardetzky TS (1999) Structural basis for paramyxovirus-mediated membrane fusion. Mol Cell 3(3):309–319
29. Weissenhorn W, Calder LJ, Wharton SA, Skehel JJ, Wiley DC (1998) The central structural feature of the membrane fusion protein subunit from the Ebola virus glycoprotein is a long triple-stranded coiled coil. Proc Natl Acad Sci USA 95(11):6032–6036
30. Colman PM, Lawrence MC (2003) The structural biology of type I viral membrane fusion. Nat Rev Mol Cell Biol 4(4):309–319
31. Walker JE (1998) ATP synthesis by rotary catalysis (Nobel lecture). Angew Chem Int Ed 37:2308–2319
32. Schlitter J (1994) Targeted molecular dynamics: a new approach for searching pathways of conformational transitions. J Mol Graph 12:84–89
33. Dubey A, Mavroidis C, Tomassone MS (2006) Molecular dynamic studies of viral-protein based nano-actuators. J Comput Theor Nanosci 3:885
34. Dubey A, Sharma G, Mavroidis C, Tomassone SM, Nikitczuk K, Yarmush ML (2004) Dynamics and kinematics of viral protein linear nano-actuators for bio-nano robotic systems. In: Proceedings of the 2004 IEEE international conference on robotics and automation, 2004 (ICRA'04), 26 Apr–1 May 2004, vol 1622. pp 1628–1633
35. Dubey A, Sharma G, Mavroidis C, Tomassone MS, Nikitczuk K, Yarmush ML (2004) Computational studies of viral protein nano-actuators. J Comput Theor Nanosci 1:18–28. doi:10.1166/jctn.2003.003
36. Lazaridis T, Karplus M (1999) Effective energy function for proteins in solution. Proteins 35(2):133–152
37. Berman HM, Westbrook J, Feng Z, Gilliland G, Bhat TN, Weissig H, Shindyalov IN, Bourne PE (2000) The Protein Data Bank. Nucleic Acids Res 28(1):235–242
38. Humphrey W, Dalke A, Schulten K (1996) VMD: visual molecular dynamics. J Mol Graph 14(1):33–38, 27–38
39. Dubey A, Tomassone MS (2009) Viral protein nano-actuators, computational studies of bio-nanomachines. In: Meyers RA (ed) Encyclopedia of complexity and systems science. Springer, New York, pp 9749–9763
40. Ferrara P, Apostolakis J, Caflisch A (2000) Thermodynamics and kinetics of folding of two model peptides investigated by molecular dynamics simulations. J Phys Chem B 104(20):5000–5010
41. Ruigrok RW, Martin SR, Wharton SA, Skehel JJ, Bayley PM, Wiley DC (1986) Conformational changes in the hemagglutinin of influenza virus which accompany heat-induced fusion of virus with liposomes. Virology 155(2):484–497
42. Crick FHC (1953) The packing of α-helices: simple coiled-coils. Acta Crystallogr 6: 689–697
43. Landschulz WH, Johnson PF, McKnight SL (1988) The leucine zipper: a hypothetical structure common to a new class of DNA binding proteins. Science 240(4860):1759–1764
44. O'Shea EK, Klemm JD, Kim PS, Alber T (1991) X-ray structure of the GCN4 leucine zipper, a two-stranded, parallel coiled coil. Science 254(5031):539–544

45. Phillips JC, Braun R, Wang W, Gumbart J, Tajkhorshid E, Villa E, Chipot C, Skeel RD, Kalé L, Schulten K (2005) Scalable molecular dynamics with NAMD. J Comput Chem 26(16): 1781–1802
46. MacKerell AD, Bashford D, Bellott M, Dunbrack RL, Evanseck JD, Field MJ, Fischer S, Gao J, Guo H, Ha S, Joseph-McCarthy D, Kuchnir L, Kuczera K, Lau FTK, Mattos C, Michnick S, Ngo T, Nguyen DT, Prodhom B, Reiher WE, Roux B, Schlenkrich M, Smith JC, Stote R, Straub J, Watanabe M, Wiorkiewicz-Kuczera J, Yin D, Karplus M (1998) All-atom empirical potential for molecular modeling and dynamics studies of proteins. J Phys Chem 102(18): 3586–3616
47. Sharma G, Rege K, Budil DE, Yarmush ML, Mavroidis C (2008) Reversible pH-controlled DNA-binding peptide nanotweezers: an in-silico study. Int J Nanomedicine 3(4):505–521
48. Sharma G, Rege K, Budil DE, Yarmush ML, Mavroidis C (2009) Biological force measurement in a protein-based nanoactuator. IEEE Trans Nanotechnol 8(6):684–691
49. Hendsch ZS, Tidor B (1999) Electrostatic interactions in the GCN4 leucine zipper: substantial contributions arise from intramolecular interactions enhanced on binding. Protein Sci 8(7):1381–1392
50. Kohn WD, Kay CM, Hodges RS (1995) Protein destabilization by electrostatic repulsions in the two-stranded alpha-helical coiled-coil/leucine zipper. Protein Sci 4(2):237–250
51. Yu Y, Monera OD, Hodges RS, Privalov PL (1996) Investigation of electrostatic interactions in two-stranded coiled-coils through residue shuffling. Biophys Chem 59(3):299–314
52. Missimer JH, Steinmetz MO, Jahnke W, Winkler FK, van Gunsteren WF, Daura X (2005) Molecular-dynamics simulations of C- and N-terminal peptide derivatives of GCN4-p1 in aqueous solution. Chem Biodivers 2(8):1086–1104
53. Mohanty D, Kolinski A, Skolnick J (1999) De novo simulations of the folding thermodynamics of the GCN4 leucine zipper. Biophys J 77(1):54–69
54. Pineiro A, Villa A, Vagt T, Koksch B, Mark AE (2005) A molecular dynamics study of the formation, stability, and oligomerization state of two designed coiled coils: possibilities and limitations. Biophys J 89(6):3701–3713
55. Nilges M, Brunger AT (1993) Successful prediction of the coiled coil geometry of the GCN4 leucine zipper domain by simulated annealing: comparison to the X-ray structure. Proteins 15(2):133–146
56. Vieth M, Kolinski A, Brooks CL 3rd, Skolnick J (1994) Prediction of the folding pathways and structure of the GCN4 leucine zipper. J Mol Biol 237(4):361–367
57. Kosztin I, Bruinsma R, O'Lague P, Schulten K (2002) Mechanical force generation by G proteins. Proc Natl Acad Sci USA 99(6):3575–3580
58. Yin H, Wang MD, Svoboda K, Landick R, Block SM, Gelles J (1995) Transcription against an applied force. Science 270(5242):1653–1657
59. Aksimentiev A, Heng JB, Timp G, Schulten K (2004) Microscopic kinetics of DNA translocation through synthetic nanopores. Biophys J 87(3):2086–2097
60. Gulla SV, Sharma G, Borbat P, Freed JH, Ghimire H, Benedikt MR, Holt NL, Lorigan GA, Rege K, Mavroidis C, Budil DE (2009) Molecular-scale force measurement in a coiled-coil peptide dimer by electron spin resonance. J Am Chem Soc 131(15):5374–5375
61. Walensky LD, Kung AL, Escher I, Malia TJ, Barbuto S, Wright RD, Wagner G, Verdine GL, Korsmeyer SJ (2004) Activation of apoptosis in vivo by a hydrocarbon-stapled BH3 helix. Science 305(5689):1466–1470
62. Futaki S (2005) Membrane-permeable arginine-rich peptides and the translocation mechanisms. Adv Drug Deliv Rev 57(4):547–558
63. Kawamura KS, Sung M, Bolewska-Pedyczak E, Gariepy J (2006) Probing the impact of valency on the routing of arginine-rich peptides into eukaryotic cells. Biochemistry 45(4):1116–1127
64. Woolley GA, Jaikaran AS, Berezovski M, Calarco JP, Krylov SN, Smart OS, Kumita JR (2006) Reversible photocontrol of DNA binding by a designed GCN4-bZIP protein. Biochemistry 45(19):6075–6084

65. Moll JR, Olive M, Vinson C (2000) Attractive interhelical electrostatic interactions in the proline- and acidic-rich region (PAR) leucine zipper subfamily preclude heterodimerization with other basic leucine zipper subfamilies. J Biol Chem 275(44):34826–34832
66. Sharma G, Mavroidis C, Rege K, Yarmush ML, Budil D (2009) Computational studies of a protein-based nanoactuator for nanogripping applications. Int J Robot Res 28(4):421–435

Index

A
AAUSAT-II Cu-besat, 86
Activation energy, 392
Active agents, 52
Active self-assembly approach, 46–47
Adaptive backstepping, 264
AERCam Sprint, 75
Agarose gel phantom, 308–309
Approach/retreat curve (A/R), 391
Artifact. *See also* Magnetic resonance imaging (MRI)
  recognition algorithms
    EM algorithm, 311
    histogram, HASTE scan, 312, 313
    scatter plot, segmented volumes, 313
    segmentation, steel sphere, 314, 315
    segmented artifacts, 311, 312
    water-filled phantom scan, 314, 315
  tracking algorithms
    center of gravity, 316
    HASTE sequence, 317–319
    template stack slice, 315
Atomic force microscopy (AFM). *See also* Virtual tooling strategy
  biomaterials, nanohandling of
    advantages, 200, 202
    biosensors, 204
    cantilevers, 201–202
    disadvantages, 201
    DNA electrical properties, 206–207
    hydrogen bonding strength, complementary DNA strands, 204–205
    intermolecular forces, analysis of, 204
    ligand–receptor binding force measurements, 204
    limitations, 202–203
    "look and move" scheme, 200
    manipulation tasks, 200
    research work, AMiR, 207–212
    sample preparation, 201
    virus shells, stability measurements, 206
    visualization, 203
  general principle, 390, 391
  imaging ultrasoft samples, 35
  loading rate, 393–394
  osmotic pressure, 389
  plastic deformation, 35
  PRC-400 self-sensing cantilever, 34–35
  quantification, DNA interactions, 394–395
  robust adaptive controller, 36–37
  rupture force, 392–393, 396
  schematic representation, 34–35
  setup, 34
  surface caracterization, 391
Attocube system, 157
Automated nanomanipulation
  advantages, 161
  depth detection, 161–162
  four-point probe measurement, nanowires, 162–163
  visual tracking, 161
Autonomous Brownian biped walker, 373
Axially symmetric bodies, 278, 279

B
Bacterial-based nanorobotics
  artificial bacterial microswimmers, 15
  biomimetics, 15
  flagella motors, 14
  magnetotactic bacteria, 15
  unicellular organisms, 14

C. Mavroidis and A. Ferreira (eds.), *Nanorobotics: Current Approaches and Techniques*, DOI 10.1007/978-1-4614-2119-1,
© Springer Science+Business Media New York 2013

Bacterial flagellar motor
description, 414–415
rotational speed
steady-state control, 419, 420
transient-state control, 418, 419
Binding type gel-microtool, 186
Bioinspired robotic swimming methods, 278
Biological cells
mechanical properties
deviation parameter, 233
myeloblasts with acute myeloid leukemia, 235–237
red blood cell, 233–235
optical stretching of
cell preparation and treatment, 227
cell stretching, 228–230
force calibration, 227–228
mechanical modeling, 230–232
Biomaterials
atomic force microscopy
advantages, 200, 202
biosensors, 204
cantilevers, 201–202
disadvantages, 201
DNA electrical properties, 206–207
hydrogen bonding strength, complementary DNA strands, 204–205
intermolecular forces, analysis of, 204
ligand–receptor binding force measurements, 204
limitations, 202–203
"look and move" scheme, 200
manipulation tasks, 200
research work, AMiR, 207–212
sample preparation, 201
virus shells, stability measurements, 206
visualization, 203
biological cells, 194–195
characteristic sizes, 193
deoxyribonucleic acid
asymmetric bonds, 198
bases of, 198
complementary base pairing, 199
conformations, 199
description, 197
electrical properties, 206–207
genetic information, 197
nucleoside, 198
nucleotides, 197, 198
phosphate and sugar residues, 198
role of, 197
transcription process, 197
dielectrophoresis
applications, 217
definition, 216
phenomenological bases, 216–217
time dependent dielectrophoretic force, 217
E. coli, 195–196
environmental scanning electron microscope, 199
future aspects, 219
ion channels, 196–197
microcapillaries, 217–218
microgrippers, 218–219
nanotweezers, 218–219
optical tweezers
applications, 214, 216
components, 214, 215
gradient force, 214
optical traps *vs*. simple spring, 214, 215
principles of, 212–213
prokaryotic *vs*. eukaryotic cells, features of, 195
scanning electron microscope, 199
Biomedical applications, nanorobotic manipulation
circular gel-microtool fabrication, 184–186
fluorescent methods, 170
functional gel-microtool
calibration, 183–184
environment sensing, 180–181
pH and temperature measurement, 186, 188
salting out concentration, 180
in situ fabrication, 181–183
microbead modified with pH-sensitive fluorescent dye, 170
microfluidic chip (see Microfluidic chip)
virus, quantitative analysis of, 170
Biomolecular motor, 412
Bionanorobotics
biomolecular motor, 9–10
CAD drawing, 9–10
components, 9
nanogripper, 11
virtual molecular dynamic simulation, 11, 12
VPL, 11
Biosensors
AFM-based structuring techniques, 209
components, automated fabrication, 209
intermolecular forces, analysis of, 204
microprinting, 208
microstamping, 208
Bipedal walker, 368

Branch migration, 359
Bridging phenomenon, 60
Bromocresol green (BCG)
  binding type gel-microtool, 186
  calibration result, 183, 184
  indicator range, 181
Bromothymol blue (BTB)
  binding type gel-microtool, 186
  calibration result, 183, 184
  circular gel-microtool fabrication, 184, 185
  indicator range, 181

C
Canadarm, 73
Cancer
  angiogenic switch, 337
  diagnosis, 340–341
  dormant phase, 337
  features, 336
  optimum capillary number, 336
  swarm of nanorobots (*see* Swarm of nanorobots)
  tissues features
  acidity, 339–340
  hyperthermia, 338–339
  hypoxia, 339
Carbon nanotubes (CNT)
  building blocks, 139–140
  filling of nanotube, 139
  mass transport between nanotube
    internanotube, 149
    molecular dynamics simulation, 150–151
  mass transport inside nanotube, 144–145
    containers, 148
    evaporation and condensation of copper, 146
    impact of cooling speed, 146, 148
    self-soldering, 146, 148
    spot welding, attogram mass delivery, 146–147
  methods
    electrostatic forces, 144
    evaporation mechanisms, 142–143
    mass delivery mechanisms, 141
    modes, 142
    thermal expansion, 140
  nanomanufacturing system, 138–139
Carbon placement tools, 103–104
Cell stretching process, 228–230
Chemical reaction network model, 366
Chromallocytes, 98
Chromosome replacement therapy, 97
Circular gel-microtool fabrication, 184–186
Circulatory system
  fractal-tree analysis, 335
  lin-lin plot, 332, 333
  log-log plot, 333
  lumped model, animal organism, 334, 335
  mitosis and growth, 332
Coexistence-type gel-microtool, 186
Coreflood testing
  outcomes, 64
  particle-free, 65
  program, 63
  rock sample, 64
CubeSat, 85–86

D
Da Vinci's Vitruvian Man, 348, 349
Deoxyribonucleic acid (DNA)
  asymmetric bonds, 198
  bases of, 198
  complementary base pairing, 199
  conformations, 199
  description, 197
  electrical properties, 206–207
  genetic information, 197
  handling and manipulation, 207–208
  nanorobotic systems (see also Bacterial-based nanorobotics)
    advantages, 358–359
    challenges of, 356–357
    kinesin, 357
    myosin, 357
    nanomachines (see Nanomachines, DNA)
    three-way DNA junction, 356
  nucleoside, 198
  nucleotides, 197, 198
  phosphate and sugar residues, 198
  role of, 197
  self-assembly
    atomic force microscope, 389–394
    DNA-based bond, 384
    global approach, 387–389
    hybridization, 394
    local approach, 386–387
    specificity analysis (see Specificity analysis)
  transcription process, 197
Dextre, 74
Diamondoid nanorobotics
  chemically actuated cantilever arrays, 94
  femtolaser surgery, 95–96
  massively parallel positional assembly, 106

Diamondoid nanorobotics (*Cont.*)
mechanosynthesis
albeit on silicon atoms, 105
carbon placement tools, 103–104
chemically active tooltip and insert handle, 102
chemical vapor deposition, 102
covalent chemical bonds, 101
DCB6Ge dimer placement tool, 100–101
2D patterns, 105
hydrogen abstraction tools, 102–103
hydrogen donation tools, 104
materials, 101
reaction sequences, 104
types of tool, 102–103
Nanofactory Collaboration, 107–108
nanomechanical design, 106–107
nanomedicine, 96
positional molecular manufacturing, 99–100
programmable positional assembly, 105–106
treatments for human diseases
chromallocytes, 98
chromosome replacement therapy, 97
Dielectrophoresis
applications, 217
definition, 216
phenomenological bases, 216–217
time dependent dielectrophoretic force, 217
Direct-gradient propulsion, 278
DNA. *See* Deoxyribonucleic acid (DNA)
5-DOF wireless micromanipulation, 288–292
Dormant cancer phase, 337

E
Efficiency index, 54–56
Elastic-flagellated robot, 244–245
Electrical SPM-based control and manipulation, 31–32
Electromechanical SPM-based control and manipulation, 32
Electroosmosis micropump, 55–56
Endovascular navigation, 247
Environment measurement gel-microtool
composition, 180
fabrication, 182
polyethylene glycol indicator, 180
Escherichia coli bacteria, 195–196
Expectation maximization (EM) algorithm, 311

F
Ferrofluids, spin-echo sequences, 309, 310
Flagellated bacteria, 412
Foot-over-foot walker, 370–372
Force–time series, 447–448
Fractal-tree description, circulatory system
Da Vinci's Vitruvian Man, 348, 349
definition, 347
symmetrical fractal tree, 350
Free energy variation computing algorithm, 387–388
Functional gel-microtool
calibration, 183–184
environment sensing, 180–181
pH and temperature measurement, 186, 188
salting out concentration, 180
in situ fabrication, 181–183

G
Gaussian mixture model (GMM), 311
GCN4mT–DNA complex, 449
GCN4 peptide-based nanoactuator
applications, 447–451
leucine zipper, 438, 439
mechanical force, 444–447
peptide design and molecular dynamic studies, 439–440
pH-dependent conformational change, 442–443
wild-type structure and mutant, 440–445
Gradient-echo sequences, 303

H
Harmonic guiding potential, 446
HASTE sequence, 317–319
Helical-flagellated robot, 244–245
Helmholtz coil configuration, 284
Hemagglutinin (HA), 426
Hemispherical electromagnetic system
MiniMag and OctoMag system, 289, 290
optimal magnetic manipulation system design, 290–292
Hofmeister series, 180
Hybrid swimming/gradient strategy, 292–293
Hydrodynamic forces, 170
Hydrogen abstraction tools, 102–103
Hydrogen donation tools, 104
Hyperthermia, 338–339
Hypoxia, 339

I
i-motif, 360
Inchworm walker, 369
Influenza virus, 427–428
Ion channels, 196–197

J
JAXA's ETS-VII, 74

K
Kinesin, 357
Kleindiek system, 157

L
Laser-free AFM imaging
  imaging ultrasoft samples, 35
  plastic deformation, 35
  PRC-400 self-sensing cantilever, 34–35
  robust adaptive controller, 36–37
  schematic representation, 34–35
  setup, 34
Lifetime, 393
Ligand-gated ion channel, 197
Lin-lin plot, 332, 333
Loading rate, 393–394
Local environmental control technique
  flagellar motor rotational speed
    steady-state control, 419, 420
    transient-state control, 418, 419
  methods and features, bacterial propulsion, 413
  Na^+ ion concentration vs. diffusion and flushing, 416
  with nano/micro dual pipettes, 416–417, 420–421
Lumped model, animal organism, 334, 335

M
Magnetically guided nanorobots
  closed loop control algorithm, 11, 13
  nanoparticle motion, 11
  navigation techniques, 13
  weak magnetic gradient, 14
Magnetic body manipulation
  field and gradient generation
    control system, 287–288
    Helmholtz coil configuration, 284
    hemispherical electromagnetic system, 288–292
    solenoids, 285–287
  field application
    drag force, 282–283
    magnetic force, 282
  Helmholtz coil configuration, 284
  magnetization, soft magnetic bodies
    demagnetization factors, 280
    ferromagnetically filled carbon nanotubes, 282
    magnetic energy and torque, 281
    magnetization angle, 280
    susceptibility tensor, 279
  swimming behavior at low Reynolds numbers, 277–278
Magnetic drug carrier fabrication
  MNPs, 294
  nanowires
    AAO templates, 296
    graphitic shells, 296, 297
    hybrid CNT-based magnetic nanostructures, 296, 297
    pulsed current electrodeposition, 296
    template-assisted synthesis, 295
Magnetic drug targeting (MDT) approaches, 326
Magnetic microparticles, 13
Magnetic nanoparticles (MNPs), 294
Magnetic resonance imaging (MRI)
  artifact imaging
    experiments, 308–310
    frequency of precession, 302–303
    k-space, 303
    magnifying glass effect, 304
    pulse sequences, 303
    spatial encoding, 303, 304
  artifact recognition algorithms
    EM algorithm, 311
    histogram, HASTE scan, 312, 313
    scatter plot, segmented volumes, 313
    segmentation, steel sphere, 314, 315
    segmented artifacts, 311, 312
    water-filled phantom scan, 314, 315
  artifact simulations
    magnetic flux density, 306
    magnetization vector, 305
    required parameters, 307
    for steel sphere, 307–308
  artifact tracking algorithms
    center of gravity, 316
    HASTE sequence, 317–319
    template stack slice, 315
  drug delivery nanorobots (see MRI-guided drug delivery nanorobots)
  magnetic propulsion, 317–319
  propulsion experiments, 320–321

Magnetic resonance navigation (MRN), 325
Magnetic steering, 245
Magnetosomes, 245
Magnetotactic bacteria (MTB), 15
Magnetotaxis system, 328
Magnifying glass effect, 304
Massively parallel positional assembly, diamondoid, 106
Mass transport system
  filling of carbon nanotube, 139
  inside nanotube, 144–145
    containers, 148
    evaporation and condensation of copper, 146
    impact of cooling speed, 146, 148
    self-soldering, 146, 148
    spot welding, attogram mass delivery, 146–147
  methods using nanotube
    electrostatic forces, 144
    evaporation mechanisms, 142–143
    mass delivery mechanisms, 141
    modes, 142
    thermal expansion, 140
  nanomanufacturing system, 138–139
  between nanotube
    internanotube, 149
    molecular dynamics simulation, 150–151
  nanotube-based building blocks, 139–140
Maxwell coil configuration, 286, 287
MC-1 magnetotactic bacterium, 326, 327
Mechanical nanomanipulation, 156
Mechanosensitive gated ion channel, 197
Mechanosynthesis, diamondoid
  albeit on silicon atoms, 105
  carbon placement tools, 103–104
  chemically active tooltip and insert handle, 102
  chemical vapor deposition, 102
  covalent chemical bonds, 101
  DCB6Ge dimer placement tool, 100–101
  2D patterns, 105
  hydrogen abstraction tools, 102–103
  hydrogen donation tools, 104
  materials, 101
  reaction sequences, 104
  types of tool, 102–103
Microbivores, 97
Microcapillaries, 217–218
Microfluidic chip
  DEP force, virus concentration, 173–175, 177–178
  experimental setup, 176–177
  fabrication of, 175–176
  photo-crosslinkable resin, 173
  photolithography, 175
  polyethylene glycol methacrylate resin, 175
  replica molding, 175
  schematic illustration, 171, 172
  single influenza virus manipulation
    chamber isolation, local polymerization, 178, 179
    deirect laser manipulation, 178
    and H292 cell contact, 178, 179
    virus transportation force, 178
  specific cell, single cell infection of, 171–172
  virus loading method, 172–173
Microgrippers, 218–219
Micromechanisms, 70
Microorganisms, locomtion of, 277
Micropropulsion, 78, 86
Microsatellites
  AAUSAT-II Cu-besat, 86
  CubeSat, 85–86
  function of, 84
  mass distribution, 84–85
  MOST, 87
NanoSail-D and O/OREOS, 87–88
  PRISMA mission, 87
  SwissCube-1 mission, 86
Microscaled objects, robot-tweezers, 226–227
Miniaturization in space robotics
  actuators, 83
  benefits, 76
  inertial navigation systems, 77
  Jet Propulsion Laboratory, 78
  MEMS and technology readiness levels, 79
  MEMS market volume, 77
  microsystems, 76
  MNT R&D per space robot class, 80–81
  mobile micro-robot, 78
  OBDH & GNC, 83
  power, 83
  selection criteria, 81–82
  sensor islands, 82–83
  spinning-in, 75
  structure, 83
  subsystem, 79
  total resources, 76
  vehicle launch, 76
MiniMag system, 289, 290, 292
Mitosis, 332
MIT SPHERES, 75
MM3A nanomanipulator, 33
Molecular positional fabriation, diamondoid. *See* Mechanosynthesis, diamondoid

Molecular spider, 376, 378
MOST, 87
Mount Everest of nanorobotics, 5
MRI-guided drug delivery nanorobots
  control approach, 260–262
  flagellum design, 244
  hydrodynamic wall effects, 245
  magnetic bead, 244
  modeling
    apparent weight, 253
    contact force, 253
    hydrodynamic drag force, 251–252
    levitation, 254–255
    magnetic force, 254
    optimal trajectory, 257–258
    resisting drag, 255–257
    state space representation, 258–259
    translational and rotational motions, 250
    Van der Waals and electrostatic forces, 253–254
  propulsion, 245
  simulations
    error on electrostatic force, 263–267
    error on magnetic force, 267–268
    parameters, 263
  state estimation, 262
  in vasculature, 246
    MRI constraints, 247–248
    physiological constraints, 248–250
Mycoplasma genitalium, 342
Myosin, 357

N
Nanites. *See* Nanorobotic system
Nanoactuator
  GCN4 peptide
    applications, 447–451
    leucine zipper, 438, 439
    mechanical force, 444–447
    peptide design and molecular dynamic studies, 439–440
    pH-dependent conformational change, 442–443
    wild-type structure and mutant, 440–445
  VPL
    $\alpha-$helix, 428–429
    coiled-coil system, 429–430
    influenza virus, 427–428
    membrane fusion, 426
    molecular dynamics simulations, 431–433
    optimal design, 433–438
    origin, 426
Nanobots. *See* Nanorobotic system
Nanobugs, 6
Nanocarriers, 58–59
Nanofactory Collaboration, 107–108
Nanofluid coreflood testing. *See* Coreflood testing
Nanohandling of biomaterials. *See* Biomaterials
Nanohand strategy, 119–121
Nanomachines, DNA
  conformational switching behavior, 359–361
  enzymatic actions
    DNA polymerases, 361–362
    ligase healing a single-stranded nick, 361
    restriction enzyme, 361, 362
  motors
    enzymatic actions, 363–366
    hybridization reactions, 367–372
  programmable, 372–377
Nanomanipulation system
  attocube system, 157
  automated nanomanipulation
    advantages, 161
    depth detection, 161–162
    four-point probe measurement, nanowires, 162–163
    visual tracking, 160–161
  Kleindiek system, 157
  robot-tweezers (see Robot-tweezers manipulation system)
  SmarAct system, 157
  teleoperated nanomanipulation
    device construction, 161
    nanomaterial characterization, 158–160
  tool strategy
    coulomb and viscous friction, 123
    lateral PSD signal, 121
    nanoparticle pushing model, 121–122
    nanorod pushing model, 122–123
  uncertainty
    AFM tip position error, 117–118
    instantaneous center of rotation, 117, 119
    nanoparticle pushing experiment, 117–118
    nanorod pushing, 118–119
  visual servoing, 163
  Zyvex system, 156–157
Nanomanipulators
  DCG system, 8

Nanomanipulators (*Cont.*)
definition, 5
MM3A, 33
nanopositioning, 6
requirements, 7
SPM, 7
STM, zenon atoms, 7
Nanomanufacturing system, 138–139
Nanomechanical cantilever (NMC) systems
controlled tip force, 39
laser-free AFM imaging
imaging ultrasoft samples, 35
plastic deformation, 35
PRC-400 self-sensing cantilever, 34–35
robust adaptive controller, 36–37
schematic representation, 34–35
setup, 34
nanofiber manipulation, 29–30
nanoobject manipulation, 30
nanorobotic manipulation, 32–33
nanoscale force tracking, 38–39
SPM
atomic force microscope, 32
generalized schematic representation, 30–31
scanning tunneling microscope, 31–32
Nanomedicine, 17–18
Nano-object manipulation
coulomb and viscous friction, 123
lateral PSD signal, 121
nanoparticle pushing model, 121–122
nanorod pushing model, 122–123
Nanopackaging
using biomaterials, 209–211
using cellulose fibrils, 212
using DNA nanowires, 211
Nanoparticle pushing
500nm pushing experiment, 129–130
NSC15/AIBS, 129
pushing velocity vs. mean pushing force, 129–130
simulation, 130–131
velocity of particle center, 130
Nanoparticle suspensions
A-Dots, 62
latex spheres, 61–62
polymer microspheres, 61–62
Nanorobotic manipulators (NRM). *See* Nanomanipulators
Nanorobotic system
characteristics, 5
definition, 3, 93
diamondoid (*see* Diamondoid nanorobotics)
fish-like nanocapsule, 21–22
history, 4
manipulation system (*see* Nanomanipulation system)
mass transport (see Mass transport system)
medical applications, 17–18
MRI-guided drug delivery (*see* MRI-guided drug delivery nanorobots)
multidisciplinary field, 5
nanocomponents, 5
PubMed database, 94
space applications, 19–20
subterranean oil reservoir applications, 20–21
swarms of (*see* Self-organized nanorobots)
types of
bacterial-based system, 14–16
bionanorobotics, 9–11
magnetically guided nanorobots, 11, 13–14
nanobugs, 6
nanomanipulators, 6–8
Nanorod pushing
angular velocity, 124
constraint condition, 129
coulomb and viscous friction, 125
equivalent resistance force, 127
experimental process, 131–132
numerical analysis, 132–134
static model, center of rotation, 123–124
surface resistance force, 126
velocity of AFM tip-particle push relationship, 128
NanoSail-D, 87–88
Nanosatellites. *See* Microsatellites
Nanoscale force tracking, 38–39
Nanotechnology, in space robotics. *See* Microsatellites
Nanotweezers, 218–219
Nanowires
AAO templates, 296
automated four-point probe measurement, 163
graphitic shells, 296, 297
hybrid CNT-based magnetic nanostructures, 296, 297
piezoresistivity characterization, silicon, 158
pulsed current electrodeposition, 296
template-assisted synthesis, 295
transfer procedure, MEMS device, 158–160
NMC systems. *See* Nanomechanical cantilever (NMC) systems
Noncontact manipulation, 170
Nonlinear model, 250

Nuclear magnetic moment
precession of, 302
relaxation trajectory of, 305
Nuclear magnetic resonance (NMR), 302–303
Nuclei spin, 302

O
OctoMag system, 289, 290
Off-axis field calculation, 286
O/OREOS, 87–88
Optical tweezers, 225
biomaterials, nanohandling of
applications, 214, 216
components, 214, 215
gradient force, 214
optical traps vs. simple spring, 214, 215
principles of, 212–213
local sensing, functional gel-microtool (see Functional gel-microtool)
single influenza virus nanomanipulation, 171–173, 178, 179
Osmotic pressure technique, 389

P
Passive agents, 52
Permanent magnets, 284
Piezoelectric gripper, 218
Ponctual, 394
Pore network, 60
Positional diamondoid molecular manufacture, 99–100
Programmable DNA nanomachines, 372–377
Programmable positional assembly, diamondoid, 105–106
Protein-based nanorobotic systems. *See* Bacterial-based nanorobotics
Protein-based nanoscale actuation
GCN4 peptide
applications, 447–451
leucine zipper, 438, 439
mechanical force, 444–447
peptide design and molecular dynamic studies, 439–440
pH-dependent conformational change, 442–443
wild-type structure and mutant, 440–445
VPL
$\alpha-$helix, 428–429
coiled-coil system, 429–430
influenza virus, 427–428
membrane fusion, 426
molecular dynamics simulations, 431–433
optimal design, 433–438
origin, 426

R
Reactive agents, 52–53
Red blood cell, robot-tweezers, 233–235
Resbots, 52–53
Reservoir nanoagents
active agents, 52
coreflood testing
outcomes, 64
particle-free, 65
program, 63
rock sample, 64
effects
Brownian motion effect, 57
low Reynolds number, 56
stickiness, 57
surface tension, 57–58
micro-nanotechnology applications in upstream E&P, 53
model, 58–59
nanoparticle suspensions
A-Dots, 62
latex spheres, 61–62
polymer microspheres, 61–62
nanotechnology efficiency index, 54–56
passive agents, 52
pore size characterization, 60–61
reactive agents, 52–53
requirements, 59–60
Resbots, 52–53
Respirocyte, 97
Robochips, 171
Robot-tweezers manipulation system
control module, 225–226
executive module, 225
mechanical properties of cells
deviation parameter, 233
myeloblasts with acute myeloid leukemia, 235–237
red blood cell, 233–235
microscaled objects, 226–227
optical stretching of cells
cell preparation and treatment, 227
cell stretching, 228–230
force calibration, 227–228
mechanical modeling, 230–232
with optical tweezer, 225
sensory module, 225–226
Robyspace, 75

Root mean square deviation (RMSD), VPL nanoactuator, 432, 433
Rover exploration system
characteristics of, 72
full-scale models of generations, 72–73
Lunar Roving Vehicles of Apollo program, 71
Rupture force, 392–393

S
Scanning electron microscopy (SEM)
description, 156
focused electron beams, 156
nanorobotic manipulation system (see Nanomanipulation system)
Scanning probe microscopy (SPM), NMC
atomic force microscope, 32
generalized schematic representation, 30–31
scanning tunneling microscope, 31–32
Self-assembly approach
DNA
atomic force microscope, 389–394
bond, 384
global approach, 387–389
hybridization, 394
local approach, 386–387
specificity analysis (see Specificity analysis)
nanorobots, 46–47
Self-docking mechanism, 345–346
Self-organized nanorobots
active self-assembly approach, 46–47
communication, 43
helicoidal propellers, 43
nanowire chemical sensors, 42
robotic artificial cells, 42
simulation, 44–46
surface markers, 42
tasks
decentralized approach, 43
global-local compilation problem, 44
shape construction, 44
Sensor islands, 82–83
Shear-thickening agents, 53
Shuttle Remote Manipulator System (SMRM), 73
Single cell phenomena, 192
SmarAct system, 157
Soft magnetic bodies
demagnetization factors, 279
ferromagnetically filled carbon nanotubes, 282
magnetic energy and torque, 281
magnetization angle, 280
susceptibility tensor, 279
Space robotics
applications
experimental system, 74–75
rover exploration system, 71–73
servicing system, 73–74
inertia forces, 88–89
micro/nanosatellites
AAUSAT-II Cu-besat, 86
CubeSat, 85–86
function of, 84
mass distribution, 84–85
MOST, 87
NanoSail-D and O/OREOS, 87–88
O/OREOS, 87–88
PRISMA mission, 87
SwissCube-1 mission, 86
miniaturization
actuators, 83
benefits, 76
inertial navigation systems, 77
Jet Propulsion Laboratory, 78
MEMS and technology readiness levels, 79
MEMS market volume, 77
microsystems, 76
MNT R&D per space robot class, 80–81
mobile micro-robot, 78
OBDH & GNC, 83
power, 83
selection criteria, 81–82
sensor islands, 82–83
spinning-in, 75
structure, 83
subsystem, 79
total resources, 76
vehicle launch, 76
spacesuit repairs, 88
Space Station Remote Manipulator System (SSMRM), 73
Spatial encoding principle, 303, 304
Special Purpose Dexterous Manipulator (SPDM), 73–74
Specificity analysis
algorithms, sequence generation of state, 397
dedicated sequence generation
algorithm, 399–400
Hamming function, 398
experimental analysis, 403
A/R curves, 402
latency time influence, 406

plateau phenomenon, 404
specificity, 404
velocity influence, 404–406
mismatch configurations, 397
theoretical analysis, 400–401
Spin-echo sequences, 303
Strand displacement, DNA, 367
Swarm of nanorobots. *See also* Self-organized nanorobots
ambient temperature detection, 343
$4F^2$ architecture, 342
malign cells, 341
nicotinamide dinucleotide, 343
self-docking mechanism, 345–346
swarm of agents, 342
Synthetic microscale medical robots, 325–326

T
Targeted molecular dynamics, VPL nanoactuator, 431
Teleoperated nanomanipulation
device construction, 161
nanomaterial characterization
AFM cantilevers, 158
electrical, 158
MEMS devices, 158–159
nanowire transfer procedure, 158–160
tensile testing, 158
Tethered cells, 418
Therapeutic magnetic microcarriers (TMMC), 325
Therapeutic self-propelled bacterial carriers, 326–328
Thermal gripper, 218
Tweezer cycling, 367–368

U
Uncertainty in nanomanipulation
AFM tip position error, 117–118
instantaneous center of rotation, 117, 119
nanoparticle pushing experiment, 117–118
nanorod pushing, 118–119
Unidirectional walker, 363
Upstream E&P, 53–54, 58

V
Viral protein linear (VPL) nanoactuator
$\alpha-$helix, 428–429
coiled-coil system, 429, 430
influenza virus, 427–428
membrane fusion, 426
molecular dynamics simulations, 431–433
optimal design
helicity and fraction, 436, 437
helix-breaker amino acid, 434
hydrogen bonds, 435
RMSD, 437
temperature effects, 435–436
wild type peptide, 434
origin, 426
Virtual tooling strategy
active probe control method, 116
nanohand strategy, 119–121
nano-object manipulation
coulomb and viscous friction, 123
lateral PSD signal, 121
nanoparticle pushing model, 121–122
nanorod pushing model, 122–123
nanoparticle pushing
500 nm pushing experiment, 130–131
NSC15/AIBS, 129
pushing velocity vs. mean pushing force, 129–130
simulation, 130–131
velocity of particle center, 130
nanorod pushing
angular velocity, 124
constraint condition, 129
coulomb and viscous friction, 125
equivalent resistance force, 127
experimental process, 131–132
numerical analysis, 132–134
static model, center of rotation, 123–124
surface resistance force, 126
velocity of AFM tip-particle push relationship, 128
uncertainty in nanomanipulation
AFM tip position error, 117–118
instantaneous center of rotation, 117, 119
nanoparticle pushing experiment, 117–118
nanorod pushing, 118–119
Vision-based contact detection method, 162
Visual molecular dynamics, VPL nanoactuator, 432, 433
Voltage-gated ion channel, 196, 197
VPL nanoactuator. *See* Viral protein linear (VPL) nanoactuator

W
Wide pH measurement gel-microtool, 186, 187